STRONG MICROWAVES IN PLASMAS

2006

Volume 2

Institute of Applied Physics
Nizhny Novgorod

RUSSIAN ACADEMY OF SCIENCES
INSTITUTE OF APPLIED PHYSICS

STRONG MICROWAVES IN PLASMAS

PROCEEDINGS
OF THE INTERNATIONAL WORKSHOP

Nizhny Novgorod,
25 July – 1 August 2005

Edited by
A.G. Litvak

In two volumes
Volume 2

Nizhny Novgorod – 2006

ISBN 5-8048-0038-8

CURRENT DRIVE AND PLASMA HEATING BY MICROWAVES IN NUCLEAR FUSION DEVICES

CONTROL OF MHD INSTABILITIES BY ECRH IN TEXTOR

E. Westerhof, A. Lazaros, A. Merkulov, F. C. Schüller, I. G. J. Classen, E. Farshi, J A. Hoekzema[1], *R. J. E. Jaspers, H. R. Koslowski*[1], *A. Krämer-Flecken*[1], *J. W. Oosterbeek*[1], *J. Scholten, O. Zimmermann*[1], *and the TEXTOR-team*[1]

Partners in the Trilateral Euregio Cluster:
FOM-Institute for Plasma Physics Rijnhuizen, Association EURATOM-FOM,
PO Box 1207, 3430 BE Nieuwegein, The Netherlands, www.rijnh.nl
[1] Forschungszentrum Jülich GmbH, Institut für Plasmaphysik,
Association EURATOM-FZJ, 52425 Jülich, Germany

The sawtooth period has been measured as a function of the EC deposition radius. The effects of current drive are identified by normalizing the response function for a discharge with ECCD to a similar discharge with pure heating. This has revealed the expected shortening of the sawtooth period when the co-ECCD is deposited just inside the $q = 1$, and lengthening of the period for deposition just outside $q = 1$.
The suppression of the $m = 2$, $n = 1$ tearing mode by localized ECRH has been studied in detail. For these studies, a reproducible 2/1 mode has been triggered by the TEXTOR DED. The suppression of this mode has been studied as a function of the deposition radius, for varying toriodal injection angles from co- to counter-ECCD, and for modulated ECRH with different phasing and duty cycles. The results show that under the conditions of the TEXTOR experiment the mode suppression is caused almost entirely by heating inside the island.

Introduction

The TEXTOR tokamak comes well equipped for studies of magneto-hydrodynamic (MHD) instabilities. Especially, the Dynamic Ergodic Divertor (DED) [1] is a flexible tool for the manipulation of the magnetic topology. It consists of 16 coils plus two compensation coils with helicity $q = 3$. It can be operated either in DC mode, or in AC mode at different frequencies up to 10 kHz. The individual coils can be powered in such a way as to produce a dominantly $m/n = 12/4$, $m/n = 6/2$, or $m/n = 3/1$ magnetic perturbation. The perturbations, generated in the 3/1 mode of operation, penetrate particularly deep into the plasma, and can be used for the controlled generation of tearing modes. In particular, a large $m = 2$, $n = 1$ side band perturbation is present, which above a certain threshold in the currents in the individual DED coils triggers an $m = 2$, $n = 1$ tearing mode that is locked to the perturbation field [2]. In addition, TEXTOR is equipped with a powerful electron cyclotron resonance heating (ECRH) system consisting of a 140 GHz, 800 kW, gyrotron with a pulse length of at least 3 s. The ECRH launcher is very flexible and is optimized towards localized power deposition: a focused beam is injected which has its waist near the plasma center with a diameter of about 1 cm. Apart from the standard diagnostics a number of advanced diagnostics are becoming routinely available on TEXTOR that will support such studies in the future. These include a high resolution burst TV Thomson scattering system and a 2D ECE-imaging system.

In this paper we describe the results of two sets of MHD experiments, in which ECRH has been used to control the MHD activity. The first set of experiments (published in Ref. [3]) concerns the control of sawtooth oscillations by electron cyclotron current drive (ECCD). Here a crucial point has been to separate the effect of the current drive from the unavoidable associated heating. This has been achieved by normalization of the sawtooth period response function in discharges with ECCD on a discharge with pure heating. The second set of experiments (published in Ref. [4]) describes the suppression of the $m = 2$, $n = 1$ tearing mode by localized ECRH/ECCD. In these experiments a reproducible 2/1 mode has been obtained by generating the mode with the help of the DED. As the mode is locked to the rotation of the DED this also provides a convenient phase reference in cases of modulated ECRH/ECCD.

Sawtooth control

Sawteeth occur when the central safety factor q_0 drops below one, and the sawtooth crash has been associated with a complete reconnection of the helical magnetic field on opposite sides of the $q = 1$ surface [5]. Porcelli et al. [6] have derived a sawtooth model in which the instability leading to the crash is triggered when the magnetic shear at $q = 1$ reaches a critical value [7]. This critical shear value depends on the plasma parameters like β and pressure gradient length inside and at the $q = 1$ surface. This suggest the possibility to control the sawtooth period by control of the evolution of the magnetic shear at $q = 1$. The most direct way to affect this shear evolution is by means of localized non-inductive current drive as with, for example, electron cyclotron waves. Experiments with ECRH and ECCD indeed show a strong influence on the sawtooth period (see e.g. [8, 9]). Modeling of the experiments on TCV with ECRH and ECCD has shown the importance of even relatively small, localized, non-inductive currents [10]. A well localized co-driven current just inside the $q = 1$ surface, would speed up the shear evolution following a sawtooth crash and, consequently, shorten the sawtooth period, whereas the same co-driven current just outside the $q = 1$ surface would slow down the shear evolution and lengthen the sawtooth period [3, 10]. The reverse of course applies for a counter-driven current.

Experiments have been performed to study the effects of ECCD and ECRH on sawteeth. The current of the target plasma was fixed at 350 kA, which corresponds to the edge value of $q_a = 4.4$. Electron temperature $T_e = 2$ keV and line averaged electron density $n_e = 2 \cdot 10^{19}$ m^{-3} were chosen to assure sufficient absorption of EC waves and providing considerable ECCD efficiency. The total plasma current, which is conserved inside the $q = 1$ surface, $I_{q=1} = 135$ kA corresponds to a $r_{q=1} = 0.3a$. To vary the ECRH/ECCD deposition a slow ramp down of the toroidal magnetic field has been applied during the ECRH/ECCD pulse. Two magnetic field ramp scenarios where used with a constant rate of 0.13 T/s. For the discharges with only EC heating and small launcher angles the magnetic field B_t was ramped down from 2.5 T to 2.1 T in three seconds, while

for the larger toroidal injection angles the magnetic field was ramped down from 2.4 T to 2.0 T. In this way for all injection angles the deposition position of ECCD was scanned from the center of the plasma to the mid radius, crossing the $q = 1$ position. The neutral beam injection (NBI) was kept on a low level of 300 kW for diagnostic purposes (CXRS). The Electron Cyclotron Emission (ECE) and Soft X-Ray (SXR) diagnostics were surveying the plasma for further sawtooth oscillation analysis.

One of the difficulties in the study of the influence of non-inductive current drive on sawteeth is to discriminate between the effect produced by the electron cyclotron current drive and a similar effect induced by the concurrent heating. To exclude the contribution of the heating to the change in the sawtooth period all discharges with ECCD have been compared with a reference discharge with only ECRH (see Fig. 1).

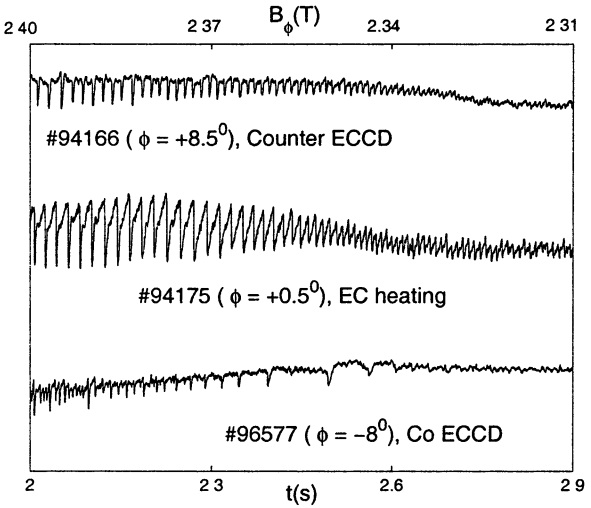

Fig. 1. Examples of ECE traces showing the behavior of sawteeth during magnetic field ramps for counter-ECCD, ECRH, and co-ECCD.

Figure 2 shows the sawtooth period normalized to the corresponding sawtooth period for the ECR heating case as a function of ECCD deposition position, $\rho_{dep} = r_{dep}/a$, for two discharges with a co-current drive. Both discharges have the same toroidal angle of the launcher mirror, $\phi = -8^\circ$ which results in a narrow ECCD deposition profile with Gaussian width of $\Delta r/r_{q=1} \approx 0.07$. The $q = 1$ surface is located around $\rho = 0.3$. One can see clear destabilization / stabilization for deposition inside / outside of $q = 1$, which is in agreement with model predictions [3]. More examples of co-ECCD with both smaller and larger toroidal injection angles showing similar results are given in Reference [3]. The results for a set of discharges with counter-drive are plotted

in Fig. 3. In this case the toroidal injection angles has been $\phi = +8.5^{\circ}$. With counter-drive the stabilization / destabilization is clearly seen to occur when the power is deposited inside / outside of $q = 1$. However, the $q = 1$ surface may well change position during the magnetic field ramp, which can possibly explain the relative shift towards the plasma center of the whole curve in Fig. 3.

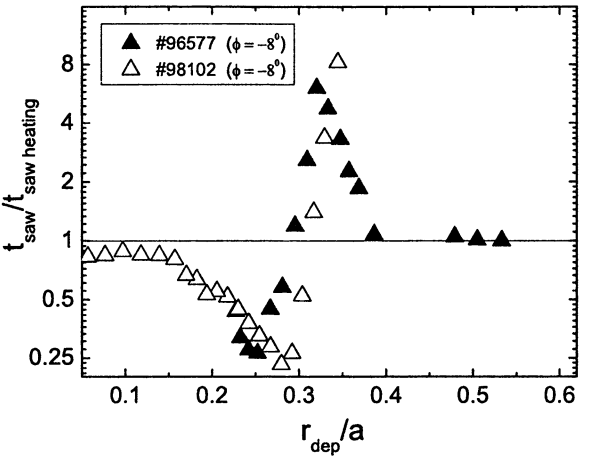

Fig. 2. Experimental observation of the sawtooth period in the presence of co-ECCD, normalized to the sawtooth period with ECRH.

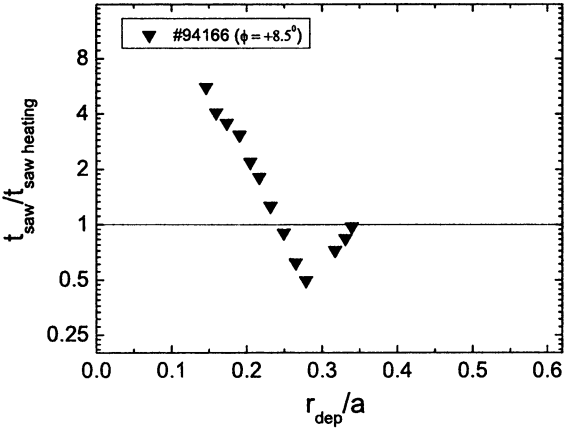

Fig. 3. Experimental observation of the sawtooth period in the presence of counter-ECCD, normalized to the sawtooth period with ECRH.

Tearing mode control

Localized heating or current drive can affect the magnetic island of the tearing mode in different ways. Firstly, it effects the island growth through heating or current drive inside the island: heating or co-current drive near the O-point of an island suppresses the island, whereas heating or co-current drive near the X-point has the opposite effect [11]. Secondly, it affects the island through changes in the equilibrium temperature and current density profile: these profile changes then lead to corresponding changes in the tearing mode stability parameter Δ' [12]. The first effect may benefit from modulated application of the ECRH in order to avoid power deposition near the X-point, while the second should be independent of the phase in which the power is applied. Which effect is dominant in a particular experiment depends on experimental conditions.

The experiments on tearing mode control [4, 13] have been carried out for fixed plasma conditions with a toroidal field of $B_T = 2.25$ T, plasma current $I_p = 300$ kA, and line averaged density $n_e = 2.0 \cdot 10^{19}$ m^{-3}. Through most of the discharge neutral beam injection (NBI) is applied at a power of 300 kW for diagnostic purposes. The DED is applied in its 3/1 mode at +1 kHz AC (implying toroidal rotation of the mode counter to the plasma current and poloidal rotation in the electron diamagnetic drift direction) and the amplitude of the current in the individual coils is ramped up to 2.0 kA. Under these conditions the threshold for the triggering of the $m = 2$, $n = 1$ tearing mode is at a DED current amplitude of about 1.6 kA. During the plateau phase of the DED current an ECRH pulse is applied and its effect on the 2/1 tearing mode is studied. By changing the vertical injection of the ECRH beam the radial location of the power deposition has been varied. Variation of the toroidal injection angle has allowed to vary between co- and counter-current drive as well as pure heating. Since the mode is locked to the DED perturbations, a DED coil current provides a conveniently stable reference signal for a phase locked modulation of the ECRH power. For these high frequencies, modulation is only possible through variation of the beam voltage, which implies a modulation between two power levels (high-low). Both duty cycle (the relative length of the high power phase) and phase (the start time of the high power phase relative to the DED current seen as a sin-wave) have been varied to study the effectiveness of modulated ECRH.

A relative measure of the size of 2/1 magnetic island is obtained from the 1 kHz oscillations observed on the electron cyclotron emission (ECE) at 141 GHz which originates from close to the $q = 2$ surface on the high field side of the tokamak. The ratio of the amplitude of these oscillations during the ECRH pulse over those during the foregoing DED plateau phase, $\tilde{T}_{\mathrm{ECRH}} / \tilde{T}_{\mathrm{DED}}$, forms a good measure of the suppression ratio of the 2/1 tearing mode by ECRH. These estimates for the suppression of the magnetic island could be confirmed by other diagnostics [13].

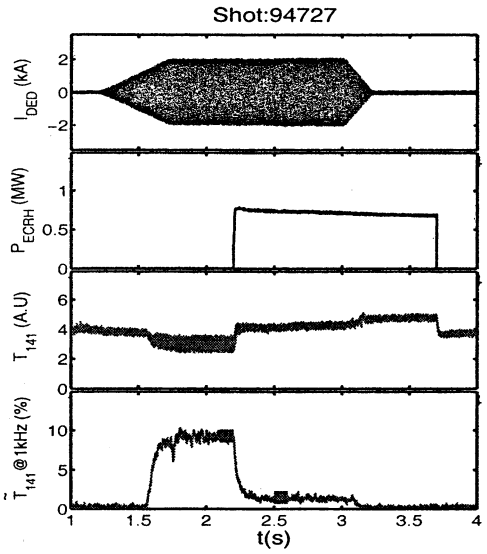

Fig. 4. The discharge scenario. First, the current (1 kHz AC) in the DED coils is ramped to 2 kA (top panel). Next, ECRH is applied (second panel). The third panel shows the 141 GHz EC emission, and the final panel the amplitude of its 1 kHz oscillations. These are a measure for the size of the 2/1 magnetic island. The ratio of the oscillation amplitudes during the boxed time intervals defines the suppression ratio $\tilde{T}_{ECRH} / \tilde{T}_{DED}$.

In Figure 4 we show the results from a typical discharge in which the ECRH power has been deposited very close to the $q = 2$ surface. The figure shows from top to bottom, the current in one of the DED coils, I_{DED}, the ECRH power, P_{ECRH}, the ECE intensity at 141 GHz, T_{141}, and the amplitude of the 1 kHz oscillations in the latter signal, $\tilde{T}_{141}$. The blue bars on $\tilde{T}_{141}$ indicate the timeframes over which the oscillation amplitudes before and during the ECRH pulse are averaged in order to obtain the suppression ratio of the 2/1 tearing mode. In this particular case, the magnetic island is almost complete suppressed and this method gives a suppression ratio of 0.10. The island is completely suppressed after the DED is switched-off. The suppression ratio is found to depend very strongly on the precise location of the power deposition. In the experiments, this location has been varied by changing the vertical injection angle of the ECRH beam. Figure 5 shows the results of two such radial deposition scans for 800 kW of injected power: in one case a toroidal injection angle of $-5°$ has been used for co-ECCD, while in the other case a toroidal angle of $+0.5°$ has been used resulting in almost pure heating. Also indicated in the Figure are the full width of the magnetic island before application of ECRH ($w/a \approx 0.13$) and the width of the ECRH deposition regions: $\Delta r_{dep}/a = 0.03$, and 0.02 (FWHM) for co-ECCD and ECRH, respectively. Clearly, the strongest suppression is

obtained when the power is deposited at the center of the magnetic island. Co-ECCD is seen to be only slightly more effective for mode stabilization than pure heating, although the largest difference between the two profiles seems to stem from the broader deposition profile in the case of co-ECCD giving rise to a broader range of deposition radii over which the mode is affected. In further study the effectiveness of current drive, we have performed a scan in toroidal injection angle ϕ thus varying the EC driven current and current density. This scan has been performed at an ECRH power of 200 kW. At this power, the mode is only partly suppressed, which should make any effect of the current drive on the suppression ratio better visible. Figure 6 shows the suppression ratios as a function of ϕ. Again the effect of the current drive is seen to be small, confirming that the dominant source for the suppression of the 2/1 magnetic island comes from heating. Calculations for these parameters predict a maximum

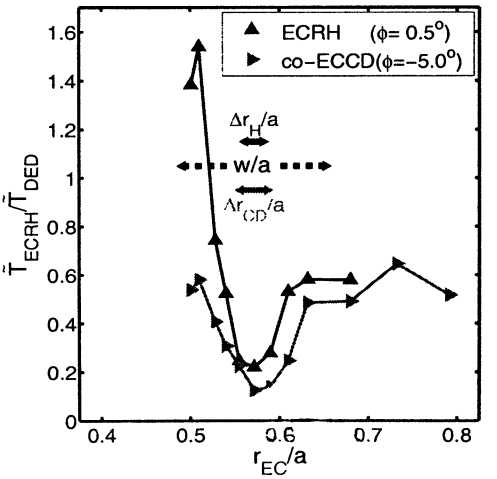

Fig. 5. The suppression ratio as a function of the 800 kW EC deposition radius. The lower curve corresponds to co-ECCD (ϕ = $-5°$), the upper to ECRH (+0.5°). The dashed black line indicates the full island size, and the two full lines the widths (FWHM) of the ECRH and co-ECCD deposition profiles.

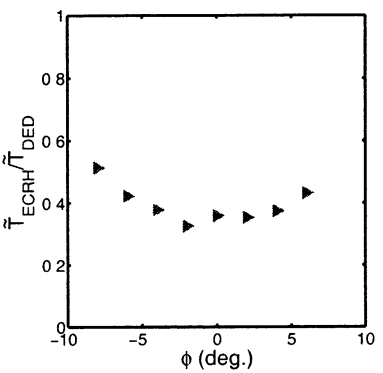

Fig. 6. The suppression ratio as function of toroidal injection angle ϕ. The ECRH power in this case is 200 kW.

driven current density of the order of $\pm 2 \cdot 10^4$ A/m^2, which is achieved at an angle -6° or $+4^\circ$ for co- or counter-drive, respectively. This is indeed relatively small compared to the current density at the $q = 2$ surface, which is estimated to be $6.5 \cdot 10^5$ A/m^2.

Previously, we have shown through the application of modulated ECRH that power deposited near the O-point of the magnetic island is more efficient for stabilization than power deposited near the X-point: in a scan of the ECRH high power phase relative to the timing of the passage of the O-point of the magnetic island through the ECRH power deposition region, the strongest mode suppression has been observed when the power is deposited at the O-point [13]. These results were obtained with modulation between a high power of 780 kW and a low power of 170 kW at a duty cycle of 50%. To further study the benefits of power modulation, we have performed a scan in duty cycle while keeping the centre of the high power phase coincident with the passage of the O-point. In this case, the power has been modulated between 400 and 70 kW. The results are shown in Fig. 7, where the 0% and 100% duty cycle points indicate the suppression ratios obtained for the injection of 70 kW and 400 kW CW, respectively. A minimum is obtained at a duty cycle of 70%. The additional power that is added beyond this point does no longer help to stabilize the mode and even leads to a small increase in its amplitude again. The dashed curve in this figure corresponds to the suppression ratio that is obtained with 200 kW CW. This corresponds to the same averaged power level as the 40% duty cycle point.

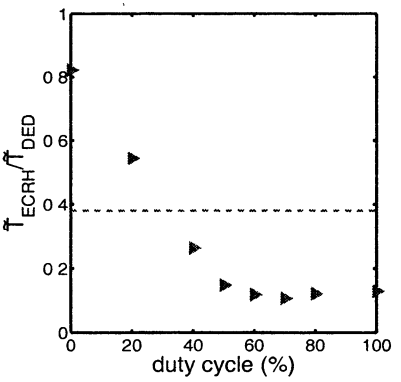

Fig. 7. The figure shows the suppression ratio as a function of the duty cycle. The duty cycle gives the length of the 400 kW high power phase which is centered at the O-point of the magnetic island. The dashed line indicates the suppression ratio for a 200 kW CW pulse.

In conclusion, the 2/1 tearing mode triggered by the DED at TEXTOR has been suppressed by properly localized ECRH. Because the mode suppression is observed to be relatively insensitive to the driven current or toroidal injection angle, heating must be responsible for the main effect. In addition, a clear benefit of power modulation is observed. This indicates that direct heating of the magnetic island and the consequent decrease of the resistivity at the O-point, rather than changes in the local temperature and current density profiles, is the dominant mechanism responsible for the suppression of the 2/1 magnetic island.

Summary and outlook

The ECRH system on TEXTOR has been used effectively for the study of two MHD instabilities. In the case of the central sawtooth instability the effect of localized current drive near the $q = 1$ surface could be well discriminated in these experiments from the effect of the concurrent heating. The theoretically predicted effects of the localized non-inductive current drive on the sawtooth period have been firmly established in these experiments. In future experiments the control of the power deposition relative to the $q = 1$ radius should be performed by control of the vertical launcher angle rather than by changes in the toroidal magnetic field. This will be possible even during an ECRH pulse with the new ECRH launcher recently installed on TEXTOR.

It has been shown that the $m = 2$, $n = 1$ tearing mode, which is generated by the dynamic ergodic divertor, can be almost completely suppressed by properly localized ECRH at the $q = 2$ surface. Heating inside the magnetic island of the mode has been shown to be the main cause of the stabilization. Further experiments will try to access regimes in which the non-inductive current drive can play a dominant role in the mode stabilization. Future experiments are being planned in which the launcher steering and gyrotron operation during tearing mode suppression experiments will be performed under feedback control.

Acknowledgement

This work, supported by the European Communities under the contract of Association between EURATOM/FOM, was carried out within the framework of the European Fusion Programme. The views and opinions expressed herein do not necessarily reflect those of the European Commission.

References

1 *Finken K.H* (Ed.). Special Issue. Dynamic Ergodic Divertor, Fusion Eng. Design **37** (1997) 335.
2 *Koslowski H R , et al ,* 31st EPS Conf. Plasma Phys., London, 28 June – 2 July 2004, ECA, Vol. **28G**, P-1.124.
3 *Merkulov A , et al ,* Sawtooth period control by localized non-inductive current drive, submitted to Nucl Fusion (2005).
4. *Westerhof E , et al.,* 32nd EPS Conf. Plasma Phys., Taragona, 27 June – 1 July 2005, Vol. **29C**, P-4.071
5. *Kadomtsev B ,* Sov. J Plasma Phys. **1** (1975) 389.
6. *Porcelli F , et al ,* Plasma Phys Control Fusion **38** (1996) 2163.
7. *Sauter O ,* in Theory of Fusion Plasmas (1998) 403.
8 *Henderson M , et al ,* Fusion Eng Design **53** (2001) 241.
9. *Westerhof E , et al ,* Nucl Fusion **43** (2003) 1371.
10 *Angioni C , et al ,* Nucl. Fusion **43** (2002) 455.
11 *Yoshioka Y , et al ,* Nucl Fus. **24** (1984) 565; Zohm H , Phys. Plasmas **4** (1997) 3433.
12. *Westerhof E ,* Nucl Fus. **27** (1987) 1929, and **30** (1990) 1143.
13 *Farshi E., et al.,* 31st EPS Conf Plasma Phys., London, 28 June – 2 July 2004, ECA, Vol **28G**, P-1.122.

HIGH POWER INJECTION AND STEADY STATE ECRH OPERATION IN LHD

H. Igami, T. Notake, Y. Yoshimura, T. Shimozuma, S. Kubo, K. Ohkubo, S. Inagaki and LHD Experimental Group

National Institute for Fusion Science, Toki, Japan

ECRH system for LHD has been improved with each experimental campaign. Recent upgrading of the high power ECRH system has achieved possibility to inject the power more than 2MW simultaneously into LHD with optimized injection condition and contributed to extend the plasma confinement database for helical systems. Formation of two kinds of improved core confinements during centrally focused high power ECRH into plasmas sustained by Co or CNTR NBI is quoted as an important issue of high power ECRH experiment. The internal structures of thermal diffusion in such plasmas have been investigated by using MECH method. On the other hand, long pulse or CW steady state operation is another main objects of LHD. One 84 GHz 200 kW CW gyrotron is installed for CW experiment. In the 8th experimental campaign, long pulse discharge over one hour was achieved. The CW gyrotron was stably operated at MOU output power of 160 kW and the input power to the plasma was about 110 kW. During the discharge, gas feed was controlled manually by mass flow controller and the central electron temperature and density were kept more than 1 keV and $1.5 \cdot 10^{18}$ /m^3.

1. Introduction

Electron cyclotron resonance heating (ECRH) is a powerful tool in magnetic fusion experiment. Well-controlled and focused microwave beam injection allows localized heating with high power density and has been expected as a dominant scenario to control the electron temperature and current profiles for the improved plasma confinement and suppression of some magneto-hydrodynamic (MHD) instabilities.

In the Large Helical Device (LHD), ECRH is used as a method of plasma initiation and electron heating. ECRH system has been improved with each experimental campaign. Eight sets of gyrotron and the transmission line for short pulse (~1 s) high power injection were operated reliably and stably throughout the last 8th experimental campaign. The maximum possible simultaneous injection power exceeded 2 MW. Well-focused microwave beam can be injected with the adjusted angle and polarization in accordance with a variety of target plasma conditions. In addition one CW gyrotron is installed and shares a transmission line with one of above transmission lines.

Several kinds of ECRH experiments have been performed with using the flexibility of this ECRH system. Formation of two kinds of improved core confinement during centrally focused high power ECRH into plasmas sustained by Co or CNTR NBI is and important topic of high power ECRH experiment. Electron heat transport characteristics of these core plasmas are investigated with using modulated ECRH (MECH). The long pulse discharge experiment

with using the CW gyrotron is another important topic. In this paper, we explain the recent state of ECRH system in the last 8th experimental campaign in section 2, then, introduce the recent topics on high power experiments in section 3 and long pulse experiments in section 4. In section 5 the summary is devoted.

2. Recent state of ECRH system for LHD

In LHD, ECRH system consists of four 168 GHz (500 kW 1 s TOSHIBA), two 84 GHz (800 kW 3 s GYCOM), two 82.7 GHz (500 kW 2 s GYCOM) gyrotrons, transmission lines and quasi-optical antennas for high power injection experiments. In addition, one 84 GHz (200 kW 1000 s GYCOM) gyrotron is installed for CW experiment (see Fig. 1).

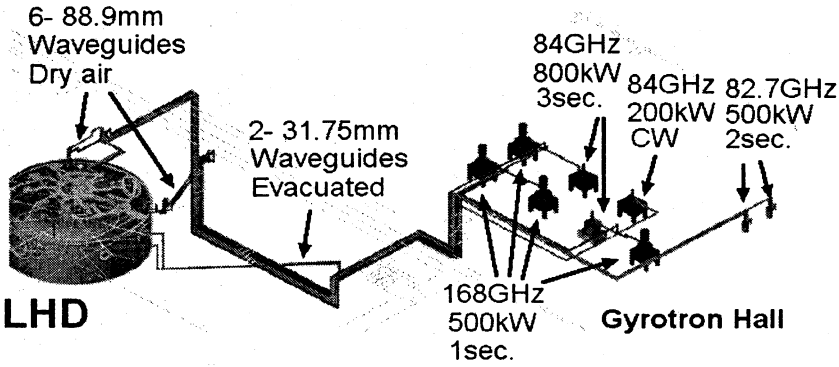

Fig. 1. ECRH system for LHD (2004)

These transmission lines have corrugated waveguides with some quasi-optical components. Miter bend type polarizers are installed in all of the transmission lines. For two of 168 GHz gyrotrons and two 82.7 GHz gyrotrons, 88.9 mm diameter non-evacuated waveguides are used and quasi-optical antennas are installed at two top ports of the LHD. These antennas can focus the beams on the equatorial plane of vertically long plasma poloidal cross-section. For the rest two 168 GHz gyrotrons, 88.9 mm diameter non-evacuated corrugated waveguides are also used and the quasi-optical antennas are installed in a horizontal port. For two 800 kW 84 GHz gyrotrons, 31.75 mm diameter evacuated waveguides are used and the quasi-optical antennas are installed at a bottom port. These antennas can focus the beams on any position of the equatorial plane of the plasma poloidal cross-section and have a wide range of scanning in the toroidal direction. The transmission line for 84 GHz CW gyrotron shares the waveguide section with one of the transmission lines for 800 kW 84 GHz gyrotrons. Single-disk windows of boron nitride, silicon nitride and diamond are used for the microwave beam injection window.

High voltage power supply systems operate these different types of gyrotrons, diode (82.7 GHz), diode CPD (84 GHz), triode CPD (168 GHz), and diode CPD CW (84 GHz CW). All of the systems equip the capability of voltage modulation for MECH. For 84 GHz CW gyrotron, a new power supply system was prepared before the 7th experimental campaign, in which the body power supply has voltage feedback control to keep the body voltage constant.

In the 8th experimental campaign, eight sets of gyrotrons and transmission line for high power injection experiments generally had been operated all throughout the campaign. The maximum possible simultaneous injection power exceeded 2 MW. And a long pulse discharge over an hour was achieved with 84 GHz CW gyrotron due to the improvement of waveguide evacuation and heat removal.

3. Results of high power injection experiment

In LHD, two types of improved core confinement have been observed depending on the direction of tangentially injected neutral beam. One shows a transition phenomena to the high electron temperature state and has a clear electron heat transport barrier (e-ITB) in counter (CNTR) neutral beam injection (NBI) plasma. Another has no clear transition and no ECRH power threshold, but shows a broad high temperature profiles with a moderate temperature gradient, which indicates the improved core confinement with additional ECRH in Co NBI plasma. Here, the CNTR direction is defined so that the NBI driven current decreases the poloidal magnetic field. In the experiments, target plasmas were produced and sustained by CNTR/Co NBI. 82.7 GHz and 84 GHz ECRH was superposed during the NBI pulse. The external perturbation methods, such as changing additional ECRH power, changing density, pellet injection were used to investigate the transition condition. Modulated ECRH power injection (MECH) of 168 GHz with 50% duty was used to investigate heat transport via heat pulse propagation.

Figure 2 shows the time evolutions of electron temperature during the additional centrally focused ECRH injected to CNTR NBI plasmas. Once the additional ECRH power exceeds a threshold level, an e-ITB and high electron temperature (T_e) state is realized around the center. This kind of transition phenomena to (from) the high-T_e state (T_e bifurcation) is induced by various kinds of external perturbations, such as additional ECRH, a little change of density, pellet injection and so on. T_e decay around the center after ECRH power off timing is slower than at the periphery and Co NBI plasma case, which is shown the next. Calculation results tell that above the threshold ECRH power, a positive electric field is produced around the core region, leading to the reduction of the electron heat diffusivity χ_e. On the other hand, Figure 3 shows the time evolutions of electron temperature during the additional centrally focused ECRH injected to Co NBI plasmas. However, calculation results tell that the electron

root (positive radial electric field) was realized over wide radial range for the cases of Co NBI target plasma.

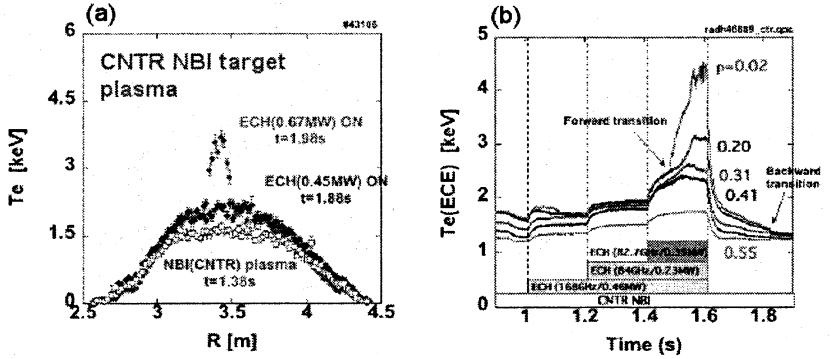

Fig. 2. Time evolution of the electron temperature profile obtained by Thomson scattering measurement during additional ECRH into the plasma sustained by CNTR NBI (*a*). Time traces of ECE signals during the step-like additional ECRH into a CNTR NBI plasma. Once the additional ECRH power exceeds the threshold level, temperatures at the center channels increase (Ref. 1) (*b*).

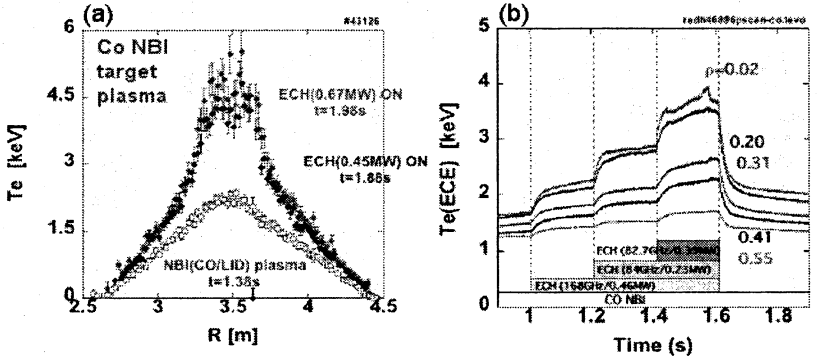

Fig. 3. Time evolution of the temperature profile obtained by Thomson scattering measurement during additional ECRH into the plasma sustained by Co NBI (*a*). Time traces of ECE signals during the step-like additional ECRH into a CNTR NBI plasma. No clear transition can be seen (Ref. 1) (*b*).

It has become clear that the difference of high T_e profile caused by just the direction of NBI driven current. When the direction of the external magnetic field is inverted in LHD, the definition of Co and CNTR for each NBI line is also inverted. e-ITB formation is observed also in the case of CNTR NBI defined in the inverted magnetic field configuration.

Microwave beam of 168 GHz was injected in the central region with 100% power modulation of 35 GHz to investigate heat transport via heat pulse propagation. In Figure 4, *a*, the time lags of modulated ECE signals at each point of

the normalized minor radius are plotted for the reference CNTR plasmas with additional ECRH cases of 0.45 MW and 0.85 MW. MECH power deposition profile calculated by a ray-tracing code is also plotted in the Figure. In Figure 4, *b*, similar plots of 0.45 MW ECRH to the reference Co NBI plasma are shown.

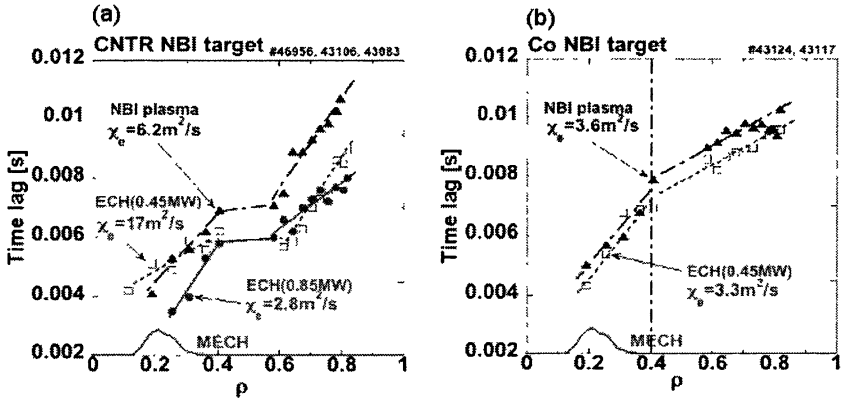

Fig. 4. Time lag of ECE signals from MECH plotted versus normalized minor radius for the case of CNTR NBI sustained plasma (*a*), Co NBI sustained plasma (*b*). MECH power deposition profile calculated by a ray-tracing code is also plotted (Ref. 1).

The electron heat diffusivity χ_e was evaluated from the relation $= V^2/4\pi f_{mod}$, assuming a constant value of χ_e and the slab model within $\rho < 0.4$, where V is a propagation velocity of the heat pulse that is calculated from the ration of propagation distance and the time lag. The modulation frequency of MECH is denoted by f_{mod}. For CNTR NBI case, χ_e increased as the additional ECRH power of 0.45 MW, however decreased once the additional ECRH power exceeded the threshold level and e-ITB is formed, 0.85 MW in this case. On the contrary, χ_e was not changed so much by additional ECRH. The confinement was not degraded even with additional ECRH power injection. The heat diffusivity normalized by the gyro-Bohm scaling $Te^{3/2}/B^2$ was reduced from 8.0 to 3.8 $m^2 \cdot s^{-1} \cdot keV^{-3/2} \cdot T^2$ with the power increase by additional ECRH, which means a kind of improved confinement except an anormalas transport part.

There is a difference in the direction of NBI driven currents between Co and CNTR directions, that is, a profile difference of the rotational transform $\iota/2\pi$. Figure 5 shows typical electron temperature profiles with calculated rotational transform profiles for CNTR and Co NBI sustained plasmas. The CNTR NBI driven current reduces the rotation transform in the core region from that for vacuum magnetic field and $\iota/2\pi = 0.5$ rational surface appears around $\rho = 0.5$. The flattening of time lag from $\rho = 0.44$ to 0.55 in Fig. 4, *a* suggests the existence of $m/n = 2/1$ magnetic island where the quick radial propagation can be driven by the fast parallel heat transport in the separatrix. A lower and flattened T_e profile can be seen below the ECRH threshold power. It ex-

tends to $\iota/2\pi = 0.5$ position. While Co NBI sustained plasmas does not have the $\iota/2\pi = 0.5$ rational surface, have big central temperature rise by additional ECRH and no threshold power exists.

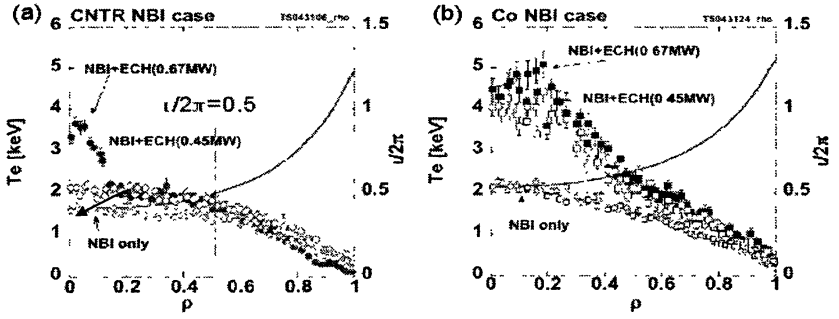

Fig. 5. Electron temperature profiles obtained by Thomson scattering measurement and calculated $\iota/2\pi$ profiles for NBI only, NBI + 0.45 MW ECRH, and NBI + 0.67 MW ECRH cases. CNTR NBI case (*a*). Co NBI case (*b*) (Ref. 1).

To clarify the effect of existence of m/n = 2/1 natural island on the high-T_e transition, the cancellation of the magnetic field was superposed by the external perturbation coils. The effect of the island cancellation field in the CNTR NBI + + ECRH plasma was investigated.

Figure 6 shows the cases without and with island cancellation. Electron temperatures increased more rapidly when the m/n = 2/1 natural island existed as shown in Fig. 6, *a*. The existence of m/n = 2/1 island or low order rational surface may facilities the transition to the high-T_e state and the formation of the e-ITB.

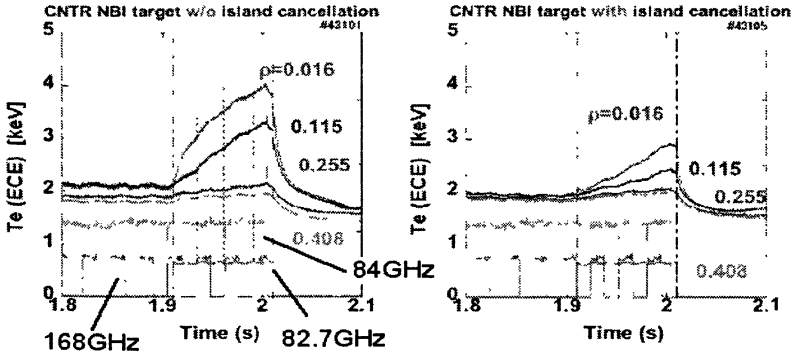

Fig. 6. Comparison of time evolutions of ECE signals in CNTR NBI + additional ECRH plasma: the case without island cancellation (*a*), the case with island cancellation (*b*), by the external perturbation coils. Timing of the additional ECRH is also shown in these Figures (Ref. 1).

Relationships between the shift of the rational surface and the change of the e-ITB structure were investigated with varying the NBI driven current in the 8th experimental campaign. As shown in Fig. 7, the driven current had unfortunately less variation to be able to observe a meaningful change of the structure. Variation of the T_e profile of Co NBI plasmas for different additional heating position was also investigated. Additional heating point was shifted for Co NBI target plasma shot by shot. The change of the structure was low. Whether it is due to the poorness of the confinement or the insufficient heating power density, the reason has not been clarified yet.

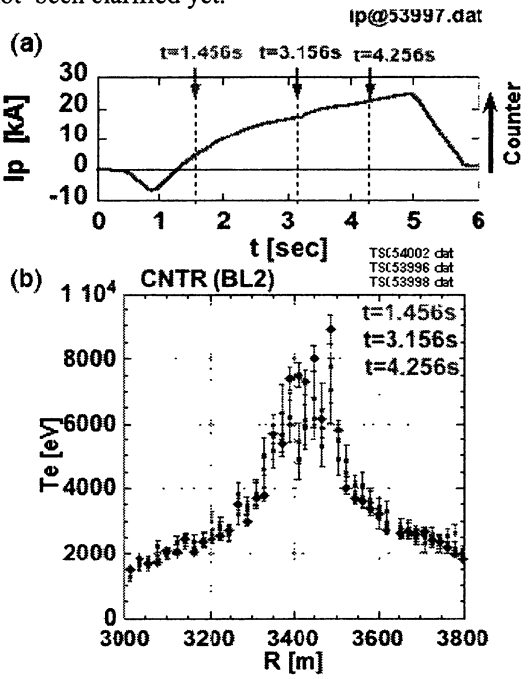

Fig. 7. Time evolution of the plasma current (*a*). Electron temperature profiles obtained by Thomson scattering measurement at t = 1.456, 3.156 and 4.256 s (*b*).

In conclusion, several transition phenomena were observed in CNTR NBI and ECRH plasmas by external perturbation methods. Heat transport study in high-T_e plasmas with and without e-ITB was performed by using heat pulse propagation excited by MECH. In CNTR NBI plasmas, the heat diffusivity within $\rho > 0.4$ once increased with the additional ECRH power, then it decreased above the threshold ECRH power. While such change of the heat diffusivity was not observed in CO NBI plasmas. However, considering the additional ECRH power, the confinement is not degraded even with additional ECRH. The existence of m/n = 2/1 island or low order rational surface may facilities the transition to the high-T_e state and the formation of the e-ITB.

4. Steady state ECRH plasma sustainment over an hour

With using 84 GHz CW gyrotron, long pulse discharge experiments have been demonstrated since the 7th experiment campaign (2004). In that experimental campaign, 75 kW power injection (100 kW at MOU output) was performed and 756 s discharge was demonstrated. In the discharge, the electron density was $2.4 \cdot 10^{17} m^{-3}$ and the electron temperature was 240 eV. The discharge was terminated due to the increase of pressure in the waveguide. Temperatures all over the transmission line were much increased up to 100 degrees by transmission loss.

Components in the transmission line were seriously damaged by heat and leaked microwave. The aluminum multi-hole corrugated waveguide of high conductance pump-out tee was deformed by thermal stress. The ceramic DC break had a clack, which led to vacuum leak and the vacuum seal of helico flex was damaged to lead leak. The resin spacer placed around the DC break was also damaged by leaked microwave. These damaged components made by GA are for pulse transmission.

To improve the evacuation, we increased the pumping port from one to nine and installed new type of water-cooling pump out tees with 1mm gap in each port. The damaged ceramic DC break was replaced by new one made of aluminum with anodized aluminum film (50 μm) on the surface. The resistance of new DC break is more than 1 MΩ at 250 V. Figure 8 shows a comparison between the 7th and the 8th experimental campaign about the pressures at each point of the transmission line. Out gassing rate decreased. The saturation pressure levels after long pulse operation decreased shot by shot.

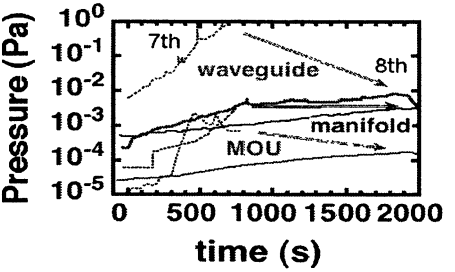

Fig. 8. Time evolutions of the pressure at each point of the transmission line. The results in the 7th and the 8th experimental campaign are plotted together for comparison (Ref. 2).

The enforcement of waveguide cooling was also done. Almost all over the transmission line was covered with water-cooling jacket.

In the 7th campaign, the output power could not achieve the specific value of 200 kW but 100 kW at MOU and only 72 kW was injected to the LHD after the transmission. A GYCOM designed mode filter was installed between MOU and the dummy load to absorb the reflected power from the dummy load or the transmission line. A pair of mode converters from HE11 mode to focused Gaussian beam is equipped on the opposite side of the wide gap in this mode filter.

The loss of HE11 mode through this mode filter is about 0.5% and the losses of higher modes are greater than 90%. After the installation, 160 kW at the MOU output was obtained. In the case of 160 kW at the MOU output, the available injection power was about 110 kW, which was estimated from the measurement at the dummy load near LHD.

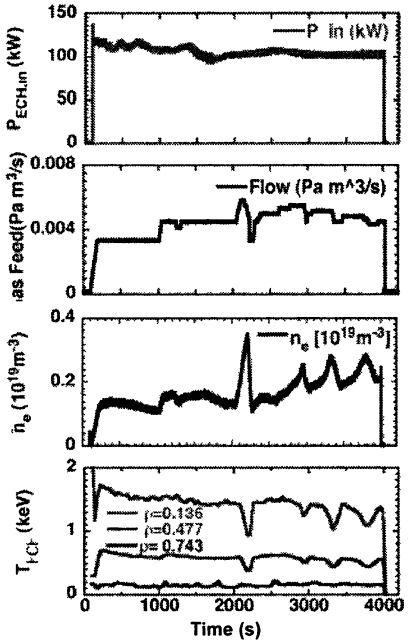

Fig. 9. 3900 s discharge waveforms. Injection power (top row), gas feed (second row), line averaged electron density at the center code (third row), electron temperature at r = 0.136, 0.477, 0.743 measured by ECE (bottom row), here ris the normalized miner radious (Ref. 2).

Pilot short pulse experiment was done to search the optimum magnetic field configuration and microwave injection condition from the corrugated waveguide horn antenna for CW experiments with using the other gyrotron, which shares the transmission line with the CW gyrotron before the long pulse experiment. Magnetic field of 1.48 T at the magnetic axis of 3.6 m was selected for CW operation. This magnetic configuration corresponds to the second harmonic heating. Figure 9 shows the waveforms of the longest continuous power injection discharge. Maximum available power was 110 kW in this shot. The experience of the previous long pulse discharge in the 7th experimental campaign told that the gas feed control is critical to keep as high density as for the power level of 100 kW without radiation collapse in LHD. The gas feeding rate was finely adjusted manually by mass flow controller during the discharge. The beginning 2000 s was devoted to keep the constant density at $1.5 \cdot 10^{18}$ m^{-3} that is about a half of the critical density for the available power. The electron temperature measured by ECE was kept more than 1.5 keV at the center. Although ECE is still grey in this regime of low density, available Thomson scattering

data in the beginning of this shot supported the ECE measurement. After 2000 s, we increased the gas feeding rate several times in attempting to raise the density higher as shown in Fig. 9, *b*. Gas feeding rate was first increased from 2050 s to 2100 s then fixed at 0.006 Pa · m^3/s to 2300 s, however the density kept increasing after the gas feeding rate was fixed, indicating that it exceeded the critical level for radiation collapse. Similar trials were performed during the same discharge. The fixed gas feeding rate at each trial was decreased however, the density increased higher and higher at each trial. The discharge was terminated manually by stopping microwave injection due to just the limitation of the data acquisition, not for any hardware troubles.

During the 3900 s (over one hour) operation, the temperature and the pressure rise in the transmission line almost saturated within the safety level due to the enforcement of the cooling and evacuation systems, except for non-cooled waveguide horn antenna as shown in Fig. 10.

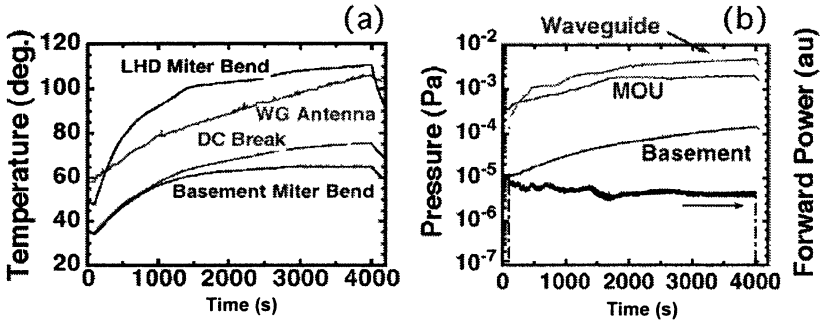

Fig. 10. Time evolutions of temperature at each point on the transmission line (*a*) and time evolutions of pressure at each ministering point in the transmission line during the 3900 s discharge (*b*).

The CW gyrotron itself was stably operated for 3900 s. As shown in Fig. 11, *a*, power supplies for the cathode and the body voltages were well regulated. The collector current was maintained at 9 to 10 A by manually controlling of the heater power as shown Fig. 11, *b*. Temperature differences at each cooling channel of the CW gyrotron components kept saturation levels as shown in Fig. 11, *c*. The waveforms of the power monitors set at the second and the last miter bend are shown in Fig. 11, *d*. The gyrotron oscillation and the modes in the transmission line were stabilized after 1500 s.

In conclusion, the installation of the mode filter into the transmission line, the CW gyrotoron was operated stably at MOU output power of 160 kW and the enforcement of the cooling and evacuation systems allowed the injection power of 110 kW into LHD for over one hour. In the longest discharge of 3900 s, the electron temperature reached about 1.5 keV and the electron density was kept $1.5 \cdot 10^{18}$ m^{-3} stably by fine gas feed control. More power is needed to achieve 10^{19} m^{-3} without the radiation.

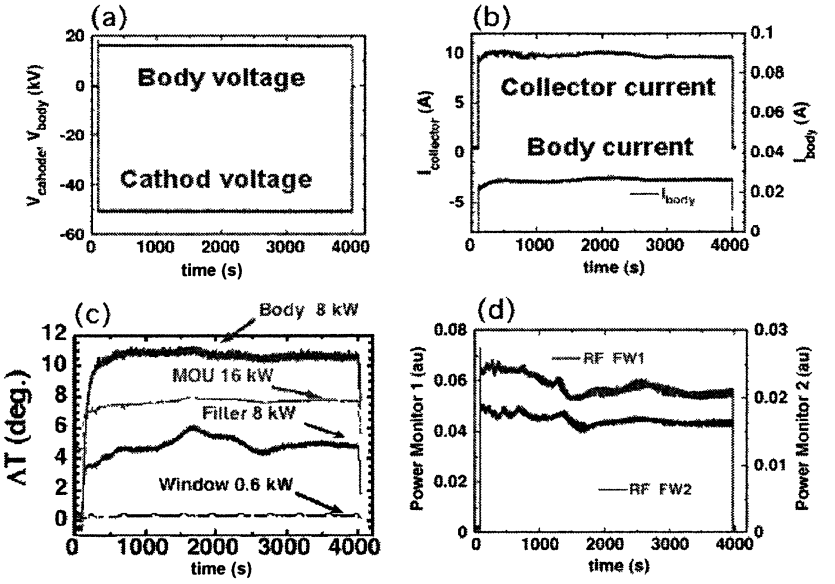

Fig. 11. Time traces of the body and cathode voltage (*a*). Time traces of the body and collector current (*b*). Time evolutions of temperature deference at each cooling channel of the CW gyrotron components (*c*). Waveforms of the power monitors set at the second (gyrotron side) and the LHD side miter bend (the forth from LHD) (*d*) (Ref. 2).

5. Summary

The recent state of ECRH system for LHD and the experimental results have been reported. With using the flexible high power injection system, formation of two kinds of improved core confinement has been investigated as an important issue of high power ECRH experiment. On another front, long pulse discharge over an hour was achieved by the CW gyrotron operation. The improvement of evacuation and heat removal in the transmission line has contributed to such stable long pulse operation.

Acknowledgements

These works have been supported by NIFS under NIFS05ULRR501, 502, 503.

References

1. *Shimozuma T., et al.*, 20th IAEA Fusion Energy Conf. 1-6 Nov. 2004 Vilamouda, Portugal, **EX/P**3-12.
2. *Kubo S., et al.*, Pro. Topical Conf. Radio Frequency Power in Plasmas, Park City, USA, 11-13 April 2005.

ECRH EXPERIMENTS IN ASDEX UPGRADE AND CONSEQUENCES FOR A NEW ECRH SYSTEM

F. Leuterer, C. Angioni, G. Gantenbein[1], *A. Manini, M. Maraschek, M. Münich, A. G. Peeters, F. Ryter, D. Wagner, H. Zohm and ASDEX Upgrade Team*

Max Planck Institut für Plasmaphysik,EURATOM Ass., D-85748 Garching, Germany
[1]Institut für Plasmaforschung, Universität Stuttgart, D-70569 Stuttgart, Germany

Electron cyclotron heating (ECRH) at 140 GHz is used in the tokamak ASDEX Upgrade for very localised heating and current drive (ECCD). This affects the confinement and the mhd-stability of the plasma. A modification of particle transport is seen in low density plasmas with central ECRH leading to changes in the density profile. Linear gyrokinetic studies indicate that the transport is determined by collisionality and by the kind of turbulence which is dominant. A similar result is obtained for the electron heat transport which increases above a threshold in the inverse electron temperature gradient scale length. Neoclassical tearing modes limit the achievable plasma pressure β_N. They can be avoided by controlling the sawtooth instability and thus the generation of seed islands. This can be done with ECCD close to the $q = 1$ surface. Already existing tearing modes can be suppressed with ECCD on the resonant flux surface whereupon β_N can be increased. This is shown in demonstration experiments. For an application to plasmas with high β_N and at different magnetic fields we need more power, a variable frequency, and a control of the precise location of the driven current.

Introduction

The present ASDEX Upgrade ECRH system consists of 4 gyrotrons (GYCOM, type Zodiak), each 140 GHz / 0.5 MW / 2 s, with 4 separate transmission lines and launchers. The launched beams are focused and have a beam waist $w_0 \approx 22$ mm located in the plasma. The narrow power deposition profile has been confirmed experimentally [1, 2]. The four independent launchers, steerable both in poloidal and toroidal directions, allow simultaneous electron heating at various locations in the plasma. This was used extensively in the transport studies presented in the first chapter. The second chapter describes experiments aimed at suppression or avoidance of neoclassical tearing modes (NTM) by localized ECCD. In the last chapter we describe our plans for a new additional ECRH system with feedback controlled power deposition and frequency step tunable gyrotrons.

Transport studies with localized ECRH

Particle diffusion

The density profile reacts quite different to central electron heating by ECRH. It may get flatter, may stay unaffected, or may even peak slightly. Two examples are shown in Fig. 1. In the low density L-mode case the electron

density profile is flattening while the temperature is increasing at constant profile shape.

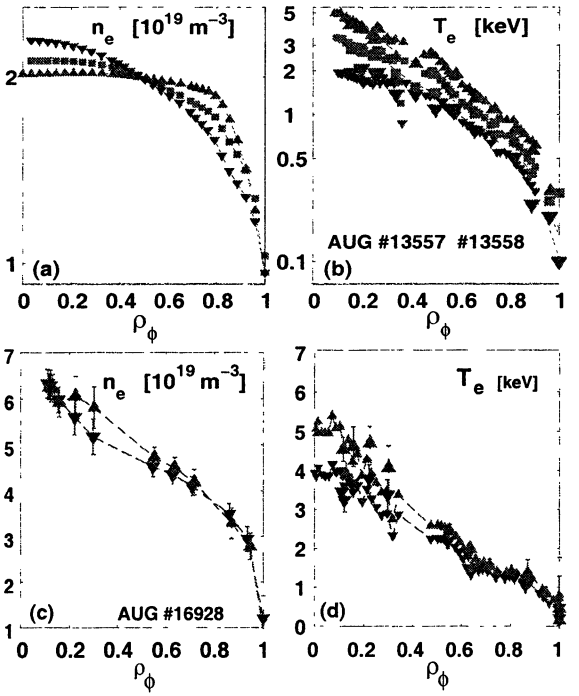

Fig. 1. Top: density and electron temperature profiles (log scale) in a low density L-mode plasma with central ECRH of 0, 0.8, and 1.6 MW. Bottom: density and temperature profiles (lin scale) in medium density H-mode plasma with central ECRH of 0, and 1.2 MW (from Ref. [3]).

A summary of many shots is shown in Fig. 2, taken from reference [3]. Here density peaking is defined by the ratio of the line averaged density along the central chord of the interferometer, H1, to that of a peripheral chord, H2. This peaking during the phase with ECRH, normalised to the peaking during the non-EC heated phase, is plotted on the x-axis, while the central line average density is on the y-axis. The non-EC heated phase is represented by an open symbol on the line $x = 1$, while the EC phase is represented by a full symbol. A displacement towards lower values on the x-axis from the open to the full symbols describes density flattening due to central ECRH. Low density L-mode plasmas generally show a strong flattening, and at intermediate density the profile does not change. In H-mode plasmas the profiles flatten at intermediate density, but remain unchanged at higher density.

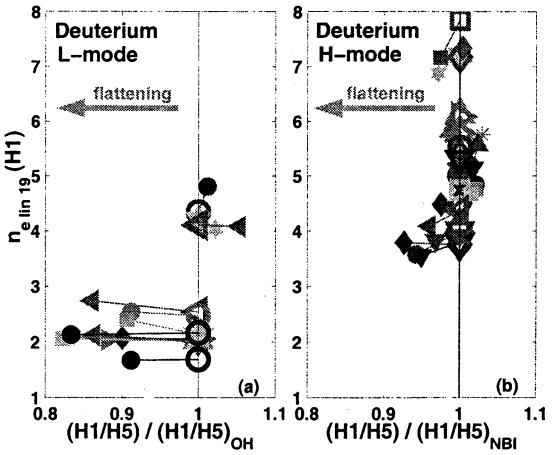

Fig. 2. Relative density peaking (horizontal axis) as a function of the line averaged density in L-mode and H-mode plasmas with central ECRH (from Ref. [3]).

An explanation of this behaviour is indicated by inspection of the expression for the thermodiffusive contribution to the total anomalous particle flux. This thermodiffusive coefficient depends on the type of the unstable mode, which characterizes the turbulence, and on its frequency. The thermodiffusive part is usually directed inward for ion temperature gradient driven instabilities (ITG), but can change sign in the instability domain of the trapped electron modes (TEM), hence becoming outward directed when the mode propagates in the electron drift direction. In this way a mechanism can be identified which leads to flatter profiles when the plasma is in an instability domain with dominant TEMs and when the electron to ion temperature ratio is increased by the application of central ECRH. Indeed the mode frequency and the thermodiffusive coefficient increase with T_e/T_i. Thus central electron heating can produce a clear effect of density flattening. This interpretation is supported by quasi-linear gyrokinetic calculations performed with the gyrokinetic code GS2, [3, 4]. Instead, when the dominant plasma instability is an ITG, the thermodiffusive term is predicted to be small and directed inwards. In this case the effect of central electron heating on the density profile is predicted to be small, leading to a slight peaking.

These theoretical predictions agree with the experimental diagrams presented in Fig. 2. Detailed calculations with the gyrokinetic code GS2 using experimentally determined parameters and identifying the mode with the largest linear growth rate, have shown that plasmas exhibiting density flattening in response to central ECRH are usually dominated by TEM instabilities. At intermediate densities in L-mode, where no flattening with central ECRH is observed, an ITG is found as dominant mode [3]. For the same reason, H-mode plasmas at intermediate densities in Fig. 2, which show small density flattening with central ECRH, are found in the TEM instability domain, while at higher

density in the ITG domain no flattening is observed. This is explained by the increasing stabilising effect of collisions on TEMs, which are dominant at low density and low collisionality, while at higher density ITGs are dominant.

Electron heat transport

Turbulence is also the reason for enhanced electron heat transport. This was shown quite clearly in low density L-mode plasmas with a plasma current of 0.8 MA, where the heat flux through the confinement region around half the minor radius was changed by a factor of 10 while keeping the heat flux at the edge of the plasma constant [5]. The temperature gradient length, $L_{T_e} = (\nabla T_e/T_e)^{-1}$, did however change only by a factor of 2. This was achieved by ECRH heating at two radial positions, $\rho_{tor} = 0.3$ and $\rho_{tor} = 0.65$, in such a way that the total ECRH power was constant but the ratio of the powers deposited at each location was varied. The results suggested the existence of a threshold in the inverse electron temperature gradient length $1/L_{T_e}$, above which the electron heat flux increases. An empirical model for this heat diffusivity proved to be very successful in describing both the experimental steady state and heat pulse diffusivities [5]. In agreement with this model the latter ones were substantially higher than the steady state diffusivities in these low density plasmas. This model also supports the hypothesis of a threshold at the normalised inverse gradient length $R/L_{T_e} \approx 4$.

We have repeated these experiments, but this time in a L-mode plasma with only 0.4 MA of plasma current, i. e. lower ohmic power input. Into this plasma we injected very low power ECRH. In this way we were able to trace the transition through the threshold in R/L_{T_e}, as shown in Fig. 3 taken from reference [6]. Figure 3, *a* shows the normalized steady state heat flux, obtained

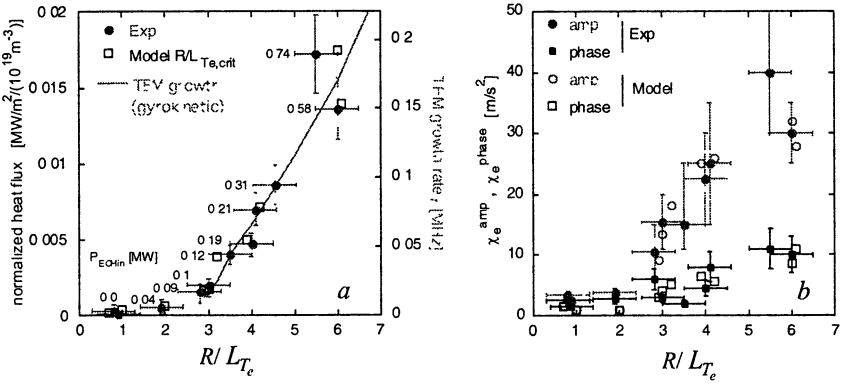

Fig. 3. Experimental electron heat flux q_e/n_e (dots) vs. R/L_{T_e} : the squares are a modeling result with an empirical critical gradient model, the solid line shows the linear growth rate of TEM modes (*a*). Experimental and modeling results for the heat pulse diffusivity (*b*) (from Ref. [6]).

from a power balance analysis, as a function of the normalized inverse temperature gradient length, while Fig. 3, *b* shows the results of the heat pulse diffusivity in these plasmas also exhibiting a jump at the threshold. The experimental results agree well with those obtained from a transport analysis using an empirical model based on a critical electron temperature gradient.

Like the previous experiments [7], these new experiments were also interpreted with linear gyrokinetic stability calculations using the GS2 code, [6]. Again TEM turbulence was shown to be the dominant mechanism for the enhanced diffusivity. The derived normalized heat flux was compared to the experimental one, matched only by one scaling factor, and is also shown in Fig. 3, *a* as the solid line. The theory fits very well to the experimental data, confirming the existence of a threshold in R/L_{T_e}, its correct value, and the importance of TEM turbulence together with collisions even in this low density plasma.

Like in the case of particle diffusion described above, an increasing collisionality should stabilise the TEM modes and ITG turbulence should then become more dominant. This was studied in a series of plasmas with increasing density [8]. The results are shown in Fig. 4. The ratio of electron to ion heat flux, the heat pulse diffusivity, and the ratio of heat pulse diffusivity to steady state heat diffusivity are plotted versus the normalised collisionality. All these quantities decrease substantially with collisionality. Also shown is a plot of the frequency of the most unstable mode obtained in a study of these plasmas with the gyrokinetic code GS2. This indicates a transition from dominant TEM modes (negative frequency) to dominant ITG modes (positive frequency) around a normalised collisionality of 1.

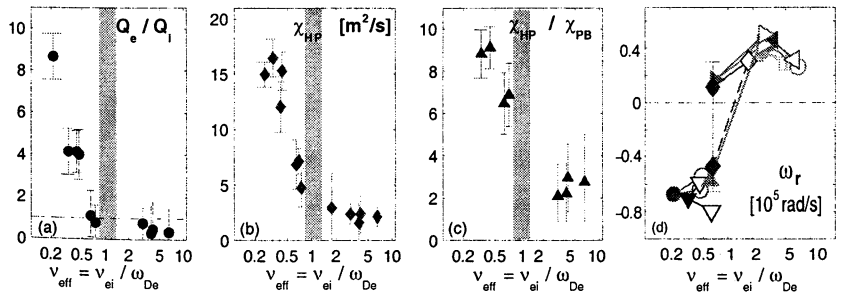

Fig. 4. Ratio of electron to ion heat flux (*a*), heat pulse diffusivity (*b*), ratio of heat pulse to power balance diffusivity (*c*), and rotation frequency from GS2 analysis (*d*) (from Ref. [8]).

Similar studies have been done in an H-mode plasma at a plasma current of 1 MA and at a higher density of $4.5 \cdot 10^{19}$ m^{-3} [9]. Thess plasmas were heated by 5 MW neutral beam injection, $\approx$ 25% of which contribute to electron heating, and $T_i > T_e$. Into this plasma we injected ECRH of up to 1.2 MW, i. e. the

electron heat flux varied by up to a factor of 2. By a variation of the poloidal launching angle the deposition was either at ρ_{tor} = 0.1; 0.35; or 0.55 while the analysis was done at ρ_{tor} = 0.25 and 0.45. In Figure 5, *a* the dots show the electron heat flux as obtained by a power balance analysis with the ASTRA transport code as a function of the local value of the product $n_e \nabla T_e$. In a series of pulses the ECRH power was slightly modulated, generating a heat wave. From the analysis of these heat waves we derived the slope $\partial q_e / \partial \nabla T_e$ which is indicated by the short lines through each point. For the data from ρ_{tor} = 0.25 we find that the doubling of the heat flux induces ≈ 50% increase in $n_e \nabla T_e$, indicating a weakly resilient profile. In contrast, at ρ_{tor} = 0.45 the same increase in heat flux induces only a variation of $n_e \nabla T_e$ by 20%, indicating more resilient profiles. Turbulent theory for the electron heat transport predicts a dependence on the normalized inverse temperature gradient scale length, R/L_{T_e}. In Figure 5, *b* we therefore plot the same data as a function of this parameter, and indeed the data are unified and form a single pattern. The electron heat transport is seen to be weakly dependent on the inverse scale length for $R/L_{T_e} < 6$, while it is strongly dependent for $R/L_{T_e} > 6$, suggesting the existence of a transition to a transport determined by turbulence. Whether this turbulence is related to ITG-, ETG- or TEM-modes can, however, not be concluded from these results.

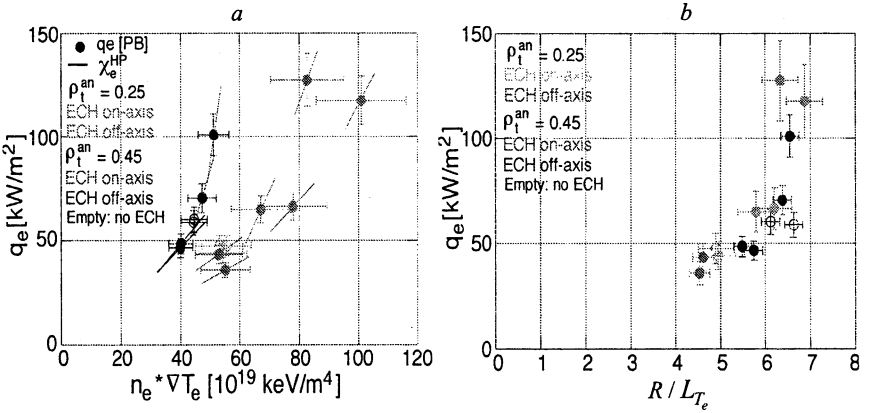

Fig. 5. Electron heat flux from power balance (dots) and $\partial q_e / \partial \nabla T_e$ from heat wave analysis at different radial locations vs. $n_e \nabla T_e$ (*a*), same data vs. R / L_{T_e} (*b*) (from Ref. [9]).

NTM control by ECCD

A main application of ECCD in ASDEX Upgrade is the control of neoclassical tearing modes (NTMs). These are resistive MHD instabilities which limit the achieveable β (plasma pressure normalized by the magnetic

pressure). They are driven unstable by the loss of bootstrap current within the associated magnetic island, which can be triggered by an externally created seed island, e. g. due to a sawtooth crash at sufficiently high local β_p [10]. Therefore, one way to get rid of NTMs is to prevent their start-up by avoiding such seed islands, which can be done by sawtooth control via ECCD near the $q = 1$ surface. However, if the NTM is already existing, a possible way to suppress it is by replacing the missing bootstrap current by ECCD within the magnetic island.

NTM suppression by replacing the missing bootstrap current

This method is based on local current drive at the resonant surface of interest, $q_{res} = m/n$. In ASDEX Upgrade the suppression of (3,2) NTMs was demonstrated up to a β_N of 2.6, obtained by 12.5 MW of neutral beam injection (NBI), with an ECCD power of 1.2 MW launched at a toroidal angle of $\varphi_{tor} = -15°$ [11]. Defining an efficiency for NTM suppression as the maximum β_N at which the mode can be suppressed, divided by the applied ECCD power [12], $\varepsilon = \beta_N / P_{ECCD}$, we get for this (3,2) suppression case a value of $\varepsilon = 2.17\ MW^{-1}$. Similarly, a (2,1) NTM could be suppressed in a plasma with $\beta_N = 1.9$, obtained with 6.25 MW of NBI, with an ECCD power of 1.8 MW launched at $\varphi_{tor} = -12°$ [13], yielding an efficiency of $\varepsilon = 1.06\ MW^{-1}$.

Localizing the driven current inside the island as long as possible is of advantage. This has been shown by a series of experiments where the toroidal injection angle was varied in otherwise identical discharges. A larger toroidal angle φ_{tor} increases the driven current I_{ECCD}, however, with a widening current profile width d, as shown in Fig. 6, *a*.

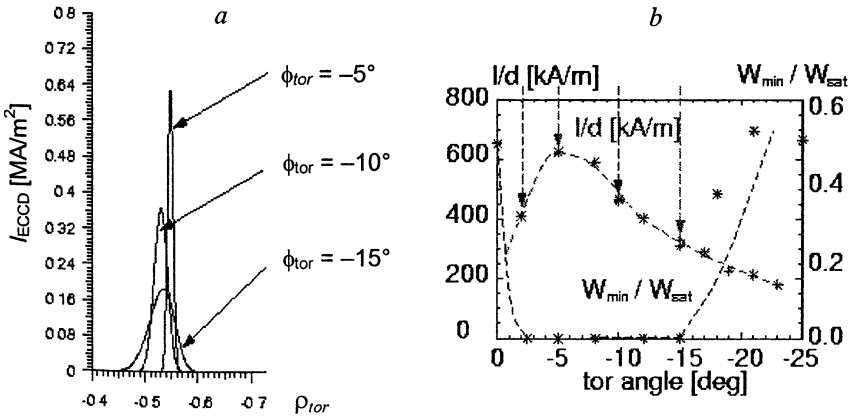

Fig. 6. Driven current profile width at different φ_{tor} (*a*), calculated current density and experimental island width W/W_{sat} (*b*) (Ref. [12]).

In Figure 6, *b* we show the results in terms of W/W_{sat}, i. e. the final island width W after ECCD application normalized by the saturated island width before ECCD is switched on [12]. It can be seen that in this series of experiments, (3,2) NTMs could be completely suppressed for a range of toroidal angles $-15° \leq \varphi_{tor} \leq -5°$. This is in qualitative agreement with the angle dependence of the current density, $j_{ECCD} \sim I_{ECCD}/d$, which is also shown in the figure. In particular, the current density j_{ECCD} has a maximum near $-5°$, although the total driven current I_{ECCD} is a factor of 2 lower than at $-15°$. For mode suppression a narrow deposition with $d < W$ is of advantage since the driven current can remain fully inside the shrinking island for a longer time. This should increase the efficiency of mode suppression. Indeed, with $-5°$ toroidal launching angle the (3,2) NTM could be suppressed at $\beta_N = 2.6$ with only 1 MW of ECCD power, and the efficiency was $\varepsilon = 2.6\ MW^{-1}$. And the (2,1) NTM could be suppressed at $-5°$ up to $\beta_N = 2.3$ with 1.4 MW of ECCD with an efficiency of $\varepsilon = 1.64\ MW^{-1}$. Our results are summarized in Table.

Experimentally achieved suppression efficiencies

mode	φ_{tor}	β_N	P_{ECCD}, MW	ε, MW^{-1}
(3/2)	$-15°$	2.6	1.2	2.17
(3/2)	$-5°$	2.6	1.0	2.60
(2/1)	$-12°$	1.9	1.8	1.06
(2/1)	$-5°$	2.3	1.4	1.64

Thus narrow deposition at small toroidal launching angle and with high current density increases the suppression efficiency. However, this also requires more effort to place and to keep the driven current centered in the shrinking island.

Avoidance of NTMs by sawtooth control

NTMs need a seed island as an initial perturbation. This is usually supplied by a sawtooth crash or a fishbone located at the $q = 1$ surface which produces a perturbation reaching the resonant q-surface of the NTM. Thus a method to avoid NTMs is the control of sawteeth.

The sawtooth amplitude and frequency can be controlled with ECCD, depending on power and location of the driven current. In H-mode plasmas heated with 5 MW of neutral beam power we achieved complete suppression of sawteeth with co-ECCD close to the $q = 1$ surface, and with counter-ECCD in the centre, [14]. This is in qualitative agreement with a reduction of the magnetic shear at the $q = 1$ surface. At a higher NBI power of 12.5 MW and $\beta_N = 2.9$, the ECCD power was not sufficient to suppress the sawteeth. However, when applied early in the discharge while the NBI power was still ramped up and NTMs were not yet destabilized, the triggering of NTMs by

sawteeth could be avoided with co-ECCD close to $q = 1$. As soon as ECCD was switched off a large sawtooth triggered the NTM [15].

The question arises whether narrow ECCD closer to the $q = 1$ surface could be more efficient, similar to the situation with the suppression of NTMs. We did a number of pulses comparing ECCD with a toroidal launching angle of $-15°$ (wide profile) and $-6°$ (narrow profile, driven current 30% less) [16]. The magnetic field was slowly varied in these pulse so that the ECCD deposition zone moved across the $q = 1$ surface and back again. Figure 7 shows some time traces: signals of two ECE channels on which we can recognize the sawteeth, the ratio of the sawtooth period with and without ECCD, the magnetic field sweep, the location of the ECCD deposition, the $q = 1$ surface from MSE diagnostics and the sawtooth inversion radius. Although a clear stabilizing (increasing period) or destabilizing (decreasing period) effect is obtained with both deposition profiles, there is not much difference in the efficiency. Only for destabilization the wide profile seems to be better. However, because of the finite sweep time across the $q = 1$ surface, it cannot be concluded that this holds also for the case of a constant magnetic field when the deposition remains much longer at the $q = 1$ surface.

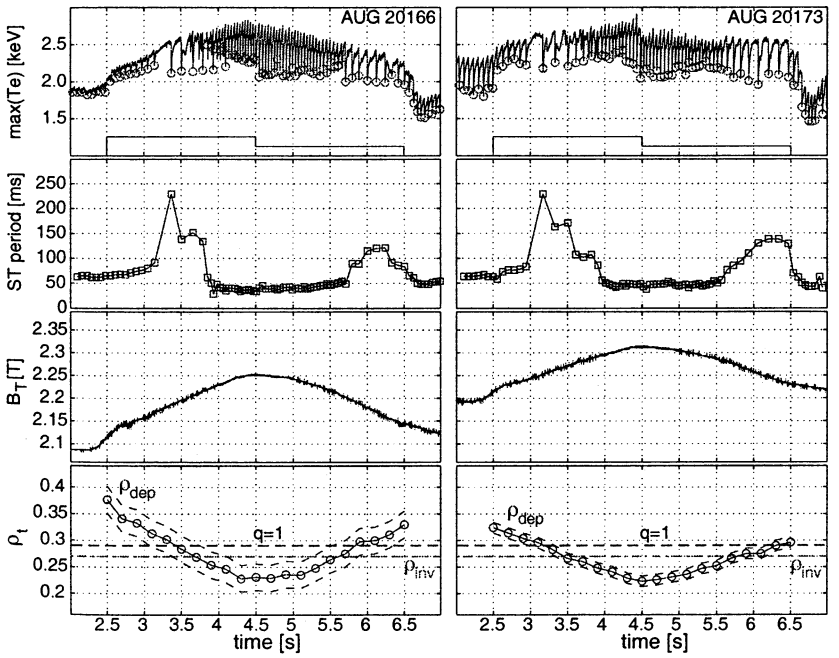

Fig. 7. Response of the sawtooth frequency on co-ECCD. The location of the driven current is swept across the $q = 1$ surface by a varying toroidal magnetic field (from Ref. [16]).

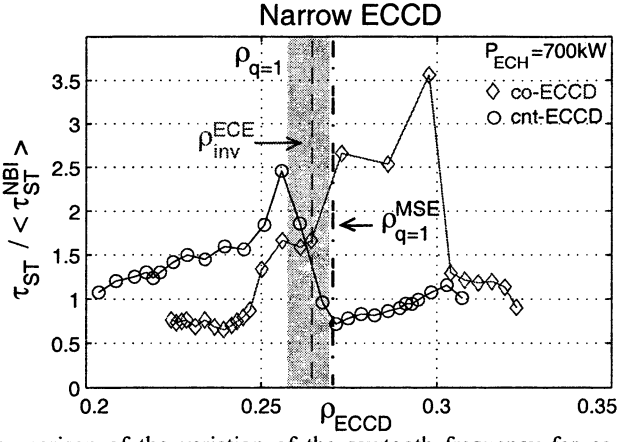

Fig. 8. Comparison of the variation of the sawtooth frequency for co- and counter-ECCD.

Similar pulses have been performed with counter-ECCD. In Figure 8 we compare the variation of the sawtooth period for the case of narrow deposition. Co-ECCD leads to stabilization outside and to destabilization just inside of the $q = 1$ surface, while for counter-ECCD this is just opposite. The crossover is clearly at the location of the $q = 1$ surface. The difference in the stabilizing effect between co- and counter-ECCD is attributed to the concomitant electron heating in the deposition zone which enhances the co- and weakens the counter-ECCD effect [16].

The new ECRH system at ASDEX upgrade

In high β plasmas our available ECRH power and pulse duration were found to be insufficient for driving the necessary current for NTM suppression. Similarly, in experiments with current profile control for reversed shear discharges or improved H-mode discharges, we need more noninductive current drive and for a longer time. For this reason we are presently installing a new system with a total power of ≤ 4 MW generated by 4 gyrotrons with a pulse duration of 10 s (maximum flat top time of ASDEX upgrade plasmas).

Another constraint, particularly in our experiments on NTM suppression so far, is the necessity to find operating parameters, mainly magnetic field and plasma current, such that the deposition zone is at the resonant q-surface on the high field side (where the current drive efficiency is maximum). Frequency variable gyrotrons would give much more flexibility in this respect. Frequency step tunability of gyrotrons has been demonstrated with short pulses [18, 19]. By changing the cryomagnetic field and the beam voltage, the gyrotron can be tuned to excite different cavity modes. In our new system we want to use this

capability. The new gyrotrons will be able to generate power at the two resonance frequencies, 105 GHz and 140 GHz, of their single disc diamond output window, but also at several frequencies within this range if they are equipped with a tunable double disc window or a Brewster angle window. We have selected four operating frequencies, 105 GHz, ≈117 GHz, ≈127 GHz and 140 GHz. The then achievable deposition range is shown in Fig. 9 and covers practically most of the operation range of ASDEX Upgrade. A first 10 s pulse gyrotron, delivering 0.9 MW at 140 GHz and 0.7 MW at 105 GHz, was presented here in this conference [20] and is already delivered to IPP.

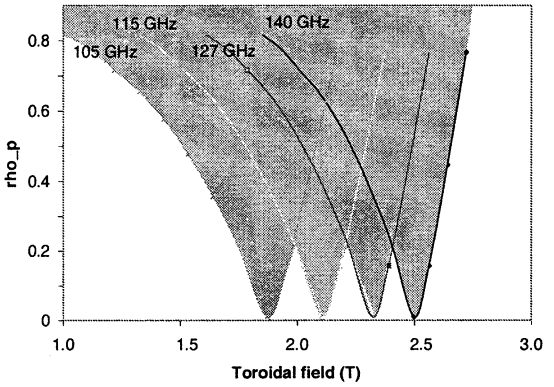

Fig. 9. Achievable deposition range with a step tunable gyrotron as a function of the toroidal magnetic field.

The narrow ECCD profile for efficient NTM suppression requires feedback control of the deposition, and thus a fast moveable mirror. Such mirrors have been installed in ASDEX upgrade and have been tested to provide the designed sweep speed of 10° in 100 ms during plasma pulses [21]. A feedback scheme, based on the online determination of the NTM- and the deposition location is in development [22].

This system, of which more details can be found in [23], is expected to be ready 2008.

References

1. *Kirov K et al*, Plasma Phys. Contr. Fusion **44**, 2583 (2002).
2. *Leuterer F. et al.*, Nucl. Fusion **43**, 744 (2003).
3. *Angioni C. et al.*, Nucl. Fusion **44**, 827 (2004).
4. *Kotschenreuther M et al.*, Comput. Phys. Commun. **88**, 128 (1995).
5. *Ryter F et al.*, Nucl. Fusion **43**, 1396 (2003).
6. *Ryter F. et al.*, Phys. Rev. Lett. 95, 040701 (2005).
7. *Peeters A.G. et al.*, Phys. Plasmas **12**, 022505 (2005).
8. *Angioni C. et al.*, Phys. Plasmas **12**, 040701 (2005).

9. *Manini A. et al.,* Plasma Phys. Contr. Fusion **46**, 1723 (2004).
10. *Zohm H. et al.,* Phys. Plasmas **8**, 2009 (2001).
11. *Gantenbein G. et al.,* Phys. Rev. Lett **85**, 1242 (2000).
12. *Maraschek M. et al.,* 20th IAEA Conf. Fusion Energy, Vilamoura, Portugal 2004, paper IAEA _CN_116/EX/7-2, accepted for Plasma Phys. Contr. Fusion.
13. *Gantenbein G. et al.,* 15th Conf. RF Power in Plasmas, AIP Conf. Proc. **694**, 317 (2003).
14. *Mück A. et al.,* Plasma Phys. Contr. Fusion **47**, 1633 (2005).
15. *Mück A. et al.,* 30th EPS Conference St. Petersburg, ECA **27A**, p. 1.131 (2003).
16. *Manini A. et al.,* 32th EPS Conference Tarragona, Spain (2005).
17. *Angioni C. et al.,* Nucl. Fus. **43**, 455 (2003).
18. *Zapevalov V. et al.,* Proc. 12th Workshop on ECE and ECRH, Aix en Provence, France (2002).
19. *Thumm M. et al.,* Fusion Eng. Des. **53**, 407 (2001).
20. *Popov L. et al.,* these proceedings, **1**, 119-124.
21. *Leuterer F. et al.,* Fusion Eng. Des. **73**, in press (2005).
22. *Keller A. et al.,* 30th EPS Conference St. Petersburg, ECA **27A**, p. 1.130 (2003).
23. *Leuterer F. et al.,* Fus. Eng. Des. **66-68**, 537 (2003).

RECENT PHYSICS RESULTS WITH ELECTRON CYCLOTRON HEATING IN TCV

A. Pochelon, S. Alberti, G. Arnoux, Y. Camenen, E. Fable, A. Mück, L. Porte and the TCV Team

Centre de Recherches en Physique des Plasmas CRPP EPFL,
Association EURATOM-Confédération Suisse,
Ecole Polytechnique Fédérale de Lausanne EPFL,
Switzerland

With its 2nd and 3rd harmonic flexible Electron Cyclotron (EC) system (3 MW at 82.7 GHz and 1.5 MW at 118 GHz), adapted to its flexible plasma shaping capabilities, TCV (Tokamak à Configuration Variable) explores a large spectrum of EC heating (ECH) and current drive (ECCD) physics, from low to high plasma densities, that is in different collisionality and confinement regimes. This paper reviews some recent highlights of TCV ECH experiments.

Second harmonic X-mode (X2) radially localized EC heating allows a variation of the normalised electron temperature gradient and electron temperature independently and over a large range. These experiments are dedicated to the separation of the effects of collisionality and plasma shape on electron heat transport.

Third harmonic heating (X3) allows initial exploration of β-limits at intermediate currents and densities. The coupling of the wave is optimised by feedback control of the mirror angle, based on a sinusoidal oscillation of the mirror angle. Since the coupling increases with electron temperature and density, best performance are obtained at the maximum of the available 3rd harmonic power and typically at 3/4 of the cutoff density, around $n_{eo} \sim (8\text{–}10) \cdot 10^{19}\ m^{-3}$. Central heating of both electron and ion species has been achieved, providing an increase of β from 1 to 2.5%, equivalent with the normalised value $\beta_N = 2$.

First evidence of EBW (Electron Bernstein Waves) global power absorption and radially localized heating in a tokamak has been obtained in an H-mode plasma. The results have been obtained using the low field side O-X-B-wave conversion scheme which becomes possible at high density ($n_{eo} \sim (20\text{–}25) \cdot 10^{19}\ m^{-3}$), a density several times overdense to 2nd harmonic O-mode.

The three kind of experiments addressed in this paper can also be seen as a set of experiments at increasingly high densities, using the adequate EC wave propagation mode (X2, X3, EBW) to provide accessibility and power absorption.

EC-System on TCV (X2, X3)

An essential part of the TCV tokamak program is dedicated to the study of the effect of plasma shape on plasma confinement and stability properties, see Fig. 1. Electron cyclotron waves (ECW), with a power coupling independent of the plasma-launcher distance, were therefore the obvious choice. Moreover, the narrow localization of the 2nd harmonic ECW X-mode (X2) power deposition is crucial for transport studies together with current profile and instability control. Third harmonic ECWs (X3), with a three times higher density cutoff, provide access to higher density, allowing the study of β-limits at intermediate currents.

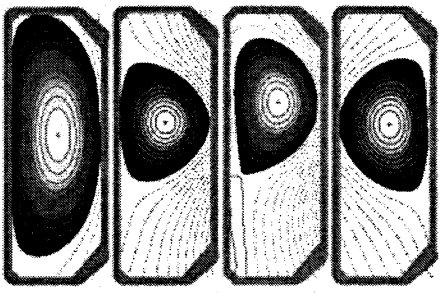

Fig. 1. Examples of plasma shapes in TCV.

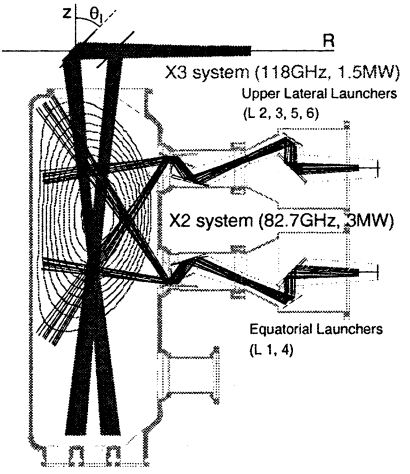

Fig. 2. X2 and X3 launchers set-up.

The TCV ECW system is composed of six 2nd harmonic X2 gyrotrons with low field side (LFS) launchers (3 MW, 2 s, 82.7 GHz, $n_{e\,cutoff\,X2} = 4.3 \cdot 10^{19}$ m^{-3}) [1] and three 3rd harmonic X3 gyrotrons using one top launcher (1.5 MW, 2 s, 118 GHz, $n_{e\,cutoff\,X3} = 11.5 \cdot 10^{19}$ m^{-3}) [2], see Fig. 2. All launchers have two degrees of freedom and can be steered in real time. The gyrotrons and matching optical units are separated from the tokamak by about 30 m of evacuated waveguides lines of 62.5 mm diameter, with a transmission efficiency of typically 95%. In the plasma, a high heating power density can be achieved, up to more than 30 MW/m^3 with central X2 injection. The relative alignment of the different X2 launcher mirrors is accomplished using the highly localised sawtooth period response at the $q = 1$ resonant surface [3]. The main codes relevant for this paper are, TORAY-GA for ray tracing, [4], ART for the conversion to electron Bernstein waves [5], Fokker – Planck CQL3D for the non-linear CD (X2&X3) [6], the inverse equilibrium code LIUQE [7] and CHEASE [8].

Access to high density with EC waves

The accessibility of EC waves depends primarily on the magnetic field. We compare the accessibility of EC waves in different machines, from the low field spherical tokamaks or compact tori (B = 0.5 T), through the rather low field TCV (B = 1.5 T, R = 0.88 m, a = 0.25 m), to the high field ITER machine (5.3 T). The accessibility limitation due to EC cutoffs is compared to the specific machine plasma density limit, given by the empirical Greenwald density limit $\langle n_{eG} \rangle = 0.27\ I_p/a^2$ [9]. The nominal ITER operation parameters are taken as a reference, also standard for the other machines envisaged, namely: safety factor $q_{95} = 3$, elongation $\kappa = 1.85$ and triangularity $\delta = 0.5$, with $q_{95} \sim (5a^2B_o/R_oI_p) \times$

$\times f(a/R) \cdot [1 + \kappa^2(1 + 2\delta^2 + \ldots)]/2$. The typical ratios of *EC cutoffs* versus *machine* accessible density range, $n_{e\ cutoff}/n_{eoG}$, are given in Fig. 3 for these conditions.

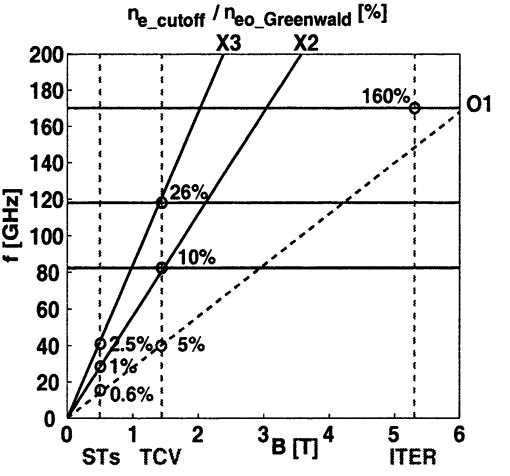

Fig. 3. Ratio of EC cutoff density to Greenwald density limit for different gyrotron frequencies and magnetic fields (in %).

In ITER, the field is sufficiently high to allow for the heating of the complete machine density range with the fundamental O-mode (O1) at 170 GHz. In spherical tokamaks however, the lowest harmonics ECWs allow only for the heating of up to a few percent of n_{eG}, thus justifying the great hopes placed in the potential of EBWs, which exhibit no principle high-density limit. In the medium field machine TCV, 10% of n_{eG} is accessible with the 2nd harmonic X-mode (X2), a range extended to 26% with the use of the 3rd harmonic X-mode (X3). The density range above X3 accessible densities could be accessed with 2nd harmonic EBWs.

If current drive using EBWs would develop in addition to heating, then there are potential applications of EBW even in high a field machine like ITER.

Electron heat transport with shape & collisionality

Increasing the energy confinement in order to limit the amount of additional heating needed for a reactor grade plasma is one of the big tasks in tokamak research. Plasma shape is one of the free parameters, which influences transport and confinement.

The effect of plasma shape on core electron heat transport in low-density L-mode plasmas is investigated in TCV using strong localized EC heating to vary both the electron temperature T_e and the normalized electron temperature gradient R/L_{T_e} [10–12]. The power is deposited at two radial locations, see

Fig. 4, one off-axis just outside the $q = 1$ surface, at ρ_1, and the other far off-axis, at ρ_2, a radius still guaranteeing full first-pass absorption. The power ratio $P(\rho_1)/P(\rho_2)$ essentially determines the electron temperature gradient, whereby the total power strongly influences T_e at mid-radius, the radius of investigation, by determining the total heat flux at the edge. Varying the two parameters $P(\rho_1)/P(\rho_2)$ and P_{tot} independently allows decoupling R/L_{T_e} and T_e, see Fig. 5. The large EC power available in TCV allows exploring a range of R/L_{T_e} three times larger than in preceding similar studies [13]. To study the effect of plasma shape, the triangularity was varied from negative to positive values, $-0.4 < \delta < +0.4$. The strong modification of the edge pedestal and stability with triangularity in H-mode [14] justifies the use of L-mode in a first study of the direct effect of plasma shape on core heat transport.

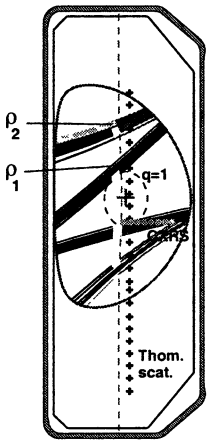

Fig. 4. EC beams for off-axis (ρ_1) and far off-axis deposition (ρ_2), with the positions of the cold EC resonance, $q = 1$ surface, Thomson and CXRS diagnostics measurements.

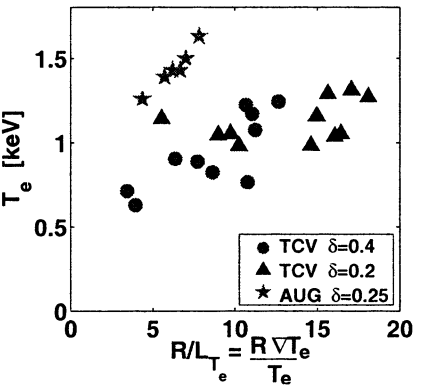

Fig. 5. Range of T_e and R/L_{T_e} explored in TCV and AUG. In TCV, T_e and R/L_{T_e} are varied independently.

Typical parameters at mid-radius are T_e = 0.6–1.3 keV, T_e/T_i = 2–4, R/L_{T_e} = 4–20, Z_{eff} = 2–5, ν_{eff} = 0.25–1, where $\nu_{eff} = \nu_{ei}/\omega_{De} \sim 0.1 R n_e^{19} Z_{eff}/T_e^2$, the collision frequency versus curvature drift frequency, is the effective collisionality relevant for micro-instabilities [15]. Simulations with the local gyro-Landau fluid code GLF23 [16] and with the global collisionless linear gyro-kinetic code LORB5 [17] show that with such parameters, trapped electron modes (TEM) are the most unstable modes, except for the very lowest values of R/L_{T_e}, where ion temperature gradient (ITG) modes dominate. In addition to the effect of

plasma shape, the experimental study focuses on the dependences of χ_e on T_e, R/L_{T_e} and ν_{eff}, plasma parameters predicted to strongly influence TEM stability.

The experimental electron heat diffusivity χ_e is found to increase strongly with the electron temperature, with no strong dependence on R/L_{ne} or R/L_{T_e}, from the whole parameter range explored, Fig. 6. This result is obtained at constant $n_e Z_{eff}$. The strong dependence of χ_e on T_e suggests a gyro-Bohm and/or a collisionality dependence.

Looking more into the details of the R/L_{T_e} dependence, it appears from Fig. 7 that for $R/L_{T_e} > 8$, the gyro-Bohm heat diffusivity does not depend on R/L_{T_e}, while at $R/L_{T_e} < 8$, TCV data are compatible with ASDEX upgrade (AUG) data showing an increase of $\chi_e/T_e^{3/2}$ with R/L_{T_e}.

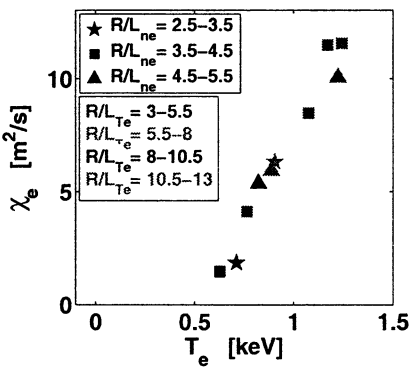

Fig. 6. Strong dependence of χ_e versus T_e at mid-radius, despite a large range of variations in R/L_{ne} and R/L_{T_e}.

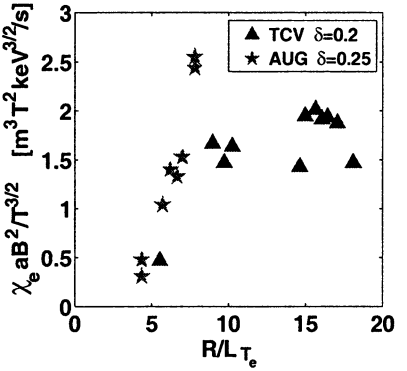

Fig. 7. Gyro-Bohm normalized electron heat diffusivity χ_e versus normalized electron temperature gradient.

The effect of plasma triangularity on electron heat diffusivity – in these TEM dominated plasmas – can first be illustrated by a specific example, which represents well the effect of triangularity on local and on global transport properties. In the experiment depicted in Fig. 8, the heating power just outside the $q = 1$ surface was adapted to get at the negative triangularity $\delta = -0.4$ the same T_e-profile than the one obtained at the positive triangularity $\delta = 0.4$ with 1.35 MW. The other parameters, n_e, Z_{eff}, q_{95} being held constant, it turns out that less than half of the power was needed at negative triangularity, compared to positive triangularity. At the negative triangularity comparatively to the positive triangularity, the (global) confinement time and confinement time enhancement factor are increased, respectively $\tau_{Ee} = 3.6 \rightarrow 7.7$ ms and $H_{RLW} = 1.5 \rightarrow 1.9$; and the (local) heat diffusivity from power balance is decreased, $\chi_e^{PB}(\rho = 0.5) =$

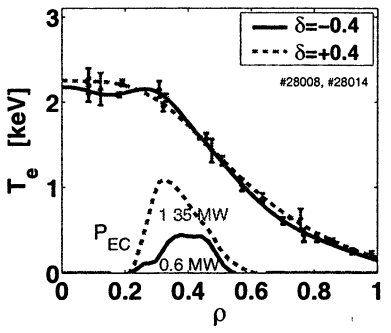

Fig. 8. Identical T_e profiles obtained at negative triangularity $\delta = -0.4$, as compared to positive triangularity $\delta = 0.4$, with half the EC power.

$= 8.5 \rightarrow 2.6$ m^2/s, with similar trend from heat pulse analysis.

Comparing the data with different values of $n_e Z_{eff}$, it appears that χ_e does not only depend on T_e, but also on $n_e Z_{eff}$ and that the heat diffusivity and the gyro-Bohm normalised heat diffusivity decrease strongly with increasing effective collisionality. The finding of a reduction of electron heat transport with ν_{eff} is consistent with ASDEX upgrade experimental results [18] and with the predicted stabilising effect of ν_{eff} on the TEM modes, as shown e. g. from GLF23 simulations.

The coupled effect of plasma triangularity and collisionality is shown in Fig. 9. The heat diffusivity does not vary significantly from $\delta = 0.4$ to $\delta = 0.2$. However, at negative triangularity, χ_e clearly decreases with decreasing δ. For the whole range of triangularity, χ_e decreases strongly with increasing ν_{eff}.

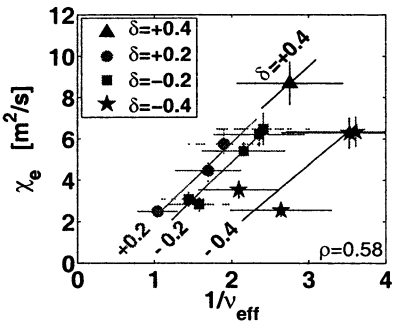

Fig. 9. Separation of shape and collisionality effects, both influencing χ_e (q_{95} = = const).

Thus, the present experiments have allowed us to separate the effect of plasma shape – here the triangularity – and collisionality on local electron heat transport. Small and negative triangularity, as well as low effective collisionality have both been shown to reduce favourably the electron heat transport, in this TEM dominated regime. Although the reason of the effect of plasma triangularity needs still to be determined, the strong effect on electron heat transport may be used as a tool to ease or control the access to electron internal transport barriers (eITB).

X3 heating for high β in H-mode

In the moderate magnetic field of TCV, the recently installed X3 system broadens the tokamak operational range, providing the possibility of heating plasmas at high density, well above the X2 cutoff density [19, 20]. To compensate for the significantly weaker absorption in X3 compared to the absorption in X2, top-launch injection is used to maximise the ray path along the resonance layer, with a shallow incidence on the resonance, thus maximising the optical depth.

The X3 mirror is located on top of TCV vacuum vessel (as shown in Fig. 2) and collects the power of three gyrotron beams. It is steerable both along the major radius ($0.8 < R < 0.96$ m) from pulse to pulse and azimuthally ($40° < \theta < 50°$) during discharges, with a maximum speed of $d\theta/dt = 20°/s$. A key characteristic of the X3 top launch is the high sensitivity of the absorption on the mirror angle θ. In a typical L-mode plasma ($n_{eo} = 4 \cdot 10^{19}$ m^{-3}, $T_{eo} = 2.7$ keV), the maximum power absorbed is typically 40–60% with a FWHM $\Delta\theta \sim 1.4°$. For a plasma with fixed n_e and T_e profiles, ray-tracing calculations show that the optimum mirror angle (at fixed mirror radius R) depends sensitively on the central density ($d\theta/dn_{eo} = 0.18°/(n_{eo}10^{19}$ m^{-3}), due to refraction) and central temperature ($d\theta/dT_{eo} = 0.2°$/keV, due to the relativistic shift). There are additional effects from the Shafranov shift and the paramagnetic cold resonance displacement ($\sim I_p^2$). This high sensitivity to the mirror angle has motivated the development of a real time control of the mirror angle.

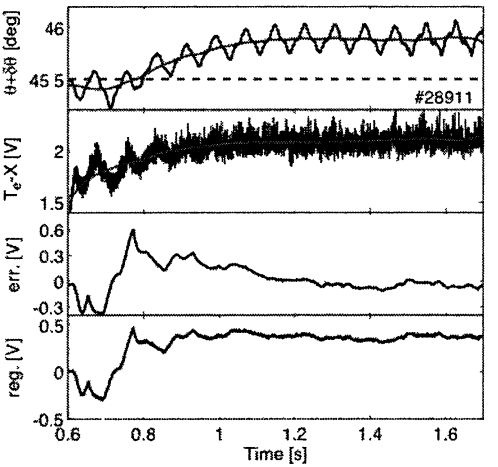

Fig. 10. X3 mirror angle feedback closed loop response. Preset (dashed) and optimal mirror angle with 13 Hz superimposed mirror oscillations, maximizing the soft X-ray T_{eX}, together with error and regulation signals.

The real-time control is based on a sinusoidal modulation of the mirror angle and a synchronous demodulation of the soft X-ray plasma response. With this system it is possible to generate an error signal proportional to $dI_X/d\theta$ (or $dT_{eX}/d\theta$ in Fig. 10) where $dI_X/d\theta$ is obtained from a central soft X-ray chord passing through plasma axis. The error signal is proportional to the slope $dI_X/d\theta$. In the closed loop system, this error signal is compared to an externally preset reference, and the difference between the error signal and the reference is fed to a PID controller. The dynamic response of the closed-loop system with a PI controller is shown in Fig. 10 where the external preset mirror angle was fixed at a value of 45.5°. After a transient period of approximately 250 ms the error signal vanishes. This real-time feedback is fully operational in L-mode plasmas, where up to full single-path absorption has been measured (DML) for

plasma densities lower than $4 \cdot 10^{19}\,m^{-3}$. At these plasma densities the calculated absorbed power fraction (TORAY) based on the assumption of a Maxwellian distribution function, is found to be significantly lower than the measured one, a difference due to the presence of the suprathermal electrons generated by the X3 heating itself.

In H-mode plasmas, due to the presence of the strong ELM perturbations, the present feedback system is not yet operational. However, the improved confinement in H-modes improves sufficiently the absorption that the need for a feedback system is less stringent.

In recent experiments dedicated to the heating of H-mode plasmas with the full installed X3 power (1.35 MW), it has been possible to reach quasi-full power absorption in a plasma with central density $n_{eo} \sim 8 \cdot 10^{19}\,m^{-3}$, owing to the electron temperature increase from 0.8 to 2.5 keV soon after heating start, leading to an increase of the absorbed power P_{abs} from 28 in Ohmic to 94% with X3 heating on.

The temporal evolution of the relevant parameters is shown in Fig. 11. At the full X3 power level, an ELMy regime fundamentally different to Ohmic/low-power-heating ELMy H-mode has been found (with large ELMs of lower frequency or small "grassy" ELMs). The presence of these ELMs allows establishing a stationary H-mode at constant density. The plasma energy increases by more than a factor two, with a very substantial increase of the ion temperature, due to collisions at these high densities.

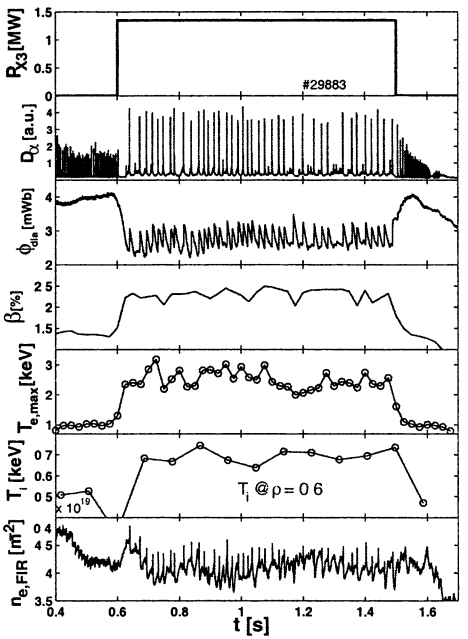

Fig. 11. β increase with X3 heating in H-mode. From top to bottom: X3 power, D_α showing ELM behaviour change, diamagnetic flux, total plasma β, Thomson scattering central T_{eo}, ion temperature at ρ = 0.6 from CXRS, line integrated density.

With the applied heating, the plasma β increases from 1 to β_{max} = 2.4%, with up to a normalised beta $\beta_N = \beta[\%]/I_N[\text{mT/MA}] = 2$ (with $I_N = I/aB \sim 1.25$ [MA/mT]), typically 3/4 of the ideal MHD Troyon pressure limit, see Fig. 12. Long stationary discharges, which are MHD stable can be obtained, but the large ELMs in these low q discharges can degrade the core confinement instantaneously [21].

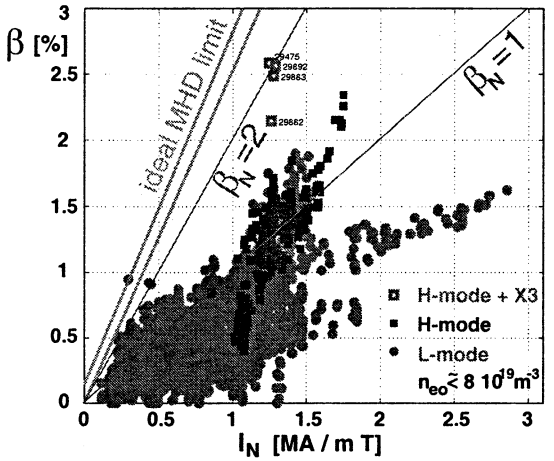

Fig. 12. β enhancement with X3 full power heating in TCV H-modes. The recent X3 heated H-modes (empty squares) reach a normalised beta $\beta_N \sim 2$, a sizable fraction of the ideal MHD Troyon pressure limit [21], also shown.

Encouraged by these results, we are presently studying the possibility of upgrading the installed X3 power on TCV by increasing the unit power of each existing gyrotron by approximately 30% (~600 kW/gyrotron) and by adding a fourth gyrotron with a LFS injection. In total, this upgrade would allow to nearly double the X3 power coupled to the plasma in X3.

Electron Bernstein wave heating in TCV

Electron Bernstein waves offer the possibility of heating low-field machines like spherical tokamaks or tokamaks with EC waves at densities far above the conventional cutoff density of O- and X-modes [22]. The first demonstration of EBWH on a torus took place on a stellarator. Bernstein waves heating can be of particular interest in low field tokamaks ($B \leq 3$–4 T), where the conventional EC cutoffs are typically lower than the Greenwald density limit.

With a low field side (LFS) launch, overdense plasmas are accessible through the double mode conversion O-X-B scheme. This scheme combines two advantages: it uses an oblique launch, minimising the risk of power reflec-

tion to the gyrotron, and permits coupling to Bernstein waves through a low-density path accessible to conventional O- and X-modes.

The refraction bends the oblique O-mode wave ray path until it nearly parallels the magnetic field lines, where O-X conversion occurs, and from where the wave propagates back towards the upper hybrid layer. The O-X conversion transmission function, as a function n of toroidal (z) and poloidal (x) refractive index is [23]:

$$T(N_x, N_z) = \exp(-\pi k_0 L_{ne} \operatorname{sqrt}(Y/2)\,[2(1+Y)(N_{z,opt} - N_z)^2 + (N_x^2)])$$

with $Y = \omega_{ce}/\omega$.

Thus, a large transmission angular conversion window requires 1) a high-density gradient, or small density scale length L_{ne}, 2) a central density n_{eo} above O-mode cutoff. The subsequent X-B conversion occurs naturally in a hot plasma close to the upper hybrid resonance layer. The converted B-wave propagates further to the centre where it is dissipated at the EC resonance harmonic. A typical O-X-B mode conversion ray path is shown in Fig. 13.

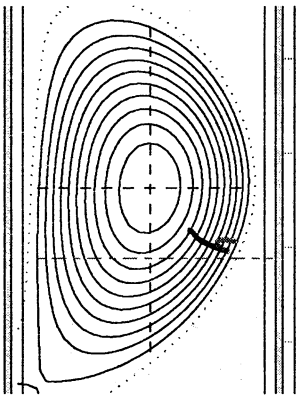

Fig. 13. Typical ray path in poloidal projection of an O-X-B wave conversion, launched from an equatorial TCV port (height indicated by the lower dotted line). The plasma magnetic axis is above equator (12 cm).

A low $q_{95} \sim 2.3$ Ohmic H-mode target plasma was developed ($I_p = 400$ kA, $\kappa = 1.8$, $\delta = 0.55$), with a slowly rising density, exhibiting ELMy and ELM-free phases, with adequate high edge density gradients. The heating studies [24] use a central density of $1.5 \cdot 10^{19}\,\mathrm{m}^{-3}$, typically half of the Greenwald density limit.

Prior to heating experiments, the value of the correct O-mode injection angles needs first to be determined. It has been noticed that the power of one gyrotron beam (0.47 MW) is influencing the H-mode properties, triggering ELMs or enhancing the D_α-emission with a delay of the order of 1–2 ms, associated with a simultaneous decrease of the power conversion. Therefore, to determine the angular conversion-absorption window without perturbing the H-mode, the power was injected in relatively short pulses at low power duty cycle (6%). The level of EC stray radiation, monitored at 180° toroidally, gives a measure of the converted power, see Fig. 14. The stray radiation is found to be low, i. e. indi-

cates good absorption, when the angle is set close to the expected optimal angle, and decreases asymptotically during the establishment of an ELM free phase.

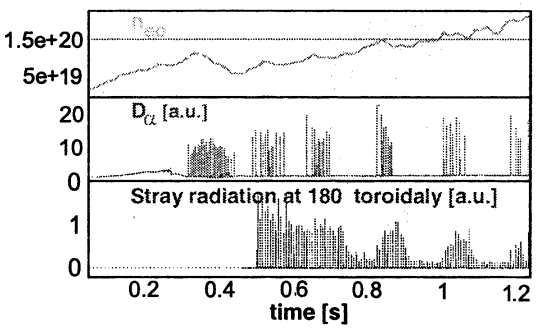

Fig. 14. ELMy H-mode with ELM-free phases, with density evolution, D_α-emission, and strong absorption (low EC stray radiation) during ELM-free periods.

A two-directional scan of the injection angle, searching for the minimum of the stray radiation around the presumed optimal angle, yields the optimal launcher angle position through interpolation. This experimental angle overlaps, within a 2° error, with the optimal angle determined from the ray tracing code ART [5], as shown in Fig. 15. This small difference is compatible with the uncertainty in the equilibrium reconstruction. In addition, the experimental window (15–20° FWHM) appears larger than the calculated one (8° FWHM), which can be due to the uncertainty in the n_e-profile determination in the region of the steep density gradient.

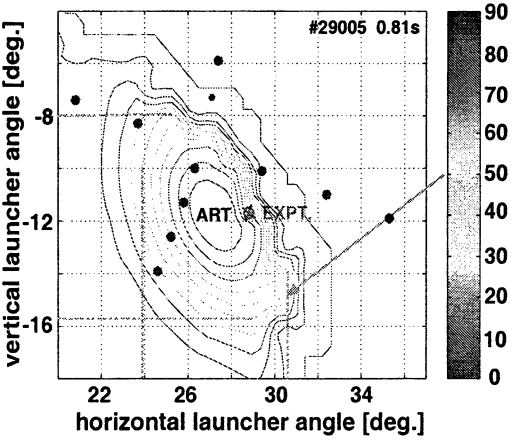

Fig. 15. Optimum angular absorption response (EXPT) from two experimental angular scan (dots) compare well with ART calculation (within 2 degrees).

With a higher duty cycle, the total power absorbed is measured from the modulated energy via the diamagnetic probe. A power of more than 60% of the injected O-mode power has been measured, as shown in Fig. 16.

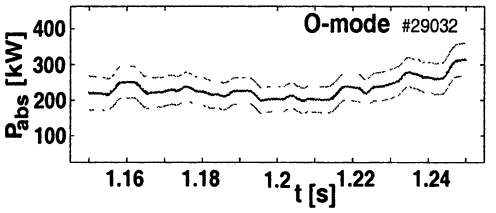

Fig. 16. Global power absorption in O-X-B conversion from the diamagnetic probe: the power absorbed (*a*), phase of DML signal vs. modulation (*b*).

With X-mode injection instead, there is no significant absorption, less than 10%, or with a knowingly wrong injection angle, the same measurement yields a very small-absorbed power.

Local power deposition is found on the soft X-ray DMPX wire-chamber camera, directly from the evolution of the soft X-ray emission at the heating pulse, as well as from Fourier transform, at a location close to the predicted power deposition from the ART code.

These high power EBH experiments demonstrate both local and global absorption of EBW wave using the O-X-B scheme in a conventional aspect ratio tokamak, in good agreement with the simulations.

Conclusions

Using the flexibility of TCV plasma shaping and the capability of varying the electron temperature and gradients with high power and localised second harmonic EC heating, it is possible to separate the independent effects of plasma shape and collisionality on electron heat transport. In these dominant trapped electron mode regimes, low and negative triangularity as well as high collisionality reduce electron heat transport.

In the moderate magnetic field TCV, third harmonic ECH X3 heating has allowed successful heating of H-mode plasmas approaching a sizeable fraction of the β-limit and demonstrating at the same time full power absorption of the X3 microwave power. At these high densities, the direct heating of the electrons by the ECWs and the indirect heating of the ions through collisions with the electrons both contribute to the plasma performance.

To add here for information, plasma scenarios in which the 2nd and 3rd harmonic EC heating systems can usefully be combined have been developed in TCV. This is the case for example in low current high elongation discharges, in which the 2nd harmonic X2 is used to increase the vertical stability margin through broadening of the current profile, while the plasma core, overdense to X2, is heated using the 3rd harmonic X3 [26].

For the first time in an overdense plasma of a conventional aspect ratio tokamak, EBWH, relying on the O-X-B mode conversion scheme, has been recently demonstrated in TCV, launching second harmonic waves from the LFS. This mode conversion scheme requires a steep density gradient at the plasma edge and a density overdense to O-mode, which both can be satisfied in TCV

Ohmic H-modes. The optimal launcher injection angles were determined experimentally from the EC stray radiation and compare well with ray tracing calculation. A global deposition exceeding 60% of the launched power was so far measured from the diamagnetic probe, and only within the prescribed conversion angular window. This heating can typically be useful in low field devices, where the conventional EC cutoffs are limiting the operation to density values well below the Greenwald density limit.

Acknowledgements

This work was partly supported by the Swiss National Science Foundation.

References

1. *Goodman T.P., et al.*, Proc. 19th SOFT, 1966, Lisbon, **I**, 565.
2. *Hogge J -Ph , et al.*, Nucl. Fus., 2003, **43**, 1353.
3. *Angioni C., et al.*, Nucl. Fus., 2003, **43**, 455.
4. *Matsuda K.*, IEEE Trans. Plasma Sci., 1989, **17**, 6.
5. *Volpe F., Laqua H.P., et al.*, Rev. Sci. Instrum., 2003, **74**, 1409.
6. *Harvey R.W., et al.*, Proc. IAEA Tech. Conf. Advanc. in Simul. and Modell. of Thermonucl. Plasmas, Montreal 1992, (IAEA, Vienna, 1992).
7. *Hofmann F., Tonetti G.*, Nucl. Fus., 1998, **28**, 1871.
8. *Lütjens H., et al.*, Computer Physics Comm., 1996, **97**, 219.
9. *Greenwald M., et al.*, Nucl. Fus., 1998, **28**, 2199.
10. *Camenen Y., et al.*, 32nd EPS Plasma Phys. Conf., Tarragona 2005, P1.052.
11. *Camenen Y., et al.*, Plasma Phys. Control. Fusion, 2005, **47**, 1971.
12. *Pochelon A., Camenen Y. et al.*, 20th IAEA Fusion Energy Conf., Vilamoura 2004, IAEA-CN-116/EX/9-1.
13. *Ryter F., et al.*, Nucl. Fus , 2003, **43**, 1396.
14. *Saibene G , et al* , Plasma Phys. Control. Fusion, 2002, **44**, 1769.
15 *Angioni C., et al.*, Phys. Plasmas, 2003, **10**, 3225.
16. *Dorland W., et al.*, Phys. Plasmas, 1997, **4**, 2482.
17. *Bottino A., et al.*, Phys. Plasmas, 2004, **11**, 198.
18. *Ryter F., et al* , Phys. Rev. Lett., 2005, **95**, 085001.
19. *Arnoux G., et al.*, Plasma Phys. Control. Fusion, 2005, **47**, 295.
20. *Alberti S., et al* , IAEA TM ECRH, Como 2005, accept. in J. Phys.: Conf. Series.
21. *Porte L , et al.*, 19th IAEA Fusion Energy Conf., Lyon 2002, IAEA-CN-94/EX/P5-15.
22. *Troyon F , et al* , Plasma Phys. Controlled Fusion, 1984, **26**, 209.
23. *Preinhaelter J., Kopecky V.*, J. Plasma Phys., 1973, **10**, 1.
24. *Mjølhus A., et al* , Plasma Phys., 1984, **31**, 7.
25. *Mück A., et al.*, 32nd EPS Plasma Phys. Conf., Tarragona, 2005, P4.410.
26. *Pochelon A., et al* , 19th IAEA Fusion Energy Conf., Lyon 2002, IAEA-CN-94/EX/P5-14.

CURRENT DRIVE, HIGH PERFORMANCE, INSTABILITY CONTROL AND PLANS FOR THE DIII-D GYROTRON INSTALLATION

John Lohr, Y. A. Gorelov, K. Kajiwara[1], *D. Ponce, R. J. La Haye, T. C. Luce, C. C. Petty, R. Prater, M. Wade*

General Atomics, San Diego, California, USA
[1]Oak Ridge Institute of Science Education, Oak Ridge, Tennessee, USA

The gyrotron complex on the DIII-D tokamak was used for 34 weeks of operation during the last experimental period. The entire complex is now shut down for a year while the DIII-D tokamak and the ECH systems undergo major modifications. The principal projects underway during this period are: rotation of one of the neutral beam lines to inject counter to the plasma current; installation of a new divertor; acquisition and installation of three new 110 GHz gyrotrons with the present 1.0 MW, 10 s performance specification; and installation and testing of a single stage 110 GHz depressed collector gyrotron having >1.0 MW long pulse capability. Following the modifications, the ECH system will comprise six production gyrotrons, plus the depressed collector prototype and a short pulse gyrotron held in ready reserve. Of these, six gyrotrons will be available for experiments at one time using the six transmission lines and three dual launchers. At least one of the launchers is expected to be capable of real time fast spatial scans at the resumption of operations.

Introduction

A multi-faceted experimental campaign has concluded on the DIII-D tokamak. In the area of evaluation of electron cyclotron current drive (ECCD) efficiency, a new technique was developed using EC injection modulated at 10 Hz to create a periodic response in the motional Stark effect polarimeter leading to a direct measurement of the spatial profile of the ECCD. Experiments on high performance operation were performed in which off-axis ECCD was used to adjust the current density profile. Noninductive discharges with about 60% bootstrap fraction were created in this way. By controlling the m/n = 3/2 island width, stationary discharges were produced having $q(0)$ slightly >1.0, which scaled to inductive ITER operation for 1 h at Q = 5–10. Preemptive injection of EC power at the $q=2$ surface was successful at preventing initiation of the m/n = 2/1 neoclassical tearing mode (NTM) and studies were performed on the control of the ECCD profile width required for stabilization of both 2/1 and 3/2 neoclassical tearing modes once the instabilities had developed. A series of measurements of the efficiencies of the separate elements of the electron cyclotron heating (ECH) transmission system and thermal performance of the articulating launchers was performed.

The DIII-D ECRH complex

During the 2004–2005 campaign, the DIII-D electron cyclotron resonance heating (ECRH) complex [1] comprised up to six gyrotrons operating

simultaneously, although the typical number of operating tubes was four, owing to several failures, which will be discussed below. The generated power was about 3 MW, of which about 2.2 MW was injected into the tokamak after passage through the transmission lines. The system includes two groups of gyrotrons in the MW class, with maximum pulse lengths at full power of 2.0 s and 10 s for the two types. Typical DIII-D maximum pulse lengths are 6–7 s and nearly all the experiments were performed with rf pulse lengths of 2–4 s. The present status of the gyrotrons that were operated during the most recent campaign is shown in Table 1.

Table 1. Summary status of the gyrotrons which have seen extensive service in the DIII-D system (τ_p is the maximum pulse length)

Gyrotron	Manufacturer	Date	P_{GEN}/τ_p (MW/s)	Operational Status/History
G1 (Katya)	Gycom*	1996	0.6/2.0	Normal operation/parasite; cathode efficiency is slowly decreasing, but operation is reliable with $P_{GEN} \sim 600$ kW.
G2 (Boris)	Gycom	2000	0.65/2.0	Removed from service in good condition for eventual use at PPPL on the National Compact Stellarator Experiment. $P_{GEN} \sim 750$ kW.
G3 (Natasha)	Gycom	2000	0.5/2.0	Retired/vacuum failure. Will be sent to PPPL for use on NCSX if repaired.
P1 (Scarecrow)	CPI†	2000	0.85/5.0	Normal operation. The gyrotron had its window replaced after failure of the aluminum seal and later had its collector replaced after a large water leak developed.
P2 (Tinman)	CPI	2000	0.65/2.0	Has a small leak in the bottom of the collector, which limits performance. The tube has been removed from service and sent to CPI for repair.
P3 (Lion)	CPI	2002	0.85/5.0	Gyrotron had a collector failure with substantial overheating, slight buckling of the structure and extensive stress cracking on the hot sides of the cooling tubes. Being repaired.

*Gycom, 46 Ulyanov St., 603950 Nizhny Novgorod, Russia.

†Communications and Power Industries, 831 Hansen Way, Palo Alto, California 94304, USA.

The oldest gyrotron in the complex, G1 (Katya), has been operating for about 8 years and has exhibited excellent reliability. This gyrotron has had a strong 100 MHz parasitic emission from the time of its first operation. The generated power from this tube has slowly decreased due to a slow decrease in cathode performance over time, but the generated power is still about 600 kW for 2 s pulse length.

In 2000, the DIII-D project acquired two similar gyrotrons from the closed Tokamak de Varennes. Both of these tubes performed well during the 2004–2005 and previous campaigns until the G3 (Natasha) gyrotron developed a vacuum leak and was removed from service. The DIII-D program plan calls for replacement of all the short pulse gyrotrons, which are limited in pulse length by heating of their boron nitride output windows, so G3 (Natasha) will not be repaired. At the end of the campaign, G2 (Boris) also was removed from service and is expected to be available to the National Compact Stellarator Experiment [2] at Princeton in about three years. Because the G1 (Katya) gyrotron is located in an area much closer to the tokamak than the other gyrotron sites, this tube is being kept in ready reserve, with the possibility of connecting to any of the six transmission lines midway between the main group of gyrotrons and the tokamak. The configuration planned for startup in late spring 2006 is shown in Fig. 1.

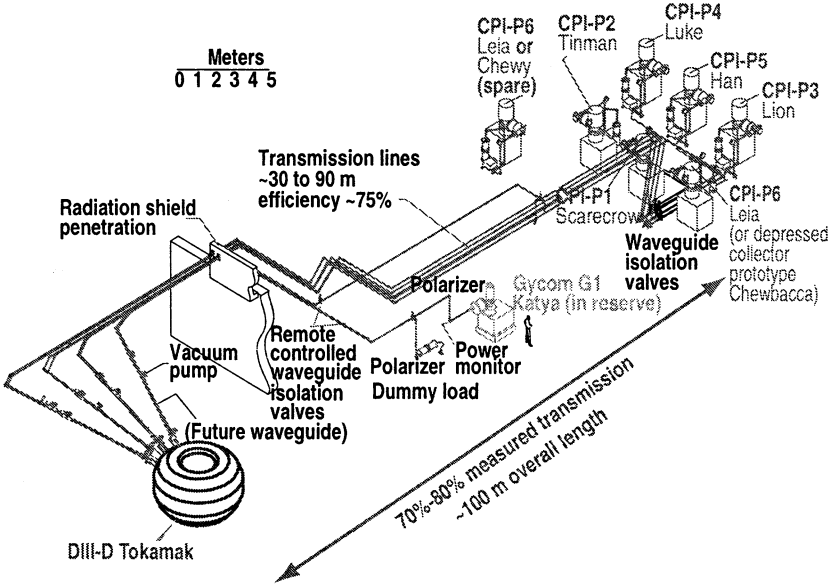

Fig. 1. Schematic diagram of the DIII-D gyrotron complex as it will exist for plasma operations in 2006. A total of six 1.0 MW, 10 s tubes will be available in addition to a depressed collector prototype operating at 1.2 MW, 10 s and a single short pulse tube, generating about 600 kW, 2.0 s in ready reserve. The system will have six transmission lines and two rapid scan launchers.

The DIII-D tokamak is presently in the middle of an extensive project to modify and upgrade the facility [3]. To provide for the possibility of balanced injection and co- versus counter-neutral beam injection experiments, one of the four NBI tanks is being rotated about 39 degrees to inject in the counter-current drive direction. At the same time, a new lower divertor geometry is being installed, which will permit higher triangularity discharges to be run. The final major element in the project will be upgrades to the gyrotron complex.

The gyrotron complex which operated for the 2004–2005 campaign will be improved for the 2006 campaign by replacement of the short pulse tubes with new tubes having CVD diamond output windows [4] and nominal 1.0 MW, 10 s output pulses [5]. These tubes are nearly identical to the first group of three long pulse tubes already installed. The major difference has been the addition of two 8 L/s vacion pumps in the region of the output window in addition to the two 75 L/s pumps in the collector. The testing to half power at 10 s pulse length for the first of the new gyrotrons was done more rapidly than had been the previous experience. About one month of around the clock operation was required, possibly because of the presence of these additional small pumps in a critical region. The first of the three new gyrotrons in this set was received at DIII-D in September and is expected to be ready for plasma operations in November. The second is expected to be finished with initial testing at CPI in November and will then begin testing at DIII-D to full parameters early in 2006. The third tube in the series will follow about 3 months later.

In parallel with the production of these three gyrotrons, CPI and the U.S. Gyrotron Development Program have built a single stage depressed collector gyrotron [6], which was tested for short pulses at 1.2 MW and measured efficiency of 44%. This gyrotron will be tested to full parameters at DIII-D during testing of the other three new tubes. Depending on the results of these tests, this tube either will remain as part of the DIII-D complex, or will be returned to CPI for modifications. There should be seven long pulse high power gyrotrons and one short pulse tube at DIII-D during the 2006 campaign, of which six can be used at any one time until additional transmission lines and launchers are completed. At least one of the dual launchers will have real time fast scan capability under control of the plasma control system. The steering mirrors will be capable of scanning at 10 deg/s for ±20 deg travel and at a rate of 100 deg/s for 2 deg movements. The positional accuracy for the rf beam will be about 1 cm at the tokamak center.

Gyrotron failures on the DIII-D system

A number of failures have occurred on the DIII-D gyrotron system during the past year. These were all related to loss of gyrotron vacuum. The Gycom gyrotron G3 (Natasha), which had been in service at DIII-D since 2000, developed a vacuum leak during normal operation. The leak was moderate, but prevented further operation. Because of plans to replace the short pulse gyrotrons

in the DIII-D system with long pulse tubes, it was decided to retire, rather than repair, this gyrotron. No specific cause of the failure was identified, although this gyrotron had been the most difficult of the short pulse tubes to operate for some time and also produced the lowest power for reliable operation.

Vacuum leaks localized to the collectors were experienced on all three of the CPI long pulse gyrotrons in the DIII-D complex. The common thread in the failures was operation during initial testing with collector power loading approaching 1 kW/cm^2. This limit had been established earlier in the gyrotron development program when initial testing at half power, 80 kV, 25 A, was performed without sweeping of the electron beams in the collectors. The cause of the first failure was cracking of the copper collector, but the cause was attributed to material problems with the copper. Following the second failure, which was concluded to have been caused by thermal stress in the copper collector, the stress calculations were revisited using more sophisticated models, with the result that a more conservative limit of 600 W/cm^2 was established. Collector sweeping during all gyrotron operation was required and stronger sweeping was implemented in order to meet the new limit. In addition, four quadrant power supplies capable of ±100 V, ±20 A were tested for use with the next group of three gyrotrons for the DIII-D system. These power supplies can produce an arbitrary time dependence of the sweep coil current. A test of a sawtooth waveform at 7 Hz gave a scalloped sweep magnetic field in the collector with minimum dwell at the low point in the collector sweep when the electron beam footprint is smallest. After limited operation under the new limit, no further failures have occurred.

One additional vacuum failure occurred in a long pulse gyrotron. In this case, the leak was in a poorly brazed joint in the cavity assembly, which could have been stressed by freezing of the stagnant cavity cooling water during a planned warm-up of the magnet over a holiday period. Although it was impossible to demonstrate bore freezing during subsequent tests, and no distortion of the cavity assembly, which could have been the result of freezing, was seen, new procedures for warming the cryogenic magnets were implemented, bore heaters were installed and a low temperature alarm was developed to forestall any similar problems. The three new gyrotrons in the current upgrade project will be equipped with cryogen-free magnets using Joule – Thomson coolers. These will not have sufficient thermal inertia to freeze the gyrotrons under any scenarios related to failure of the magnet cryostat vacuum, quench or warm-up.

Thermal measurements and analyses

Temperature measurements of gyrotron cooling water and launcher mirrors are used on the DIII-D ECH system to provide calibrated injected rf power on a shot by shot basis and provide a diagnostic of the performance of the launchers. These measurements will be described in this section.

A total of approximately 2 MW is dissipated in the gyrotron cooling water during pulses at full power operation. This water is circulated through several circuits and the temperature rise and measured flow can be used to determine the power loading on the various gyrotron components calorimetrically and to calculate the generated rf power. The maximum water pressure is about 10 bar. Coupled with measurements of the transmission line efficiencies, these thermal measurements permit the rf power injected into the tokamak to be inferred. After passing through the gyrotron cooling circuits, the water flows to a cooling tower heat exchanger and then returns to the gyrotrons in a closed circuit loop. Unfortunately, in the DIII-D system the mixing of the water is extremely poor, therefore packets of heated water produce ghost ΔT signals with similar time dependence to the real time signal that can, after the firing of several rf pulses, interfere with the accuracy of the real time measurement. Circuits which have long cooling times, such as the dummy loads (*D/L*) and the matching optics units (MOU), are especially susceptible to errors from ghost heat pulses, while fast responding circuits such as the output window and cavity, have very small ΔT signals with attendant signal/noise measurement difficulties. The characteristics of the calorimetry measurements on the DIII-D systems are presented in Table 2.

Table 2. Calorimetry circuit characteristics for a 1 s rf pulse at ~700 kW generated rf power. The power for each circuit is given as a percentage of the generated rf power

Calorimetry circuit	Flow (l/min)	Time response (s)	Power (%)	ΔT (°C)
Collector	1200	20	220	4.0
Cavity	80	10	2.3	1.0
Diamond window	20	5	0.2	0.3
BN window	28	400	4	0.2
MOU	12	200	5–18	1.0
Waveguide *D/L*	240	20	60	10
Backstop *D/L*	30	300	40	2.0

The long time constant calorimetry data were analyzed by developing an analytical fitting function which takes into account the heating portion and then the cooling portion of the measurement cycle, the specific heats of the various components and coolant, heat transfer coefficients and suitable boundary conditions. The problem and the quality of the fit to the calorimetry response using this function are illustrated in Fig. 2, in which it is clear that the function provides an excellent fit to the calorimetry characteristic and results in a decrease in the scatter in the data for pulses of various lengths from ±15% to about half that value.

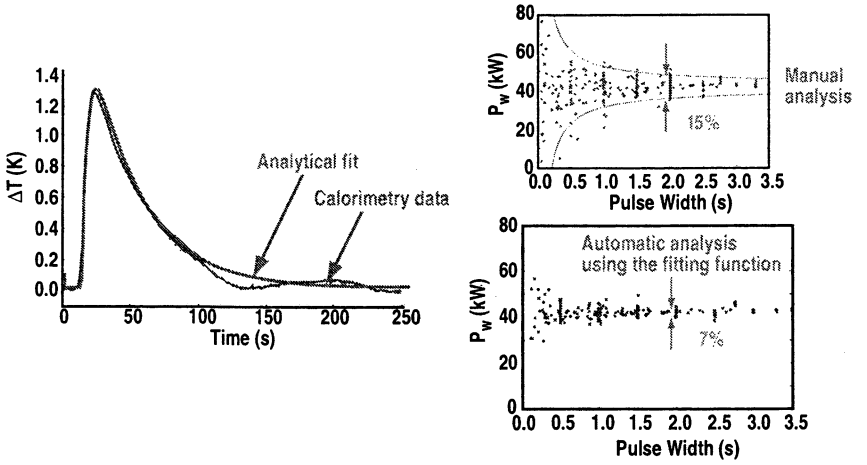

Fig. 2. On the left a typical calorimetry trace is shown, with ghost ΔT signals registered as variations from an exponential characteristic after the end of the heating pulse. The analytical fitting function is seen to provide a good representation of the data and in the summaries of a number of pulses on the right, is seen to reduce the scatter in the measurement by about a factor of 2, with statistical accuracy approaching ±5% for the longer pulses. For the gyrotron cavity, P_W, the power absorbed by the cooling water, is about 40 kW.

The data, including the time dependent flow from the vortex flow monitors, are acquired during and after an rf pulse and then are fit once the data acquisition has been completed. The data are archived, analyzed for accuracy, corrected for the measured transmission line efficiencies and then are added to the DIII-D database for that shot. Conditioning pulses in between tokamak discharges invalidate use of the MOU calorimetry for power determination, but in such cases the system disregards the MOU data. In general, calorimetry on the cavity cooling has provided the best accuracy, although this relies on a prior determination of the relationship between cavity heat load and generated rf power. The system provides a power measurement with better than ±7% accuracy on each tokamak shot. Efforts are underway to develop a suitable rf pickoff near the DIII-D machine for providing real time power measurements, but thus far the calorimetric measurement has provided the best accuracy.

Performance of the launcher mirrors in the DIII-D vacuum vessel [7] is measured using resistance temperature devices (RTDs) attached to the back surfaces of the mirrors and by relating the time dependent measurements of these temperatures to the mirror surface temperatures using experimentally verified models. Each launcher has a pair of mirrors to focus and direct the rf beam. The fixed focusing mirrors are Glidcop and are securely mounted to the launcher structure. The steering mirrors have flat copper reflecting surfaces which are bonded to a laminated structure of copper and stainless steel designed to reduce

eddy current induced loads. The mirrors are radiatively cooled to the launcher shroud and have performed well. Temperature measurements from the RTDs are shown in Fig. 3 for a series of rf pulses into the DIII-D vessel during plasma operations.

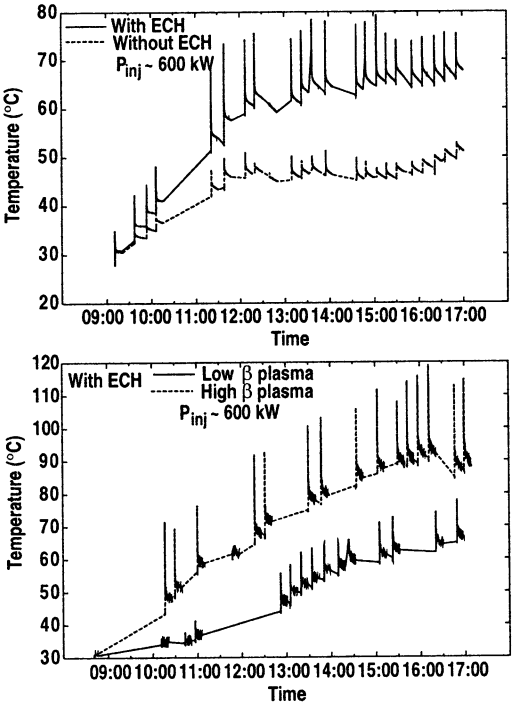

Fig. 3. The daily record of RTD measurements comparing equivalent ECH and no ECH shots at about 600 kW injected power for 2 s pulses in the upper figure and ECH shots at high and low beta in the lower figure. For the worst case, ECH at high beta, the peak RTD measurement was 120 °C late in the day. In the comparison between ECH and no ECH shots, it is seen that about half of the power loading was from plasma radiation, and half from heating by the rf reflected from the steering mirror.

During the course of a day's tokamak operations using about 600 kW injected power at 2 s pulse length, the temperatures measured by the RTDs on the back surfaces of the mirrors ratchet up to about 100 °C during the periods between rf pulses. The maximum increases are about 20 °C during the pulses. As can be seen in the upper portion of Fig. 3, which presents a comparison of the measurements for plasma operation with and without ECH, plasma radiation accounts for about half of the heating of the mirrors. The worst case is documented in the lower part of the figure, which shows the difference between high and low beta operation with rf injection. The maximum measured tem-

perature on the back of the mirror approaches 120 °C during the pulses late in the day when the baseline temperature has increased to about 90 °C. Calibration of the thermal response of the system using heat sources or ice applied to the mirror surfaces permits the peak surface temperature on the mirror to be inferred from the RTD measurements on the back surface. Such a calculation is summarized in Fig. 4, where the model was used to calculate the peak mirror surface temperature for a 1.2 MW 5 s rf pulse with Gaussian profile and the worst case polarization with the electric vector in the plane of the reflection. The peak surface temperature for this case is calculated to be about 500 °C, which is acceptable for Glidcop. After two years of experimental operation, there was evidence of isolated tracking on the mirror surfaces, but the overall condition was excellent.

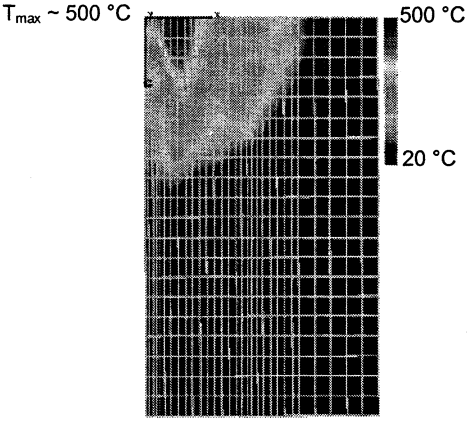

Fig. 4. Based on calibrated model calculations and the data shown in Fig. 3, the maximum mirror surface temperature for a 1.2 MW, 5 s rf pulse is predicted to be about 500 °C, which is an acceptable result for these radiatively cooled mirrors. The model invokes symmetry and shows the temperature on one quarter of the mirror surface.

Summary of experimental results

The DIII-D facility was active for a total of 34 experimental weeks during the 2004–2005 campaign. This was the longest period of continuous operation in the history of the facility and was done to create a time window to accommodate the major modifications discussed above. The typical schedule was two or three weeks of plasma operations followed by one or two weeks of maintenance activity. Many of the experiments made use of the ECH system and for some the system was a major element. Some of the ECH-related experiments will be described briefly.

A major line of investigation continued to be suppression of NTMs [8] using ECCD to restore a stable current density profile and eliminate islands that

decrease confinement and can lead to disruptions. Attention continued to focus on the m/n = 2/1 and 3/2 modes. In Figure 5, a shot is shown which is particularly complete in its illustration of the effects. Beta increased as the neutral beam power was increased. When β_N, a normalized indicator of beta, reached about $4 \times l_i$, the 2/1 NTM began to grow, decreasing β_N. The NTM was immediately suppressed by 2 MW of ECCD applied at the $q = 2$ surface, after which it was possible to restore the previously unstable β_N by ramping up the neutral beam injection (NBI) power. When one gyrotron dropped out, it was impossible to maintain the suppression and the NTM returned.

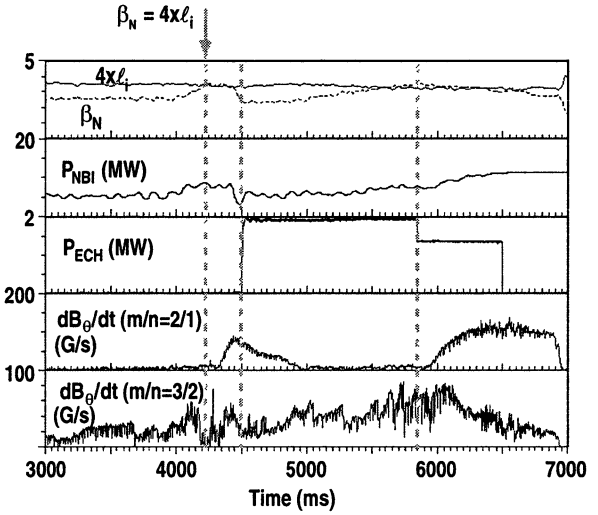

Fig. 5. Evolution of a discharge in which ECCD applied at the $q = 2$ surface suppressed the m/n = 2/1 NTM. The mode returned when one gyrotron dropped out and the rf power decreased.

A significant development in the NTM suppression experiments was preemptive NTM suppression, which is shown in Fig. 6. The previously described shot was followed by a shot on which ECCD at the $q = 2$ surface was applied prior to the development of the 2/1 NTM. Increasing the neutral beam power then increased β_N to the threshold in the previous discharge for driving the NTM unstable, but it did not grow until after the ECCD terminated. This result is significant for large machines like ITER, because it means that the possibility exists to increase the operating window for the machine without getting perilously close to conditions for disruption.

Although operation of the ITER device is still many years away, its operational scenarios are being investigated on a number of tokamaks worldwide. At DIII-D, plasma shaping studies coupled with active control of the $q(r)$ profile with nearly fully noninductive current drive are leading to operational scenarios

for ITER which push the ITER extrapolation to higher beta and better overall performance. Discharges in this Advanced Tokamak (AT) scenario [9], Fig. 7, have strongly inverted $q(r)$ profiles, with $q_{min} > 2$, which is controlled by relatively low EC driven current at large values of normalized radius, $\rho \sim 0.55$.

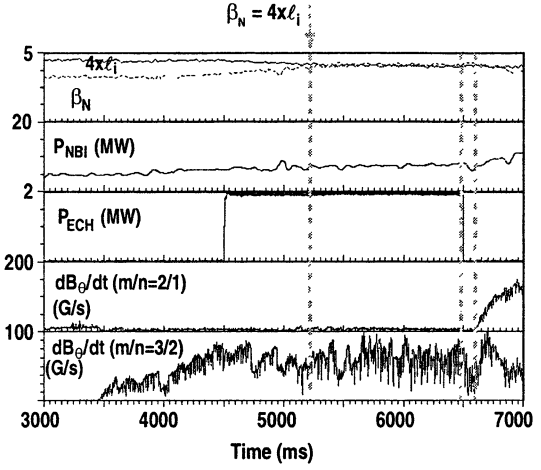

Fig. 6. Preemptive suppression of the 2/1 NTM is demonstrated. In this discharge, co-ECCD at $q = 2$ was applied prior to growth of the 2/1 NTM and the mode onset was delayed until the termination of the ECCD.

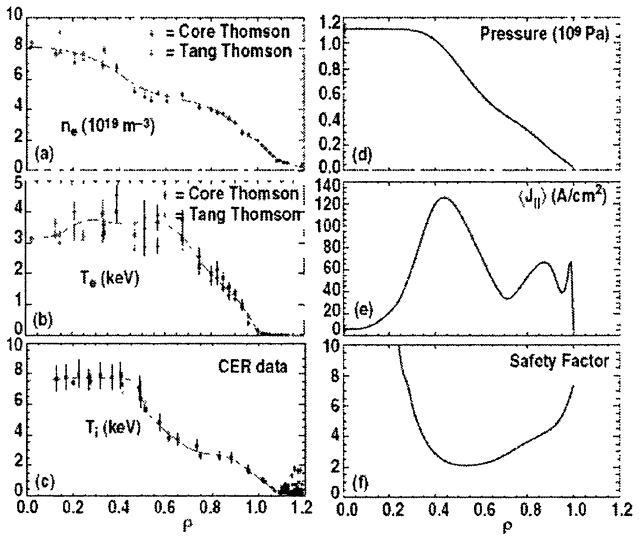

Fig. 7. The DIII-D AT scenario has a strongly inverted q profile, with hollow current density profile and $q_{min} \sim 2$. The mode is not stationary on DIII-D with the non-inductive power available at present.

These discharges are formed by ramping down the toroidal field while ramping up the plasma current and have $\beta_T \sim 6\%$, $\beta_N \sim 6 \times l_i$. Although the discharges are developed using non-stationary techniques as seen in Fig. 8, the high performance phase is quasi-stationary or over 2 s with a large noninductive current fraction and probably can be sustained with higher noninductive current drive. Very small ECCD compared with other noninductively driven currents can have a disproportionate effect on the performance of the AT discharges, as in the case where only about 5% of the total current is due to ECCD at $\rho \sim 0.55$.

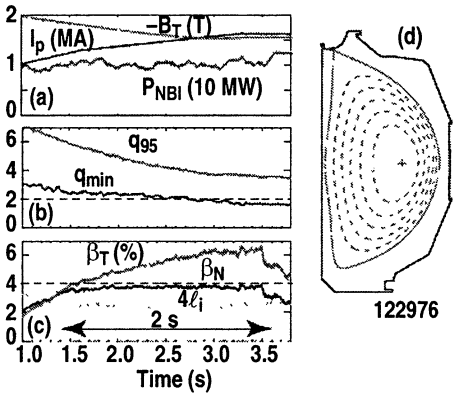

Fig. 8. At present, advanced tokamak discharges are produced on DIII-D by noninductive means, such as this example where the toroidal field was ramped down and the current ramped up to maintain a quasi-stationary configuration with high performance.

It is probable that very high performance discharges can be achieved in ITER using the AT scenario, but the machine can also be successful with more modest extrapolations from present device performance when plasma parameters can be controlled, possibly using innovative techniques. In DIII-D, a specific mode called the "Hybrid Mode" [10] has been studied, which makes use of the fact that the width of the 3/2 NTM island can be controlled by ECCD and this in turn can affect $q(0)$. In suppressing the NTM, co-ECCD is applied at the q surface corresponding to the mode and the island width shrinks. When counter-ECCD is applied at the same q surface, the island grows. To some extent the central temperature is affected by the presence of the island, as can be seen in Fig. 9, where ECE T_e data shows that periodic changes in the electron temperature at the island location periodically affect the central temperature with a phase shift. This can be used to control the central q value, through coupling between $T_e(0)$ and the current density, at a value slightly greater than 1.0 for long periods of time as seen in Fig. 10.

The potential for control is shown in Fig. 11, in which $q(0)$ is plotted as a function of island width for two discharges in which co- and counter-ECCD were used and a search algorithm was used to place the ECCD at the island location.

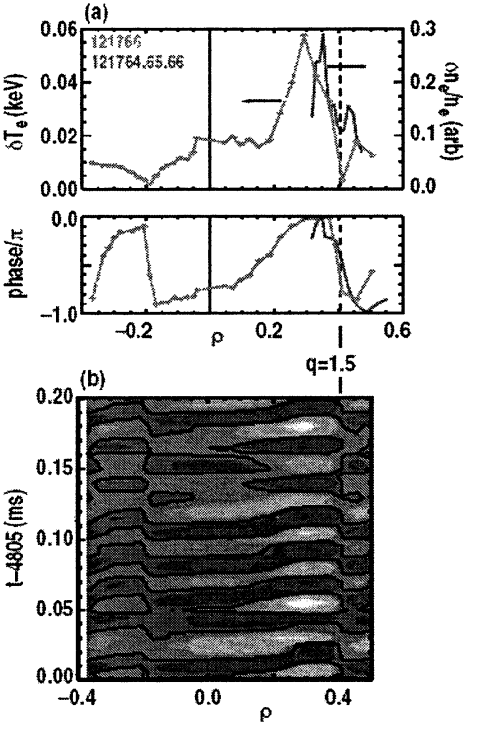

Fig. 9. The fluctuations in T_e at the 3/2 NTM island location affect the central temperature and hence the central current density.

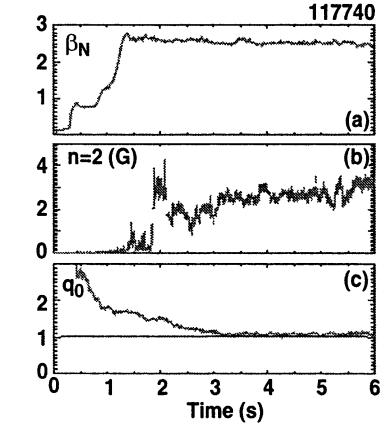

Fig. 10. By controlling the width of the NTM island with co- and counter-ECCD, $q(0)$ can be held slightly >1.0 for extended periods of time. This mode of operation is called the "Hybrid Mode".

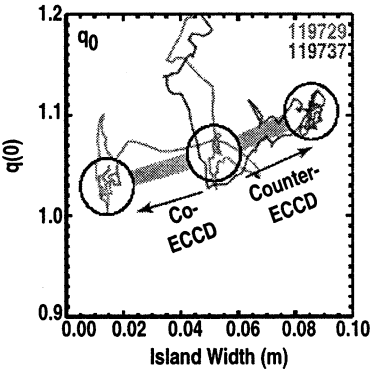

Fig. 11. Two discharges are shown in which co- and counter-ECCD was used to affect the island width for the 3/2 NTM. Co-ECCD shrinks the island and counter-ECCD increases the size, with concomitant effect on the q profile.

To summarize, the Hybrid Mode makes use of inductively driven main plasma current, and does not represent a radical departure from present tokamak operational scenarios. The operation is very robust and stable and $q(0)$ can be controlled in part by regulating the width of the 3/2 island with ECCD. The mode extrapolates from the DIII-D operation to one hour discharges in ITER with $Q \geq 10$.

Summary

When the DIII-D facility resumes operations in mid 2006, the ECH complex will include six gyrotrons with 1.0 MW nominal output for 10 s pulse length. An additional gyrotron in this class will be available in reserve and one short pulse gyrotron will be available as a hot spare, able to be incorporated into the system on any of the waveguide lines. The next series of experiments will focus on applying this nearly factor of two increase in power and long pulse capability to extensions of a wide range of experiments in support of the ITER development.

Acknowledgement

This work was supported in part by the U.S. Department of Energy under DE-FC02-04ER54698 and DE-AC05-76OR00033.

References

1. Lohr J., *et al.,* Fusion Sci. Technol. **48**, 1226 (2005).
2. Neilson G.H., *et al.,* J. Plasma Fusion Res. **78**, 214 (2002).
3. Luxon J.L., *et al.,* Fusion Sci. Technol. **48**, 807 (2005).
4. Thumm M., Diamond and Related Materials **10**, 1692 (2001).
5. Blank M., *et al.,* Proc. Int. Workshop on Strong Microwaves in Plasmas, A.G. Litvak, Editor. Russian Academy of Sciences, 2003, vol. 1, p. 7.
6. Felch K., Blank M., Borchard P., Cahalan P., Cauffman S., Chu T.S., Jory H , Recent ITER-Relevant Gyrotron Tests, Proc. 3rd IAEA Technical Meeting on ECRH Physics and Technology for ITER, to be published in J. Physics, Conference series.
7. Kajiwara K., *et al.,* Radio Frequency Power in Plasmas, Wukitch and Bonoli, Editors, American Institute of Physics, 2005, p. 407.
8. La Haye R.J., *et al.,* Phys. Plasmas **9**, 2051 (2002); La Haye R.J., Fusion Sci. and Technol. **48**, 906 (2005).
9. Greenfield C.M., Fusion Sci. Technol. **48**, 1178 (2005).
10. Politzer P.A., *et al* , The Role of the *m/n* = 3/2 Tearing Mode in the Hybrid Scenario in DIII-D, Proc. 3rd Euro. Conf. Plasma Phys., and General Atomics Report GA-A25094 (2005).

ELECTRON CYCLOTRON HEATING AND CURRENT DRIVE ON TORE SUPRA 2002–2005

M. Lennholm, J. F. Artaud, F. Bouquey, G. Berger-By, J. Clary, C. Darbos, R. J. Dumont, L. G. Eriksson, G. Giruzzi, F. Imbeaux, M. Jung, R. Lambert, R. Magne, A. Montecot, S. Poli, F. Rimini, D. Roux, E. Traisnel, J. L. Segui, X. Zou

Association Euratom-CEA,DSM/DRFC,CEA/Cadarache,
13108St. Paul-lez-Durance, France

The ECRH/ECCD system on Tore Supra, with its front steering antenna and its long pulse capability makes it ideal for testing essential technical and physics issues for ITER. This paper report the experimental results obtained and the technical evolution of the system since the last "Strong Microwaves in Plasmas" workshop. The observation of a clear synergistic effect between Electron Cyclotron Current Drive and Lower Hybrid Current Drive in fully non-inductively driven plasmas allowing a significant reduction in the Lower Hybrid power required to drive the plasma current is one of the major results of recent experiments. In another series of experiments ECCD has been exploited for studies of advanced scenarios with strongly or weakly reversed shear, resulting in high core electron temperatures and steep gradients The operation of the system was halted for a year following a water leak in the armored water bellows feeding cooling water to the antenna mobile mirror. This incident highlighted the difficulty of cooling mobile components inside the vacuum vessel and a major modification in the mirror cooling system was implemented as a consequence. With these modifications the first test of control of the ECRH/CD injection angle in real time should proceed in the upcoming experimental campaign.

Introduction

At the previous "Strong Microwaves in Plasmas" conference, held in 2002, the Status of the Tore Supra Electron Cyclotron Heating and Cur rend Drive System was reported together with the Physics results achieved in its first operational years [1]. The present paper starts where the previous paper left off. In the following, we will describe the ups and downs of the continuing evolutions of gyrotrons and antenna as well as a few selected experimental results obtained over the past 3 years.

Gyrotron evolution

As described in [1] the second gyrotron delivered to Tore Supra achieved 300 kW for 111 s in 2001. This result, though a world record at the time, did not fulfil the specifications (400 kW for 210 s). The limitation was seen as a strong out gassing in the gyrotron commencing around 60 seconds into a pulse. Spurious oscillations observed in the gyrotron output spectrum were shown to originate in the "injector" (the mode converter that converts the high order mode in

the gyrotron cavity to a Gaussian beam). These spurious modes could, according to calculations, explain additional losses inside the gyrotrons of about 10 kW [2, 3].

In collaboration with Thales Electron Devices (TED), a modified gyrotron has been designed and constructed. The cooling of the mirror box which focuses the beam emitted by the injector onto the gyrotron window has been enhanced and well cooled areas have been made from stainless steel to enhance RF absorption while less well cooled areas are made from copper to reduce local RF heating (Fig. 1). The ion pumps which maintain the gyrotron vacuum, originally situated inside the gyrotron, have been moved outside the gyrotron volume and protected from stray microwave radiation by copper grills. In addition the original cylindrical injector has been replaced by a conical injector (Fig. 2) with an angle of 0.1°, which according to theoretical calculations should be sufficient to eliminate the spurious oscillations [4, 5].

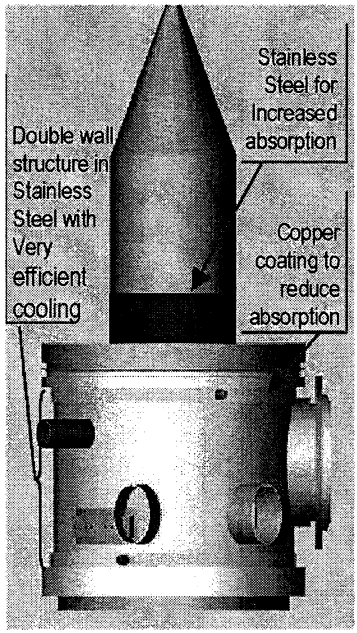

Fig. 1. Gyrotron cooling upgrade

In factory tests at Thales Electron Devices (TED) with pulse lengths up to 5 s, the redesigned gyrotron showed improved behaviour and very rapid conditioning. No spurious oscillations were observed, confirming that the conical injector indeed resolved this problem. In a series of 5 second pulses repeated with a duty cycle of 10% excessive heating of the transmission line connected to the gyrotron was observed. The cause of this overheating was found to be the poor quality of the beam emitted by the gyrotron. In fact subsequent detailed measurements have shown that the gyrotron emits a double hump beam which is much too wide at the interface with the waveguide to achieve decent coupling to the HE11mode (Fig. 3) [4, 5]. Despite these problems it was decided to proceed with high power tests at Cadarache. The focusing mirror in the MOU was redesigned for better coupling to the HE11mode and additional cooling was installed on the transmission line. Unfortunately, as testing was about to start, the gyrotrons saffire window was damaged by arcing, preventing any further testing.

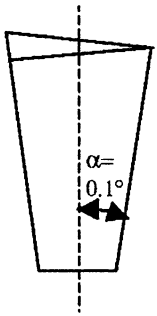

Fig. 2. Conical injector

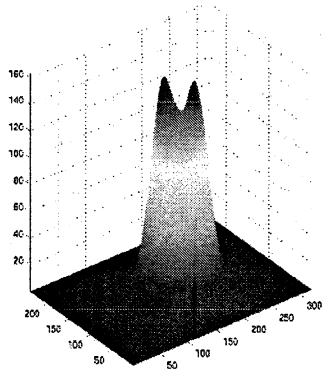

Fig. 3. "Double hump" Gyrotron output beam.

While we feel uncertain whether we can purchase gyrotrons "polluted" by spurious oscillations or emitting a double beam and while continuing investigations have failed to explain the double beam, manufacture of gyrotrons has been halted pending a decision œ or preferably an explanation and remedy for the double beam.

Antenna

The direction of the beam launched by the antenna can be varied both toroidally and poloidally by moving mobile mirrors situated inside the vacuum vessel. The position of each mobile mirror is controlled in real time with a time response of the order of 0.5 s by two stepper motors. The mobile mirrors are cooled through armoured bellows with water at pressures up to 30 bar and with temperatures up to 150 deg. [1, 2, 6]. These bellows remain, as mentioned in [1, 6], the most critical parts of the antenna and unfortunately this has been proven correct, as the bellows have ruptured twice in the past years. The second rupture followed tests of the real time injection angle control and was the result of approximately 100 full range movements. The rupture was caused by a twisting torque applied to the bellows during mirror movements. In the original design only two bellows, one for inlet water and one for outlet water, were used for each mirror. With such a design and given the fact that the mirrors rotate about two perpendicular axes it is impossible to avoid subjecting the bellows to twisting torques. As a consequence the mirror cooling was redesigned, using four bellows per mirror, two taking up the rotation around a vertical axis of the frame supporting the mirror, and two taking up the rotation around a horizontal axis of the mirror with respect to the frame. To assure the reliability of the new layout, the bellows were endurance tested in the new design configuration. Several design iterations were necessary in order to find a satisfactory design allowing 50000 cycles of full range movement. Figure 4 shows photographs of the original, two bellows, layout together with the new, four bellows, layout [7].

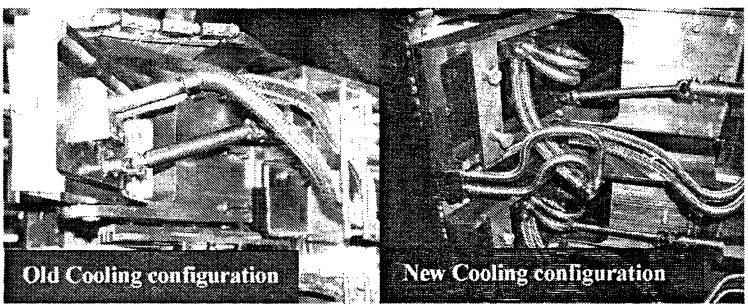

Fig. 4. Antenna cooling before and after modification

Real time control of injection angles

The toroidal and poloidal injection angle are controlled using two stepper motors for each of the three mobile mirrors. The architecture of the injection angle control is illustrated in Fig. 5. The stepper motors are controlled from the central ECRH fast controller via a serial link and local stepper motor controllers. The positions of the pushrods driven by the stepper motors, which in turn rotate the mobile mirrors around vertical and horizontal axes, are measured by linear motion potentiometers. Using these measurements, which are acquired in real time by the fast controller, closed loop control of the injection angles have been demonstrated [7]. As seen in Fig. 5 the ECRH fast controller also communicates in real time, via a reflective memory network, with a central control computer and with a range of different plasma diagnostics. Using this facility closed loop control of a variety of plasma parameters using the ECRH injection angles as the actuator is feasible and the first experiments demonstrating this are planned for the upcoming experimental campaign.

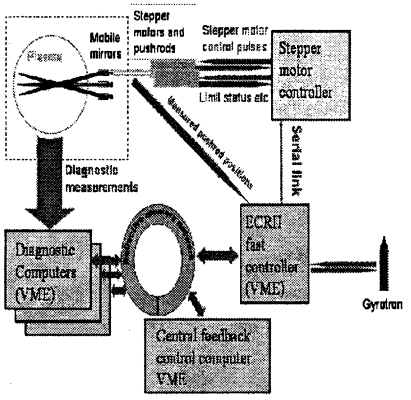

Fig. 5. Real time injection angle control

Polarisation

The Tore Supra ECRH system is designed for power deposition near the fundamental Electron Cyclotron resonance when the maximum toroidal field is used and near the second harmonic electron cyclotron resonance in pulses at reduced toroidal field. To assure maximum absorption in these two cases the polarisations of the waves launched by the antenna have to be adjusted to couple to the Ordinary mode (O-mode) and extraordinary mode (X-mode) respectively. As the injection angles – in particular the toroidal angle – vary, the polarisation of the wave should vary in order to maintain pure O-mode or pure X-mode injection. The polarisation is adjusted using two corrugated mirrors situated in the matching optics unit at the output of the gyrotron. Figure 6 shows the required corrugated mirror settings to achieve pure O-mode (or X-mode) injection as a function of the toroidal and poloidal injection angles.

The polarisation calculations [6] have been verified through low power measurements as shown in Fig. 7 [8], where the measured and calculated ellipticities are compared. The polarisation has also been verified at high power during

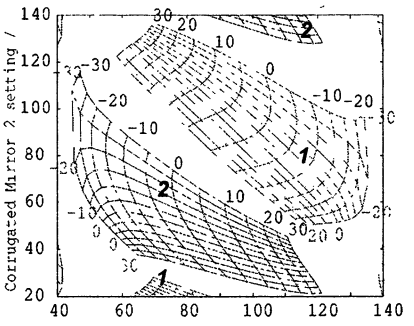

Fig. 6. Polarising mirror setting for pure X (*1*) or O (*2*) mode injection as a function of injection angles.

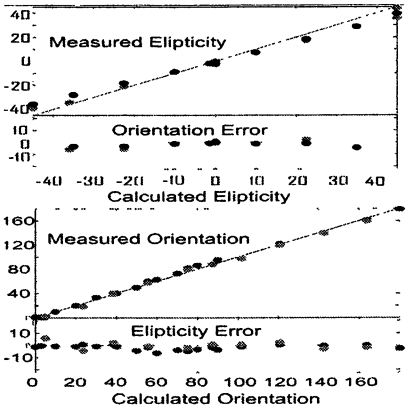

Fig. 7. Low power polarizer verification

plasma experiments [6]. For the time being the Polarising mirrors can only be varied between plasma pulses, as manual intervention is required. A system for real time control of the position of these mirrors is being studied. Meanwhile, almost pure O- (or X-) mode coupling is achieved over the full range of poloidal injection angles if the Toroidal injection angle is only varied by a few degrees around the value for which the polarisers are adjusted. As a consequence good mode purity can be maintained in real time control experiments without adjusting the polarising mirrors, as long as the control algorithm primarily varies the poloidal injection angle.

Experimental results

One of the most – if not the most – important assets ofECRH/ECCD over other means of plasma heating is its very localized and controllable power deposition. Over recent years ECRH plasma experiments exploiting this property have been performed using the two available gyrotrons, to inject up to 800 kW of ECRH/ECCD power for up to 31.5 seconds. A number of different results have been achieved, a few of which will be detailed in the following sections.

LH-ECCD synergy

The Tore Supra Tokamak is a long pulse machine, in which superconducting coils produce a toroidal field of up to 4 T. Using a combination of inductive and non-inductive Lower Hybrid (LH) current drive, the plasma current can be sustained for times which are long with respect to typical resistive diffusion times. In such long pulses in conditions of full non-inductive current drive – the longest of which has lasted for > 6 minutes with a plasma current of 0.5 MA – the primary fluxis controlled to maintain zero loop voltage and the plasma current is kept constant by real time control of the LH power.

Figure 8 shows a typical – though fairly short – pulse operating in this scenario. After and initial inductive current ramp-up phase current in the flat-top phase is 100% non-inductively driven, mostly by LH current drive, the bootstrap current giving only a small contribution. In the current flattop the density is $1.5 \cdot 10^{19} m^{-3}$ and the central electron temperature reaches 7 keV. In the middle of the current flat top a pulse of 700 kW of ECCD is applied for 10 s and, as a result, the Lower Hybrid power required to sustain the plasma current is reduced by approximately 500 kW. Simplistically speaking 500 kW of LH power has been replaced by 700 kW of EC power. This would correspond to an EC current drive efficiency which is almost the same as the current drive efficiency of LH. According to theoretical calculations, confirmed by experiments, such current drive efficiency cannot be achieved with EC alone. The experiment has been carried out with a variety of different deposition radii for the ECCD power. Figure 9 shows a comparison of the additional current driven in the presence of ECCD over and above the current which LH alone would have driven given a plasma with the same temperature, density etc. It also shows the current which ECCD should have driven in these plasmas in the absence of LH [9].

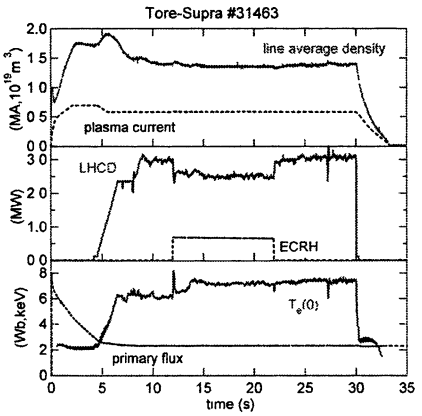

Fig. 8. EC-LH synergy pulse

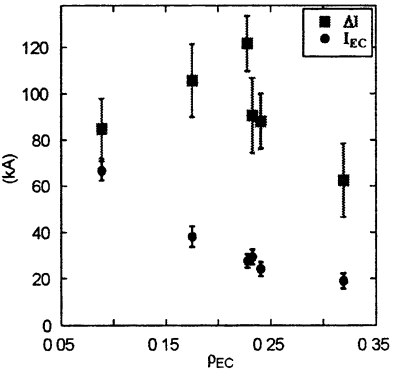

Fig. 9. Predicted EC current I_{EC} and total measured current minus LH current ΔI

In order to explain the observation, a synergistic effect – which has been theoretically predicted – between LH and EC has to be evoked. The Simple explanation of this theory is that the EC waves heat electrons with parallel velocities at the lower end of the LH tail moving them to higher parallel velocities where the LH current drive efficiency is enhanced. A synergy factor ($F_{syn} = \Delta I / I_{EC}$) [10] has been defined as the ratio of the two currents shown in Fig. 9. Figure 10 shows very good agreement between the measured synergy factor and values predicted from Kinetic Theory using a 3d Fokker plank code [11].

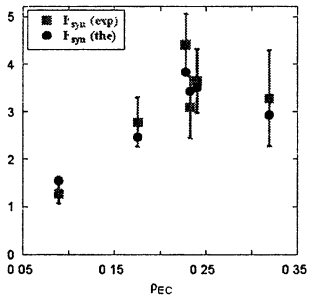

Fig. 10. Predicted and measured synergy factors

Although the overall current drive efficiency is not above that of LH alone, the importance of this observation is that the synergy current is driven in the region of EC absorption and thus not only the EC current but also a significant part of the LH current benefits from very narrow localization in minor radius. Thus the high current drive efficiency of LH can be combined with the narrow driven current profile associated with ECCD. This in turn can significantly reduce the overall power needed for current profile control for advanced scenario development and mode stabilisation. The synergistic effect is a positive indication that a combination of LH and EC current drive can be a very efficient tool to achieve control of the q-profile.

Advanced scenario development

In another set of experiments ECCD has been exploited for detailed control of the current profile [12]. The aim is to reproduce the improved confinement scenarios achieved on other machines by creating a flat or hollow current profile with the use of heating early in the initial current ramp-up phase.

Figure 11 shows the time evolution of such a pulse on Tore Supra. High central electron temperature is obtained and sustained into the current flat top. Very steep temperature gradients are observed in the initial phase. These steep temperature gradients, located around a normalised minor radius of 0.2, are associated with very hollow q-profiles with q_{min} also located near minor radius of 0.2. The good confinement is lost at the occurrence of the first sawtooth when q_{min} reaches 1.

Figure 12 shows electron temperature profiles for a series of similar pulses using either on-axis counter ECCD or off axis co ECCD or a combination of the two. For the on axis shots the results with and without added ICRH power are also shown. At a first glance it seems that the on axis counter current case is clearly the best. On second thoughts, however, the very narrow region of high temperature, associated with very high temperature gradients not far from the centre represents a rather unstable situation. As the aim is to create an improved confinement – and to sustain it for long periods – the ideal situation would be to create the steep temperature gradients at larger minor radii. In order to achieve this, co-current off axis ECCD is probably more desirable, although this would require more ECCD power – and/or a use of the LH EC synergy effect. Achieving improved confinement over a significant part of the plasma volume and sustaining this for a significant periodis an essential element in advanced tokamak operation scenarios for ITER. Future experiment on Tore Supra will focus on this line of research.

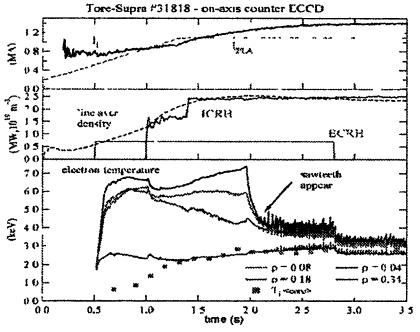

Fig. 11. ECCD in current ramp up

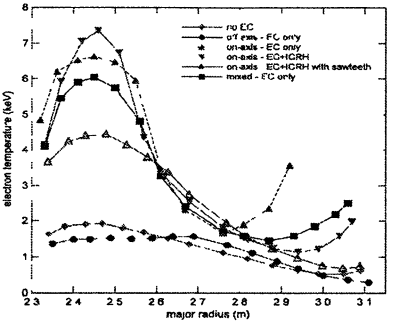

Fig. 12. Electron temperature profiles

Future experiments

The principal aim of the ECRH system on ITER is the control of neoclassical tearing modes (NTMs). Without active control, these modes are predicted to severely limit ITER performance. While the standard approach to NTM control is to use ECCD to drive current inside the NTM islands another approach employs ECCD indirectly to avoid the creation of seed islands for the NTMs. The seed islands are typically triggered by large sawtooth crashes. In present machines the stabilising effect of central Ion Cyclotron(IC) heating or current drive can produce such large sawteeth. In ITER a similar stabilization is predicted to be caused by alpha particles. By driving current locally near the $q = 1$ surface the sawteeth can be de-stabilised resulting in smaller sawtooth crashes. This in turn would prevent the creation of large seed islands triggering NTMs. This approach has been demonstrated on JET using Central ICCD to create large sawteeth and off axis ICCD to drive current near $q = 1$ [13, 14]. In these experiments the destabilising effect was lost when the $q = 1$ surface moved away from the position where the off axis current was driven, highlighting the need for feedback control of the location of the driven current

The possibility to control the EC injection angles in real time makes Tore Supra ideally suited to demonstrate long term Sawtooth destabilisation with ECCD. Figures 13, 14 show results of simulations performed in preparation for such Sawtooth control. Figure 13 shows the EC power deposition profiles calculated using the REMA [15] ray tracing code for two different poloidal injection angles generating current slightly outside and slightly inside the $q = 1$ surface. Figure 14 shows a simulation based on a very simple Sawtooth model of closed loop control of the Sawtooth period. The simulation shows that long term closed loop control of the Sawtooth frequency and hence of the size of the Sawtooth should be feasible on Tore Supra.

Conclusions. In the period 2002–2005 the technical work on the Tore Supra ECRH system has focusedon the improvement, in collaboration with TED of the 118 GHz Gyrotron, and on modifications to the ECRH antenna. The internal

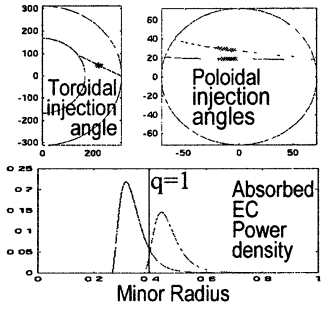

Fig. 13. EC power deposition near $q = 1$

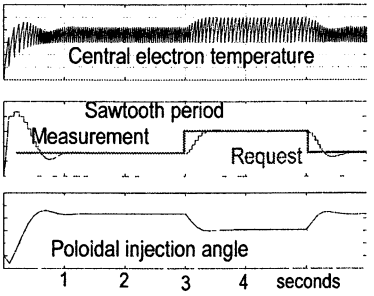

Fig. 14. Simulation of Sawtooth control

gyrotron cooling has been improved and the cylindrical injector inside the gyrotrons has been replace by a conical injector. While these modifications have succeeded in removing spurious oscillations and in reducing the conditioning requirements, the gyrotrons output beam is no longer a pure Gaussian beam. Investigations of the origin of this problems are still ongoing. Following a leak in the water bellows feeding the Antenna mobile mirrors situated inside the tokamak, the cooling system for these mirrors has been redesigned and the new design which was en-durance tested up to 50000 has been implemented.

Despite these technical problems, significant experimental results have been achieved. The predicted synergy between EC and LH waves have been demonstrated, raising hopes that this mechanism can be exploited to develop a current drive system with the current drive efficiency of LH and with the narrow – and controllable – current drive location of EC. In experiments using ECCD for initial current profile tailoring improved confinement has been triggered during the current rise and maintained for up to 1 secondinto the current flattop.

With real time control of the EC injection angles available, feedback control of MHD modes will be attempted in the coming campaign with special focus on control of Tearing modes and of the Sawtooth frequency which is a scheme for NTM avoidance envisaged for ITER.

References

1. *Lennholm M. et al.,* Proc. 5th SMP, Nizhny Novgorod (2003), p. 409.
2. *Darbos C. et al.,* Fusion Engineering and Design, vol. 56-57 (2001), p. 605.
3. *Darbos C. et al.,* Proc. EC12, Aix-en-Provence, 2002.
4. *Darbos C. et al.,* Proc. 3rd IAEA TM on ECRH in ITER, 2005.
5. *Darbos C. et al.,* Proc. EC13, Nizhniy Novgorod, 2004.
6. *Lennholm M. et al.,* Nuclear Fusion, vol. 43 (2003), p. 1458.
7. *Lennholmet M. et al.,* Proc. 3rd IAEA TM on ECRH in ITER, 2005.
8. *Berger-By G. et al.,* Proc. EC13, Nizhny Novgorod, 2004.
9. *Giruzzi G. et al.,* Phys. Rev. Lett., vol. 93 (2004), 255002.
10. *Dumont R.J., Giruzzi G., Barbato E.* Phys. Plasmas, vol. 7(2000), p. 4972.
11. *Giruzzi G.,* Plasma Phys. Cont. Fusion, vol. 35 (1993), A123
12. *Rimini F.G et al.,* Plasma Phys. Cont. Fusion, vol. 47, № 6 (2005), p. 869.
13. *Bhatnagar V.P. et al.,* Nuclear Fusion, vol. 34 (1994).
14. *Eriksson L.-G.,* Phys. Rev. Lett., vol 92 (2004).
15. *Krivenski et al.,* Nuclear Fusion, vol 25 (1985), p. 127.

THE FIRST EXPERIMENTAL RESULT OF ELECTRON BERNSTEIN WAVE HEATING IN LHD

H. Igami, T. Notake, Y. Yoshimura, T. Shimozuma, S. Kubo, S. Inagaki, K. Ohkubo, K. Nagasaki[1] *and LHD Experimental Group*

National Institute for Fusion Science, Toki, Japan
[1] Institute of Advanced Energy Kyoto University, Uji, Japan

Electron cyclotron resonance heating (ECRH) by mode-converted electron Bernstein wave (EBW) was tried in the Large Helical Device (LHD) for the first time. When a quasi-X (QO) wave is injected from the high field side so that it can directly access the upper hybrid resonance (UHR) layer, power absorption takes place at the low field side of the ECR layer although the incident beam approaches ECR layer from the high field side. While in the case of quasi-O (QO) wave injection at the same angle, power absorption takes place at the high field side of the ECR layer. As the polarization of the incident electromagnetic wave is gradually changed from QO wave to QX wave shot by shot, each amount of the power absorbed at the high field side and the low field side of the ECR layer changes relative to the change of polarization. These results suggest that ECRH by mode-converted EBW was performed.

Introduction

ECRH by EBW have been long attracted as a possible way to heat the overdense (where $\Omega_e < \omega_{pe}$) or low temperature region of plasmas [1–7], in which the conventional way of ECRH with usual ordinarily (O) or extraordinarily (X) propagation wave is not applicable. Since EBW has no density limit of propagation and are strongly absorbed in the Doppler shifted ECR layer even the electron temperature is low. However, EBW is electrostatic wave and cannot propagate in vacuum. Therefore EBW should be excited at the upper hybrid resonance (UHR) layer via mode conversion process by injection of electromagnetic (EM) waves from the outside of the plasma. One way to excite EBW is to inject the X (or QX) wave from the high field side so that it can directly access the UHR layer (XB method) [8]. In this case, the injected X wave is fully mode-converted to EBW without any reflection. XB method is available if the electron density in the high field side is less than two times of the plasma cutoff density. We tried ECH by EBW for the first time in the 8th experimental campaign of LHD by XB method and have had some evidence of ECRH by mode converted EBW.

Experimental results and discussion

Figure 1 shows plasma cross-sections and the vacuum trajectories of the incident beam projected on the plane which is created by the incident beam vector and the major radius. In these cases, the magnetic axis is located at 3.55 m from the center of the torus, and the magnetic field strength at the axis is 2.789 T.

84 GHz microwave is injected from the bottom port. In the case of *a* and *b*, the beam sticks through the ECR layer located in the high field side. If the plasma exists, the beam might approach the UHR layer directly from the high field side and it is expected that EBW can be excited in the UHR layer if the incident wave is QX wave. Though the beam encounters the fundamental ECR before it reaches the UHR layer, it may pass through the ECR layer without strong absorption because the electron temperature is low in that peripheral region. Thus we can view this ECR layer located in the high field side as the "XB access window".

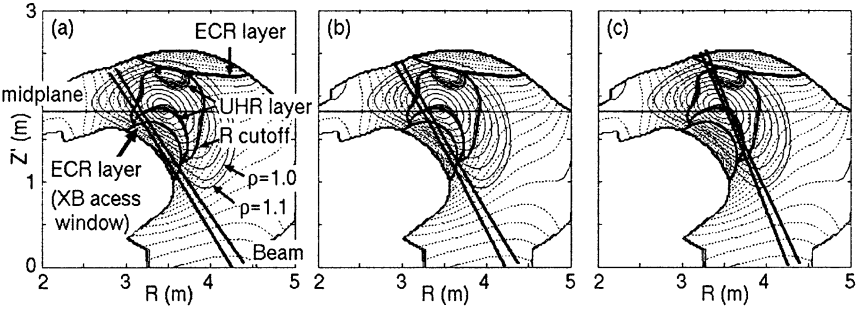

Fig. 1. Plasma cross-sections and vacuum beam trajectories projected on the planes created by the incident beam vector and the major radius for the cases of radial and toroidal beam focal point on the mid-plane, (Rf, Tf) is (3.15 m, –0.75 m) (*a*), (3.23 m, –0.75 m) (*b*), (3.55 m, –0.75 m) (*c*).

Figure 2 shows the waveforms when 84 GHz QX wave beam was obliquely injected to the toroidal direction with 100% power modulation of 34 Hz. In this experiment the target Ne plasma was sustained by neutral beam injection. The averaged line density at the center code is less than the cutoff density, however EBW can be excited if the QX wave reach the UHR layer. With the power modulation, the diamagnetic signal and the ECE signals were also modulated thus we can guess some power absorption took place. The focal point of the incident microwave beam was moved from the inner side to the outer side of the vacuum vessel as shown in Fig. 1. At each point, both QX and QO waves were injected shot by shot. Modulated ECE signals were detected through all cases.

The results of FFT analysis of these modulated ECE signals are shown in Fig. 3 for each injection case. In both cases of *a* and *b*, where the beam sticks though the "XB access window" the narrow peak of the amplitude appears in the inner, low field side of the ECR layer in the case of QX wave injection though the beam approaches the ECR layer from the outer high field side and the bottom of the phase is located at the peak. While in the case of QO wave injection, the peak appears in the outer, high field side of the ECR layer and the bottom of the phase is located at the peak of outer side. On the other hand, in the case of *c*, where the beam deviates the "XB access window", the QX wave encounters the right hand cyclotron cutoff and suffers reflection, while the QO wave runs close to the ECR layer without reflection. In Figure 3 something like

a peak of the amplitude and a bottom of the phase can be seen around $\rho = 0.4$ (in case of *c*) in the case of QO wave injection, on the contrary nothing like a peak can be seen in the case of QX wave injection.

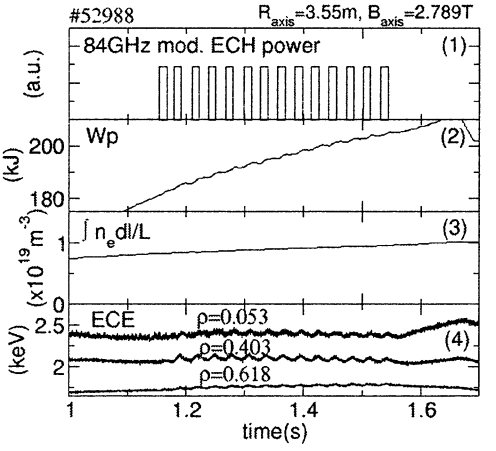

Fig. 2. Discharge waveforms. Injected power (*1*). Diamagnetic current (*2*). Line averaged density at the center code (*3*). ECE signals at ρ = 0.053, 0.403, 0.618 (*4*).

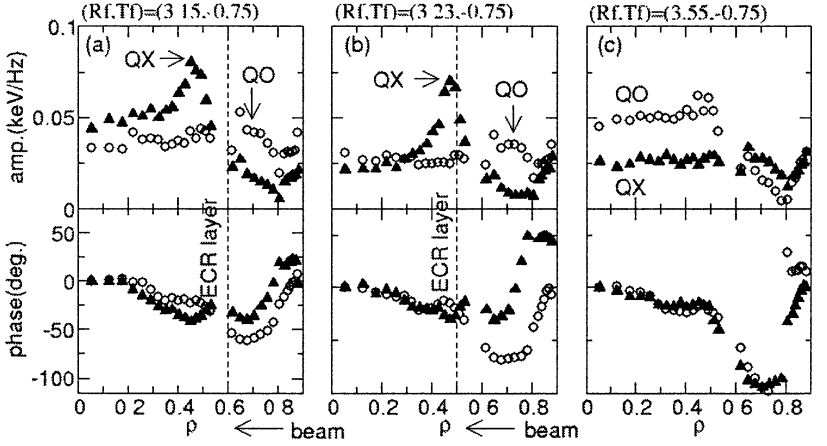

Fig. 3. Profiles of the amplitude of FFT spectrum at 34 Hz (above row) and the phase (bottom row) for each beam focal point on the mid-plane. Black triangles represent the case of QX mode injection and white circles represent the case of QO mode injection. Those *a*, *b* and *c* correspond to the cases of *a*, *b* and *c* in Fig. 1 respectively.

We gradually changed the polarization of the incident microwave beam from the QX wave to the QO wave shot by shot at the same direction as shown in Fig. 1, *a*. In Figure 4, *a*, we can see the amplitude of the peak in the inner side becomes low, while the amplitude of the peak in the outer side becomes

high as the QX wave component decreases. In Figure 4, *b*, there can be seen two bottoms of the phase both in the inner and outer side for these cases of QX and QO mixed wave injection.

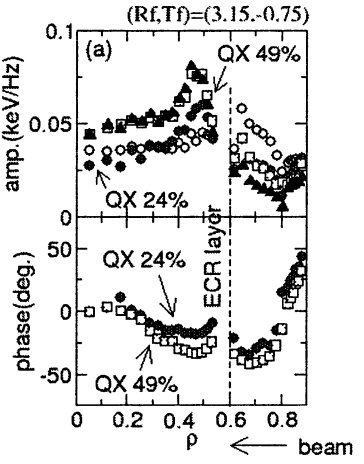

Fig. 4. Profiles of the amplitude of FFT spectrum at 34 Hz (above row) and the phase (bottom row) for the case of focal point on the mid-plane, (Rf, Tf) is (3.15 m, –0.75 m). Squares represent the case where the QX wave copmponent is 49%. Hatched circles represent the case where the QX wave power component is 24%. In the above row, the profiles of QO and QX wave injection are also plotted with white circles and black triangles.

From these experimental results, we can say that in the case where the incident microwave beam was directed to the "XB access window", waves injected as QO wave and as QX wave were absorbed in different mechanisms. In the case of QO wave injection, as the beam came close to the ECR layer from the outer side, the wave might absorbed in the outer side of the ECR layer by usual cyclotron dumping of normal mode. On the other hand, in the case of QX wave injection, the wave might be mode-converted to EBW in the UHR layer successfully and propagated via some complicated trajectory, then was absorbed in Doppler-shifted ECR layer.

Summary

ECRH by XB method was tried in LHD for the first time. In the case where QX wave beam was injected toward the "XB access window", local power absorption took place in the inner low field side of the ECR layer though the incident beam approaches the ECR layer from the outer high field side of the ECR layer at first. This result might be the evidence that ECRH by mode converted EBW took place.

References

1. *Preinhaelter J., Kopecky V*, J. Plasma Phys., 1973, **10**, 1.
2. *Maekawa T., et al.*, J. Phys. Soc. Japan, 1980, **48**, 247.
3. *Nakajima S., Abe H.*, Phys. Lett A, 1987, **28**, 295.
4. *laqua H.P., et al.*, Plasma Phys. Control Fusion. 1999, **41**, A273.
5. *Ram A.K., Schultz S.D.*, Phys. Plasmas, 2000, **7**, 4084.
6. *Cairns R.A., Lashmore-Davies C.N.*, Phys. Plasmas, 2000, **7**, 4126.
7. *Nagasaki K., Yanagi N.*, Plasma Phys. Control Fusion. 2002, **44**, 409.
8. *Maekawa T., et al.*, Phys. Rev. Lett., 2001, **86**, 3783.

ABOUT CYCLOTRON PARAMETRIC INTERACTION AND MANLEY — ROWE RELATIONS

M. A. Erukhimova, M. D. Tokman

Institute of Applied Physics RAS, Nizhny Novgorod, Russia

On the basis of different schemes of parametric interaction of electromagnetic waves with ensembles of magnetized electrons we determine the basic common signs of processes of parametric interaction that contradict with the customary Manley – Rowe relations.

Introduction

A variety of interesting effects can be observed in complex systems of parametric interaction of coherent waves in the medium of relativistic magnetized electrons. In our previous papers [1–5] different regimes of so called inversionless amplification of cyclotron radiation were revealed in such systems and investigated. In these regimes two HF waves with frequencies ω_1 and ω_2 are amplified simultaneously being coupled parametrically by means of created preliminary modulation at the differented frequency $\Omega = \omega_1 - \omega_2$ in the electrons medium which is stable ("not inverted") against cyclotron generation of each of two monochromatic waves separately. At first sight such processes are forbidden by well-known Manley – Rowe relations that couple each of two waves in any multi-wave nonlinear process. For considered waves such relation has the form:

$$\frac{W_1}{\omega_1} + \frac{W_2}{\omega_2} = \text{const},$$

where W_j is the energy of radiation at the corresponding frequency ω_j. The Manley – Rowe relations are clearly interpreted at the photon language as the conservation low for number of photons in the scattering process. But it is important to have in view that the Manley – Rowe relations are strictly proved in the medium which is transparent at every frequency involved in the multi-wave process.

In the regimes of inversionless cyclotron amplification two different mechanisms turning over the Manley – Rowe relations were revealed. The first one corresponds to the parametric interaction of two waves in the medium where the *active* response is formed upon the action of monochromatic waves. The active response is formed by the particles *resonant to the waves*; i. e. the energy $mc^2\gamma_R$ and longitudinal velocity $V_{\|R}$ of such electrons obey the synchronism conditions:

$$\omega_j = N_j \frac{eB_0}{mc\gamma_R} + k_{\|j} V_{\|R}.$$

(Here $k_{\|j}$ is the longitudinal component of wave vector of the j-wave, B_0 is the absolute magnitude of the constant magnetic field, e and m – electron's

charge and mass, c is the light velocity). This mechanism can be characterized as the parametric interaction in the medium with modulated conductivity.

In the second mechanism unlike the first one the conversion of Manley – Rowe relations can not be explained at the photon language as combination of scattering of photons and burning of photons due to one-photon resonances. In the second regime the simultaneous amplification of two waves takes place in the medium which produces *reactive response* at the wave's frequencies, the amplification is possible *in the absence of particles, resonant to the waves*. The second mechanism can be characterized as the parametric interaction in the medium with modulated *in opposite phases* partial susceptibilities.

In both regimes of cyclotron inversionless parametric instability the resonant interaction of the beating wave (at frequency $\Omega = \omega_1 - \omega_2$) with electrons is of principal value, the medium *is not transparent* at least at the beating frequency. More over it was shown that the process of simultaneous amplification instead of scattering runs during limited time interval after interaction switching on at the moment $t = 0$. The time restriction condition can be written in the following form:

$$\left(\Omega - \left(N_1 - N_2\right)\frac{eB_0}{mc\gamma} - \left(k_{\|1} - k_{\|2}\right)V_{\|}\right)t < 1 . \qquad (1)$$

(This inequality must be fulfilled for every gamma-factor γ and longitudinal component of velocity $V_{\|}$ of electrons from ensemble.) The inequality (1) can be interpreted as conservation of the synchronism between all particles of ensemble and the beating wave during interaction.

In the present paper we demonstrate that the denoted two different mechanisms of the inversionless amplification conflicting with the Manley – Rowe relations can be realized in the stationary regimes in presence of pumping wave with the differented frequency and wave vector; i.e. in the three-waves system. The customary method of description of multi-wave processes not depending on the moment and character of interaction switching on can be used. As result more common formulation of the attributes peculiar for the schemes of parametric interaction not restricted by the Manley – Rowe relations, are formulated.

The first regime

The first regime can be demonstrated by the example of the following system. Two probe HF coherent waves and LF pumping wave propagate at the same direction transversely to the constant magnetic field $\mathbf{B_0} = \mathbf{z_0}B_0$:

$$\mathbf{E} = \mathbf{y_0}\,\mathrm{Re}\sum_{j=1}^{2} E_j \exp\left(ik_j x - i\omega_j t\right) + \mathbf{y_0}\,\mathrm{Re}\sum_{j=1}^{2} E_p \exp\left(i\kappa x - i\Omega t\right).$$

Here $\Omega = \omega_1 - \omega_2$, $\kappa = k_1 - k_2$. HF waves and pumping wave are resonant with relativistic electrons at two high harmonics of gyro-frequency and the differented gyro-harmonic, correspondingly:

$$\omega_j = N_j \frac{eB_0}{mc\gamma_R},\ \Omega = (N_1 - N_2)\frac{eB_0}{mc\gamma_R}.$$

The medium is the low-density plasma; the energy of electrons in ensemble is slightly disturbed near the resonant value. The amplitude of the pumping wave is fixed. The parameter of interest is the nonlinear (quadratic over the pumping wave amplitude) susceptibility at the frequencies ω_1 and ω_2. This system can be analyzed on the basis of the kinetic equation [1, 2]:

$$\frac{\partial f}{dw} + \frac{eB_0}{mc\gamma}\frac{\partial f}{d\theta} + \sum_{j=1}^{2}\left(F_j \frac{\partial f}{dw}\right) + F_p \frac{\partial f}{dw} = 0, \qquad (2)$$

where $f(w, \theta, t, X)$ is the electron distribution function, $w = \gamma - \gamma_R$, θ is the gyrophase; $F_j = -G_j(e/mc)\mathrm{Re}(E_j \exp(ik_j X + iN_j\theta - i\omega_j t))$, $F_p = -G_p(e/mc)\mathrm{Re} \times$ $\times (E_p \exp(i\kappa X + i(N_1 - N_2)\theta - i\Omega t))$, $G_{j,p}$ – coupling parameters. The unperturbed distribution function $f_0(w)$ is "not inverted", i. e. $\partial f_0/\partial w(w=0) < 0$.

The result of the analysis of this system for the purpose of inversionless amplification is negative. The parametric interaction of probe waves by means of LF pumping wave can not provide their simultaneous amplification.

We have found that the situation can be cardinally changed by including any dissipative mechanism of interaction to the system, thus adding the corresponding "collision" term in the simplest form to the kinetic equation (2):

$$\frac{\partial f}{dw} + \frac{eB_0}{mc\gamma}\frac{\partial f}{d\theta} + \sum_{j=1}^{2}\left(F_j \frac{\partial f}{dw}\right) + F_p \frac{\partial f}{dw} = -\nu(f - f_0).$$

The basic result is the following. If the dissipation rate ν is sufficiently large, so that the following condition is fulfilled:

$$\left|\Omega - (N_1 - N_2)\frac{eB_0}{mc\gamma}\right| < \nu, \qquad (3)$$

the parametric interaction by means of sufficiently strong pumping wave can lead to the simultaneous amplification of two HF probe waves in the inversionless electron medium. Under condition $\nu << \omega_j \langle \Delta w \rangle / \gamma_R$, which means that the dissipation does not change the linear response of the medium upon the HF waves, the simultaneous amplification of two HF waves is realized if the following condition is fulfilled:

$$\frac{G_p e |E_p|}{2mc\nu}\left|\frac{\partial^2 f_0}{\partial w^2}\right|_{(w=0)} > -\left.\frac{\partial f_0}{\partial w}\right|_{(w=0)}.$$

The mechanism of inversionless amplification in this system can be formulated as the parametric interaction of two waves by means of modulation of conductivity of the medium, which is formed by the particles which are resonant both to the probe and pumping waves. The sufficiently strong modulation of conductivity is excited if the pumping wave is intensive enough. It is

especially important that the resonant interaction of the medium with the LF pumping wave has essentially dissipative character. It is important that due to sufficiently fast dissipative processes the phase of complex amplitude of the excited distribution function modulation has inessential dependence on the energy.

The second regime

The second mechanism of inversionless amplification, – parametric interaction by means of *anti-phase modulation of reactive partial susceptibilities*, – is conditioned by the cyclotron interaction modified by Doppler effect; the necessary type of modulation is provided by the dependence of the modulation phase on the sign of Doppler shift of synchronism. This type of parametric instability process in steady regime can be presented by the example of the following system.

Two HF electromagnetic probe waves with circular polarization propagate along the constant magnetic field in opposite directions; the longitudinal wave plays the role of the LF pump:

$$\mathbf{E} = \sum_{j=1}^{2} \mathrm{Re}\left((\mathbf{x_0} + i\mathbf{y_0}) E_j e^{ik_j z - i\omega_j t} \right) + \mathbf{z_0}\, \mathrm{Re}\left(E_p e^{i\kappa z - i\Omega t} \right), \quad k_1 > 0, \quad k_2 < 0 .$$

We have shown that in this system the simultaneous amplification of two electromagnetic waves is possible in the absence of electrons resonant with these HF waves. As the necessary condition we should again to assume, that the dissipative process with sufficiently large rate are included to the system, so that the following condition is fulfilled:

$$\left| \Omega - \kappa V_{\|} \right| < \nu . \tag{4}$$

Simultaneously, the dissipative rate ν must be small, so that the interaction of electromagnetic waves with electrons can be considered as nonresonant, i. e. purely reactive:

$$\nu << \left| \omega_j - \frac{eB_0}{mc\gamma} - k_j V_{\|} \right| . \tag{5}$$

As it follows from analysis of time-limited nonresonant amplification without pumping [3, 4], this regime, particularly, is possible for ensemble of nonrelativistic particles in presence of constant magnetic field. For this case the following kinetic equation describes the system:

$$\frac{\partial f}{\partial t} + V_{\|} \frac{\partial f}{\partial z} + \frac{eB_0}{mc} \frac{\partial f}{\partial \theta} + \sum_{j=1}^{2} \frac{1 - k_j V_{\|} / \omega_j}{V_{\perp}} \mathrm{Im}\left(\frac{eE_j}{m} e^{ik_j z + i\theta - i\omega_j t} \right) \frac{\partial f}{\partial \theta} +$$

$$+ \sum_{j=1}^{2} \mathrm{Re}\left(\frac{eE_j}{m} e^{ik_j z + i\theta - i\omega_j t} \left(\frac{1 - k_j V_{\|} / \omega_j}{V_{\perp}} - \left(1 - k_j V_{\|} / \omega_j\right) \frac{\partial}{\partial V_{\perp}} \right) f \right) -$$

$$- \mathrm{Re}\left(\frac{eE_p}{m} e^{i\kappa z - i\Omega t} \frac{\partial f}{\partial V_{\|}} \right) = -\nu (f - f_0) .$$

It can be shown that in the simplest case, when $\omega_1 \approx \omega_2 \approx \omega$, $k_1 \approx -k_2 \approx k$, $\omega << eB_0/(mc)$, the condition of simultaneous amplification of two electromagnetic probe waves (taking into account conditions (4) and (5)) takes the form:

$$\frac{1}{2} k \frac{e|E_p|}{m} > \nu^2 \frac{\omega mc}{eB_0}.$$

In this regime the simultaneous amplification of two waves is provided by parametric interaction by means of excited modulation of the distribution function with anti-symmetrical dependence of the modulation amplitude on the longitudinal velocity. The necessary type of modulation can be formed under action of the longitudinal pumping wave if only the active interaction of the electron medium with the pumping wave has the dissipative character.

Resume

We considered the systems of three-waves interaction that are not described by the Manley – Rowe relations. The following reasons can be revealed. The principal aspect of these systems is the combination of three-waves (or parametrical) process with the resonant interaction of the radiation with electrons-oscillators at every frequency or at least at differented (low) frequency. The last case is especially surprising, but it has the right to exist, because the Manley – Rowe relations are strictly proved for multi-waves interaction in reactive at every frequency medium. It is especially worth to note that for considered regimes to be realized in classical system the sufficiently wide frequency band of resonant interaction with LF pumping wave must overlap the spectrum of the corresponding LF transitions in electrons system. This requirement is described by the conditions (3) and (4). But the time restriction condition of instability in the medium without dissipation (1) can be formulated in the same way. So the Manley – Rowe relations can be conversed if there is resonant interaction of the electrons medium with LF pumping wave or LF beating wave and the corresponding resonance band is sufficiently large due to dissipative processes or restricted time of interaction.

This work was supported by grants: RFBR 03-02-17234, RFBR 04-02-17042, ISTC A-1095.

References

1. *Gaponov-Grekhov A.V., Tokman M.D.*, JETP, 1997, **85** (4), 640.
2 *Erukhimova M A., Tokman M.D.*, JETP, 2000, **91**(2), 255-264.
3 *Erukhimova M.A., Tokman M D.*, Strong Microwaves in Plasmas, 2003, **2**, 544.
4 *Erukhimova M.A., Tokman M D.*, Radiophysics and Quantum Electronics, 2003, **46** (4), 249-266.
5. *Erukhimova M.A., Tokman M.D.*, Opt. Commun., 2005, **250** (4-6), 355-369.

STUDY OF MICROWAVE TRANSMISSION THROUGH THE PLUG REGION WITH BEACH GEOMETRY IN THE GAMMA 10 TANDEM MIRROR

T. Saito, D. Nagai, Y. Tatematsu, K. Nozaki, N. Machida, T. Kaitsuka, Y. Kamata, O. Watanabe, H. Hojo, I. Katanuma, K. Sakamoto[1], *T. Imai, T. Cho*

Plasma Research Center, University of Tsukuba, Ibaraki 305-8571, Japan
[1] Naka Fusion Research Establishment, JAERI, Ibaraki 311-0193, Japan

Electron heating with new high power gyrotrons at the plug region of GAMMA 10 has generated a record value of the axial ion confining potential. Measurement of microwave transmission through the plug region indicates penetration of finite power beyond the fundamental resonance surface. This means that electron heating in the low field side takes place. The measured transmission rate is consistent with calculation with a newly developed full Maxwell code.

Introduction

Microwave power with a frequency of 28 GHz is injected onto a fundamental electron cyclotron resonance (ECR) surface at the plug region of GAMMA 10 for generation of an axial ion confining potential. Recently, high power heating experiment has started with newly installed high power gyrotrons with an output power up to 500 kW [1, 2].

The plug region has beach geometry, where the magnetic field strength varies along a magnetic field line. To avoid right-hand cutoff in the low field side, the heating power is injected from the high field side. According to the cold plasma theory, the parallel refractive index becomes infinite at cyclotron resonance as shown in Fig. 1 and no power is transmitted across the resonance surface. On the other hand the Budden tunneling theory predicts finite power transmission to the low field side.

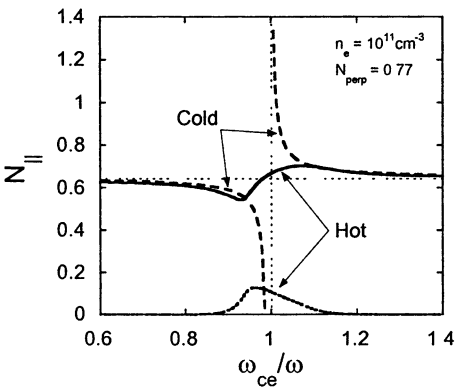

Fig. 1. Dispersion of EM Wave near electron cyclotron resonance surface. N_{perp} is fixed at 0.77.

Accurate evaluation of power absorption rate is very important for efficient potential generation. Experimentally, finite power is detected on an array of open-ended rectangular waveguides installed in the vacuum region across the resonance surface. This means that the microwave power penetrates to the low field side beyond the resonance surface and the cutoff region. This is consistent with the Budden theory for tenuous plasma. However, for more detailed analysis of power transmission, calculation including the finite temperature effect is necessary [3]. Then, as plotted in Fig. 1, the real refractive index becomes finite and continuous in the resonance-cutoff region. The absorption coefficient can be evaluated from the imaginary part of the refractive index (dotted line).

Penetration of the heating power beyond the resonance surface indicates that electrons are heated in the low field side as well as in the high field side. Thus, the spatial profile of power absorption along the propagation direction is very important. Moreover, information of the radial profile of power absorption is highly requisite for control of the radial potential profile. Theoretically, we calculate wave propagation and the power transmission rate with a finite difference time domain (FDTD) full Maxwell code including cyclotron absorption [4]. Comparison of the measurement with the calculation provides information about the spatial profile of power absorption.

High power heating at the plug region

This section gives a brief description of the experimental setup. For more detail, see Refs. [5, 6]. Figure 2 shows the axial distributions of the on-axis

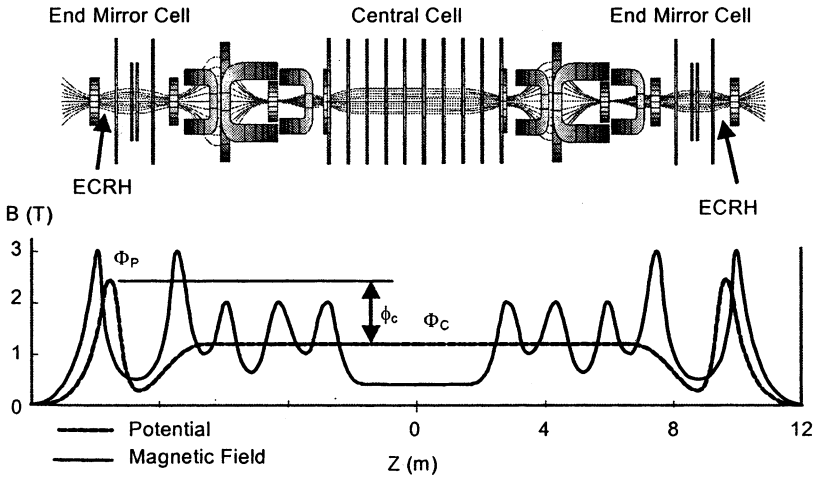

Fig. 2. Axial distributions of the on-axis magnetic field strength (solid line) and the electrostatic potential (dotted line) of GAMMA 10.

magnetic field strength and a typical electrostatic potential in GAMMA 10. Fundamental ECRH (plug ECRH) is applied at the plug position (B_p = 1 T) between the mid plane (B_b = 0.5 T) and the outer mirror throat (B_m = 3.0 T) of the end mirror cell. Although, second harmonic ECRH is applied to the mid-plane of the end mirror cell, Fig. 2 indicates only the plug ECRH for simplicity.

A new high power 28 GHz gyrotron has been installed for the west side plug ECRH. Microwave power is transmitted through 63.5 mm diameter corrugated waveguides into the GAMMA 10 vacuum vessel. Then, it is radiated from the high field side. The radiated microwave has linear polarization and it is mostly coupled to the X-mode for the present geometry. The power profile on the resonance surface is designed to be almost axi-symmetric by using two profile-tailoring mirrors [7]. Plasma is produced and sustained with a fast ICRF wave. A slow ICRF wave heats the central cell ions [8]. The electron density n_{ec} in the central cell is in the range of (2 – 3) × 10^{12} cm^{-3}, and the ion temperature perpendicular to the magnetic field T_{ic} is several keV. The electron density at the plug region is in the order of 10^{10} cm^{-3} to 10^{11} cm^{-3} during plugging.

On application of the plug ECRH, the plug potential Φ_P becomes the largest of the potentials along the magnetic field line, and a large ion confining potential $\varphi_C = \Phi_P - \Phi_C$ is generated, with Φ_C being the central cell potential. The increment in Φ_P strongly depends on the plug ECRH power P_{plug}. Figure 3 plots Φ_P and Φ_C obtained from the three stages of experiment: before high power heating (denoted with crosses), high power operation of existing gyrotrons (open triangles), and experiment with new gyrotrons (closed triangles). The attainable value of Φ_P increases with P_{plug} and φ_c does. The maximum values of φ_c at the three stages are 0.8, 1.4 and 2.5 kV. The value of 2.5 kV is the new record.

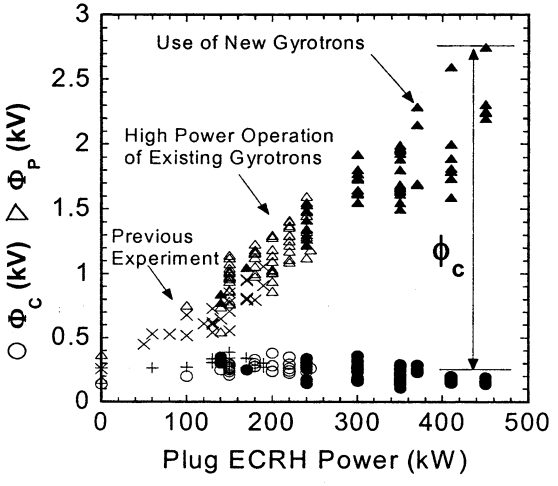

Fig. 3. Potentials as functions of the plug ECRH power P_{plug}

Microwave transmission measurement

An array of open-ended rectangular waveguide (WR-28) is used to measure the spatial distribution of the transmitted power. This array is installed in the vacuum region opposite to the antenna across the resonance layer. Microwave with the same polarization as that of the incident wave is received with each waveguide. The power transmission rate T is evaluated as the ratio of the transmitted power measured with plasma to that without plasma.

Figure 4 plots a time evolution of the radial profile of the transmission rate T evaluated with the array of six WR-28 waveguides. The plug ECRH is applied from 160 ms to 185 ms. Channel five corresponds to the central ray of the incident microwave beam. The radial profile of T varies during the ECRH pulse. This suggests time variation of the density profile at the plug region. The value of T for the central ray is small and becomes less than 0.1 in the latter half of the ECRH pulse.

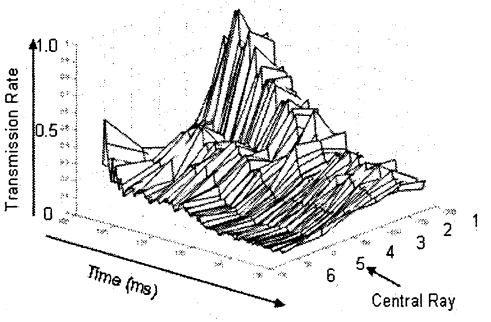

Fig. 4. An example of time evolution of the radial profile of microwave transmission rate.

Calculation with full Maxwell code

Electron heating in the high field side always occurs. However, occurrence of low field side heating depends on the absorption profile. Recently, a full Maxwell FDTD code of wave propagation has been developed [4]. It is applicable to beach geometry and includes cyclotron absorption. Calculation with this code shows that, for a typical density regime of the plug region of GAMMA 10, microwave power launched from the high field side is not fully absorbed before the resonance surface but a finite fraction penetrates into the low field side [9].

Figure 5 depicts wave propagation calculated with this code. The magnetic field profile and the density distribution simulate the plug region. A heating wave with frequency of 28 GHz is launched in linear polarization from the high field side with the same angle to the machine axis as that in the experiment. The wave field penetrates beyond the resonance surface for low density as plotted in

Fig. 5, *a*, and the wave energy is absorbed in both sides of the resonance surface. This is consistent with the experimental observation. Therefore, low field side heating occurs for the typical experimental condition [2]. On the other hand, for high density, the injected power is almost absorbed before the resonance surface as shown in Fig. 5, *b*. Experimentally, the transmitted power becomes almost zero for electron density roughly higher than 10^{11} cm^{-3}.

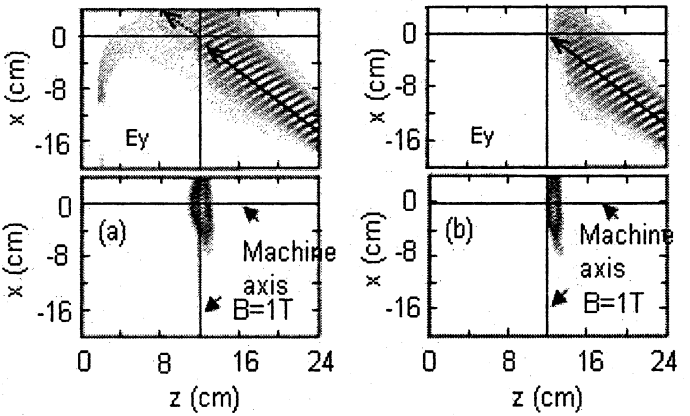

Fig. 5. Calculation of wave propagation (upper) and absorption profile (lower) through the fundamental resonance surface for 3×10^{10} cm^{-3} (left) and 3×10^{11} cm^{-3} (right).

Figure 6 plots the measured power absorption rate along with the calculated one as function the electron density n_{ep} at the plug. The experimental data are evaluated for the central ray. The absorption rate A is simply evaluated as $A = 1 - T$. The experimental value of A represented by open diamonds increases with n_{ep} and reaches nearly unity for n_{ep} larger than 3×10^{11} cm^{-3}. The calculated value indicated with solid circles also increases with the electron density and also practically complete absorption is predicted for n_{ep} larger than 3×10^{11} cm^{-3}. Thus, calculation well reproduces measurement.

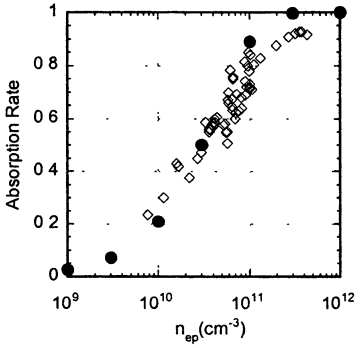

Fig. 6. Absorption rate as functions of the electron density at the plug.

Usually, n_{ep} ranges from 5×10^{10} cm^{-3} to 1×10^{11} cm^{-3} and absorption rate more than 0.5 is expected. Within this density range, substantial power absorption occurs in the low field side. This indicates that electrons are heated in the low field side as well as in the high field side. This is very important from the viewpoint of the mechanism of potential generation.

Conclusions

High power electron heating has been carried out at the plug region of GAMMA 10 by using new high power gyrotrons and the ion confining potential has attained to a record value. Microwave transmission rate has been measured with an array of open-ended rectangular wave guides. The measured value is consistent with calculation of a newly developed full Maxwell code. For usual regime of the electron density at the plug, finite power propagates beyond the fundamental resonance surface. This means that electron heating in the low field side can occur. Evaluation of the two dimensional absorption profile is the next task for control of the radial potential profile.

References

1. *Cho T. et al.*, 20th IAEA Fusion Energy Conf., EX/9-6Rd.
2. *Saito T. et al.*, J. Plasma Fusion Res., 2005, **81**, 288.
3. *Ellis R.F. et al.*, Phys. Fluids, 1983, **26**, 1528.
4. *Hojo H. et al.*, J. Plasma Fusion Res., 2004, **80**, 175.
5. *Saito T. et al.*, J. Plasma Fusion Res., 2001, Ser. **4**, 61.
6. *Saito T. et al.*, Fusion Engineering and Design, 2001, **53**, 267.
7. *Tatematsu Y. et al.*, Jpn. J. Appl. Phys., 2005, **44**, 6791.
8. *Ichimura M. et al.*, Nucl. Fusion, 1999, **39**, 1995.
9. *Tatematsu Y et al.*, J. Plasma Fusion Res., 2004, **80**, 360.

MICROWAVE EMISSION FROM A DENSE PLASMA IN GLOBUS-M TOKAMAK THROUGH LINEAR CONVERSION OF BERNSTEIN WAVES

M. A. Irsak, S. V. Krikunov, M. M. Larionov, K. M. Novik, V. V. Rozhdestvensky, A. N. Saveliev

A. F. Ioffe Physico-Technical Institute, St.-Petersburg, Russia

In spherical tokamak, ST, experiments dense plasma, $n_e(0) \sim 5 \cdot 10^{13}$ cm^{-3} is confined in rather weak magnetic field, B(0) ~ 0.5 T. Problem is discussed, how the electron cyclotron, EC, heating and current drive by gyrotrons and microwave emission diagnostics can be used in ST plasma, [1–3]. Cutoff conditions for electromagnetic waves of EC frequency range of ordinary, O, and extraordinary, X, polarizations are formed in this overdense plasma, T_p (0) >> T_{ce} (0). Theory predicts that at certain conditions the absorption of externally launched waves and the plasma thermal emission in a vacuum can be related to the electron Bernstein, EB, plasma waves propagating in the overdense plasma and undergoing strong absorption near EC resonance and its harmonics. The emission and the absorption of O and X waves originate through conversion of EB and X waves near the upper hybrid resonance, UHR, $T^2 = T_p^2 + T_{ce}^2$. Then the X mode can both partly penetrate into vacuum through the evanescent layer at plasma periphery, if it is narrow enough, case EB–X, or to be converted into O mode freely propagating into vacuum, if X–O conversion is realized at a certain angle of wave propagation relative to the magnetic field B, case EB–X–O. Measurements of the thermal microwave emission at several frequencies, T, its angular and polarization dependence can help in understanding the complicated processes of conversion, propagation and absorption of EB waves in overdense plasma. Main questions arising are: 1. Optimal frequency. 2. Optimal wave launching scheme, polarization and wave direction relative to B_{tot}. 3. The efficiency of conversion 0, energy losses due to reflection and absorption of converting waves. The efficiency of linear conversion into EBW is supposed to be the same for reverse process of thermally excited EBW conversion into X and O waves emitting in a vacuum. Some results obtained in Globus-M experiment [3, 4] are described below. The geometry and dimensions of this tokamak are shown in Fig. 1. Its discharge current of 200–250 kA lasts about 70 ms. The toroidal magnetic field $B(0)$ at R = 36 cm is 0.4 T and changes strongly along R due to low aspect ratio, A = 1.5. Its distribution along R is shown in Fig. 2, B_{tot} includes poloidal and paramagnetic components. Typical density profiles, parabolic and steep, are also shown in Fig. 2. These data were used in numerical simulation of EBW conversion, propagation and absorption in Globus-M plasma. In Figure 3 the dependence on frequency, T, of wave interaction with plasma of ST is explained. 12 GHz is T_{ce} at the central $R(0)$ = 36 cm, strong dependence of T_{ce}

and harmonics, $2T_{ce}$, $3T_{ce}$, on R is shown. Conversion of X, O, EB waves is localized in the narrow zone C near the external boundary of a plasma volume. Zone C includes O and X wave cutoffs and UHR for the range of ω studied. The absorption of EBW and its thermal excitation by plasma electrons take place in zones A_1, A_2, A_3 near the fundamental and harmonic EC resonance positions. These zones are rather broad and are shifted outside from T_{ce} positions due to Doppler shifts and toroidal corrections. Figure 3 shows us that only waves of a low $T < 15$ GHz can arrive to the center of a plasma volume and be absorbed there. At $\omega > 15$ GHz the EBW are absorbed by harmonics near to the periphery. Numerical modeling of dependence of conversion efficiency, $\eta(\varphi, \theta)$, on wave vector direction in poloidal θ and toroidal φ planes is shown in Fig. 4. Contours are surrounding angular zones, where $\eta > 20\%$ for X and O modes of linearly polarized waves of pointed T, η_{max} for every zone is pointed also. Direction $\theta = 0$, $\varphi = 0$ is along R and perpendicular to B_{tor}.

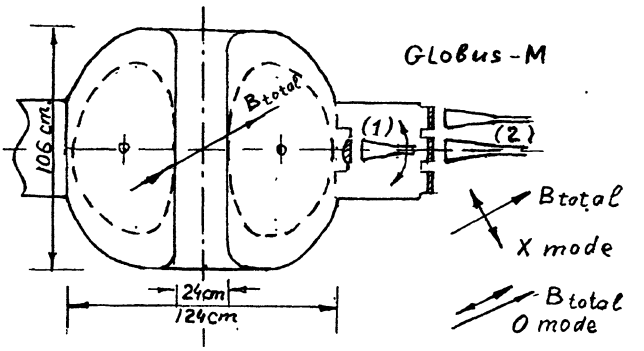

Fig. 1. Globus-M and microwave horn antenna positions in numerical simulation (*1*) and in experiment (*2*).

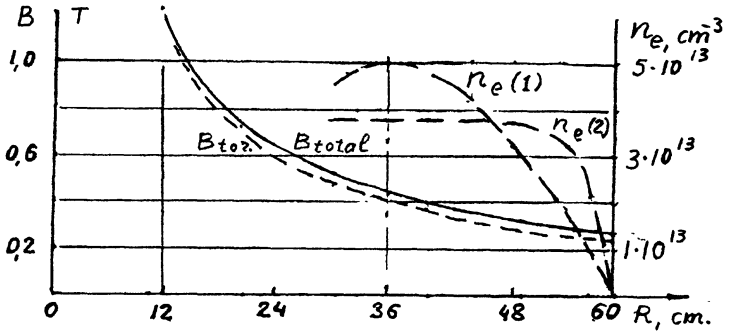

Fig. 2. Magnetic field (B_{total}) and plasma density ($n_e(1)$, $n_e(2)$) distributions along R, accepted for numerical simulation. ECR frequency at $R(0) = 36$ cm is 12 GHz.

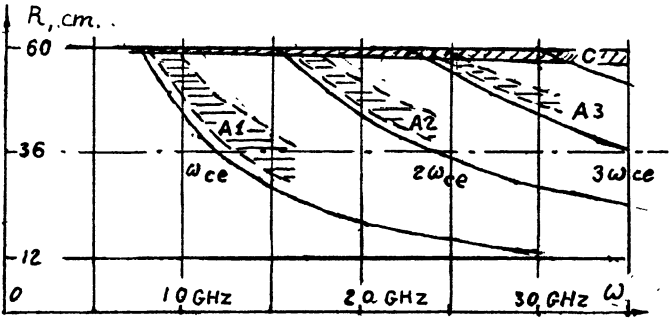

Fig. 3. The scheme of positions of conversion (C) and EBW absorption zones (A_1, A_2, A_3) in equatorial plane, depending on frequency ω. ECR and harmonics are shown also.

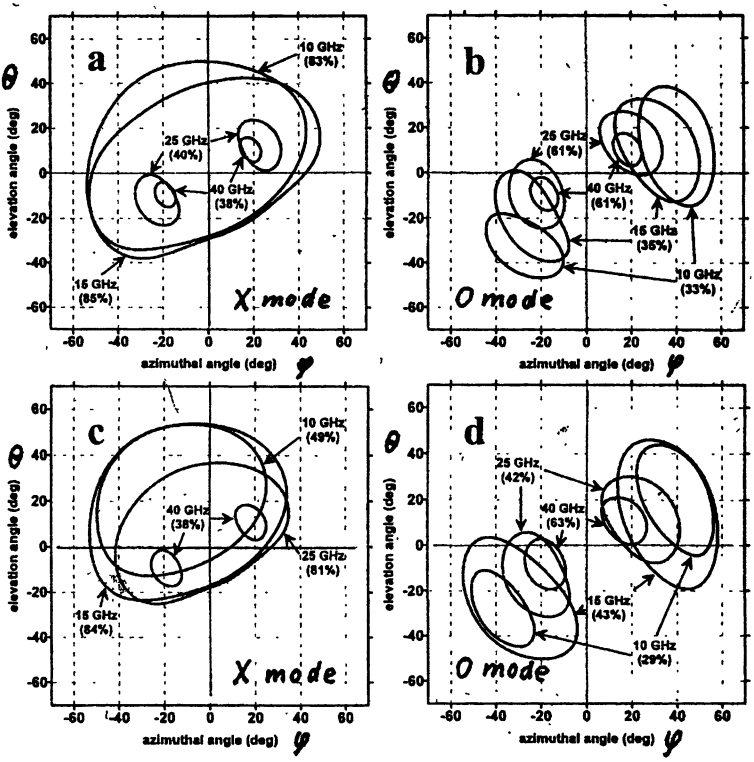

Fig. 4. Angular zones of transparency for EBW conversion into O and X waves, $\eta > 20\%$, for some frequencies: *a*, *b* – grad $n_e = 0.5 \times 10^{13}$ cm^{-4}, *c*, *d* – grad $n_e = 1.5 \times 10^{13}$ cm^{-4}.

Transparent zones are broad at lowest T and become narrow at highest ones. The optimal orientation of antenna for wave launching and emission reception can be determined from Fig. 4. Strong dependence of $\eta(\theta, \varphi)$ on density gradient in conversion zone is suppoused. So calculations are complited for gradient $n_e = 0.5 \cdot 10^{13}$ cm^{-4}, parabolic profile, case *a*, *b*, and for gradient $n_e = 1.5 \cdot 10^{13}$ cm^{-4}, steep profile, case *c*, *d*.

Figure 5 presents examples of ray tracing for EBW of $T = 15$, 20, 25 GHz excited near the equatorial plane. The bunch of rays was chosen corresponding to the diagram of a horn antenna in position (*1*), Fig. 1. The zones of absorption and of thermal excitation of EBW are shaded. Waves of 15 GHz penetrate to the central zone, waves of 20, 25 GHz are absorbed near the 2-nd, 3-th EC harmonics. Absorbing zones are rather broad in R direction. Numerical simulation results allow us to conclude that the optimal condition for EBW excitation and penetration in a central part of Globus-M plasma is X-mode conversion at $T = 12$–15 GHz. These results are taken into account in real measurements.

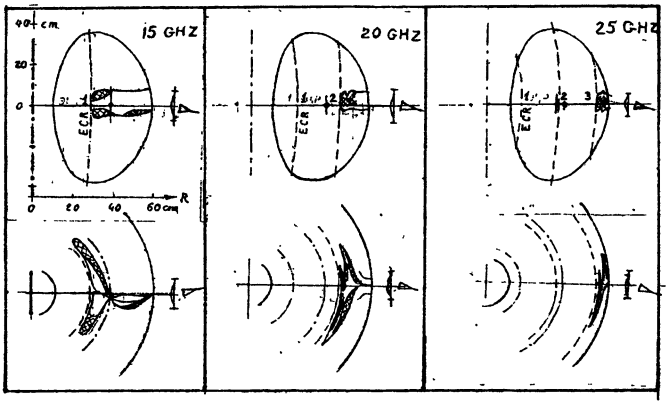

Fig. 5. Ray tracing prediction of propagation and absorption of EBW, excited near the equatorial plane, for some frequencies. The bunch of rays corresponds to the horn antenna diagram.

In experiment the radiation temperature of microwave emission, T_{rad}, was measured by absolutely calibrated, in eV, heterodyne receivers in the range of $T = 10$–25 GHz. Usually two frequencies were registered at once. Antennae of a horn type receiving linearly polarized waves of O or X modes were placed in non-optimal position (*2*), Fig. 1, in rather long distance of a plasma looking through a quartz window in direction perpendicular to B_{tot}, ($\varphi = 0$, $\theta = 0$, Fig. 4). The change of this direction was not possible. Some results of emission measurements in ohmic discharges at $I = 180$–240 kA, $B(0) = 0.4$ T are presented in Fig. 6. $T_e(0) = 400$–500 eV was measured by Thomson scattering. Dependencies of T_{rad} on T and mean plasma density, n_e, in O and X

polarizations were studied. At the same time hard X-ray radiation, HXR, controlling the runaway level in a plasma was registered. Typical recordings of microwave emission at several T are shown in Fig. 6. In the left column the traces of X-mode signals in discharges with low HXR level are shown. Probably the thermal emission is observed in this case. The scale of T_{rad} in eV is pointed. The trace of a mean density signal is shown also. In the right column we present the comparison of O and X modes of emission at 25 GHz and 15 GHz. In this case at rather low n_e HXR signal is strong as a runaway beam is produced in a plasma. Strong flash of non-thermal emission with $T_{rad} > 500$ eV arises in the beginning of a discharge. Besides the 15 GHz signal shows a modulation by MHD oscillatios of sawtooth type.

In conclusion the following features of really observed emission can be noted:

1. In spite of cutoffs for O and X waves localized near the plasma boundary the microwave emission is observed in all range of T studied confirming the mechanism of EBW convesion in O and X waves radiating in a vacuum.

2. In discharges without strong HXR emission the level of T_{rad} is low, < 100 eV, and is less than $T_e(0)$ = 400–500 eV. This result can be explained partly by non- optimal position of receiving antenna and partly by the limited rate of conversion efficiency, $\eta < 100\%$, Fig. 4.

3. The T_{rad} level is clearly dependent on T, its maximum is at 15 GHz confirming the theoretical prediction. The dependence of T_{rad} on plasma density is strong, (Fig. 6, left).

4. The T_{rad} dependence on wave polarization is not found. O and X signals are roughly equal not corresponding the theory.

5. Strong fluctuations of emission signals are observsd especially at lowest T reflecting oscillatios in the zone of conversion. These oscillations can reduce the efficiency of EBW–X–O process.

6. In the case of discharges with strong HXR radiation confirming appearance of accelerated electrons strong flash of non-thermal microwave emission, $T_{rad} > 500$ eV, is developed mostly in initial and final stages of a discharge. Non-thermal emission is observed in low density discharges, $n_e(0) < 2 \cdot 10^{13}$ cm^{-3}.

7. Besides of a direct emission through EBW–X and EBW–X–O conversions leading to penetration of plasma waves through the cutoff zones multiple reflections of microwaves on discharge chamber walls and plasma cutoff surfaces leading to X and O mode mixing and angular scattering should be taken into account for explanation of experimental results.

This experiment was supported by RFBR grants № 02-02-17683, № 04-02-16404.

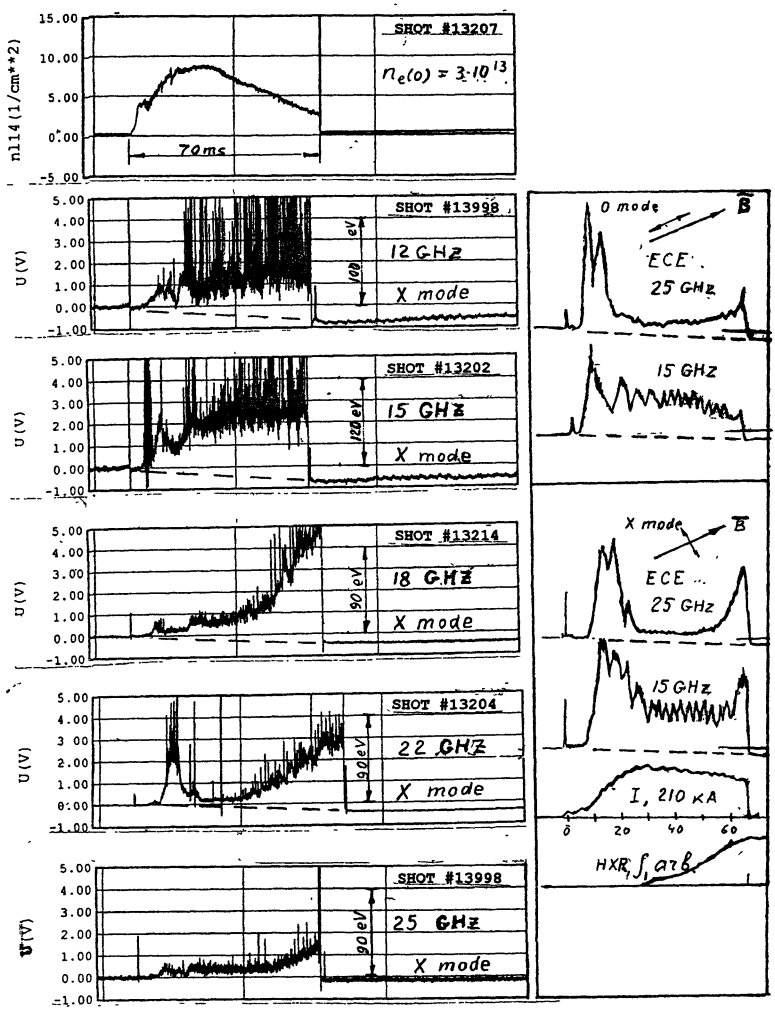

Fig. 6. Microwave emission traces at some frequencies. At the left – X mode, discharges with low HXR emission. At the right – comparison of O and X modes, discharges with runaways and strong HXR emission.

References

1. *Bers A et al*, Proc.12-th Workshop on ECE and ECRH. Aix-en-Provence, France, May 2002, p. 12.
2. *Ram A K et al*, ibid, p. 131.
3. *Piliya A D. et al.*, Plasma Phys. Control Fusion., 2005, 47, p. 2029.
4. *Gusev V K*, Strong Microwaves in Plasmas, 2000, v. 1, p 223
5 *Gusev V.K et al.*, Zh Techn Fiz. 1999, 69, p. 58.

O-X TRANSFORMATION IN TWO-DIMENSIONALLY INHOMOGENEOUS MAGNETIZED PLASMA

E. D. Gospodchikov, E. V. Suvorov

Institute of Applied Physics RAS, Nizhny Novgorod, Russia

Peculiarities of O–X transformation in two-dimensional inhomogeneous magnetized plasma are analyzed. It is shown, what for the optimal beam even neglecting the curvature of cut-off surfaces the transformation is of two-dimensional nature, thus must be treated beyond the scope of the well-known one-dimensional approach. Approximate partial differential equations for rf field in the transformation region are derived and solved. Transformation coefficient and recipe of matching procedure for given distribution of RF electromagnetic fields in the quasi-optical beam are obtained.

1. Introduction

In ECR heating of toroidal plasma there is a well known problem of wave penetration into central parts of plasma column when the plasma density is above the critical one: $N_e > N_c = \omega^2 m / \left(4\pi e^2\right)$. One possible way of solving this problem is the so-called O–X–B coupling process. The process is based on a number of mode transformations in inhomogeneous plasma. A LFS launched ordinary wave (O-mode) is transformed into an extraordinary wave (X-mode) near critical surface ($N_e = N_c$). An electron Bernstein wave (EB wave) is generated from the slow X-wave originating at the upper hybrid resonance layer. Since for EB waves there is no density limit, they propagate towards central parts of plasma column with the dense plasma where they are absorbed in the cyclotron resonance region.

Efficiency of O–X–B process is mainly determined by efficiency of O–X transformation. In the one-dimensional approximation this process is rather well investigated (see, e. g. [1, 2]). But dispersion properties of cold magnetized plasma depend on two parameters: $\upsilon = \omega_{pe}^2 / \omega^2$ and $u = \omega_{ce}^2 / \omega^2$, where ω_{pe} is plasma frequency and ω_{ce} is electron cyclotron frequency. In a toroidal magnetic trap, the surfaces of constant magnetic field strength ($u = \text{const}$) and of constant plasma density ($\upsilon = \text{const}$) are not coinciding in general. This means that even neglecting the curvature of these surfaces the transformation is of two-dimensional nature, and must be treated beyond the scope of the usual one-dimensional approach.

In the present work peculiarities of O–X transformation in a magnetized plasma with two-dimensional inhomogeneity are investigated basing approximate wave equation for the 2D model of magnetic field and plasma density distributions in a tokamak. Differences between 2D case and 1D case are shown in

Fig. 1 where cut-off surfaces for extraordinary and ordinary waves are displayed. 2D case corresponds to cut-off surfaces crossing, while in 1D approach cut-off surfaces are parallel.

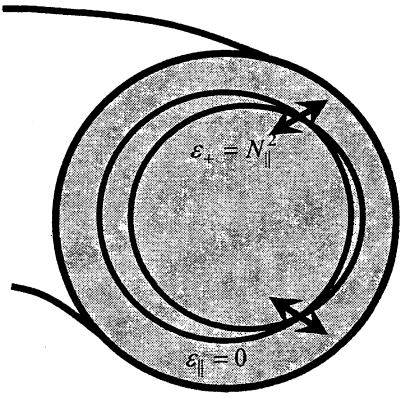

Fig. 1. Cut-off surfaces of ordinary ($\varepsilon_\parallel = 0$) and extraordinary ($\varepsilon_+ = N_\parallel^2$) waves in poloidal section of tokamak.

2. Approximate wave equation

We consider a model distribution of plasma parameters in which the magnetic field is directed along z axis and the magnetic field strength and the plasma density are dependent on the co-ordinates (x, y) orthogonal to this direction: $N_e = N_e(x,y)$, $B = B(x, y)$. In such a situation component of refractive index parallel to the magnetic field ($N_\parallel$) is conserved and dependence of electric field on co-ordinates may be taken in the form:

$$\mathbf{E}(x,y,z) = \mathbf{F}\left(x,y,N_\parallel\right)\exp\left(ik_0 N_\parallel z\right). \tag{1}$$

Let us take the origin of co-ordinate system (x,y) in the point where curves $\varepsilon_\parallel(x,y) = 0$ and $\varepsilon_+(x,y) = N_\parallel^2$ are crossing (with $\varepsilon_+ = 1-\upsilon/\left(1+\sqrt{u}\right)$ and $\varepsilon_\parallel = 1-\upsilon$); these curves bound evanescence regions for the left-polarized X and O waves with fixed longitudinal refractive index $N_\parallel$ [1] and let the direction of x axis be defined from the following:

$$\mathbf{l} \uparrow\downarrow \mathbf{x}, \qquad \mathbf{l} = \frac{\nabla\varepsilon_+}{\left|\nabla\varepsilon_+\right|} + \frac{\nabla\varepsilon_\parallel}{\left|\nabla\varepsilon_\parallel\right|}. \tag{2}$$

Monochromatic electromagnetic field distribution is governed by well known general wave equation:

$$\mathrm{rotrot}\,\mathbf{E} - k_0^2\,\hat{\varepsilon}\,\mathbf{E} = 0\,, \tag{3}$$

where $k_0 = \omega/c$ and $\hat{\varepsilon}$ is dielectric tensor of cold magnetized plasma.

Stix components are used for the description of electric field:

$$\mathbf{E} = \begin{pmatrix} E_- \\ E_+ \\ E_\parallel \end{pmatrix}, \quad E_\pm = \frac{E_x \pm iE_y}{\sqrt{2}}, \quad E_\parallel = E_z . \tag{4}$$

Substituting Eq. (1) into (3) and using standard simplifying expansion procedure [2] over small parameter λL^{-1} (λ is the wavelength, and L is scale of inhomogeneity) we get in the first order the following set of equations for electric field components F_+, F_- and $F_\parallel$:

$$\begin{cases} \left(N_\parallel^2 - \varepsilon_+(x,y)\right)\dfrac{\sqrt{2}\omega}{cN_\parallel}F_+ = -i\dfrac{\partial F_\parallel}{\partial x} + \dfrac{\partial F_\parallel}{\partial y} \\ \varepsilon_\parallel(x,y)\dfrac{\sqrt{2}\omega}{cN_\parallel}F_\parallel = i\dfrac{\partial F_+}{\partial x} + \dfrac{\partial F_+}{\partial y} \\ F_- = 0. \end{cases} \tag{5}$$

In obtaining Eqs. (5) the following parameters are considered to be small:

$$\frac{1}{k_0 N_\parallel}\left|\frac{1}{F_{+,\parallel}}\frac{\partial F_{+,\parallel}}{\partial x}\right|, \quad \frac{1}{k_0 N_\parallel}\left|\frac{1}{F_{+,\parallel}}\frac{\partial F_{+,\parallel}}{\partial y}\right|, \quad \left|\varepsilon_+ - N_\parallel^2\right|, \quad \left|\varepsilon_\parallel\right|. \tag{6}$$

The first two parameters represent slightly corrected modifications of small parameter λL^{-1} and the two remaining are small due to vicinity of the region under consideration to the transformation point.

The set of Eqs. (5) may be rearranged in a more pleasant and symmetric form:

$$\begin{cases} \left(\cos\alpha \cdot x' + \sin\alpha \cdot y'\right)A_+ = -\left(i\,\partial/\partial x' - \partial/\partial y'\right)A_\parallel \\ \left(\cos\alpha \cdot x' - \sin\alpha \cdot y'\right)A_\parallel = -\left(i\,\partial/\partial x' + \partial/\partial y'\right)A_+ \end{cases} \tag{7}$$

after the following normalization of field components and co-ordinates:

$$A_{+,\parallel} = \left|\nabla\varepsilon_{+,\parallel}\right|^{-1/2} F_{+,\parallel} \quad x' = \left(N_\parallel/\sqrt{2}k_0\right)^{-1/2}\left(\left|\nabla\varepsilon_+\right|\left|\nabla\varepsilon_\parallel\right|\right)^{1/4} x,$$

$$y' = \left(N_\parallel/\sqrt{2}k_0\right)^{-1/2}\left(\left|\nabla\varepsilon_+\right|\left|\nabla\varepsilon_\parallel\right|\right)^{1/4} y,$$

with 2α being the angle between directions $\nabla\varepsilon_+$ and $\nabla\varepsilon_\parallel$.

The second terms in the left-hand sides of Eqs. (7) are responsible for the 2D properties of transformation; they should be taken into account, when $\alpha >> \lambda L^{-1}$. In particularly case of T-10 tokamak, the latter inequality may be valid for displacement of microwave launching point from equatorial plane more than approximately 30°.

3. Solution of approximate equations

Eqs. (7) have the partial solution of the following form:

$$A^0_{+,\|} = \pm C_1 e^{\frac{1}{2}\left(i\cos\alpha x'^2 + \sin\alpha y'^2\right)} + C_2 e^{\frac{1}{2}\left(i\cos\alpha x'^2 + \sin\alpha y'^2\right)}. \quad (8)$$

The first term of this solution corresponds to the beam propagating in the direction of plasma density increase, and the second term corresponds to the beam propagating in the opposite direction.

Using the constant variation technique for case of beam propagating to dense plasma and taking (for definiteness) positive sign of angle α one can get general solution of Eqs. (7) in the form:

$$A_{+,\|} = \pm\sum_{n=0}^{\infty} A_n e^{i\frac{1}{2}x' - \frac{1}{2}y'^2\sin\alpha} D_{in\tan\alpha}\left(\sqrt{2\cos\alpha}e^{-i\pi/4}x'\right) H_n\left(\sqrt{\sin\alpha}\,y'\right) + \quad (9)$$

$$+\left(refl.\,wave\right),$$

where A_n are arbitrary constants, $H_n(\xi)$ are Hermit polynomial and $D_v(\xi)$ are parabolic cylinder functions correspondingly. The second term corresponding to reflected wave is not presented explicitly because of its rather complicated form.

Functions

$$f_n(y') = e^{-\frac{1}{2}y'^2\sin\alpha} H_n\left(\sqrt{\sin\alpha}\,y'\right) \quad (10)$$

form orthogonal basis with the scalar product

$$\int_{-\infty}^{\infty} f_n f_m dy' = 2^n n!\sqrt{\pi}\delta_{nm}. \quad (11)$$

This fact essentially simplifies the calculation of coefficients A_n in solution (9); for a given field distribution $A^{inc}_{\|}(y')$ (corresponding to $x' \to -\infty$) in beam incident to the transformation region:

$$A_n = \frac{1}{\sqrt{2^n n!\sqrt{\pi}}} \int_{-\infty}^{\infty} A^{inc}_{\|}(y') f_n(y') dy'. \quad (12)$$

Relations (9) and (12) get full solution for the wave tunneling through the evanescent region.

4. Coefficient of O–X transformation and optimal beam

The transformation coefficient T_n for basis functions (10) can be obtained from asymptotics of parabolic cylinder functions [2]:

$$T_n = \exp\left(-\pi n\tan\alpha\right). \quad (13)$$

The transformation coefficient for wave beam (9) with fixed $N_{\|}$ is a weighted sum of basis transformation coefficient (13)

$$T\left(N_{\|}\right)=\sum_{n}\left|A_n\right|^2 T_n \Big/ \sum_{n}\left|A_n\right|^2 . \tag{14}$$

Transformation coefficient for incident wave beam with arbitrary distribution over transverse coordinates $E^{inc}(y',z)$ takes the form:

$$T=\frac{1}{P_0}\int_{-\infty}^{\infty}\sum_{n=0}^{\infty}\left|\int_{-\infty}^{\infty}\int_{-\infty}^{\infty} e^{-ik_0 N_{\|} z} E^{inc}\left(y',z\right) f_n\left(y'-y_0'\left(N_{\|}\right)\right)dy'dz\right|^2 T_n\, dN_{\|}, \tag{15}$$

where $P_0=\int_{-\infty}^{\infty}\sum_{n=0}^{\infty}\left|\int_{-\infty}^{\infty}\int_{-\infty}^{\infty} e^{-ik_0 N_{\|} z} E^{inc}\left(y',z\right) f_n\left(y'-y_0'\left(N_{\|}\right)\right)dy'dz\right|^2 dN_{\|}$,

and $y_0'\left(N_{\|}\right)=-\left(N_{\|}-N_{\|}^0\right)\left(\sqrt{2}k_0 N_{\|}\right)^{1/2}\left|\nabla\varepsilon_-\right|^{1/4}\left|\nabla\varepsilon_+\right|^{-3/4}\sin^{-1}\alpha$.

Displacement $y_0'\left(N_{\|}\right)$ in Eq. (15) reflects $N_{\|}$-dependence of the position of the point defined by crossing of curves $\varepsilon_{\|}(x,y)=0$ and $\varepsilon_+(x,y)=N_{\|}^2$.

For every $N_{\|}$ there is an optimal distribution $E^{inc}\propto\exp\left(-y^2/2L_{opt}^2\right)$, with

$$L_{opt}^2(N_{\|})=\frac{N_{\|}}{\sqrt{2\left|\nabla\varepsilon_+\right|\left|\nabla\varepsilon_{\|}\right|}k_0\sin\alpha}. \tag{16}$$

Taking into account displacement $y_0'\left(N_{\|}\right)$ one can construct an optimal distribution corresponding to fully transformed beam:

$$E_{opt}^{inc}(y,z)=\int_{-\infty}^{\infty} G\left(N_{\|}\right)\exp\left(-\frac{1}{2L_{opt}^2(N_{\|})}\left(y-\frac{N_{\|}-N_{\|}^0}{\left|\nabla\varepsilon_+\right|\sin\alpha}\right)^2+iN_{\|}k_0 z\right)dN_{\|}. \tag{17}$$

For example for "normal" weight function $G\propto\exp\left(-\left(N_{\|}-N_{\|}^0\right)^2 k_0^2 L_z^2\right)$:

$$E\propto\exp\left(-a_1 y^2-a_2 z^2-ia_3 yz+iN_{\|}^0 k_0 z\right), \tag{18}$$

with $a_1=\frac{1}{2L_{opt}^2}\left(1-\frac{\left(N_{\|}^0\right)^2}{2k_0^2 L_z^2 L_{opt}^2\left|\nabla\varepsilon_+\right|^2\sin^2\alpha}\right)$, $a_2=\frac{1}{4L_z^2}$, $a_3=\frac{1}{2L_z^2}\sqrt{\frac{\left|\nabla\varepsilon_-\right|}{\left|\nabla\varepsilon_+\right|}}$.

5. Conclusion

Theory of O–X transformation is developed with taking to account variation of a magnetic field strength on a flux surface within the two-dimensional model of magnetic field and plasma density distributions in a tokamak. The set of approximate wave equations for distribution of an electromagnetic field in two-dimensionally inhomogeneous transformation region is obtained and analyzed. Basing on a full analytical solution of the system the O–X transformation efficiency is found. The solution is formulated in a convenient form as a sum over discrete basic terms related to a specific full orthogonal basis representing the electric field in a wave beam. It is demonstrated that even neglecting the curvature of the flux surfaces, the transformation may be essentially two-dimensional due to finite angle between surfaces of constant magnetic field magnetic field intensity and of constant plasma density. The most pronounced feature of 2D transformation is existence of the "optimal" beam exhibiting full transformation instead of "optimum" plane wave specific for one-dimensional geometry.

This work is partially supported by 03-02-17466 RFBR grant and 047.016.016 NWO-RFBR grant.

References

1. *Preinhalter J, Kopecky V.* // J. Plasma Phys. 1973. V 10 P. 1.
2. *Tokman M.D.* // Plasma Phys. 1985. V 10. P 1205.

COUPLING ION BERNSTEIN WAVES TO TOKAMAK PLASMAS BY WAVEGUIDE ANTENNAS

G. L. Ravera, C. Castaldo, R. Cesario, P. Papitto

Associazione EURATOM-ENEA sulla Fusione, C.R. Frascati, Frascati, Italy

The Ion Bernstein Wave (IBW) experiment on the FTU tokamak is aimed at heating the plasma bulk ions by utilising the mode-conversion of lower hybrid (LH) waves coupled by two waveguides' antennas. The results show that the antennas couple the useful LH wave and that moderate effects of non-linear physics, such us parametric instabilities and ponderomotive effects, occur in the edge. The RF system at the frequency of 433 MHz is powered by two klystrons connected to standard rigid coaxial lines. In the paper the RF design, construction and exploitation of the alumina vacuum tight window of the antenna will be reported. The presence of such component allows transmitting high RF power, since breakdown-free operations are obtained by working with high pressure in most of the antenna regions.

Introduction

The main goal of the IBW experiment on FTU at the frequency of 433 MHz is to demonstrate that the Ion Bernstein Waves can be coupled to tokamak plasmas by waveguide antennas. Operating with a toroidal magnetic field of 7.9 T, the fourth ion cyclotron harmonic of the hydrogen is located at about one third of the minor radius (two thirds for the layer of the ninth harmonic of Deuterium).

The design of the system started after the good results of the IBW experiments on ALCATOR C and PLT. In the following, as a consequence of the negative results on DOUBLET III-D and TFTR concerning the plasma heating effectiveness of the IBW waves, the Frascati experiment had the further goal to prove that IBW can heat the ions and improve the confinement through induced plasma sheared flows. The relatively high operating frequency and the use of a waveguide launcher might produce results clearer that in previous experiments. The IBW experiment on FTU started in 1997 by utilizing only one launcher. In 2001 a second launcher was installed in a different equatorial port. In the last campaign, about 0.5 MW of RF power have been coupled into H or D majority plasmas. The design of a new vacuum tight ceramic window made possible the coupling of a higher RF power. The paper reports the design and construction criteria of the vacuum windows, built in collaboration with the Princeton Plasma Physics Laboratory (PPPL) USA. In addition it describes the tests of the windows performed in ENEA Frascati.

Waveguide antennas

After the installation of the second waveguide antenna, the IBW launching system consists of two antennas installed in two different equatorial ports of FTU.

Each antenna is made by a grill of two phased, reduced sizes (400 × 29.5 mm at the mouth), waveguides joined together along their broad side (Fig. 1).

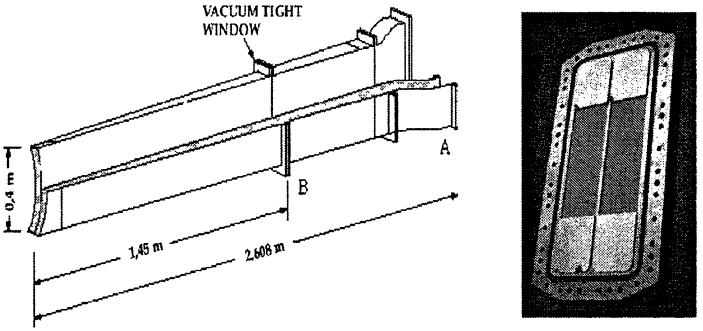

Fig. 1. IBW launcher schematic and double vacuum window

A single double tight window separates the pressurized region of the launcher from its terminal section exposed to the vacuum vessel.

Tight vacuum windows

In the first antenna setup (1995), the vacuum windows were located far from the plasma (about 2.5 m); in this condition the maximum-coupled RF power was only 10 kW for each waveguide. The limiting factor was ascribed to multipactor discharges induced by electron cyclotron resonance in the external vacuum region of the launcher exposed to the residual toroidal magnetic field of the machine. The present solution with ceramic windows located closer to the antenna mouth (about 1.4 m), locating the electron cyclotron resonance region in a pressurized section of the launcher, allowed to consistently increase the IBW power. Two different types of high power RF window were considered; the analysis of the two solutions by means of the "High Frequency Structure Simulator" (HFSS) code eventually allowed choosing the component with the best performances.

Windows with rectangular dielectric

In the geometric model of this RF component, shown in Fig. 2, the dielectric (alumina ceramic with permittivity 9.7 and loss tangent 10^{-4}) is centered in a transverse plane of the rectangular waveguide (400 × 76 mm) between two symmetric metallic frames used as matching elements.

The dielectric height corresponds to the minor dimension of the waveguide (b = 76 mm) while its thickness and length (x) are defined by the simulation. The dimensions of ceramic and metallic frame (thickness and width) have been optimised by minimizing the reflection coefficient taking into account that in

matched conditions the impedance of the window $(L/C)^{1/2}$ must be equal to the wave impedance of the waveguide $(L_0/C_0)^{1/2}$. The diagram in Fig. 3 shows all the simulation resultsrange 10.3–20 mm, the best results are obtained for a dielectric thickness of 15 mm (reflection coefficient S_{11} lower than –40 dB and insertion loss of about –0.22 dB at 433 MHz).

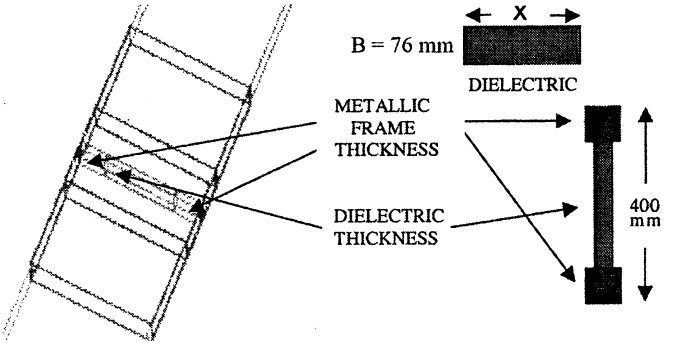

Fig. 2. Geometrical model of window with rectangular dielectric

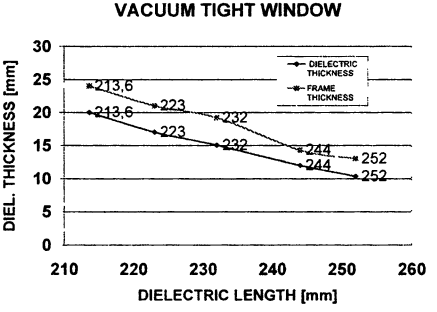

Fig. 3. Dielectric and frame thickness versus width dielectric at 433 MHz.

Window with posts matching

The second type of window presents dielectric frames with circular edges (radius 38 mm) and the same thickness of the previous one (15 mm for the dielectric and 19.1 mm for the metallic frame). The rounded corners reduce the eventuality of fracture of the dielectric due to thermal stresses during the brazing process. Figure 4, *a* gives the geometric model of the window assembled in the rectangular waveguides (400 × 76 mm).

The dielectric and the symmetric metallic frame are placed in the transverse plane of the waveguide and the dimensions shown in Fig. 4, *a* minimizes the reflection coefficient. In this case the window presents a mismatching (VSWR = 1.8); the insertion in the pressurized region of the waveguide of two

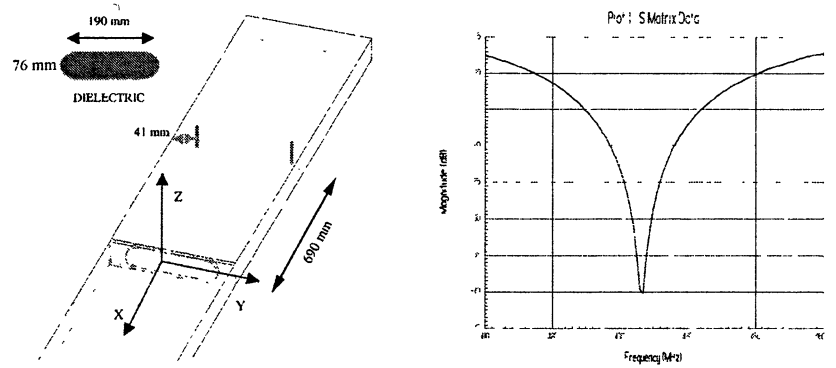

a) Geometry *b*) S_{11} amplitude [dB]

Fig. 4. High power tuning window with cylindrical metallic posts and dielectric with circular side.

symmetrical metallic posts with diameter 1 cm, allows the matching of the RF structure. The position of the posts is optimized after the evaluation of the window scattering parameters and the characterization, in terms of reflection coefficient (amplitude and phase), of the symmetric posts versus their positions along the broad dimension of the waveguide. With the positioning shown in Fig. 4, *a* the S_{11} amplitude is about –38 dB at $f = 433$ MHz.

Tight windows performance comparison

In the Table the performance of these two different windows with the same dielectric and metallic frame thickness are compared. The electric field is evaluated at $f = 433$ MHz for a RF power of 300 kW in matching condition and with VSWR = 4.

According to this table, the window with rectangular dielectric presents electric field, RF power loss and reflection coefficient lower than the second one, In addition the realization of the rounded window with posts is more complicated and expensive than the first one, therefore it was decided to build and install rectangular windows.

Windows performance

	S_{11} (dB)	Ploss (%)	Electric field (kV/cm)
Vacuum window (15 mm)	–45	0.4	2.4 @VSWR = 1 3.65 @VSWR = 4
Vacuum window with Post (15 mm)	–38	0.7	3.5 @ VSWR = 1 6 @ VSWR = 4

Construction and test of new windows

Vacuum windows with these characteristics have been built in collaborations with PPPL, which realized the brazing of two big alumina sleeves into a titanium frame. This window is composed of a tight alumina slab (type AD 995, cross section 232 × 76 mm, thickness 15 mm) brazed into a titanium frame (cross section 84 × 76 mm, thickness 19.10 mm), which acts also as adapting iris. Two double tight windows have been characterized in ENEA. The low power measurements have been made using the test set up given in Fig. 5. At the operating frequency of 433 MHz the measured S_{11} amplitude is about –20 dB and the insertion loss –0.17 dB.

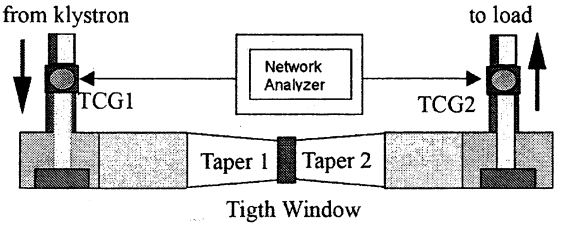

Fig. 5. Test set-up

TGC = Coax to waveguide transition

In the high power test the maximum launched RF power is 400 kW for one second. All the tests have given satisfactory results and now these double windows are in operation in the IBW antennas.

Conclusions

The primary goal of the IBW experiment, transmission of high power through waveguides and coupling to the plasma (0.4 MW routine power with two launchers, corresponding to a power density of 15 MW/m^2 at the mouth) of a lower hybrid wave useful for IBW conversion, has been successfully achieved. This goal has been obtained after the realization of the new vacuum tight alumina window. In the next FTU experimental campaigns further features of IBW will be tested.

Acknowledgement. The authors would like to thank the ENEA (Frascati) RF group (Aquilini, Petrolini, Di Giovenale and Zampelli) for their activity in the IBW system. They wish also to thank Francesco Mirizzi, Angelo Antonio Tuccillo and Massimo Papalini for their collaboration to this paper.

References

1 *Papitto P. et al*, Proc. 19th SOFT Lisbon, Portugal, 1996, p. 613–616.
2. *Cesario R. et al.*, Phys. Plasma, **8**, No. 11 (Novembre 2001), p. 4721–4724.
3. *Cardinali A. et al.*, Nucl Fusion, **42**, No. 4 (April 2002), p. 427-440.
4. *Castaldo C et al.*, Nucl. Fusion, **44**, No 1 (January 2004), L1-L4.

LOW- AND HIGH-POWER INVESTIGATIONS OF AN ITER REMOTE STEERING LAUNCHER MOCK-UP

W. Kasparek[1], V. Erckmann[2], G. Gantenbein[1], B. Plaum[1], K. Schwörer[1], R. Wacker[1], M. Grünert[1], F. Hollmann[2], L. Jonitz[2], H. P. Laqua[2], G. Michel[2], F. Noke[2], F. Purps[2], D. Wagner[2], A. V. Chirkov[3], G. G. Denisov[3], S. V. Kuzikov[3], K. Ohkubo[4], A. Bruschi[5], S. Cirant[5], F. Gandini[5], A. G. A. Verhoeven[6], ECRH groups at IPP Greifswald[2], FZK Karlsruhe[7] and IPF Stuttgart[1]

[1]Institut für Plasmaforschung, Univ. Stuttgart, 70569 Stuttgart, Germany
[2]MPI für Plasmaphysik (IPP), EURATOM Association, 17491 Greifswald, Germany
[3]Institute of Applied Physics, RAS, 603600 Nizhny Novgorod, Russia
[4]National Institute for Fusion Science, 322-6 Oroshi-cho,Toki, 509-5292, Japan
[5]Istituto di Fisica del Plasma, EURATOM-ENEA-CNR, 20125 Milano, Italy
[6]FOM Institute for Plasma Physics, EURATOM Association, Nieuwegein, Netherlands
[7]Forschungszentrum Karlsruhe, EURATOM Association, D-76021 Karlsruhe, Germany

For the upper launchers of the 170 GHz electron cyclotron resonance heating (ECRH) and current drive system of ITER, "remote steering" based on the imaging properties of corrugated square waveguides is the reference option. In the last years, a variety of numerical simulations and experimental investigations of a remote steering launcher (RSL) mock-up were performed and demonstrated the feasibility of this concept.
In this paper, low- and high-power experiments of a remote steering antenna mock-up are presented and compared. The tests included recording of radiation patterns, ohmic loss measurements, and exploration of the limits for breakdown. All measurements were performed with a straight launcher mock-up as well as with a dog-leg version with two integrated mitre bends It is shown that the usable steering range of the antenna is ±12°, and that optimized mitre bends can be integrated without prohibitive extra loss. Consequences for the design of the upper launcher on ITER are discussed.

1. Introduction

The International Thermonuclear Experimental Reactor (ITER) will be equipped with a 170 GHz electron cyclotron resonance heating (ECRH) system, which can be applied for localised heating or current drive (ECCD) in the plasma [1]. The upper launcher concept under investigation is the so-called remote-steering launcher as proposed in [2], which is developed by a European consortium [3] as well as in Japan and the U.S. [4]. The launcher basically consists of a corrugated square waveguide with a steerable mirror at the entrance of the guide.

Square corrugated waveguides show imaging characteristics [5]: Within the paraxial approximation and for balanced conditions, the propagation constants of the hybrid modes $HE_{m,n}$ differ by a multiple of $\Delta k = \pi\lambda/(4a^2)$. Here, λ is the vacuum wavelength and a is the side of the waveguide. Of particular interest is a waveguide length of

$$L = 4a^2/\lambda. \quad (1)$$

For this case, the phase difference of adjacent modes at the waveguide output is $\delta \approx (2n + 1)\pi$, and an antisymmetric image of the input field is generated. Thus, if a beam is injected into such a waveguide at an angle φ, the identical beam is emitted from the waveguide end at the angle $-\varphi$. This feature can be used for the design of a remote steering antenna and is illustrated in Fig. 1 by a calculation of the field in the mid-plane of the waveguide for the case of $\varphi = 5°$. For a continuous angular scan, the modulus of φ is restricted to $|\varphi| < 12°$ due to the breakdown of the paraxial approximation, as shown in Fig. 2. At larger angles, revivals of the beam occur; consequences from this behaviour are extensively discussed in [6]. Further theoretical and experimental works on remote steering antennas is found in [7, 8, 9].

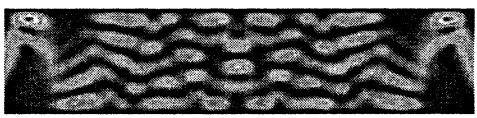

Fig. 1. Field distribution in the mid-plane of the square waveguide for $\varphi = 5°$. Parameters: $a = 60$ mm, $f = 140$ GHz, $L = 6.62$ m.

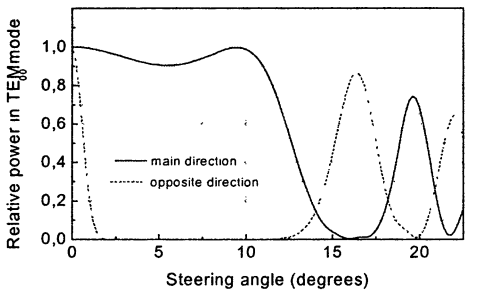

Fig. 2. Gaussian beam purity as function of φ. Solid line: main (antisym.) direction, dotted line: opposite direction.

This paper summarizes experiments performed with a four-wall corrugated square waveguide antenna with transverse dimension $a = 60$ mm. The corrugation profile was rectangular with a depth of $d = 0.45$, a width of $b = 0.4$ mm and a period of $p = 0.7$ mm. The length of the waveguide was matched to the frequency according to (1) with a small correction of 0.986 [6] to optimize it for $\varphi = 10°$. The low-power experiments were performed at 148 GHz and 158 GHz, therefore the waveguide length was $L = 7.0$ m and $L = 7.5$ m, respectively; for the high-power test at 140 GHz, $L = 6.62$ m was used. Most experiments were done with a straight waveguide. However, as in ITER, a reduction of the neutron flux to the vacuum window and the steering mechanism might become necessary, a "dog-leg"-version of a remote-steering antenna with 2 mitre bends was investigated.

Low-power experiments were performed at IPF Stuttgart by injecting a Gaussian beam from a lens horn via a scanning mirror into the waveguide and recording near- and far-field patterns by field scanners and a vector network analyzer. The high-power tests [10] (pulses up to 700 kW, 10 s) were performed at the ECRH facility of the future stellarator W7-X at IPP Greifswald, where

a 140 GHz, 10 MW CW ECRH system is presently being installed employing optical transmission [11]. For the tests, the beam from the "Maquette" gyrotron was detoured in front of the dummy load by a fixed beam shaping mirror and a rotatable mirror and directed into the square corrugated waveguide as shown in Fig. 3. For long-pulse measurements, the power was dumped into a spherical load from IFP Milano [12] at the end of the waveguide.

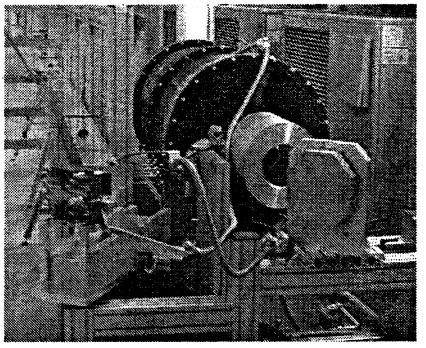

Fig. 3. Experimental set up for the high-power test of the remote steering antenna. The beam coming from the gyrotron via the first part of the transmission line is detoured in front of the dummy load and injected via a beam forming mirror and a steering mirror into the square waveguide.

2. Near-field patterns, mode purity

In low-power experiments, amplitude and phase distributions at the exit aperture of the square waveguide have been recorded as function of the steering angle. High agreement with theory is found [7]. An example for $\varphi = 0°$ and $\varphi = 10°$ is shown in Fig. 4. The picture shows that the amplitude distributions at the waveguide exit are practically identical. The phase distribution for $\varphi = 0°$ is flat within $\pm 20°$ showing that an axial beam will be radiated from the waveguide. At $\varphi = 10°$, the observed phase slope corresponds to a beam which is radiated with this angle.

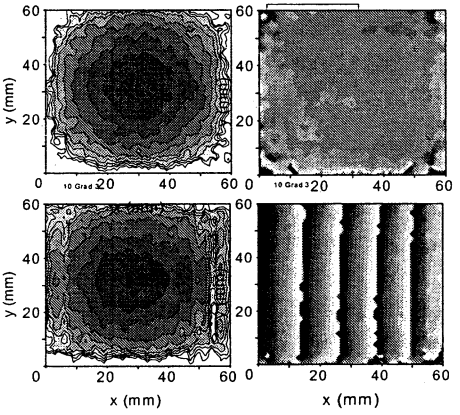

Fig. 4. Amplitude and phase distributions in the exit aperture of the square waveguide for $\varphi = 0°$ and $\varphi = 10°$ (3 dB and 20° per level).

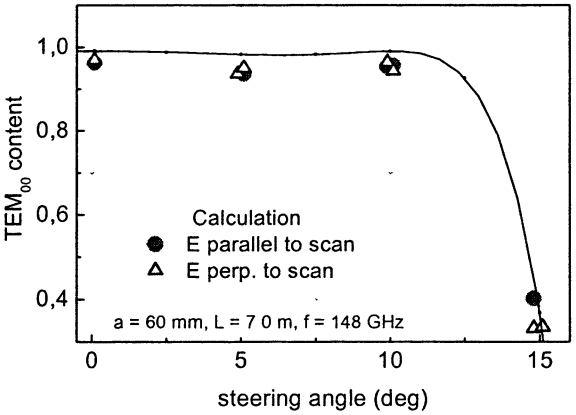

Fig. 5. TEM_{00} mode contents of the radiated beam as function of the steering angle. Line: numerical calculation. Symbols: meas. values for polarization parallel (dots) and perpendicular (triangles) to the steering plane.

From the Gaussian beam mode analysis [13] of the near-field, the complete information of the radiated beam can be obtained: TEM_{00} mode purity, radii and positions of the waist in the steering plane and the plane perpendicular to it, as well as the beam axis. As an example, Fig. 5 shows the TEM_{00} mode purity as function of the steering angle. One can see that a mode purity of typically 95% was reached for $|\varphi| \leq 10°$, in good agreement with theory. Note here, that the calculated mode purity is for a Gaussian beam which is optimally matched to the output field, in contrast to the calculation in Fig. 2, where the mode purity with respect to a beam with identical parameters as the input beam is plotted.

3. Radiation patterns

Low-power records of the radiation pattern show a low side-lobe level and thus confirm the high mode purity obtained from the investigations of the near-field (example in Fig. 6). For both polarizations, results are similar. It could be demonstrated that elliptically polarized radiation keeps its polarization characteristics. With a beam injected with a linear polarization at 45° with respect to the steering plane, the measured field pattern shows no decrease in the co-polarized power at large scanning angles (Fig. 6). The cross-polarized power in the range of $-10° < \varphi < 10°$ is below 2%. This result however holds only for balanced hybrid conditions in the waveguide (groove depth near to $\lambda/4$), which were obtained at a frequency of 158 GHz. This finding is in good agreement with theory based on integral equations or impedance calculations of the waveguide wall [8, 14], but reveals inaccuracies in the propagation constants calculated with the available scattering matrix code [15].

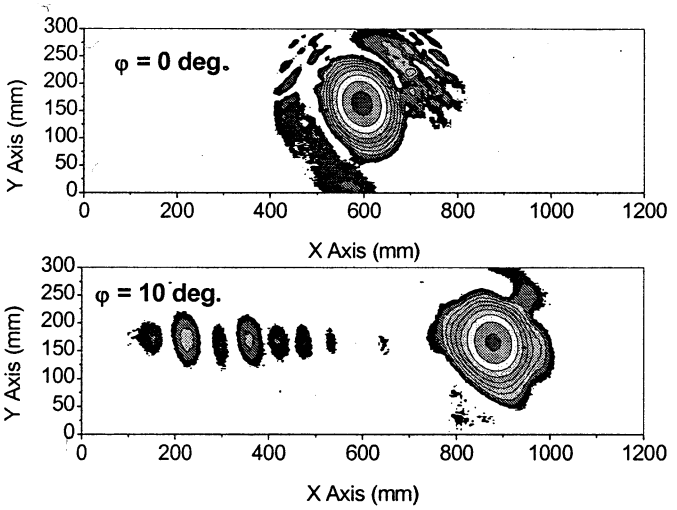

Fig. 6. Radiation patterns for the four-wall corrugated square waveguide at $\varphi = 0°$, and 10°, $f = 158.0$ GHz, $L = 7.5$ m, linear polarisation at 45° with respect to scanning plane. Scale: 3 dB/colour.

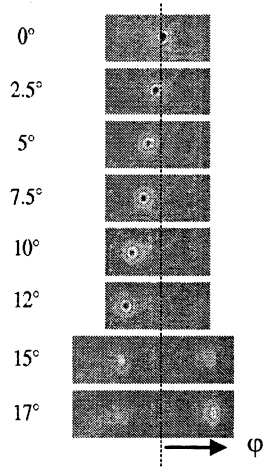

Fig. 7. Thermographically recorded far-field patterns of the remote steering antenna for various steering angles and polarization perpendicular to the steering plane.

In the high-power tests, far-fields were recorded by transmitting short pulses onto an absorbing screen and recording the temperature patterns with an infrared camera. Figure 7 shows the far-fields for both polarization planes. One can see a good beam quality for steering angles up to 12.5°, which is more than the nominal steering range proposed for ITER. At higher angles, a lobe in the opposite direction develops in good agreement with theory (cf. Fig. 2) and the low-power measurements.

4. Ohmic losses

For high-power applications of the remote steering launcher, the total transmission efficiency and especially the ohmic loss is of interest. Low-power measurements of the transmission efficiency with respect to the main lobe normalized to the value at $\varphi = 0°$ show a light drop with increasing steering angle. Assuming a coupling and transmission loss of 2% for $\varphi = 0°$, the power transmission coefficient can be fitted by $\eta \approx 0.98–0.005\varphi$ [°]. This result was rather independent of polarization. With high-power, a similar measurement was not possible due to insufficient reproducibilty of the gyrotron and lack of equipment. To determine the ohmic loss of the waveguide, an approach was chosen based on the ohmic loss for a single reflection of the radiation at the waveguide wall. The total ohmic loss can then be determined by calibrating the calculated relative power distribution on the waveguide wall (cf. Fig. 1) with the experimental result and subsequent integration over the waveguide. In a low-power experiment, the single reflection loss as function of the steering angle ($\varphi = 90° - \alpha$, where α is the angle of incidence) and polarization was measured in a 3-mirror set up [16]. The absorption coefficient A for one reflection could be fitted to $A_{\parallel} = 0.0098 \cdot \sin\varphi$ and $A_{\perp} = 0.003 \cdot \sin\varphi$ for parallel and perpendicular polarization, respectively. In the high-power test [10], the temperature distribution on the waveguide wall after a long pulse was measured. The temperature near the inner waveguide wall was recorded by a 2D array of thermal sensors in the area, where the first reflection of the beam occurs. The measured values were fitted to a Gaussian temperature profile, which allows the estimation the heat energy content and thus the ohmic losses of the first reflection of the beam. For instance, for a beam power of 500 kW at $\varphi = 11.6°$, the resulting losses for the first reflection are 0.9 kW (0.18 %) and 0.3 kW (0.06 %) for parallel and perpendicular polarization, respectively. These values are in good agreement with the results obtained from the resonator measurements. In Figure 8, the resulting total loss of the waveguide as function of the steering angle is plotted.

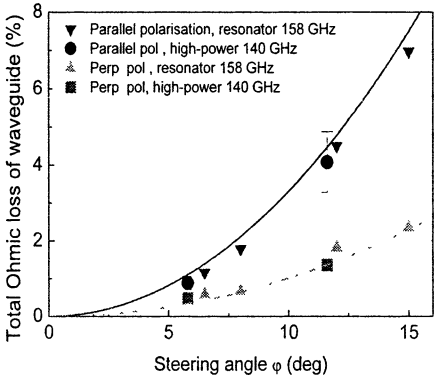

Fig. 8. Calculated total ohmic loss of the remote steering antenna as function of φ, based on resonator measurements (up- and down triangles) and high-power tests (squares and circles) for perpendicular and parallel polarization, respectively.

Additionally, thermal imaging was used to monitor the power distribution on the wave-guide wall. These data confirm the ohmic loss measurements. As Figure 9 shows, a good agreement between measurement and calculation is obtained.

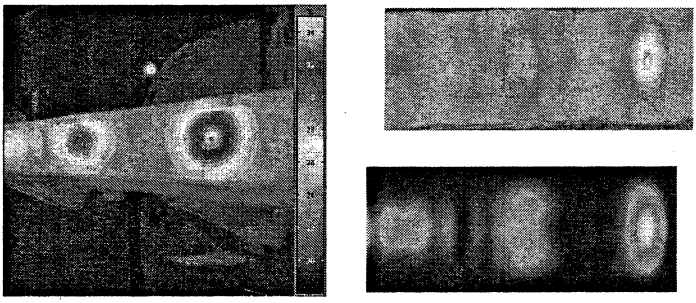

Fig. 9. Left: thermographic image of the outer waveguide wall. Right: rectified thermal image (top) and calculated power density (bottom). Parameters: $\varphi = 11.6°$, P = 500 kW, pulse $\tau = 8$ s, parallel polarization.

5. Implications for the integration of mitre-bends

For ITER, mitre bends might be needed in the remote steering antenna to reduce the neutron flux to the window. A configuration with two bends (for 140 GHz: 3.1 m straight – 90° bend – 0.28 m straight – 90° bend – 3.24 m straight) was tested with both polarizations.

Mitre bends in square waveguide exhibit three sources of loss: firstly, the unavoidable ohmic absorption in the mirror, secondly, diffraction in the plane of the bend due to the missing waveguide wall, and thirdly – as main contribution – diffraction in the plane perpendicular to the bend arising from the discontinuity of the corrugations. Theory [8] claims that diffraction in the plane of the bends is negligible (typ. less than 0.5%), provided that the bends are positioned in the middle between entrance and exit, as was the case in the experiments. A series of measurements [8] and theoretical considerations [15] showed, that minimum diffraction loss from the waveguide wall was obtained when the corrugations within the bend were rotated by 45° (i.e. parallel to the mirror), and with an increased depth of $d_{MB} = \sqrt{2} \cdot d = 0.63$ mm.

Low- and high-power far-field patterns measured with these optimized bends give practically identical results concerning steering range, however, the side-lobe level slightly higher (< -17 dB for $|\varphi| \leq 10°$) owing to enhanced diffraction loss. An example from the high-power measurements is given in Fig. 10.

In the area of the mitre bends, a thermal problem occurs: the temperature increase was about 3 times higher than the peak temperature at the beginning and end of the waveguide (Fig. 11). These high losses can be explained by the

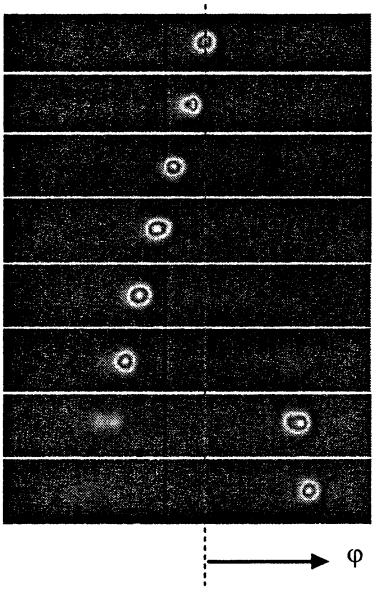

Fig. 10. Far-field patterns for "dog-leg"-version for φ = 0°, 2.5°, 5°, 7.5°, 10°, 12.5°, 15°, and 17.5°. Parallel polarization, 2 mitre bends in the middle of the guide, 0.28 m apart.

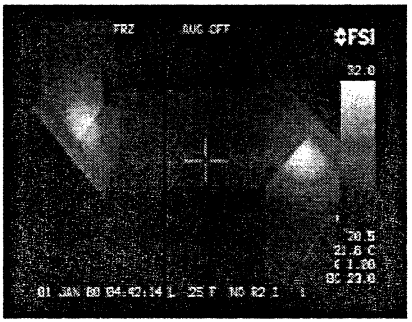

Fig. 11. Thermal image of the mitre bends

fact, that the corrugation in the triangular areas of the bends has a larger depth, and that for angles around 12°, local maxima of the wall fields are coincident with the positions of the bends [10]. By optimum positioning of the mitre bends, this problem could be reduced.

6. Arcing problems

In the straight waveguide, pulses with powers up to 700 kW and durations up to 10 s were transmitted through the waveguide, and no limits due to arcing were found. Note that this result was obtained in operation under atmospheric pressure with a waveguide, which employed rectangular corrugations as it was designed only for low-power tests.

In the waveguide with the mitre bends, arcing limited the operating parameters. To achieve high energies for measuring the temperature increase, periodic pulses (10 ms, duty cycle 0.5) were transmitted.

7. Consequences for the application on ITER at 170 GHz

In the following, some consequences as well as possible improvements for the application on ITER at 170 GHz are discussed. It is assumed, that the waveguide consists of pure copper and is operated at a surface temperature of 200 °C. The waveguide cross-section is quadratic with $a = 44$ mm, the length is taken as $L = 4.33$ m. The power at the waveguide entrance is 2 MW.

For the input beam at the high-power tests, a small ratio between input beam waist w_0 and waveguide width a of $w_0/a = 0.28$ was chosen. This is not optimum with respect to beam divergence, however, it does strongly reduce the risk of arcing at the waveguide entrance and in the mitre bends. By careful optimization of the input beam with respect to width and amplitude profile, a relative reduction of the beam divergence can be obtained. A study [17] shows that high performance can be obtained by imaging the HE11-pattern of the cylindrical waveguide to the input of the square waveguide, resulting in a J_0 pattern. Limits are imposed by truncation of the input beam at the window and waveguide entrance (reflections!) as well as at the waveguide exit.

The overall ohmic loss for the ITER RS launcher is expected to be slightly less compared to the results given in Fig. 8, if the results are scaled with the ITER data given above. At the maximum steering angle of $\varphi = 12°$, a total ohmic loss of 4% is expected for parallel polarisation (worst case) with a maximum wall loading of 2.3 MW/m^2. Note that the operation of the upper launcher will be with elliptical polarisation, i. e. a mixture of parallel and perpendicular polarisation.

The use of mitre bends in the upper launcher of ITER is possible; however, a few percent of extra loss must be taken into account. The strong heating of the waveguide wall in the mitre bends can be handled, but should be avoided as far as possible. One means is the positioning of the bends at places where the field strength on the wall is low. A first analysis of the problem shows, that the loss of the bends can be reduced if mitre bends with higher deflection angles are used. This leads to less rotation of the polarization and thus to a lower diffraction loss. For this case, the depth of the grooves in the mitre bends can be reduced and therefore, the ohmic loss is reduced as well. Additional investigations are needed to further optimize the mitre bends along these guidelines. Note that the neutronics calculations for the present design show that mitre bends are not necessary.

The tests of the mock-up were performed under atmospheric conditions, using a waveguide with rectangular corrugation profile (originally not designed for high-power). As ITER will operate the launcher under vacuum and will use a rounded corrugation profile, the arcing limits should be much higher. Therefore arcing problems for ITER conditions appear not to be a major problem provided that collection of dust in the grooves of the waveguide is avoided.

8. Summary

Low-power as well as high-power investigations of a remote steering launcher mock-up in the frequency range of 140 GHz to 158 GHz demonstrate a continuous steering range of $-12° < \varphi < 12°$ with high mode purity. The measured ohmic loss of the corrugated square waveguide is relatively high (up to 5% at $\varphi = 12°$), which however can be handled. In the high-power experiments (700 kW, 10 s), no arcing was observed for the straight setup in spite of operation under atmospheric pressure. If necessary, mitre bends could be integrated into the launcher; however, evacuation of the waveguide (as foreseen in ITER) is required to avoid arcing. In summary, no major obstacles were identified so far for the application of the remote steering antenna on ITER.

Acknowledgement

Part of this work was carried out under the EFDA technology research programme activities. The ECRH for W7-X is built up in the frame of the project PMW hosted at FZK Karlsruhe (collaboration between FZK Karlsruhe, IPP Garching and Greifswald, and IPF Stuttgart).

References

1. *Zohm H.*, Proc. 13th Joint Workshop on ECE and ECRH, May 2004, Nizhny Novgorod, Russia, http://www.ec13.iapras.ru/.
2. *Prater R. et al.*, Proc. 10th Joint Workshop on ECE and ECRH, Ameland, The Netherlands, 1997, ed. by T. Donne and A.G.A. Verhoeven, World Scientific, Singapoore, 1997, pp. 531-540.
3. *Verhoeven A G.A. et al.*, in Strong Microwaves in Plasmas 2005, ed. A.G. Litvak, IAP RAS, Nizhny Novgorod, 2005.
4. *Takahashi K., Moeller C. et al.*, Fusion Eng. Design **65** (2003), 589-598.
5. *Semenov L., Rivlin A.*, Laser Focus (Feb. 1981), 82-84.
6. *Ohkubo K. et al.*, Fusion Eng. Des. **65** (2003), 657-672.
7. *Moeller C.P.*, Proc. 23rd Int. Conf. On Infrared and Millimeter waves, eds. T.J. Parker and S.R. Smith, Colchester, 1998, 116-118.
8. *Denisov G.G., Kuzikov S.V., Kobayashi N.*, Int J. Infrared and Millimeter Waves, **22** (2001), 1735-1760.
9. *Kasparek W. et al.*, Nucl. Fusion **43** (2003), 1505-1512.
10. *Plaum B et al.*, Proc. 13th Joint workshop on ECE and ECRH (EC-13), Nizhny Novgorod, May 2004.
11. *Kasparek W. et al.*, in Strong Microwaves in Plasmas, ed. A.G. Litvak, Nizhny Novgorod, Russia, 2003, Vol. 1, 333-339.
12. *Cirant S. et al*, these proceedings, Vol. 1, p 347-352.
13 *Kogelnik H.*, Microwave Research Institute Symposia Series, Polytechnique Press, New York, 1964. Vol 14, p. 333-347.
14. *Kok Y, Gallagher N.J.*, J. Opt. Soc. A, **5** (1988), 65-73.
15. *Wagner D et al.*, Int. J. IR and Millimeter Waves, **20**, (1999) 567-582.
16. *Kasparek W, Fernandez A., Hollmann F., Wacker R*, Measurement of ohmic loss of metallic reflectors at 140 GHz by a 3-mirror resonator technique, Int J Infrared and Millimeter Waves, **22** (2001), 1695-1707.
17. *Kasparek W., Plaum B., Schwörer K.*, Final report on RS Launcher Design, EFDA Tech. Work 2005 TW5-TPHE-ECHULB5, del. (a) 5.1 and (a) 5.2.

MILLIMETER-WAVE DESIGN OF THE ITER UPPER ECRH LAUNCHER

A. G. A. Verhoeven, B. S. Q. Elzendoorn, W. A. Bongers, A. Bruschi[2], S. Cirant[2], I. Danilov[1], A. Fernandez[5], G. Gantenbein[3], M. F. Graswinckel, R. Heidinger[1], W. Kasparek[3], K. Kleefeldt[1], O. G. Kruijt, B. Lamers, B. Piosczyk[1], B. Plaum[3], D. M. S. Ronden, G. Saibene[6], H. Zohm[4]

FOM-Institute for Plasma Physics Rijnhuizen, Association EURATOM-FOM, Trilateral Euregio Cluster, Nieuwegein, The Netherlands, www.rijnh.nl/ITERECRH,
[1]Forschungszentrum Karlsruhe, Association FZK-EURATOM, [2]CNR,Milan,
[3]Univ Stuttgart, [4]Max-Planck, Garching, [5]Ciemat, Madrid, [6]EFDA, Garching

An ECRH (electron-cyclotron resonance heating) launching system for the ITER upper ports is being designed. The aim of the system is to inject Electron Cyclotron Waves (ECW) in the ITER plasma in order to stabilize neoclassical tearing modes (NTM). Each of the four upper-port launchers consists of six mm-wave lines capable of transmitting high power up to 2 MW per line at 170 GHz. In order to exploit the capability of ECW for localized heating and current drive over a range of plasma radii in ITER, the ECH&CD upper port launcher must have a beam steering capability. The Remote Steering (RS) principle has great advantages, because it enables to avoid steerable mirrors with flexible cooling lines at the plasma-facing end of the launcher. The principle consists of a long, corrugated, square waveguide having the steerable optics placed outside of the first confinement boundary of the vacuum vessel. All vulnerable components are far away from the hostile plasma environment. Furthermore, the RS launching system enables to do maintenance on the system during shutdown, without affecting the torus vacuum and the blanket cooling circuits.

1. System lay-out

Starting from the gyrotrons, the mm-wave power will be transmitted towards the tokamak by circular evacuated waveguides with an aperture of 63.5 mm. Steering of the beam over a range of $\pm$ 12° will be achieved by a mirror system consisting of a combination of curved and rotating mirrors. Via the mirror system the beam will be directed into a square corrugated waveguide of 44×44 mm with a length of 4.4 m. A single-disk diamond window and an isolation valve will provide the tritium boundary between the primary and secondary vacuum. At the end of the square waveguide, mm-wave beams will be guided through penetrations in the front-shield blanket module by a set of 2 fixed mirrors towards the ITER plasma. The mirrors will have focusing properties in both directions. This will result in an effective steering range in the plasma such that all the flux surfaces can be reached at a major radius of the ITER plasma of 5650 mm at horizontal locations between 1900 and 3300 mm. The latest 3-D CATIA model (June 2005) incorporates the newest requirements on steering range and launching angles, following from recent physics-based performance analysis [1, 2].

2. Design parameters

At the start of this work, we came to the reference model. This is now obsolete, but a good indication how the work evolved from the start, where the design was based on 3 ports, each carrying 8 beam lines at a frequency of 170 GHz. In the reference model a single end mirror directed the beam to the proper position in the plasma by focusing the beam in both directions, poloidal and toroidal. The input scanning range was set at $\pm$ 12°, the maximum that can be handled by the remote-steering square waveguide. Both the angles α (the poloidal launching angle, the angle between the poloidal component of the nominal beam centerline and the horizontal plane) and β (the toroidal launching angle, the angle between the nominal beam centerline and its poloidal component) were set in the way as given by the beam tracers [1, 2]. The resulting α scan in the plasma covered the full range for all the ITER scenarios. The angle β was optimized as follows: upper row: –18°, lower row: –20° [3, 4].

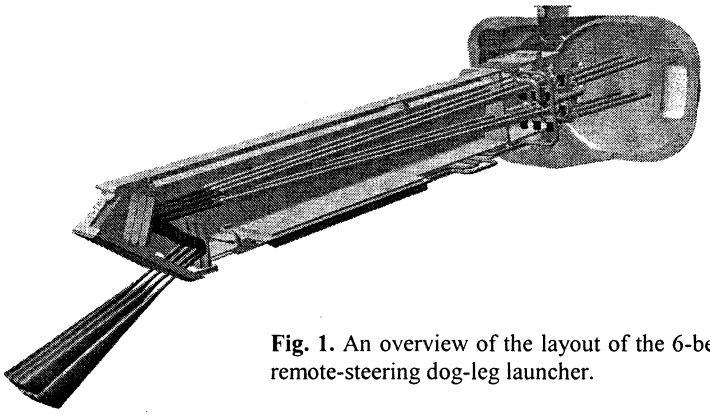

Fig. 1. An overview of the layout of the 6-beamline remote-steering dog-leg launcher.

The 2-MW ECRH mm-wave system has to operate under various vacuum conditions. The transmission line is partly quasi optical, at the location of the remote steerable mirror and at the location of the plasma facing fixed mirror, see Fig. 1. As the primary vacuum boundary a diamond window is placed after the steerable mirror in order to prevent tritium and beryllium contamination. Maintenance on the system after DT operation is foreseen, depending on the resulting neutron load in the port-duct. Behind the diamond window an isolation valve and the entrance of the square corrugated waveguide are located.

3. Mirror steering mechanism

As it leaves the gyrotron, the mm-wave beam is guided through a waveguide with a circular cross-section of 63.5 mm. Steering of the beam is

achieved by a steerable mirror mechanism, placed at the end of the circular waveguide, see Fig. 2, top.

The spot size at the beginning of the square waveguide has to be limited, therefore a fixed, curved mirror (*M1*) will focus the beam. The steerable mirror (*M2*) makes a combined translating and rotating movement in the drawing plane in order to steer the beam through the waveguide aperture.

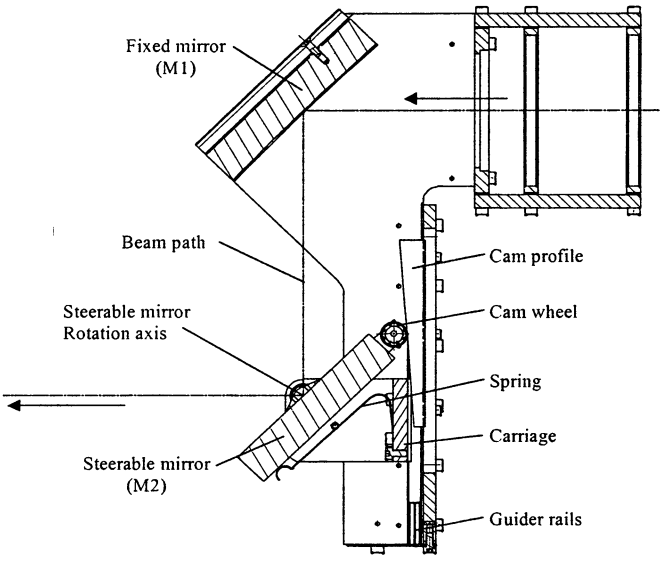

Fig. 2. Mirror steering mechanism, cross section. The set-up is such that the beam axis crosses the waveguide axis always at the point of entry of the waveguide.

Although the mm-wave beam enters the diamond window under angles as large as 12 degrees, the maximum reflection on the window is always lower than 1%.

4. Reference model

For the reference model the single-end-mirrors in the front shield direct the beam under the required angles α and β into the plasma, while focusing the beams in both planes.

The mirrors are elongated in the beam plane to accommodate the steering range of ± 12 degrees from the square waveguide, see Fig. 3. Active cooling is foreseen for these mirrors, and they will be bolted or welded to the port plug structure. Focusing is optimized in the plane orthogonal to the beam plane for a spot size 2.1 meters from the mirror. Focusing in the beam steering plane is more difficult because the incident beam from the square waveguide moves over the mirror surface. If there is focusing in the beam steering plane this re-

duces the effective steering range. Therefore focusing of the beam is a tradeoff between steering range and spot size [5, 6].

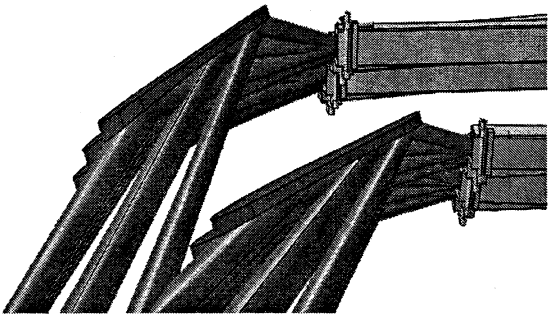

Fig. 3. The front mirrors in the reference set-up

5. Dog-leg option

The latest optimization of the remote-steering set-up has resulted in the dog-leg option. Here, the front mirror is replaced by a set of 2 mirrors. The set-up is arranged in such a way that 2 beams (one from the upper row and one from the lower row) use a common first front mirror (*M1*, on top, see Fig. 4) and also a common second front mirror (*M2*, the lower one). In this way Din (the distance between the output of the square waveguide and the first front mirror) could be increased substantially to as much as 900 mm [7]. An important improvement of this set-up is a substantial reduction in the power density on the front mirrors. Now a value substantially below a maximum peak level of

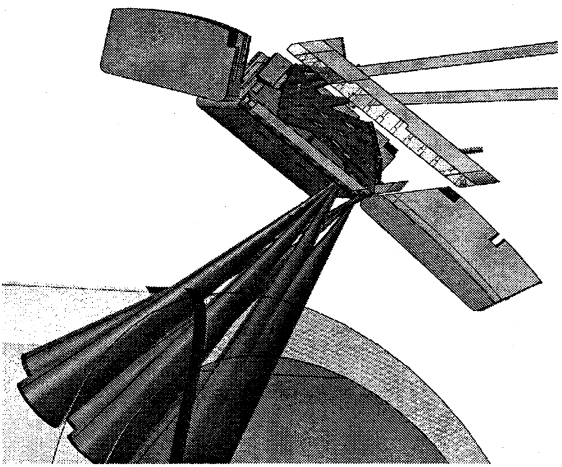

Fig. 4. The dog-leg lay-out

10 MW/m^2 could be achieved. The exact value depends on further optimizations. An important issue is the possibility to avoid an overlap of the two beams on the same mirror for all the angles that are required for sending the beams to each location.

Another optimization criterion is, of course, the beam size in the plasma at the point of absorption of the mm waves. In this set-up, the beams that are directed to the plasma have a much lower Z position, leading to relative better NTM stabilization performances.

The mechanical lay-out has undergone quite a number of improvements. The construction is much more robust now, e.g., all the former clashes with the port-plug sidewalls could be avoided now. The steering plane can be vertical now allowing easier access to the isolation valves, diamond windows and steering mechanisms. Furthermore, the opening required into the first wall panel is reduced to the smallest area that can be achieved for all RS launcher variants, the required cut into the neighboring lower regular blanket module is practically negligible.

6. Maintenance

One of the major features of the ECRH RS launching system is the possibility to do hands-on maintenance. All sensible mm-wave components are located in the secondary vacuum containment "the mini duct". By removing the mini-duct door, all steering components will come out of the port-duct and can be placed in an area of the ITER upper floor were radiation is more moderate, see Fig. 5.

Checking, repairing and exchanging steering components will be taken into account during the design process. Further it should be mentioned that for having maintenance on the mm-wave system the blanket cooling system and the torus vacuum remain unaffected [8].

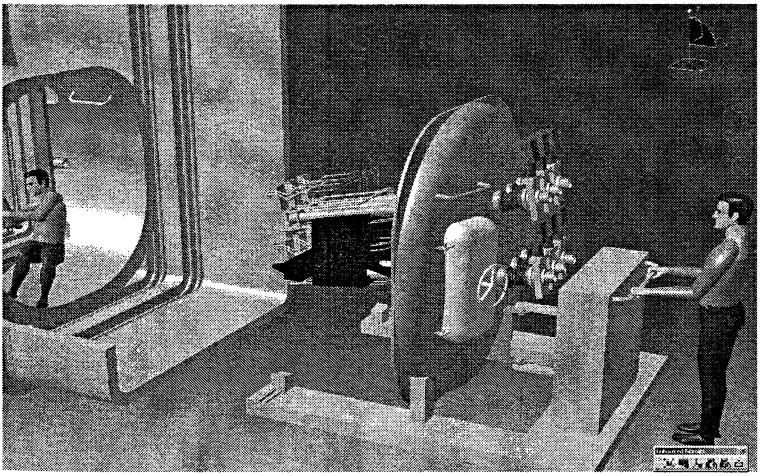

Fig. 5. Hands-on maintenance inside the mini duct in the port cell

7. First low-power measurements

A full-scale model of the entire mm-wave part of the proposed ITER ECRH upper-port launcher has been designed in all details. All components have been procured and assembled at the FOM institute. In Figure 6 the following elements can be identified. On the top left side a taper transforms the small rectangular waveguide size of the low-power source into the "standard" ITER circular waveguide size of 63.5 mm. Following the taper some corrugated circular waveguides can be identified, amongst them two miter bends. These miter bends can be used in two configurations. Either grooved plates are included to allow for an elliptical polarization of arbitrary orientation and ellipticity. Or flat, water-cooled plates can be incorporated that can handle a power of 2.2 MW for cw operation for future long-pulse testing purposes.

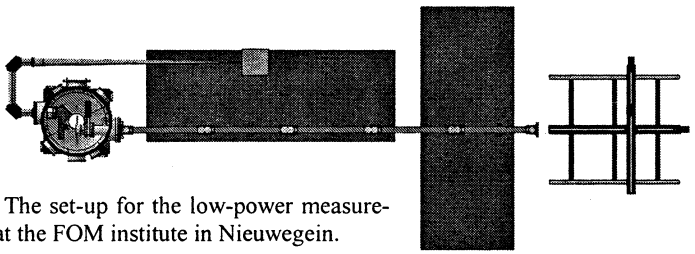

Fig. 6. The set-up for the low-power measurements at the FOM institute in Nieuwegein.

From here, the mm-wave beam enters the vacuum vessel, where the mirror-steering mechanism is located, see chapter 3. Here, the beam falls first on the fixed focusing mirror and then on the movable plain mirror. From here the beam goes through the diamond window and the isolation valve into the square corrugated waveguide under the chosen angle between +12° and –12°. At the end of the 4.4 m long square waveguide the beam continues through another vacuum window under the same (but opposite) angle. Here an x-y-z scanner is located that measures the beam at a number of frequencies at each position. A full overview of the low-power measurements performed in Nieuwegein is given in [5]. An example is given in Fig. 7, where a measurement is performed at a scanning angle of 12°.

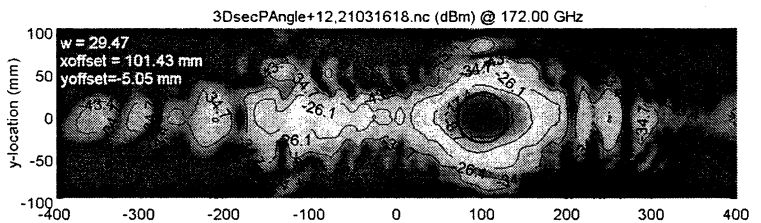

Fig. 7. Low-power measurement at a scanning angle of 12°. Measurement performed at a distance of 500 mm from the end of the square corrugated waveguide.

Although, the beam shows a very nice sharp beam in the proper direction, also a small fraction of the power (less then 1%) is going into other directions, clearly seen on the picture because of the very high dynamic range (> 100 dB) of the measuring device.

A second measurement shows (in Fig. 8) the propagating under –6° in the horizontal plane at a distance between 0 and 900 mm from the exit of the square corrugated waveguide.

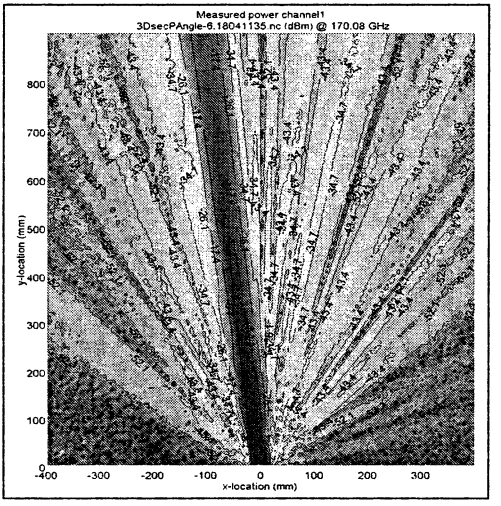

Fig. 8. Low-power measurement at a scanning angle of –6°. Measurement performed in a horizontal plane.

In June 2005 the entire set-up was transported to FZK in Karlsruhe, Germany where the system will be connected to a high-power gyrotron in order to perform tests at ITER-relevant power levels, see Fig. 9. These tests will be very close to the ITER conditions, at a frequency of 170 GHz, evacuated system, diamond window included in the test set-up. These tests can also be seen as a next step after very promising high-power tests in Greifswald [9] and Naka [10].

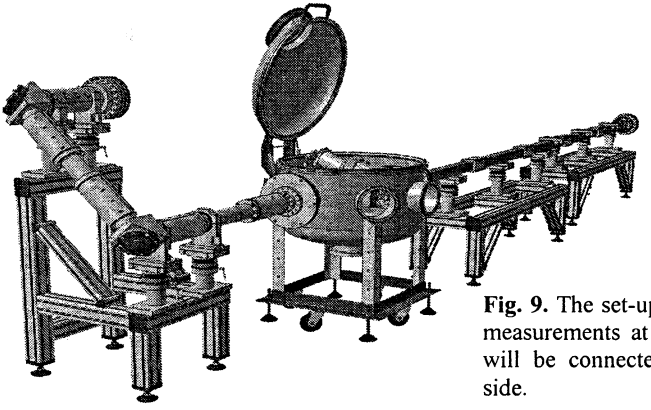

Fig. 9. The set-up for the high-power measurements at FZK. The gyrotron will be connected at the upper left side.

8. Conclusions

The design analyses and the detailed design of the mm-wave layout of the remote-steering concept for the upper-port launcher have demonstrated the feasibility of the remote-steering approach in the ITER environment. Furthermore, a full-scale mock-up line has been designed and built for testing at the appropriate ITER frequency and power level. Both low- and high-power measurements confirm the expected behavior of the remote-steering launching system and its compatibility with ITER.

Acknowledgement

The early work on this topic was an important first step by R. Prater, C. P. Moeller [11]. This work is supported by the European Communities under the contract of Association between EURATOM and FOM, with financial support from NWO. This work was carried out under the EFDA technology research programme activities, EFDA technology task TW3-TPHE-ECHULA and B1. The views and opinions expressed herein do not necessarily reflect those of the European Commission.

References

1. *Zohm H., et al.*, Comparison of the performance of different options for the ITER ECRH Upper Launcher, Third IAEA Technical Meet. ECRH Physics and Technology for ITER, 2–4 May 2005, Società del Casino, Como, Italy.
2. *Volpe F., et al.*, Resiliency of ITER ECRH Upper Launcher to Steering Errors and Changes of Profiles and Integration with Equatorial Launcher, *ibid.*
3. *Heidinger R., et al.*, Structural integration studies for the ITER ECRH Upper Launcher, *ibid.*
4. *Verhoeven A G.A., et al.*, Design of the mm-wave system of the ITER ECRH Upper Launcher, Proc. 13th Joint Workshop on Electron Cyclotron Emission and Electron Cyclotron Heating. Nizhny Novgorod, 2005, Ed. A. Litvak, p. 281.
5. *Graswinckel M F., et al.*, Low power measurements on a remote steering upper port launcher mockup for ITER, Third IAEA Technical Meet. ECRH Physics and Technology for ITER, 2–4 May 2005, Società del Casino, Como, Italy.
6. *Bruschi A., et al.*, Advanced Optics for the Remote Steering ITER ECRH Upper Launcher, *ibid.*
7 *Ronden D M S, et al.*, Integration of a dog-leg beam routing for the remote steering upper port launcher for ITER, *ibid.*
8. Oxford Technologies: http //www.oxfordtechnologies.co.uk/
9 *Plaum B., et al.*, High-power tests of a remote steering Launcher mock-up At 140 GHz, *ibid.*
10. *Takahashi K., et al*, Development of Equatorial EC Launcher Components for ITER, *ibid.*
11. *Prater R., Moeller C.P., et al.*, A design study for the ECH launcher for ITER, Proc. 10th Joint Workshop on ECE and ECH Ed. A.J H. Donne and A.G A. Verhoeven Ameland, the Netherlands, World Scientific, 1997, p. 531.

PARAMETRIC DECAY INSTABILITY ACCOMPANYING ELECTRON BERNSTEIN WAVE HEATING IN MAST

A. Surkov[1], *G. Cunningham*[2], *A. Gurchenko*[1], *E. Gusakov*[1], *V. Shevchenko*[2], *F. Volpe*[2]

[1]Ioffe Institute, St.-Petersburg, Russia
[2]EURATOM/UKAEA Fusion Association, Culham Science Center, Abingdon, OX14 3DB, UK

First observations of LF waves generated in the EBW heating experiments on MAST are reported. The radiation is postulated to arise due to the parametric decay of the pump UH wave into another UH wave and LH wave. The theoretical study of this instability is performed and the threshold power is calculated. The development of the decay instability during the heating pulse is interpreted as an indication of substantial coupling of the microwave power to the UHR in the MAST experiment.

Introduction

Electron cyclotron heating was shown to be effective in stellarator and tokamak plasmas. Unfortunately its application to spherical tokamaks (STs) is substantially limited by high plasma density and relatively low magnetic field typical for these devices. This ST feature has a strong effect on the electromagnetic wave propagation. In the microwave frequency region, characteristic surfaces, like the upper hybrid resonance (UHR) and cut-offs are very close to the plasma edge. As a result electromagnetic (EM) waves are unable to penetrate into the plasma interior. The only way to overcome this difficulty is to use a linear conversion of the incident EM wave into the electron Bernstein wave (EBW) at the UHR. EBW has no density limit and can, in principle, carry the radio frequency power deep into the plasma. The feasibility of this plasma heating scheme is under investigation now on the MAST tokamak at Culham, UK.

The wave propagation in the UHR, where the wave electric field increases, is usually distorted by nonlinear effects at a power density level exceeding $\sim 1\ \mathrm{kW \cdot cm^{-2}}$ typical for EBW heating experiments [1–3]. In particular, parametric decay instabilities can cause an anomalous reflection and absorption of the incident power. In experiments [1, 2] generation of low-frequency (LF) waves has been observed. These waves were identified as lower-hybrid (LH) waves, which are the only waves able to reach the small scales of the pump UH wave and satisfy the wavelength matching condition for the decay instability. In the present paper the first observations of LF waves generated in the EBW heating experiments on MAST are reported. The radiation is postulated to arise due to the parametric decay of the pump UH wave into another UH wave and LH wave. The theoretical study of this instability is performed and the threshold power is calculated.

Experimental results

The EBW heating system in the MAST tokamak allows up to 1 MW microwave power at 60 GHz to be launched into the plasma in 7 beams. The coupling to EBW is optimized by a system of steerable focusing mirrors. At a certain orientation of the microwave antenna the steep growth of 100 MHz RF radiation (Fig. 1, *c*) during the heating pulse (Fig. 1, *a*) was registered by the specially designed RF antenna situated in the edge plasma at 5 cm outside the separatrix. The maximum of the registered RF radiation corresponds to the over-dense (Fig. 1, *b*) and ELM-free (Fig. 1, *c*) plasma. That provides high density gradient at the UHR region, which is the necessary condition for the heating wave mode conversion to EBW.

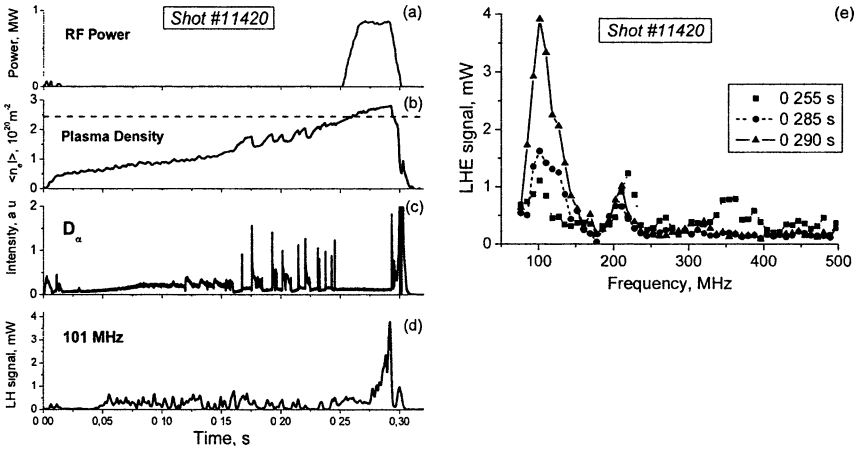

Fig. 1. RF power injected into the plasma (*a*), line integrated density (*b*), lower hybrid emission (LHE) signal measured at 101 MHz (*c*), D_α emission intensity (*d*), LHE spectrum measured at different time slices (*e*).

Due to the fact that the observed RF signals have frequencies close to the LH resonance frequency in the UHR region (calculated taking into account a local impurities level) we postulate that the radiation is generated by the parametric decay instability occurring at the UHR.

Theoretical analysis

We consider a slab plasma model and 1D problem of parametric decay, assuming that the pump UH wave propagates along the inhomogeneity direction x as well as the reflected UH wave. We analyze the "high-frequency" case, specific for MAST conditions, when the pump frequency is more than twice the

ECR frequency in the UHR: $\omega_0 > 2\omega_{ce}$. In this case the UH waves dispersion curves (Fig. 2, *a*) do not possess a turning point and transformation to Bernstein wave occurs without a change of group velocity sign. The opposite direction of the daughter waves propagation between the decay points (Fig. 2, *a*) corresponds to the situation where a feedback loop and, therefore, an absolute parametric decay instability [4] is possible.

We are interested here in the fundamental mode of this instability, which usually has a minimal threshold and corresponds to the decay points x_{d1} and x_{d2} (Fig. 2, *b*) being close to each other ($x_{d1} \simeq x_{d2} \equiv x_d$) and to the LHW turning point. In this case the situation under consideration is similar to the decay problem, when two daughter waves have the cut-off. Namely our problem is equivalent to that studied in [5], where one of the cut-offs is far from the feed-back loop, where the decay wave energy is circulating (Fig. 2, *c*).

Keeping in mind this analogy, we consider the equations, describing the complex amplitudes ϕ_1, ϕ_2 of the daughter waves potentials

$$\phi_{uh} = \tfrac{1}{2}\left(\phi_1(x)\exp\left[ik_1 x\right] + c.c.\right),$$

$$\phi_{lh} = \tfrac{1}{2}\left(\phi_2(x)\exp\left[i\kappa_* x\right] + c.c.\right).$$

We use the following notation: k_0, k_1 are the constant values denoting the wavenumbers of the UH waves in the vicinity of the LHW turning point. The transformation wavenumbers κ_*, k_* of LH and UH waves are given by $\kappa_*^2 = \omega_{pe} N_z^{lh} / [c\ell_T(\omega_2)]$,

$k_*^2 = \omega_{ce}\sqrt{1 + N_z^{uh\,2}} / [c\ell_T(\omega_0)]$, where

$$l_T^2(\omega) = \frac{3}{2}\left(\frac{\omega_{pe}^2}{\omega^2 - \omega_{ce}^2}\frac{V_{Te}^2}{\omega^2 - 4\omega_{ce}^2} + \frac{\omega_{pi}^2 V_{Ti}^2}{\omega^4}\right)$$

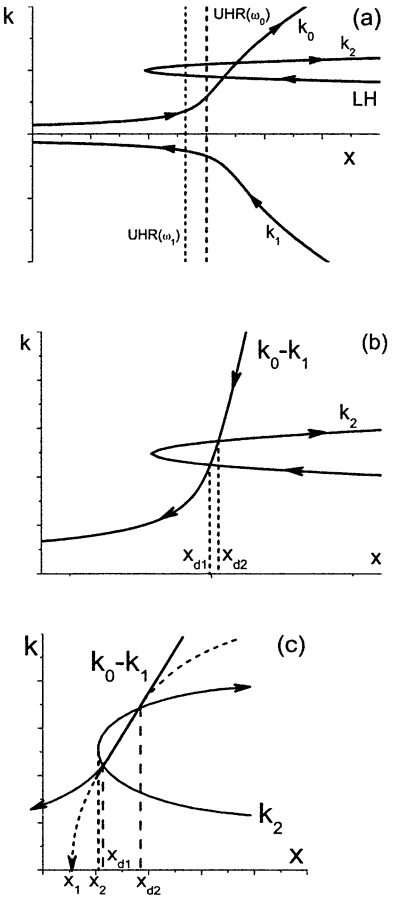

Fig. 2. Dispersion curves for pump UH wave k_0, reflected UH wave k_1 and LH wave k_2 (*a*, *b*). Arrows denote group velocity direction. Three-wave interaction, when two waves possess turning points (*c*).

and N_z^{lh}, N_z^{uh} are the toroidal refraction coefficients of the corresponding waves.

In the vicinity of the LHW turning point the equations in question [6] can be represented as

$$\begin{cases} \tilde{\phi}_1 + \alpha_1 (x - x_1)\tilde{\phi}_1 = V_{12}\, e^{-iKx}\phi_2 \\ \phi_2 + \alpha_2 (x - x_2)\phi_2 = V_{21}\, e^{iKx}\tilde{\phi}_1 \end{cases} \qquad (1)$$

where $\mu = (k_*/k_1)^4$, $\tilde{\phi}_1 = \phi_1^*\, e^{-i\Delta kx}$, $\Delta k = k_1(1+\mu)/(5+\mu)$, $K = k_0 - k_1 - \kappa_* + \Delta k$,

$$\alpha_1 = \left[(5+\mu)\ell_T^2(\omega_1)L(x_d)\right]^{-1}, \qquad \alpha_2 = \left[4\ell_T^2(\omega_2)L(x_d)\right]^{-1}$$

and $L(x_d)$ is the inhomogeneity scale:

$$L^{-1}(x) = \frac{d\ln n}{dx} + \frac{2\omega_{ce}^2}{\omega_{pe}^2}\cdot\frac{d\ln B}{dx}.$$

The quantity x_1 denotes a virtual turning point for the UH wave $x_1 = x_d - \ell_T^2(\omega_1)L(x_d)k_1^2(1+\mu)^2/(5+\mu)$, while x_2 gives the real turning point of the LH wave $x_2 = x_d + 2i\omega_2''\omega_{pe}^2 L(x_d)/(\omega_2\omega_{ce}^2)$, which is slightly shifted to the complex plane due to ω_2, which is the imaginary part of the LH wave frequency $\omega_2 = \omega_2' + i\omega_2''$, describing the growth rate of the instability. The interaction coefficients take the form

$$V_{12} = -\frac{ie}{2m_e}\frac{\kappa_*^2 E_0^*}{\omega_{ce}^2(5+\mu)\ell_T^2(\omega_1)k_1}, \qquad V_{21} = \frac{ie}{2m_e}\frac{k_1 E_0}{\omega_{ce}^2\ell_T^2(\omega_2)}$$

where E_0 is an amplitude of the pump wave electric field. According to [5] the absolute instability threshold for the fundamental mode of the system (1) is determined by the equation $V_{12}V_{21}\left(\alpha_2^2 - \alpha_1^2\right)^{-1/3} \simeq 0.2$. This gives the following expression for the parametric decay, producing the LH wave with $N_z^{lh} \simeq c/(5V_{Te})$, which can be shown to have the minimal threshold

$$\frac{P_i^*}{\pi\rho^2}\left[\frac{\mathrm{W}}{\mathrm{cm}^2}\right] = 2\cdot 10^{-3}\left[\frac{\mathrm{W}}{\mathrm{cm}^{2/3}\mathrm{T}^{1/3}\mathrm{GHz}^{1/3}\mathrm{eV}^{13/6}}\right]\cdot\frac{f_0^{1/3}\tilde{T}^{11/12}T_e^{5/4}B^{1/3}}{L^{4/3}} \qquad (2)$$

where $\tilde{T} = T_e + 4T_i$ and ρ is the electric field e-fold radius of the heating beam. All the plasma parameters here should be taken at the UHR position.

Discussion

For MAST experiment parameters $f_0 = \omega_0/(2\pi) = 60$ GHz, $T_e \sim T_i = 140$ eV, $B = 0.38$ T, $L = 3$ cm the threshold (2) is equal to $P_i^*/(\pi\rho^2) \approx 260$ W/cm^2, which gives $P_i^* \approx 80$ kW for the beam of $\rho = 10$ cm

radius. This power was well exceeded in every heating beam in the recent MAST experiments.

It should be noted that the actual power P_i^* is less than the heating beam power due to the conversion efficiency in the UHR, which is less than 100%. In case of the MAST experiments the UHR accessibility window position is rather hard to control and its angular width is small ($3° \div 5°$). Under these conditions the decay instability excitation can be considered as a proof of the successful injection of the power exceeding the threshold, given by (2), into the plasma. It can be concluded that in these experiments the coupling efficiency of at least one of the heating beams was not less than 50%.

Due to the inhomogeneity scale in the denominator of (2), which is a rapidly growing function of the heating frequency (e. g., for linear density profile $L \propto f_0^2$), the instability threshold increases with decreasing frequency. Thus, to optimize the EBWH experiment, the decrease of the heating frequency can be recommended. It leads additionally to the broadening of the accessibility window, hence simplifying the design of the experiment. Unfortunately ion and electron temperatures in the UHR are decreased at lower frequencies due to the UHR shift to the plasma periphery. That gives the reverse tendency to the threshold behaviour, which however can be expected to be overcome by minor heating power deposition in the UHR vicinity.

Conclusion

Generation of lower hybrid waves has been observed in EBW heating experiments on MAST for the first time. Theoretical study of corresponding decay instability of the pump wave induced backscattering was performed. The threshold power was estimated for typical parameters in MAST. It was shown that the backscattering parametric decay instability can arise only if the pump power exceeds 80 kW in any beam, so there is an indication of substantial coupling of the microwave power to the UHR in the MAST experiment.

The work was partly funded by the UK Engineering and Physical Sciences Research Council, by EURATOM, by the RFBR (project no. 04-02-16404) and by the scientific school support program 2159.2003.2. A.V. Surkov is thankful to the Dynasty foundation for supporting his research.

References

1. *McDermott F S., Bekefi G. et al.*, Phys. Fluids, 1982, **25**, 1488.
2. *Bulyginsky D G., Dyachenko V. V. et al.*, Plasma Phys. Rep., 1986, **2**, 138.
3. *Laqua H. P., Erckmann V. et al.*, Phys. Rev. Lett., 1997, **78**, 3467.
4. *Piliya A. D., Fedorov V. I.*, Zhurnal Tekhnicheskoi Fiziki (Sov. J Tech. Phys.), 1974, **44**, 1092.
5. *Piliya A. D., Fedorov V. I.*, Zhurnal Eksperimental'noi i Teoreticheskoi Fiziki (JETP), 1975, **68**, 987.
6. *Gusakov E., Surkov A.* Proc. 12th Int. Congress on Plasma Physics, Nice (France, 2004) http://hal.ccsd.cnrs.fr/ccsd-00001866/en/
7. Pilya A. D., Tregubova E. N. Plasma Phys. Control. Fusion., 2005, **47**, 143.

INVESTIGATION OF SMALL-SCALE COMPONENT OF TOKAMAK PLASMA TURBULENCE BY CORRELATIVE UPPER HYBRID RESONANCE BACKSCATTERING DIAGNOSTIC

A. B. Altukhov, L. A. Esipov, A. D. Gurchenko, E. Z. Gusakov, M. Yu. Kantor, D. V. Kouprienko, A. Yu. Stepanov

Ioffe Physico-Technical Institute, St.-Petersburg, Russia

The new diagnostic technique for investigation of ETG mode-scale tokamak turbulence – correlative enhanced scattering is developed at the FT-2 tokamak. Fine scale drift wave modes possessing unusually high frequency are observed using this technique in the ohmic discharge under conditions when the ETG mode should be unstable.

Electrostatic fine scale electron temperature gradient (ETG) mode turbulence is discussed nowadays as a possible candidate for explanation of the anomalous electron energy transport in tokamak plasmas, especially in transport barriers [1–5]. According to theoretical and computational analysis of [1, 2], performed using gyrokinetic approach in flux tube geometry, this turbulence, possessing shortest wave length in the electron gyroradius range, can nevertheless cause a substantial heat flux due to formation of streamers at the nonlinear stage of its evolution. On contrary, the global fluid simulations [3–5] have shown much smaller heat flux, which was explained by instability saturation at a lower level due to toroidal mode coupling. These contradictory theory predictions have not been checked yet experimentally, due to complications caused by extremely small scale of ETG modes. The attempt to develop the experimental tool for ETG mode study using the upper hybrid resonance backscattering diagnostics (UHR BS) [6] is presented in this paper.

The experiment is performed at the FT-2 tokamak ($R = 55$ cm, $a = 8$ cm, $B_T \approx 2.2$ T, $T_e(0) \approx 500$ eV, $I_p = 19 \div 37$ kA, $n_e(0) = (2 \div 4) \times 10^{19}$ m^{-3},) where a movable focusing double antennae set, allowing off equatorial plane plasma X-mode probing from high magnetic field side with maximal vertical displacement $y_a = \pm 2$ cm is installed. The beam radius at the UHR position, where the probing frequency ($52 \div 69$ GHz) satisfies condition $f_i^2 = f_{ce}^2(R) + f_{pe}^2(r)$, is $\rho \approx 0.7 \div 0.9$ cm. The scheme of the UHR BS is shown in Fig. 1. The probing wave electric field, radial and poloidal wave number grows rapidly in the vicinity of the UHR, where the BS efficiency $S_{BS}(q_R)$ possesses sharp maximum [6, 7]. The diagnostics benefits of this growth leading to high localization, enhanced sensitivity to sub-millimeter scales and substantial frequency shift of the BS wave (Enhanced Doppler effect) [8]. In this experiment the probing wave UHR layer was situated at $r > 4$ cm, where condition for the ETG mode excitation [2] $L_T < 1.25\, L_n$ was fulfilled, as it is seen in Fig. 2. The UHR BS spectra obtained in 32 kA ohmic discharge at different probing frequencies

and, correspondingly, UHR positions are shown in Fig. 3. The BS spectrum is weakly shifted and symmetric at the edge, whereas its shift and asymmetry grows, when moving inward. At $r_{UH}=5.6$ cm the second line possessing more than twice higher frequency shift appears in the spectrum. At $r_{UH}=5$ cm its amplitude exceeds the amplitude of the first line. The spatial distribution of their amplitude normalized to the ECE signal is shown in Fig. 4.

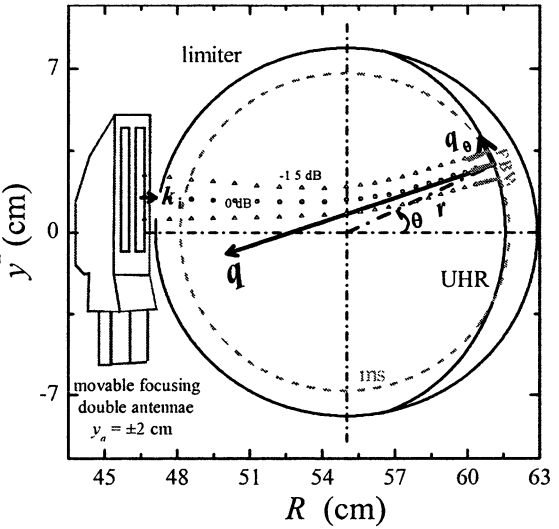

Fig. 1. Poloidal FT-2 section. ($\mathbf{k_i}$ – incident wave vector; $\mathbf{q}$, $\mathbf{q_\theta}$ – fluctuation wave vector at BS efficiency maximum and its poloidal projection; circles – central ray of the probing beam, triangles – beam at 1.5 dB power suppression level; ms – magnetic surface).

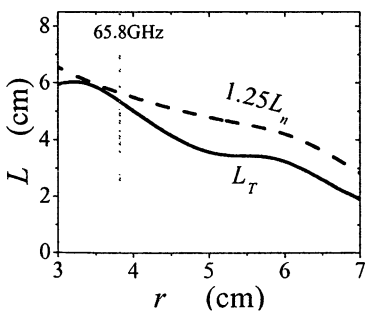

Fig. 2. Comparison between the electron temperature L_T and electron density L_n scale length in 22 kA discharge.

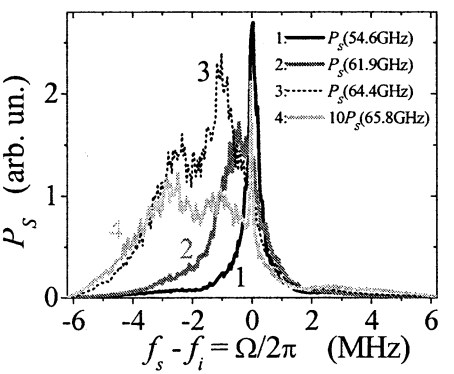

Fig. 3. UHR BS spectra: $r_{UH}=7.9$ cm (*1*), 6 cm (*2*), 5.6 cm (*3*), 5 cm (*4*).

As it is seen, the amplitude of the low frequency (LF) satellite decreases when moving inward whereas the high frequency (HF) satellite's amplitude increases. The observation of the doublet in the UHR BS signal is most likely associated with simultaneous excitation of two different drift modes in FT-2 plasma. To check this supposition the wave number spectrum of turbulence was investigated with correlation technique [9].

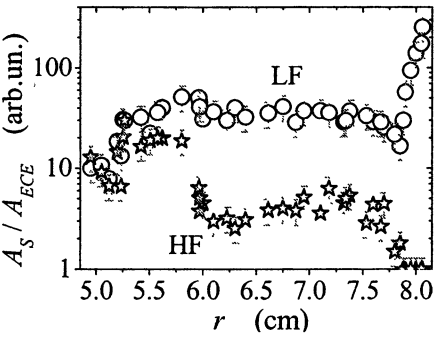

Fig. 4. LF & HF satellite's normalized spectral amplitudes profiles.

Two BS signals at close probing frequencies (with difference Δf_i) measured simultaneously were utilized for the cross-correlation function (CCF) computation. The normalized CCF obtained at the reference frequency 61.9 GHz in 32 kA discharge at $y_a = 1.5$ cm is shown in Fig. 5 (a – real part; b – imaginary). The Δf_i width of the high coherency region there decreases with growing turbulence frequency Ω. As a result, the higher wave numbers q_R should correspond to higher Ω in the cross-correlation spectrum (CCS), obtained by Fourier transform from the CCF dependence on the UHR spatial separation, proportional to Δf_i. The corresponding CCS proportional to the product of density fluctuations spectral power density and $S_{BS}(q_R)$ is shown in Fig. 6, a. The imaginary part of the CCS (Fig. 6, b), which should be zero in theory, determines the accuracy of our procedures. The UHR BS spectrum, obtained from the CCS multiplying

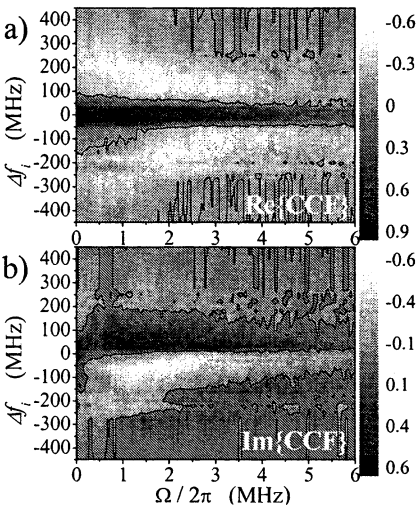

Fig. 5. Normalized CCF for $r_{UH} = 6.4$ cm

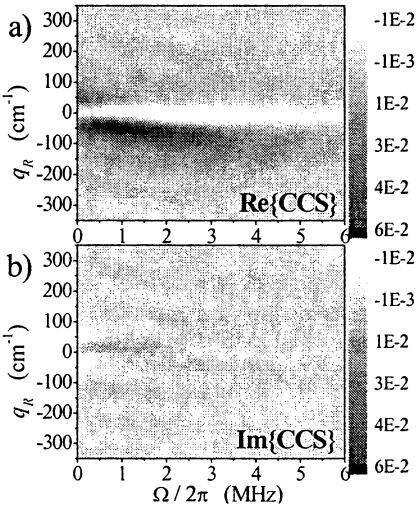

Fig. 6. CCS for $r_{UH} = 6.4$ cm

it by the signal frequency spectrum (integral in q_R), is shown in Fig. 7, *a* and Fig. 8, *a* for two extreme cases of dominating LF and HF satellites, correspondingly. The first case, in which low q_R in the interval 25 – 100 cm^{-1} and frequency less than 1 MHz are measured, is typical for the plasma edge. The second spectrum, where frequencies are higher than 2 MHz and q_R reach 250 cm^{-1} is never observed at the edge, but in the central region at $r < 5$ cm.

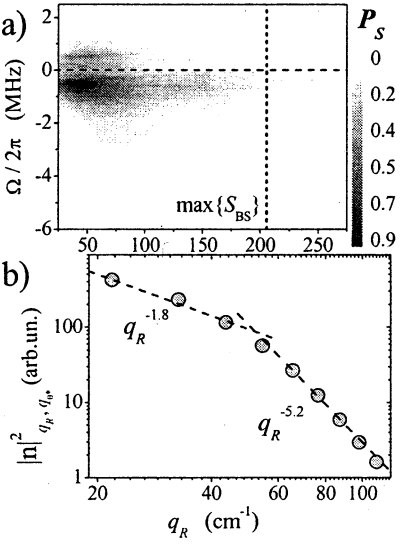

Fig. 7. UHR BS signal spectrum (*a*) and turbulence wave number spectrum (*b*) for 32 kA, 61.9 GHz (r_{UH} = 6.4 cm).

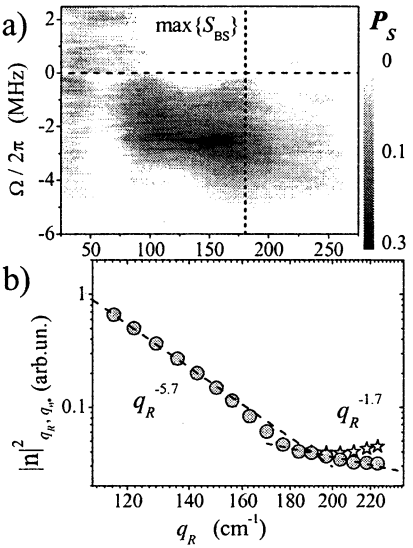

Fig. 8. UHR BS signal spectrum (*a*) and turbulence wave number spectrum (*b*) for 22 kA, 65.8 GHz (r_{UH} = 3.8 cm).

To obtain the turbulence wave number spectrum $|n|^2_{q_R,q_\theta,\Omega}$ from these figures we supposed that the UHR BS spectrum is determined by the turbulence spectrum, BS efficiency, as well as by the antenna beam, and given by integral over poloidal wave number q_θ of fluctuations: $P_{BS}(q_R,\Omega) = \int |n|^2_{q_R,q_\theta,\Omega} S_{BS}(q_R) F^2(y) dq_\theta$, where the antenna beam power distribution in the vertical direction on the UHR is given by $F^2 = \exp\{-2(y-y_*)^2/\rho^2\}$. We also account for the relation [8] between poloidal wave number of fluctuations contributing to the signal q_θ and vertical displacement of the point where backscattering happens $q_\theta = 2k_{0*}(y/y_*) + q_R \cos\gamma_*(y/y_*)$, (here y_* gives the vertical position of the centrum of the spot illuminated at the UHR surface; $k_{0*} + (q_R/2)\cos\gamma_*$ is the poloidal wave number of the probing wave possessing in the UHR radial wave number $q_R/2$. We assume here the drift mode type of turbulence, for which the fluctuation frequency is proportional to the poloidal

wave number. The nonlinear broadening of turbulence spectrum is described by the following expression: $|n|^2_{q_R,q_\theta,\Omega} = |n|^2_{q_R,q_\theta} \exp\{-(q_\theta - \Omega/V_\theta)^2 / \Delta q_\theta^2\} \times$

$\times \sqrt{\pi} / \Delta q_\theta$.

As a result of fitting procedure, the turbulence spectral parameters are obtained. In the case of Fig. 7, *a* (32 kA) they are as follows: $V_\theta = 3.1$ km/s, $q_{0*} = q_0(y_*) = 13$ cm^{-1}, $\Delta q_0 = 13$ cm^{-1}, $q_R^{\max} = 50$ cm^{-1}. The reconstructed turbulence q_R spectrum in this case is shown in Fig. 7, *b* in double logarithmic scale. It scales as $q_R^{-1.8}$ for $25 < q_R < 50$ cm^{-1} and as $q_R^{-5.2}$ for $50 < q_R < 100$ cm^{-1}. This behavior is similar to that observed on Tore Supra tokamak for ITG mode turbulence [10]. In the case of HF satellite of Fig. 8, *a* (22 kA) the fitting parameters are $V_\theta = 2.5$ km/s, $q_{0*} = 64$ cm^{-1}, $\Delta q_\theta = 24$ cm^{-1}, $q_R^{\max} = 160$ cm^{-1}. The turbulence q_R spectrum in this case is shown in Fig. 8, *b*. Its quick, as $q_R^{-5.7}$, decay at $50 < q_R < 180$ cm^{-1} saturates at higher wave numbers. The frequency of turbulence modes producing BS in this case are much higher than in Fig. 7, *a* as well as the range of wave numbers where they are observed is not usual for ITG or TEM mode. It is natural to associate this mode with the ETG mode which should be unstable under the experiment conditions. The parameters of these modes were directly compared in the experiment at 32 kA current, where they were observed simultaneously (Fig. 9, *a*). The LF satellite at 1 MHz is larger there than the HF satellite at 2.4 MHz, which possesses higher q_R. The fitting for these two satellites results in parameters: $V_\theta = 2.7$ km/s, $q_{0*} = 23$ cm^{-1}, $\Delta q_\theta = 19$ cm^{-1} for ITG mode and $V_\theta = 5.6$ km/s, $q_{0*} = 27$ cm^{-1}, $\Delta q_0 = 10$ cm^{-1} for ETG mode. The huge excess of the HF mode phase velocity provides additional argument in favor for its physical difference. The turbulence q_R spectrum reconstructed for these modes is shown in Fig. 9, *b*.

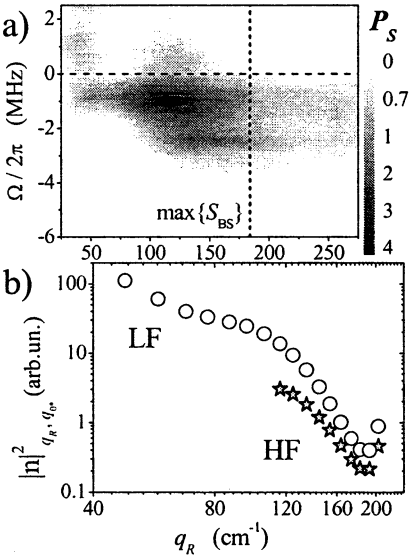

Fig. 9. UHR BS signal spectrum (*a*) and turbulence wave number spectrum (*b*) for 32 kA, 64.4 GHz ($r_{UH} = 5.6$ cm).

Conclusions

Summarizing the results of the paper we would like to state that two modes are found in the UHR BS spectra under conditions when the threshold for the

ETG mode instability $L_T < 1.25\,L_n$ is overcome. The first possessing frequency less than 1 MHz and radial wave number $25 < q_R < 150\,\mathrm{cm}^{-1}$ is localized at the plasma edge and most likely associated with the ITG mode. Its wave number spectrum is quickly decaying in the way similar to that observed at Tore Supra. The second possessing frequency higher than 2 MHz and radial wave number $q_R > 150\,\mathrm{cm}^{-1}$ is associated with the ETG mode. Its phase velocity is twice as high and amplitude is growing towards the centre. In the region of observations its level is comparable to that of the ITG mode, been however much smaller than the later one at the edge.

Financial support of RFBR grants 04-02-16534, 05-02-16569, scientific schools state program HIII-2159.2003.2, INTAS grant 01-2056 and NWO-RFBR grant 047.016.015 is acknowledged.

References

1. *Jenko F., Dorland W., et al.,* Phys. Plasmas, **7**, 1904 (2000).
2. *Jenko F., Dorland W., Hammett G.W.,* Phys. Plasmas, **8**, 4096 (2001).
3. *Labit B., Ottaviani M,* Phys. Plasmas, **10**, 126 (2003).
4. *Li J., Kishimoto Y,* Phys. Plasmas, **11**, 1493 (2004).
5. *Lin Z., et al.,* IAEA-CN/TH/8-4 (2004).
6. *Novik K.M., Piliya A. D.,* Plasma Phys. Control. Fusion, **35**, 357 (1993).
7. *Bulyiginskiy D.G., Gurchenko A D., et al.,* Phys. Plasmas, **8**, 2224 (2001).
8. *Altukhov A.B., Gurchenko A.D., et al.,* 30 EPS Conf. Control Fusion and Plasma Physics, ECA **27A** (2003), P-4.170pd.
9. *Gusakov E.Z., et al.,* Plasma Phys. Control. Fusion, **42**, 1033 (2000).
10. *Hennequin P., et al.,* Plasma Phys. Control. Fusion, **46**, B121 (2004).

EVIDENCE OF GYROTRON PERTURBATION IN COLLECTIVE THOMSON SCATTERING BELOW GYRO-RESONANCE IN FTU

U. Tartari, G. Grosso, G. Granucci, L. V. Lubyako[1], A. G. Shalashov[1], E. V. Suvorov[1], F. P. Orsitto[2], A. Simonetto, S. Nowak, F. Volpe[3], V. Muzzini, S. Garavaglia, G. Grossetti

Istituto di Fisica del Plasma, CNR-ENEA-EURATOM Ass., Milano, Italy
[1]Institute of Applied Physics, Russian Academy of Science, Nizhny Novgorod, Russia
[2]CRE-ENEA Laboratories, ENEA-EURATOM Ass., Frascati, Italy
[3]UKAEA, Culham, United Kingdom

We report the observation of anomalous spectra in Collective Thomson Scattering below gyro-resonance in FTU, ascribed to a perturbation of the gyrotron output due to back-reflection of the X component of the probing beam at a cutoff layer met in the beam-injection port. The main implications of these results are shortly discussed.

The diagnostic experiment of Collective Thomson Scattering (CTS) at 140 GHz in the high-field tokamak FTU ($R = 0.93$ m; $a = 0.3$ m; $B = 4 \div 8$ T; $I_p = 0.4 \div 1.2$ MA) is aimed at spatially-resolved measurements of the ion temperature with the final goal of demonstrating high-density CTS in the X-mode. Actually strong anomalous spectra often including lines are systematically detected at spectral power densities orders-of-magnitude stronger than predicted for the ion-thermal spectra.

CTS in FTU is the first diagnostic experiment in a fusion-relevant device with propagation below gyro-resonance, $\omega < \omega_{ce}$. Significant advantages of this configuration, recognized of primary interest in the perspective of alpha-CTS in ITER [1], are minimization of electron cyclotron (EC) noise and accessibility of both modes from the low-field side. CTS in the X-mode at low enough frequency is expected to allow operation both at high density, with acceptable refractive effects, and at high temperature, avoiding the prohibitive black-body EC emission levels typical of an ignited device [1]. This ITER relevance provided a strong motivation to a detailed investigation of our unexpected results.

A layout expressly designed in view of CTS at high density is exploited in the experiment. One of four 140 GHz, 0.5 MW gyrotrons available for ECRH provides the probing source. The transmitting and receiving antennas, of quasi-optical type, are accommodated in two ports of the same poloidal section. Due to the narrowness of the ports, six mirrors are required to propagate and properly steer the beams. To allow both antenna alignment and CTS measurements off-axis, the two plasma-facing mirrors can be rotated about a vertical axis. Besides taking advantage of the circular cross-section of the FTU plasma, refractive effects are minimized by the use of an orthogonal ($\theta_s \cong 90°$) scattering

geometry with up-down symmetry. The beam propagation directions being tilted toroidally, the polarization is elliptic and a modal mixture is propagated in the plasma in absence of polarization control. This was the case in the measurements here reported. Pure X-mode operation at high density having been postponed to a final phase, a linear horizontal polarization borrowed from ECRH has been currently launched.

A quasi-homodyne radiometer with a voltage-controlled BWO acting as local oscillator is used for signal detection and a spectrum analyzer with $j \leq N = 32$ channels of width $\Delta f_j = 0.1 f_{j0}$, f_{j0} being their central frequency, to spectrally resolve the spectra. The detection bandwidth is $\Delta f_{tot} = 0.050 \div 1.2$ GHz. Antenna decoupling not exceeding $50 \div 60$ dB, the requirement of a stray-radiation rejection capability of the order of 90 dB, mandatory for reliable operation, is satisfied by the use of a 20-cavity notch filter with 100 dB peak attenuation.

Considerable improvements were introduced both in the setup and in the operational procedures to support the investigation. In particular, fine matching of the gyrotron and notch-filter frequencies, achieved by small ($\leq$ 1%) variations of the gyrotron-magnet current, provided $a \cong 40$ dB increase in stray-radiation rejection and high symmetry, to within ± 10 MHz, in spectral analysis.

Evidences and interpretation

Orders-of-magnitude variations in spectral power density are exhibited by the anomalous spectra in different plasma conditions. No clear correlation with the plasma parameters could be found, however, in spite of good shot-to-shot reproducibility. The estimated enhancement of the spectra with respect to ion-thermal spectra can be as high as $\approx 10^4$. A variety of behaviors, including oscillations and decay, are exhibited in spectra from a single shot. The spectra detected in aligned- and misaligned-antenna conditions are much similar, showing that the thermal-CTS geometry is not involved in their excitation. A low-frequency feature with shape approaching $S \propto 1/f$ is common to all spectra. In some shots only this feature is exhibited. In the majority of cases spectral lines with recurrent frequency patterns are observed (Figs. 1 and 2). High-frequency ($0.8 \div 1.1$ GHz) lines are much more frequent than low-frequency lines ($0.2 \div 0.3$ GHz). A multiplet structure is suggested in both cases.

Attempts were initially made of interpreting the anomalous spectra in terms of plasma-wave interactions, as regads the line features, and of high-frequency micro-turbulence or coherent modes, as regards the $1/f$ feature. Beam-plasma interaction at the first transit and signal collection through a multiple wall-reflection process were necessarily assumed in these attempts. The possible occurrence of a gyrotron perturbation was considered only after their failure,

mainly due to a lack of reproducibility of the relevant features in subsequent measurements.

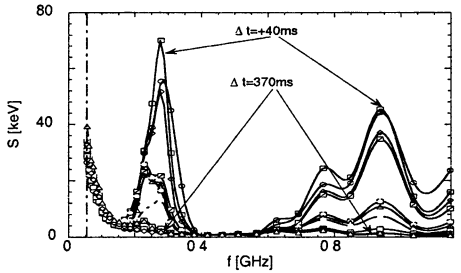

Fig. 1. Spectral sequence from a single shot (27359) exhibiting, besides the $1/f$ feature, both low- and high-frequency lines. Here the lines quickly reach a maximum and then progressively decay. Integration time: 30 ms.

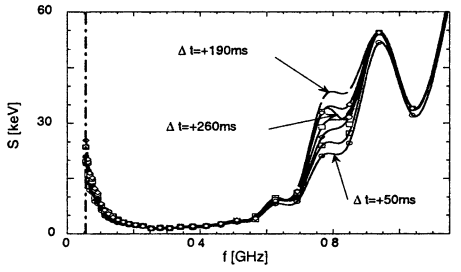

Fig. 2. Spectral sequence from a single shot (27343) exhibiting only high-frequency lines. Here all lines are stable except one, which exhibits an oscillating behavior. Integration time: 36 ms.

While we looked at the gyrotron perturbation mainly in global terms neglecting details, a qualitative interpretation of the spectral features in this frame poses no major problems provided a reflection coefficient R of at least 5% in power is made available [2]. The crucial question to be answered was that of if and how the FTU plasma could cause this relatively high reflection coefficient. At high enough R both unmatched-cavity modes at frequency patterns $\Delta f_R \equiv 1/\tau = v_g/2L_R$, with v_{gr} the group velocity and L_R the load distance, and secondary matched-cavity modes (spurious gyrotron lines) may be jointly excited. The plasma-gyrotron distance in FTU being $L_R \approx 30$ m, leading to $\Delta f_R \approx 5$ MHz, however, it is easily realized that at best only a low-frequency pattern, seen as line broadening, may be produced by a primary perturbation directly excited by the far plasma-load. To explain the occurrence of spectral lines it must be further assumed that a secondary perturbation by a near load, e. g., the gyrotron window, (low-frequency lines), and secondary matched-cavity modes (high-frequency lines) are also indirectly excited by this load. These simple considerations motivated our considering the perturbation strong.

Only a small continuous feature at very low frequency, unambiguously identified as the (unperturbed) gyrotron-noise spectrum, is observed in shots performed in the vacuum vessel without plasma. This seemed to support the idea that the FTU plasma was either directly or indirectly implied in causing the perturbation. However, in CTS most of the beam power being in all cases dissi-

pated through a multiple wall-reflection process, the conditions in the shots in the plasma and in those in vacuum could be reasonably expected to be much similar. Significant differences could have arisen at best only due to orders-of-magnitude increments of the stray-radiation level following a modification of the multiple wall-reflection process by plasma refraction. Both simple reasoning and a number of experimental evidences clearly demonstrated that this was not the case. Anomalous spectra were detected also in shots at very low density, hence with negligible refraction. A dedicated monitor set at the receiver input provided direct confirmation that the stray-radiation level in shots with and without plasma was much similar and, on symmetry considerations, the same conclusion applied to the transmission side. Finally, the spectra observed in shots at $B = 6$ T, hence with a partially absorbing EC layer in the plasma spoiling multiple wall-reflections, were found even stronger than those observed in shots at $B = 7$ T, where no absorption at all occurred. The same was true for the spectra from shots made at "half" gyrotron power (170 kW) compared to those at "full" power (370 kW).

A first insight in the nature of the perturbation came from the observation that significant spectral enhancements, with maxima exceeding several keV, were noticed in spectra from shots performed still in vacuum but now with the toroidal magnetic field applied. Showing that the perturbation was related, not to the FTU plasma as such, but to the application of the magnetic field in the plasma build-up process, this brought us to focus the attention on possible unexpected effects of "hidden" resonances and cutoffs. Consider a beam propagating, instead than from the top as in the CTS geometry, radially horizontally from the low-field side in a plasma at $B = 5.5$ T. As Figure 3 shows, while the beam component polarized in the O-mode freely propagates after partial absorption at the resonant layer, the component in the X-mode is totally reflected at the cutoff layer that is crossed previous to the former. In the CTS geometry a much similar situation is met in the beam-injection port. In absence of injected beam the resonant and cutoff layers are only virtual, but will become active as soon as a breakdown plasma with not too low density is produced in the port by ionization of the residual gas by the beam itself. The back-reflected signal producing the perturbation is ascribed to this kind of process.

Following this explanation, the strength of the gyrotron perturbation is determined, besides the incident polarization, by the density and the composition of the breakdown plasma, hence by scarcely controllable parameters like the rate of gas puffing, the rate of gas desorption from the walls, etc. This explains our difficulties in establishing correlations between the spectral behavior and the main plasma parameters. We further stress that in our quasi-optical antennas, while poloidal in the first tract, the reflection plane is tilted when the beam propagates in between the last two mirrors. Do to this the modal partition at the resonant layer is different from that propagated in the plasma.

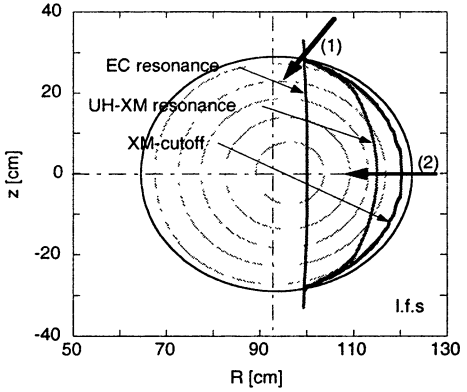

Fig. 3. Resonant and cutoff layers at $B = 5.5$ T. It is seen that, while a beam injected in the CTS geometry (*1*) may still freely propagate, a beam injected radially horizontally from the low-field side (*2*) crosses a cutoff layer, which causes the back-reflection of the beam component in the X-mode.

Figure 4, where the normalized isolines of B in a poloidal section of the port are plotted, shows the shape of the resonant layer and the location of the last two antenna mirrors. The resonant layer is seen to cross these mirrors, around which the breakdown plasma is accordingly formed, both for $B = 6$ T and for $B = 7$ T, the field values more frequently applied in the shots. Due to the tenuousness of the breakdown plasma, the cutoff layer strictly approaches the resonant layer.

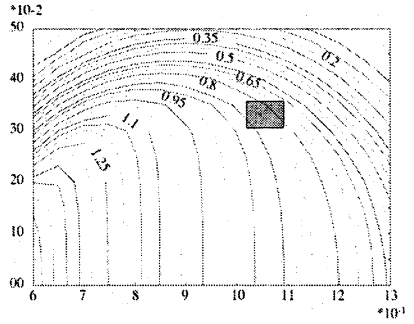

Fig. 4. Isolines of the toroidal field in a poloidal section of the beam-injection port normalized to $B = 1$ on the vessel axis. The small box shows the position of the last two mirrors. The resonant and cutoff layers cross the mirror surfaces both for $B = 6$ T and $B = 7$ T (isolines at 0.71 and 0.83).

A pictorial and rather shocking evidence of the process described above was achieved by direct inspection of the transmitting antenna after deinstallation. Wakes were found on the surfaces of both the 5-th and the 6-th mirror and two small holes pierced in the latter. The small region covered by the wakes has the same slope of the isolines and its width corresponds to the displacement of the critical layers for the B-range covered in the shots. The mutual distance of the holes corresponds to the displacement in passing from $B = 6$ T to $B = 7$ T. The poloidally projected mirror surfaces being partially overlapped, the holes are the result of a progressive erosion of one them due to arcing along a conductive channel parallel to the magnetic-field lines. The presence of Fe and Ni

peaks only in a few of the shots involved showed that, although likely to have become more frequent in time, arcing is but a side-effect. Conferring a metallic content to the breakdown plasma, however, sporadic arcing contributes to explain the apparently random behavior of the spectra.

Discussion

Being associated to the presence of a parallel conduction channel, arc formation is clearly limited to our layout and in principle can be easily prevented by a suitable modification of the antenna. An issue of general relevance is nevertheless highlighted by our results since in the CTS configuration with $\omega < \omega_{ce}$ the resonant and cutoff layers are unavoidably crossed, hence a breakdown plasma possibly formed, in the beam-injection port in any viable geometry. The necessity therefore arises, to avoid the back-reflection, of ensuring pure O-mode polarization locally in this port, which constraint is in contrast with the basic requirement, pure X-mode propagation in the plasma, of CTS at high density.

A viable solution could be strong local pumping in the beam-injection port in order to bring the breakdown plasma "below threshold". The effectiveness of such solution however is made problematic by the scarce controllability of the parameters involved. A more realistic and possibly complementary solution could be recourse to a polarizing antenna to provide pure O-mode polarization up to just beyond the critical layers and pure X-mode polarization thereafter. A matter of concern, especially at the MW power levels envisaged for alpha-CTS in ITER, might be the power-handling capability of the $\lambda/4$-corrugated mirrors required to rotate the polarization.

References

1. *Meo F., Bindslev H., Korsholm S.B., Tsakadze E.L., Walker C.I., Woskov P., Vayakis G.,* Rev. Phys. Instrum., 2004, **75**, 3585.
2. *Grudiev A., Jelonnek J., Schuenemann K.,* Phys. Plasmas, 2003, **8**, 2963; *Glyavin M.Yu., Zapevalov V.E.,* Int J. Infr. & Mill. Waves, 1998, **19**, 1499.

REAL-TIME ECE IDENTIFICATION AND ECRH/ECCD CONTROL OF MAGNETIC ISLANDS IN A TOKAMAK

E. Lazzaro, J. Berrino[1], *S. Cirant, F. Gandini, G. Granucci*

Istituto di Fisica del Plasma Euratom-ENEA-CNR Ass., Milan, Italy
[1]Universita' degli Studi di Milano, Milan, Italy

A challenging task for achieving reliable tokamak operation is the realization of real-time diagnostics and control of low-order tearing-mode magnetic islands by means of localized rf.-driven current. The experimental task involves the identification of the radial and angular position of the rotating islands and the location of the deposition radius of the rf. power. Here we present the first experiment of real-time island detection/suppression on a tokamak obtained applying fast signal correlation and PLL techniques to ECE signals on an automatic digital device installed on the FTU tokamak.

The electron cyclotron emission (ECE) spectrum from a tokamak plasma in the microwave range, as detected by receiving antennas parallel to the equatorial plane, is well known to provide information on the electron temperature profile, $T_e(R)$, along the major radius R. Multichannel acquisition of the related fluctuations signals can provide information on several *turbulent* and *coherent* processes perturbing the equilibrium configuration. In particular, coherent perturbations due to resistive instabilities can be monitored with space and time resolutions appropriate for their real-time control.

The helical magnetic perturbations of the type

$$\delta\mathbf{B} = \mathrm{Re}\sum_{m,n} \delta\mathbf{b}_{m,n}(r)\exp[i(m\theta - n\phi) - i\omega t] \qquad (1)$$

tear and reconnect the magnetic surfaces threaded by field lines that are "closed", i. e. with rational safety factor, $q = m/n$, (m, n integers), developing magnetic islands that cause distortions of the $T_e(R)$ profile by partial flattening across the magnetic-island full width,

$$W(t) = 4\sqrt{r_s L_s \delta b_r(t)/B_0}\,,$$

with $L_s = q^2 R/q' r_s$ the local magnetic-shear length, at $r = r_s$. The magnetic islands appear, grow and rotate at a frequency in the range $\omega_{*i} < \omega < \omega_{*e}$, where $\omega_{*,\alpha}(\alpha = e, i)$ are the drift frequencies [1]. The evolution of $W(t)$ is governed by the back e.m.f. equation for the helical magnetic flux. The rate of growth is described by the non-linear instability index

$$\Delta'(W) = \frac{64 L_s}{c B_0 W^2}\int_{-\infty}^{\infty} \mathrm{d}x \oint J_{\parallel} \cos\xi \mathrm{d}\xi\,,$$

which depends on the parallel current profile.

In low-collisionality, neoclassical regimes at finite $\beta_p = 8\pi n\kappa T/B_0^2$ the additional contributions to $J_{||}$ depend non-linearly on W and the equation for $W(t)$ takes the modified Rutherford form:

$$\frac{\tau_R}{r_s^2}\frac{\partial W}{\partial t} = \Delta_0' + \frac{a_{bs}\varepsilon^{1/2}L_q}{L_p}\frac{\beta_p(t)}{W}\left(\frac{1}{1+W_d^2/W^2} - \frac{W_{pol}^2}{W^2}\right) - \Delta_{EC}'(W,\delta\phi), \quad (2)$$

where the r.h.s. presents a superposition of non-linear physical effects that determine the growth or decay of an initial seed island, W_{seed}, when β_p exceeds a critical value. Differently from classical TMs, non-linear neoclassical tearing instabilities (NTMs) can grow even if $\Delta_0' \le 0$. In equation (2) τ_R is the local resitive diffusion time-scale, L_q, L_p are the typical q and pressure profile scale-lengths, and $\varepsilon = r_s/R$. Further, the first term in brackets is the destabilizing contribution due to the local reduction of the neoclassical bootstrap current, a_{bs} is a numerical coefficient, and W_d a scale-length associated with the competition between parallel and perpendicular heat-transport conductivities [2]. The second term in brackets is associated with the frequency- and collisionality-dependent ion polarization drift current required by current closure. The relevant scale-length is of the order of the poloidal Larmor radius and is defined by [3]:

$$W_{pol}^2(\omega) = \varepsilon\frac{L_q}{L_p}g(\nu_{ii},\varepsilon)\rho_{0i}^{\ 2}\frac{T_e}{T_i}\frac{\omega(\omega-\omega_{*pi}-\kappa\omega_{*Ti})}{\omega_{*e}^{\ 2}}. \quad (3)$$

Finally in equation (2) the last term, that has the explicit form

$$\Delta_{EC}' \equiv \frac{8q\delta_{EC}}{\pi W^2}\eta\left(\frac{W}{\delta_{EC}}\right)\left(\frac{J_{EC}}{J_{boot}}\right)\cos\delta\phi(t), \quad (4)$$

describes the contribution of externally rf.-driven current densities, J_{EC}, to the control and quench of the NTMs, achieved by balancing the deficit in the J_{boot} term [5]. An expression similar to eq. (4) can be written when no ECCD is generated but ECW-heating effects are present [6].

The scaling of the neoclassical term with W is particularly important in the determination the rf. power required to suppress a saturated island. While the problem is still open, recent theoretical work [3] on the effects of parallel-pressure perturbations within an island suggests a change of the scaling of the bootstrap term from $a_{bs}W/(W^2+W_d^2)$ to the more favourable $a_{bs}W_d^4W/(W^6+W_d^6)$. A practical criterion is that the ECW power should generate the non-inductive current inside the island, $\delta_{EC} \approx W$, with a ratio $J_{ECCD}/J_{boot} \approx 1$, δ_{EC}, $\eta(W/\delta_{EC})$ and $\delta\phi(t)$ being respectively the local ECW-power deposition width, the current-drive efficiency, and the phase mismatch between the

power source and the island reference frame centered on the "O" point. These key parameters characterize the ECCD term as a "steering function", $u(t)$, for the control problem and are calculated using ECCD and EC beam propagation theories for given plasma data and given beam launch direction.

Strategies of control of magnetic islands by EC waves

A necessary requisite for the control-action by EC waves to be effective is the ability: a) of identifying in real time the relevant state-variables, namely the radial location of the magnetic island (r_s), the radial location of the ECW-power absorption (r_{dep}), and the amplitude (related to W), frequency and phase of the perturbation; b) of varying accordingly, still in real time, the control variables, i. e., basically the beam direction, as defined by proper toroidal and poloidal launching angles, and the duty cycle of the modulation of the beam power.

In all the several proof-of-principle experiments of NTM feedback control already performed in tokamaks [6–9], the strategy was essentially based on the use of signals from Mirnov coils, due to the poloidal field oscillations, $\varepsilon_B = |\delta B_0|$, the amplitude of which provided the error to be minimized. In the alternative strategy developed for the FTU tokamak instead we have chosen as error-signal the position mismatch, $\varepsilon_r = |r_s - r_{dep}|$. In the following these two strategies are referred to respectively as "search and suppress" (SS) and "just align" (JA) [10].

The SS strategy offers the advantage that the response of the state variable (the Mirnov signal) to the steering action (modification of r_{dep}) and the decision to be taken accordingly are both simple: if $|\delta B|_\theta$ decreases then keep going in the same direction otherwise move r_{dep} in the opposite direction. However, the effect on the mode-amplitude becomes evident only when r_{dep} approaches r_s and this means that in principle the search is blind unless the absorption is almost on the target. Further, beam steering has to be adjusted, to place r_{dep} on the resonant surface, on the basis of a real-time reconstruction of the equilibrium. This additional computation, to be done in real time, complicates the method since it requires much arbitrary *a priori* information, with significant risk of misalignment.

Opposite to SS, the JA method is apparently more complicated since it requires an active and reliable measure of both r_{dep} and r_s in real-time, but has the great merit of using only factual experimental measurements. Below we show how the experimental tracking of r_{dep} can be performed exploiting ECW-power modulation and an automatic procedure applicable on high-performance tokamaks.

Formally the process described by eq. (1), with its associated constraints, e. g., the frequency evolution, belongs (at least in its linearised form) to a class that is well known in the theory of multi-stage decision processes [11, 12].

It consists in reducing the state $W(t)$ to zero in minimal time by a suitably chosen steering function, $u(t)$, dependent on a finite set of control parameters. The formal solutions of this problem show that the optimal steering functions, $u^*(t)$, are of the bang-bang (discontinuous) form. Thus proper use of all the power available must be made in order for the objective to be reachable in minimum time. In what follows we show the results of the application of this type of strategy to the experiment on the FTU tokamak.

ECE signal treatment

The natural variable of state, $|\delta B|_0 \propto |\delta B|_r \propto W^{1/2}$, is replaced by the coherent temperature fluctuation, $\delta T_e(r,t)$, detected by the ECE diagnostics on several channels corresponding to definite R locations. The typical signal $\delta T_e(r,t)$ is a superposition of coherent fluctuations and of noise that must be filtered out. In $(r, \vartheta, R\phi)$ coordinates, and for $r/R << 1$, it can be represented by

$$\delta T_e(r,t) = \delta T_e(r)\cos(m\vartheta - n\phi - \Delta\varphi(t)) .$$

The radial-profile distortion associated with an island is governed by the heat-transport equation with different parallel and perpendicular heat conductivities, $\kappa_{\|} >> \kappa_{\perp}$, and has the structure:

$$\delta T_e = CT_0 X^{1/2} K_{1/4}\left(\frac{X^2}{4}\right)\int_0^X \mathrm{d}z z^{-1} K_{1/4}^{-2}\left(\frac{z^2}{4}\right)\int_z^\infty \tau^{3/2} K_{1/4}\left(\frac{\tau^2}{4}\right)\mathrm{d}\tau , \qquad (5)$$

where

$$X = 4(r - r_s)/W_c , \; C = W^2 |T_0'|/(16W_c)$$

and

$$W_c = \sqrt{4.8} W_d \text{ is } \propto \left(\kappa_{\perp}/\kappa_{\|}\right)^{1/4} .$$

This solution is anti-symmetric with respect to the radius of the rational surface. Therefore the fluctuation amplitude is $\delta T_e \cong 0$ both on the island centre, r_s, and at the "X" stagnation point and this is the main information on island localization provided by the amplitude of the ECE signals.

In some cases direct monitoring of the radial anti-symmetry of the ECE signal may turn out ambiguous. This taking into account, we have developed a different, more robust method for radial island location based on monitoring both the "phase contrast" between pairs of oscillation signals and the expectation value of their correlation over a time interval τ long compared with the oscillation period:

$$P(r,r_1) \equiv \left\langle \delta T_e(r)\delta T_e(r_1)\cos\xi(t)\cos\left(\xi(t) + \delta\phi_{r,1}\right)\right\rangle_\tau = \\ = \frac{1}{2}\delta T_e(r)\delta T_e(r_1)\cos\left(\delta\phi_{r,1}\right). \qquad (6)$$

The generic phase difference between two channels, $\delta\phi_{r,1} = k(r - r_1)$, with $k \cong 2\pi/W$, becomes π if the perturbation is odd close to the rational surface. In particular, considering a point on the *left* and one on the *right* of the rational surface, the expansion of the normalized correlation function around $r = r_s$,

$$P_N(x) \equiv \cos\delta\phi_{r,1} = \cos(kx + \pi),$$

depends continuously on x and takes the values $P_N(\mp W/2) = 1$ for $\delta\phi(\mp W/2) \approx 0, 2\pi$ and $P_N(0) \cong -1$ for $\delta\phi(0) \approx \pi$. Therefore $P_N(x)$ has a maximum concavity at the rational surface $x = 0$ and this can be monitored sampling pairs of ECE channels as a sequence $P_{ij} \approx 1 \to -1 \to 1$ across the island position.

This principle is implemented in the basic algorithms for ECE detection and control developed and installed on FTU, based on four digital signal processors (DSPs) on a VME board. The first algorithm filters the noise and yields the oscillating ECE signal of the *i-th* channel as

$$o_i = \mathrm{ECE}_i - \langle \mathrm{ECE}_i \rangle_{\tau_1},$$

with τ_1 a suitable averaging time scale. Another time average over $\tau_2 > \tau_1$ is performed to get the normalisation amplitude,

$$\mathrm{A}_i = \sqrt{\langle o_i^2 \rangle_{\tau_2}}, \quad o_i^{norm} = o_i / \mathrm{A}_i .$$

The correlation function $P_{ij} = \langle o_i^{norm} o_j^{norm} \rangle_{\tau_3}$ is constructed with an average over $\tau_3 > \tau_2 > \tau_1$. Usually $j = i + 1$ but larger steps can be used. $P_{ij} = 1$ means that a coherent oscillation is present, and $P_{ij} = -1$ that a phase jump $\Delta\varphi = \pi$ occurs. The localization algorithm evaluates the P_{ij} concavity in real-time by finite differences.

The different averaging time-scales are parameters to be adjusted to cope with high-frequency noise and thermal transport time constants. The averages are performed with a first-order digital filter approximating a low-pass filter with a pole in the integration time-scale, τ_c. Another digital phase-locked-loop (PLL) algorithm allows tracking and locking to the frequency and phase of the mode in a few oscillation cycles.

The block diagrams of the filter and the frequency-tracking PLL algorithm are shown in Fig. 1. The difference equation of the filter (Fig. 1, left) is

$$I(1) = K_1 \cdot o(1); I(k) = K_2 \cdot I(k-1) + K_1 \cdot o(k),$$

where the constants K_1 and K_2 are defined as $K_1 = \tau_{sample}/(\tau_{sample} + \tau_c)$ and $K_2 = \tau_c/(\tau_{sample} + \tau_c)$, with τ_{sample} the sampling period and $o(k)$ the input signal

at time $k \cdot \tau_{sample}$. These real-time operations allow identification of all the active modes at once as well as the plasma radius where a π phase-jump occurs. The control-action by the actuator requires real-time tracking of the deposition radius of the peak rf.-power (depending on the beam launch angle) to implement the JA procedure.

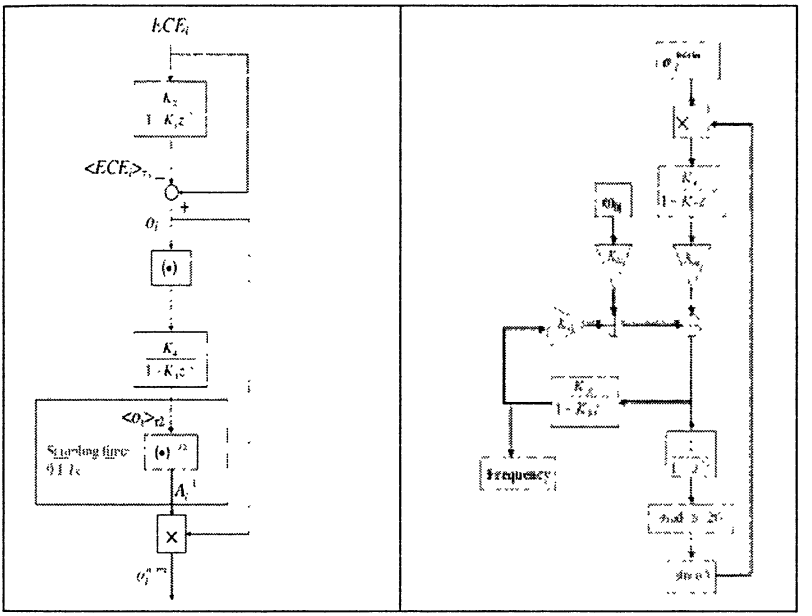

Fig. 1. Left: block diagram of ECE signal filter. Right: block diagram of PLL for mode-frequency tracking.

In the FTU experiment the actuator, based on the ECRH system [13], consists of four GYCOM gyrotrons (140 GHz, 500 kW, 0.5 s) that feed the microwave power through an oversized corrugated circular waveguide to a launcher focusing the beams into the plasma. The beams can be steered shot by shot, both poloidally and toroidally, by four independent mirrors. In the initial phase, where r_{dep} is determined, each *k-th* gyrotron is modulated with a low duty-cycle waveform (10% on "ping" and 90% off) at a different frequency. The correlation function between the *i-th* induced temperature oscillations, $\delta T_{e,i}$, as detected by ECE, and the *k-th* gyrotron power ping, $g_{i,k}$, is calculated as

$$P_{i,k} = \left\langle o_i^{norm} g_k \right\rangle_{t_3}.$$

The peaks of $P_{i,k}$ allow real-time tracking of the r_{dep} of many beams. Then a decisional algorithm (Fig. 2, right) selects the ECW-deposition peak closest to the selected magnetic island and switches to 90% duty cycle the corresponding

gyrotron, leaving a dip of 10% to continue the tracking of the r_{dep}. The four gyrotrons are fed by two tetrodes in series that can be modulated separately and independently.

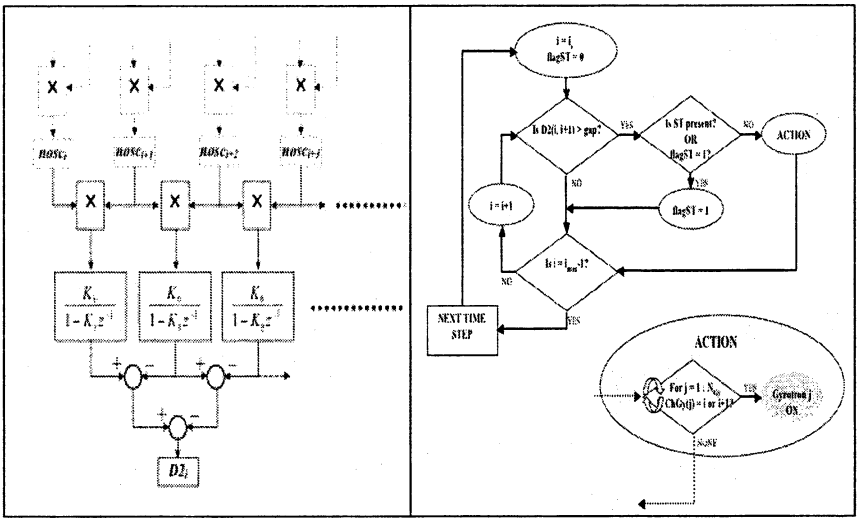

Fig. 2. Left: block diagram of the finite-difference algorithm for P_{ij}. Right: principle of the decisional algorithm for alignment of r_{dep} onto r_s.

Results of automatic TM stabilization experiments on FTU

In a number of FTU shots, with B = 5.54 T, I_p = 500 kA, $n = 7 \times 10^{19}$ m^{-3}, $T_e(0)$ = 1.85 keV, tearing modes (TMs) were present and successful automatic detection/control of these modes by ECRH was obtained with the system described above using two gyrotrons, both with purely poloidal injection angle. Here we present a single significant example. Figure 3, where the ECE temperature profile of shot 27714 is plotted, shows the identification in real time of r_{dep} of gyrotrons *1* and *3*. Figure 4, where the ECE channels 3, 2 and 1 are displayed for the same shot, in turn shows the onset of a (m = 2, n = 1) tearing mode in the same shot at t = 0.58 s. The two lower traces show the low duty-cycle polling regime of gyrotrons *1* and *3*, the subsequent automatic turning-on to full duty cycle of gyrotron *3* (while gyrotron *1* remains low) and the successful action on the mode terminating with its suppression at t = 0.62 s.

More details are shown in Fig. 5, where the traces of the ECE channels in the top-left frame show the appearance of a mode on channel *9* at t = 0.56 s. This is confirmed by the phase inversion between channels *9* and *10* seen in the top-right frame at t = 0.6038 s and by the Mirnov signal in the fourth frame. The large signal on chan. *8* is likely the consequence of asymmetric shape of the magnetic island, and deserves further study. The ping waveforms of the "far"

and "near" gyrotrons seen in frame 2 further show the onset of the high duty-cycle at $t \sim 0.60$ s and its quenching effect on the mode ending with full suppression at $t \sim 0.63$ s.

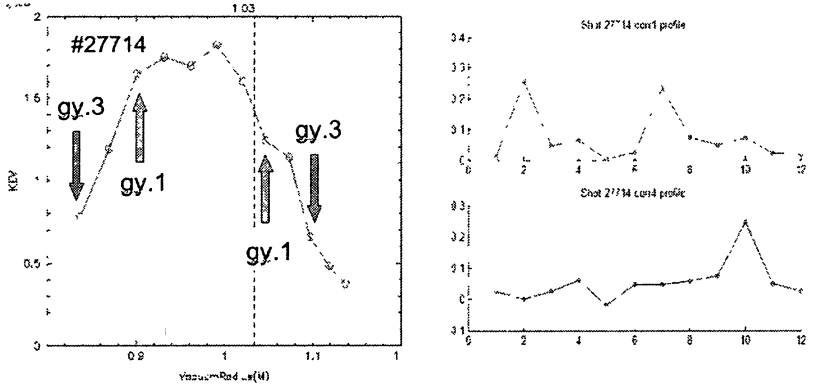

Fig. 3. Left: T_e profile and gyrotron power deposition positions in FTU shot 27714. Right: identification of r_{dep} of gyrotrons *3* (top) and *1* (bottom).

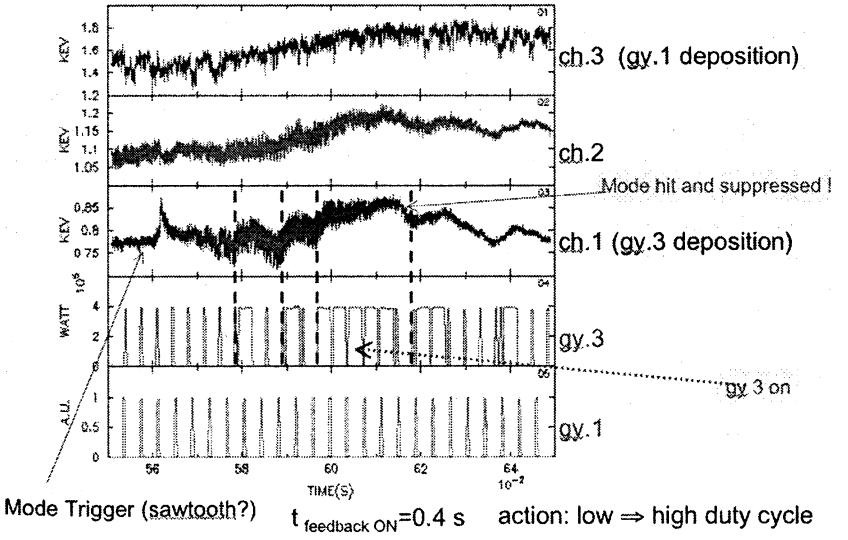

Fig. 4. Top traces: T_e ECE signals for shot 27714. Lower traces: waveforms of gyrotrons *3* (top) and *1* (bottom).

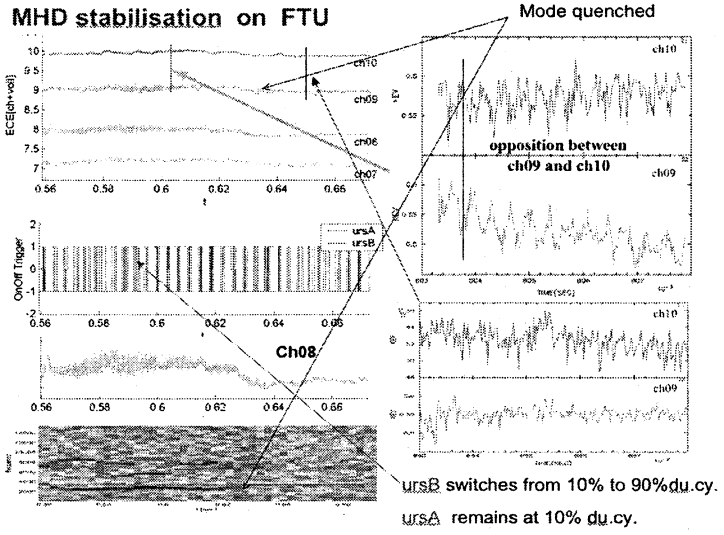

Fig. 5. Top-left frame: T_e ECE signals for FTU shot 27714. Right frames: ECE signals on expanded scale. Second frame: gyrotrons pulsed waveforms. Third frame: signal on chan. *8*. Bottom frame: Mirnov spectrogram showing the presence of a mode and its subsequent quench.

Conclusions

A new strategy for the use of ECW power to control magnetic islands has been conceived and successfully tested with a purpose-built digital device on the FTU tokamak. The principle of monitoring the radius of ECW-power deposition by suitable modulation and correlation with temperature fluctuations, together with cross-correlation-based tracking of islands, has been proven feasible in real time and as such applicable to steer the movable mirrors of the ECW launchers in high-performance tokamaks.

References

1. *Waelbroeck F.L., Connor J W., Wilson H.R.,* Phys. Rev. Lett., 2001, **87**, 215003.
2. *Fitzpatrick R.,* Phys Plasmas, 1995, **2**, 825.
3. *Smolyakov A I., Hirose A., Lazzaro E., Re G., Callen J.D* , Phys. Plasmas, 1995, **2**,1581.
4. *Smolyakov A.I., Lazzaro E.,* Phys. Plasmas, 2004, **11**, 4353.
5. *Sauter O.,* Phys. Plasmas, 2004, **11**, 4808.
6. *Cirant S. et al.,* Proc. 18-th Int. Conf. on Fusion Energy, 2000, Sorrento, IAEA CD-ROM file EX3/3.
7. *Zohm H. et al.,* Phys. Plasmas, 2001, **8**, 2009.
8. *La Haye R. et al.,* Phys. Plasmas, 2002, **9**, 20051.
9. *Isayama A. et al.,* Nucl. Fus., 2003, **43**, 1272.
10. *Berrino J., Lazzaro E , Cirant S. et al.,* Nucl. Fus., 2005, **45**, 1272.
11. *La Salle J.P.,* Proc. Nat. Acad. of Sciences, 1959, **45**, 573.
12. *Bellman R., Glicksberg I., Gross O.,* Q. Appl. Math , 1956, **14**, 11.
13. *Tuccillo A. et al.,* Fus Sc. and Techn., 2004, **45**, 459.

ECR TRANSPORT IN HOT TOKAMAK PLASMAS WITH ECCD/ECRH-PRODUCED SUPERTHERMAL ELECTRONS

K. V. Cherepanov, A. B. Kukushkin, L. K. Kuznetsova, E. Westerhof[1]

NFI RRC "Kurchatov Institute", Moscow, Russia
[1]FOM-Institute for Plasma Physics, Rijnhuizen, Association, EURATOM-FOM, Trilateral Euregio Cluster, The Netherlands, www.rijnh.nl

First results on evaluating the role of ECCD/ECRH-produced superthermal electrons, simulated with numeric code TORBEAM+RELAX, on the ECR transport in hot tokamak plasmas, simulated with numeric code CYNEQ, show that for ITER-like conditions the net EC power loss radial profile in the plasma core is sensitive to contribution of superthermal electrons.

1. Introduction

Fokker – Planck modeling of the electron velocity distribution (EVD) for ECRH and ECCD showed the possibility of appreciable deviation from a Maxwellian for high enough intensity of the injected wave [1].

For hot ($T_e > 10$ keV) plasmas confined by a strong toroidal magnetic field ($B > 5$ T), the superthermal electrons may influence the transport of electron cyclotron radiation (ECR) in the entire spectrum, not only at the low harmonic numbers of the fundamental frequency, which are directly involved in ECRH and/or ECCD. The contribution of superthermal electrons to ECR transport in such plasmas was shown to strongly influence the profile of the net ECR power loss, $P_{EC}(r)$ [2]. In particular, for ITER-like conditions (ITER reference scenario 2, "Inductive", $T_e(0) \sim 25$ keV), the presence of ~10% fraction with locally doubled temperature in the plasma core makes the value $P_{EC}(0)$ a noticeable part of the fusion power in the core. This conclusion qualitatively agrees with the {ASTRA + CYTRAN} code-based analysis [3] which showed significance of local/global contribution of ECR for strictly maxwellian EVD in the ITER regimes with somewhat higher temperatures (ITER reference scenarios "Steady-State", $T_e(0) \sim 35$–45 keV).

Here we present first results of evaluating the impact of ECCD/ECRH-produced superthermal electrons on the ECR transport in hot tokamak plasmas for ITER-like conditions. These include (i) Fokker – Planck modeling of EVD for ECRH and/or ECCD via successive use of the numerical codes TORBEAM [4] and RELAX [5], and (ii) subsequent modeling of the $P_{EC}(r)$ profile, using the numerical code CYNEQ [2].

2. Fokker – Planck modeling of electron velocity distribution

Method of calculating the EVD is as follows. First, the beam tracing code TORBEAM [4] calculates a power deposition profile $P_{ECRH}^{TORBEAM}(r)$ and provides the beam width, w, and the variation of parallel refractive index, $\Delta N_{||}$, on the set of magnetic flux surfaces. Second, the fully relativistic Fokker – Planck code RELAX [5] takes w and $\Delta N_{||}$ from TORBEAM and calculates deposition $P_{ECRH}^{RELAX}(r)$ with allowance for resonance broadening [5, 6].

The results of calculations of the ECRH power deposition profile and the EVD for ITER-like conditions are given in Figs. 1–3. Here we do not deal with the ITER geometry and perform a calculation for concentric circular flux surfaces with the proper central density ($n_e(0) = 10^{20}$ m^{-3}) and temperature ($T_e(0)/T_e(a) = 25/2$ keV) and dimensions $R = 6.2$ m and $a = 2.0$ m from ITER, for beams launched in the equatorial plane to fit with use of the mid-plane launcher in ITER rather than the upper launcher.

3. Transport of plasma's self ECR in tokamak plasma with ECRH/ECCD-produced superthermal electrons

The code CYNEQ is applicable to hot toroidal non-circular plasmas with a strong enough reflection of EM waves from the wall. In this case, the high harmonic numbers of the fundamental EC frequency dominate in the EC transport. This enabled S. Tamor [7] to reduce the ECR transport problem to a 1D one, in which the net ECR power loss profile, P_{EC}, depends on the magnetic surface only, and the EC intensity is isotropic and homogeneous in the major part of the reduced phase space {radiation frequency, magnetic surface} (cf. Eq. (2) in [8(A)]). Therefore, for evaluating the effect of superthermals on the $P_{EC}(r)$ profile, the code CYNEQ needs the EVD as a function of radial coordinate/magnetic surface (i. e. EVD is averaged over magnetic surface) and modulus of electron velocity (i. e. EVD is averaged over pitch angles). In principle, this pitch angle average will be a function of the bounce angle and thus not constant on the flux surface. Just to estimate the effect, we proceed by extracting only the deviation from a maxwellian with respect to electron energy and neglect any pitch angle dependence.

The results of calculations for the $P_{EC}(r)$ profile with the code CYNEQ are given in Figs. 4, 5.

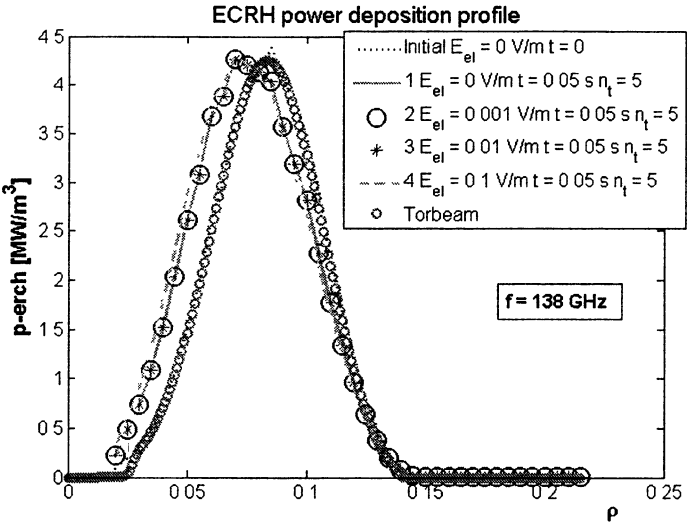

Fig. 1. Power deposition profile, as a function of normalized radius $\rho = r/a$, calculated with the codes TORBEAM (small circles) and RELAX (all others) for perpendicular launch ($\beta = 0$), $f = 138$ GHz, O mode, $n = 1$, 20 MW ECRH. The steady-state EVD is obtained by iterations in time (n_t – number of iterations, time step 0.01 s). The curves are shown for various values of the electric field E_{el}.

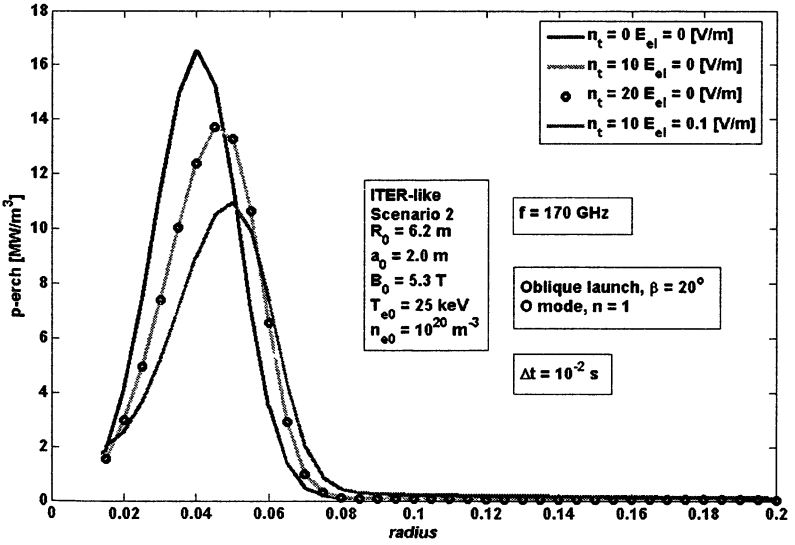

Fig. 2. Power deposition profile, similar to Fig. 1, for oblique launch ($\beta = 20°$), $f = 170$ GHz

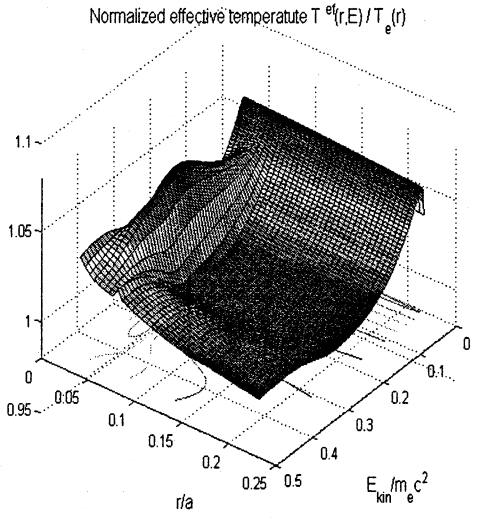

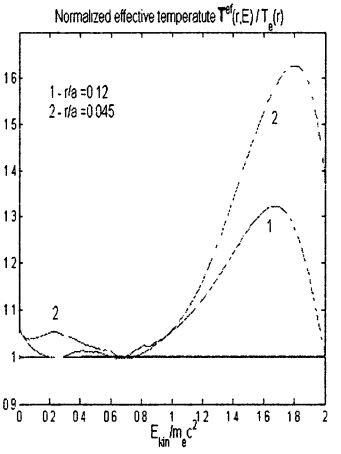

a

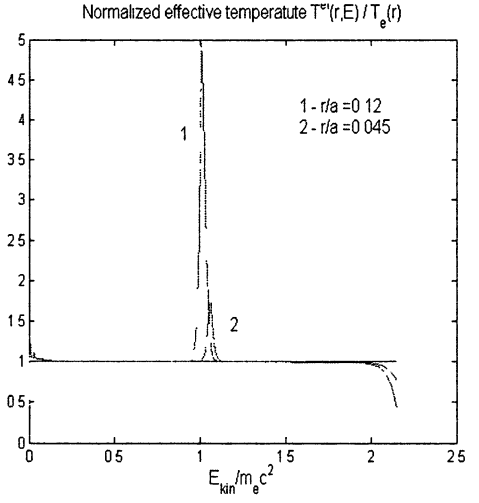

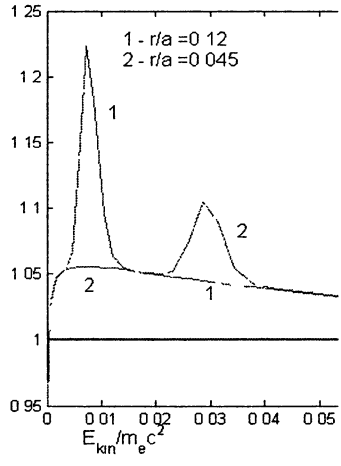

b

Fig. 3. The ratio of the effective temperatures (defined as EVD's slope with respect to electron energy *E)* $T_{ef}(E) \equiv -\left\{\partial \ln[f(E)]/\partial E\right\}^{-1}$, for disturbed EVD, averaged over pitch angles, and undisturbed maxwellian background, as a function of normalized radius and electron kinetic energy, for ECCD in the range r/a = (0, 0.2): oblique (β = 22°, f = 170 GHz) (*a*) and perpendicular (β = 0, f = 138 GHz) (*b*) launches.

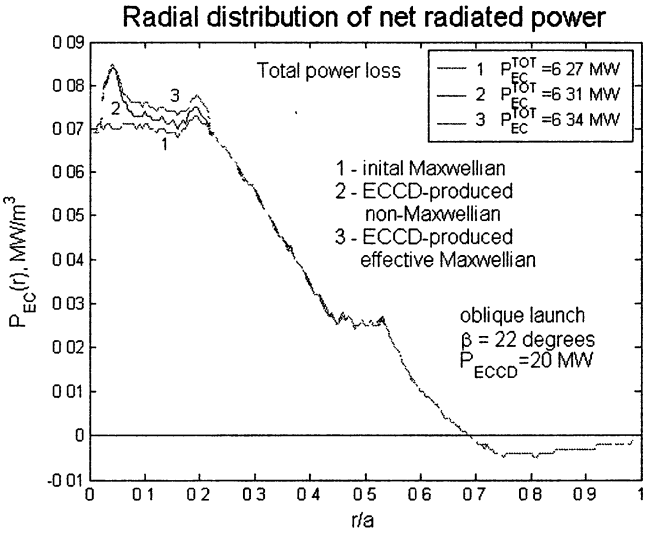

Fig. 4. Comparison of radial profiles of net ECR power loss for maxwellian background plasma (curve *1*), non-maxwellian EVD produced by ECRH/ECCD of Fig. 3, *a* (curve *2*), and maxwellian EVD with the same relativistic mean electron energy (curve *3*), for wall reflection coefficient R_W = 0.6. Similar picture (without, however, the peak at $r/a \sim 0.05$) takes place for EVD of Fig. 3, *b*.

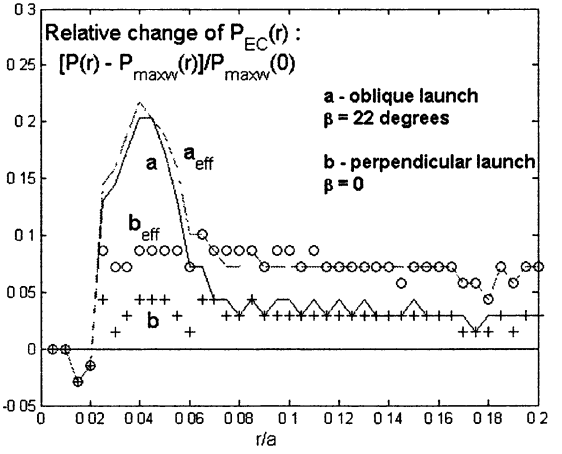

Fig. 5. Relative change of radial profiles of the net ECR power loss for EVD disturbed by ECCD/ECRH for oblique (solid curve, *a*) and perpendicular (crosses, *b*) launch (for EVD of, respectively, Fig. 3, *a* and Fig. 3, *b*) vs. profile for background maxwellian. Similar comparison of the effective maxwellian (i. e. maxwellian EVD with the same relativistic mean electron energy) is given by the curve a_{eff} and the circles b_{eff}.

4. Conclusions

1. The EC absorbed power density, calculated with TORBEAM+RELAX code, may attain ~10 MW/m^3 for ITER-like conditions, for 20 MW total absorbed power and wave beam focusing in the plasma core (cf. Figs. 1, 2).

2. For perpendicular launch, the impact of 20 MW ECRH on the profile of net ECR power loss, $P_{EC}(r)$, calculated with CYNEQ code, appears to be small (~ few percents in the core), similarly to the case of EVD's distortions caused by the plasma's self emitted ECR of ~15 MW total intensity (inside the plasma column, for wall reflection coefficient $R_w = 0.6$) (cf. Figs. 7, 8 in [2]).

3. For oblique launch (injection angle $\beta \sim 20°$) the contribution of ECCD to $P_{EC}(r)$ grows by up to ~20% in the core, because of larger values of electron velocities, responsible for the ECRH power absorption.

4. The calculated steady-state ECRH/ECCD-disturbed EVD, converted to Maxwellian with the same relativistic mean electron energy, produces similar or slightly larger effect on $P_{EC}(r)$ (Fig. 5).

The authors thank D.A. Shuvaev for valuable assistance. The work is partly supported by the NWO-RFBR Grant Nr.047.016.016.

References

1. *Harvey R.W., et. al.*, Phys. Rev. Lett., 1989, 62, 426.
2. *Cherepanov K.V., Kukushkin A.B*, Proc. 20th IAEA Fusion Energy Conf., Vilamoura, Portugal, 2004, TH/P6-56.
3. *Albajar F., Bornatici M., Cortes G, et. al.*, Nucl Fusion, 2005, 45, 642, Proc. 20th IAEA Fusion Energy Conf., Vilamoura, Portugal, 2004, TH/P4-18.
4. *Poli E., et al.*, Comp Phys. Commun , 2001, 136, 90.
5. *Westerhof E., Peeters A.G., Schippers W.L.*, Rijnhuizen Report RR 92-211, 1992.
6. *Westerhof E.*, Proc. 9th Joint Workshop ECE & ECH, 1995, p. 3
7. *Tamor S.*, (A) Fusion Technol., 1983, 3, 293; Nucl. Instr. and Meth. Phys. Res., 1988, A271, 37; (B) Reps. SAI-023-81-110-LJ/ LAPS-72 and SAI-023-81-189-LJ/ LAPS-72, La Jolla, CA: Science Applications, 1981.
8. *Kukushkin A.B.*, (A) Proc. 24th EPS Conf. Contr. Fusion & Plasma Phys , Berchtesgaden, 1997, ECA vol. 21A, Part II, p. 849-852; (B) Proc. 14th IAEA Conf. Plasma Phys. & Contr. Fusion, Wuerzburg, 1992, vol. 2, p. 35-45; JETP Lett., 1992, 56, 487.

ELECTROMAGNETIC WAVE BEAMS IN SMOOTHLY INHOMOGENEOUS ANISOTROPIC MEDIA

A. I. Smirnov, A. A. Balakin, M. A. Balakina, G. V. Permitin

Institute of Applied Physics, RAS, Nizhny Novgorod, Russia

An asymptotic description in the short-wavelength limit is developed for propagation of quasi-monochromatic electromagnetic wave beams in smoothly inhomogeneous anisotropic (including gyrotropic) media with spatial dispersion Proposed method is consisted in derivation of quasi-optical equation for the slow-varied scalar beam amplitude from Maxwell equations. This parabolic equation is written in orthogonal coordinates system attached to the central geometrical optical ray. Transversal localization of wave beam near the central ray allows to separate and sequentially derive the focusing (or defocusing) and aberrations terms The case of account of only quadratic phase corrections (the so called nonaberrational approximation) is considered in detail.

1. Introduction

Quasi-optical description of wave fields by means of parabolic equation (with imaginary diffusion coefficient) for slow and smooth envelopes (complex amplitude) of wave packets takes the intermediate position between the geometrical optics (GO) and the full wave theory. In the small-angle approximation quasi-optics (QO) takes into account diffraction effects for beams wide on the wave length scale. In contrast to GO quasi-optics is never a subject to local and integral differential catastrophes – so it describes fields in the vicinity of focal points and caustic surfaces correctly and provides the continuous transition from the one characteristic diffraction zone to another. It is not independent fully from GO though, since it uses the last for separation of the rapidly oscillating factor – namely the carrier of wave packets. But for this it is enough to calculate in GO approximation the only one ray (the so called reference ray) that may be chosen henceforth in capacity of the bearing curve for curvilinear orthogonal coordinates system following the beam.

Consistent derivation of quasi-optics for isotropic smoothly inhomogeneous media may be found in [1–3]. The object of the present work is the generalization of quasi-optical theory on smoothly inhomogeneous magneto-active plasmas for those cases, when it may be described by the model of dielectric with Hermitian permittivity tensor $\varepsilon_{ij}(\mathbf{r},\mathbf{k})$ ($\mathbf{k}$ is the current wave vector). Only monochromatic ($\exp(-i\omega t)$ processes) wave beams in stationary media will be considered.

For the system of wave equations for electric field in magneto-active plasmas

$$\hat{L}_{ij}E_j = 0, \quad (i,j=1,2,3) \tag{1}$$

with integro-differential operator $\hat{L}_{ij}$ the eikonal equation

$$\det\left\|\delta_{ij}p^2 - p_i p_j - \varepsilon_{ij}(\mathbf{r},\mathbf{p})\right\| = 0 \tag{2}$$

may be easily written, where $\mathbf{p} = \nabla\psi$, ψ is eikonal (wave phase $\varphi = k_0\psi$). However in such form the eikonal equation proves to be quite complicated. It is convenient to rewrite it relative to refraction index $n_j(\mathbf{r},\mathbf{p})$ for one of possible modes:

$$H = (\nabla\psi)^2 - n_j^2(\mathbf{r},\nabla\psi) = 0. \tag{3}$$

Yet after writing the exact expression for refraction index out even without the spatial dispersion and using Appleton – Hartree formula the expression (3) will turn out quite cumbersome. Nevertheless (3) allows calculate the reference ray of the wave beam by means of the system of Hamiltonian canonical equations:

$$\frac{d\mathbf{r}}{d\tau} = \frac{\partial H}{\partial \mathbf{p}} = \mathbf{s}\cdot S_0, \qquad \frac{d\mathbf{p}}{d\tau} = -\frac{\partial H}{\partial \mathbf{r}}, \tag{4}$$

where $\mathbf{s}$ is the unit vector tangent to the ray and $S_0 = |\partial H/\partial \mathbf{p}|$. Variable τ is related to the length of a ray arc as $ds = d\tau\cdot S_0$. The central (reference) ray of the wave beam will be considered to be constructed somehow, i. e. dependences $\mathbf{r} = \mathbf{r}_0(s)$, $\mathbf{p} = \mathbf{p}_0(s)$ are known.

The curvilinear orthogonal coordinates system (s,ξ_1,ξ_2) may be attached to the central ray: $\mathbf{r} = \mathbf{r}_0(s) + \xi_1\mathbf{o}_1(s) + \xi_2\mathbf{o}_2(s)$, where s is the reference curve arc length, (ξ_1,ξ_2) are coordinates perpendicular to the one, unit vectors of which $\mathbf{o}_1$ and $\mathbf{o}_2$ are turning at moving along the ray relative to natural Darboux trihedron in accordance with Rytov's law. The angle ϑ between principal normal and axis ξ_1 submits to equation $d\vartheta/ds = T$, where T is the reference ray torsion. The metric tensor $g_{ij}(i,j=1,2)$ of the coordinates system (s,ξ_1,ξ_2) is equal to:

$$g_{00} = h_s^2;\ g_{ij} = \delta_{ij};\ g_{0i} = 0;\ h_s = 1 - K(\xi_1\cos\vartheta + \xi_2\sin\vartheta),$$

where K is the reference ray curvature.

2. The wave beam equations

In magneto-active plasmas wave vectors surfaces $H(\mathbf{r}=\mathbf{r}_0,\mathbf{p}) = 0$ ($\mathbf{p}$ is the current wave vector normed on k_0) are quite complicated and multiform. They can include both prominent and concave or prominent-concave parts, lines of inflection and lines of internal conic refraction, where Gauss curvature turns into zero, they can leave to infinity. Using the fact that wide wave beam has narrow angle spectrum one may represent vector $\mathbf{p}$ in the form

$$\mathbf{p} = \mathbf{p}_0(s) + \boldsymbol{\kappa}, \qquad |\boldsymbol{\kappa}| \ll |\mathbf{p}_0|, \tag{5}$$

where $\mathbf{p}_0(s)$ is the value in a point on the reference ray, in vicinity of which wave vectors surface may be approximated by the surface of the second order.

The substitution of complicated surface of wave vectors by paraboloid is possible only for processes with narrow angle spectrum. For the wave beam it is equivalent to that it's characteristic transversal dimensions $\Lambda_\perp$ exceeds essentially wave length: $\lambda/\Lambda_\perp \ll 1$. In those cases then $\Lambda_\perp$ in it's turn is much smaller than characteristic transversal scales of heterogeneity of refraction index ($\Lambda_\perp / L_n \ll 1$) eikonal equation may be expanded in the form of asymptotic series in transversal coordinates ξ_i to within quadratic terms. Broadly speaking the expanding in κ and ξ should be followed by the account of the curvature of the coordinates system (s,ξ_1,ξ_2), i. e. one should expand Hamiltonian of the form

$$H\left(\mathbf{r}_0+\boldsymbol{\xi},\mathbf{p}_{0,\perp}+\boldsymbol{\kappa}_\perp+\frac{\mathbf{s}}{h_s}\left(p_{0,s}+\kappa_s+\frac{\dot{\mathbf{p}}_{0,\perp}\boldsymbol{\xi}}{S_0}\right)\right)=0,\ \boldsymbol{\xi}=\xi_1\mathbf{o}_1+\xi_2\mathbf{o}_2.$$

As a result one can derive shortened eikonal equation of the form

$$\kappa_s+T_{ij}(s)\cdot\kappa_i\kappa_j-\Phi_{ij}(s)\cdot\xi_i\xi_j+B_{ij}(s)\cdot\frac{1}{2}\left(\kappa_i\xi_j+\xi_i\kappa_j\right)=O\left(\left(\lambda/\Lambda\right)^2,\left(\Lambda/L_n\right)^2\right),\quad(6)$$

$$T_{ij}=\frac{1}{2}\frac{\partial^2 H}{\partial\kappa_i\partial\kappa_j},\quad B_{ij}=\frac{\partial^2 H}{\partial\xi_i\partial\kappa_j}-\frac{1}{S_0}\frac{\partial H}{\partial\xi_i}\frac{\partial^2 H}{\partial\kappa_s\partial\kappa_j},\quad \vartheta_j=(K\cos\vartheta,K\sin\vartheta),$$

$$\Phi_{ij}=\frac{1}{2}\left(\frac{\partial^2 H}{\partial\xi_i\partial\xi_j}+\frac{1}{S_0^2}\frac{\partial H}{\partial\xi_i}\frac{\partial H}{\partial\xi_j}\frac{\partial^2 H}{\partial\kappa_s^2}-2\frac{1}{S_0}\frac{\partial H}{\partial\xi_i}\frac{\partial^2 H}{\partial\xi_j\partial\kappa_s}-2\frac{\partial H}{\partial\xi_i}\vartheta_j\right).$$

After application of the Shrödinger procedure by means of substitution

$$\boldsymbol{\kappa}\to\frac{1}{ik_0}\nabla,\quad\left(\kappa_i\to\frac{1}{ik_0}\frac{\partial}{\partial\xi_i},\ \kappa_s\to\frac{1}{ik_0}h_s\frac{\partial}{\partial s}\right)$$

in reduced eikonal equation (6) one can derive QO equation for the smooth envelope of the wave process. In neglecting of the right part of (6) we have the so called nonaberrational approximation[1]:

$$\left(ik_0\frac{\partial}{\partial s}+T_{ij}(s)\frac{\partial^2}{\partial\xi_i\partial\xi_j}-k_0^2\Phi_{ij}(s)\xi_i\xi_j+\right.$$
$$\left.+ik_0B_{ij}(s)\left(\frac{1}{2}\delta_{ij}+\xi_i\frac{\partial}{\partial\xi_j}\right)\right)W=0.\quad(7)$$

Note, that the shortened equation (7) can be derived directly from the Maxwell equations provided we shall seek the solution in the form of asymptotic series in small parameter $\mu=\max\left\{\Lambda_\perp/L_n,\lambda/\Lambda_\perp\right\}$:

[1]One should note, that in quasi-optics the nonaberrational approximation describes arbitrarily strong astigmatism which in traditional optics is accepted to consider like aberrations.

$$\mathbf{E} = \left(W(\mu^2 s, \mu\xi_1, \mu\xi_2)\mathbf{e}_0 + \mu\mathbf{E}_1 + \mu^2\mathbf{E}_2 + \ldots\right) \times \\ \times \exp(ik_0 \int p_{0,s}(s)ds + ik_0 \mathbf{p}_{0,\perp}\xi), \tag{8}$$

where $\mathbf{e}_0$ is the polarization on the reference ray $\mathbf{r}_0(s)$, $\mathbf{E}_1$ and $\mathbf{E}_2$ are polarization corrections. If we substitute the field in form (8) to (1) and limit ourselves by terms of the second order then after some cumbersome algebra we shall come to parabolic equation (7). At that expressions for polarization corrections of the first and second orders are:

$$\mathbf{E}_1 = W \cdot \xi_i \left(\frac{\partial \mathbf{e}_0}{\partial \xi_i} - \frac{1}{S_0} \frac{\partial H}{\partial \xi_i} \frac{\partial \mathbf{e}_0}{\partial \kappa_s} \right) + \frac{1}{ik_0} \frac{\partial \mathbf{e}_0}{\partial \kappa_i} \frac{\partial W}{\partial \xi_i},$$

$$\mathbf{E}_2 = \frac{1}{ik_0 S_0} \frac{\partial \mathbf{e}_0}{\partial \kappa_s} \frac{\partial W}{\partial s} - \frac{1}{2k_0^2} \frac{\partial^2 \mathbf{e}_0}{\partial \kappa_i \partial \kappa_j} \frac{\partial^2 W}{\partial \xi_i \partial \xi_j} +$$

$$+ \frac{1}{ik_0} \left(\xi_i \frac{\partial W}{\partial \xi_j} + \frac{\delta_{ij}}{2} W \right) \cdot \left(\frac{\partial^2 \mathbf{e}_0}{\partial \xi_i \partial \kappa_j} - \frac{1}{S_0} \frac{\partial H}{\partial \xi_i} \frac{\partial^2 H}{\partial \kappa_s \partial \kappa_j} \right) + \frac{1}{2} W \xi_i \xi_j \times$$

$$\times \left(\frac{\partial^2 \mathbf{e}_0}{\partial \xi_i \partial \xi_j} + \frac{1}{S_0^2} \frac{\partial H}{\partial \xi_i} \frac{\partial H}{\partial \xi_j} \frac{\partial^2 \mathbf{e}_0}{\partial \kappa_s^2} - 2 \frac{1}{S_0} \frac{\partial H}{\partial \xi_i} \frac{\partial^2 \mathbf{e}_0}{\partial \xi_j \partial \kappa_s} - \frac{2}{S_0} \frac{\partial H}{\partial \xi_i} \vartheta_j \frac{\partial \mathbf{e}_0}{\partial \kappa_s} \right).$$

3. The solution of nonaberrational equation

The general solution of equation (7) with initial field distribution $W|_{s=0} = W_0(\xi_1, \xi_2)$ may be represented as

$$W(\tau, \xi_1, \xi_2) = \frac{k_0^2}{4\pi^2} \int_{-\infty}^{\infty} \int_{-\infty}^{\infty} \tilde{W}(\kappa_1, \kappa_2) D \exp(ik_0 \Psi(\xi_1, \xi_2; \kappa_1, \kappa_2)) d\kappa_1 d\kappa_2, \tag{9}$$

$$\tilde{W}(\kappa_1, \kappa_2) = \int_{-\infty}^{\infty} \int_{-\infty}^{\infty} W_0(\xi_1, \xi_2) \exp(-ik_0(\xi_1\kappa_1 + \xi_2\kappa_2)) d\xi_1 d\xi_2,$$

$$\Psi = \alpha_{ij}\xi_i\xi_j + \beta_{ij}\xi_i\kappa_j + \gamma_{ij}\kappa_i\kappa_j \quad (i, j = 1, 2).$$

Parameters $\alpha_{ij}, \beta_{ij}, \gamma_{ij}$ and D are determined by the solution of the system of the ordinary differential equations

$$\begin{aligned} &2\dot{\alpha}_{ij} + 2B_{kj}\alpha_{ki} + T_{kn}\alpha_{ki}\alpha_{jn} + \Phi_{ij} = 0, \\ &2\dot{\beta}_{ij} + 2B_{ki}\beta_{kj} + T_{kn}(\alpha_{in}\beta_{kj} + \alpha_{ki}\beta_{jn}) = 0, \\ &2\dot{\gamma}_{ij} + T_{kn}\beta_{ki}\beta_{jn} = 0, \\ &2\dot{D} + DT_{ij}\alpha_{ij} + DB_{ij}\delta_{ij} = 0 \end{aligned} \tag{10}$$

with initial conditions $\alpha_{ij}(s=0) = 0$, $\beta_{ij}(0) = \delta_{ij}$, $\gamma_{ij}(0) = 0$ and $D(0) = 1$.

Despite considerable difference of (7) from the analogous equation for isotropic media an important property remains valid: Gaussian beams stay Gaussian. Equivalently relates to beams the transversal distribution of which is described by Hermitian functions[1].

Determining of the field distribution in Gaussian form:

$$W = A(s)\exp(\sigma_{ij}\xi_i\xi_j)$$

one can derive from (10) a system of the ordinary differential equations for elements of the complex matrix $\sigma_{ij}(s)$:

$$\dot{\sigma}_{ij} = -ik_0\Phi_{ij}/2 + (\sigma_{kj} + \sigma_{jk})(-B_{ik} + iT_{km}(\sigma_{mi} + \sigma_{im})/k_0). \qquad (11)$$

The amplitude factor $A(s)$ at this is determined by the ratio

$$A(s) = \exp\left[\int (2i(\sigma_{11}T_{11} + \sigma_{22}T_{22})/k_0 + 4i\zeta T_{12}/k_0 - (B_{11} + B_{22})/2)\mathrm{d}s)\right].$$

As it is clear from (10), (11) the calculation of Gaussian beams structure in frames of nonaberrational approach reduces to the solution of the system of ordinary differential equations and computation of integral convolutions. Though the possible (in future) account of aberrations and dissipation makes the direct numerical simulation of the wave beam propagation along the reference ray by means of shortened parabolic equation far more preferable. Such method has been approved for equation (7) and gives good coincidence with exact solutions derived from (11).

4. Conclusion

Nonaberrational approximation is well fit to numerical simulation. Procedure comes to solution of the system of ordinary differential equations along the propagation path and further taking of sample integrals in observation region. Moreover, nonaberrational QO approximation stays informative even beyond its applicability domain and allows (by extension of the system of ordinary differential equations) take into account aberrations caused by anisotropy and heterogeneities of the medium.

The work is supported by RFBR grant № 03-02-17466 and NWO–RFBR grant № 047.016.016 (04-02-89005 HBO-a).

References

1. *Permitin G.V., Smirnov A.I.*, Zh. Eksp. Teor. Fiz., 1996, **109**, 736.
2. *Kondrat'ev I.G., Permitin G V, Smirnov A.I.*, Izv. VUZov, Radiofiz., 1980, **23**, 1195.
3. *Permitin G.V, Smirnov A.I.*, Zh. Eksp. Teor. Fiz., 2001, **119**, 16.
4. *Pereverzev G V.*, Phys. Plasmas 1998, **5**, 3529.

[1] Note. that in frames of nonaberrational approximation the behaviour of Gaussuan beams may be described by means of the so called complex GO (see [4]). In principal any initial distribution $W_0(\xi_1,\xi_2)$ may be expanded in Hermitian functions but relations (9) – (11) are more convenient for calculations.

STATISTICAL ANALYSIS AND MODELING OF TURBILENT PROCESSES IN ECRH PLASMA OF MODERN STELLARATORS

N. N. Skvortsova[1], *V. Yu. Korolev*[2], *G. M. Batanov*[1], *A. E. Petrov*[1], *K. A. Sarksyan*[1], *N. K. Kharchev*[1], *J. Sanchez*[3], *S. Kubo*[4]

[1]Prokhorov Institute of General Physics, Moscow, Russia
[2]Moscow State University, Moscow, Russia
[3]EUROATOM-CIEMAT, Madrid, Spain
[4]National Institute of Fusion Research, Toki, Japan

Experiments in ECH plasma in three stellarators have shown the occurrence of steady-state low-frequency strong structural turbulence throughout the entire plasma column. A key feature of strong structural turbulence is the presence of stochastic plasma structures. A new mathematical model is proposed for the probability distributions of the characteristics of the processes observed in turbulent plasmas. The model is based on formal theoretical considerations related to probabilistic limit theorems for a nonhomogeneous random walk and has the form of a finite mixture of Gaussian distributions. The reliability of the model is confirmed by the results of a statistical analysis of the experimental data on density and local flux fluctuations in plasmas of the L-2M, LHD, and TJ-II stellarators with the use of the estimation–maximization algorithm. It is shown that low-frequency structural turbulence in a magnetized plasma is related to non-Brownian transport, which is determined by the characteristic temporal and spatial scales of the ensembles of stochastic plasma structures.

1. In many toroidal and linear devices, low-frequency (LF) turbulence in the plasma core and at the plasma periphery has the form of strong structural (SS) turbulence. The term "strong structural turbulence" means that there are ensembles of stochastic, nonlinearly interacting plasma structures against the background of well-developed steady-state plasma turbulence. In the case of LF SS plasma turbulence in stellarators: time samples of any fluctuating plasma parameter are bursty in character; such time samples are more adequately described by finite-duration oscillating wavelets rapidly decaying in time; the observed wavelet spectra contain quasi-harmonics, and their correlation functions have oscillating tails; nonlinear structures comprise a considerable fraction (from 10 to 30% in different plasma regions) of the turbulence energy; turbulent fluctuations in LF SS turbulence are correlated over the entire plasma volume via ensembles of stochastic plasma structures [1, 2]. The main characteristic feature of LF SS turbulence is that the probability density functions (PDFs) of the fluctuating parameters differ from a normal distribution: the observed PDFs are leptokurtic and are characterized by heavier tails. Non-Gaussian PDFs of stochastic plasma processes point to the non-Brownian (anomalous) motion of particles in stochastic fields [3].

2. There have been many attempts to explain the observed leptokurtic PDFs of fluctuation amplitudes. The most progress in solving this problem has been

achieved with the use of the limit theorems for a homogeneous random walk with discrete or continuous time. According to these theorems, the so-called stable or fractionally stable PDFs characterized by power-law tails can be used as an alternative to a Gaussian distribution [4–6]. However, stable or fractionally stable models sometimes fail to provide an adequate description of plasma turbulence. A basic assumption underlying these models is the absence of the second moment (variance) of the distribution of random particle jumps and/or the absence of the first moment (mathematical expectation) of the distribution of time intervals between the jumps [7]. For this assumption to be valid, it is necessary that, at the least, these random variables with positive probabilities could take arbitrary large values. It is evident that this assumption fails to be valid in practice, because the recorded processes are always limited in space and time, so the above random variables possess all the moments. A new mathematical model is proposed for the probability distributions of the characteristics of the processes observed in turbulent plasmas. The model is based on formal theoretical considerations related to probabilistic limit theorems for a nonhomogeneous random walk and has the form of a finite mixture of Gaussian distributions [8]. In contrast to traditional models, our mathematical models are based on limit theorems for a nonhomogeneous continuous-time random walk. This walk differs from a homogeneous walk in that the distributions of the random time intervals between successive jumps of a walking particle are, in general, different. The assumption of the nonhomogeneity (different distributions of the time intervals between successive jumps) of a random walk is consistent with a concept that the rate of the coordinate increment of a particle that undergoes Brownian motion in a turbulent medium is essentially nonhomogeneous. The parameters of turbulent plasma fluctuations observed in tokamaks and stellarators are nonhomogeneous in both space and time. The most reasonable stochastic models of nonhomogeneous chaotic point processes are doubly stochastic Poisson processes, which are also referred to as Cox processes [9]. When compound Cox processes are used as models of a nonhomogeneous random walk describing the observed turbulent plasma process, the form of the mixing distribution in the limiting law is completely determined by the character of the accumulated intensities and, hence, by the statistical features of changes in the instantaneous intensities of elementary processes. Statistical analysis of the distribution of the increments [3] of turbulent plasma processes reduces to the separation of mixtures, i. e., to the statistical determination of the mixing distribution of the control process, which is an unknown parameter of the statistical problem under consideration. Without going into analytical details, we note that, using the general limit theorems for compound Cox processes, it is possible to theoretically justify models for the distributions of the increments of turbulent plasma processes in the form of more general finite shift-scale (drift-diffusion) mixtures of normal distributions as $\sum_{j=1}^{n} p_j \Phi\left(\frac{x-a_j}{\sigma_j}\right)$, where a_j is the

drift coefficient and σ_j is the diffusion coefficient of the j-th component. It is this approach that we used in statistically analyzing the processes observed [10]. To fit a mixture of normal distributions to a data sample, we must solve the problem of separating the mixture of distributions:

$$f(x) = \sum_{j=1}^{k} p_j \frac{1}{\sqrt{2\pi}\sigma_j} \exp\left(-\frac{(x-\mu_j)^2}{2\sigma_j^2}\right) = \sum_{j=1}^{k} p_j \phi(x, \mu_j, \sigma_j); \quad \sum_{j=1}^{k} p_j = 1.$$

When the number k of the mixture components is fixed, the parameters of the model can be efficiently estimated by the EM-algorithm [11].

3. The detailed description of parameters of TJ-II, L-2M and LHD stellarators is given in [12–14]. Fluctuations were measured by different methods over all volume of plasma (Table).

Device	L-2M	LHD	TJ-II
Measurement in the edge plasma	Probes (density, potential, flux fluctuations)		
Measurement near the mid-radius of plasma	2-mm scattering (density fluctuations)		2-mm scattering (density fluctuations)
Measurement near the center of plasma	Gyrotron radiation scattering (density fluctuations)		

4. Plasma fluctuations in TJ-II were measured in the most quiescent plasma region: far from the heating microwave region (where energy is deposited in the plasma) and also far from the chamber wall and the edge plasma (where energy is dissipated). This region may be considered as an inertial interval for the nonlinear turbulent state of the entire plasma column. It is primarily in this region that energy is redistributed among different nonlinear states under steady-state conditions. However, even in this case, the hypothesis of the normal distribution of the increments of the magnitudes of plasma density fluctuations is discarded for the number of observations more than 10^4 because the P value in the Kolmogorov – Smirnov goodness-of-fit test is less than 0.05. As is well known, the P value shows the degree of assurance that the adopted model is realistic. The hypothesis of the form of a distribution is not discarded if the P value computed for statistical packages is higher than a given confidence level (which is usually taken to be 0.05). For a long sample of $3 \cdot 10^4$ data points acquired over 60 ms (i. e., over almost the entire discharge), the histogram of increments is fitted with a good accuracy by a mixture of three Gaussian distributions (Fig. 1), the contribution of the fourth component is insignificant.

The scattered signal from the heating microwave region in LHD and L2-M seems to be less homogeneous than the time sample of fluctuations from TJ-II. The sample of increments from 2000 points from the ordinary regimes was not

described by a normal distribution in both devices. However, these samples are modeled with a probability more than 85% by a three-component mixture of normal distributions.

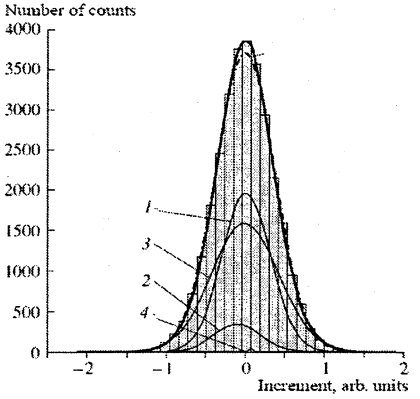

Fig. 1. Modeling of the PDF of a time sample of the increments of plasma density fluctuations in TJ-II (shot no. 8227) by a scale mixture of four Gaussian distributions marked by *1*, *2*, *3*, and *4*. $P = 0.8385$.

Plasma experiments provide a unique possibility of studying the diffusion of ensembles of particles by directly measuring turbulent plasma fluxes. Local fluxes were measured in the edge plasma of the L-2M stellarator [2]. The values of the local particle flux measured in successive instants constitute a time sample of a stochastic diffusion process, which can be studied by the same methods of spectral, correlation, and probability analysis as any other stochastic process.

The hypothesis of a normal distribution for PDF of turbulent flux is discarded because the P value equals zero. The histogram is fitted with a probability of 97% by a mixture of three normal components. The presence of the third component with a large average and a dispersion that is significant in spite of the small weight of the component (in Fig. 2 $p_3 = 0.09$).

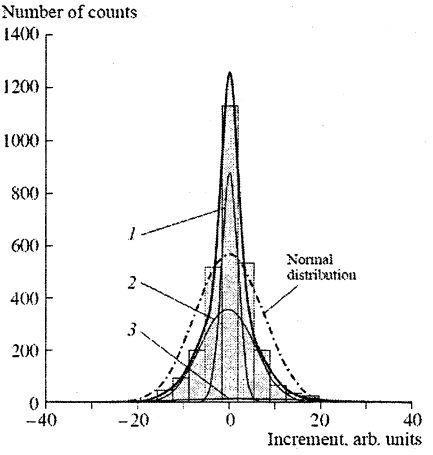

Fig. 2. Modeling of the PDF of a time sample of the increments of the local flux in the low-temperature plasma of L-2M (shot no. 44487) by a scale mixture of three Gaussian distributions marked by *1*, *2*, and *3*. $P = 0.98$.

5. Nonhomogeneous (over time) random walks with a continuous time (e. g., those described by generalized Cox processes) turn out to be convenient and adequate mathematical models for describing the processes under consideration on a microscopic level. These models make it possible to apply Gaussian processes with a random time (the so-called subordinated Gaussian processes) to describing the observed processes. Since finite mixtures of normal distributions model the one-dimensional distributions of the increments of these processes, the subordinated processes describing the intensity of local events have discrete distributions. This means that, in the processes observed in low-frequency structural plasma turbulence, a finite number of characteristic processes can be distinguished, each of which is characterized by its own intensity of the local events. We used the EM-algorithm to model the increments of density fluctuations of high-temperature plasmas of L-2M, LHD, and TJ-II and the increments of the local fluctuating flux in the edge plasma of L-2M. Distributions of the increments are well fitted by finite mixtures of normal distributions with the same number of the mixture components in L-2M, LHD, and TJ-II, which have different magnetic field configurations.

Since the distributions of the increments of the LF SS turbulent processes are well fitted by finite mixtures of normal distributions, the local (in time and space) character of these processes is described by classical normal (Gaussian) diffusion. This does not mean, however, that the resulting motion of particles will also be Brownian. The increments of these processes are associated with a finite number of types of diffusion. Since each type of dynamic structures in plasma turbulence is characterized by its own diffusion coefficient, the separation of the mixture into a finite number of components means that the stochastic character of the observed plasma turbulence is related to a finite number of dynamic structures (a finite number of the main interacting processes).

References

1. *Sarksyan K.A , Skvortsova N.N., Kharchev N.K., Milligen B.F.,* Plasma Phys. Rep., **25,** 312 (1999).
2. *Batanov G.M. et al ,* Zh. Eksp. Teor. Fiz., **78,** 974 (2003).
3. *Batanov G M. et al.,* Plasma Phys. Rep., **28,** 111 (2002).
4. *Gonchar V.Yu. et al.,* Plasma Phys. Rep., **29,** 380 (2003).
5. *Van Milligen B.Ph., Sanchez R., Carreras B.A.,* Phys. Plasmas, **11,** 2272 (2004).
6. *Zaslavsky G.M.,* Phys. Reports, **371,** 461 (2002).
7. *Uchaikin V.V., Zolotarev V.M.,* Chance and Stability: Stable Distributions and their Applications, 1999.
8. *Skvortsova N.N et al.,* Plasma Phys. Reports. **31**. 57 (2005); *Bening V., Korolev V.,* Generalized Poisson Models and their Applications in insurance and finance. VSP, The Netherlands, 2002; *Grandell J.,* Mixed Poisson Processes. Chapman & Hall, London, 1997.
11. *Aevazyan S.A., Bukhshtaber V.M., Enyukov I.S., Meshalkin L.D.,* Applied Statistics: Classification and Reduction of Dimensions, Moscow, 1989.
12. *Abrakov V.V et al.,* Nucl. Fusion., **37,** 233 (1997).
13. *Alejaldre C. et al.,* Plasma Phys. Controlled Fusion., **41,** B109 (1999).
14. *Motojima O. et al.,* Phys. Plasmas., **6,** 1843 (1999).

THE PAM FOR JET. PRELIMINARY DESIGN OF THE MAIN MICROWAVE COMPONENTS

F. Mirizzi, Ph. Bibet[1], A. A. Tuccillo

Associazione ENEA-EURATOM sulla Fusione, C.R. Frascati, Frascati, Rome
[1]Association CEA-EURATOM, C.E. Cadarache, St. Paul lez Durance, France

The Passive Active Multijunction (PAM) is considered as a promising candidate launcher for Lower Hybrid (LH) waves in the harsh plasma environment of ITER. The good coupling properties foreseen by theory for this launcher have been demonstrated by testing a prototype on the Frascati Tokamak Upgrade (FTU). The technological aspects of this launcher will be assessed with a more comprehensive experiment now in preparation on Tore Supra. Both machines, FTU and Tore Supra, work with L-mode plasma edges. JET appears then as the natural candidate to test a PAM launcher in ITER-like conditions on advanced scenarios with H-mode plasma edges. The feasibility of such an experiment has been considered in Europe and has triggered a preliminary design activity of the launcher. The present paper reports the study of the main RF components of this design.

Introduction

LH waves have been used in many experiments in the last two decades demonstrating the best current drive efficiency at low plasma temperature among the existing heating systems. More recently LH waves have been largely used, also in real time, to control plasma current profiles via off axis current drive, thus contributing to the progress of Advanced Tokamak scenarios. LH is therefore the best candidate for controlling q-profiles in partially (hybrid regime at I_P = 12 MA) and fully non-inductive steady-state operations (I_P = 9 MA) in ITER. The PAM is the present design for the LHCD launcher for ITER [1] due to its good coupling characteristics, its mechanical stiffness and the possibility of installing a built-in, effective and reliable water-cooling system. Following the successful test on FTU of the coupling characteristics of a PAM [2, 3], a similar launcher is in construction to test its long pulse capabilities on Tore Supra. A complete characterization of this launcher would require the test of its coupling characteristics and power handling capabilities in the ITER-like conditions, that can be obtained in JET. JET shape, dimensions and plasma scenarios will in fact provide an overall comprehensive test of a PAM launcher to be extrapolated to ITER. Furthermore the replacement of the present, damaged, launcher with a PAM would endow JET of a launcher with increased coupling capabilities. This would allow more reliable LH operations in the severe conditions of advanced scenario plasmas up to a power level of 5 MW.

The PAM for JET

The design of the PAM launcher for JET is based on the preservation of the lay out of its LH system (f = 3.7 GHz) and the reuse of most of the components of the present launcher. On the base of the worldwide extant LHCD experiments (Fig. 1), the power density in the active waveguides has been safely set to 25 MW/m^2.

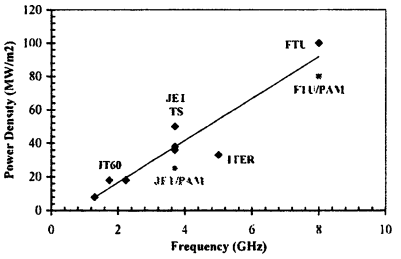

Fig. 1. Power density in LH experiments

The $N_{\parallel}$ peak must be close to 1.84 to do not change the radiated power spectrum with reference to the present JET launcher. These constraints bring to an elementary PAM module including 4 active (72 × 20 mm) and 4 passive (72 × 8 mm) waveguides arranged on two toroidal rows. The uneven width of the waveguides assures, as indicated by the SWAN code [4], the maximization of the radiating surface of the active waveguides and the good coupling properties of the whole launcher.

To minimize the amount of the RF power reflection at the launcher input, taking advantage from (profiting of) the multi-junction (MJ) effect [4], the phase pitch between two toroidal active waveguides is set to 270°. Six PAM modules arranged in a single toroidal row form a PAM block. The whole launcher is composed of six poloidally stacked PAM blocks. A single 650 kW klystron feeds two poloidally adjacent modules (Fig. 2); the complete launcher is then fed by 18 klystrons. The total radiating surface is larger than 0.2 m^2, allowing a maximum injected power of 5 MW. For this configuration the computed maximum power directivity is 75% with a power reflection coefficient less than 3% when the phase shift between adjacent toroidal modules is set to 135°. The overall preliminary design of the PAM for JET is given in a companion paper [5] in this workshop.

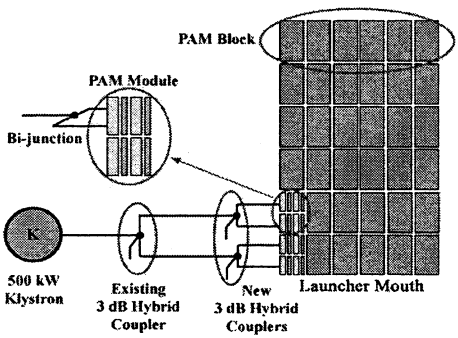

Fig. 2. PAM launcher for JET, schematic lay-out

The main microwave components

In this preliminary design phase only the 3 dB hybrid coupler, the E-plane bi-junction and the fixed phase shifter have been considered. In addition theirs combinations have been studied to investigate the performance of a single elementary PAM module from the microwave point of view. The study has been done using the High Frequency Structure Simulator (HFSS) release 9.02, an interactive software package, based on finite element solvers, developed by ANSOFT, running on a workstation with 2 GHz clock and 2 GB RAM.

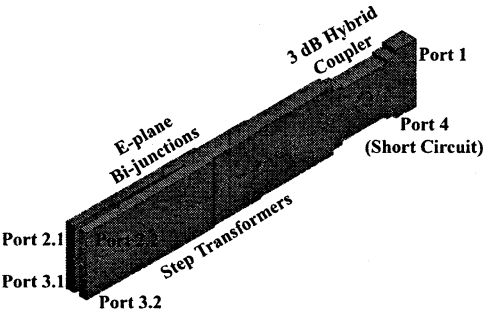

Fig. 3. The simplified PAM module.

The PAM module

The studied PAM module, whose HFSS model is given in Fig. 3, includes the 3 dB hybrid coupler and the E-plane bi-junctions; step transformers connect parts of the module having different cross sections. The fourth port of the hybrid coupler is terminated by a short circuit, as for the couplers used in Tore Supra, to avoid problems generally arising from matched dummy loads (need of a cooling unit, arching, etc.).

It does not includes the passive waveguides, only relevant for the coupling performance of the launcher, and the 270° built in phase shifters, to avoid to overload the computer during the computation. The main performances of the structure in matched conditions, in term of S-parameters, are given in Fig. 4, *a*.

According to this diagram, the frequency bandwidth of the module is essentially determined by the reflection amplitude at the input port (S11), which is lower than –37 dB in the range 3.62–3.73 GHz (Δf = 110 MHz). The couplings to the four output ports are very well balanced (S1,2.1 through S1,3.2 are all in the range $-6 \div -6.05$ dB, corresponding to a RF power difference between the four ports lower than 0.17%) in a wider frequency range (3.4–3.8 GHz, Δf = 400 MHz). Fault conditions have also been considered, in particular a short circuit in one out of the two output waveguides of each bi-junction. The analysis shows (Fig. 6, *b*) that, in the frequency bandwidth determined by S11 in matched conditions, the two bi-junctions are effectively uncoupled because a short circuit in one of them does not significantly influence the coupling to the

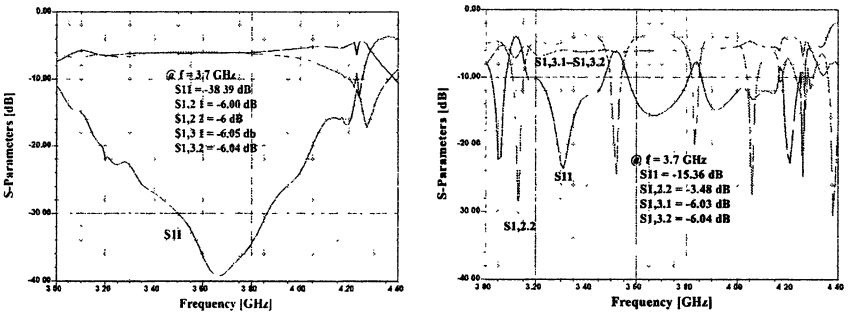

a) Fully matched conditions b) Short circuit at port 2.1

Fig. 4. PAM module: S-parameters amplitude [dB]

two output waveguides of the remaining matched one (S1,3.1 = –6.05 dB, S1,3.2 = –6.04 dB). There is instead a considerable increase of the power reflection at the input port (S11 = –15.4 dB) while the transmitted RF power of the faulty bi-junction is conveyed into the remaining matched port (S1,2.2 = –3.5 dB).

The 270° phase shifter

A fixed phase shift between two rectangular waveguides carrying the TE_{10} mode is simply obtained by modifying the width of one of them to change the phase velocity of the related electromagnetic wave. Two different phase shifters have been studied, the first one using tapers and the second one using step transformers as matching devices between the two sections of the waveguide with unequal width. In Figure 5 is given the HFSS model of the taper based phase shifter in connection to the related bi-junction; the optimised dimensions of the whole structure, section by section, are also shown.

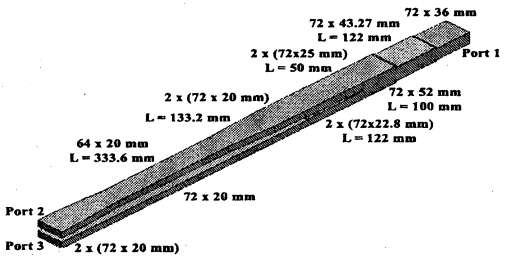

Fig. 5. The 270°, taper-based, fixed phase shifter

Looking at the amplitude of the S-parameters, the performance of the whole structure is imposed by the E-plane bi-junction that determines the sharp and deep peak of S11 = –47 dB at 3.7 GHz (Fig. 6, *a*). The frequency bandwidth is only 40 MHz (but larger than the 10 MHz klystron frequency bandwidth) at –35 dB (–20 MHz at –40 dB). In this frequency range the power difference between the two output waveguides, mainly due to their dimensionally unequal cross sections, is lower than 2.5%. With reference to the phase, if a 270 ± 5° value

is accepted as phase shift between the two output waveguides, the frequency bandwidth of the structure is about 80 MHz around 3.7 GHz (Fig. 6, *b*). The analysis of the step transformer based phase shifter gives the same results, so that the final choice between the two alternative types of device must be based on different approaches.

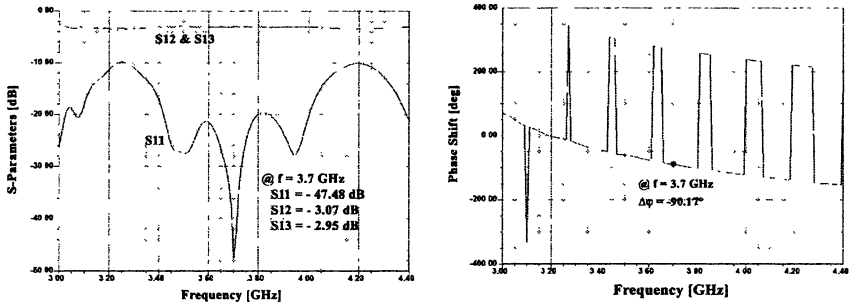

a) S-parameters amplitude [dB] b) Phase shift [deg]

Fig. 6. Performance of the 270°, taper-based, fixed phase shifter

Conclusions. Following a successful test on FTU of a prototype PAM launcher, a definitive test of a similar launcher on JET, where ITER-like conditions can be routinely obtained, is highly advisable to completely ascertain the PAM reliability for the next machines. To substantiate a concrete proposal to the scientific community, a preliminary, but exhaustive, study of a PAM launcher for JET has been done, showing its technical feasibility. The study includes also the design of the relevant main microwave components of the launcher. All of them have been optimised in term of S-parameters (amplitude and phase) and for some of them fault conditions have been analysed. Significant combinations of components have also been considered. The simulation shows good performances for all the components and their assemblies and do not put in evidence critical parts. The design must be completed with the analysis and the choice of the most suitable construction techniques.

References

1. *Bibet Ph., Mirizzi F*, Report on ITER FEAT LHCD launcher, Final report of EFDA contract FU05 - CT 2001-00019 (CEA. EFDA/00-553, ENEA: EFDA/00-554), July 2001.
2. *Mirizzi F. et al.*, Experiment with the PAM launcher for FTU. Proc. 20th SOFE S. Diego, CA, USA, 2003, p. 512-515.
3. *Pericoli Ridolfini V. et al.*, LHCD and coupling experiments with an ITER-like PAM launcher on the FTU tokamak. Nucl. Fusion 45 (2005), p. 1085-1093.
4 *Moreau D., Nguyen T.K.*, Coupling of slow waves near the lower hybrid frequency in large tokamaks, CEA Internal Report EUR-CEA-FC-1246, CEA Cadarache, 1983/84, p. 51-70.
5. *Bibet Ph. et al*, JET passive active multijunctuon lower hybrid launcher, these proceedings, Vol. 2, p. 554-558.

JET PASSIVE ACTIVE MULTIJUNCTION LOWER HYBRID LAUNCHER

Ph. Bibet[1], *J. Belo*[2], *B. Bertrand*[1], *J. P. S. Bizarro*[2], *R. Cesario*[3], *A. Kaye*[4], *F. Leguern*[5], *A. Lioure*[5], *J. Mailloux*[4], *F. Mirizzi*[3], *C. Portafaix*[1], *P. Testoni*[6], *A. A. Tuccillo*[3], *J. C. Vallet*[1], *B. Walton*[4]

[1]Association Euratom-CEA, CEA/DSM/DRFC, CE Cadarache,13108, St Paul lez Durance France,
[2]Centro de Fusão Nuclear, Associação Euratom-IST, Instituto Superior Técnico, 1049-001 Lisboa Portugal,
[3]Associazione ENEA–EURATOM sulla Fusione, C. R Frascati, P.O. Box 65,00044 Frascati, Rome, Italy,
[4]UKAEA, Culham Science Centre, Abingdon, Oxon, OX14 3EA,UK,
[5]EFDA Close Support Unit, Culham Science Centre, Abingdon, Oxon, OX14 3EA,UK,
[6]Consorzio RFX, Corso Stati Uniti 4, 35127, Padova, Italy

Lower Hybrid power in the range of 5 MW will be needed to maintain the required current profile in Advanced Tokamak discharges in JET at ITER relevant β and ρ^*. To couple reliably this power in discharges with Elmy edge, a Passive Active Multijunction (PAM) has been designed A PAM experiment on JET would also allow testing this type of launcher in operative scenarios as close as possible today to ITER coupling conditions. A preliminary coupler design has been completed. Firstly the physic rationale for the choice of the antenna parameters will be presented then an overall description of the antenna with the results on coupling studies will be given.

1. Introduction

LH current drive (LHCD) is widely used and has even boosted the research in Advanced Tokamak (AT) regimes [1]. LHCD is used to control the current profile in the low beta phase of discharges. In this way the q profile is tailored to the one necessary in the high performance phase with the double advantage of avoiding large relaxation and reducing the power threshold to access the regime [2]. The LHCD is then used to maintain the q profile throughout the high beta phase thus allowing long steady operation in condition of enhanced performance [3].

In the Hybrid regime, it allows forming and maintaining low shear q profiles with $q_0 \geq 1$ in discharges with dominant ICRH [4]. The use of LHCD in these discharges prevents sawteeth re-appearance making possible the scenario also in condition of dominant electron heating.

In JET, to realize AT scenarios in ITER relevant conditions, a more resilient LH antenna to electron density change is necessary. The existing JET launcher is presently damaged, limiting the injection power capability to 3–4 MW.

The present proposed LHCD antenna for ITER is based upon the PAM concept [5]. The antenna is made of active rectangular waveguides arrays with quarter wavelength passive waveguides set in between. The passive waveguides

are fed through plasma reflected power by cross coupling with the active ones. The PAM design allows inserting very efficient cooling in the thick wall left available behind the passive waveguides. In long operation and even more on ITER, it is compulsory to have an efficient launcher cooling to remove the heat due to the neutron attenuation, RF losses and plasma radiation. Theoretical coupling computations have shown that the power reflection coefficient of a PAM launcher is very small even near the electron cut-off density. The PAM concept has been tested on FTU Tokamak [6] confirming these results.

On ITER, the LH antenna will be installed flush to the wall, 12 cm away from the separatrix in plasma edge typical of H modes with heavy Elms activity. Before installing a LH system on ITER based on a PAM launcher, it would be advisable to test this antenna concept on a machine able to provide operational conditions as close as possible to those expected on ITER.

2. Present LHCD antenna concept

There are presently 3 different antenna concepts for LHCD launcher:

The conventional one based upon independently fed wave guides array. The advantages are a wide $N_{\parallel}$ flexibility and a high power directivity, i. e. larger than 80%. The drawbacks are that coupling properties highly depend upon the electron density. Generally this type of launcher is equipped with a large number of RF windows.

The multi-junction based on the splitting in the E-plane, generally in a multiple of 2, of the feeding waveguides. Geometrical phase shifters are then inserted in the elementary waveguides to reach the desired phase velocity. The phase shift between 2 neighbours wave guides is 90 degrees. This leads to a power reflection coefficient reduction from ρ at the antenna tip to ρ^2 at the antenna input and good coupling properties on a wide electron density range. The total number of RF windows is generally smaller than in traditional antenna. Conversely the $N_{\parallel}$ flexibility and also the power directivity are smaller.

Finally the PAM is a multi-junction having passive waveguides inserted between active ones, consequently its radiating surface is smaller by a fraction up to a factor two than that of a multi-junction. Its coupling properties are good even near the electron cut-off density n_{ec}. The behaviour of the power reflection coefficient variation versus density for these antennae is compared in Fig. 1. Here the

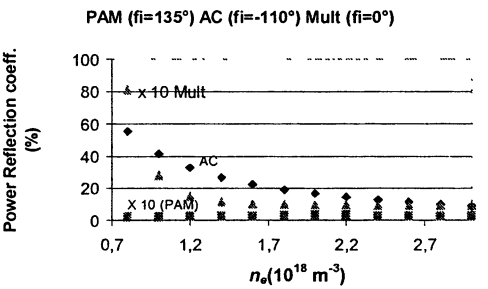

Fig. 1. Power reflection coefficient versus electron density.

computation is shown for the actual FTU antennae at a 8 GHz frequency: conventional (labelled AC), multi junction (labelled mult) and PAM.

3. $N_{\parallel}$ choice

To define the best $N_{\parallel}$ for the JET PAM a reference shot (#53429) has been remodelled with the power spectrum generated by the PAM. The actual equilibrium and plasma data of that shot have been retained in the simulation while ray tracing and Fokker – Planck code have been used [7] with three different $N_{\parallel}$ values: 1.83, 2.3, 2.8. The objective of the simulation being to form and sustain Internal Transport Barriers (ITB) with the new spectrum, the value of 1.83 has been retained. The results of the simulation are shown in Fig. 2.

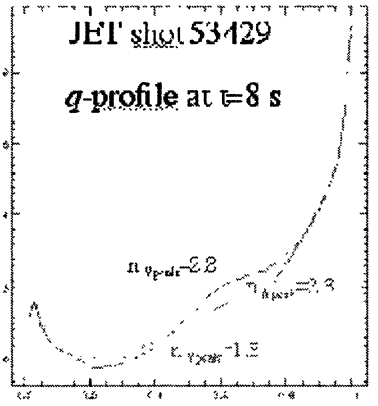

Fig. 2. Q profile versus the normalized radius and different $N_{\parallel}$ values

4. Overview of the PAM for JET

The foreseen antenna for JET is made of 6 PAM blocks vertically stacked (Fig. 3). One block is made of 6 modules. For each module, a RF window is linked to a vertical hybrid junction having a short circuit on its equilibrium port. Each output feeds a 270 degrees E-plane bi-junction through an E-plane quarter wavelength transformer. That leads to a 36 RF windows array fed by eighteen 650 kW klystrons at the input and 12 × 12 active wave guides and 12 × 13 passive wave guides at the antenna front. The main properties of the RF components have been studied in [8].

The antenna is designed to radiate a spectrum having its $N_{\parallel}$ main peak equal to 1.9 ± 0.3 when the input phase is changed from ± 90 degrees. The toroidal pitch is 37 mm.

Fig. 3. Overall view of the PAM for JET

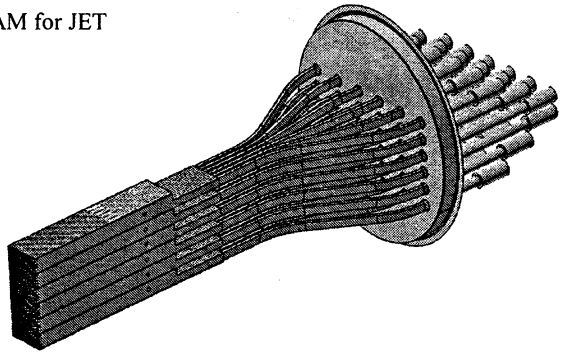

In order to inject a power of 5.2 MW at a 25 MW/m^2 power density, the width of active wave guides has been chosen larger than the passive ones: 20 versus 8 mm.

5. Coupling studies

Coupling studies have been performed using HFSS finite element code from Ansoft and SWAN coupling code [9]. Considering 4 bi-junctions with a 135 degrees input feeding phase, the average power reflection coefficient and the power directivity have been computed depending on the electron density. The active wave guide width has been changed from 14 mm to 20 mm. The coupling is very good even near n_{ec} (Fig. 4), and the best results are obtained for a 20 mm width.

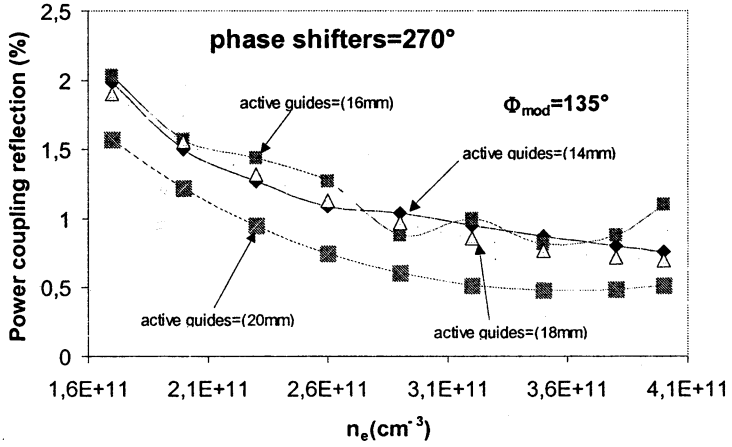

Fig. 4. Power reflection coefficient versus electron density

The obtained power directivity increases when the electron density is near n_{ec} i. e. $1.7 \cdot 10^{11}$ cm^{-3} at 3.7 GHz. In that case too, the best value is obtained in the 20 mm case (Fig. 5).

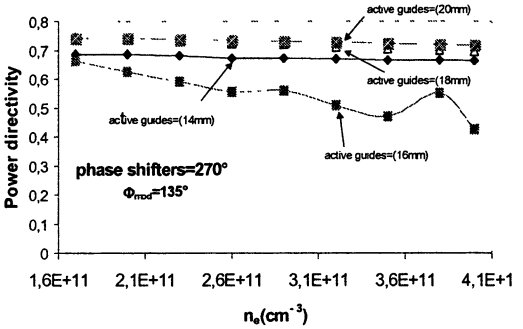

Fig. 5. Power directivity versus electron density

When a vacuum gap is added between the antenna and the electron density cut off layer, it is found that the average power reflection coefficient stays smaller than 10% up to 5 mm vacuum gap. The optimum power directivity of 75% is obtained for the case with 14 mm width. In the case of a 20 mm width, the power directivity decreases with the gap thickness.

6. Conclusion

The blueprint of the PAM for JET is completed. The antenna is designed to inject 5.2 MW at a power density of 25 MW/m^2 radiating a spectrum having a $N_{||}$ main peak value of 1.9.

The test of such a concept presently proposed for the ITER LHCD system on a machine with similar physics scenario with H mode end Elms is of high relevance. JET is well suited to perform such an experiment.

References

1. *Tuccillo A.A. et al.*, Progress in Lower Hybrid, a tool for advanced regimes on ITER, 32nd EPS, Tarragona, 2005.
2. *Challis C.D. et al.*, Plasma Phys. Control. Fusion, **44**, No 9 (2002) 2063.
3 *Crisanti F. et al*, Phys Rev. Lett., **88**, 145004-1 (2002).
4. *Gormezano C. et al*, Plasma Phys. Control Fusion, **46**, No 12B (December 2004) B435-B447.
5. *Bibet Ph. et al.*, Overview of the ITER FEAT LH system, Fusion Engineering and design, 66-68 (2003), p. 525-529.
6 *Pericoli V. et al*, Experimental test of an ITER-like Passive Active Multi-junction Lower Hybrid RF launcher on the FTU tokamak, 31st EPS Conf., London, 2004.
7. *Cesario R et al.*, PRL, April 2004.
8. *Mirizzi F. et al.*, The PAM for JET, Preleminary design of the main microwave components, these proceedings, vol. 2, p. 549-553.
9 *Moreau D., Nguyen T.K.*, Coupling of slow waves near the lower hybrid frequency in large tokamak, Report EUR-CEA-FC-1246.

EC PLASMA RADIATION UNDER MAGNETIC FIELD STRUCTURE VARIATION BY INDUCED OH CURRENT IN THE L-2M STELLARATOR

D. K. Akulina, G. A. Gladkov, S. E. Grebenshchikov, O. I. Fedyanin, S. V. Shchepetov and L-2M Team

A. M. Prokhorov General Physics Institute, RAS, e-mail: akulina@fpl.gpi.ru

Results are presented of experiments in the L-2M stellarator (R = 100 cm, a_p = 11.5 cm, $B(0)$ = 13.4 kGs) in which the magnetic structure was modified by induced OH current in the range I_p = ±(0–14) kA, and the ECE response to a change in the magnetic configuration was studied. The plasma was heated by a gyrotron beam (P = 200 Kw at $2\omega_{He}$, X-mode). The average plasma density was varied over a wide range n_e = = (0.5–2)·10^{13} cm ^{3}. In the basic magnetic field configuration in the absence of a current, the rotational transform varies from $i/2\pi(0)$ = 0.2 on the axis to $i/2\pi(a_p)$ = 0.8 at the plasma boundary. In the presence of a positive current up to $+I_p$ = 13.5 kA, the corresponding values of rotational transform were $i/2\pi(0)$ = 1.2 and $i/2\pi(a_p)$ = 0.9. The experiments with positive currents have shown that the radiation temperature increases with current as compared to the case I_p = 0. When the current reaches I_p = (11–14) kA and $i/2\pi(0)$ achieve ≅ 1, a strong modulation appears in the ECE signals measured over all the plasma radius, the ECE spectrum changes, and the intensity decreases. In the presence of a negative current I_p = –(0–13) kA, the rotational transform is negative $i/2\pi(0)$ = –0.4 and attains $i/2\pi(a_p)$ = 0 7 on the boundary. The ECE temperature and suprathermal radiation decreases steadily at high and low n_e = (2–0.5)·10^{13} cm^{-3} plasma densities.

Introduction

The structure of a magnetic field and its principal and peculiar features occupied attention of researches since the invention of closed toroidal magnetic confinement systems. Considerable recent attention has been focused on the question concerning the existence of internal transport barriers (ITBs) in tokamak and stellarator plasma, and special experiments have been carried out to clarify how the generation of such barriers depends on the particular characteristics of the magnetic field. The stellarator magnetic field configuration is created by external coils, without inducing currents. The characteristics of magnetic configurations of stellarators differ markedly from one device to another.

The L-2M stellarator has a substantial rotational transform, increasing from $i(0)/2\pi$ = 0.2 to $i(a_p)/2\pi$ = 0.8 at I_p= 0 and a large shear. Characteristic of this stellarator is a low field B_{min} in the ECRH region and, consequently, almost total absence of trapped particles in this region [1]. The L-2M stellarator differs radically in this respect from other stellarators. In L-2M, as in the other stellarators, the population of "locally trapped particles" increases toward the plasma edge because the field ripple increases near the helical winding. The ITB generation mechanism appears to be different for tokamaks and

stellarators. In [2], the conditions for the ITB generation in LHD were discussed in detail. The authors pointed out that, the ITB generation in stellarators is primarily due to a high value of the radial electric field E_r related to dT_e/dr. A series of experiments were performed in TJ-II to clear up the role of the magnetic field structure and rational magnetic surfaces in the generation of ITBs [3]. The authors suggest that the presence of the rational surface in the microwave absorption region is the major cause of the formation of e-ITBs in TJ-II.

The general view of the receiving system. receiving antennas

The plasma radiation is received by antennas positioned in different sections of the stellarator, both on the inside and outside of the chamber. This arrangement of antennas allows ECE measurements at the low-field side (LFS) and high-field (HFS). For ECE measurements we have chosen two sections referred below to as "basic" and "vertical". A gyrotron heating beam is launched in the section with basic magnetic configuration The receiver has the channels with the following frequencies: 68 GHz ($\rho = +r/a_p = 0.67$), 70 GHz (0.46), 71 GHz (0.58), 72 GHz (0.29), 74 GHz (0.11), 76.5 GHz (–0.11), 78 GHz (–0.3), 79.5 GHz (–0.46), and 81 GHz (–0.6), which are appropriate for ECRH experiments when the magnetic field at the axis is $B(0) = 1.34$ T.

Magnetic field structure and rotational transform in vacuum and in the presence of OH current

The radial profile of the OH current and the rotational transform in the presence of current was calculated with $Z_{ef}(r) = \text{const}$ [$j(r) \sim T_e^{3/2}$]. In the calculations the trapped particles effect was taken into consideration. Figs. 1a–1c show the $i/2\pi$ as a function of r/a_p, where $a_p = 11.5$ cm is the mean radius of the magnetic flux surface. The $+I_p$ increase the rotational transform (the "positive" current); the dependences $i(r)$ are presented for the currents $I_p = 0$ and $I_p = 0$–13.4 kA. It is seen in Fig. 1a that the $m/n = 2/1$ resonance and the $m/n = 1/1$ resonance can appear at the plasma center and at the edge.

The calculated value of the shear defined as $\theta = r(di/dr)/i$ is shown in Fig. 1b. Similar dependences for the total rotational transform when the OH current $I_p = -(0–13.4)$ kA is directed so as to decrease i ("negative" current) are presented in Fig. 1c. It is seen in Fig. 1c that the $i/2\pi(0)$ varies from –0.8 to $i/2\pi(a_p) \sim 0.7$. The presence of iota = 0 inside the plasma column can lead to a substantial destruction of the magnetic structure.

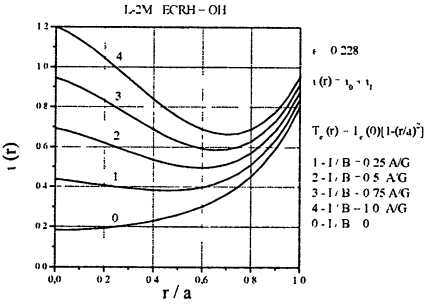

Fig. 1a. Calculated radial profiles of the net rotational transform in the plasma with positive current.

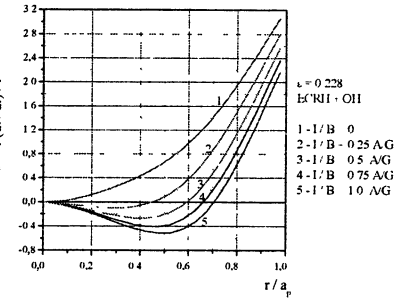

Fig. 1b. Radial profiles of the shear in the plasma with positive current I_p = (3.4–13.4) kA.

Fig. 1c. Calculated radial profiles of the net rotational transform in the plasma with negative current I_p = –(3.4–13.4) kA.

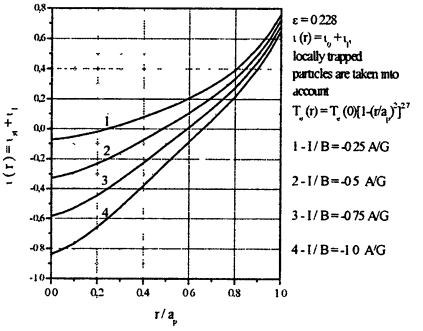

Experimental results. Experiments in the absence of an OH current

In the ECRH experiments in the absence of an OH current, we find that the bootstrap current and the current produced by a microwave beam (namely, CD) add up to no more than $I_{bs,cd} \sim 2$ kA. Based on measurements of the vacuum magnetic structure and estimates of the effect of this current, we can assume that the rational rotational transform $i/2\pi = 0.5$ takes place near the normalized radius $\rho = 0.8$, i. e., not far from the plasma boundary. First we consider the ECE spectrum in the case of $I_p = 0$. Figure 2 shows the results of measurements of the spectrum ($T_{e,rad}$) in the frequency range 68–81 GHz during the steady-state phase of the discharge. The ECE measurements covered a wide plasma region from $\rho = -0.6$ to $\rho = +0.67$. The temperature profile $T_e(r)$ at large plasma radii (ρ = 0.6–1) was independently measured by spectroscopic technique. The gyrotron power in these experiments was $P \sim 200$ kW. It will be recalled that a distortion of the ECE spectrum and the appearance of an additional peak at

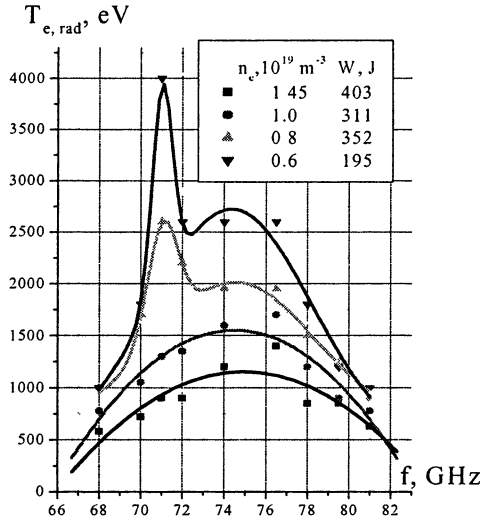

Fig. 2. ECE spectra for various values of the average plasma density $n_e = (0.6–1.45)\cdot10^{13}$ cm^{-3}.

low frequencies (72–68 GHz) is attributed to a deviation of the electron energy distribution function from Maxwellian and to the generation of suprathermal electrons that radiate at lower frequencies because of the relativistic shift of their gyrofrequency (see also our previous works [4]). The effect of the absorption of ECE signals coming the regions of the (LFS) and (HFS) are described in [5]. Recall that the receiver of the radiation at a frequency of f = 71 GHz is placed in the "vertical" section, where the EC wave propagates through the HFS region without absorption. For this reason, the amplitude of the radiation at f = 71 GHz is maximum. In this experiment, a non-thermal spectrum was observed as the average plasma density was decreased to ~ $n_e < 0.810^{13}$ cm^{-3}. This is demonst-rated by Fig. 2 and which show the dependence of $T_{e,rad}$ and the energy W on the average plasma density n_e. It is seen from Fig. 2 that, with a decrease in the density, the temperature increases, whereas the plasma energy W drops, which is indirect evidence that the electron energy distribution differs from Maxwellian.

As the second peak appears in the temperature distribution derived from the ECE intensity, caution is required in the determination of T_e in the case of a non-Maxwellian electron energy distribution which appears at high values of heating power per electron. As a reference diagnostic in this case, we can use measurements of diamagnetic signals and fields produced by Pfirsch – Schluter currents. It is felt that the curves in Fig. 2 for an average density n_e = (1.45–0.9)$\cdot10^{13}$ cm^{-3} can characterize the ECE signals at frequencies 68–81 GHz as a T_e, because the measured energy W is consistent with the dependence $W \sim Kn_eT_e(0)$, where K is a form-factor, and any additional peaks do not appear in the temperature curves.

At an average density of $n_e < 0.8\cdot10^{13}$ cm^{-3}, the second peak appears in the ECE; these measurements conflict with the dependence $W \sim Kn_eT_e(0)$ (the diamagnetic signal drops while the apparent temperature increases), and the effective temperature deduced from the radiation intensity can only be characterized as T_{rad}. We decreased the density down to $n_e = 0.32\cdot10^{13}$ cm^{-3} and thus increased the heating energy per electron; however, we did not observe either an increase in the diamagnetic signal or the temperature profile modification

characteristic of the ITB. For this reason, we can conclude that, with the available structure of the magnetic field, the internal transport barrier in L-2M is either absent or indistinguishable from the effect of suprathermal radiation.

Experiments with an additional positive OH current I_p = +(0–14) kA at an average plasma density of $n_e = (0.8–1)\cdot10^{13}$ cm^{-3}

The OH current was gradually increased so as to achieve various rational values of the rotational transform up to $i/2\pi(0) = 1$ inside the plasma. The results of experiments with currents $I = 0–14.2$ kA are summarized in Fig. 3. The density value was chosen such that suprathermal radiation was absent at $I_p = 0$. It is seen from Fig. 3 that the ECE spectra measured in the presence and absence of the current differ markedly. An additional peak appears at low frequencies $f = 74–68$ GHz (suprathermal radiation) in the presence of the current, whereas this peak is absent when $I_p = 0$. The curves are similar in shape at currents below 9.3 kA. The intense oscillations throughout the plasma column observed when the current achieve $I_p \geq 11$ *kA*, and this involves a decrease in the $T_{e,rad}$. Calculations show that these currents result in a rotational transform $i(0)/2\pi \sim 1$ at the magnetic axis and a small shear, which is favorable to development of intense oscillations. The second peak associated with suprathermal disappears at high currents. The distribution function with electron energies above 5 keV in the tail was measured with a soft X-ray Si(Li) spectrometer.

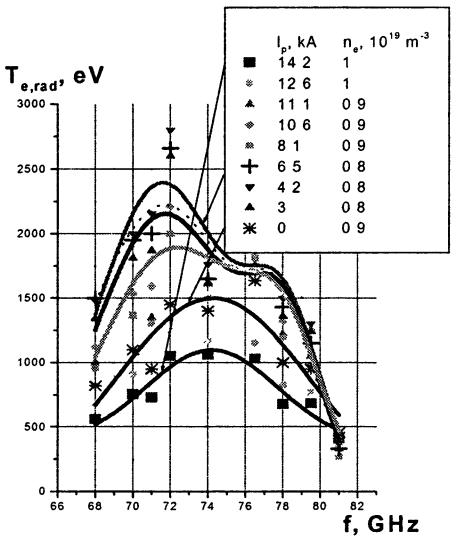

Fig. 3. ECE spectra ($T_{e,rad}$) for various values of positive current I_p = 0–14.2 kA at an average plasma density of $n_e = (0.8–1)\cdot10^{13}$ cm^{-3}.

Experiments with an additional negative OH current I_p = –(0–13) kA at an average plasma density of $n_e = 0.5\cdot10^{13}$ cm^{-3}

Figure 4 shows the ECE spectrum at currents of $I_p = -(0–13)$ kA and a low average plasma density $n_e = 0.5\cdot10^{13}$ cm^{-3}. In contrast to the experiments with positive current, the suprathermal radiation decreases substantially as the

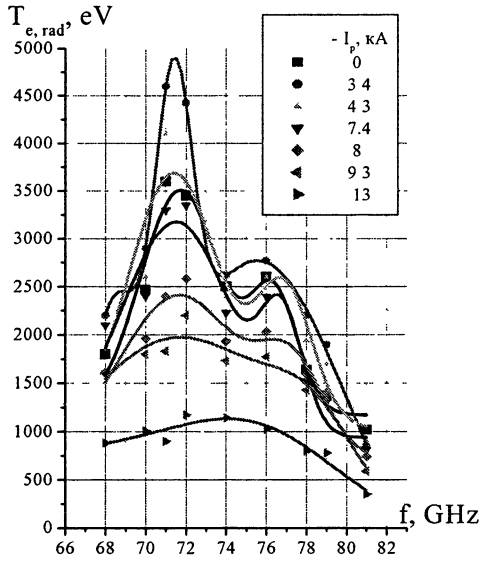

Fig. 4. ECE spectra ($T_{e\,rad}$) for various values of negative current I_p = –(3.4–13) kA at an average plasma density of $n_e = 0.5 \cdot 10^{13}$ cm^{-3}.

amplitude of the plasma current increases. As seen from Fig. 4, the suprathermal radiation almost disappears at currents of I_p = –(9.3–13) kA. In the experiments with negative currents, we did not observe large-amplitude oscillations in the ECE signals as occurred in the experiments with positive currents. The ECE spectra of the plasma with densities of n_e = (1.7–2.)·10^{13} cm^{-3} and negative plasma currents of I_p = = –(0–13.5) kA was per-formed also. The suprathermal radiation was absent in this case. The electron temperature decreases steadily with increasing current.

Conclusions

An additional OH current $I = \pm$ (0–14) кА was induced in the ECR heated plasma in which case the rotational transform on the axis could be varied from $i(0)/2\pi$ = –0.8 to $i(0)/2\pi \leq 1.2$. At $+I_p$ up to I_p = +9 kA the temperature and suprathermals increases in comparison with I_p = 0 discharges. At I_p = +(11–13) kA, MHD activity is observed in the plasma over the entire cross section; this affect accounts for a change the ECE spectrum and a decrease in the plasma temperature. The reverse situation takes place at $-I_p$: the $T_{e,rad}$ steadily decreases with increasing current At plasma densities below $n_e \leq 0.8 \cdot 10^{13}$ cm^{-3} and power $P \sim 200$ kW in the currentless plasma, the energy deduced from diamagnetic signals disagrees with the energy $W \sim Kn_eT_e(0)$ calculated with T_e determined from ECE measurements. Hence, the temperature in this case can only be characterized as T_{rad}, because the electron energy distribution is non-Maxwellian.

References

1 *Akulina D , Batanov G., Berezhetskii M. et al* , Plasma Phys Reports, 29, 1028 (2003).
2. *Ida K., Ohyabu N., Morisaki T. et al* , Phys. Rev Lett , 88, 015002-1, (2002).
3. *Estrada T , De la Luna E., Ascasibar E. et al.,* Plasma Phys. Controlled Fusion 44, 1615-1624 (2002).
4. *Akulina D., Batanov G , Berezhetskii M et al.,* Proc. 12th Workshop on ECE and ECRH (EC-12), Aix-en –Provence, 2002, 413-418.
5. *Lontano M., Pozzoli R., Suvorov E.,* Il Nuovo Cimento 6313, 529 (1981).

THE IMPROVED CONFINEMENT IN T-10 AND TEXTOR BY THE CHANGE IN MAGNETIC SHEAR AROUND RATIONAL Q-SURFACES WITH ECRH

G. M. D. Hogeweij[1], F. C. Schüller[1], V. F. Andreev[2], I. S. Bel'bas[2], A. J. H. Donné[1], A. Merkulov[1], K. A. Razumova[2], S. Varshney[1], E. Westerhof[1], the T-10 team[2] and the TEXTOR team[3]

[1] FOM-Institute for Plasma Physics Rijnhuizen, Association EURATOM-FOM, partner in the Trilateral Euregio Cluster, The Netherlands; www.rijnh.nl
[2] Nuclear FusionInstitute, RRC, "Kurchatov Institute", 123182 Moscow, Russia
[3] Institut für Plasmaphysik, Forschungszentrum Jülich GmbH, Association EURATOM-FZ-Jülich, partner in the Trilateral Euregio Cluster, Germany

It has been observed in both the T-10 and the TEXTOR tokamaks that it is possible to create transiently an improved core confinement after switch-off of a carefully deposited *off-axis* ECRH-pulse [1]. The phenomenon is sensitive to power-level and duration of the ECRH-pulse. Explanation was sought in a transiently established electron-ITB at rational q-surfaces in an area of low shear that is formed after a sawtooth-free period during the ECRH-pulse.

Although the arguments in favour of this explanation were strong some questions remained:

– Is the electron-ITB occurring at $q = 1$ or at $q = 3/2$?

– If it is $q = 3/2$, one expects that low shear around a rational surface will lead to a growth of islands with $m/n = q_{rat}$ and therefore with spoiled confinement.

– If it is $q = 1$, then a normal sawtooth crash ends the period of improved core confinement and theories explaining sawtooth crashes should be applicable [2].

Recently TEXTOR discharges have led to longer periods of improved confinement up to 45 ms. There are indications that the ITB is at $q = 1$, because:

– r_{inv} of the first sawtooth after ECRH is as large as the ITB-radius;

– the crash agrees with [2] and sawtooth (de)stabilization at other tokamaks;

– there are no signs of a 3/2 precursor to the crash.

This means that with heating alone the improvement will be transient. Only current drive by ECCD or LHCD will keep the low shear stationary, which is needed to maintain the ITB and to avoid the 1/1 precursor to the sawtooth crash.

References

1. *Razumova K.A. et al*, Nucl. Fus., 44 (2004), 1067-1074.
2 *Porcelli F. et al*, Plasma Phys. Contr. Fusion, 38 (1996), 2163.

COMPARISON OF HEAT PULSE PROPAGATION ACROSS INTERNAL TRANSPORT BARRIERS IN JT-60U, LHD AND T-10 PLASMAS IN A PRESENCE OF ECRH

S. V. Neudatchin[1], *S. Inagaki*[2], *T. Takizuka*[3], *K. Itoh*[2], *N. Hayashi*[3], *V. I. Ilin*[1], *I. A. Isayama*[3], *A. Ya. Kislov*[1], *S. V. Krylov*[1], *Yu. D. Pavlov*[1], *Y. Sakamoto*[3], *N. Tamura*[2]

[1]Nuclear Fusion Institute, RRC "Kurchatov Institute", Moscow Russia
[2]National Institute for Fusion Science, Oroshi-cho 322-6, Toki 509-5292, Japan
[3]Japan Atomic Energy Agency, Naka Fusion Research Est., Naka, 311-093, Japan

Understanding of properties of internal transport barrier (ITB) is of importance for the fusion research of toroidal magnetic confinement. Abrupt and non-local confinement bifurcations inside and around ITBs (ITB-events) have been found in JT-60U. Non-local features of transport have been reported recently in LHD. The present paper is aimed at showing the dual nature of transport (local and non-local simultaneously). We study the transport properties of strong ITBs by the analyzing the inward and outward heat pulse propagation (HPP) in JT-60U The heat pulses (induced by ITB-events or sawtooth-like crash) propagate slowly inside strong ITB with dynamic electron heat diffusivity $\chi_e^{HP} \sim 0.1$ m^2/s. By contrast, the heat pulse propagates fast ($\chi_e^{HP} \sim 1$ m^2/s) in the zone between two ITBs. In T-10, ITB has been recently recognized by means of analyses of HPP induced by central ECRH-onset and cold pulse propagation (CPP) by off-axis ECRH cut-off in a sawteeth-free plasma created by off-axis ECRH. The influence of current rump-up on CPP characteristics is demonstrated also. New details of slow inward CPP induced by spasmodic shrinking of the wide zone with low transport formed by large C_8H_8 pellets in LHD are also described. In all three devices, inward/outward HPP and CPP propagate slowly and diffusively ($\chi_e^{HP} \sim 0.1$-0.3 m^2/s). The so-called "heat pinch" is either absent or small enough (the upper limit of inward electron heat pinch velocity is evaluated to be below 1 m/s).

1. Introduction

The relationship between local and non-local properties of the transport in toroidal magnetic devices is not yet obvious. Initially, non-local (global) transport bifurcations have been observed at fast L–H–L transitions in some normal shear (NrS) regimes of JET [1] and JT-60U [2]. These experiments deny the paradigm of transport locality, i. e. that heat flux is always the function of plasmas local measured parameters such as electron temperature T_e, electron density n_e, safety factor q, etc. Another type of abrupt and non-local confinement bifurcations inside and around internal transport barriers (ITBs) have been found in JT-60U and called ITB-events [3]. Furthermore, the ITB and the edge transport barrier (ETB) evolve together at global L–H–L transitions in JT-60U reverse shear (RS) plasmas, with an abrupt jump of electron heat diffusivity $\delta\chi_e$ covering wide region ($0.3 < r/a < 1$) in a ms timescale [4]. Several types of transport at ITB-events correlate with the presence of multiple levels of reduced transport in strong ITBs [5]. Recently, the short-timescale (ms) correlation between T_e

rise in the centre ($0 < r/a < 0.4$) and the evaporation of small C_8H_8 pellet at the edge has been found in some regimes in LHD [6, 7]. These experiments highlight global features of transport in LHD as well. Abrupt reduction of core χ_e has been observed in some regimes in T-10 [8].

The present paper is aimed at showing the dual nature of transport (local and non-local simultaneously). After a non-local bifurcation of transport, the heat pulse propagation (HPP) and cold pulse propagation (CPP) across ITBs in different machines with different physics of ITB formation and various sources of HPP/CPP (including CPP/HPP created by non-local bifurcations) are well described by the simple diffusive equation. Section 2 contains examples of HPP/CPP across ITBs in JT-60U, LHD and T-10. Analysis of HPP in the region between two ITBs in JT-60U is fulfilled also. Section 3 highlights similarity of HPP/CPP in the three machines. Discussion and conclusions are the content of Section 4.

2. Analysis of HPP (CPP) in JT-60U, LHD and T-10

In the beginning of this section, we analyze examples of HPP at JT-60U. Sawtooth-like crash creates outward HPP in shot RS 36614 (see timetraces in [9] also). Profiles of T_e before and after the crash (under $P_{NB} = 5.4$ MW, $P_{EC} = 1.2$ MW, $W = 3.2$ MJ, measured with 12-channels radiometer) are shown in Fig. 1, *a* by solid and dashed curves, respectively. Figure 2, *b* shows shifted timetraces of T_e (ch. 9–12) with 2.7 cm distance between channels. T_e rises after the crash at ch. 9 and 10. Bold solid lines show calculations of HPP from ch. 9 to ch. 11–12 with $\chi_e^{HP} = 0.1$ m^2/s (faster compare with experiment, see detail of the method e. g. in [10]) and dashed solid curve represents calculations with $\chi_e^{HP} = 0.04$ m^2/s. Heat wave does not propagate at ch. 11 and one cannot obtain the χ_e^{HP} value but can only estimate its upper limit $\chi_e^{HP} < 0.05$ m^2/s. Figure 2, *a* shows the evolution of T_e measured with 12-channel ECE heterodyne radiometer in L-mode 1.5 MA/3.7 T shot 32423 (for shot details see [10, 11]). Figure 2, *a* illustrates ITB formation via ITB-events and further ITB-splitting into two ITBs (see detail description in Figures 1–3 in [11]). The analysis of outward heat pulse propagation induced by localized T_e rise at ITB-event C (see detail in [10], arrow in Fig. 2, *a* indicates the region of HPP) shows $\chi_e^{HP} \approx \chi_i^{HP} \approx \chi_{i\,neo} =$ $= 0.1$ m^2/s (dynamical values of heat diffusivities and neoclassical ion heat diffusivity). Before the time F (shown in Fig. 2, *a* by a vertical line), the first weak ITB takes up position between ch. 2 and ch. 6, and the second strong ITB is located between ch. 10 and ch. 12. An abrupt rise of T_{e9-11} (T_e at ch. 9–11) at the time F corresponds to ITB-event F and creates inward and outward HPPs shown in Fig. 2, *a* by arrows. The inward HPP between ITBs is illustrated in detail in Fig. 2, *b*. Heat wave arrives at ch. 8 with a few ms delay after the time F; the delay increases at ch. 7 and ch. 6.

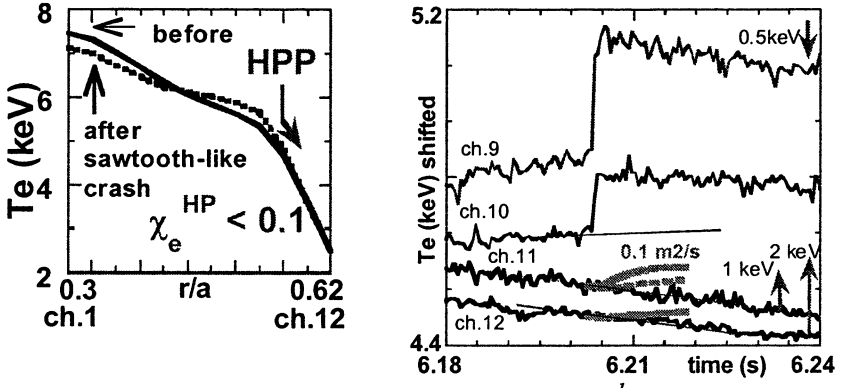

a *b*

Fig. 1. T_e profiles before and after crash in RS JT-60U shot 36614 with NBI and ECRH (*a*). Extremely slow HPP from ch. 10 to ch. 11, 12 (bold solid and dashed lines – calculations with $\chi_e^{HP} = 0.1$ m^2/s and 0.04 m^2/s) (*b*).

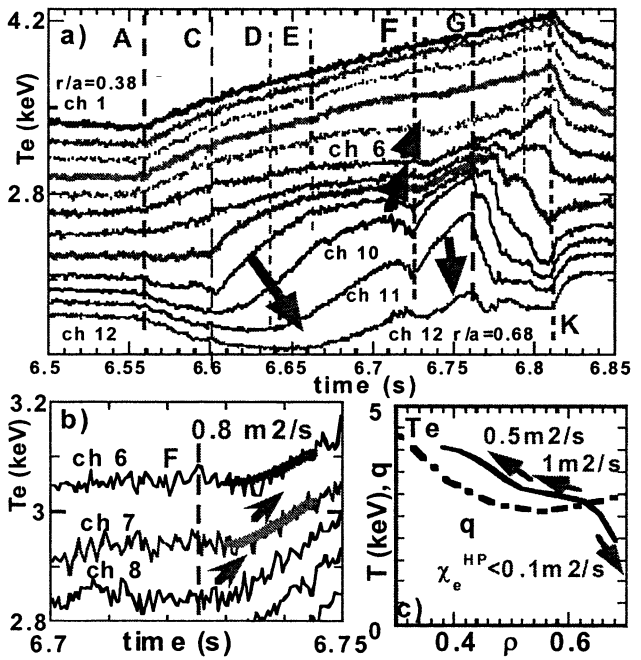

Fig. 2. T_e evolution in JT-60U RS shot 32423 during strong ITB formation via ITB-events *A* and *C* (arrow – slow HPP after time *C*) (*a*); further ITB splitting into two ITBs and inward/outward HPPs (arrows) are observed after ITB-event *F*. Inward HPP between two ITBs induced by event *F* (*b*); bold lines are calculation results with $\chi_e^{HP} = 0.8$ m^2/s. T_e and q profiles near $t = 6.72$ s (*c*); arrows indicate schematically zones of HPP with values of χ_e^{HP}.

Regarding perturbations of heat sources and n_e in the region of HPP study, HPP is analyzed with the simplified transport equation for δT_e, as usually (see [9] and references therein):

$$1.5 n_e \partial \delta T_e / \partial t = \mathrm{div}(n_e \chi_e^{\mathrm{HP}} \nabla \delta T_e),\ r_1 \le r \le r_8,$$

with zero initial condition $\delta T_e(r, 0) = 0$, right boundary condition $\delta T_e(r_e, t)$ taken at ch. 8 from experiment, and $\nabla \delta T_e(r_1 = 0, t) = 0$. Bold lines drawn in Fig. 2, *b* represent calculations with $\chi_e^{\mathrm{HP}} = 0.8$ m^2/s. Series of calculations with some variation in the background T_e subtraction give $\chi_e^{\mathrm{HP}} = 0.7$–$1.3$ m^2/s. Fast HPP occurs in low gradient region with R/L_{T_e} ($\equiv R\nabla T_e/T_e$) = 5 (see Fig. 2, *c*) and reflects L-mode transport in the region between two ITBs. Later, HPP decelerates inside weak ITB (between ch. 6 and ch. 4), and calculations give $\chi_e^{\mathrm{HP}} = 0.4$ m^2/s (0.3÷0.6 m^2/s) in the region with higher $R/L_{T_e} = 9$–10. As for outward HPP from ch. 11 to ch.12, series of calculations with various subtraction of background T_e results in $\chi_e^{\mathrm{HP}} < 0.1$ m^2/s at very high values R/L_{T_e} (up to 40–45). Similar low values of $\chi_e^{\mathrm{HP}} = 0.1$ m^2/s (inside strong ITB in RS plasmas) have been also reported at inward HPP induced by ITB-event [9].

In LHD plasmas, ITBs have been observed for the central ECRH in low-density shots; they are associated with the transition from ion root (low radial electric field E_r) to electron root (high E_r) [12, 13]. In the present paper, we focus on CPP created by a new phenomenon (see [14] for detail), which takes place after an injection of large TESPEL pellets. Evaporation of large TESPEL pellet creates a hollow profile of electron density n_e. After an initial decay, the electron temperature T_e starts to rise rapidly. Later, when the T_e value exceeds the level observed before injection, an abrupt decay of T_e ("event") appears at periphery. The events penetrate gradually deeper and deeper toward the plasma center. We interpret this behaviour as a step-wise shrinking of the zone with strongly reduced transport, which is initially formed by the evaporation of the pellet. Each event creates an inward CPP. Numerical analysis gives very low values of $\chi_e^{\mathrm{CP}} \approx 0.3$–$0.4$ m^2/s (0.15 m^2/s in some of the zones) at $0 < r/a < 0.8$ (by order of magnitude below the power balance values in usual shots). Comparison of CPP analysis at both sides of the plasma column confirms the validity of our results. Figure 3, *a* shows an example of slow inward CPP created by event. The evolution of δT_e ($r/a = 0.555$, t) calculated with $\chi_e^{\mathrm{CP}} = 0.14$ m^2/s is shown by a bold solid curve in Fig. 3, *a*. The calculated CPP with $\chi_e^{\mathrm{CP}} = 0.5$ m^2/s (bold dotted line) is obviously faster and strongly deviates from the experiment. In usual LHD shots, the values of χ_e^{CP} and χ_e^{HP} are much higher (order of 2 m^2/s, see [7, 15]). Nevertheless, Fig. 3, *b* clearly shows the decay of amplitude and rising delay of HPP (diffusive features) arriving during outward propagation of heat wave induced by ECRH-on in shot 45475 (2.3 MW NBI injected power). Calculations with $\chi_e^{\mathrm{HP}} = 1.7$ m^2/s are shown in Fig. 3, *b* with bold lines ($r/a = 0.191$ is taken as boundary condition). These calculations

nearly fit experimental data. Calculations with $\chi_e^{HP} = 4$ m^2/s are shown in Fig. 3, *b* with dashed lines.

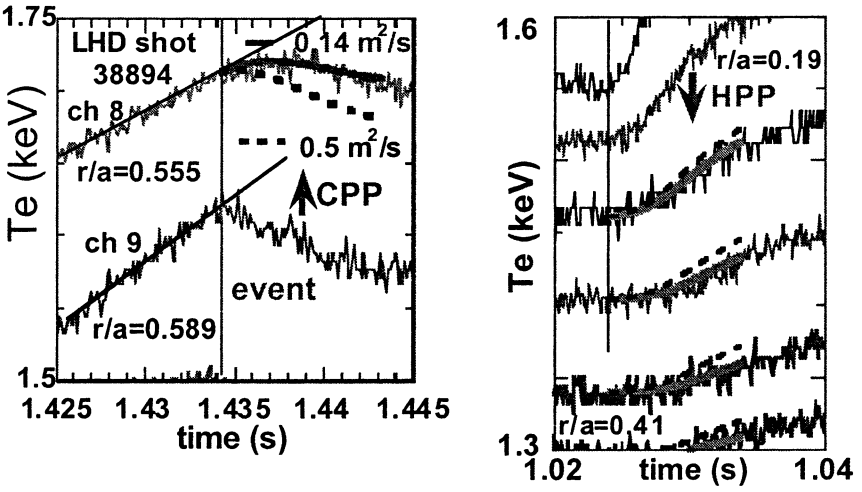

a *b*

Fig. 3. Slow inward CPP in LHD (*a*): bold line is calculation result with $\chi_e^{HP} = 0.14$ m^2/s and dotted bold line is calculation with $\chi_e^{HP} = 0.5$ m^2/s (faster as compared with experiment); CPP is created by spasmodic shrinking (events) of the zone with reduced transport formed earlier by evaporation of large C_8H_8 pellet. Diffusive HPP created by ECRH-on in LHD L-mode shot 45475 (solid bold lines – calculations with $\chi_e^{HP} =$ $= 1.7$ m^2/s and dashed lines – calculations with $\chi_e^{HP} = 4.0$ m^2/s) (*b*).

In T-10, ITB has been recently found by means of HPP and CPP analysis in a sawtooth-free plasma created by off-axis ECRH [7, 16]. Figure 4, *a* shows CPP created by off-axis ECRH cut-off (0.22 MW) in 0.22 MA/2.33 T shot 37421. Calculations with $\chi_e^{CP} = 0.1$ m^2/s inside $r/a < 0.3$ are shown by bold solid lines in Fig. 4, *a* (dotted bold lines are calculated with $\chi_e^{CP} = 0.2$ m^2/s) and $\chi_e^{CP} \approx 0.15$ m^2/s at $0.3 < r/a < 0.4$.

Figure 4, *b* represents HPP in shot 35764 at ~0.5 MW central ECRH (130 GHz) superimposed on the background created with ~0.4 MW of off-axis ECRH. Some asymmetry of T_e increase at LFS and HFS is clearly observed. Bold lines illustrate calculations performed for LFS and HFS data. Nevertheless, the asymmetry of χ_e^{HP} values is not significant (0.24 m^2/s at $-0.26 < r/a < -0.18$, 0.3 m^2/s at $0.2 < r/a < 0.4$).

Recently, we have studied the influence of the current ramp-up (started 30 ms before HPP/CPP) on the heat propagation characteristics in T-10. The idea was to combine the decrease of q (inside $r/a < 0.4$) during HPP/CPP with gradual penetration of q reduction from periphery. Figure 5, *a, b* presents the scenario of 3 shots with pure off-axis ECRH. Partial ECRH cut-off (absorbed

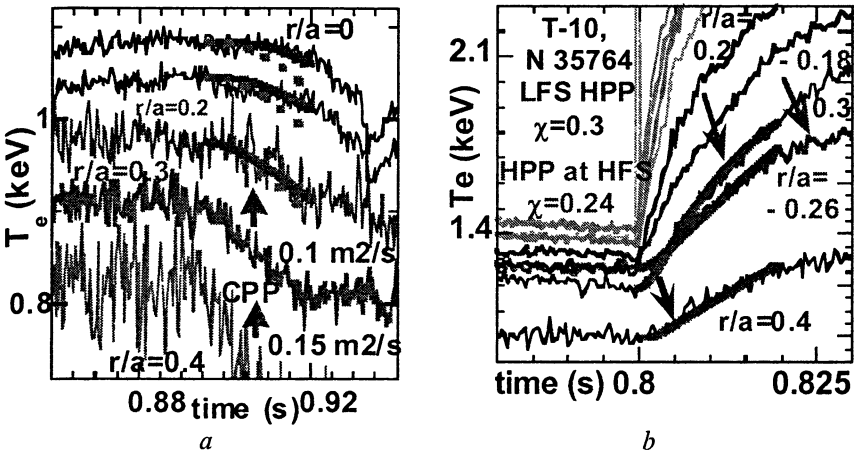

a *b*

Fig. 4. CPP in T-10 induced by off-axis ECRH cut-off (*a*), bold and dotted lines represent calculations with χ_e^{CP} = 0.1 m^2/s and 0.2 m^2/s. HPP in T-10 created by central ECRH-on superimposed on background formed by off-axis ECRH (*b*), bold lines – calculations with χ_e^{HP} = 0.3 m^2/s at LFS and 0.24 m^2/s at HFS.

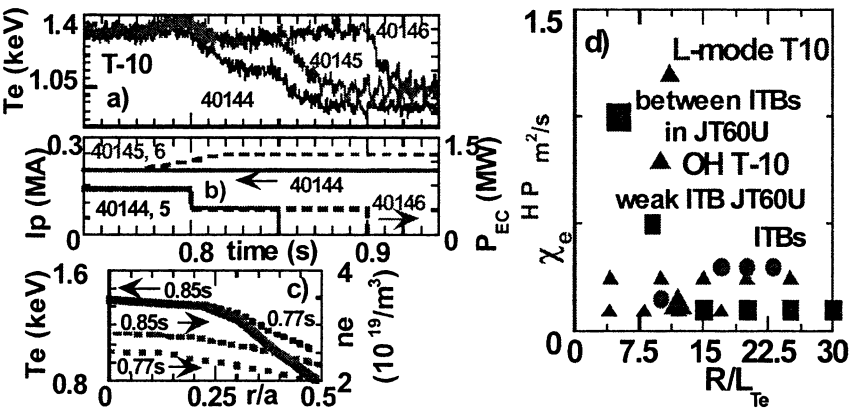

Fig. 5. Evolutions of $T_e(r/a = -0.25)$, I_p and ECRH power for three shots in T-10 (*a–b*); $T_e(r/a < 0.3)$ does not decay at the swith-off of ECRH for current ramp-up shots. Profiles of T_e and n_e for different times in shot 40145 (*c*); T_e is stable in center. Dependence of $\chi_e^{HP,CP}$ on R/L_{T_e} in JT-60U (squares), inside of ITB in LHD (circles: typical L-mode level is 1.5–3 m^2/s), and in T-10 (triangles: bold triangle is result of [17]) (*d*).

power near 0.3 MW) occurs in all shots at t = 0.8 s, and 0.4 MW power persists longer. Without I_p ramp-up (shot 40144) T_e decays to lower level, while with I_p ramp-up (shots 40145, 40146 with I_p rise from 0.2 MA to 0.25 MA during 50 ms) T_e in central part holds at the same level for a long time (see Fig. 5, *a*

and T_e profiles in Fig. 5, *c*). R/L_{T_e} value rises by 1.7 times at r/a = 0.3–0.45. We just have repeated these experiments under better control of mirror position (in principle, injection was perpendicular in the above-described) and found the same phenomena at the angle equal to six degrees. The phenomenon is absent at perpendicular injection.

3. Comparison of HPP/CPP characteristics

Figure 5, *d* demonstrates the dependence of $\chi_e^{HP,CP}$ on R/L_{T_e}. A square at low R/L_{T_e} = 5 shows large χ_e^{HP} between two ITBs in JT-60U (see Fig. 1, *b*), the next square at R/L_{T_e} = 9–10 depicts HPP inside weak ITB (see Fig. 1, *c*), and a row of squares schematically shows various slow HPPs across strong ITBs. Two triangles around R/L_{T_e} = 9–11 represent T-10 Ohmic and L-mode (small power) values, while rows of triangles show values for CPP (χ_e^{CP} = 0.1 m^2/s, see Fig. 4, *a* and [7, 16]) and HPP during the evolution of R/L_{T_e} (see Fig. 4, *b* and [16]). A bold triangle displays T-10 result obtained 15 years ago [17]. Critical value of R/L_{T_e} lies around 6–8 for JT-60U and 8–10 for T-10. Strong reduction of $\chi_e^{HP,CP}$ values in comparison with L-mode ones is obvious in both cases. A circle at moderate value of R/L_{T_e} = 10 represents CPP at r/a = 0.55 in LHD (see Fig. 3, *a*) and a row of circles shows similar CPP at r/a = 0.7 (exact values of R/L_{T_e} depend on the way of space averaging). These values of χ_e^{CP} around 0.3 m^2/s, which are routinely obtained at inward CPP created by the events inside $r/a < 0.8$, are indeed very low compared with the typical values of χ_e^{HP} = = 1.5–2 m^2/s at r/a = 0.2–0.5 (see Fig. 3, *b* and [5, 7]). Earlier in LHD, similar value of $\chi_e^{CP} \approx 0.3$ m^2/s was observed once only in the case of CPP inside magnetic island formed by an external perturbation magnetic field [18].

In all HPP/CPP experiments described above, the value of "heat wave sharpness" $S_h = |(\delta\nabla T_e/\delta T_e)/(\nabla T_e/T_e)|$ is very high (above 5), which characterizes the sensitivity of the diffusive term ($\chi_e^{HP,CP}\delta\nabla T_e$) to terms proportional to δT_e such as convective (perturbation of convective heat flux) and convective-like terms (dependence of χ_e on T_e, etc.) (see [1, 10, 15]). For HPP with $S_h >> 1$, $\delta(\nabla T_e/T_e)$ is almost proportional to $\delta\nabla T_e$. In the presence of so-called "heat pinch" (i. e. strong inward heat flux $n_e V_{T_e} T_e$), HPP with $S_h >> 1$ allows to estimate the uppermost limit of V_{T_e} (if V_{T_e} is constant with time) as $V_{T_e\ \mathrm{uppermost}} \approx \chi_e^{HP,CP}(\nabla T_e/T_e)$ (see detail in [10]). A more realistic estimation is $V_{T_e\ \mathrm{upper}} \approx 0.7\chi_e^{HP,CP}(\nabla T_e/T_e)$ (if the convective flux compensates 70% of the diffusive flux and $\chi_e^{HP,CP} \approx 3\chi_e^{PB}$). The upper limit of V_{T_e} lies below 0.5 m/s in

most of the above-described experiments (1 m/s in some cases including HPP between ITBs in JT-60U).

4. Discussion and conclusions

The non-local nature of transport in many regimes of JET, JT-60U and in some regimes of LHD and T-10 is obvious [1–7]. In JT-60U, ITB-events occur with triggers (or precursors) and without visible triggers [3–4, 9–11]. Reference [19] describes the new type of edge-core instant interplay in JT-60U high-β_p plasmas. Abrupt in time (ms timescale) and wide in space (~0.4 of minor radius) reduction of electron heat flux in the core (ITB-event) is correlated in ms timescale with the start of ELM's series that create enhanced level of H_α. This result enables to give an opportunity to form ITB instantly and non-locally by creation of "proper" MHD-activity.

In order to understand non-local property of the transport coefficient, theoretical models have been discussed, either based on the statistical excitation of long-range perturbations (e. g. [20]) or on the spatial spreading of turbulence (e. g. [21–22]). At the same time, it is not always easy to find relationship between turbulence measurements and the transport level. A recent JT-60U paper highlighted that the ion heat transport and the particle transport correlate with the measured density fluctuations, while the electron heat transport seems to be decoupled with the measured density fluctuations [23]. No evidence of the turbulence reduction has been found in LHD at the time of abrupt decrease of the electron heat transport in the core simultaneously with the pellet evaporation at the edge [24]. In T-10, a strong local decrease in the turbulence level and poloidal coherency is clearly seen for radii $0.25 < r/a < 0.35$ after ECRH switch-off [25]. Moreover, measurements show that the usual mechanism of turbulence stabilization by $E_r \times B$ shear flows is not able to describe low transport. Shot with slow CPP shown in Fig. 3, *a* belongs to this series of discharges.

In some LHD experiments heat waves propagate in non-diffusive manner (i. e. one-dimensional heat transport equation is not able to describe experiment) [7, 26]. The two-dimensional heat transport equation (due to the presence of a magnetic island structure e. g. $m/n = 2/1$) can explain non-diffusive features of HPP in some LHD regimes [26].

After a non-local bifurcation, the transport is local and diffusive. Simple diffusive equation gives good description of all cases of inward and outward HPP/CPP in JT-60U, LHD and T-10 reported in the present paper and in earlier Refs. [1, 7, 9, 10, 16, 17]. The conditions and physics of ITB formation are different for the above-mentioned cases. Nevertheless, HPP and CPP manifest similar low values of dynamic electron heat diffusivity $\chi_e^{HP} \sim 0.1–0.3$ m^2/s. To the contrary, the heat pulse propagates faster ($\chi_e^{HP} \sim 1$ m^2/s) in the zone between two ITBs and low T_e gradients in JT-60U (L-mode trend). The so-called "heat pinch" is either absent or small enough (the upper limit of inward electron heat pinch velocity is evaluated to be below 1 m/s).

Acknowledgements. The authors are indebted to all members of JT-60, LHD and T-10 teams for fruitful collaborations. Part of this work was performed during SVN's stay at NIFS under the visiting professor programme and at JAERI under JAERI fellowship programme in 2001. In Japan this work was partially supported by the Grant-in-Aid for Specially-Promoted Research of MEXT (16002005), and in Russia by Nuclear Science and Technology Department of Minatom RF and by RFBR Scientific school grant 1608-2003.2.

References

1. *Neudatchin S.V., Cordey J.G., Muir D.G.,* Proc. 20th EPS Conf. Controlled Fusion and Plasma Physics, 1993. Vol **I** (EPS), p. 83.
2. *Neudatchin S V, Takizuka T., Shirai H., Isei N., Kamada Y., Koide Y., Sato M., Azumi M.,* Japan J. Appl. Phys., 1996, **35,** 3595.
3. *Neudatchin S V., Takizuka T, Shirai H., Fujita T., Isei N., Isayama A., Koide Y., Kamada Y.,* Plasma Phys Control. Fusion, 1999, **41**, L39.
4. *Neudatchin S.V, Takizuka T., Shirai H., Fujita T., Isayama A., Kamada Y., Koide Y., Suzuki T., Takeji S.,* Plasma Phys. Control. Fusion, 2002, **42,** A383
5. *Inagaki S., et al.,* Proc. 20th IAEA Fusion Energy Conf., 2004, EX/P2-12.
6. *Tamura N., et al.,* submitted to Phys. Plasmas.
7. *Neudatchin S., Inagaki S., Itoh K., Kislov A., Kislov D., Krupin D, Kubo S., Lysenko S., Ohkubo K., Pavlov Y., Poznyak V., Shimozuma T., Sushkov A., Yakovlev M., Ida K.,* J. Plasma and Fusion Res Series, 2004, **6**, 134.
8. *Sakamoto Y., et al.,* Nucl. Fusion, 2004, **44,** 876.
9. *Neudatchin S.V., Takizuka T., et al.,* Proc. 18th IAEA Fusion Energy Conf., 2000, (Vienna: IAEA), CR-ROM file EXP5/01.
10. *Neudatchin S V., Takizuka T., Shirai H., Fujita T., Isayama A., Koide Y., Kamada Y.,* Plasma Phys. Control. Fusion, 2001, **43,** 661.
11. *Neudatchin S.V., Takizuka T., Hayashi N., Isayama A., Shirai H., Fujita T., Kamada Y., Koide Y., Suzuki T.,* Nucl. Fusion, 2004, **44,** 945.
12. *Shimozuma T., et al.,* Plasma Phys. Control. Fusion, 2003, **45,** 1183.
13. *Ida K., et al.,* Phys. Rev. Lett., 2003, **91**, 085003.
14. *Neudatchin S V., Inagaki S., Itoh K., Tamura N., Tanaka K., Ida K., Kalinina D., Yakovlev M., Nagayama Y., Kawahata K., Sudo S., and LHD Experimental Group,* 2005, Spasmodic space-time evolution of reduced electron heat transport formed by injection of large C_8H_8 pellets into LHD plasmas, Plasma Phys. Control Fusion (submitted).
15 *Inagaki S., et al.,* J. Plasma and Fus. Res. Ser., 2001, **5,** 409.
16. *Neudatchin S.V., Kislov A.Ya., Krupin V.A., Lysenko S.E., Pavlov Yu.D., Syshkov A.V., Borshagovskii A.A., Chistyakov V.V., Ilin V.I., Piterskii V.V., Poznyak V.I., Roi I.N.,* Nucl. Fusion, 2003, **43**, 1405.
17. *Bagdasarov A.A., Vasin N.L., Neudatchin S.V., Savrukhin P.V,* Proc. 15th Int. Conf., 1991, Vol. **1** (Vienna: IAEA 1991), 523.
18. *Inagaki S., et al.,* Phys. Rev. Lett., 2004, **92,** 55002.
19. *Neudatchin S., Takizuka T., Hayashi N., Isayama A., Shirai H., Fujita T., Kamada Y., Koide Y., Itoh K, Miura Y.,* J. Plasma Fusion Res., 2003, **79,** 1218.
20. *Itoh S.-I, Itoh K,* Plasma Phys. Control. Fusion, 2000, **43,** 1055.
21. *Hahm T.S., Diamond P.H., Lin Z., Itoh K., Itoh S.-I.,* Plasma Phys. Control. Fusion, 2004, **46,** A323.
22 *Hahm T.S., Diamond P.H., et al.,* Phys. Plasmas, 2005, **12,** 090903.
23 *Takenaga H, et al.,* Temporal variation of density fluctuation and transport in reversed shear plasmas on JT-60U, Plasma Phys. Control. Fusion, 2005 (submitted).
24. *Inagaki S., et al,* Abrupt reduction of core electron heat transport in response to edge cooling in LHD, Plasma Phys. Control. Fusion, 2005 (submitted).
25. *Vershkov V.A., et al,* Nucl Fusion, 2005, **45,** S203.
26 *Yakovlev M., Inagaki S., et al.,* Phys. Plasmas, 2005, **12,** 092506.

EFFECT OF ECR HEATING ON IMPURITY TRANSPORT AND RADIATIVE LOSSES IN TOKAMAK PLASMAS

N. Timchenko, V. Lisitsa, A. Dnestrovskij, L. Kuznetsova, D. Petrov, D. Shuvaev, E. Westerhof[1]

Russian Research Centre "Kurchatov Institute", Moscow, Russia
[1]FOM-Institute for Plasma Physics Rijnhuizen, Association EURATOM-FOM, Trilateral Euregio Cluster, The Netherlands, www.rijnh.nl

Experimental and calculated data on impurity transport and radiative losses are presented for T-10 tokamak conditions. Data on radiative power obtained by AXUV detectors demonstrate a strong redistribution over the minor radius of radiative losses under ECR heating. Regimes with argon seeded plasmas with both Ohmic and ECR heating were considered. A strong modification of radiative power profile during the transition from the Ohmic to ECR regime was observed.

The modeling is based on the EC heating code TORBEAM, transport code ASTRA and the impurity transport and radiation code. The distribution over charge states of impurity components was calculated with account of transport and charge-exchange with neutrals. The transport coefficients were obtained as a result of comparison of calculated radiation with experimental data. In the calculations the radiation power contribution from all impurity components was obtained. The experimentally observed increase of neutral density in the ECRH regime was taken into account in the calculation of the radiative power losses.

The modeling demonstrates a strong modification of transport coefficients resulting in increased diffusion after the transition from Ohmic to ECRH regimes

Introduction

Modern tokamak investigations deal with two main radiative processes involved in the energy balance, namely: the plasma heating by electron cyclotron radiation and the plasma cooling due to radiative losses on impurities present in plasma. The ECR heating is mostly related to the central hot plasma and it is strongly selective in minor radius. The energy balance between strong central heating and plasma periphery cooling can result in a sharp increase of electron temperature gradients and in the increase of transport coefficients both for electron thermal conductivity and impurity transfer. In addition, the application of centrally deposited ECR heating flattens the electron density profile in the core and, consistently with higher diffusion, can cause the impurities to flow out. The goal of the present paper is to make an analysis of a redistribution of impurity radiative losses under ECR heating for T-10 tokamak conditions (R/a = = 1.5 m / 0.3 m, I_{pl} = 225 kA, B_{tor} = 2.5 T, $T_e(0)$ = 1–2 keV, ECRH ~1 MW).

The experiment and diagnostics

The radiation in the T-10 tokamak is measured by the diagnostic system based on silicon AXUV (Absolute eXtreme Ultra Violet) photodiode detectors

[1]. The region from the center to the experimental measurements at 28 cm is under consideration in the calculations.

Time traces of unfolded signals (emissivity) in an argon puffing shot are shown in Fig. 1. Argon was injected into the plasma (R/a = 1.5 m/0.3 m, I = 250 kA, B_{tor} = 2.5 T) in the Ohmic heating phase and ECR heating was switched on at t = 700 ms. It is seen that after ECRH application the radiation signal after a sharp increase decreases for central chords during approximately 50 ms and remains unchanged at the periphery (at r = 26 cm chord). Taking into account that the density and temperature remain constant during this period in the EC regime, it can be supposed that the radiation redistribution happens due to the pump out of impurities from the plasma center. The emissivity change over minor radius for the transition from OH to EC regimes is presented in Fig. 2. Such a radial redistribution of radiation losses can be connected with three reasons: (1) change of electron density and temperature profiles, (2) increase of neutral fraction in the ECR regime, (3) modification of impurity transport. The mechanisms responsible for the changes in the radiative loss profiles are investigated below.

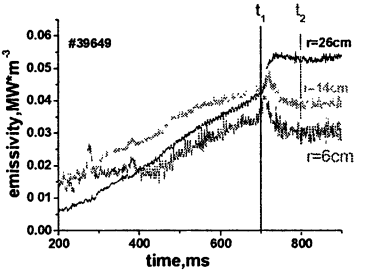

Fig. 1. Time traces of AXUV emissivity power given at different radii.

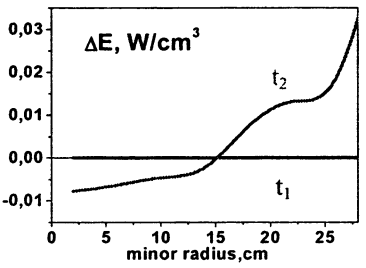

Fig. 2. Profiles of AXUV emissivity change ΔE after ECRH switch on.

The analysis methods and results

The modeling of the effects has been done in the frame of the transport impurity code [2], and radiation losses were estimated using the model of average ion charge [3].

The radial transport equations together with ionization balance were used in the form for each impurity charge component density n_i^Z:

$$\frac{\partial n_i^Z}{\partial t} = \frac{1}{r}\frac{\partial}{\partial r} r\left(D(r)\frac{\partial n_i^Z}{\partial r} - V(r) n_i^Z \right) + \\ + S_{i-1} n_{i-1}^Z - S_i n_i^Z + R_{i+1} n_{i+1}^Z - R_i n_i^Z , \quad (1)$$

where $D(r)$ and $V(r)$ are the diffusion coefficient and convection velocity for all impurity components, $S_i(T_e, Z_i)$, $R_i(T_e, Z_i)$ are ionization and recombination rates including the charge-exchange recombination for a specific ion with the charge Z_i.

Simultaneously we modeled the heat transport with the help of transport code ASTRA [4] and TORBEAM code [5] for EC wave beam tracing and heating. The radial distribution of electron heat conductivity in the OH and ECRH regimes are presented in Fig. 3. One can see an essential increase of heat transport in the ECRH regime, both OH and ECRH heat conductivities dominating strongly the neoclassical value.

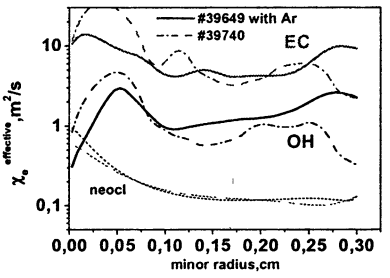

Fig. 3. The radial distribution of electron heat conductivity in the OH (black) and ECRH (grey) regimes for shots with (solid) and without (dash dotted) Argon puffing. Neoclassical conductivity is also shown (dotted).

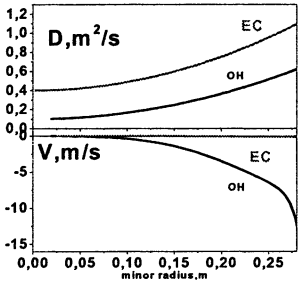

Fig. 4. Impurities transport coefficients used in modeling in OH (black) and ECRH (grey) regimes.

The impurity diffusion coefficients and convection velocities in a simplified treatment used to fit the experimental data are shown in Fig. 4. The diffusion coefficients in the ECRH regime are higher than in the OH regime while the inward convection at the edge has almost vanished at the edge in the ECRH regime. It is seen that the increase of impurity diffusion coefficient in the ECRH regime in comparison with OH regime corresponds to the enhancement of electron heat conductivity. The different impurities species have been taken into account for the solution of Eq. (1). The emissivity data for intrinsic impurities iron and carbon together with argon seeded impurity are presented in Fig. 5. In calculations, the impurity transport coefficients and the sources of the neutral atoms of impurities were determined also consistently with the value of Z_{eff} that was found with ASTRA code in the main components transport modeling using the experimental loop voltage. The Table demonstrates the contribution from different impurities species to radiative losses, average density and Z_{eff}. It had been taken into account also that ECR heating causes the increase of the neutral flux into the plasma resulting in a change of the impurity ionization balance and enhanced cooling of the plasma periphery. Calculated and experimental emissivity profiles for OH and ECRH regimes replicate quite well as shown in Fig. 6.

The carbon impurity charge component density profiles are presented in Fig. 7. It is seen that carbon nuclei dominate over the main plasma except the periphery beyond a 20 cm minor radius. The ECRH input power causes the outflow of the carbon nuclei from the plasma center diminishing the impurity density at the center.

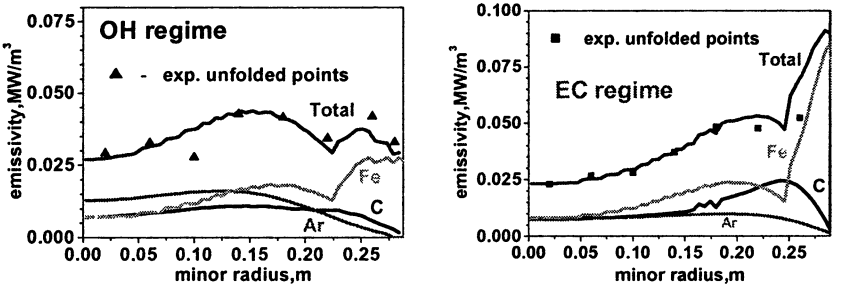

Fig. 5. The calculated total and component (Iron, Carbon and Argon) of impurity radiation profiles for OH (*a*) and ECRH (*b*) regimes. Experimental AXUV radiation points.

Radiative losses, average density and Z_{eff} for different impurities species at ECRH

	C	Ar	Fe	Sum	Photodiodes
P_{rad}, kW	34	19	49	102	107
<n>, %	3	0.1	0.03		
Z_{eff}	1.9	1.2	1.05	2.15	

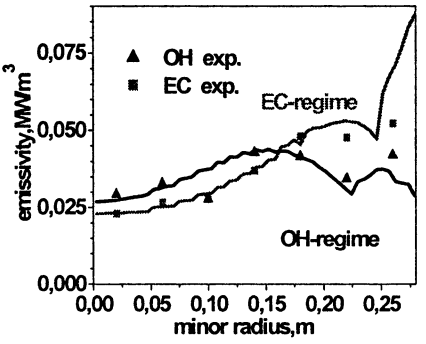

Fig. 6. Total emissivity for OH (black) and ECRH (grey) regimes calculated (lines) and experimental (points).

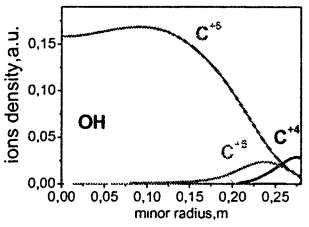

a

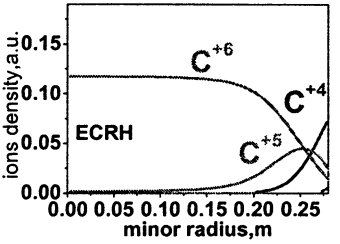

b

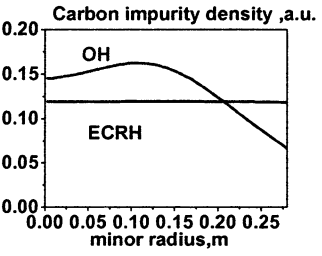

c

Fig. 7. Carbon impurity charge component density profiles in OH (*a*) and ECRH (*b*) regimes. Total carbon density profile in OH and ECRH regimes (*c*).

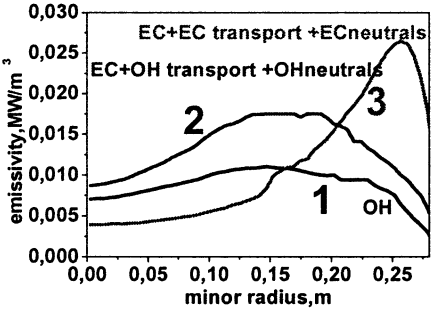

Fig. 8. The emissivity profiles resulting from the modeling for intrinsic carbon impurity for OH regime (curve *1*), for ECRH parameters with the same impurity transport coefficients as in OH regime (curve *2*) and for ECRH regime with the modified impurity transport (curve *3*).

Another example of the emissivity profiles resulting from the modeling for intrinsic carbon impurity is presented in Fig. 8. It is seen that the change of neutral density and temperature profile only without changing of impurity transport coefficients fails to explain the dramatic redistribution of radiative losses observed after ECRH switching on (see Fig. 1).

Conclusion

On-axis ECR heating causes impurity transport increase whereas another effects on emissivity such as increased neutrals flow and changed T_e are less

important. As a result the redistribution of impurities charge balance and densities profiles together with decrease of impurities density in the plasma center takes place. A strong increase of impurity diffusion coefficients under the condition of on-axis ECRH heating is in a qualitative correspondence with the increase of the heat transport coefficients. Our result for T-10 tokamak is in an agreement with the result for impurity transport analysis made for ASDEX-U tokamak in regime with the ECR heating [6]. The results data of impurity transport analysis are of importance for understanding the impurity behavior in future tokamak reactor with central heating.

The authors are grateful to V. Vershkov for helpful discussion.

The work is supported by NWO-RFBR Grant Nr.047.016.016 and Grant RFBR Nr. 04-02-17567, Scientific School Grant 5899.2003.2 and 2024.2003.2.

References

1. *Timchenko N.N. et al.*, 30th EPS Conf. Contr. Fusion and Plasma Phys., St. Petersburg, 2003, Vol. 27A, P-2.74.
2. *Dnestrovskii Yu.N., Strijov V.F.* The model of impurity diffusion in Tokamaks: Preprint IAE 3779/6, Moscow, 1983 (in Russian).
3. *Post D.E. et al.*, Atomic Data and Nucl. Data Tables, 1977, 20, 397-439.
4. *Pereverzev G, Yushmanov P.*, ASTRA Automated System for Transport Analysis in a Tokamak: IPP-Report 5/98, 2002.
5. *Poli E. et al.*, Computer Phys. Commun. 2001, 136, 90-104.
6. *Dux R. et al.*, 30th EPS Conf. Contr. Fusion and Plasma Phys., St. Petersburg, 2003, Vol 27A, P-1.132.

RECENT RESULTS OF STUDIES OF FLUCTUATIONS IN HIGH-TEMPERATURE PLASMA OF MODERN STELLARATORS BY MICROWAVE SCATTERING TECHNIQUE

N. N. Skvortsova[1], *G. M. Batanov*[1], *L. V. Kolik*[1], *A. E. Petrov*[1], *A. Pshenichnikov*[1], *K. A. Sarksyan*[1], *N. K. Kharchev*[1], *Yu. V. Khol'nov*[1], *S. Kubo*[2], *J. Sanchez*[3]

[1]Institute of General Physics, Moscow, Russia
[2]National Institute of Fusion Science, Toki, Japan
[3]Euroatom-CIEMAT, Madrid, Spain

Plasma density fluctuations in the heating region of the L-2M stellarator were measured from microwave scattering at the second harmonics of the heating gyrotron radiation. In the TJ-II stellarator, a separate 2-mm microwave source was used to produce a probing beam; the measurements were performed at the middle of the plasma radius. In TJ-II, plasma density fluctuations were studied in experiments with the neutral beam injection. Plasma density fluctuations in the heating region of the LHD stellarator were measured from microwave scattering at the fundamental harmonic of the heating gyrotron radiation. New results were obtained with the use of a small-angle scattering of the heating gyrotron radiation in LHD.

The new results of the investigations of fluctuations of hot stellarator plasma are represented. Microwave scattering diagnostics are described that allow direct measurements of the turbulent processes in a high-temperature plasma of magnetic confinement systems. The parameters of plasma density fluctuations were studied by the conventional technique of measuring the scattered 2-mm radiation of a separate low-power microwave source and also by measuring the scattered radiation of the heating gyrotron [1, 2]. Experiments on studying the characteristics of fluctuations in high-temperature plasma by microwave-scattering techniques were carried out in three stellarators: L-2M, LHD, and TJ-II.

The L-2M stellarator has a two-pole winding. The plasma is produced and heated under ECR conditions at the second harmonic of the electron gyrofrequency with the help of a 75-GHz gyrotron. The LHD device is the largest modern superconducting heliac with a divertor. In this experiment, the plasma was created and heated under ECR conditions at the fundamental and second harmonics of the electron gyrofrequency by several 168-GHz and 84-GHz gyrotrons. The TJ-II device is a stellarator with four-pole winding. In this experiment, the plasma was produced and heated by a 53.2-GHz gyrotron at the second harmonic of the electron gyrofrequency. The detailed description of parameters of TJ-II, L-2M and LHD devices is given in [3–5].

1. For the TJ-II device, a 2-mm scattering technique was elaborated for studying fluctuations in the high-temperature core plasma. Plasma density fluctuations were measured from signals scattered from the inner plasma region lying at the middle of the plasma radius; the poloidal and radial dimensions of this region were about 4 cm. We measured plasma density fluctuations with wavenumbers 3 and 6 cm^{-1}. The homodyne detection of the scattered signals was employed.

This diagnostic was used in the experiments with additional NBI heating of ECRH target plasma. The conditions of these experiments are described in [6]. Figure 1 shows how the plasma density and Hα intensity change after NBI is switched on; the start time of NBI is indicated by an arrow. The figure also shows the behavior of the RMS of fluctuation amplitudes. It is seen that the RMS drops during the NBI pulse. It will be recalled that the scattered signal is proportional to the square of the plasma density. However, the observed drop in the RMS level cannot be attributed to increased refraction, because the monitor (direct) channel indicates the absence of such a strong refraction.

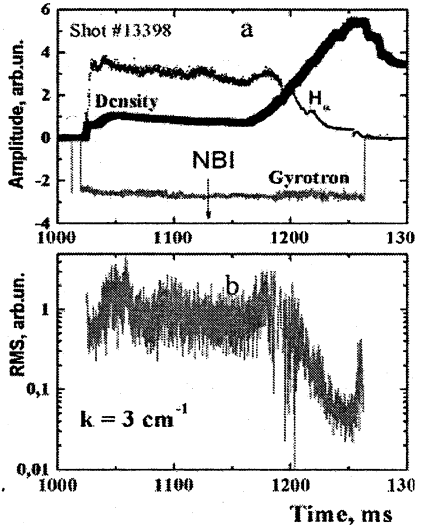

Fig. 1. The behavior of the plasma density and Ha intensity after NBI is switched on (*a*), the corresponding drop in the RMS level of fluctuations (*b*).

This is evidence that conditions change substantially in comparison with the target ECRH plasma. There are at least two instabilities: drift-dissipative instability and the instability driven by trapped electrons, that can give rise to fluctuations in ECRH plasma. Conditions that provoke the onset of these instabilities were considered in [2]. It is shown that a necessary condition for drift-dissipative instability is $d\ln T_e / d\ln n > 2$, whereas the instability driven by trapped electrons can arise at a weaker condition $(dT_e / dr)\cdot(dn / dr) > 0$. On the other hand, with the method of mixture separation it is shown that only one of

these instabilities may be responsible for growth of fluctuations at the plasma middle radius in TJ-II [7].

Figure 2 shows the temporal evolution of Fourier spectra of fluctuations characteristic of the ECRH and ECRH/NBI regimes (before and after NBI is switched on). In the NBI regime, the density increases and the electron temperature decreases. The temperature profile flattens and becomes similar in shape to the density profile. The conditions for drift-dissipative instability, which are determined by a difference between the density and temperature gradients cannot be realized in this case. Furthermore, just after the neutral injection is switched on, high frequencies disappear in the fluctuation spectra, which is typical of the drift-dissipative instability.

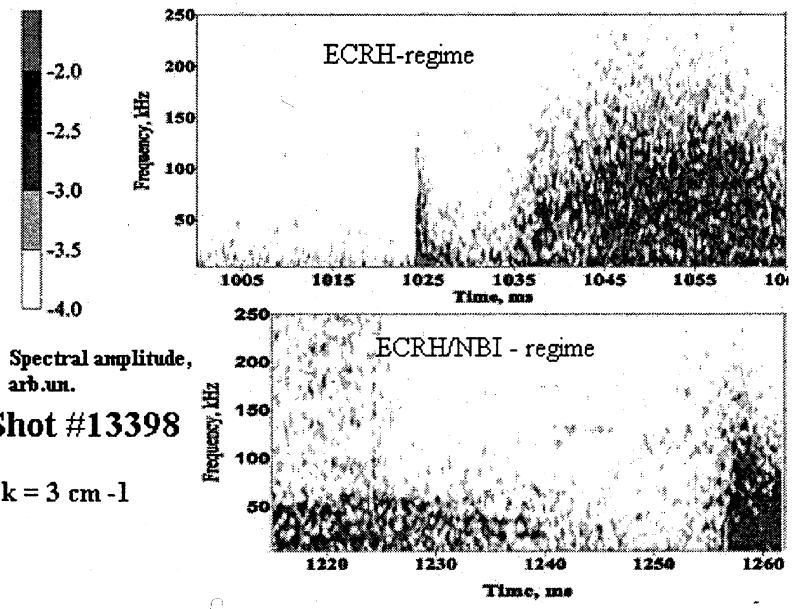

Fig. 2. Temporal evolution of Fourier spectra of density fluctuations in the ECRH and ECRH/NBI regimes.

2. Microwave radiation from the heating gyrotron was launched into the vacuum chamber of the L-2M stellarator as a linearly polarized Gaussian beam. At the plasma boundary, the incident linearly polarized wave splits into extraordinary and ordinary waves. At densities typical of the existing toroidal devices, the plasma is transparent to ordinary waves, and it is optically thick for extraordinary waves. The fact that the incident radiation excites two waves in the plasma is unfavorable for ECR plasma heating, because the single-pass absorption of the heating wave in the plasma decreases [8]. On the other hand, the ordinary wave can be used as a probing wave in scattering diagnostics. Fluctua-

tions were measured in the heating region in L-2M. We studied the increments of density fluctuations with $k = 40$ cm^{-1} (second-harmonic gyrotron scattering [9] with a 1-MHz sampling rate) in the steady-state phase of a discharge (2000 data points). These data do not obey a normal distribution. However, even a three-component mixture of normal distributions $f(x; p, \mu_1, \mu_2, \mu_3, \sigma_1, \sigma_2, \sigma_3) =$

$$= \sum_{k=1}^{3} \frac{p_k}{\sqrt{2\pi}\sigma_k} \exp\left\{-\frac{(x-\mu_k)^2}{2\sigma_k^2}\right\},$$ with parameters: $p_1 = 0.1521$, $\mu_1 = 0.0037$, $\sigma_1 = 0.0013$, $p_2 = 0.6497$, $\mu_2 = -0.0023$, $\sigma_2 = 0.0134$, $p_3 = 0.1982$, $\mu_3 = 0.0031$, and $\sigma_3 = 0.0034$ fairly well describes this time sample: the P value is 0.9688. Figure 3 presents a histogram of the increments for a time sample of plasma density fluctuations in L-2M and the corresponding model distributions.

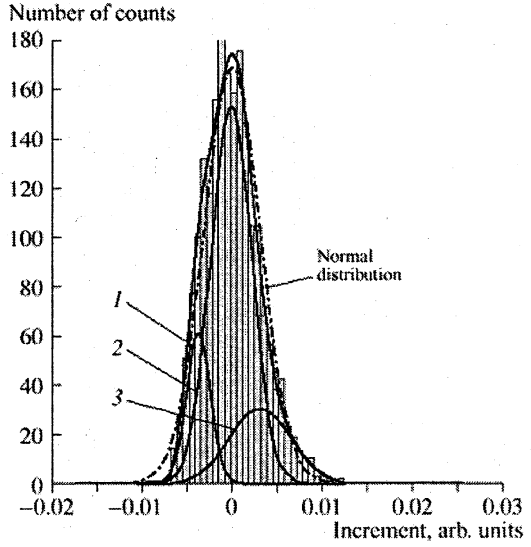

Fig. 3. Modeling of the PDF of a time sample of the increments of plasma density fluctuations in L-2M (shot no. 54 215) by a scale mixture of three Gaussian distributions marked by *1*, *2*, and *3*.

3. The gyrotron scattering diagnostics was elaborated and mounted in the LHD device with the purpose of measuring fluctuations in the central region of the plasma column [9]. As in L-2M, the radiation from the gyrotron (84 GHz) was partially converted into the ordinary wave. In the previous experiments the geometry of gyrotron scattering was closer to the backward Bragg scattering, the microwave radiation was scattered by plasma density fluctuations with a wavelength of $k \sim 25$–34 cm^{-1}. In the resent experiments gyrotron forward scattering was measured on fluctuations with a wavelength of $k \sim 3$ cm^{-1}. The Fourier spectrum of these fluctuations is represented in Fig. 4.

Fig. 4. FFT spectrum of plasma density fluctuations ($k \sim 3$ cm^{-1}). Forward gyrotron scattering. Shot 55993. $t = 0.17$–0.52 s.

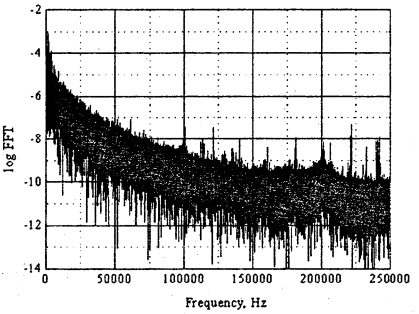

4. Conclusions

1. It is shown that fluctuations at the middle radius ($r/a \sim 0.5$) of TJ-II can be attributed to drift-dissipative instability. The level of fluctuations in the ECRH/NBI regime decreases by a factor of 10–50 in comparison with the ECRH regime.
2. In the high-temperature central plasma and the low-temperature edge plasma of L-2M, LF structural turbulence is well described by scale mixtures of normal distributions with the same number of mixture components.
3. With the method of forward gyrotron scattering, Fourier spectra of plasma density fluctuations were measured for the first time in LHD.

References

1. *Batanov G.M. et al*, Pis'ma Zh. Eksp. Teor. Fiz. **72**, 250 (2000).
2. *Batanov G.M. et al.*, Plasma Phys. Rep., **29**, 363 (2003).
3 *Abrakov V.V. et al.*, Nucl. Fusion **37**, 233 (1997).
4. *Alejaldre C. et al.*, Plasma Phys. Controlled Fusion **41**, B109 (1999).
5. *Motojima O. et al.*, Physma Plasmas **6**, 1843 (1999).
6. *Hidalgo C. et al.*, Nuclear fusion. **45** (2005), in print; *Skvortsova N.N. et al.*, Plasma Phys. Rep. **31**, 57 (2005).
8. *Suvorov E.V., Frayman A.A.*, Fiz. Plazmy, **6**, 1161 (1980).
9. *Batanov G M et al*, Plasma Phys. Rep., **29**, 1019 (2003).
10. *Skvortsova N.N. et al.*, J. Plasma Fusion Res., **5**, 328 (2002).

A FAMILY OF CALORIMETRIC LOADS FOR HIGH POWER MILLIMETRIC WAVELENGTH BEAMS

S. Cirant, W. Bin, A. Bruschi, F. Gandini, G. Granucci, V. Mellera, V. Muzzini, N. Spinicchia, C. Sozzi

Istituto di Fisica del Plasma, CNR, Milano, Italy

The paper describes the design, calculation and performances of a family of calorimetric matched loads to be used with high power, millimeter wave gyrotrons for ECRH applications in plasma physics. All the loads in the family are based on the same identical concept of a copper sphere coated on the inside with a partially absorbing ceramic layer. Different applications are foreseen, from a precise characterization of the e.m. beam power distribution in short pulses (up to 0.1 s), to the absorption and calorimetric measure of beams at 2 MW, CW. The loads differ mainly in the way in which heat is removed, and calorimetry is performed.

The availability of an appropriate sink for the e.m. power delivered by any new microwave source is obviously necessary for a successful completion of the development process. "Appropriate" means, in substance, that the sink withstands the delivered power, it does not interfere with the source operation and provides the measure of the soaked power. An additional but most useful feature is that it can be used in every operating condition.

An ideal load for the development of high power gyrotrons for ECH therefore should have less than 1% reflectivity in the Gaussian mode (back-reflection), a maximum of 5% reflectivity in high order modes, a power handling capability in excess of 2 MW, high precision calorimetric capability both in short pulse for gyrotron's first operation and characterization and in long pulse or CW for gyrotron development to full specs, and it should be vacuum compatible.

However strange it might appear, the main limit to having all these features in one single object is not in the electromagnetics but in the calorimetry, since a system designed for CW operation will be drastically different from the one used at short pulse.

Within this frame of reference, "short" means shorter than the thermal characteristic time constant, where the dominant time constant is the one of the gyrotron system τ_{gyro}. We assume that for multimegawatt mm-wave gyrotrons "short" means less than 0.1 s. Conversely, the thermal time constant of the load τ_{load} is a free parameter, to be optimized in dependence to the application foreseen and the operating temperature of the load itself T_{load}, which is proportional to the heat stored in the load (with coolant) $H_{load} = P_{absorbed}\tau_{load}$. In order to keep T_{load} within safe limits (in the coolant or in any part of the load) even at very high absorbed power (P_{gyro}), τ_{load} must be kept adequately small. Roughly speaking $\tau_{load} = \tau_{mat} + \tau_{liq}$, where τ_{mat} is the characteristic time constant in the body of the load, related to the thermal resistance from the absorbing layer up to the coolant, and τ_{liq} is the time-of-flight from inlet to outlet of the liquid coolant.

In a good CW design τ_{mat} will be kept to a minimum by appropriate design of the cooling channels (the golden rule is here to bring the coolant as close as possible to all directly heated points), while fast flows will keep τ_{mat} low.

In case of short, or very short pulse length t ("very short" means here shorter than $0.1\tau_{load}$), $T_{load,pulse}$ should be scaled with respect to the steady temperature $T_{load,CW}$ by a factor $e^{-t/\tau_{LOAD}}\ t/\tau_{LOAD}$, easily in the order of 1/10000 during early phases of gyrotron development and test. In order to have measurable $T_{load,pulse}$ for calorimetric purposes, it follows that $\tau_{load,pulse} >> \tau_{load,CW}$. The difference can be accomplished to some extent by reducing the coolant speed, but by not much more than a factor in the order of 10÷100. A factor 10 more could be accomplished by sophisticated and very precise temperature measurements. The remaining factor 10 must be achieved with a different design of the cooling circuit, in order also to limit the mass of the coolant in the load.

A good approximation to the ideal load is a family of models having an identical absorbing core and electromagnetic design, but a different thermal time constant and heat removal scheme for different applications. A very flexible electromagnetic design, applicable to all cases where a Gaussian beam is used, is the integrating sphere [1], having an aperture for beam coupling and absorbing walls for sinking the coupled power. The overall reflectivity R can be written as:

$$R = \frac{\rho \cdot \frac{S_{port}}{S_{total}}}{1 - \rho \cdot (1 - \frac{S_{port}}{S_{total}})}$$

where ρ, S_{total} and S_{port} are respectively the (average) wall reflectivity, the total absorbing surface and the area of the input port. Average wall reflectivity can be adjusted either by coatings of different material or different thickness. The diameter of the sphere is the other parameter which can be used for the achievement of the specified overall reflectivity.

In spite of the relatively complex fabrication, the constant curvature of a spherical absorbing cavity offers decisive advantages in the design and realization of high power matched loads: it provides the highest uniformity in the distribution of e.m. fields and heat flux at the wall, with the lowest possible peak values (field & heat flux) for a given input power and load size. If the input beam is well characterized, the sphere allows a good predictability of critical features (heat flow, fields, overall reflection), with a minimum risk of wrong design and unexpected behavior. Last but not least, a good precision in manufacturing is possible.

Basic structure and concept

The main components of each load of the group, designed for operation in the mm-wave band and at the MW power level, is a spherical copper shell, 600 mm inner diameter, with a thin (2÷3 mm) or thick (40 mm) wall for the

operative test of different construction processes. The inside is coated with high temperature ceramics, deposited by plasma spray with a thickness in the range 100÷300 μm. Several different ceramics have been tested both with respect to electromagnetic and thermal properties [2], Chromia (Cr_2O_3) being presently considered as the most promising.

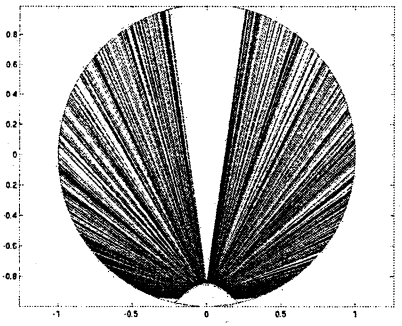

Fig. 1. Scheme of the load and of the primary illumination resulting from the combination of the input beam size and of the shape of the diverging mirror.

A diverging mirror, made of polished copper, is positioned oppositely to the entrance, with the surface designed for providing a primary illumination of the cavity wall such that the overall thermal loading after many reflections is most uniform (Fig. 1). A cooling spiral is wounded on the outside in a way dependent on the application (Short Pulse or CW). All loads can be made vacuum compatible, and can be used in evacuated ECH systems.

Ceramic coating and thermal loading

The wall reflectivity and the absorbing coating is the most critical element of the load. Low reflectivity means low overall reflection and uniform wall loading, but great sensitivity to the operating conditions and input beam anomalies. Low wall losses would imply worst performances (higher heat load inhomogeneity and higher overall reflectivity) but a better use the smoothing effect of multiple reflections. Figure 2 shows the wall reflectivity dependence for a Cr_2O_3 coating at 140 GHz with thickness. A value of $\rho \approx 0.6$ has been chosen for most of the loads.

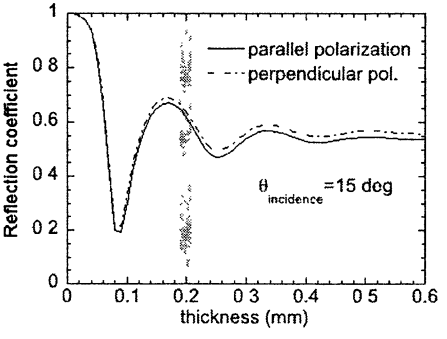

Fig. 2. Wall reflection coefficient vs. Cr_2O_3 thickness at 140 GHz. The vertical bar show the precision achievable by the coating process.

Low thickness is preferable from the thermal point of view, since heat removal is fast enough to

allow low temperatures and gradients (Fig. 3). However this implies operation in a regime more sensitive to coating errors.

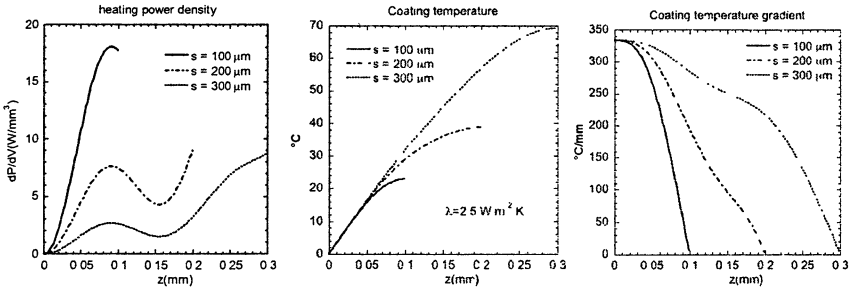

Fig. 3. Heating power density, temperature and temperature gradient inside the coating material in function of its thickness, at the same absorbed power.

A thickness in the range of 70 μm is chosen for low-energy (very short pulses) applications, while for most powerful uses a thickness around 200 μm is preferred.

For reflectivity in the range up to $\rho \approx 0.6$ thermal loading tends to pile up around the entrance port mostly because of the overlapping of the few first reflections, in spite of different shapes of the diverging mirror. Figure 4 shows the calculated wall heat flux for the mirror/beam combination with the lowest heat load peak. Another side effect of first-reflections is the creation of the interference pattern observed in real loads.

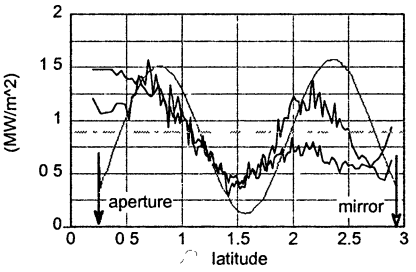

Fig. 4. Total heat flow at the wall (irregular curve) vs. the position along the meridian for an inner diameter of 600 mm and a total power of 1 MW. The dotted curve is the primary wall illumination, tailored for minimum peak value near the entrance.

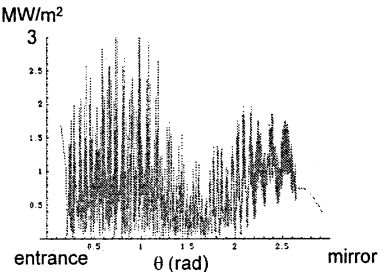

Fig. 5. Heat flow in Fig. 4 is obtained by overlapping many rays, random in phase. Contrarily, Fig. 5 takes into account the few first reflected rays with appropriate phases, showing interference patterns.

The sphere diameter is the main parameter determining the heat flux at the wall, which is in the order of 0.8 MW/m^2 for an i.d. of 600 mm and 1 MW total power. In principle, thermal wall loading distribution can be controlled by an appropriate shaping of the coating thickness along the meridian from the mirror edge to the entrance aperture.

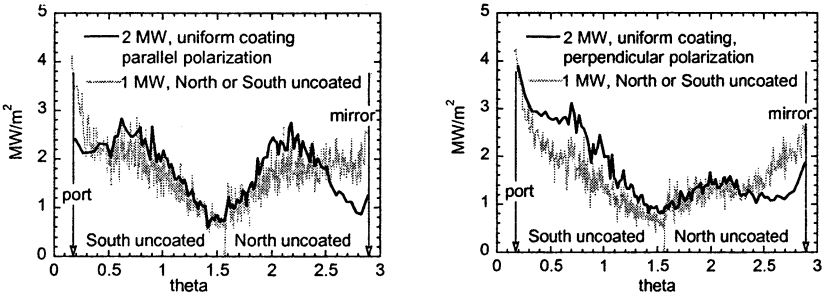

Fig. 6. Calculation of the heat flux at the wall for the two polarizations (left and right figure) in case of uniform coating, full power (black curves) and in the case (gray) of only a half sphere coated, the other one uncoated, but with half power.

In practice, this would require an accurate preparation of the coating process to be reliable and reproducible. However, a very simple thickness shaping method provides a very important option: if only one half sphere is coated, and the other one is finished with bare copper, wall reflectivity $\rho \approx 1$, the heat flux at the coated wall, and the electric fields inside the cavity, are nearly doubled. Figure 6 shows the results of different calculations covering the different cases (perpendicular or parallel polarization, north or south hemisphere uncoated). The importance of such a possibility is related to the fact that loads designed for a certain power level could be tested at about half power, which means that loads designed for the next generation sources could be tested with already available units.

Reflections and pre-load

Load reflection can be considered as made of a purely backward component (directly from the diverging mirror), and a wide-angle component originated by multiple reflections.

Although the reflecting mirror has a cusp, which should prevent reflection directly backwards, finite cusp radius and diffraction determine a finite (< 1%) reflectivity in this direction. Multiple-rays calculations show that up 10% of the input power can be reflected at large angle, which however is limited in a defined cone with an aperture of about 60° (Fig. 7 and 8).

The power coming out from the load at large angles is reflected back into the load by a mirror arrangement designed to act as a back-reflector. Figure 7, right, shows an example of this. The pre-load has no effect on the narrow input beam. The trapping effect of the preload is shown in Figs. 8 and 9, which show respectively the angular pattern of the reflected radiation and the measured gyrotron power with and without pre-load. While large angle rays are suppressed, the bolometric power is increased by 10%, confirming the quantitative estimate of the radiation that would escape without preload.

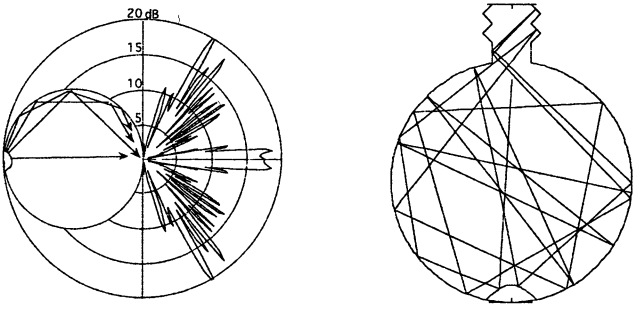

Fig. 7. Load reflections (left) are grouped in a narrow backward beam (originated from the mirror) and a broader emission from multiple reflections. The broad-angle reflection can be re-injected in the load by a pre-load section (right).

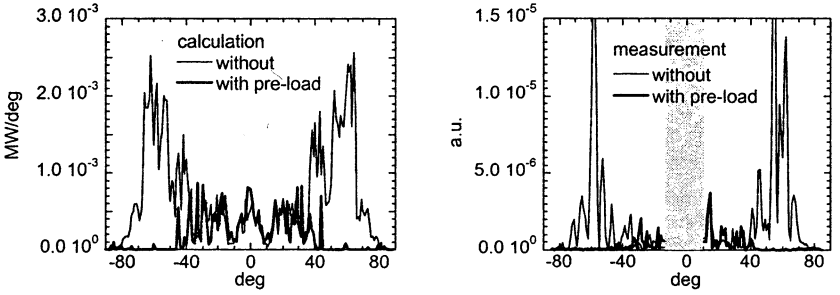

Fig. 8. Calculated (left) and measured (right) effect of the preload in preventing reflection from the load at large angles from the symmetry axis.

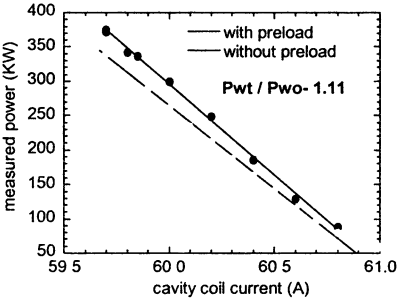

Fig. 9. Bolometric gyrotron output power vs. cavity field, measured with and without preload, all other parameters being the same.

Thin-wall 2 MW, 0.1 s diagnostic load

During the development phase of a new gyrotron the load should provide good diagnostic of the output beam and full power handling capability at short pulse length, usually up to 0.1 s. This is accomplished in a spherical load with a thin wall, with a cooling circuit designed to remove from shot to shot the heat

absorbed. Figure 10 shows an image of half a sphere immediately after the creation of the cooling channel, which is done by electroforming in order to not introduce any stress and deformation in the sphericity of the copper shell.

Bolometric measurements performed on the coolant give the total absorbed power. In addition, the thin wall allows a better description of the power distribution by an IR imaging of the temperature distribution on the sphere (Fig. 11). An even more direct picture of the beam power is obtained by the infrared image of the backside of the diverging mirror, if its thickness is appropriately chosen (Fig. 12).

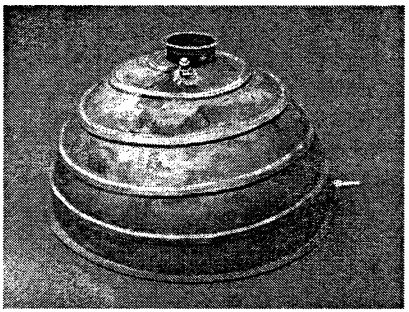

Fig. 10. Picture of one half of the load for short pulse operation, 2 MW. The thin copper shell (3 mm) and the electroformed cooling channel are shown.

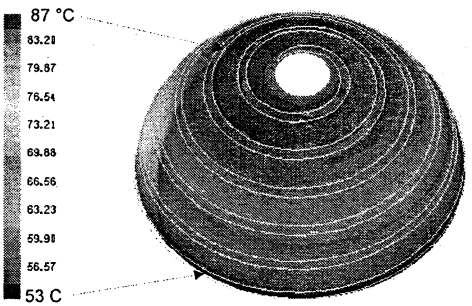

Fig. 11. Calculated temperature distribution on the sphere after 0.1 s at 2 MW (multiple reflections). Wall thickness is 3 mm (copper).

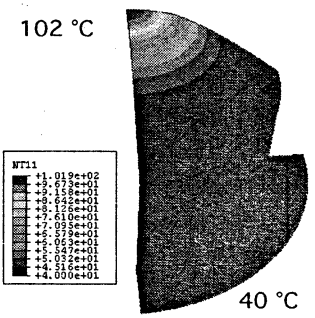

Fig. 12. Calculated temperature distribution on diverging reflector after 0.1 s at 2 MW (first reflection). Mirror thickness is 5 mm (copper).

The time constant for complete recovery of the initial temperature is approximately 60 s in this case, which means that during the pulse length of 0.1 s the heating is purely adiabatic and the local temperature increase depends on heat flux wall and thickness only.

The lowest thickness value is, on the other end, limited by mechanical stability of the sphere under vacuum. Extensive calculations, including buckling, show that the wall should be at lest 1.75 mm thick. A typical thickness for safe handling of 0.2 MJ pulses is 3 mm for a sphere with a diameter of 600 mm.

Thick-wall, 1 MW, long pulse

For high energy (long pulse) applications the thin shell with loose cooling spiral cannot be used any more. An alternative, which has been tested up to 700 kW/1 s and 500 kW/10 s at 140 GHz, is made of a thick copper shell with the cooling pipe immersed. The copper shell is obtained by casting, followed by machining to required shape. Some heat is stored in the body, which helps in handling high peak powers (MW) for relatively long pulses (10 s). The system seems unfit to true CW operation.

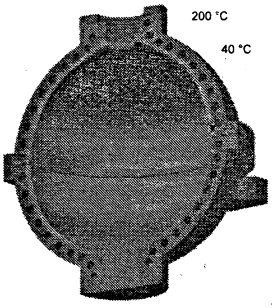

Fig. 13. Section of the thick wall load, showing the cooling channel and the temperatures for a steady 1 MW input.

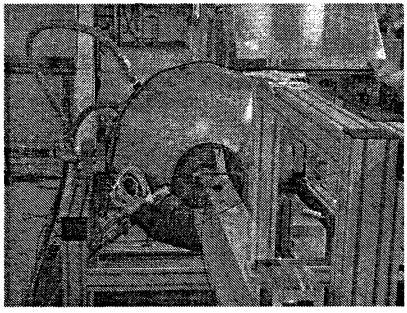

Fig. 14. Picture of the load positioned at the end of a remote steering waveguide for high power tests.

Thin wall 2 MW, CW design

The load envisaged for high power (2 MW) CW operation has a thin shell, and the cooling system is composed by several adjacent spirals, covering the entire surface of the sphere. With this arrangement both the time constant for heat transfer across the body and heat storage are minimum. Figures 15 and 16 show in more detail this arrangement for heat removal. The cross section of each channel is 9.5 × 2 mm, and the water flows at speed of 10 m/s. The high velocity provides sub critical, bubble free operation even in the presence of a wall temperature slightly in excess of the boiling point of the coolant. To give an example, at the points close to the entrance aperture where the heat flux reaches maximum value of 3 MW/m^2, the critical heat flux above which vapor bubbles might develop is 33 MW/m^2 at the foreseen water speed and channel size. The tenfold safety margin makes the risk of bubble formation very unlikely, which is the most severe concern in a parallel configuration of the cooling channels. The presence of a bubble reducing to one third the mass flow would bring the copper temperature above 180 °C, which is unacceptable, in half a second. On the other end, vaporization increases the heat transfer capability by a significant amount, and it is taken into account.

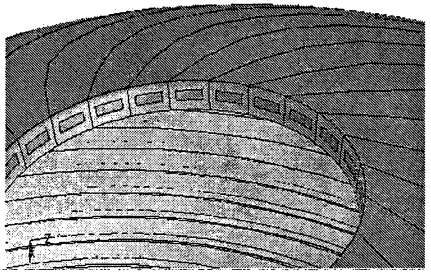

Fig. 15. Cooling spirals are adjacent in the 2 MW CW load for the fastest heat transfer.

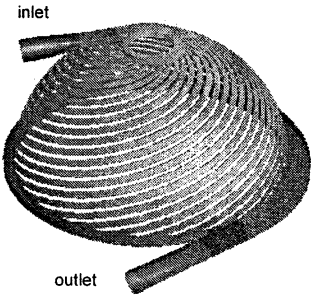

Fig. 16. The design of the water distribution provides low pressure drop and even distribution in the parallel channels.

The design of the water inlet and outlet manifold must provide an equal distribution of the coolant flow in all channels (10 ± 0.5 m/s, according to calculations). The temperature distribution at 2 MW, steady state input is shown in Fig. 17. On the hot size, facing the Cr_2O_3 coating, the peak value is safely 40 °C less than crystallization temperature. On the water side the temperature is slightly above boiling point, but heat flux is largely under-critical and no vapor bubbles are being developed.

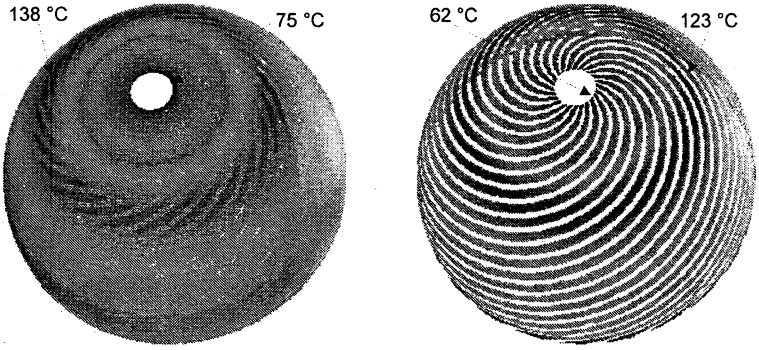

Fig. 17. Temperature distribution in the hot internal side (left), and on the water side (right) of the copper shell at 2 MW, steady state

References

1. *Bruschi A. et al.*, Nucl. Fusion, **43**, No. 11, November 2003, 1513.
2. *Gandini F. et al.*, 29th Int. Conf. IRMMW, Karlsruhe, 2004.

PLASMA BREAKDOWN USING SECOND HARMONIC ECH IN HELICAL SYSTEMS

K. Nagasaki[1], *Á. Cappa*[2], *Y. Yoshimura*[3], *T. Mizuuchi*[1], *F. Sano*[1], *H. Okada*[1], *S. Kobayashi*[1], *K. Kondo*[4], *K. Takahashi*[4], *F. Castejón*[2], *F. Tabarés*[2], *A. Fernández*[2], *E. de la Cal*[2], *T. Estrada*[2], *V. Tribaldos*[2], *D. Tafalla*[2], *H. Shidara*[5], *Heliotron J Team, TJ-II Team and CHS Team*

[1]Institute of Advanced Energy, Kyoto University, Japan
[2]Laboratorio Nacional de Fusión, CIEMAT, Spain
[3]National Institute for Fusion Science, Japan
[4]Graduate School of Energy Science, Kyoto University, Japan
[5]Centre de Recherches en Physique des Plasmas, Switzerland

Plasma breakdown using second harmonic electron cyclotron (EC) waves has been studied experimentally in three helical devices, Heliotron J, TJ-II and CHS. Comparison of the experimental results among three devices shows a common feature that the plasma starts up from the good confinement region and strongly depends on the nonlinear interactions with the electric field of local beam rather than the multi-reflected field. This suggests that the confinement of high energy electrons generated by ECH has a dominant role in the second harmonic plasma breakdown.

1. Introduction

Electron cyclotron waves of fundamental and second harmonic resonance frequencies are routinely used for plasma start-up and heating in toroidal fusion plasmas. The fundamental plasma breakdown can be explained simply by a linear theory, while the second harmonic plasma breakdown requires consideration of nonlinear wave-particle interactions, since the linear energy increment of seed electrons is proportional to the gyroradius squared, which is practically zero at the initial phase. According to a nonlinear theory [1–3], the accelerated electrons should be confined well for causing electron avalanche until they collide with neutrals.

The ECH is also an attractive scheme for start-up scenario in tokamaks. Low voltage start-up is very important for large tokamaks to reduce large voltage spike for plasma breakdown. In ITER, for example, the toroidal electric field less than 0.3 V/m is required because of slow voltage diffusion through the thick vessel wall [4]. In JT-60U tokamak, the breakdown loop voltage was reduced to 0.26 V/m by 200 kW fundamental ECH [5]. However, much higher EC power was required for the second harmonic ECH-assisted startup.

It is noted that the plasma breakdown occurs under different conditions between tokamaks and helical systems. In tokamaks, the confinement in breakdown phase is very poor because of no nested flux surfaces, while in helical systems, confining magnetic field structure is generated by external coils from the beginning of discharges. However the breakdown physics should be the

same in both toroidal devices. The study of plasma breakdown in helical system will give some insight to effective EC assisted start-up in tokamaks.

2. ECH systems

The ECH system is utilized for plasma production and heating in helical systems. Since the helical system has three dimensional magnetic field structure, a wide range of the injection angle and the precise control of the polarization mode are required to achieve the efficient single pass absorption. Recent technological progress can lead to the sophisticated launching of a focused Gaussian beam with the polarization and launching angle controllable. Table shows the main features of ECH systems for three fusion devices. All the ECH systems have a capability of controlling the input power, injection angle and wave polarization, which makes it possible to study the dependence of plasma breakdown on the ECH conditions.

ECH systems for Heliotron J, TJ-II and CHS

	Heliotron J	TJ-II	CHS
Frequency	70 GHz	53.2 GHz	53.2 GHz 106.4 GHz
Power	0.4 MW	0.3 MW×2	0.3 MW 0.4 MW
Pulse length	0.2 s	0.5 s	0.1 s
Injection mode	Focused /non-focused Gaussian	Focused Gaussian	Focused Gaussian
Injection angle	Controllable	Controllable	Controllable
Polarization	Controllable	Controllable	Controllable
Reference	[7]	[8]	[9]

The three fusion devices, Heliotron J, TJ-II and CHS have their similar major and minor radii, ECH power and magnetic field strength. The mod B structure is saddle type for CHS, and monotonic for TJ-II likely as tokamaks. The Heliotron J device has both mode B structures depending on the toroidal angle. Plasmas are produced by only ECH without ohmic current.

3. Experimental results

The experimental results on plasma breakdown using second harmonic EC waves are described in this section. More details of the experimental results are given in Ref. [9, 11, 12]. A few ms after the ECH turn-on, the H_α signal starts to rise up, and then the line averaged electron density signal shows a slow increase. The H_α signal has a peak before the electron density is saturated. Figure 1 shows the examples of the plasma shape at the initial phase, which is a tan-

gential view measured with a CCD camera. At the second harmonic ECH, the plasma is first produced like a "snake" around the magnetic axis, and then expands towards the edge region. This is confirmed in the edge plasma measurement with a Langmuir probe. The ion saturation current at the scrape-off layer appears a few msec after the core electron density starts to rise up.

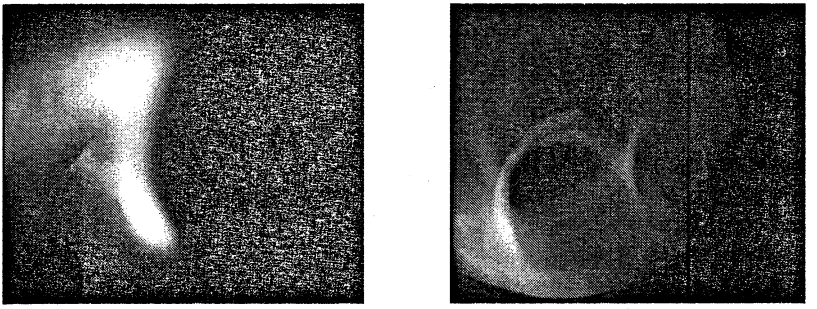

a *b*

Fig. 1. Tangential view of initial plasma in Heliotron J measured with CCD camera, (*a*) second harmonic ECH and (*b*) fundamental ECH.

This time evolution is contrast with the fundamental breakdown. In Heliotron J, the fundamental plasma breakdown occurs at the magnetic field regime, $\omega_0/\omega \geq 0.52$, that is, when the resonance appears inside the Heliotron J vacuum chamber. The initial plasma is produced in the edge region where the fundamental EC resonance is located. Such a breakdown does not happen when the second harmonic resonance is located at the edge. These indicate that the breakdown process is different between the fundamental and second harmonic ECH. The second harmonic breakdown starts from the good confinement region, while the fundamental breakdown occurs along the resonance layer.

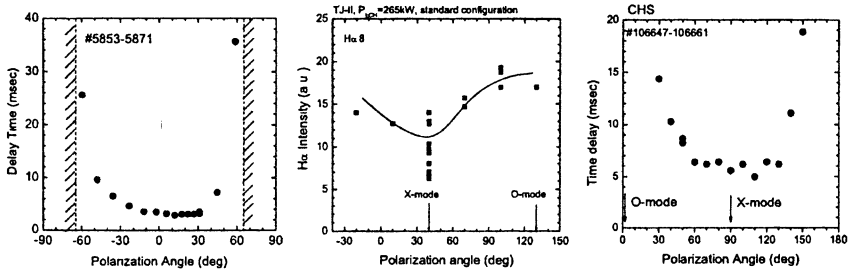

a *b* *c*

Fig. 2. Dependence of second harmonic plasma breakdown on wave polarization in (*a*) Heliotron J, (*b*) TJ-II and (*c*) CHS.

Figure 2 shows the dependence on the polarization of EC waves. In all devices, the shortest time delay is obtained for the X-mode polarization, and it is

longer as the X-mode fraction is decreased. In Heliotron J and CHS, no breakdown occurs when the X-mode fraction is less than a critical value of total ECH power. This power is close to the threshold power in the power scanning experiment. The experimental results indicate that the X-mode polarized waves have a dominant role rather than the multireflected absorption. In the fundamental plasma breakdown, on the other hand, no polarization dependence is observed. The time delay is short ~1 ms compared to the second harmonic plasma breakdown.

To investigate how the change in position of the interaction volume affects the plasma breakdown and where the plasma is produced, the crossing point between the ECH beam and the resonance layer is shifted from on-axis to off-axis in Heliotron J. The breakdown occurs earlier when the crossing point is located on axis. It is delayed when moving the crossing point toward the edge region. A similar dependence is found in the magnetic field scan. The time delay becomes shorter and the peak H_α intensity is high when the crossing position is near the magnetic axis. The position of snake plasma moves as the resonance layer is shifted. As shown in Fig. 3, the snake plasma is generated on axis when the resonance layer is located near magnetic axis, and it moves outward as the resonance is shifted from the center. The snake position agrees with a calculation of magnetic field line tracing.

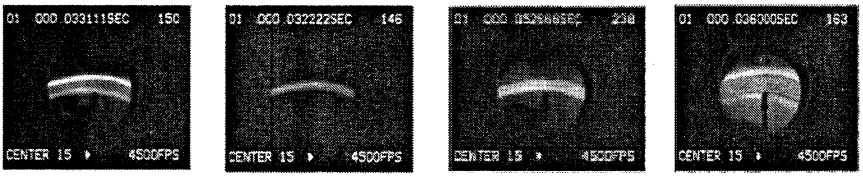

a *b* *c* *d*

Fig. 3. Horizontal views of initial plasmas in Heliotron J at $\omega_0/\omega = 0.46$ (*a*), $\omega_0/\omega = 0.48$ (*b*), $\omega_0/\omega = 0.50$ (*c*) and $\omega_0/\omega = 0.5$ (*d*).

The emission detected by the H_α array when all the power is coupled to the O-mode is represented in Fig. 4. A shift of the breakdown time (breakdown propagation) is observed. No delay occurs between core channels covering around 1.5 cm of plasma. This is consistent with the beam size at the resonance crossing point. The rest of channels show an increasing delay as the H_α line of sight moves towards the edge. The maximum delay occurs for the last channel in the O-mode case.

The Heliotron J device has a high flexibility to change the magnetic field spectrum. It is theoretically predicted that the bumpiness (mirror ripple) component has a strong influence on the particle confinement [13]. Figure 5 shows the plasma breakdown characteristics as a function of the bumpiness. The components, B_{04} and B_{14}, correspond to the bumpiness and the helicity, respectively. In the bumpiness scanning experiment, the rotational transform and plasma vol-

ume are set as almost unchanged. To study the role of accelerated electrons generated by ECH on the breakdown phase, the bumpiness is changed by controlling the ratios of coil currents. As the bumpiness decreases, the time delay is longer, and the breakdown is considerably delayed when the bumpiness is around zero. This result indicates that the control of bumpiness affects the breakdown through the confinement of accelerated electrons.

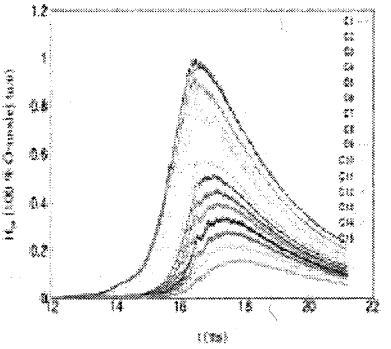

Fig. 4. Time evolution of 15 channel H_α signals in TJ-II

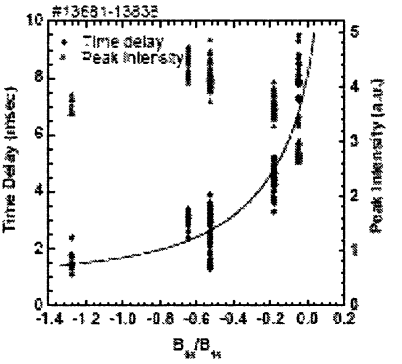

Fig. 5. Dependence of time delay on bumpiness components in Heliotron J

4. Conclusion

The plasma breakdown by using second harmonic ECH has been studied experimentally in Heliotron J, TJ-II and CHS. The experiment scanning the wave polarization indicates a common feature that the plasma breakdown is early when the X-mode polarization is chosen as the launching mode. The electric field of local EC beam is responsible for plasma production rather than the multi-reflected field. The condition for effective plasma breakdown is that the crossing point should be located on the magnetic axis with a large bumpy field component. This implies that the confinement of accelerated electrons generated by ECH is important for the second harmonic ECH plasma breakdown.

References

1. Carter M.D., et al , Nucl. Fusion, 27 (1987), 985.
2 *Cappa Á., et al*, Nucl. Fusion, 41 (2001), 363.
3. *Cappa Á., Castejón F.*, Nucl. Fusion, 43 (2003), 1421.
4 *Lloyd B., et al.*, Plasma Phys. Contr. Fusion, 38 (1996), 1627.
5 *Kajiwara K., et al.*, Nucl Fusion, 45 (2005), 694.
6 *Shidara H., et al* , Fusion Science and Technology, 45 (2004), 41.
7. *Fenández A , et al* , Int. J. IRMMW, 22 (2001), 649
8. *Yoshimura Y*, J. Plasma Fusion Res SERIES, 6 (2004).
9. *Nagasaki K , et al* , Nucl Fusion, 45 (2005), 13.
10. *Cappa Á , et al.*, 32nd EPS Conf , Tarragona, 2005
11. *Yokoyama M., et al.*, Nucl. Fusion, 40 (2000), 261.

TRANSPORTATION OF RADIATION THROUGH OPAQUE MAGNETOACTIVE PLASMAS BY MEANS OF PARAMETRICALLY INDUCED TRANSPARENCY

A.Yu. Kryachko, M.D. Tokman, E. Westerhof[1]

Institute of Applied Physics Russian Academy of Sciences, Nizhny Novgorod, Russia
[1]FOM-Institute for Plasma Physics Rijnhuizen, Association EURATOM-FOM, Trilateral Euregio Cluster, The Netherlands, www.rijnh.nl

We discuss the applications of the effect of parametrically induced transparency for diagnostics of dense toroidal plasma. We investigate the nonlinear mode conversion in inhomogeneous medium, which significantly influences on the whole effectiveness of the scheme. Numerical calculations are provided for the parameters corresponding to the TEXTOR tokamak.

Introduction

One of the traditional applications for the nonlinear theory of electromagnetic waves is the transport of radiation through an opaque medium [1]. In references [2–5] it was proposed to perform this transport by means of the "classical" version of electromagnetically induced transparency (EIT). EIT is a variant of 3-wave interaction in a nonlinear medium when the appropriate synchronism conditions are fulfilled for the frequencies and wave vectors of the waves (see e. g. [6]). In particular, the possibility of nonlinear transport of radiation through a non-transparent toroidal plasma in the region of upper-hybrid resonance (UHR) was considered in [5]. As it was proposed in [5], the signal wave (s-wave) is carried through the opaque plasma region by beating between the drive wave (d-wave) and a quasi-electrostatic "transporting" wave (t-wave). The t-wave is excited by the beating between s-wave and d-wave at the boundary of the opaque region.

In real applications it is difficult task is to provide the focused high-power drive wave over the whole opaque region. But significant simplification is possible if the t-wave is electromagnetic and its group velocity never comes to zero in plasma. In this case it is necessary to apply the drive only in the region of effective nonlinear interaction between s-wave and t-wave. Then exited t-radiation will go to the vacuum and the s-wave intensity can be determined via the appropriate postprocessing of received t-radiation (because the amplitude of s-wave unambiguously determines the amplitude of excited t-wave). We call this variant parametrically induced transparency (PIT). We discuss the possibility to apply the PIT scheme in plasma diagnostics for getting the information about the intensity of spontaneous emission, "separated" from the vacuum by an opaque region near the surface of UHR in dense toroidal plasma.

Effectiveness of transformation in inhomogeneous plasma

We will consider the propagation of monochromatic waves in a weakly inhomogeneous and a weakly nonlinear medium without thermal dispersion

(i. e. the tensor of dielectric permittivity is hermitian and does not depend on the wave vector **k**) with the 3-wave synchronism conditions, corresponding to the LF drive (this case is investigated the most detailed):

$$\omega_t = \omega_s + \omega_d\,,\ \mathbf{k}_t = \mathbf{k}_s + \mathbf{k}_d\,. \tag{1}$$

In a weakly inhomogeneous medium the following small parameter can be introduced: $\mu = (k_{s,t,d}L)^{-1}$ and the waves and polarization of the medium can be represented, using the approach of geometrical optics:

$$\begin{cases} \mathbf{E} = \mathrm{Re}\sum_{j=s,t,d}\mathbf{e}_j(\mathbf{r})A_j(\mathbf{r})\exp\left(i\int\mathbf{k}_j\mathbf{dr} - i\omega_j t\right), \\ \mathbf{P} = \mathrm{Re}\sum_{j=s,t,d}\mathbf{P}_j(\mathbf{r})\exp\left(i\int\mathbf{k}_j\mathbf{dr} - i\omega_j t\right). \end{cases} \tag{2}$$

Here, L is the scale length of inhomogeneity, $\mathbf{e}_{s,t,d}$ are the unit linear polarization vectors of the waves,

$$\begin{aligned} \mathbf{P}_s &= \hat{\chi}_0^s\mathbf{e}_s A_s + \hat{\chi}^s\mathbf{e}_t\mathbf{e}_d^* A_t A_d^* \exp\left(-i\int(\mathbf{k}_s + \mathbf{k}_d - \mathbf{k}_t)\mathbf{dr}\right), \\ \mathbf{P}_t &= \hat{\chi}_0'\mathbf{e}_t A_t + \hat{\chi}'\mathbf{e}_s\mathbf{e}_d A_s A_d \exp\left(i\int(\mathbf{k}_s + \mathbf{k}_d - \mathbf{k}_t)\mathbf{dr}\right), \end{aligned} \tag{3}$$

$\chi^{s,t}{}_{0pm}$ and $\chi^{s,t}{}_{pmn}$ are the two-index linear and three-index nonlinear susceptibility tensors. If the coupled wave equations, describing the propagation of the waves, are ordered in the parameter μ and only terms linear in μ and retained, one can obtain the following system of coupled equations:

$$\begin{cases} \mathbf{p}_s\nabla A_s + \dfrac{A_s}{2}\mathrm{div}\,\mathbf{p}_s = i\dfrac{\omega_s}{4}\mathbf{e}_s^*\hat{\chi}^s\mathbf{e}_t\mathbf{e}_d^* A_t A_d^* \exp\left[i\int(\mathbf{k}_t - \mathbf{k}_d - \mathbf{k}_s)\mathbf{dr}\right], \\ \mathbf{p}_t\nabla A_t + \dfrac{A_t}{2}\mathrm{div}\,\mathbf{p}_t = i\dfrac{\omega_t}{4}\mathbf{e}_t^*\hat{\chi}'\mathbf{e}_s\mathbf{e}_d A_s A_d \exp\left[-i\int(\mathbf{k}_t - \mathbf{k}_d - \mathbf{k}_s)\mathbf{dr}\right]. \end{cases} \tag{4}$$

Here, $\mathbf{p}_{s,t} = (c^2/16\pi\omega_{s,t})d\lambda_{s,t}/d\mathbf{k}_{s,t}$, $\lambda_{s,t}(\omega_{s,t},\mathbf{k}_{s,t})$ are the eigenvalues of operator $D^{s,t}{}_{pm} = k^2_{s,t}\delta_{pm} + (k_{s,t})_p(k_{s,t})_m - (\omega^2_{s,t}/c^2)\varepsilon^{s,t}{}_{pm}$ (see [7]), $\varepsilon^{s,t}{}_{pm} = \delta_{pm} + 4\pi\chi^{s,t}{}_{0pm}$ is a linear tensor of dielectric permittivity of the medium, δ_{pm} is the Kronecker tensor, c is the velocity of light. When the nonlinear right-hand side terms in (4) are zero, these equations have integrals $\mathrm{div}(\mathbf{p}_{s,t}|A_{s,t}|^2) = 0$, describing the conservation law for energy fluxes $\mathbf{I}_{s,t} = \mathbf{p}_{s,t}|A_{s,t}|^2$ (see [7]). In the presence of nonlinear interaction, Eqs. 4 give the Manley – Rowe relations [6]:

$$\mathrm{div}\left(\mathbf{p}_s|A_s|^2/\omega_s + \mathbf{p}_t|A_t|^2/\omega_t\right) = 0\,, \tag{5}$$

describing the conservation of the number of quanta. For LF drive stimulated scattering from s-photons to t-photons occurs and the sum of quanta is preserved. Analogous relations exist when the modification of the number of d-photons is taken into account, but we neglect the back influence of the s- and t-waves on the drive wave.

Now we will consider a 1D problem, when the medium is inhomogeneous along the x-axis. Let the synchronism condition be satisfied in the whole space for the components of wave vectors perpendicular to x-axis, and at point $x = x_0$ for the components directed along x-axis. For a linear layer: $k_{sx} + k_{dx} - k_{tx} =$

$= \beta(x-x_0)$, β = const, the system (4) can be written as the well-known equation of a parabolic cylinder [8]:

$$d^2U/d\eta^2 + \left(\nu + 1/2 - \eta^2/4\right)U = 0. \qquad (6)$$

Here, $\nu = i16\pi^2[(d\lambda_s/dk_{sv})(d\lambda_t/dk_{tv})]^{-1}|A_d|^2|\chi^s_{pmn}(e_s)_p(e_t)_m(e_d)_n|^2/\beta$, $\eta = \beta^{1/2}(x-x_0)\times$ $\times\exp(-i\pi/4)$, $U = (p_{sv}/\omega_s)A_s\exp[(i/2)(\int(k_{sv}+k_{dv}-k_{tv})dx)]$.

Using the known properties [8] of Eq. 6 and requiring that in the limit $x\to\infty$ the solution corresponds to transmitted wave, one can obtain the following transformation coefficient $T_s = I_{s2}/I_{s1}$, determining the ratio between energy fluxes I_{s1} and I_{s2} of incident and transmitted waves respectively: $T_s = \exp(-2\pi|\nu|)$. For LF drive the incident photons are partially scattered into t-photons and $T_s < 1$. The coefficient of transformation into the t-wave $T_t = I_t/I_{s1}$ can be obtained using the Manley – Rowe equations (5): $T_t = (\omega_t/\omega_s)(1 - T_s)$. Here, I_t is the energy flux in the t-wave. For weak transformation $|\nu| << 1$ T_t has the form $T_t = (\omega_t/\omega_s)2\pi|\nu|$. Using the expressions for the nonlinear susceptibilities the value of T_t can be estimated as:

$$T_t \approx 2\pi\xi\omega_t\omega_s L/\left|k_s(x_0)V_sV_t\right|. \qquad (7)$$

Here, $\xi = (eA_d/mc\omega_d)^2$ is the dimensionless intensity of the drive wave, L is the inhomogeneity scale, $V_{s,t}$ are the group velocities of the waves, e and m are the electron charge and mass. The transformation coefficient is determined by quite complex relations and the values of L and $V_{s,t}$ should be calculated using the real profiles of plasma parameters. However, the calculation of T_t can be simplified. The nonlinear dispersion relation can be approximated by two hyperbolas in the vicinity of the point x_0: $[k_s(x)-k_s(x_0)-a_1(x-x_0)][k_s(x)-k_s(x_0)-a_2(x-x_0)] = \delta$ and the parameters of the approximation unambiguously determine the transformation coefficient:

$$T_t = \left(\omega_t/\omega_s\right)2\pi\delta/\left|a_1 - a_2\right|. \qquad (8)$$

Applicability of PIT scheme for toroidal devices

We performed 1D calculations to investigate the possibility of output of extraordinary mode from the region of UHR to the vacuum in a toroidal plasma in the low-field side (LFS) direction. The main aim of this section is to explore the possibility of a proof of principle experiment of the PIT regime in a tokamak. For the high power drive wave, such an experiment could make use of existing high power mm-wave sources that are being used for electron cyclotron resonance heating or current drive.

Let the x-axis of the Cartesian coordinate system be directed along the plasma density gradient, the z-axis coincide with the direction of the toroidal magnetic field, and the point $x = 0$ correspond to the plasma boundary on the LFS. For simplicity we assume, that all three waves propagate perpendicular to the external magnetic field, which is typical for toroidal devices. Let the signal wave and drive waves be extraordinary waves, so that the t-wave also is an extraordinary wave (because ordinary waves have orthogonal polarization and are

not excited). As an example the configuration and parameters, typical for the TEXTOR tokamak [9] were considered. The profiles of plasma density $N(x)$ and toroidal magnetic field $B(x)$ were chosen as follows:

$$N(x) = N_0\left\{1-(x-r_0)^2/r_0^2\right\},\ B(x) = B_0R_0/(R_0+r_0-x). \qquad (9)$$

Here, $R = 1.75$ m and $r_0 = 47$ cm are the major and minor radius of the tokamak, respectively. N_0 and B_0 are the plasma density and magnetic field in the center of the torus. The values of N_0 and B_0 can be varied in some range and will be specified further. It is assumed that the gyrotron radiation, used for plasma heating also plays the role of drive wave. This allows us not to have a separate source of high-power radiation for the PIT observation. For the current TEXTOR configuration the heating radiation is injected from the LFS and its frequency is of the order of the second EC harmonic: $\omega_d \sim 2\omega_{H0}$, $\omega_{H0} = eB_0/mc$.

The main idea of the diagnostic technique is the following. The plasma produces radiation at one of the EC harmonics, which is partially represented as electron Bernstein waves. These waves propagate to the UHR region and are transformed into extraordinary electromagnetic waves. An extraordinary wave is considered as the s-wave and during propagation from the UHR region toward the plasma center it is transformed into a t-wave by the means of PIT. In rare plasma ($\omega_{p0}^2 < \omega_s^2 - \omega_{H0}^2$) the opaque region for the signal wave is situated only on the low-field part of the plasma, therefore the signal wave can be observed on the high-field side (HFS) of the torus by standard means without usage of PIT. Real applications of PIT look much more promising in dense plasma ($\omega_{p0}^2 > \omega_s^2 - \omega_{H0}^2$), when the opaque region for the s-wave has the form of a "ring", surrounding the plasma center and therefore the signal wave is "trapped" inside the plasma. The PIT scheme can be a good solution here to "extract" this "trapped" spontaneous emission of Bernstein waves to the vacuum. For the parameters considered the conditions of dense and rare plasma are fulfilled for LF and HF drive, respectively.

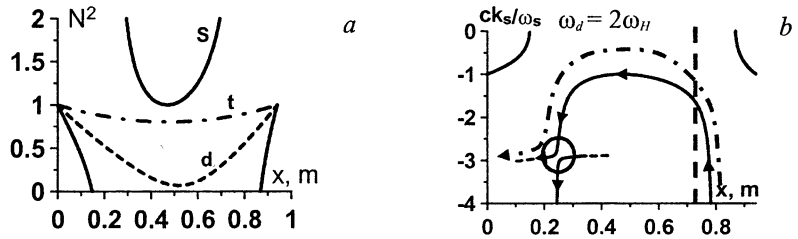

Fig. 1. PIT in a dense plasma: *a* – linear refractive indices for the s-, t- and d-waves; *b* – nonlinear PIT dispersion curves for the s-wave. The circle shows the region of transformation. The place is shown, where heating is applied ($\omega_d = 2\omega_H$). $\xi = 2.5\cdot10^{-4}$, $\omega_d = 2\pi\cdot160$ GHz, $\omega_s = 2\pi\cdot120$ GHz, $\omega_t = 2\pi\cdot280$ GHz, $N_0 = 10^{14}$ cm^{-3}, $B_0 = 2.3$ T.

Figure 1 shows the dispersion curves for LF drive (dense plasma). The dash-dotted arrow shows how the wave propagates from the UHR region at the HFS. In the beginning this is the emission at frequency ω_s and then in the pres-

ence of the drive the wave at LFS is transformed into the t-wave, which propagates toward the plasma boundary and goes to the vacuum. The transformation coefficient T_t here is one of the most important characteristics, determining the effectiveness of the PIT scheme. For a drive intensity I_d = 100 kW·cm^{-2} the conversion efficiency T_t, calculated from Eq. 8, is of the order of $5 \cdot 10^{-2}$. The theoretical estimations, according to the Eq. 7, give a value of the same order. The values of distance L and group velocities $V_{s,t}$ are the following: L = 3 cm, $V_s = 0.008\ c$, $V_t = 0.9\ c$.

The investigations performed show that if the size of tokamak or the energy flux of the drive is increased by 10 times (the new energy flux is then I_d = 1 MW cm^{-2}), then up to 30% of radiation power can be transported from the UHR region. But even for the given parameters the conversion efficiency T_t seems to be high enough for the stable observation of t-wave against the plasma noise background at frequency ω_t:

$$T_t >> \max\left(\tau_C, \tau_4\right). \qquad (10)$$

Here, $\tau_C \sim k_t r_0 \gamma_C / \omega_t$ and $\tau_4 \sim \pi (T/mc^2)^3 (\omega_p/\omega_{H0})^2 k_t R_0$ are the collisional plasma optical depth (determined by Coulomb collisions) and collisionless one at frequency $\omega_t = 4\omega_{H0}$ respectively, T is the plasma temperature, γ_C is Coulomb collision frequency [10], $\omega_p = (4\pi e^2 N_0/m)^{1/2}$ is the electron plasma frequency. For T = 1 keV and other parameters as for Fig. 1 $\tau_C \sim 5 \cdot 10^{-5}$, $\tau_4 \sim 2 \cdot 10^{-3}$, which at least 1 order less than the value of T_t.

Conclusion. In this work we investigated the effect of PIT, which is a variant of parametric 3-wave interaction. This effect looks simpler and more promising for diagnostics applications in nuclear fusion, than "standard" electromagnetically induced transparency. The general theory of 3-wave interaction in an inhomogeneous medium is provided for the consistent investigation of PIT. We investigate the nonlinear mode conversion, which is critical for the effectiveness of the PIT scheme. Numerical calculations are provided for the parameters corresponding to the TEXTOR tokamak.

This work is supported in part under NWO-RFBR grant no. 047.016.016, ISTC grant no. A-1095 and RFBR grant no. 04-02-17042. A.Yu. Kryachko is also grateful to the "Dynasty" foundation for support.

References

1 *Litvak A.G.*, in Reviews of Plasma Physics, Ed by M A. Leontovich, Consultants Bureau, New York, 1986, **10**, 164.
2 *Gordon D.F*, *Mori W B*, *Joshi C*, Phys. Plasmas, **7**, 3145 (2000); **7**, 3156 (2000).
3. *Litvak A.G.*, *Tokman M D*, Phys. Rev. Lett., **88**, 095003 (2002).
4. Kryachko A Yu , Litvak A.G., Tokman M.D , Nucl Fusion, **44**, 414 (2004).
5 *Kryachko A Yu.*, *Tokman M.D.*, Plas. Phys. Rep., **31**, 229 (2005).
6. *Bloembergen N*, Nonlinear Optics, Benjamin, New York, 1965.
7 *Tokman M.D*, *Westerhof E.*, *Gavrilova M A.*, Nucl. Fusion, **43**, 1295 (2003).
8 *Yanke E*, *Emde F.*, *Lesh F.*, Spccial Functions, Nauka, Moscow, 1977.
9 *Samm U*, Fusion Sci. Technol., **47** (Special Issue on TEXTOR), 73 (2005).
10. *Zheleznyakov V V*, Radiation in Astrophysical Plasmas, Kluwer Academic Publishers, Dordrecht/Boston/London, 1996

MODELLING OF O-X-B AND B-X-O CONVERSION OF ELECTROMAGNETIC RADIATION IN T-10 TOKAMAK PLASMAS

A. G. Shalashov, M. A. Balakina, E. D. Gospodchikov, O. B. Smolyakova

Institute of Applied Physics, RAS, Nizhny Novgorod, Russia

O-X-B conversion in tokamak plasmas is considered within the generalised geometrooptical approximation with taking into account the thermal and relativistic effects in a dielectric tensor. Relativistic effects are shown to be of importance for the cyclotron absorption of electron Bernstein wave generated in the O-X-B process. Plasma heating and spontaneous emission resulted from direct and inverse O-X-B processes are analysed in a particular case of T-10 tokamak.

1. Introduction

The problem of electron cyclotron resonance (ECR) heating and current drive in dense plasma has been widely discussed in connection with optimized stellarators and spherical tokamaks characterized by high plasma density confined at comparatively low magnetic field in which either incident electromagnetic waves could not propagate into the core plasma, or ECR absorption is inefficient. One of the promising ways to overcome this difficulty is based on linear conversion of the electromagnetic waves into the electrostatic electron Bernstein (EB) waves, which have no density cut-offs and are heavily damped in a wide range of cyclotron harmonics numbers.

EB waves may be effectively excited via so called O-X-B process proposed in [1, 2] and demonstrated in a number of experiments, e. g. [3–6]. In this scheme the ordinary (O) wave launched from the low field side transforms to the extraordinary (X) wave in the vicinity of the O mode cutoff surface. In order to provide high efficiency of O-X conversion the wave beam should propagate within a particular narrow angular range with respect to a static magnetic field. After transformation X wave continues propagation to the inner part of a plasma column; however with high enough plasma density the direction of propagation may reverse, so X wave reaches the upper hybrid resonance (UHR) layer at outer plasma region where secondary transformation occurs to EB wave propagating again towards the plasma center.

On the other hand, EB waves excited spontaneously in the core plasma may become observable due to the linear conversion (in particular, due to inverse O-X-B process) into the electromagnetic waves capable of propagation in vacuum. This opens new possibilities of exploiting electron cyclotron emission for diagnostics of overdense plasmas [4, 7].

In this paper excitation, propagation and damping of EB waves in tokamak geometry is considered within the generalised ray tracing technique with taking into account thermal and relativistic effects in a dielectric tensor. The importance of such generalization is shown in Part 2; ray tracing code is described in Part 3; in Part 4 direct and inverse O-X-B processes are analysed in a particular case of T-10 tokamak.

2. Relativistic effects on a wing of a cyclotron absorption line

A specific feature of O-X-B process is excitation of strongly damped EB waves propagating with large values of longitudinal refractive indexes with respect to a static magnetic field. This may be understood having in mind that longitudinal refractive index is slowly varying in a tokamak geometry and it should be close to the optimal value $N_{\|} \sim 1$ on the critical surface to provide effective O-X transformation. Therefore, resonant interaction occurs far from the relativistic cutoff, i.e. $\upsilon_{\|} << N_{\|} c$, and the resonant velocity is mainly determined by the non-relativistic Doppler condition, $\upsilon_{\|} = (\omega - n\omega_{ce})/k_{\|}$, here all quantities have their usual meaning.

Let us compare non-relativistic and relativistic absorption coefficients under conditions of strong cyclotron damping when rf power is deposited mainly to energetic electrons. The non-relativistic absorption coefficient in a Maxwellian plasma may be expressed as follows:

$$\mu_c^{nonrel} = A \exp(-\upsilon_{\|}^2 / \upsilon_e^2), \quad \upsilon_e = (2T_e / m_e)^{1/2} \tag{1}$$

where υ_e is the electron thermal velocity, A is slowly varying coefficient assuming that the condition $\upsilon_{\|} >> \upsilon_e$ is fulfilled. Neglecting the perpendicular electron velocity in the relativistic ECR condition ($\upsilon_{\perp} \approx \upsilon_e << \upsilon_{\|}$), one can obtain relativistic formula for absorption coefficients,

$$\mu_c^{rel} \approx A' \exp(-\upsilon_{\|}'^2 / \upsilon_e^2), \quad \upsilon_{\|}' \approx \upsilon_{\|} + \upsilon_{\|}^2 / (2N_{\|} c) \tag{2}$$

that differs from the non-relativistic Eq. (1) only by definition of the resonant velocity, $\upsilon'_{\|}$, in which relativistic mass factor γ is taken into account. With accuracy of the order of $\upsilon_{\|} / (N_{\|} c) << 1$, one can consider that $A = A'$. Finally, the ratio between relativistic and non-relativistic absorption coefficients may be approximated by the simple equation [8, 9]:

$$\mu_c^{rel} / \mu_c^{nonrel} \approx \exp[-\upsilon_{\|}^3 / (N_{\|} c \upsilon_e^2)]. \tag{3}$$

Note, that relativistic modification of the resonant velocity is small compared to its value, but not necessary small compared to the thermal velocity. This results in significant modification of ECR absorption coefficient on a wing of the absorption line when $\upsilon_{\|}^3 / (N_{\|} c \upsilon_e^2) \geq 1$. More detailed study [8] shows that in inhomogeneous magnetic field the relativistic effects are important when condition

$$N_{\|} \leq (\upsilon_e / c) \ln^{3/2}(\tau / 2\sqrt{\pi}) \tag{4}$$

is fulfilled with τ being the total optical thickness of the plasma layer.

In a particular case of EB wave absorption in T-10 tokamak the term in square brackets in Eq. (1) is of the order of unity at the maximum of rf power deposition. Therefore the relativistic effects are essential for definition of power deposition profiles as illustrated in Fig. 1. Corresponding absorption coeffi-

cients obtained in non-relativistic and weakly relativistic assumptions differ approximately twice, which is in very good quantitative agreement with an estimation given by Eq. (3). Note that the main fraction of rf power is deposited to suprathermal electrons with longitudinal velocities 2 – 3 times greater than the thermal velocity.

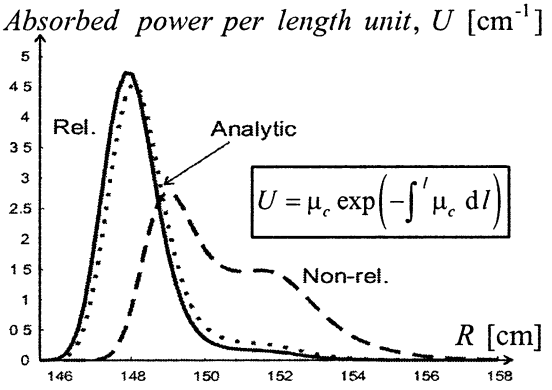

Fig. 1. Absorbed power as a function of the major radius: comparison of weakly relativistic (solid line) and non-relativistic (dash) calculations. Dots show analytical result corresponded to the absorption coefficient obtained by multiplication of the non-relativistic absorption coefficient by correcting factor defined by Eq. (3).

3. Weakly relativistic ray-tracing code

The ray-tracing code is based on the full-wave weakly relativistic dispersion relation for the perpendicular component of refractive index:

$$A(N_{\|}, N_{\perp}) \cdot \left[N_{\perp}^2 - X_1(N_{\|}, N_{\perp})\right] \cdot \left[N_{\perp}^2 - X_2(N_{\|}, N_{\perp})\right] = 0. \qquad (5)$$

Here term A defines the hot electrostatic EB wave, X_1 and X_2 define propagation of two electromagnetic waves, in cold plasma limit the coefficients do not depend on $N_{\perp}$. Definition of these coefficients and more detailed description of the code one can find in [9, 10]. Keeping $N_{\|}$ as a parameter allows imposing this quantity to be real valued what greatly simplifies numerical calculations of the relativistic dispersion functions.

For three branches of Eq. (5) the ray Hamiltonians D_i may be composed in the form, that allows standard ray tracing calculations of the trajectory corresponded to the total O-X-B process:

$$\frac{d\mathbf{r}}{ds} = \frac{\partial D_i}{\partial \mathbf{N}}, \quad \frac{d\mathbf{N}}{ds} = -\frac{\partial D_i}{\partial \mathbf{r}}, \quad D_{1,2} = \mathrm{Re}(N_{\perp}^2 - X_{1,2}), \; D_3 = \mathrm{Re}\, A. \qquad (6)$$

Propagation of O wave from the vacuum up to the cutoff region where the O-X transformation occurs and propagation of X wave from the cutoff to the turning point (where $\partial\omega / \partial N_{\perp} = 0$) is described by Hamiltonian D_1; further propagation

of X wave up to UHR is described by D_2; propagation of EB wave from UHR layer is described by D_3. For not ideal conditions for the O-X transformation, the ray trajectory breaks due to evanescent region which is present in the vicinity of O mode cutoff. In this case we trace the O wave ray up to the reflection point, then make a jump through the evanescent region in the direction of ∇n_e, then start a new ray for X wave with the same $N_{||}$, for more details see [9]. After ray is defined, the radiative transport equation is solved along the ray modelling O-X-B heating or spontaneous B-X-O emission with the thermal emissivity and absorption coefficient being assumed.

4. O-X-B heating and B-X-O radiation in T-10 tokamak plasma

Modelling experimental conditions at T-10 tokamak we shall use the following reference parameters: major radius 150 cm; minor radius 30 cm; on-axis magnetic field 2.5 T (corresponds to gyrofrequency 70 GHz); central electron temperature 0.9 keV and plasma density 10^{14} cm^{-3}; O-X-B heating is provided by a gyrotron source with frequency 83 GHz.

A typical ray trajectory and dispersion curve corresponded to this set of parameters are shown in Fig. 2. Point *A* marks the position of O-X transformation at the critical (O mode cutoff) surface; *B* marks the X mode turning point; *C* marks the position of X-B transformation at UHR layer; *D* marks the maximum rf power deposition point.

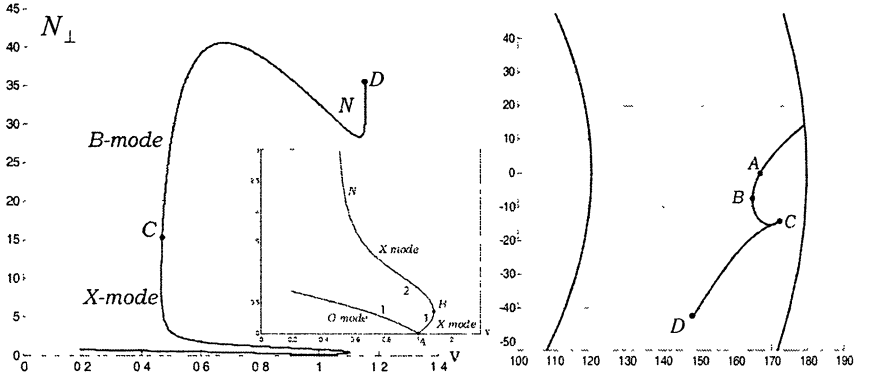

Fig. 2. Left: $N_\perp$ as a function of $\upsilon = (\omega_{pe}/\omega)^2$ along the ray, right: the ray trajectory viewed from a top of toroidal chamber for O-X-B process at T-10 tokamak.

Ray tracing calculations show that at T-10 tokamak O-X-B converse-on may be realised in a fairly broad range of parameters. Some examples are presented in Fig. 3, where flux surface coordinate and relative width of the ECR interaction region is plotted. Figure 3, *a* illustrates the idea that localisation of power deposition during O-X-B heating experiment may be naturally controlled by variation of a magnetic field strength in the installation. Figure 3, *b* is more

relevant to electron cyclotron emission diagnostics based on B-X-O process – it is shown the position of spontaneous emission region for EB waves at different frequencies. Like in usual ECE diagnostics, plasma cord may be scanned with acceptable localisation varying the frequency of the receiver, what opens possibility, e. g., for electron temperature diagnostics inside the overdense plasma region based on B-X-O conversion.

Variation of parameters on both plots in Fig. 3 is limited by appearance of "exotic" situations that break O-X-B scheme. For example, at low magnetic field EB waves are poorly absorbed due to ECR layer being too far. Instead of being absorbed, EB waves meet UHR layer where they transform to X waves, and then the process repeats. So combination of X and EB waves gets trapped inside the UHR layer. Another situation realises with radiation frequency increase, when the X wave turning point (point *B* in Fig. 2) corresponds to the plasma density which is higher than the central plasma density. In this case, after O-X transformation slow X wave can not reach UHR layer and gets trapped inside the O mode cutoff surface.

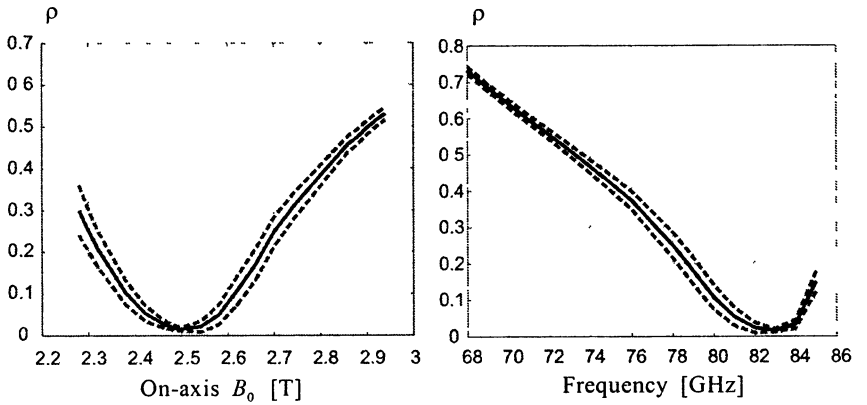

Fig. 3. Position of the center (solid line) and characteristic width (dash) of the ECR interaction region: left – dependence on a static magnetic field strength at the fixed frequency 83 GHz, right – dependence on a frequency for the fixed on-axis magnetic field 2.5 T. Vertical axis shows normalised effective radius of a flux surface.

Both aforementioned "exotic" regimes are characterized by non-local power absorption (with a low local damping rate but quite long radiation path due to the trapping). Therefore such regimes seem to be mainly of theoretical interest.

5. Conclusions

Generalised geometro-optical ray tracing approach is considered with taking into account all thermal and relativistic effects in the plasma dielectric tensor in application to modelling of O-X-B processes in hot plasmas. It is shown

that even at rather moderate electron temperatures (about 1 keV) the relativistic effects are essential at calculation of the cyclotron absorption of electron Bernstein waves.

Direct and inverse O-X-B processes are analysed in a particular case of T-10 tokamak. Localisation of the power deposition profiles for O-X-B plasma heating at frequency 83 GHz is identified. Emission of spontaneously excited Bernstein waves resulted from B-X-O conversion is studied, and possibility is demonstrated of local electron temperature measurements inside the overdense plasma region at the central flux surfaces by means of registration of B-X-O spectra in the 68–85 GHz range.

Acknowledgements

Authors gratefully acknowledge Prof. M. D. Tokman for the valuable discussions. The work is supported by RFBR grant No. 03-02-17466 and NWO–RFBR grant No. 047.016.016 (04-02-89005 HBO-a).

References

1. *Preinhalter J., Kopečky V.*, J. Plasma Phys., 1973, **10**, 1.
2. *Maekawa T. et al.*, Phys Rev. Lett., 1978, **40**, 1379.
3. *Laqua H.P. et al.*, Phys. Rev. Lett., 1997, **78**, 3467.
4. *Laqua H.P. et al.*, Plasma Phys. Contr. Fusion, 1999, **41**, A273.
5. *Pinsker R.I. et al.*, AIP Proc., 2001, **595**, 350.
6. *Shevchenko V.F. et al.*, Phys. Rev. Lett , 2002, **89**, 265005.
7. *Shevchenko V.F. et al.*, Plasma Phys. Rep., 2000. **26**, 1000.
8. *Shalashov A.G., Gospodchikov E.D* , To the theory of cyclotron absorption on a wing of line (submitted to Plasma Phys. Rep., 2005).
9. *Balakina M.A., Shalashov A G., Gospodchikov E D., Smolyakova O.B.,* Geometrooptical modeling of the O-X-B conversion of electromagnetic radiation in tokamak plasmas: Report of IAP RAS № 677, Nizhny Novgorod, 2005 (in Russian).
10. *Balakina M.A. et al.*, Plasma Phys. Rep., 2003, **29**, 53.

MICROWAVE DISCHARGES IN GASES AND OTHER APPLICATIONS OF HIGH-POWER MICROWAVES

DEVELOPMENT OF MPACVD TECHNOLOGY FOR HIGH-RATE DIAMOND PRODUCTION

A. L. Vikharev, A. M. Gorbachev, A. V. Kozlov, V. A. Koldanov, A. G. Litvak, N. M. Ovechkin, Yu. V. Bykov, G. G. Denisov, V. V. Parshin, D. B. Radishev

Institute of Applied Physics RAS, Nizhny Novgorod, Russia

The paper reviews the results of investigations of polycrystalline diamond film deposition in MPACVD reactors at 2.45 GHz frequency and in novel MPACVD reactor based on 10 kW gyrotron operating at frequency 30 GHz. The influence of increasing the operating frequency of microwaves in CVD reactor that exceeds the conventionally used frequency 2.45 GHz on diamond deposition process is discussed. Polycrystalline diamond films were grown on silicon substrates with 40–75 mm diameter. The growth rate of diamond films, their quality and morphology at wide variation of process parameters (gas pressure, substrate temperature, microwave power, methane concentration) in different gas mixtures were investigated. The diamond growth processes in 2.45 GHz and 30 GHz MPACVD reactors are compared.

Introduction

Among the various techniques for chemical vapor deposition (CVD) of diamond films (DFs), the microwave plasma-assisted CVD (MPACVD) has gained the widest application [1, 2]. Currently, several types of MPACVD reactors are commonly used. They differ in the shapes of the reaction chambers, and, correspondingly, the geometry of the electromagnetic field in the area of plasma formation near the substrate [3–5]. These devices are resonance-type reactors, and the plasma in them is produced in the shape of a sphere or hemisphere. The diameter of the homogeneous plasma near the substrate does not exceed a half of the wavelength. The plasma is maintained by microwave radiation that has frequency of 2.45 GHz or 915 MHz. Therefore, the largest diameters of the grown diamond films are 60–75 mm and 100–120 mm, respectively. In these CVD reactors high quality diamond films (having thermal conductivity 15–18 W/cm·K) are grown at the low rate of 1–2 μm/h. As a result, artificial CVD diamond in spite of its unique properties is not wide used material. Wide application of CVD diamond films specially in electronic devices and optics could be expected if the following conditions of diamond coating process will be carried out simultaneously: the deposition rate is higher than 10 μm/h, the size of diamond film area is larger than 100 cm^2 and growth of quality diamond films with high thermal conductivity and optical transperancy occurs. For obtaining such diamond film growth the novel millimeter wave plasma-assisted CVD reactor was suggested [6].

In this paper the results of investigations of polycrystalline diamond film deposition in MPACVD reactors at 2.45 GHz frequency and in novel MPACVD reactor based on 10 kW gyrotron operating at frequency 30 GHz are

presented. Polycrystalline diamond films are grown on silicon substrates with 40–75 mm diameter. The growth rate of DFs, their quality and morphology at wide variation of process parameters (gas pressure, substrate temperature, microwave power, methane concentration) in gas mixtures H_2/CH_4 and $Ar/H_2/CH_4$ are investigated. The diamond quality is characterized using Raman Spectroscopy and Atomic Force Microscopy. The diamond growth processes in 2.45 GHz and 30 GHz MPACVD reactors are compared.

Methods of improvement CVD technology

In order to introduce quality diamond films into wide application, it is necessary to improve the technique of the deposition in order to increase the growth rate. Two methods could be considered for improvement of polycrystalline diamond film deposition: 1) operation with pulse-periodical plasma generation in traditional 2.45 GHz frequency band, 2) operation with CW plasma generated by microwaves with sufficiently higher frequency than the conventionally used frequency 2.45 GHz, for example, at frequency 30 GHz. Let us consider the specific features of mentioned methods.

The growth rate of DF in MPACVD reactor is determined by the values of concentrations of carbon-containing radicals and hydrogen atoms near the substrate [2]. In a pulsed microwave discharge with a relatively low repetition rate (up to several hundred hertz), the concentration of chemically active particles (hydrogen atoms and carbon-containing radicals) is appreciably modulated. According to results obtained in the papers [7, 8], the growth rate G and relative defect density X_{def} (that determines film quality) may be estimated by the following formulae:

$$G \propto \frac{[CH_3]_{sur}[H]_{sur}}{3\cdot 10^{15}\,\mathrm{cm}^{-3} + [H]_{sur}}, \quad X_{def} \propto \frac{G}{[H]^2_{sur}}. \tag{1}$$

Here, $[H]_{sur}$ and $[CH_3]_{sur}$ are the densities of hydrogen atoms and CH_3 radicals near the substrate surface, respectively. The gas-phase reaction $CH_4 + H \rightarrow \rightarrow CH_3 + H_2$ usually proceeds fairly rapidly; as a result, the density of CH_3 radicals is in equilibrium with the atomic hydrogen density. Therefore, dependences (1) are quadratic in the atomic hydrogen density, so the modulation of the atomic hydrogen density should result in an increase in G and/or a decrease in X_{def}, provided that the mean density is kept constant.

The specific features of the second method could be also explained on the basis of the formulae (1). The formulae (1) show that the diamond film quality and growth rate are determined by density of atomic hydrogen at the substrate surface. The main channel for dissociation of hydrogen molecules in MPACVD reactors, even at high temperatures of the gas ($T_g \sim 3000$–3200 K) is dissociation by an electron impact [9]. Therefore, an increase in the value of electron density, N_e, in the plasma of a CVD reactor should result in a higher density of atomic hydrogen.

The value of electron density N_e in the plasma maintained by the microwave field in resonance-type reactors [3–5] grows up to the point, at which the nonlinear effect of microwave field skinning starts to manifest itself. So, the characteristic dimension of the plasma at the substrate in a reactor is equal approximately to the depth of the skin layer. In the case of the parameters used traditionally in MPACVD reactors (gas temperature $T_g \sim 2700$–3000 K depending on the specific power absorbed into the plasma, and the initial pressure of the gas mixture 50–200 Torr) the density of the gas near the substrate corresponds to the minimum of the Pashen curve for maintenance of a continuous microwave discharge [10], at which the electron collision frequency is of the order of the wave frequency. Under the conditions when $\nu \geq \omega$ and $N_e \leq N_{c0}\nu/\omega$ the depth of the skin layer is equal to

$$\delta \approx 2(c/\omega)(N_{c0}/N_e)[(\omega^2+\nu^2)/\omega\nu], \qquad (2)$$

where $N_{c0} = m\omega^2/4\pi e^2$ is the critical density, ω is the wave frequency, ν is the electron collision frequency with neutral particles, and m and e are mass and charge of electrons, respectively. At a fixed depth of the skin layer (e. g. for resonance-type reactors this value is of the order of $\delta = \delta_0 \approx 1 \div 2$ cm) from the above relation for δ we obtain that the value of electron density in the plasma is proportional to the frequency of the microwave radiation:

$$N_e \propto N_{c0}(c/\delta_0\omega)[(\omega^2+\nu^2)/\omega\nu] \propto \omega. \qquad (3)$$

Hence, the densities of both the electrons and radicals in non-equilibrium plasma of MPACVD reactors may be increased with an increase in the frequency of microwave power. Due to a higher frequency of the microwave radiation, the plasma produced near the substrate will have higher electron density, and, correspondingly, higher density of radicals and atomic hydrogen, thus providing a higher rate of the diamond film growth as compared to the traditional plasma reactors with a microwave discharge.

Below the results of diamond growth in pulsed 2.45 GHz CVD reactor and in novel 30 GHz CVD reactor are presented.

Diamond growth in pulsed 2.45 GHz MPACVD reactor

In the series of experiments [11–13] the comparison of pulsed and CW regimes of MPACVD reactor operation was performed. The study had the aim to examine how the pulsed regime of maintaining the microwave plasma affects the plasma parameters, the density of atomic hydrogen and the diamond film growth rate in hydrogen-methane mixture.

Figure 1 shows a scheme of the experimental setup. The CVD reactor used in these experiments is similar in design to that designed at the Michigan State University [3]. The discharge was produced in cylindrical cavity *1* excited by the TM_{013} mode of coaxial waveguide *2* at a frequency of 2.45 GHz. The coax-

ial waveguide was connected to rectangular waveguide *3* and then to magnetron *5* through circulator *4*. Discharge *6* was bounded by quartz cell *7*, which was connected to vacuum chamber *8*. The reactor was equipped with automatic pump-out and let-in systems (9 and *10*, respectively), which held the gas flow rate and pressure inside the chamber at a fixed level. Both these systems and magnetron power supply *11* were controlled by PC *12*, which made possible long-term automated reactor operation.

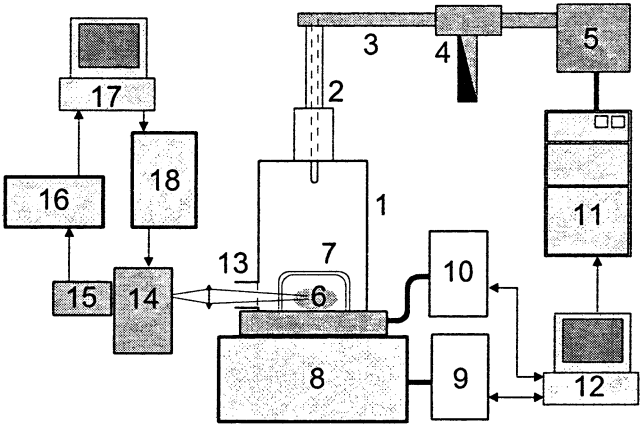

Fig. 1. Experimental setup: *1* – cylindrical cavity, *2* – coaxial waveguide, *3* – rectangular waveguide, *4* – circulator with the absorber of reflected microwaves, *5* – magnetron, *6* – microwave discharge, *7* – quartz cell, *8* – buffer vacuum volume, *9* – pump-out system, *10* – let-in system, *11* – magnetron power supply, *12* – control PC, *13* – diagnostic window, *14* – MDR-41 monochromator, *15* – photomultiplier, *16* – digital oscilloscope, *17* – PC, and *18* – monochromator controller.

The experimental setup was used to study diamond film synthesis in hydrogen-methane mixtures at pressures of 10–150 Torr. The methane concentration was varied from 0.1 to 10%, and the hydrogen flow rate was varied from 50 to 200 sccm. The 5-kW magnetron allowed stable discharge operation in both regimes. Experiments with continuous microwave discharges were carried out at incident powers of 1.5 and 3 kW. Experiments with pulsed discharges were carried out under the following conditions: the mean microwave power was 1.5 kW and 3 kW, the pulse duration was $\tau = 5$ ms, and the repetition rate was $F = 100$ Hz. Diamond films were deposited onto a 40 mm-diameter silicon substrates. The substrate temperature was measured by optical and IR pyrometers.

We compared the growth rate in the continuous and pulsed regimes of reactor operation at the same mean power 1.5 kW. The pressure in the pulsed regime was higher than in the continuous one and was chosen so as to make the visually observed dimensions of the plasma equal in both regimes. In that case the main specific power absorbed in the plasma and the substrate temperature

were also equal. In the continuous regime, the pressure was p = 50 Torr, whereas in the pulsed regime, it was p = 70 Torr. The growth rate was determined as the ratio of the mass of the film produced to the deposition time and the linear growth rate was calculated, assuming the diamond film to be uniform. Figure 2 shows the dependences of the growth rate on the methane percentage in the gas mixture for pulsed and continuous microwave discharges. It can be seen that, the results obtained for pulsed and continuous discharges at the same pressure (50 Torr) are generally the same; this is because the volume occupied by the discharge is large and, accordingly, the mean power density absorbed in the plasma is lower in the pulsed regime. As the gas pressure in the pulsed regime is increased to 70 Torr (in this case, the plasma volume and the mean absorbed power density are the same in both regimes), the DF growth rate in a pulsed discharge becomes larger than that in a continuous discharge.

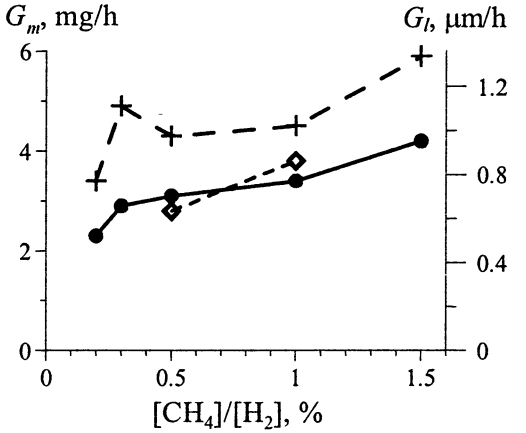

Fig. 2. Mass (left ordinate) and linear (right ordinate) growth rate of DFs vs. methane concentration in an H_2/CH_4 gas mixture in pulsed (crosses and diamonds) and continuous (circles) microwave discharges at a hydrogen flow rate of 200 sccm, gas pressures of 50 Torr (diamonds and circles) and 70 Torr (crosses), substrate temperatures of T_g = 880 °C (crosses and circles) and 850 °C (diamonds).

The DF growth rate depends on the atomic hydrogen density near the substrate surface (see formulae (1)). For this reason, it was necessary to compare the atomic hydrogen densities in continuous and pulsed microwave discharges. The atomic hydrogen density [H] was measured using the well-known actinometric method, which is based on the comparison of the radiation intensities of atomic hydrogen and an actinometer – a small admixture of a chemically inert gas to the gas mixture [14]. Figure 3 shows the atomic hydrogen density [H] determined under the conditions of our experiments on DF deposition. It can be seen that the maximal atomic hydrogen density in a pulsed microwave discharge at a pressure of 70 Torr (curve *1*) is considerably higher than that in a

continuous microwave discharge at a pressure of 50 Torr (curve *3*). In contrast, in a pulsed discharge at a pressure of 50 Torr, the maximal atomic hydrogen density is only slightly higher than that in a continuous discharge at the same gas pressure.

The results of measurements of the atomic hydrogen density can be used to explain the observed increase in the DF growth rate in a pulsed microwave discharge in comparison to that in a continuous discharge. We note that, during a microwave pulse, the atomic hydrogen density was several fold higher than the atomic hydrogen density in a continuous discharge (Fig. 3, curves *1*, *3*). Probably, the atomic hydrogen density averaged over the repetition period of microwave pulses was somewhat higher than that in a continuous discharge, since the DF growth rate was somewhat higher in a pulsed discharge (see formula (1)). The measurements of the atomic hydrogen density during the all repetition period of microwave pulses were made in paper [15]. These measurements confirmed the made conclusion.

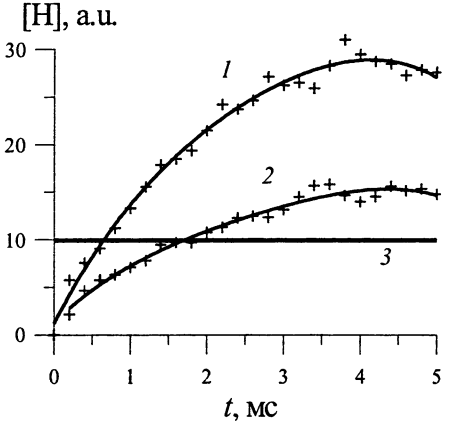

Fig. 3. Comparison of the atomic hydrogen densities in pulsed and continuous discharges used to study the DF growth rate (see Fig. 2): *1* – pulsed discharge at a pressure of 70 Torr, *2* – pulsed discharge at a pressure of 50 Torr, and *3* – continuous discharge at a pressure of 50 Torr.

We note that the pulsed and continuous regimes of the CVD reactor should be compared at different gas pressures at which the dimensions of the plasma glow, the mean absorbed microwave power, and the substrate temperature are the same in both regimes. At a mean power of 1.5 kW, this was the case at gas pressures of 50 and 70 Torr for the continuous and pulsed regimes, respectively. At the mean power of 3 kW the chosen pressures for comparison of CW and pulsed regimes were different: 90 and 130 Torr, respectively.

At the mean power of 3 kW the diamond depositions during long-term processes (100 hours) for the CW and pulsed discharges were carried out. Figure 4 shows the diamond disks with silicon substrates grown at CW and pulsed regimes. The thicknesses of diamond disks grown in CW and pulsed regimes were different – 120 and 550 μm, respectively. It means that growth rate in pulsed discharge was sufficiently higher than when we used CW discharge.

a *b*

Fig. 4. Photographs of the diamond disks with silicon substrates grown in CW (*a*) and pulsed (*b*) regimes, deposition time is 100 h in both cases.

The quality of the obtained diamond films was studied using Raman scattering spectra. The Raman spectra of the films were taken using a 514.5 nm Ar^+ laser operating at the beam power of 50 mW and a spectrometer with a CCD array. Figure 5 shows the Raman scattering spectra of two disks deposited at different regimes of CVD reactor operation.

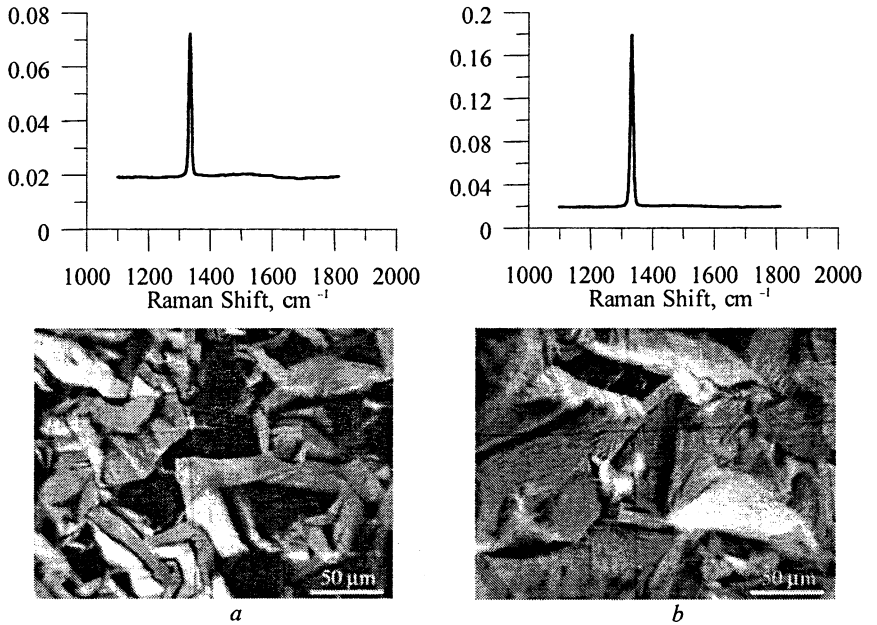

a *b*

Fig. 5. Raman scattering spectra and microphotographs of the surface of diamond disks grown in CW (*a*) and pulsed (*b*) regimes.

As it is seen in Fig. 5 both disks had very close texture. The quality of the disks in terms of Raman spectra was the same also. So the pulsed regime of CVD reactor operation demonstrated the higher growth rate of diamond disk than that in the CW regime without decreasing the diamond quality.

Diamond growth in millimeter wave CVD reactor

In comparison with resonance-type CVD reactors in the case when the plasma is created by means of short-wave microwave radiation, the required diameter of the plasma near the substrate exceeds the length of the electromagnetic wave significantly. Therefore, production of the plasma using short-wave microwave radiation with higher frequency than 2.45 GHz can be realized only with the use of an electrodynamic system of the quasi-optical type.

Figure 6 shows a general schematic diagram of the developed 30 GHz gyrotron-based system for diamond film deposition. The plasma layer near the substrate is formed by means of a microwave discharge in four crossing wave beams. An area of enhanced field intensity is formed in the region where four beams are intersecting in pairs, and where the steady-state microwave discharge is sustained. By changing the shape and the diameter of the transverse cross-section of the beams one can control the dimensions and shape of the plasma.

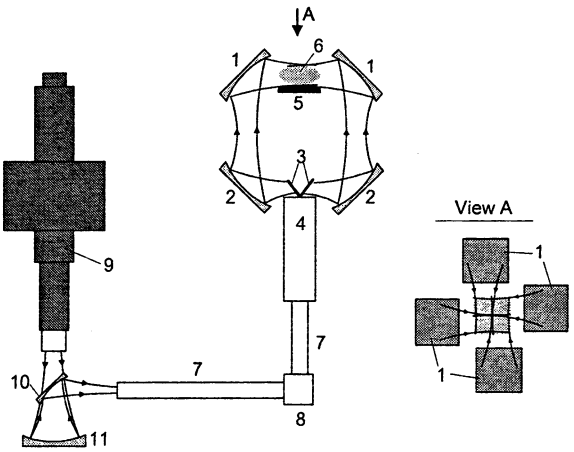

Fig. 6. Schematic diagram of the gyrotron-based system: *1* – top focusing mirrors, *2* – bottom focusing mirrors, *3* – plane mirrors, *4* – wave beam spliter, *5* – substrate, *6* – plasma maintenance region, *7* – circular corrugated waveguide, *8* – mitre bend, *9* – gyrotron, *10* and *11* – mode converter into a Gaussian beam.

In this gyrotron-based system the four focusing mirrors *1* direct the microwave radiation into the area over the substrate *5*, near which the plasma is main-

tained. In its turn, the radiation is transferred to mirrors *1* by means of the system of mirrors *2* and *3*. Formation of four coherent beams takes place at the output from the oversized square waveguide *4* due to the effect of image multiplication during propagation of an electromagnetic wave [16]. The quasi-Gaussian beam is delivered to the input of waveguide *4* from an oversized circular waveguide with a corrugation surface *7*. Such a waveguide provides propagation of an electromagnetic wave with the nearly Gaussian transverse distribution of the field. In its turn, the linearly polarized microwave radiation from the gyrotron *9* in the form of a Gaussian beam is sent to the input of this waveguide *7* by means of mirrors *10* and *11*.

A plasma reactor is a part of the gyrotron-based system, Fig. 7. In the reactor the microwave beams *2* are directed by mirrors *1* to the discharge area *3*. The substrate is positioned on the substrate holder *4* which is placed below the discharge area. The discharge area is restricted from above by a metal shield *5*. The working gas mixture *6* is fed into the plasma reactor through openings in the shield. The exhaust gas *7* is pumped out through openings in the substrate holder. The metal shield, substrate holder and some other elements of the plasma reactor are cooled by water *8*. The temperature of the substrate is controlled by means of a thermocouple positioned in an opening in the top part of the substrate holder *4*.

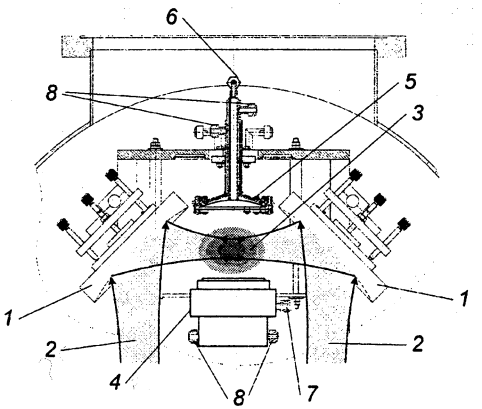

Fig. 7. Schematic diagram of the plasma reactor: *1* – focusing mirrors, *2* – wave beams, *3* – discharge area, *4* – substrate holder, *5* – metal shield, *6* – gas mixture feed-in, *7* – exhaust gas pump-out, *8* – water cooling channels.

For the deposition of diamond films the gas mixture $Ar/H_2/CH_4$ was chosen because of the possibility to grow polycrystalline as well as nanocrystalline diamond films by variation of the content of argon in the mixture [17]. The in-

vestigation of polycrystalline diamond film deposition was carried out at wide variation of process parameters. The content of methane in the three-component mixture varied in the range from 0.5% to 2%, and that of argon, from 50% to 75%, while the total gas flow was 400 sccm. The 30 GHz reactor could be operated across a range of the gas pressure from 100–400 Torr and input microwave power from 5 to 8 kW. Diamond films were grown on 2 mm thick (100) oriented silicon with 60–75 mm diameter. Before deposition process the silicon substrates were mechanically seeded with a 2 μm diamond powder. The duration of thin films deposition was 1–3 hours.

The average growth rate was determined based on the data about the mass of the deposited diamond film under the assumption that the film thickness is equal across the substrate surface. The growth rate is compared with respect to the variation of the methane concentration in Fig. 8. It shows a linear increasing trend with increasing CH_4 concentration at gas pressure 200 Torr and argon concentration of 75%.

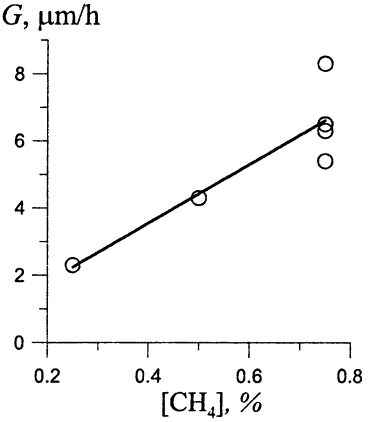

Fig. 8. The growth rate versus methane concentration at gas pressure 200 Torr.

The film morphology was observed using an optical- and an atomic force microscopes. The morphologies of polycrystalline diamond films were very much a function of the growth conditions. Optical microphotographs of two films grown with CH_4 concentration of 0.75%, substrate temperature 790–850 °C and gas pressure 200 Torr are shown in Fig. 9. Difference of growth temperature is reflected to the film texture. Figure 9 shows also the Raman scattering spectra from the center of two films deposited at different substrate temperature. The film quality in terms of Raman spectra decreased a little from the center to the edge of the films. But nevertheless this 30 GHz plasma reactor demonstrated the growth of high quality diamond films with a high rate.

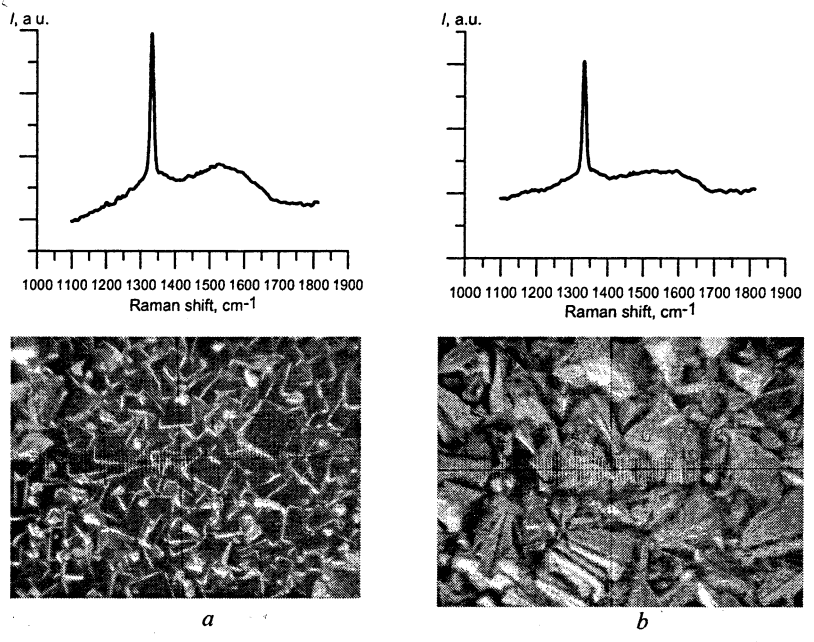

Fig. 9. Raman scattering spectra and microphotographs of the surface of diamond films grown in 30 GHz plasma reactor at different substrate temperatures: 800 °C (*a*) and 850 °C (*b*); deposition time is 3 h in both cases.

Comparison with results obtained in 2.45 GHz CVD reactor

In order to undertake a correct comparison between the diamond film deposition processes in the 2.45 GHz and 30 GHz reactors, a series of investigations of diamond film deposition has been carried out with the same gas mixture composition, pressure, gas flow rate, substrate temperature and the input microwave power. The 2.45 GHz ellipsoidal cavity reactor [4] has been selected for comparison. Shown in Fig. 10 are the Raman scattering spectra and microphotographs of surface of the films deposited with $Ar/H_2/CH_4$ gas mixture in two reactors. It should be noted that in the 2.45 GHz CVD reactor diamond film deposition was carried out during 8 hours at an average deposition rate of 1.9 μm/h, whereas in the 30 GHz CVD reactor diamond film deposition was carried out during 3 hours at an average deposition rate of 9 μm/h. In both reactors the process parameters were the following: gas pressure 200 Torr, substrate temperature 820 °C, input microwave power 6 kW, argon concentration 75%, methane concentration 0.75%. The accomplished experiments demonstrate that in the 30 GHz reactor the deposition rate is higher. This can be explained by the

fact that in the 30 GHz reactor the discharge was located along the substrate and the discharge power density (W/cm^{-3}) was sufficiently higher.

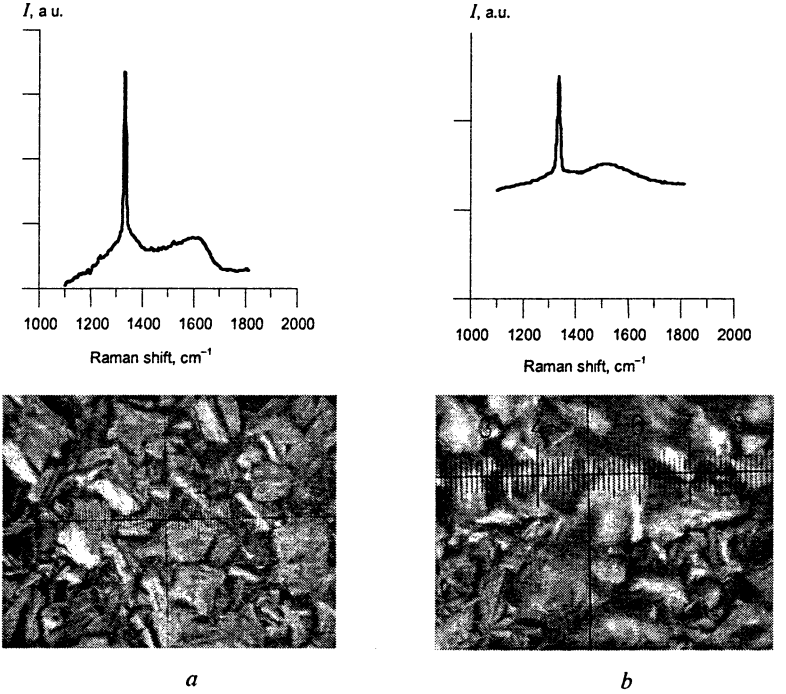

Fig. 10. Raman scattering spectra and microphotographs of the surface of diamond films grown in two CVD reactors: in the 30 GHz CVD reactor, deposition time is 3 h (*a*), in the 2.45 GHz ellipsoidal cavity reactor, deposition time is 8 h (*b*).

Conclusion

In traditional MPACVD reactor at 2.45 GHz frequency the comparison of the growth rate in the continuous wave and pulsed regimes of reactor operation was carried out. Using the results of measurements of the atomic hydrogen density and the DF growth model proposed in [7], it is possible to explain the fact that the DF growth rate in the plasma of a pulsed microwave discharge is larger than that in a continuous microwave discharge at the same mean microwave powers and mean absorbed power densities in both regimes. The larger DF growth rate in a pulsed discharge can be explained by the strong modulation of the atomic hydrogen density.

A novel microwave plasma-assisted CVD reactor using a 30 GHz, 10 kW gyrotron has been designed, built and launched for operation. The microwave output of the gyrotron was transformed into four gaussian beams which main-

tained a stable localized plasma layer in the region of the wavebeam intersection.

Gyrotron operating parameters and gas conditions were found for a steady state gas discharge plasma. Discharge has a disc shape with diameter equal to the substrate diameter and a thin thickness. Such a shape of the discharge made it possible to achieve sufficiently high discharge power density.

30 GHz CVD reactor demonstrated the growth of high quality diamond films with a high deposition rate. Polycrystalline diamond films were grown with deposition rate up to 9 μm/h on silicon substrate of 60–75 mm in diameter. The growth rate of diamond films in the 30 GHz reactor was shown to be 5 times greater than the growth rate in the 2.45 GHz reactor under identical gas mixture parameters.

References

1. *Bachmann P.K.*, in Handbook of Industrial Diamonds and Diamond Films, Ed. by M.A. Prelas, G. Popovici, and L.K. Bigelow, New York-Basel-Hong Kong, Marcel Dekker, 1998, p. 821.
2. *Grotjohn T.A., Asmussen J.*, in Diamond Films Handbook, Ed. by J. Asmussen and D.K. Reinhard, New York, Marcel Dekker, 2001, p. 211.
3. *Asmussen J.*, in High Density Plasma Sources, Ed. by O.A. Popov, Park Ridge, NJ, Noyes, 1995, p. 251.
4. *Funer M., Wild C., Koidl P.*, Appl. Phys. Lett., 1998, **72,** 1149.
5. *Besen M.M., Sevillano E., Smith D.K.*, US Patent 5,556,475, Sep. 17, 1996.
6. *Vikharev A.L., Gorbachev A.M., Litvak A.G., Bykov Yu.V., Denisov G.G., Ivanov O.A., Koldanov V.A.*, Proc. Int. Workshop: Microwave Discharges: Fundamental and Applications, Ed. by A. Ohl, Greifswald, INP, 2003, p. 84.
7. *Goodwin D.G.*, J. Appl. Phys. 1993, **74,** 6888 and 6895.
8. *Goodwin D.K., Butler J.E.*, in Handbook of Industrial Diamonds and Diamond Films, Ed. by M.A. Prelas, G. Popovici, and L.K. Bigelow, New York-Basel-Hong Kong, Marcel Dekker, 1998, p. 527.
9. *Markelevich Yu.A., Rakhimov A.T., Suetin N.B.*, Fizika Plazmy, 1995, **21,** 921 (in Russian).
10. *Vikharev A.L., Ivanov O.A., Kuznetsov O.Yu., Stepanov A.N.*, Sov. J. Plasma Phys., 1987, **13,** 648.
11. *Akhmedzhanov R.A., Vikharev A.L., Gorbachev A.M., Koldanov V.A., Radishev D.B.*, Diamond and Related Materials, 2002, **11**, 579.
12. *Vikharev A.L., Gorbachev A.M., Koldanov V.A., Akhmedzhanov R.A., Radishev D.B., Grotjohn T.A., Zuo S., Asmussen J.*, Diamond and Related Materials, 2003, **12**, 272.
13. *Vikharev A.L., Gorbachev A.M., Koldanov V.A., Radishev D.M.*, Plasma Physics Reports, 2005, **31,** 338.
14. *Coburn J.W., Chen M.*, J. Appl. Phys., 1980, **51**, 3134.
15. *Koldanov V.A., Vikharev A.L., Gorbachev A M., Muchnikov A.B., Radishev D.B.*, these proceedings, vol. 2, p. 767-772.
16. *Denisov G.G., Kuzikov S.V.*, Proc. Int. Workshop: Strong Microwaves in Plasmas, Ed. by A.G. Litvak, N. Novgorod, IAP, 2000, p. 960.
17. *Gruen D.M.*, Annu. Rev. Mater. Sci., 1999, **29,** 211.

PROSPECTS OF MATERIALS PROCESSING BY MICRO- AND MILLIMETRE WAVES

M. Willert-Porada

Chair of Materials Processing, University of Bayreuth, Bayreuth, Germany

The demand for high quality, energy efficient material processing technology opens up new possibilities for utilisation of electromagnetic radiation with micro- and millimetre wavelength. There are two major driving forces for such a development: maturity of micro- and millimetre wave devices and increased fundamental knowledge about primary and secondary effects upon interaction of materials with high frequency electromagnetic radiation.

Introduction

The use of high frequency electromagnetic radiation is the foundation of plant production on earth. Although only a small fraction of the sunlight (provided by the natural fusion reactor "sun") in the wavelength range of 0.4–0.7 μm is consumed upon photosynthesis, the average annual terrestrial Net Plant Production, NPP, of monomeric and polymeric organic compounds amounts around 130 GT [1], representing the largest production system on Earth[1].

Unfortunately, the processing principle of photosynthesis fueled by sunlight can not be directly adopted to metals, ceramics, polymers or composites made out of them: the biological system provides only very few catalysts for a photochemical production and for processing of such "synthetic" materials. For heating purposes in materials processing, concentrated sunlight is currently gaining importance, based on "solar furnaces", which collect the sunlight by means of a heliostat and a mirror or which convert the photon energy of the visible part of sunlight into lower frequency IR-radiation by means of ceramic collectors [2]. Such devices offer certain advantages as compared to monochromatic sources, like e. g., a LASER (Light Amplification by Stimulated Emission of Radiation) [2].

Although not based on natural sunlight, utilisation of high frequency electromagnetic energy sources, which deliver micro- and millimetre waves, has already revolutionised materials processing technology within the last 20 years, not so much in the area of synthesis but in many other processes, like e. g., melting, curing, annealing, cutting, welding, sintering or coating. This development was enabled by the technological maturity of many new devices, mainly different types of lasers, focussed IR-heaters and microwave sources, like e. g., klystrons, magnetrons and gyrotrons. They can be employed either for direct

[1] Assuming a smaller aquatic NPP.

heating of solid materials or for indirect energy deposition by means of a gas plasma or short wavelength radiation emitted from ionised gases.

The paper discusses examples for processing different classes of materials by direct exposure to mm- and μm-waves as well as on combined processing by simultaneous use of direct and indirect energy deposition into a material.

Choice of energy sources

At the UV- and visible range of the electromagnetic spectrum, corresponding to 0.3 – 1.0 μm wave length, different laser types are used for a wide range of processes with a very high energy density applied to the material, as shown in Table 1.

Table 1. Average properties of common micro- and millimetre and centimetre wave sources for material processing

Source	λ [μm]	η [%]	P [kW]	Examples of Application
Excimer laser (ArF, He/Cd)	0,193–0,325	< 1	10^5pulsed	PLD, PLA, Microstructuring
Ar, He/Ne	0.488–0.632	0.1–1.0	10^2 pulsed	Curing, Cleaning
Diode laser	0.810–0.940	0.1–4.0	10^2 pulsed	different
Nd-YAG	1.064	5.0	10^2 pulsed	Melting, Sintering
CO_2	10.6	5.0–10.0	10^2cont.	Cutting, Welding, Drilling
Gyrotron < 100 GHz	~1000	30–40	10–40	Sintering, Welding, Plasma
Magnetron 2.45 GHz	12.000	~ 65	1–100[2]	Sintering, Drying, Plasma
Klystron 0.915 GHz	32.000	~ 75	~ 100	Curing, Drying, Plasma

The major area of application is processing of metals and semiconductors, mainly in high trough-put operations like hardening, drilling, cutting and welding of complex shaped parts in e. g., automotive industry or cutting, etching, doping and curing in semiconductor industry.

For comparison, examples of microwave sources are also shown in Table 1; over the whole microwave frequency range the following sources are presently available with cw power levels as indicated: magnetrons 0.915 and 2.45 GHz, 1–100 kW; klystrons 0.47–18 GHz, 1 kW–1 MW power for telecommunication and research; gyrotrons 24–140 GHz and power levels of 10 kW to 1 MW. Peak power output of up to 100 MW is possible, comparable with laser sources. In

[2] Private communication, Tschunke, 2003.

Table 2 characteristic properties of laser, plasma and solar beams as energy source for materials processing are shown [2], using a comparable wave length in all these sources.

Table 2. Comparison of laser, thermal plasma and concentrated solar beams as energy sources for materials processing

Source	Flux density W/cm³	η [%]	$P_{average}$ [kW]	Surface area [cm²]
CO_2-Laser	10^3–10^6	5–10	2–5	<1
Nd-YAG	10^5–10^9	1–5	~0.5	<1
Plasma	10^4	25	10–20000	~100
Solar furnace	10^3	60	<1000	~1000

The "natural" mm-wave radiation has the advantage of large area processing, not achievable by lasers but similar to plasma sources. Opposite to laser, materials selection for microwave processing was quite narrow in the past. The majority of the early work on microwave processing of materials was devoted to dielectric ceramics [3–6]. Now recognition has grown, that semiconducting and metallic materials can be processed by microwave radiation as well [7–10].

Secondary effects from interaction of materials with micrometre and millimetre wave radiation

As shown in Eq. 1, in bulk solids only few parameters govern the penetration depth δ of monochromatic, high frequency electromagnetic radiation into a material: the complex conductivity σ*, the magnetic susceptibility μ_r as material properties, and the frequency f of the externally applied radiation. The well defined penetration depth of high frequency electromagnetic radiation into a metal or semiconductor is a pre-requisite for the controlled energy deposition in a surface near area, leading to fast melting and evaporation of the material. Fast melting or evaporation occurs because heat generation by dissipation of the mm- and μm-wave radiation exceeds significantly the capability of the material to transport heat into the remaining volume by conduction or convection. In addition, a very high power density exists also in the surface near gas phase, due to reflection of the radiation from the material. As a consequence, ionisation and plasma ignition might occur as secondary effect.

$$\delta = \frac{1}{\sqrt{\pi \cdot f \cdot \mu_0 \mu_r \cdot \sigma^*}}. \tag{1}$$

As soon as a plasma, which absorbs the electromagnetic energy, is formed, it screens the processed material off from the laser or microwave radiation. Depending upon the electron and ion temperature, UV-radiation might be emitted from the plasma and re-absorbed by the material. Particularly upon laser proc-

essing of metals high energy photons might be generated, which contribute to heating, evaporation and further ionisation of the material. The absorption coefficient of the electron gas in metals is much higher for UV-radiation than for IR-radiation. Metal heating can therefore become very efficient due to the secondary effect of plasma generation [11], as shown in Fig. 1.

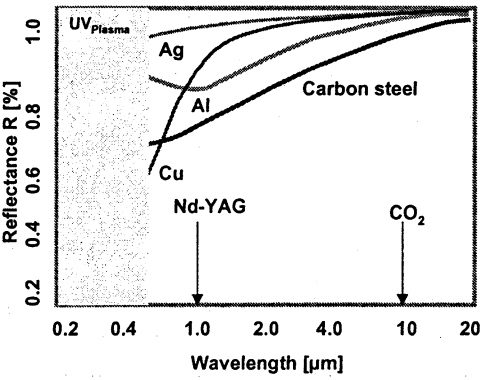

Fig. 1. Laser radiation is reflected from bulk metal surface – penetration depth into the metal is only few nm, but it increases with decreasing wave length of the radiation.

There are some subtle differences with respect to secondary effects, when laser and microwave processing of materials is compared. Upon microwave processing the strong dependence of dielectric properties on temperature might become a dominating effect. As shown in Fig. 2, a "hysteresis" of penetration depth of the microwave radiation has to be taken into account, when heating of a material occurs by microwave losses [5]. Therefore, although at low temperature dissipation of microwaves might occur in the volume of the material, upon temperature increase the depth of penetration can be significantly reduced and the power density per volume therefore strongly increased, leading to plasma formation. In case of metals, efficient heating might still go on, e.g., due to UV-emission from plasma, not due to the "screened off" microwave radiation. For other materials the electronic conductivity as well as ionic conductivity can dominate the process at such "combined" millimetre and micrometre wave exposure.

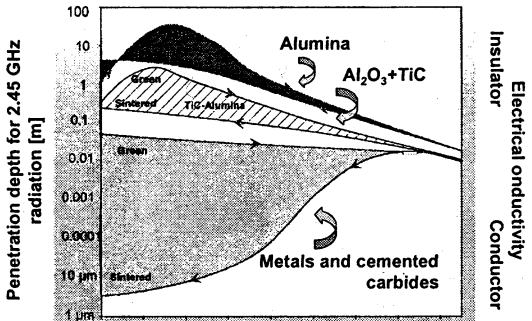

Fig. 2. Penetration depth, related to energy deposition and hysteresis of penetration depth upon microwave sintering of materials.

Direct energy dissipation from the microwave radiation into the material depends only on the local electric field strength, E_{local}, as shown in Eq. (2), and on the electric/dielectric properties of the material processed.

$$P_{abs} = \mathrm{Re}(\sigma^*) \cdot E_{local}^2 = \left(\sigma + \omega\varepsilon_0\varepsilon_r''\right) \cdot E_{local}^2 . \qquad (2)$$

If the effective electrical field strength, E_{eff} depending upon the frequency ω of the electromagnetic radiation and the collision frequency of electrons, ν_{eff} exceeds a threshold value γ, governed by the concentration of neutral species n_0, than dielectric break down of the gas atmosphere occurs, as shown in Eq. (3). The only material property, which contributes to this process is the vapor pressure of easy ionisable atoms or molecules, escaping from the processed material.

$$E_{eff} = E_0 \Big/ \sqrt{1 + \frac{\omega^2}{\nu_{eff}^2}}, \qquad \gamma = \left[\frac{E_{eff}}{n_0}\right] \geq \gamma_{critical} . \qquad (3)$$

The role of the temperature dependence of loss behaviour is usually defined for an "ideally isotropic and monolithic" material. When local electrical field strength and evaporation due to heating is taken into account, then the real structure of the materials plays an important role in high frequency electromagnetic processing of materials. As shown schematically in Fig. 3 for a porous powder compact made of a metal powder, real materials display many interfaces with a whole range of electrical conductivity values, corresponding to different heating mechanisms, including plasma discharge.

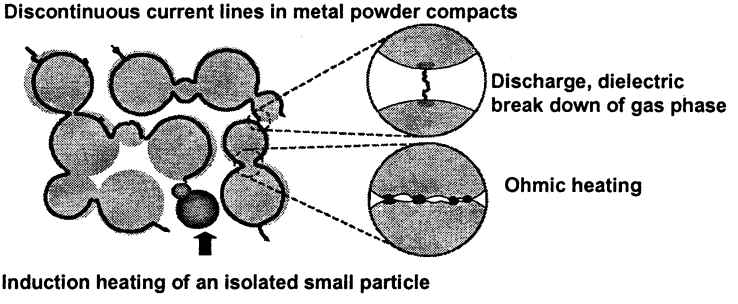

Fig. 3. Contribution of different energy dissipation mechanisms to microwave heating based on the real structure of a porous metal compact (after [12]).

The role of plasma upon microwave processing of materials is described in detail in [12]. An industrially interesting example of "combined processing" are functionally graded cutting tools, where coating or surface treatment is intentionally combined with sintering by a controlled combination of direct microwave heating with a superimposed microwave plasma treatment.

The contribution of additional mm- and μm-waves (generated by the interaction of the processed material with the "monochromatic" laser or microwave radiation as a "secondary" effect) to ignition of plasma and to it's sustained presence is not understood in detail yet for such processes like e. g., Selective Laser Sintering [11, 13], Laser Assisted Microwave Processing [14, 15] or Plasma-CVD-Coating of fibres and particles [16]. All these processes work at ambient pressure, in many different reactive or inert atmospheres.

From laboratory scale experiments some empirical findings are available, which will be presented in the next chapter.

Simultaneous exposure to different mm- and μm-wave radiation for material processing

For SLS an empirical formula for a plasma formation threshold, I_{plasma}, upon laser processing is given by Eq. (4), utilising the pulse duration τ, the pulse repetition rate ν and the average pulse power P_0 as a measure for the peak power (valid for 0.248 – 10.6 μm and pulse duration from 10 ns to 1 ms [17]).

$$I_{plasma} = 4 \times \frac{10^4}{\sqrt{\tau}}, \qquad \nu_{plasma} = \frac{P_0}{\tau_P \cdot \pi \cdot r_B^2} \cdot \frac{1}{I_{plasma}}. \tag{4}$$

Such a plasma might be destructive because of the recoil pressure generated as the plasma escapes from the surface. With respect to low surface roughness and stress free surface layers therefore alternative μm- or mm-wave sources could become attractive.

An interesting comparison, with respect to the pressure exerted at the solid surface could be drawn between laser (Nd:YAG) processing and Laser Assisted Microwave Processig, LAMP, using the laser for surface preheating and a 2.45 GHz, 1 atm Ar-plasma for coating a solid ceramic surface of composition A with another ceramic of composition B [14]. As can be seen from Table 3, the "ignition" temperature T_{crit} depends clearly on a certain concentration of ionisable atoms in the gas layer above the ceramic surface. After plasma ignition, microwave power is increased to a level which sustains the plasma and the focussed laser beam is used to guide the surface attached plasma ball over the surface [19].

The ion pressure p_{ion} of the near surface gas discharge is calculated according to Eq. (5) [20].

$$p_{ion} = 2 m_{ion} n_{ion} \nu_2, \tag{5}$$

m – mass of the ion; n – ion density; ν – ion velocity (calc. from temperature).

A value of 0.003–0.009 Pa is obtained, in comparison to the equivalent photon pressure of a laser beam depositing a comparable amount of photons to account for the energy absorbed by the solid. Details are given in [19]. The "laser only" processing would exert a 10 times higher photon pressure of 0.060 Pa. In order to achieve high surface quality, LAMP could therefore be superior over

pure laser processing. Furthermore, the electric efficiency of a 2.45 GHz microwave source is much higher than for an Nd-YAG laser (p_{max} = 90 W).

Table 3. Partial pressure of different metals in neutral and oxidizing atmosphere

Metal	neutral	at 0,2 bar O_2	T_{crit} [°C]
	p(Me) [bar]	p(Me) [bar]	
Ni (NiO)	$3{,}15 \cdot 10^{-8}$	$8{,}82 \cdot 10^{-12}$	1200
Zn (ZnO)	$4{,}48 \cdot 10^{-8}$	$1{,}50 \cdot 10^{-11}$	850
Mg (MgO)	$3{,}25 \cdot 10^{-8}$	$9{,}28 \cdot 10^{-12}$	1450
Sn (SnO_2)*	$4{,}58 \cdot 10^{-8}$	$1{,}05 \cdot 10^{-14}$	1210

From model experiments on binary oxides a simple relation between material and process parameters has been developed, which allows the prediction of a critical surface temperature as a threshold for the ignition of a surface plasma, as shown in Table 3. The important feature is the metal concentration of the vapor phase, which is sufficient to reduce the break down strength of the surface-near gas phase. Experimental evidence was found, that a partial pressure of 10^{-8} bar metal atoms is needed.

Combined laser and microwave heating was used for the formation of an eutectic ZrO_2-NiO ceramic, utilized as anode material in solid oxide fuel cells [19]. In Figure 4 the powder granules are shown. Radiant heating is not sufficient to develop locally an eutectic melt – temperatures exceeding 1800 °C at high O_2-activity are needed and, in addition, extensive mass and charge transport. Upon conventional heating no eutectic microstructure formation was observed.

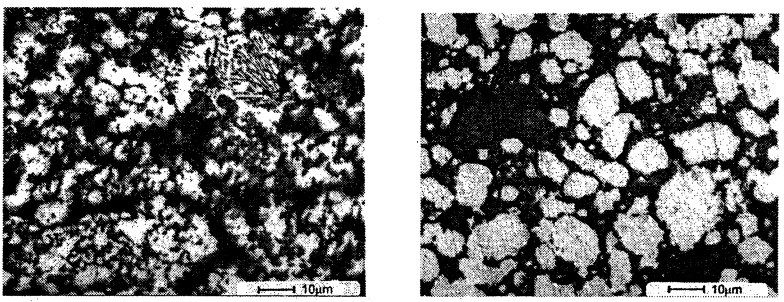

Fig. 4. Eutectic NiO-ZrO_2 ceramic after radiant heating (right) and laser or microwave heating (left) at 1800 °C.

For processing of finely divided materials, like fibers or particles, laser application is limited to process control, e. g., upon flame pyrolysis of combustible precursors [18]. Opposite to this, microwave radiation combined with a microwave plasma can easily be used for coating or surface etching of particles or short fibers in a fluidised bed reactor, as shown in Fig. 5. Contribution from plasma can be recognised by the much smaller particle size and a denser coating with TiN deposited on carbon fibers.

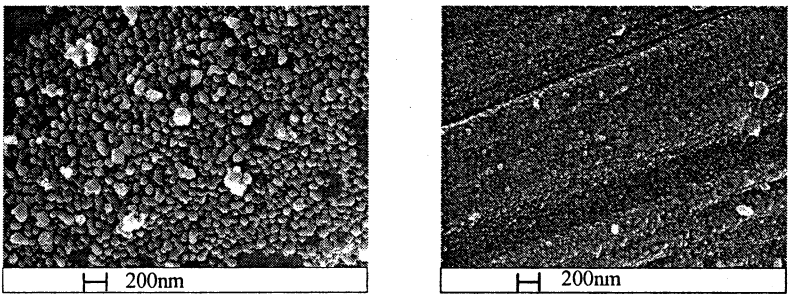

Fig. 5. SEM-image to show TiN-coating microstructure on carbon fibre upon microwave only (2.45 GHz) heating (left) and plasma + microwave heating (right) for comparable time, temperature and CVD-parameters.

Prospects of mm- and µm-wave processing of materials

The potential of high frequency electromagnetic radiation with mm- and µm-wavelength for the development of a very efficient industrial material processing technology is very high, based on the numerous up- and down-conversion paths for such radiation upon interaction with different classes of materials. The defined penetration depth of laser and microwave radiation into metals and ceramics enables the control of the thermal field inside the material, over a large range of dimensions, from bulk down to surface treatment and individual particle coating. Secondary effects, mainly connected with atmospheric plasma, can be applied concomitantly with direct heating. Based on fundamental criteria and monochromatic radiation sources, simultaneous application of few distinguished wave lengths together with polychromatic radiation should contribute to significant reduction of energy consumption for materials processing.

Acknowledgement

Financial support of the Bavarian Ministry for Science, Research and Arts, through the programme "New materials", X/1-27/52c(16)-10b/25428 is gratefully acknowledged.

References

1. *Townsend C.R., Harper J.L., Begon M.*, Essentials of Ecology, Blackwell Science, 2000.
2. *Flamant G., Ferriere A., Laplaze D., Monty C.*, Solar Processing of Materials: Opprtunities and new Frontiers, Solar Energy, Vol. 66 (2), 117-132 (1999).
3. *Wroe F.C.R., Rowley A.T.*, Microwave enhanced sintering of ceramics, in Ceram. Trans., 59, 69-76 (1995).
4. *Müller H., Mehringer R.*, Microwave processing of ceramics at 28 GHz frequency, cfi, Berichte der Deutschen Keramischen Gesellschaft, 1999.
5. *Gerdes T., Willert-Porada M.*, Technology Development for Microwave Sintering of Silicon Nitride Components in a Hot-Wall Applicator, 9th Cimtec World Ceramic Congress, Ceramics: Getting into 2000's – Part C, Ed. P. Vinzenzini, Techna Srl, 1999, 379-388, and lit. cited therein.
6. *Willert-Porada M., Bartusch W., Dhupia G., Müller G., Nagel A., Wötting G.*, Material and Technology Development for Microwave Sintering of High Performance Ceramics, in Ceramics-Processing, Reliability, Tribology and Wear, Ed. G. Müller, Wiley-VCH, 2000, p. 87-93, Euromat, Vol. 12.
7. *Sato M., Takayama S., Ochiai T., Kagohashi A.*, Development of microwave kilns for industries in Japan, 9th Int. Conf. Microwave and High Frequency Heating, Loughborough, September 2003.
8. *Kolaska H., Rödiger K., Willert-Porada M, Gerdes T.*, Verbundwerkstoff und Verfahren zu seiner Herstellung (Mikrowellensintern), Ger. Pat. Appl. P 43 40 652.1, (1993); DE 43 40 652 A1, PCT/DE95/00548.
9. *Willert-Porada M., Gerdes T., Kolaska H., Rödiger K.*, Einsatz von Mikrowellen zum Sintern pulvermetallurgischer Produkte, Pulvermetallurgie in Wissenschaft und Praxis, Bd. 11, Hrsg. H. Kolaska, DGM Informationsges. mbH P. 177-210 (1995).
10. *Roy R., Agrawal DK., Gedevanishvili S., Cheng J.*, Full sintering of powdered-metal bodies in a microwave field, Nature. Vol. 399. P. 668-670 (1999).
11. *Fischer P., Romano V., Weber H.P., Karapatis N.P., Boillat E., Glardon R.*, Sintering of commercially pure titanium powder with a Nd:YAG laser source, Acta Materialica, 51, 1651-1662 (2003).
12. *Gerdes T., Willert-Porada M.*, The role of plasma upon microwave sintering, MAPEES, 2004, Trans. Tech. Publ. (in print 2005).
13. *Fischer P., Karapatis N.*, A model for the interaction of near infrared pulses with metal powders in selective laser sintering, Appl. Phys., A74, 467-474 (2002).
14. *Gerk Ch., Willert-Porada M.*, Laser assisted microwave processing as a new tool in ceramic processing, Ceram. Trans., Vol. 111, 451-458 (2001); DE 199 51 143 A1, 2001.
15. *Willert-Porada M.*, Simultaneous Use of Different High Frequency Energy Sources for Material Processing, MAPEES 2004, Trans. Tech. Publ. (in print 2005).
16. *Tap R., Willert-Porada M.*, Dual Zone PE-CVD Circulating Fluidized Bed Reactor, IEEE Trans. Plasma Sci., IEEE Trans. Plasma Sci., Vol. 32 (5), 2085-2092 (2004).
17. *Rubahn H.-G.*, Laseranwendungen in der Oberflächenphysik und Materialbearbeitung, Teubner Studienbücher, 1996.
18. *Lee D., Choi M.*, Control of size and morphology of nano-particles using CO_2 laser during flame synthesis, J. Aerosol Sci., Vol. 31, 1145-1163 (2000).
19. *Gerk Ch.*, PhD Thesis Herstellung keramischer Eutektika durch simultanen Laser- und Mikrowelleneinsatz, Bayreuth, 2001.
20. *Schmoll R.*, Plasma-Wand Wechselwirkung strukturierter Materie, PhD Thesis, Ruhr Universität Bochum, 1995.

MULTIPACTOR DISCHARGE ON METALS AND DIELECTRICS. STATE OF THE ART

V. Semenov, V. Nechaev, E. Rakova

Institute of Applied Physics, Russian Academy of Sciences,
Nizhny Novgorod, Russia

This paper presents an overview of the multipactor phenomenon including recent theoretical achievements in the understanding of this phenomenon. Both two-surface and single-surface multipactor are considered. The classical results of the resonance multipactor theory are presented and generalized taking into account more complicated regimes of electron motion. The problem of output window failure in high power microwave generators is discussed in the context of multipactor discharges on dielectric surface. Specifically it is demonstrated that under certain conditions multipactor development is possible on the window surface even in the absence of dc electric and/or permanent magnetic fields, which typically are considered as necessary prerequisites for returning electrons back to the surface of emission. The necessity of numerical simulations for accurate predictions of the multipactor threshold is underlined.

Introduction

The design of novel accelerators for charged particles and the progress in plasma heating in fusion installations depend crucially on an increase in available microwave power. Increased power levels are also required in radar systems. As a result of this tendency, the problem of the electric breakdown strength of different rf and microwave components becomes more and more important. At present the most advanced high power systems operate close to vacuum conditions in order to avoid breakdown caused by gas discharges. However even vacuum cannot guarantee that no breakdown will occur as long as there is a contact of a strong electromagnetic field with dielectric or metal objects. The specific discharge which is called the multipactor [1–3] is typically considered as an important mechanism for such a breakdown under vacuum conditions.

The multipactor discharge manifests itself as an avalanche-like increase in the number of free electrons inside vacuum components of rf and microwave systems. It is caused by the process of secondary electron emission accompanying collisions of energetic electrons with solid surfaces. The phenomenon was discovered 70 years ago [4] and has been intensively studied both experimentally and theoretically during the past 50 years. The interest in the multipactor phenomenon is still very strong due to the sharp increase in the number of applications where operation can be disturbed by this kind of discharge. Specifically during the past decade multipactor discharges have been a serious concern by causing output window failure in high power microwave devices [5–9]. During the same period, multipactor has also become a severe problem in space borne rf communications [10, 11]. To solve this problem, the European Space Agency has organized a special international workshop (MULCOPIM), which

is held at ESTEC each second year. Since the multipactor discharge is an undesirable phenomenon, the main concern in this field is to be able to make accurate predictions for the multipactor threshold in different rf components.

Basic multipactor models

The secondary emission yield exceeds unity when an electron hits a solid surface with an impact velocity, V_i, which lies in a certain interval between the first V_1, and the second, V_2, cross-over points (see Fig. 1). The particular values of V_1 and V_2 depend on material but typically the first cross-over point corresponds to an electron energy in the range 30–100 eV whereas the second cross-over point corresponds to an energy 0.5–5 keV. The impact electron energy clearly depends on rf field amplitude. Therefore in order to predict the multipactor threshold in terms of rf power one should calculate a number of successive electron trajectories starting from different points of the solid surface at different times and find the corresponding series of impact electron velocities. A solution of this problem requires tremendous numerical simulations for each particular system. Examples of such calculations for waveguides, cavities, coaxial lines, etc. can be found in Refs. [12–17]. Reliable simulations of multipactor present a challenge because it is difficult to specify which particular properties of the secondary emission and which particular number of electron trajectories that must be taken into account. A better understanding of this problem becomes possible when the multipactor is studied within a simplified model which can be considered as the basic one.

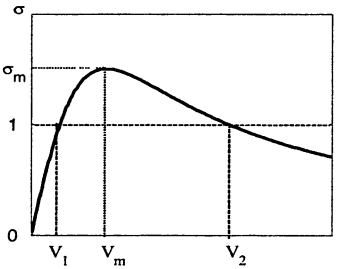

Fig. 1. Qualitative plot of the secondary emission yield vs. the impact electron velocity.

At present three qualitatively different basic models are used to study the multipactor. The most well known is the one describing the two-surface multipactor in a gap between two parallel metal plates exposed to an rf voltage [18]. Two others are associated with the single surface multipactor on a dielectric [2, 19] (where the basic model assumes the rf electric field to be parallel to the surface of emission) or on a metal [20, 21] (where the rf electric field is normal to the surface of emission). All basic models consider spatially uniform rf electric fields and neglect the action of the rf magnetic field on the electron motion. Under this approximation, the single-surface multipactor is possible only if

there is an additional force which pushes the emitted electrons back to the surface of emission. Within the basic models, the returning force is caused by either a uniform dc electric field which is perpendicular to the surface and/or by a uniform permanent magnetic field which is parallel to the surface.

The above approximations make it possible to calculate any electron trajectory analytically. Nevertheless a study of the multipactor avalanche remains a challenge because it is necessary to calculate a series of successive trajectories which requires solving a number of transcendental equations. The general analysis only makes it possible to reduce the number of parameters which control the multipactor development. For example, when the surface emission properties are fixed, the basic model of the two-surface multipactor is completely determined by the electron oscillatory velocity, $V_\omega = eE_\omega/m\omega$, (where E_ω and ω denote rf field amplitude and frequency respectively) and normalized gap width, $l = \omega L/V_\omega$ (where L denote the distance between the electrodes). Similarly the basic model of the single-surface multipactor is completely determined by V_ω and such dimensionless parameters as E_{dc}/E_ω and ω_c/ω (where E_{dc} and ω_c denote the dc field strength and the electron cyclotron frequency in the permanent magnetic field, respectively).

Resonance theory of multipactor on metal

The normal component of the rf electric field on the surface of emission plays an important role in the multipactor development. In the presence of such a field, the secondary electrons can actually leave the emission surface only during half of the rf period, otherwise the rf field pushes them back immediately. Therefore a multiplication of electrons can only occur due to a sufficiently long series of successive electron trajectories which all start with the appropriate phase of the rf field. This idea is the basis of the so called resonance multipactor theory, which determines periodically repeated and stable series of successive electron trajectories.

The classical resonance theory analyzes the periodicity of the trajectory in a restricted sense, namely as the equality between the electron flight time and an odd number of half rf cycles (in the case of the two-surface multipactor) or an integer number of complete rf cycles (in the case of the single-surface multipactor). Furthermore, this type of resonance is called classical and simple respectively. Evidently, the requirements of existence and stability of classical resonant trajectories demand some correlation between the system parameters.

A detailed study based on the basic model demonstrated [22, 23] that stable resonance of two surface multipactor is possible only inside a set of relatively narrow well separated bands of the normalized gap width. These bands are localized around $l = \pi n\left(1+V_0/V_\omega\right)$ as shown in Fig. 2 (here n is an odd number

called the resonance order and V_0 stands for the electron initial velocity). In the case of the stable classical resonance the impact electron velocity is close to $2V_\omega$. Therefore the criterion for electron multipacting can be formulated as

$$V_1 < 2V_\omega < V_2, \quad l \approx \pi n\left(1+V_0/V_\omega\right). \tag{1}$$

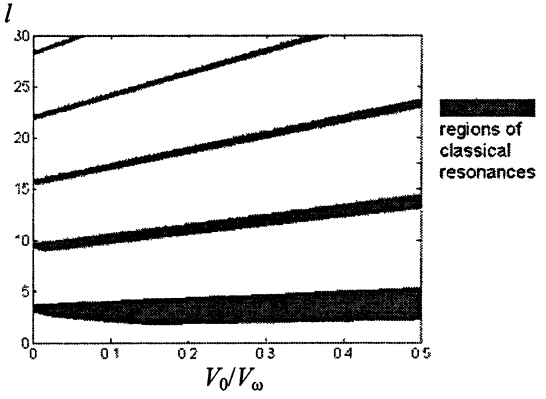

Fig. 2. The classical resonance zones (shaded areas) of the two-surface multipactor.

In complete agreement with these predictions, no multipactor was detected in experiments [18, 24] when $2V_\omega < V_1$ or $l < \pi$. However, other predictions of the resonance theory were not confirmed. Specifically the first multipactor zone ($n = 1$) was found to be considerably wider and the higher zones often overlap in experiment. As a result the current ESA standard for the two-surface multipactor threshold can be presented as a combination of inequalities [24]:

$$2V_\omega > V_1, \quad l > \pi. \tag{2}$$

An application of the classical resonance theory to the basic model of the single-surface multipactor on a metal surface also gives a set of separated regions in parameter space where the resonant electron trajectories are stable [20, 21]. In the case of zero magnetic field, the multipactor resonance zones can be presented in a form which is very similar to (1) [25]:

$$V_1 < 2V_\omega < V_2, \quad E_{dc}/E_\omega \approx -\left(1+V_0/V_\omega\right)/\pi n, \tag{3}$$

where in contrast to (1), the number n is an arbitrary integer and negative values of the dc electric field strength correspond to direction outwards. In general cases the resonance zones have to be calculated numerically and are shown in Fig. 3. As can be seen from this figure, the resonance zones are significantly affected by the initial electron velocity, especially in the case of strong magnetic fields ($\omega_c > \omega$). It should also be mentioned that multipactor resonance is impossible when ω_c is close to higher harmonics of the rf frequency ($\omega_c = s\omega, \quad s = 2,3,4,\ldots$).

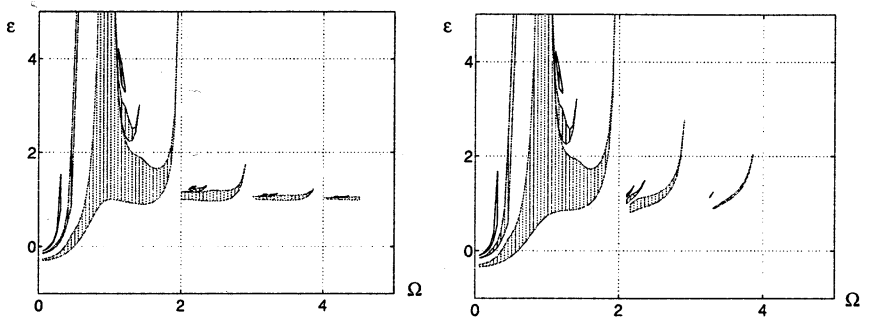

Fig. 3. The three first classical resonance zones of the single-surface multipactor on a metal plane ($\varepsilon = E_{dc}/E_{\omega}$ vs. $\Omega = \omega_c/\omega$). To the left: $V_0 = 0$, to the right: $V_0 = 0.1V_{\omega}$.

Complicated multipactor resonances

A discrepancy between the classical resonance theory and experimental results stimulated a search for more complicated periodical series of successive electron trajectories [26–28] within the basic model of the two-surface multipactor. This search was completed only recently [23, 29] using direct numerical calculations of the electron trajectories in a wide range of parameters. A lot of new resonance regimes were found both for two- and single-surface multipactor. Some results of the calculations are illustrated in Figs. 4–6 where the successive flight times and impact velocities are shown for some particular system parameters chosen outside the resonant zones. When the system parameters are chosen inside a resonance zone, both the flight times and the impact velocities approach finally the constant values predicted by the simple resonance theory. However for non-resonant parameters the series of electron trajectories can be very complicated. Specifically when the normalized gap width, l, becomes larger than the upper boundary of any resonance zone, the simple two-surface resonance becomes impossible. As a result the successive flight times begin to oscillate around and between different resonant values. In definite bands of l (with width greater than the resonance bandwidth), these oscillations are periodical and (what is more important) accompanied by relatively small fluctuations of the impact velocity (Fig. 4, left). Such regimes are called hybrid resonances. When the parameter l becomes smaller than the lower boundary of the resonance zone, the simple multipactor resonance becomes unstable. This means that any small deviation from the resonant trajectory results in an increase of flight times and impact velocity fluctuations. However, attraction to the resonant trajectory does not disappear completely and finally the fluctuations saturate at some level (Fig. 4, right). These regimes are called multiphase resonances.

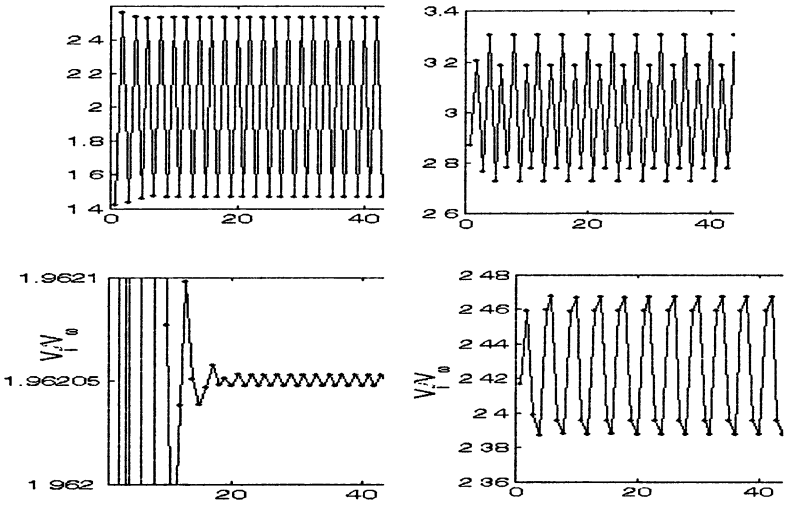

Fig. 4. Normalized (to half the rf period) electron flight times (upper trace) and normalized (to V_ω) electron impact velocities (lower trace) vs. the number of successive electron trajectory. To the left: hybrid resonance ($l = 8.56$, $V_0 = 0.7V_\omega$); to the right: multiphase resonance ($l = 14.0$, $V_0 = 0.7V_\omega$).

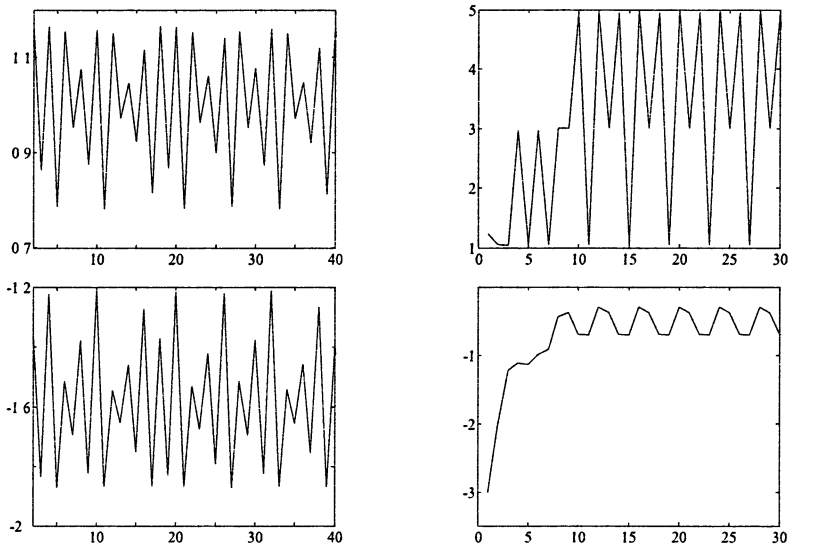

Fig. 5. Normalized (to rf period) electron flight times (upper trace) and normalized (to V_ω) electron impact velocities (lower trace) vs. the number of successive electron trajectories. Left: multiphase resonance ($\omega_c = 0$, $E_{dc} = -0.268E_\omega$, $V_0 = 0.1V_\omega$); right: hybrid resonance ($\omega_c = 0.56\omega$, $E_{dc} = 0.55E_\omega$, $V_0 = 0.1V_\omega$).

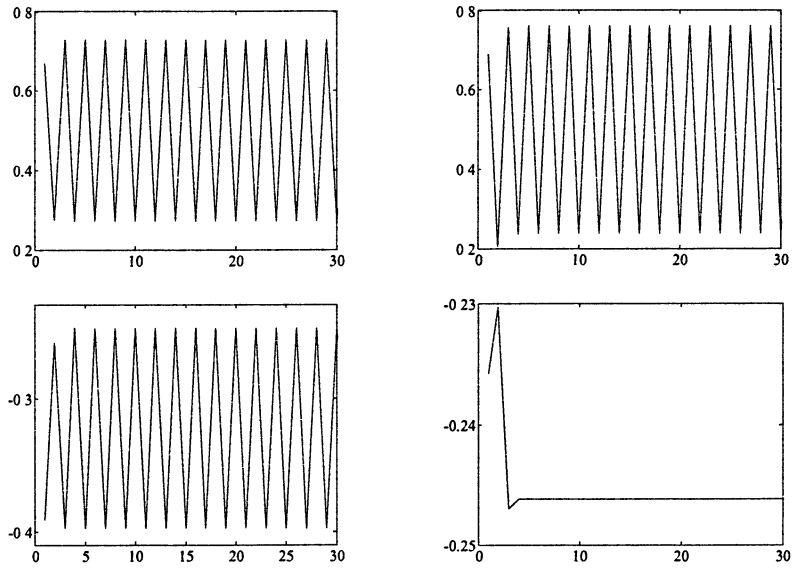

Fig. 6. Normalized (to rf period) electron flight times (upper trace) and normalized (to V_ω) electron impact velocities (lower trace) vs. the number of successive electron trajectory. Left: sub-resonance ($\omega_c = 1.9\omega$, $E_{dc} = 0.87E_\omega$, $V_0 = 0.02V_\omega$); right: sub-resonance ($\omega_c = 2\omega$, $E_{dc} = 0.83E_\omega$, $V_0 = 0.02V_\omega$).

Again the width of the l-band where fluctuations of the impact velocity are relatively small is not negligible compared to the resonance bandwidth. It should be noted here that small fluctuations of the impact electron velocity mean that the multipactor avalanche may occur in the regions of hybrid and multiphase resonances too, provided the first inequality in (1) is fulfilled.

Detailed numerical simulations of successive electron trajectories demonstrated [25, 29] that the simple resonance theory is neither complete for the single-surface multipactor. In the parameter regions between the classical resonance zones, many hybrid and multiphase resonances were found, characterized by moderate fluctuations of the electron impact velocity (Fig. 5). A particular study of a case when $\omega_c \approx 2\omega$ (the simple multipactor resonance is impossible in this case) revealed absolutely new and quite unexpected regimes of electron motion which can be called sub-resonances since each rf period contains two successive electron flights (Fig. 6). The impact velocity is considerably smaller than V_ω in this case, but its relative fluctuations are small and therefore the electron avalanche can grow provided the amplitude of the rf field is high enough. When the electron cyclotron frequency is exactly equal to twice the rf frequency ($\omega_c = 2\omega$), the parameters of the sub-resonance regime can be ex-

pressed in explicit analytical form: the electron flight times are one fourth and three fourths of the rf period respectively, the corresponding starting phases are

$$\varphi_2 = \varphi_1 + \pi/2\,, \quad -\pi < \varphi_1 < -3\pi/2, \tag{4}$$

the strength of the dc field is related to the starting phases according to:

$$E_{dc} = -2E_\omega(\cos\varphi_1 + \sin\varphi_1)/3, \tag{5}$$

and finally the impact electron velocities are the same and equal to

$$V_i = V_0 + V_\omega \frac{\sqrt{2}}{3}\cos\left(\varphi_1 + \frac{\pi}{4}\right). \tag{6}$$

Effect of electron velocity spread

The above results demonstrate clearly that the simple theory of resonance multipactor on a metal surface is incomplete since inside a considerable fraction of the parameter space between the classical resonant zones, more complicated resonant regimes are also possible. However similar to the classical theory, the above study of successive electron trajectories assumed a fixed value of the electron initial velocity and thereby treated the secondary electron emission as a completely deterministic process. As a result, the multipactor zones remain separated in parameter space even when all complicated resonances are included. The real emission process is stochastic by nature and is characterized by some spread of electron initial velocity. The latter effect should blur all boundaries of the particular resonance zones since their position in parameter space is sensitive to the value of the electron initial velocity. On the other hand, fluctuations of initial velocity can be treated as a specific loss mechanism for electrons from the particular resonance zones. Therefore the effect of the velocity spread can be quite different depending on the value of the secondary emission yield, σ. In the case of relatively weak secondary emission, the multipactor can be suppressed inside some zones whereas in the opposite case (sufficiently strong secondary emission) one should expect overlapping of different multipactor zones.

Taking V_T as a characteristic value of the electron velocity spread one can predict that a considerable perturbation of the simple two-surface resonance will occur for orders $n > (2/\pi)\sqrt{V_\omega/V_T}$ [23]. Usually in practice $V_T \geq 0.1V_\omega$, which means that any simple resonance of order $n > 1$ is disturbed by the velocity spread. On the other hand, an overlapping of the simple resonance zones can be expected only when $n > 4V_\omega/V_T$ or $l > 4\pi V_\omega/V_T$. For the limiting case $l >> 4\pi V_\omega/V_T$, the approximate theory predicted complete suppression of the multipactor if $\sigma < \sigma_{th} \cong 1.96$ [30]. However, numerical simulations [31, 32] demonstrated that even the lower multipactor zones may overlap (Fig. 7) due to

the existence of the hybrid and multiphase resonances, as has also been confirmed by experiments. The threshold value, σ_{th}, for multipactor suppression inside a wide gap was found to be $\sigma_{th} \cong 1.6$.

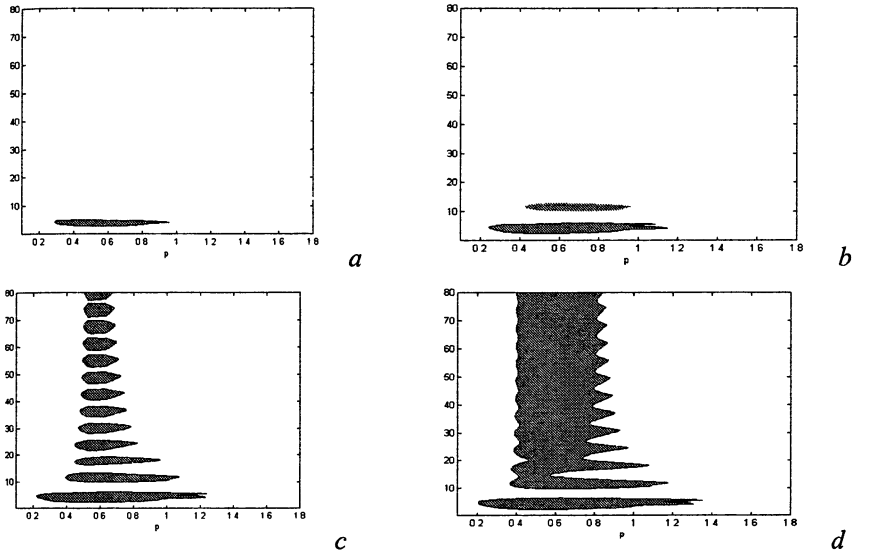

Fig. 7. Susceptibility diagrams of the two-surface multipactor in terms of l versus the normalized oscillatory velocity $p = V_\omega / V_m$ depending on the maximum value of the secondary emission yield (The shaded area indicates a region of parameters where the multipactor occurs). The normalized velocity spread is $w_T = (V_T / V_m)^2 = 3 \cdot 10^{-2}$ in all Figs.; σ_m is 1.3 (*a*), 1.5 (*b*), 1.6 (*c*), 1.7 (*d*).

Multipactor on an output rf window

The single surface multipactor discharge is an important failure mechanism of output windows in high power microwave devices. The basic model for analyzing this effect assumes the microwave electric field to be parallel to the surface of the window [2]. Under this condition a secondary electron can leave the surface of emission at any time and therefore it is not necessary to look for resonant electron trajectories. On the other hand the electron flight time and impact velocity differ from zero only when there is a finite value of the electron initial velocity. Therefore neither this velocity nor its spread can be neglected and the multipactor study requires numerical simulations from the very beginning. Detailed numerical simulations have been carried out using different algorithms [19, 33] and the corresponding susceptibility multipactor diagrams are

shown in Fig. 8 for the case of zero permanent magnetic field. These simulations also have revealed that it is possible to use a very simple estimate to predict conditions for multipactor build-up, viz:

$$V_1^2 < \langle V_i^2 \rangle < V_2^2, \tag{7}$$

where the angular brackets denote averaging over electron emission and flight time. In the particular case when the returning forces are weak (when the electron flight time is much greater than the microwave period), the average impact velocity coincides with the oscillatory one and the multipactor threshold can be expressed as

$$V_\omega^2 > V_1^2. \tag{8}$$

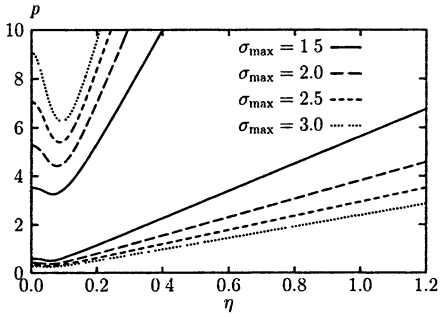

Fig. 8. Susceptibility diagrams of the multipactor on a dielectric window in terms of $p = V_\omega / V_m$ versus normalized dc electric field $\eta = eE_{dc}/m\omega V_m$ for different maximum values of the secondary emission yield. Normalized velocity spread $w_T = (V_T/V_m)^2 = 0.667 \cdot 10^{-2}$.

Formally the latter expression is valid when the returning force goes to zero. However the electron flight time goes to infinity in this case and the rate of the multipactor avalanche becomes infinitely small. Moreover in the case of weak returning forces electrons move far away from the surface of emission and the basic approximation of uniform microwave electric field is violated. This means that the basic model is not able to explain the main peculiarity of experiments, which demonstrate that multipactor development on a dielectric surface is possible even in the absence of static fields [5, 9].

To understand this phenomenon one should study the electron motion more accurately taking into account the spatial non-uniformity of the microwave field and the action of the microwave magnetic field as well. Detailed analysis of these effects within the context of multipactor breakdown was started only recently [6, 8, 34]. First, the exact solution of the equation of motion for an electron in a plane electromagnetic wave shows that the radiative field pressure is large enough to return electrons to the surface of emission if the amplitude of the incident wave is high enough to fulfill the following inequality:

$$V_\omega^2 > 4V_0 c \tag{9}$$

where c is the light velocity in vacuum. Second, it was demonstrated that the condition of electron return is very sensitive even to small reflections of the incident electromagnetic wave due to the effect of the Miller force on the electron motion in a non-uniform electromagnetic field [35]. Figure 9 demonstrates the reduction of the multipactor threshold (in terms of the incident wave amplitude) for increasing reflection coefficient in the case when the reflection gives rise to a minimum of the microwave field amplitude on the window: $E_\omega = E_0 \cdot (1-R)$. On the other hand, positioning the dielectric window at the maximum of the electric field amplitude seems a very promising method to avoid the multipactor at all.

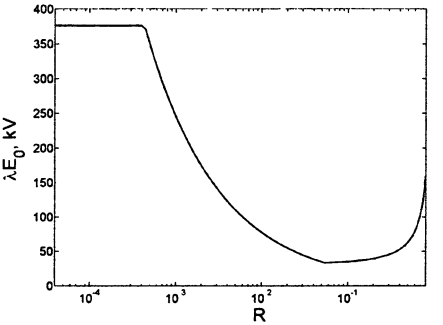

Fig. 9. The multipactor threshold in terms of the product λE_0 (λ is the wavelength, E_0 is the amplitude of the incident wave) vs. the reflection coefficient R of the incident electromagnetic wave. The energy of the first cross-over point and the electron initial energy are taken to be 50 eV and 3 eV respectively.

Conclusion

Studies of the basic multipactor models demonstrate that the classical resonance theory is incomplete and its concomitant results cannot be used for reliable predictions of multipactor-free regions in parameter space. In practice any situation when the electron oscillatory velocity exceeds half the first cross-over velocity ($V_\omega > V_1/2$) in the vicinity of a solid surface should be treated as potentially dangerous from the multipactor point of view. In the latter case, more accurate predictions can only be done using numerical simulations which must take into account both a spread of the electron initial velocity and the actual dependence of the secondary emission yield on the impact electron velocity. Knowing the first cross-over point is not enough to determine the multipactor threshold. The microwave field can itself generate the returning force for the secondary electrons and thereby provide the necessary conditions for the single surface multipactor. In this case the multipactor threshold can be sensitive to the over all distribution of electromagnetic field inside the entire vacuum volume of the device. In particular a local reduction of the electric field amplitude near the solid surface is not sufficient to reduce the danger of the multipactor breakdown.

Acknowledgement

This work was performed within the joint CNES-Chalmers-IAP project and was also supported by INTAS under Grant No. 03-53-4213 and by the Russian Basic Research Foundation through grant No. 03-02-16357a.

References

1. *Vaughan J.R.M.*, IEEE Trans. Electron Devices, 1988, **35**, 1172.
2. *Kishek R.A. et al.*, Phys. Plasmas, 1998, **5**, 2120.
3. *Kovalev N.F. et al.*, IEEE Trans. Plasma Sci., 1998, **36**, 246.
4. *Farnsworth P.T.*, J. Franklin Inst. 1934, **218**, 411.
5. *Neuber A. et al.*, IEEE Trans. Plasma Sci., 1998, **26**, 296.
6. *Neuber A. et al.*, J. Appl. Phys., 1999, **86**, 1724.
7. *Ang L.K. et al.*, IEEE Trans. Plasma Sci., 1998, **26**, 290.
8. *Valfells A. et al.*, IEEE Trans. Plasma Sci., 2000, **28**, 529.
9. *Anderson R.B. et al.*, Rev. Sci. Instrum., 2001, **72**, 3095.
10. *Raboso D.*, Vacuum Electronics Conf., 2000, 14.4.
11. *Ludovico M. et al.*, IEEE MTT-S, 2002, **3**, 2077.
12. *Chojnacki E.*, Phys. Rev. ST Accel. Beams, 2000, **3**, 032001.
13. *Geng R.L.*, Proc. PA Conf., IEEE, 2003, **1**, 264.
14. *Devanz G.*, Phys. Rev. ST-Accel. Beams, 2001, **4**, 012001.
15. *Somersalo E. et al.*, Proc. PA Conf, IEEE, 1996, **3**, 1500.
16. *Riyopoulos S.*, Phys. Plasmas., 1999, **6**, 372.
17. *Yamaguchi S. et al.*, IEEE Trans. Nucl. Sci., 1992, **39**, 278.
18. *Hatch A.J., Williams H.B.*, Phys. Rev., 1958, **112**, 681.
19. *Kishek R.A., Lau Y.Y.*, Phys. Rev Lett., 1998, **80**, 193.
20. *Vance E.F.*, J. Appl. Phys., 1963, **34**, 3237.
21. *Blyakhman L.G., Nechaev V.E.*, Sov. Phys. Tech. Phys., 1984, **54**, 1269.
22. *Shemelin V.D.*, Sov. Phys. Tech. Phys., 1986, **31**, 1029.
23. *Kryazhev A. et al.*, Phys. Plasmas., 2002, **9**, 4736.
24. *Woode A., Petit J.*, ESA J., 1990, **14**, 467.
25. *Semenov V. et al.*, Phys. Plasmas., 2005, **12**, 073508.
26. *Sombrin J.*, Effect multipactor, CNES Report No. 83/DRT/TIT/HY/119/T.
27. *Gilardini A.L.*, J. Appl. Phys., 1992, **71**, 4629.
28. *Gilardini A.L.*, J. Appl. Phys., 1995, **78**, 783.
29. *Buyanova M. et al.*, Proc. MULCOPIM 2005, ESTEC, 135.
30. *Grishin L.V. et al.*, Lebedev Physics Institute Series, Consultants Bureau, New York, 1977, **92**, 63.
31. *Sakamoto K. et al.*, J. Phys. D, 1989, **22**, 1840.
32. *Sazontov A. et al.*, Phys. Plasmas., 2005, **12**, 053102.
33. *Sazontov A. et al.*, Phys. Plasmas., 2005, **12**, 093501.
34. *Semenov V. et al.*, Proc. MULCOPIM 2005, ESTEC, 119.
35. *Gaponov A.V., Miller M.A.*, Sov. Phys. JETP, 1958, **7**, 168.

APPLICATION OF STEADY STATE MICROWAVE DISCHARGES IN NUCLEAR TECHNOLOGY

A. A. Skovoroda, V. M. Kulygin, V. P. Smirnov, A. V. Timofeev, V. A. Zhil'tsov

RRC "Kurchatov Institute", Institute of Nuclear Fusion, Moscow, Russia

Two nuclear technologies developed in OGRA department of Institute of Nuclear Fusion RRC "Kurchatov Institute" are discussed: Plasma Neutralizer for ITER NBI heating and Plasma Separator for treatment of Spent Nuclear Fuel and Radioactive Wastes.

Microwave discharge is intensively used in different applications. In this report only two examples of microwave discharges used in nuclear technologies are discussed.

Plasma neutralizer

The Plasma neutralizer (PN) could be an attractive upgrade for Neutral Beam Injection Systems based on Negative Ion Beam acceleration with further electron stripping (NNBI), see Fig. 1.

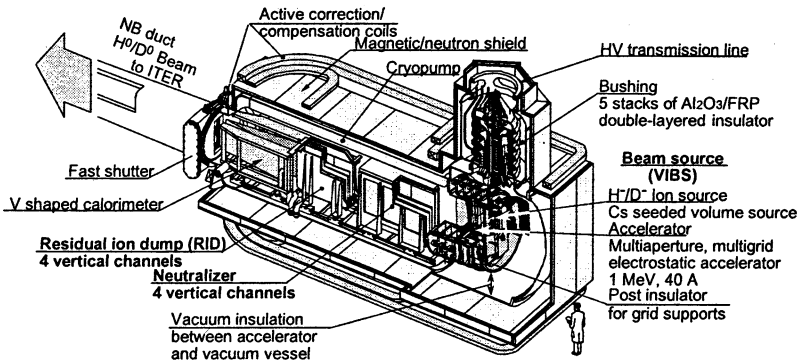

Fig. 1. ITER NBI

Gas neutralization to be in routine use and can provide the stripping efficiency ~60%. Use plasma instead of gas gives significant improvement of efficiency up to ~80%. The main problems here are the high efficiency of steady state plasma production and small divergence of beam after the PN [1]. To solve these problems the ECR microwave discharge in large volume 3D multicusp magnetic trap was proposed [2]. On Figure 2 the magnetic field and plasma geometry is shown. The magnetic field is small in all plasma volume

except the surface. In the magnetic slits the ECR condition is satisfied for 7 GHz microwave (2 klystrons, 50 kW). The special kind of plasma surface discharge was investigated in cut-off conditions [3]. The wave input and the plasma waveguide geometry is shown on Fig. 3.

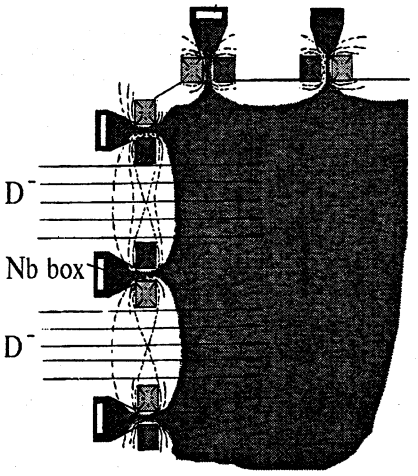

Fig. 2. The coils and plasma geometry on the wall of 3D multicusp trap. The closed plasma collectors (gas box) and the beam openings are shown.

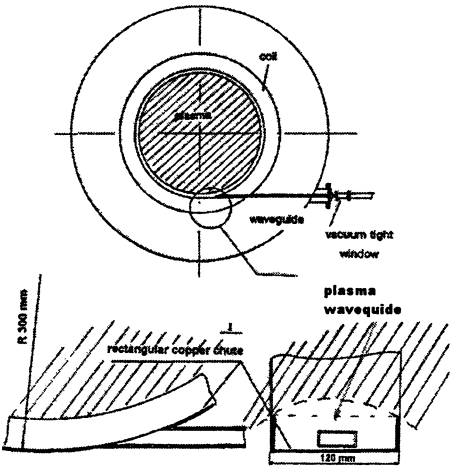

Fig. 3. Microwave input and the plasma waveguide geometry in PNX-U installation.

The experimental device PNX-U was installed to examine the general principles of proposal. On Figure 4 the PNX-U device is demonstrated. See details in [4].

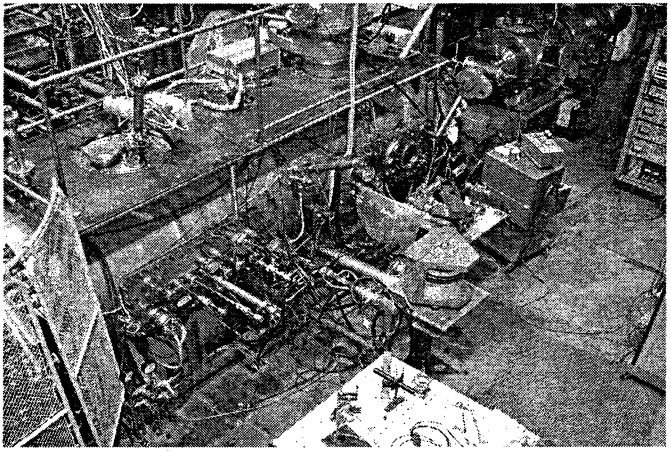

Fig. 4. PNX-U device

The large quantity of items was investigated on this installation:

1) energy confinement time scaling;
2) specific power cost of steady state operation, power balance;
3) plasma ionisation degree;
4) mechanism of PN volume plasma infilling, plasma uniformity;
5) electron and ion densities and temperatures, its special distribution;
6) multi-charged ion generation (for Argon);
7) choice of working gas, gas recycling, gas boxes influence;
8) plasma density limitation at ECR plasma generation;
9) cross magnetic field plasma losses.

We review the main physical and technological results only.

The obtained parameters

1. Target Thickness, nl, $0.2 \cdot 10^{15}$ cm^{-2}. This is 1/10 of needed for ITER.
2. Plasma Volume, V, 0.5 m^3.
3. Power density <0.1 $W \cdot cm^{-3}$. This is needed value for ITER.
4. Ionization degree on the beam trace >90%.

Volumetric and shallow forms of discharge

On Figure 5 these two forms are shown. The volumetric form is needed for PN. We find the conditions when the volumetric form is stable and the transition to shallow form is absent.

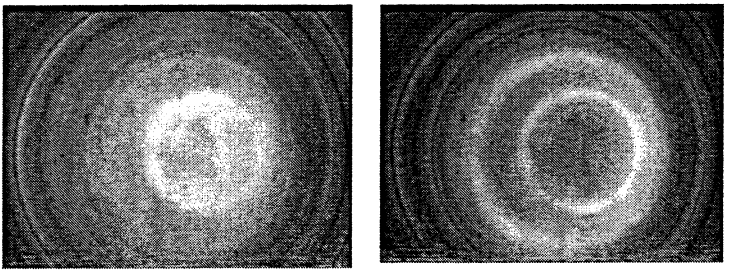

Fig. 5. Volumetric (left) and shallow (right) forms of microwave discharge in PNX-U

Ambipolar Confinement of Cold and Highly Ionized Plasma in Multicusp Trap at ECR Heating

Very high efficiency of plasma production (high ionized, cold plasma with density 10^{12} cm^{-3} in the volume 0.5 m^3 is produced by 50 kW) was achieved due

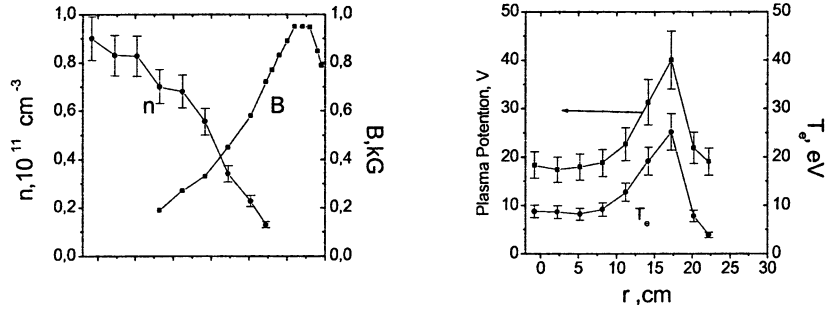

Fig. 6. Radial profiles of plasma density n, plasma potential V_{pl}, magnetic field B, Electron temperature T_e in PNX-U at 5 kW power (probe measurements).

to ambipolar confinement of ions. On Figure 6 the measured radial profiles of plasma potential, density and electron temperature are shown.

The electron temperature inhomogeneity due to ECR heating on the periphery leads to potential barrier formation. The physics of discharge in PNX-U is explained on Fig. 7.

Using the PNX-U results the PN for ITER is designed [5]. On Figure 8 the project of PN for ITER with SuperConductor magnet system is shown.

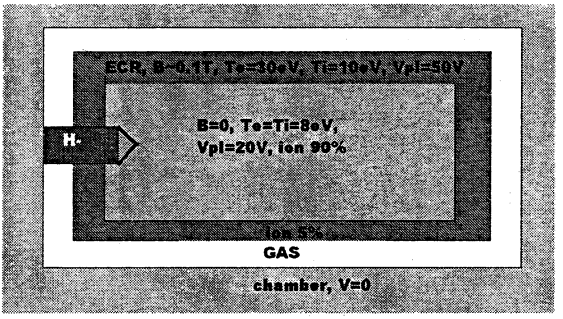

Fig. 7. Discharge in PNX-U. On the wall the potential in zero, the gas is concentrated on the periphery, in the ECR region the gas ionization is produced (source of charged particles), in the center the high ionized plasma is confined with potential barrier.

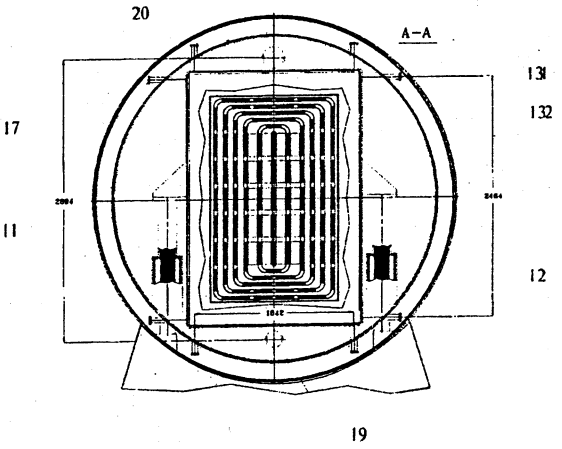

Fig. 8. Project PN for ITER with SC magnet (frontal view)

The experimental investigations, calculations and design developmental works demonstrate that the Plasma Neutralizer scheme on the base of multicusp magnetic trap with strong microwave periphery ECR plasma generation is found rather perspective for further development as an element of N-NBI for full-scale fusion systems.

Plasma separator

The Plasma separator (PS) could be an attractive supplement for nuclear Fast Reactor [6]. The Technology of Fuel Processing must separate fission products excluding Pu detachment.

To demonstrate the role of PS in fuel processing the composition of fuel assembly for fast reactor BREST-1200 is shown on Fig. 9.

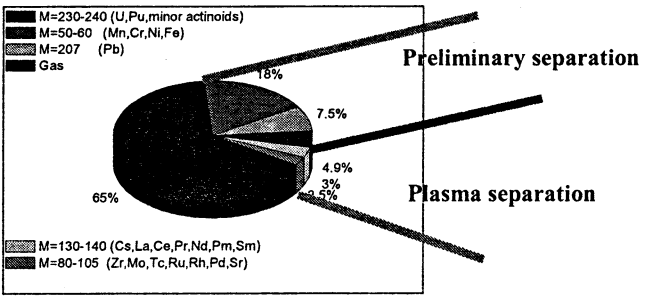

Fig. 9. Composition of fuel assembly

One can see that plasma separated components have half as much mass number as fuel components and small quantity. The large quantity of elements can be separated preliminary. The possible steps of such technology system are shown on Fig. 10.

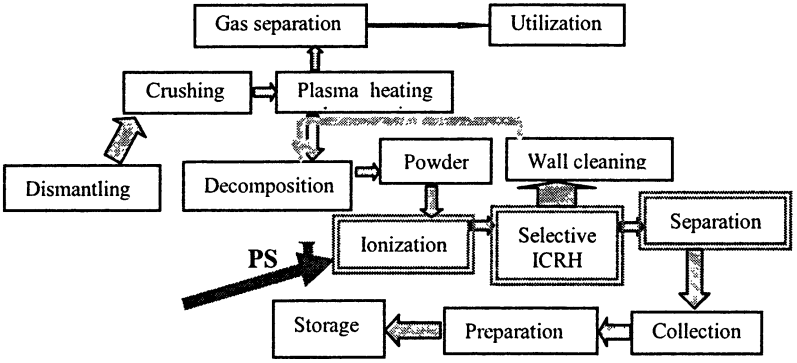

Fig. 10. Technology steps with use of PS

For plasma separation the fuel components are ionized in plasma source forming the stream. Then, the separated elements are selectively heated by ICR and selected in toroidal field. Due to reducing of magnetic field B the increased perpendicular energy $E_{\perp}$ of selected ions is transformed in the longitudinal en-

ergy $E_{\|}$. The toroidal drift $V_{dr} = \left[c\left(2E_{\|} + E_{\perp}\right)\right] / eBR$, where R is toroidal radius, results in vertical displacement $\Delta z[\text{cm}] \sim 0.2\sqrt{\Delta E[\text{eV}]M}$ (at $B = 0{,}1$ T on 1/4 of tore) of separated particles.

The principal PS scheme is shown on Fig. 11.

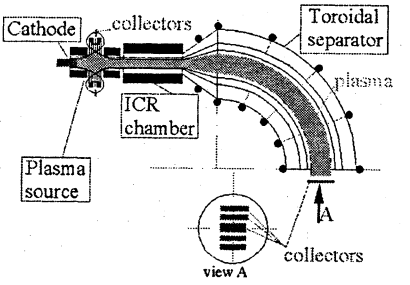

Fig. 11. PS Scheme: ECR Plasma Source + Selective ICR Heating + + Toroidal Separator.

The Experimental Model PS-1 is designed and constructed. The first Step (without the toroidal separator) should start close of year. On Fig. 12 the PS-1 device is shown. The parameters: the maximal magnetic field strength 0.7 T, 7 GHz 50 kW klystrons in ECR Plasma Source, 0.15–0.25 MHz 6 kW ICR Heating, 1–3 kV, 30 kW biasing in cathode spattering system, buffer gas Ar. The coming plasma stream parameters: plasma density 10^{12} cm^{-3}, electron temperature 3–10 eV, sputtering rate <0.05 kg/h.

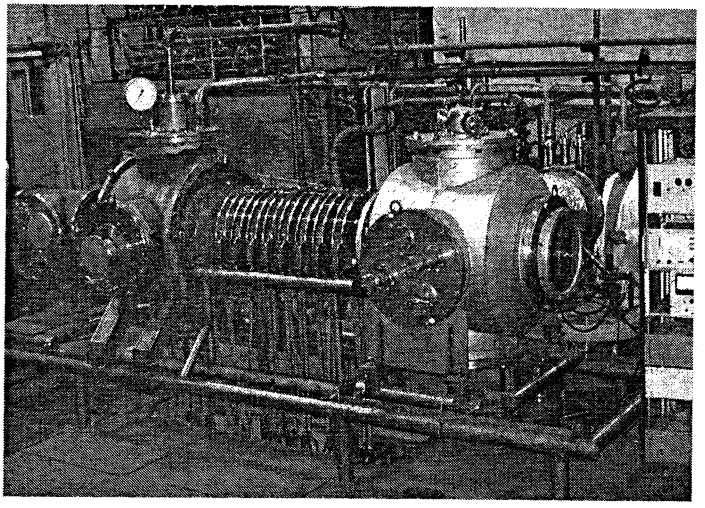

Fig. 12. PS-1 installation (Step 1)

The detailed construction of PS-1 (Step 1) is shown on Fig. 13. The distribution of magnetic field along the axis is shown too.

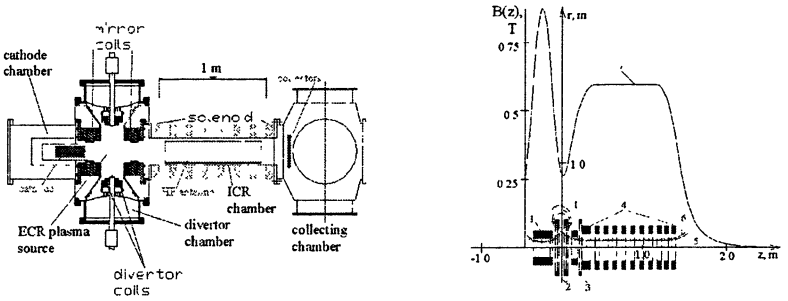

Fig. 13. Magnetic system of PS-1 (Step 1) and distribution of magnetic field along the axis.

The main items planed to investigate on experimental model PS-1:

1) conversion of solid materials into plasma stream;
2) specific power cost of steady state operation, power balance;
3) divertor MHD stabilization and wall protection;
4) eCR source of metallic plasma;
5) electron and ion densities and temperatures, its spatial distribution;
6) plasma stream limitation at ECR plasma generation;
7) minimisation of multi-charged ions generation;
8) selective ICRH of ion groups;
9) depolarisation of separated flow;
10) collectors for separated ions.

We comment the 1, 3 and 8 items only. The conversion of solid materials into plasma stream will be investigated in the test experiment with multi-component metallic plasma. On Figure 14 the scheme of such experiment is shown.

The plasma In + Cu + Ar will be produced by Indium vapor, Cu cathode sputtering and wall protection by Ar gas shielding and magnetic divertor. The limiter in plasma source outlet forms the stream.

The divertor in plasma source play the role of MHD stabilizer too. The parameters of plasma are large enough for appearance of flute like instabilities. The Kadomtsev criterion of stability

$$W = \nabla p \cdot \nabla U + \gamma p \frac{(\nabla U)^2}{U} \geq 0, \qquad (1)$$

where p – plasma pressure, $U = \oint \frac{dl}{B}$, $\gamma = 5/3$ (integration along field line), is satisfied at pressure profile $p \sim U^{-5/3}$. In divertor configuration $U \to \infty$ on the separatrix due to $B \sim 0$ and, hence, $p \sim 0$ on the periphery. The condition (1) is obtained for isotropic plasma. The situation is more favorable in anisotropic case [7]. On Figure 15 the calculated MHD stable pressure profiles for different degree of anisotropy are shown.

Ion Cyclotron Resonance heating in separation system differs from ICRH in thermonuclear installations. The specific effects were investigated theoretically in [8].

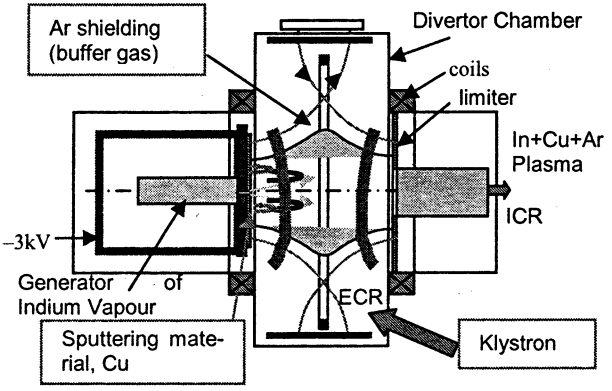

Fig. 14. Test experiment on plasma production (ECR zone, separatrix field lines and divertor plates are shown).

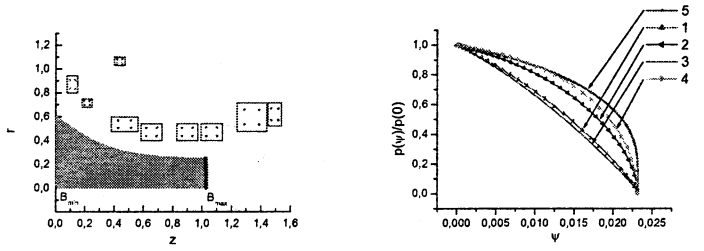

Fig. 15. Divertor configuration (left) and MHD stable pressure profiles (right); (ψ is a magnetic flux) for different degree of plasma anisotropy (*1* – high anisotropy, *5* – isotropy).

Archimedes Technology Group, Inc. San Diego, USA develops the Archimed Filter™ (see Fig. 16) for treatment of Radioactive Wastes [9].

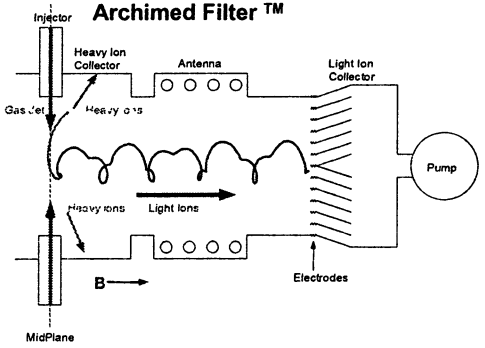

Fig. 16. Principle of separation

The rotating plasma is used for separation of heavy and light ions. On Figure 17 the conceptual difference between Archimed Filter Techonology (left) and our Stream Technology of separation is shown.

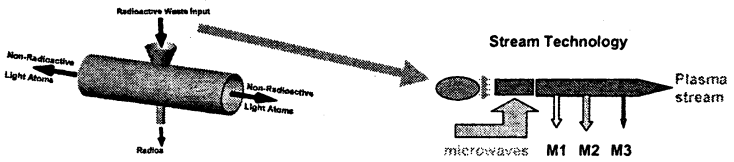

Fig. 17. Archimed Filter (left) and Stream Technology (right)

The Plasma Separator can change the technology of fuel processing and the treatment of radioactive wastes. But the experimental investigations in Russia and USA began only.

Reference

1. *Skovoroda A.A., Zhil'tsov V.A.*, Plasma Phys. Control. Fusion, 2001, **43**, 929.
2. *Skovoroda A.A., Zhil'tsov V.A.*, Strong Microwaves in Plasmas, Institute of Applied Physicas, Nizhny Novgorod, 1996, V. 1, 368.
3. *Gildenburg V.B., Skovoroda A.A.*, Plasma Phys Reports, 1998, **24**, 339.
4. *Zhil'tsov V.A et al.*, Nuclear Fusion, 2000, **40**, 3Y, 509.
5. *Kulygin V.M. et al.*, Nuclear Fusion, 2001, **41**, 355.
6. *Smirnov V.P. et al.*, Plasma Separation of SNF&RAF, Proc. 9th Conf. Selection af Atoms and Molecules, Zvenigirod, Russia, 2004, 7.
7. *Arsenin V.V., Kuyanov A.Yu.*, Plasma Phys. Reports, 2001, **27**, 675.
8. *Timofeev A.V.*, Plasma Phys. Reports, 2005, **31**, N12.
9. *Ahlfeld C.E., Gilleland J.G., Wagoner J.W.*, Waste Management Conference, Tucson, USA, February 23-27, 2003.

ECR ION SOURCE WITH QUASI-GASDYNAMIC PLASMA CONFINEMENT REGIME

A. F. Bohanov, S. V. Golubev, I. V. Izotov, S. V. Razin, A. V. Sidorov, V. A. Skalyga, A. V. Vodopyanov, V. G. Zorin

Institute of Applied Physics RAS, Nizhny Novgorod, Russia

Increasing of microwave pumping frequency in ECR ion sources is a subject of great interest now. Condition of gyroresonance requires increasing of magnetic field of a trap for plasma confinement as consequence. Traditional "min B" method of MHD plasma stabilization in such sources for magnetic field more than 1 Tesla looks impossible because baffling complexity of magnetic line structure. By now a number of methods of plasma stabilization in axisymmetrical traps of fusion mirror machines have been tested. Application of these methods in ECR ion sources of multicharged ions with pumping by millimeter waves seems to be fruitful.

A review of last investigations on creation of dense plasma with multicharged ions under ECR condition in mirror and cusp magnetic traps as well as on high current ion beam formation from such plasma carried out at the Institute of Aplied Physics are presented.

Introduction

Electron cyclotron resonance sources of multicharged ions (MCI) have become widely spread recently. One of the major trends in their development is defined by the demand to increase the ion current. Obviously, this requires the density of the plasma, from which the ions are extracted, to be increased. The increase in the ion current was first shown to be possible in Ref. [1] on the base of a semi-empirical scaling. It was observed in [1] that an increase in frequency of microwave pumping may lead to an increase in a density of a plasma, and, as a consequence, to an increase in the ion current. This conclusion rests upon the experimental fact: in real ECR ion sources (ECRIS) the plasma density should be a few times smaller than the cut-off density for a given microwave pumping frequency [1]:

$$\frac{4\pi \cdot N_e \cdot e^2}{m_e} = \omega_0^2 < \omega^2,$$

where N_e is an electron density in the plasma, e and me are the electron charge and mass, respectively. That is why increasing of microwave pumping frequency in ECR ion sources is a subject of great interest now.

As demonstrated in [2], as the trapped plasma density exceeds a certain threshold value, the electron velocity distribution function (EDF) alters dramatically, and a regime of plasma confinement changes from the classical to the quasi-gasdynamic one. In quasi-gasdynamic regime plasma confinement time can be not very high but anyway confinement parameter is still high enough for multicharged ions generation due to high plasma density. It was shown that

such transition to quasi-gasdynamic confinement regime leads to a great enhancement of extracted ion current.

A few years ago we made a lot of estimations connected with transition from classical confinement to quasi-gasdynamic. The dependence of threshold plasma density on plasma parameters for SMIS 37 ion source [3] is presented in Fig. 1.

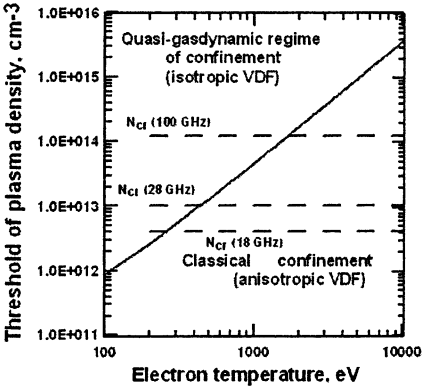

Fig. 1. The border between the three regimes of plasma confinement.

But applying of microwaves with higher frequency demands to construct magnetic systems for plasma confinement different from classical ones. Condition of gyroresonance requires increasing of magnetic field of the trap for plasma confinement as consequence. Traditional "min B" method of MHD plasma stabilization in such sources for magnetic field more than 1 T looks impossible because baffling complexity of magnetic line structure. By now a number of methods of plasma stabilization in axisymmetrical traps of fusion mirror machines have been tested. Application of these methods in ECR ion sources of multicharged ions with pumping by millimeter waves seems to be fruitful.

A review of last theoretical and experimental investigations on creation of dense plasma with multicharged ions under ECR condition in mirror and cusp magnetic traps as well as on high current ion beam formation from such plasma carried out at the Institute of applied physics are presented in this paper shortly.

Modeling of the plasma confinement in a quasi-gasdynamic magnetic trap

The effectiveness of multicharged ions generation in a plasma is determined entirely by the product of plasma density and confinement time (the confinement parameter). The problem of calculation of plasma confinement time in the magnetic traps was considered in a number of studies of various authors.

However in the case of quasi-gasdynamic confinement regime the distribution function is isotropic due to the high collision frequency, so plasma lifetime can be found from more simple considerations. The approach developed for the investigation of gas-dynamic traps in [4] is convenient. It is supposed that plasma density N_e is approximately homogeneous along the magnetic field tube. Plasma flux S through the plugs of any magnetic tube can be written in the form:

$$S = N_e s V_s , \tag{1}$$

where s is total square of cross-sections limiting the volume of magnetic tube between magnetic plugs, V_s is ion-sound velocity. Then the longitudinal plasma lifetime in this tube τ_l is equal to ratio of total plasma amount in the tube to the outgoing flux

$$\tau_l = \frac{N_e \cdot V_p}{S} = \frac{V_p}{s \cdot V_s} , \tag{2}$$

here V_p is the volume of magnetic tube limited by magnetic plugs. For the traps with long uniform part (length >> magnetic lines radius of curvature) the expression (2) gives simple well-known formula

$$\tau = \frac{R \cdot L}{2 \cdot V_s} .$$

If magnetic trap has a complicated configuration of the magnetic field lines the plasma lifetime can be estimate numerically. We call ratio V_p/s in (2) the effective trap length (the analogue of $RL/2$ value for mirror trap with long uniform part of the magnetic field, R is mirror ratio). It can be found in the case of quasi-gasdynamic regime that plasma lifetime is determined only by ion-sound velocity and trap geometry.

To simulate the ECR breakdown in nitrogen, we employ the set of ionization balance equations for ions with charge i:

$$\frac{\partial N_i}{\partial t} = (k_{i-1,i} N_{i-1} - k_{i,i+1} N_i) \cdot N_e - \frac{N_i}{\tau_i} . \tag{3}$$

Here τ_i is the confinement time for an ion with charge state i, $k_{i,i+1}$ is a rate coefficient of electron impact ionization.

Equation for the electron density:

$$\frac{\partial N_e}{\partial t} = N_e \cdot \sum_{i=0}^{6} k_{i,i+1} N_i - \frac{N_e}{\tau_e} . \tag{4}$$

The neutral gas density N_0 is governed by the equation:

$$\frac{dN_0}{dt} = I(t) - k_{0,1} N_0 N_e , \tag{5}$$

where $I(t)$ is the rate of gas influx to the trap.

The set of equations is completed by the quasineutrality condition:

$$\frac{1}{\tau_e} = \frac{1}{N_e} \sum_{i=1}^{7} \frac{iN_i}{\tau_i} \tag{6}$$

and also the equation for electron temperature must be added:

$$\frac{3}{2} \cdot \frac{d(N_e \cdot T_e)}{dt} = \frac{P}{L} - \frac{N_e \cdot T_e}{\tau_e} \cdot \ln \sqrt{\frac{M}{< Z > \cdot m_e}} - \sum_{i=0}^{6} k_{i,i+1} \cdot N_e \cdot N_i \cdot I_i \,. \tag{7}$$

Here P is the RF intensity, L – trap length, I_i – ionization potential. Simulations were mainly done for nitrogen plasmas. Generalization for other types of gasses can be done easily.

Some results of numerical calculations are presented together with experimental ones in the next paragraph.

Experimental results

The experimental research presented in this work was carried out on the SMIS 37 stand. Gyrotron generating radiation at the frequency of 37.5 GHz, with the power up to 100 kW, and pulse duration up to 1.5 ms was used as a source of pulsed microwave radiation. Ion extraction and ion beam formation were achieved by means of a traditional two-electrode extracting system with Pierce geometry electrodes. A plasma electrode with 1 mm extraction hole was placed at an arbitrary distance from the trap plug. Maximum 55 kV voltage was supplied to the extractor. Spectral analysis of the extracted beam of positive ions was performed by means of a magnetostatic analyzer. The main part of experimental results in this paper were obtained with using of a cusp magnetic trap and they shortly compared with a case when a simple mirror trap was used. Experiments with a simple mirror trap were described in [5]. The interest to an ECR ion source based on a cusp magnetic trap is connected with absolute plasma MHD stability in it, which can not be realized in a simple mirror trap. This fact allows to obtain stable extraction currents and high experiment reproducibility.

Measurements of the total ion current were made for different distances between the extractor and the magnetic trap. Results of these measurements are given in Fig. 2 together with the theoretical curve. The solid curve is the result of calculations of the ion flux from the trap through a hole 1 mm in diameter. The calculations were made for the plasma parameters corresponding to the conditions of the described experiment assuming that the ion current density behind the plug is inversely proportional to the magnitude of magnetic field (plasma spread along magnetic lines). The experimental dots correspond to the measured sum of currents at the Faraday cup (placed immediately behind the puller) and at the puller. Measurements at each distance were made for the optimal extraction voltage at which the Faraday cup current is maximal. Maximum current density of ion beam which was successfully extracted in experiments is equal to 1.2 eA/cm^2.

Fig. 2. Total current of extracted ions at the Faraday cup and at the puller measured in experiment (dots) and results of calculation of total current (solid curve) for different positions of the extraction system.

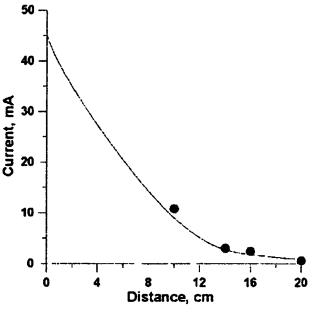

The maximum extracted ion current in the case of a simple mirror tarp was very close to the presented one for a cusp trap.

The ion spectrum at 20 kV extraction voltage and magnetic field in the plugs along the longitudinal axis of 1.7 T, given that gas input into the trap was optimized for the maximum value of N^{3+} ion current, is presented in Fig. 3.

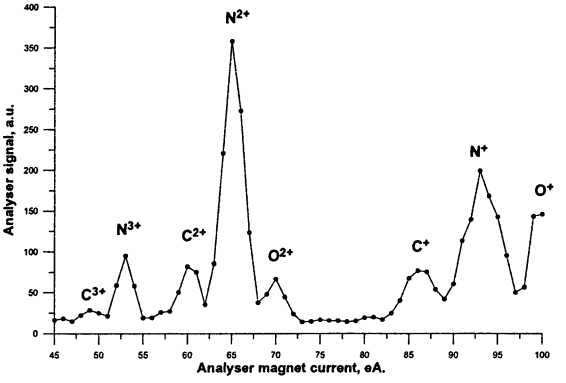

Fig. 3. Charge state distributions in the beam for the extraction voltage of 20 kV

The presence of carbon and oxygen impurities is evidently connected with the gas flux from the walls of the vacuum chamber under the action of plasma bombardment. If a simple mirror tarp is used the average ion charge can be significantly higher (up to 4) [5]. But in this case ion current is not stable during a pulse and that is why the search of new MHD stabilization methods for ECR ion sources with pumping frequencies higher than 28 GHz is a subject of a great interest.

To demonstrate the effect of trap length in quasi-gasdynamic regime of plasma confinement we made experiments for different values of effective length of cusp trap. An ability of average ion charge rising due to increase of effective trap length evidently presented in Fig. 4.

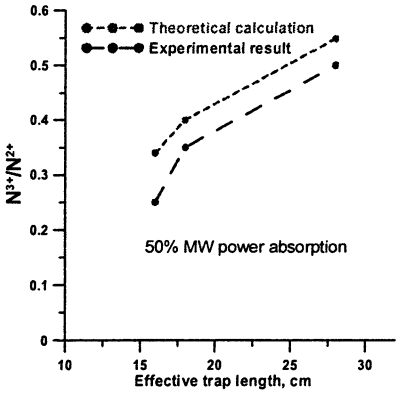

Fig. 4. Ratio of N^{3+} and N^{2+} current for different trap lengths.

Presented results shows that ECR ion source with quasi-gasdynamic regime of plasma confinement can be considered now as a ultra high current source of multicharged ions with not high average charge. Good correspondence between theory and experiment shows that quasi-gasdynamic regime of plasma confinement can be easily modeled and numerical calculations can be effectively used for designing of a future devices.

Modern applications

Realization of the European program for neutrino oscillations research, "Beta Beam Project" [6], requires that high-power short-pulse (10 to 100 μs) beams of multicharged ions of radioactive isotopes of gases (^{6}He or ^{18}Ne) be created. A possible way to achieve formation of such beams is associated with the use of a pulsed ECR source of multi-charged ions (MCI). Application of modern classical ECR ion sources for this is not feasible, since the time of gas breakdown and the plasma density's reaching the stationary level is too long (over 1 ms) as compared with the required pulse duration. This leads to prohibitively high losses of expensive isotopes in the ion line during this stage, since the extraction system is tuned to a specific (stationary) plasma density, and a quality ion beam can be produced efficiently only after the plasma density reaches that level. In order to reduce the impact of this channel of ion losses, it is necessary to shorten the time of development of the microwave discharge.

It has been shown that it is possible to reduce significantly the time of plasma parameters' reaching the stationary level by using microwave radiation with frequencies that are higher, than those, at which the quasi-gasdynamic regime of plasma is realized.

Figure 5 shows the surface, which shows the time of the electron density's reaching its stationary value, N_{st}, versus the frequency and power of the microwave pumping. During that time the plasma density reaches 98% of N_{st}. It is

seen from the Figure that the growth time becomes sufficiently shorter as the frequency of the microwave pumping grows.

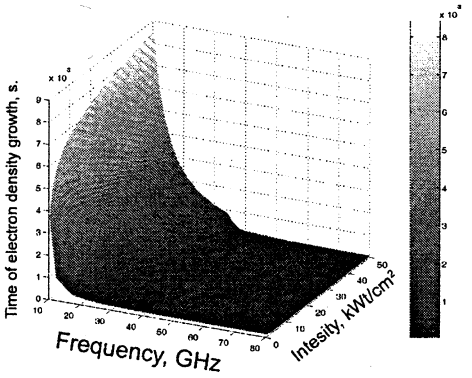

Fig. 5. Time of electron density growth versus frequency and power of the pumping

The particles extracted at the stage of plasma breakdown and degeneration cannot be utilized by the user efficiently. Their number is proportional to $\int_0^{\tau_{st}} Sdt$, where S is plasma flow from the trap, and τ_{st} is time of reaching the steady-state level. The η parameter that determines efficiency of using extracted isotope ions parameter can be written down in the following form:

$$\eta = \frac{S_{st}\Delta t}{\int_0^{\tau_{st}} Sdt}, \tag{8}$$

where S_{st} is plasma flow having reached the steady state, and Δt is characteristic pulse duration. Figure 6 shows the dependence of $1/\eta$ on the pumping parameters. It is easily seen that at the frequencies over 40 GHz the relative losses fall off abruptly and, hence, efficiency of the use of radioactive ions grows.

Figure 7 shows the oscillogram of the ion beam, which was obtained using a Faraday cup on the SMIS'37 experimental stand, and the numerically calculated flow of the plasma from the trap. The oscillogram was obtained under the following conditions: the microwave pumping frequency was 37 GHz, power, 10 kW/cm^2, initial density of electrons, 10^6 cm^{-3}, the density of neutrals was half of the critical density of electrons, nitrogen was used as a working gas. It is seen that the agreement is quite good. This, in its turn, makes it possible to hope that the forecasts based on these calculations and other pumping parameters are adequate.

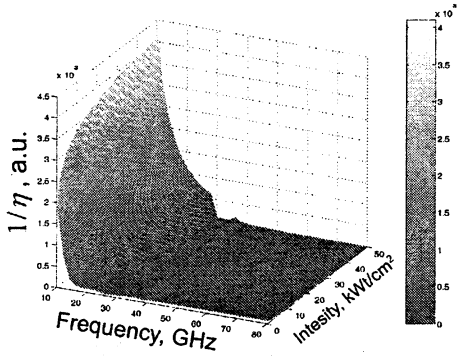

Fig. 6. Specific losses versus frequency and power of the pumping

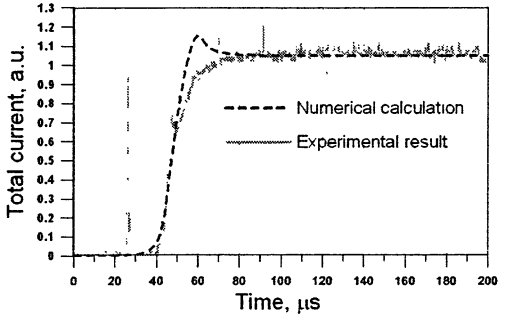

Fig. 7. Comparison of the experimental results and numerical calculations. Black line is experimental current to FC, grey line is calculated total current.

Presented results show that quasi-gasdynamic ECR ion source can be successfully used in such project.

Future perspectives

In this part some future plans of experiments on plasma creation in open magnetic traps under conditions of powerful ECR pumping on frequencies from 37.5 GHz and higher are discussed.

In nearest future we plan to make experiment with modified cusp trap with MW pumping on 75 GHz. We give as an example (see Fig. 8) calculation of the efficiency of formation of multicharged nitrogen ions in the cusp based ECR source using a gyrotron with the radiation frequency of 75 GHz and power of 400 kW which we intend to try on the SMIS stand. Such a gyrotron with a modified trap is expected to produce and confine plasma with a density of $6 \cdot 10^{13}$ cm^{-3} and electron temperature of about 100 eV.

Fig. 8. Charge state distribution of nitrogen ions: $N_e = 6 \cdot 10^{13}$ cm^{-3}, $T_e = 100$ eV.

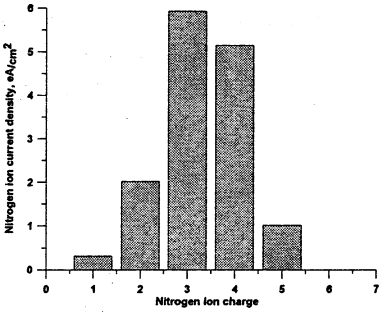

Conclusion

As a result of quasi-gasdynamic regime of plasma confinement investigations a prototype of a new ECR ion source with ultra high ion current density was created. Calculations which are in a good agreement with experimental results showed an ability of significant increase of average ion charge in a beam due to higher frequency of pumping microwaves and modifications of magnetic field structure. Thus investigation of ECR sources of multicharged ions with quasi-gasdynamic regime of plasma confinement and powerful gyrotron pumping seems to be fruitful.

Acknowledgments

The authors are grateful to M. Kazakov (IAP RAS) for his help with the experiments and technical assistance. This work was supported by INTAS grant 01 0373 and RFBR grant 05-02-17187.

References

1. *Geller R.*, Electron Cyclotron resonance Ion Sources and ECR Plasmas, Institute of physics publishing, UK, London, 1996.
2. *Ryutov D.D.*, Plasma Phys. Controlled Fusion, **28**, 191 (1986).
3. *Golubev S.V., Razin S.V., Semenov V.E., Smirnov A.N., Vodopyanov A.V., Zorin V.G.*, Rev. Sci. Instrum., **71**(2), pt. 2, 669-671 (2000).
4. *Mirnov V.V., Ryutov D.D.* Pis'ma v Zh. Thekh. Fiz. **5**, 678 (1979).
5. *Golubev S., Mansfeld D., Razin S.V., Skalyga V., Vodopyanov A., Zorin V., Murugov V., Senik A., Kravchenko A., Litvin D., Misko V., Petrov S., Geller R., Lamy T., Sortais P., Thuillier T.* ECR Ion Sources: Recent Developments, Proc. 5th Int. Workshop: Strong Microwaves in Plasmas; Ed. by A.G. Litvak, Nizhny Novgorod, Russia, 2003, v. 2, p. 618-630.
6. http://beta-beam.web.cern.ch/beta-beam/

MODELING OF ELECTRON DISTRIBUTION FUNCTION IN A LOW DENSITY ECR DISCHARGE WITH POINTWISE MAPPINGS

V. L. Erukhimov, V. E. Semenov

Institute of Applied Physics, Nizhny Novgorod, Russia

Numerical modelling of ECR discharge provides quite a few challenges both from the view point of theory and computations. The state-of-art codes either make strong assumptions or are extremely computationally expensive. A new numerical model based on a pointwise mapping of single particle parameters over one bounce time period is discussed in the paper. The method is a good compromise between model validity and computational cost. The proof-of-concept for this model is presented by analyzing formation of electron distribution function under the conditions of strong ECR diffusion and low plasma density. The results are verified against the integration of exact electron motion equations.

ECR discharge in a magnetic trap is nowadays a popular method of creation and sustaining of high density plasma used in many research and industrial applications. However there is a lack of understanding in the physical processes governing the formation of plasma. A key factor for the performance of ECR discharge tools such as ECR ion sources, is the profile of the electron distribution function (EDF). The theory of EDF formation is where complexity of each process such as ECR heating is combined with a large number of factors that have to be accounted for – such as various sorts of collisions, ionization, ambipolar losses – and unavailability of sensors to produce necessary experimental evidence. The numerical investigation of the problem is quite challenging too. The most of the EDF models can be clustered in two groups: bounce-averaged kinetic equation solvers and Particle-In-Cell (PIC) solvers. The former (see [1–3]) tends to make too strong assumptions about the model and is not suited to deal with large spread in energy scales (from several eV ionization up to hundreds keV ECR-heated electrons) while the latter does brute-force integration of electron motion equations with time scale of order of electron cyclotron period and hence is extremely computationally expensive. This paper discusses the development of a new numerical model that relaxes many of the assumptions made by bounce-averaged kinetic equation solvers but keeps the integration time scale of order of electron bounce period making the computations on large discharge times such as 100 ms feasible. The most challenging part of the model is accounting for ECR heating that possesses various effects such as stochastic heating and superadiabatic limit [5–7], relativistic Doppler shift [8] and ECR diffusion into the loss cone [9]. The next section provides a brief overview of the whole model (see the detailed description in [10]), then we focus on the details of computing ECR heating for single electron, verify our results against

the brute-force integration of motion equations and then provide the results of modeling the breakdown stage of ECR discharge.

Overview of the model

The EDF is modeled as a finite set of particles that are characterized by their spatial positions, velocities and the number of electrons they represent. The dynamics of EDF is modeled on two levels. The particle level takes care of calculating trajectories of single particles under the assumption of constant global parameters (such as density, profile of EDF, ambipolar potential etc.). The calculation uses adiabatic invariants to recalculate velocities of particles from one point to another as well as a special mapping accounting for ECR heating that is described in the next section. Collisions (both electron-electron and electron-ion) are modeled using Monte-Carlo (MC) method. The parameters level, in its turn, calculates ionization, updates the global parameters and numerical model-specific parameters such as time step. It can also change the number of particles together with the number of electrons they represent in order to increase the precision and/or keep calculation feasible. Latter is crucial for modeling an exponential burst of the particles number in breakdown conditions.

ECR heating of a single electron

We consider an electron moving in an axial symmetric magnetic trap and interacting with a wave propagating along the trap axis. It was shown [5, 6, 11] that the energy exchange between electron and wave takes place in a narrow region near the ECR point where the wave frequency ω equals electron cyclotron frequency ω_c. The width of the region Δz is much less than the length of a bounce oscillation for the most of electrons. A 5 keV electron with bounce oscillation length of 20 cm will have $\Delta z = 0.5$ cm. The width increases with electron energy according to the following scaling: $\Delta z \propto \varepsilon^{1/3}$. In fact we can consider the interaction of electron with the wave as a process that takes place exactly at the ECR point. We can calculate electron velocity represented by its longitudinal $V_{\parallel}$ and transverse $V_{\perp}$ components with regard to the magnetic field of the trap as well as by the cyclotron phase θ relative to the wave phase. We will express these values right after electron's pass through ECR point as a function of same variables taken after the previous pass:

$$\begin{cases} V_{\perp,n+1}^2 = V_{\perp,n}^2 + V_a^2 - 2V_{\perp,n}V_a\cos\theta_n \\ V_{\parallel,n+1}^2 = V_{\parallel,n}^2 \\ \theta_{n+1} = \theta\left(V_{\perp,n}, V_{\parallel,n}, \theta_n\right) \end{cases} \quad (1)$$

Here $V_a\left(V_{\perp,n}, V_{\parallel,n}\right)$ characterizes the intensity of ECR heating process and is a function of wave and trap parameters, n counts the number of passes through ECR. An analytical expression for V_a is given in [5, 7, 14]. Although one can write an analytical expression for $\theta\left(V_{\perp,n}, V_{\parallel,n}, \theta_n\right)$ (see [7]), numerical experiments show that straightforward application of such an expression to (1) results in electron trajectories that are qualitatively different from what is obtained by brute force integration of motion equations [6]. A better approximation is to consider θ as a random variable that is sampled from a given distribution function $F(\theta)$. We choose the distribution function such that (1) applied to a problem of calculating electron trajectories gives the same result as the brute-force integration of electron motion equations.

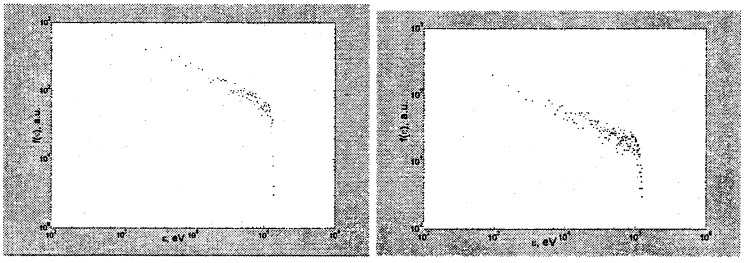

a *b*

Fig. 1. Distribution of electron energies after $t = 10^{-6}$ s of ECR heating with wave intensity S = 10^4 W/cm^2: calculated by integration of motion equations (*a*); by using a pointwise mapping (1) with sampled θ (*b*).

In order to choose the right $F(\theta)$ we have run the calculation of 10^4 electron trajectories by integrating their motion equations with random starting conditions (arbitrary position inside the trap, mean energy about 10 eV and large pitch angle that prevented spending calculation time on particles that leave the trap). Figure 1, *a* shows the distribution function of electrons over energies after 1 μs of ECR heating. Obviously the region below 100 keV corresponds to the stochastic heating and is well described by the Fokker–Plank equation for the

EDF [12–13]. The electrons with higher energies are affected by so-called superadiabatic limit [5–7] that prevents them from further heating. The critical energy ε_{st} can be estimated analytically [6] and this is in good agreement with the results of numerical modeling. This region can also be described with a Fokker–Plank equation with coefficients calculated from the simulation statistics in order to provide a good fit to Fig. 1, *a*. A steep decline in the EDF profile is provided by high values of dynamic friction coefficient.

We seek for $F(\theta)$ such that for $V_\perp > V_a$ the mapping (1) generates a kinetic equation in the Fokker–Plank form with coefficients corresponding to [12–13] for $\varepsilon < \varepsilon_{st}$ and to the simulation statistics for $\varepsilon \geq \varepsilon_{st}$:

$$F(\theta;\varepsilon) = \begin{cases} \dfrac{1+\alpha(\varepsilon)}{2\pi}, -\dfrac{\pi}{2} \leq \theta \leq \dfrac{\pi}{2} \\ \dfrac{1-\alpha(\varepsilon)}{2\pi}, \dfrac{\pi}{2} \leq \theta \leq \dfrac{3\pi}{2} \end{cases}. \qquad (2)$$

Here $\alpha(\varepsilon) = \dfrac{\pi}{6}\left(\dfrac{\varepsilon_a}{\varepsilon}\right)^{1/2} << 1$ for the stochastic region (where ε_a is the kinetic energy of electron with velocity v_a) and $\alpha(\varepsilon) \sim 1$ for superadiabatic region. Note that in the stochastic region $\alpha(\varepsilon)$ is always strictly positive (although usually much less than unit). This indicates that the distribution of θ is slightly nonuniform. The assumption of uniform distribution of θ together with (1) gives an EDF profile that is quite different from the results of brute-force electron motion equations integration presented in Fig. 1, *a* (see [5–6] for more details). For $V_\perp < V_a$ we choose $\alpha(\varepsilon) = 0$ although the choice of $F(\theta)$ is not crucial – the term V_a^2 in the first equation of the mapping (1) will prevail over the term with the random variable θ.

The choice of $V_a(V_\perp, V_\parallel)$ is also very important. Although this dependence has been studied analytically [14] some of the results are very approximate.

For $V_a < V$ we choose $V_a = V_a^0\left(\dfrac{V_a^0}{V}\right)^{2/3}$, where $V = \sqrt{V_\perp^2 + V_\parallel^2}$. This corresponds to [5] and is in agreement with numerical simulation (see Fig. 2). For $V_a > V$ V_a is equal to constant V_a^0. The constant is chosen empirically from the simulation and is scaled proportionally to the amplitude of the wave electric field.

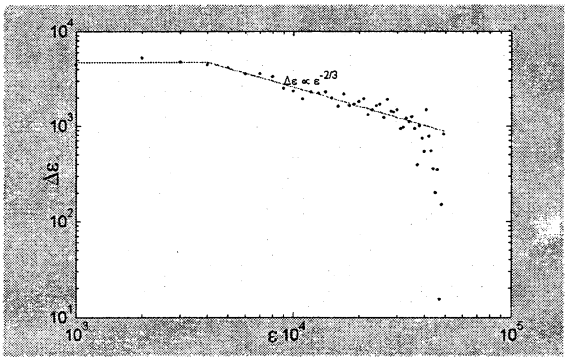

Fig. 2. Average change $\Delta\varepsilon$ of electron energy ε during one pass through ECR, calculated by brute force integration of electron motion equations. Wave intensity $S = 10^4$ W/cm^2, frequency $\nu = 37$ GHz.

Results

Due to lack of space we provide here only the results for plasma growth rate in a breakdown problem. The growth rate in inverse seconds is plotted in Fig. 3 against neutral gas density and position of ECR. These results are in qualitative agreement with analytical expressions for the density growth rate provided in [9].

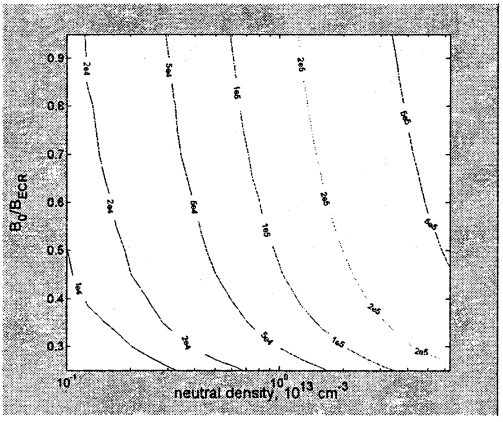

Fig. 3. Growth rate for plasma density in a breakdown problem plotted in s^{-1} against density of neutral gas (hydrogen) and ratio of minimum trap magnetic field B_0 to the magnetic field in the ECR point B_{ECR}. Wave intensity $S = 10^4$ W/cm^2, frequency $\nu = 37$ GHz.

References

1. *Girard A., Pernot C., Melin G.*, Phys. Rev. E, **62**, 1, 1182 (2000).
2. *Girard A., Lecot C., Serebrennikov K.*, J. Comp. Phys , **191**(1), 228-248 (2003).
3. *Kasheev A.V., Suetin N.V.*, IEEE Trans. Plasma Sci., **23**(4), 591 (1995).
4. *Shirkov G., Alexandrov V., Preisendorf V. et al.*, Proc. 15th Int. Workshop ECR Ion Sources, 2002.
5. *Jaeger F., Lichtenberg A.J., Lieberman M.A.*, Plasma Phys., **14**, 1073 (1972).
6. *Lieberman M.A., Lichtenberg A.J.*, Plasma Phys., **15**, 125 (1973).
7. *Timofeev A.V.*, Plasma Phys., **1**, 88 (1975) [in Russian].
8. *Zhiltsov V.A., Skovoroda A.A., Timofeev A.V. et al.*, Plasma Phys. Reports, **20**(3), 242-251 (1994).
9. *Suvorov E.V., Tokman M.D.*, Plasma Phys. Reports, **15**(8), 934-943 (1989) [in Russian].
10. *Erukhimov V.L., Semenov V.E.*, 2D Numerical Model of ECR Discharge With Pointwise Mappings, Rev. Sci. Instruments [accepted for publication].
11. *Kuckes A.F.*, Plasma Phys., **10**, 367 (1968).
12. *Mauel M.E.*, Phys. Fluids, **27**, 2889 (1984).
13. *Berk H.L.*, J. Plasma Phys., **20**, 205 (1978).
14. *Canobbio E.*, Nucl. Fusion, **9**, 27 (1969).

SUPERSONIC PLASMA AERODYNAMICS

V. M. Shibkov

Physical Department of Moscow State University, Moscow, Russia

The results of researches of low-temperature non-equilibrium plasmas in supersonic streams of the air and air-hydrocarbon fuel which has been carried out at Physical Faculty of the Moscow State University [1–16] within last several years are submitted in the report.

Advances in aviation technology call for research and development aimed at creating new efficient means for controlling the gas flow parameters near an aircraft's surface, heat and mass transfer in the boundary layer, and flow separation; reducing the frontal and surface friction; and delaying the laminar-turbulent transition; as well as for reducing the ignition time and controlling the combustion of supersonic fuel flow in a ramjet engine. A new solution to these problems is application of different gas discharges. This has given rise to a new field of research in plasma physics, supersonic plasma aerodynamics, which is rapidly progressing today [1, 2]. Specifically, it is conjectured that placement of plasma object in front of and on the lifting surfaces of the vehicle will improve its aerodynamic characteristics and use of a non-equilibrium gas-discharge plasma will reduce the fuel ignition time in a hypersonic ramjet engine. However, although the discharge in the gas flow has been studied for many years, the physics of discharge in the supersonic flow is still in its infancy. Many problems remain to be solved, among which the organization of electric gas breakdown; optimization of creation of the discharge in the supersonic air flow; maintenance of plasma objects in the gas flow; influence of the flow on the plasma parameters, and influence of the discharge on the supersonic flow characteristics; studying of process of ignition and burning of air-hydrocarbon mixtures under conditions of low-temperature plasma; research of the physical and chemical processes proceeding at initiation of ignition of gaseous fuel with the help of non-equilibrium plasma; carrying out of mathematical modelling of influence of the gas discharge on initiation of ignition and stabilization of burning of the supersonic streams of hydrocarbon fuel.

Some years ago it was offered to create plasma before flying vehicle and on its external surfaces for improvement of the aerodynamic characteristics of an aeroplane. The first laboratory experiments have shown an opportunity of a drag reduction at creation of the discharges of direct and alternative currents before a body, streamlined supersonic airflow (Fig. 1 and Fig. 2). However electrode discharges in gasflow are unstable and spatially non-uniform. Such discharges result in strong erosion of electrodes and model surface and reliably are not reproduced in various realizations (Fig. 3). There was a task of search of optimum ways of creation of non-equilibrium plasma in supersonic flow.

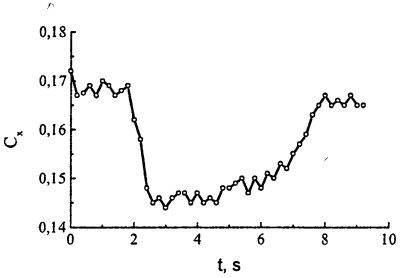

Fig. 1. Time dependence of head resistance coefficient for ceramic model with a spherical head part. Flow Mach number $M = 4$, direct current discharge with $I = 4$ A [1].

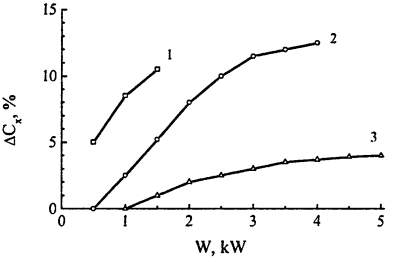

Fig. 2. Drag reduction as a function of the discharge power: *1* – high-frequency discharge $f = 50$ Hz, *2* – direct current discharge (nose electrode – the cathode), *3* – direct current discharge (nose electrode – the anode) [1].

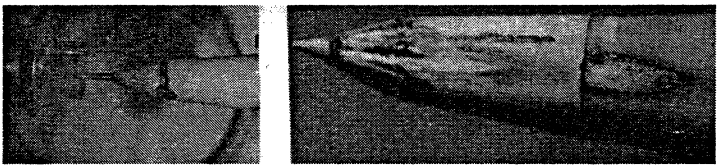

a *b*

Fig. 3. Common view of a model surface after several realizations of the electrode discharge: *a* – dc transversal discharge at $i = 2.6$ A, pulse duration $\tau = 5$ s, $M = 2.3$; *b* – high-frequency longitudinal discharge at $i = 1.5$ A, pulse duration $\tau = 3$ s, $M = 4.0$ [1].

At our laboratory for purposes of drag reduction and ignition electrodeless freely localized and surface microwave discharges have been offered and investigated [3–16]. A study of the properties of a microwave discharge removed both from the discharge chamber walls and from the radiation sources is topical from the point of view of both the solution of a number of fundamental problems of plasma physics and its practical application. Most of gas discharges are produced with the use of single- or multielectrode energy supply systems. From the practical standpoint, such systems are poorly suited to remotely control plasma production in a certain spatial region, e. g., ahead of a body moving with a supersonic velocity in the dense atmosphere (rather than at its surface). Electrodeless systems in which freely localized discharges are produced using focused microwave beams are best suited for this purpose.

In a freely localized discharge, the electric field is localized in the waist region of a focused microwave beam. Microwave beams can be focused in both

motionless gases and gas flows. Gas breakdown in a microwave discharge occurs over a time that is shorter than the time during which the gas propagates through the discharge; therefore, the discharge is not blown off by the supersonic flow. In contrast, in a transverse electrode discharge, the current frozen in the moving plasma is carried away from the electrode gap and forms an unsteady current loop. Hence, the plasma of a freely localized discharge can exist in a specified region of space during the entire microwave pulse. It was demonstrated experimentally that the discharge was not blown off by a supersonic flow from the focal region of a focused microwave beam. The experiments also showed that the power required for producing a microwave discharge depended only slightly of the flow velocity. Thus, there was almost no difference between the situation in which a freely localized microwave discharge was initially excited in motionless air and then a supersonic flow was switched on and the opposite situation in which a supersonic flow was initially switched on and then a microwave discharge was produced in the flow. Note that, under our experimental conditions, the gas flow velocity was much lower than the discharge propagation velocity and the supersonic air flow with a Mach number of $M = 2$ only slightly affected gas heating.

Microwave discharge before the conic body, streamlined by supersonic stream of air with Mach flow number $M = 2$ at air pressure $p = 60$ torr and microwave pulse duration $\tau = 30$ μs is shown in Fig. 4. This type of microwave discharge can be used for management of a stream near to a surface of the vehicle, for drag reduction of the flying device and for ignition of air-fuel supersonic stream.

In our experiments, we studied the influence of a nonequilibrium plasma on the combustion kinetics of a gaseous hydrocarbon fuel using the ignition of a supersonic propane-air flow with a Mach number of $M = 2$ as an example. For ignition, we used a freely localized microwave discharge. A microwave discharge was excited in motionless air inside the aerodynamic channel; the plasma 1–2 cm in size was produced near the initiator (Fig. 5, *a*). The discharge dimensions were found to increase with increasing power and duration of the microwave pulse. Figure 5, *b*, *c* shows photographs of freely localized microwave discharges in supersonic air and air-propane flows in the aerodynamic channel. It turned out that the supersonic flow of a gaseous hydrocarbon fuel was easy to ignite by a microwave discharge. In our experiments, the combustion of a supersonic air-propane flow was successfully initiated by microwave beams with a duration as short as $\tau = 25$ μs. It should be noted that a repetitive transverse electrode discharge ensures the ignition of a supersonic air-propane flow only at pulse durations of no less than 100–150 μs, whereas the microwave pulse duration required for ignition is much shorter. This indicates that the number of active particles produced in a microwave discharge is much larger than that in a dc electrode discharge.

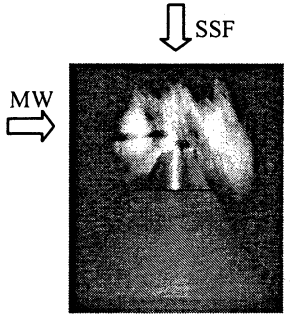

Fig. 4. Freely localized microwave discharge before the conic body, streamlined by supersonic stream of air. $M = 2$, $p = 60$ Torr and $\tau = 30$ μs.

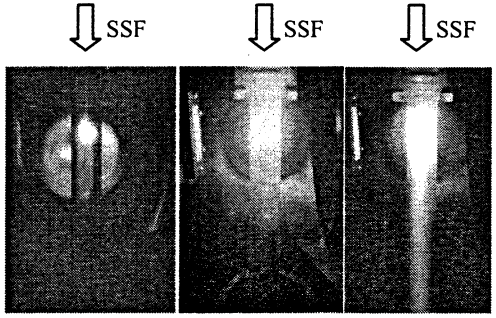

Fig. 5. The general view of a freely localized microwave discharge produced in motionless air at a microwave power of $W_p = 100$ kW (plot *a*) and in supersonic ($M = 2$) air and air-propane flows at $W_p = 200$ kW (plots *b* and *c*, respectively). The static air pressure in the chamber is $p = 60$ Torr, and the microwave pulse duration is $\tau = 100$ μs.

Another way of plasma creation under condition of gas flow, offered in our laboratory, is the new version of a surface microwave discharge, namely, a microwave discharge on an external surface of a dielectric body streamlined by supersonic flow of air. It is known that at creation of the microwave discharges inside dielectric tube, filled by gas at low pressure, the electromagnetic energy delivered to system is transformed to a surface wave. Thus, there is a self-sustaining system when a plasma medium created by the surface wave is necessary for a surface wave existence, i.e. the presence of plasma is a necessary condition for spreading of a surface wave. The surface wave is travelled in space so long as its energy is sufficient for creation of plasma with electron density no less than a critical value. This paper deals with a surface microwave discharge outside a dielectric body in a low-pressure chamber. In this case plasma supported by a surface microwave is formed on an external surface of a dielectric antenna.

The common side view of a surface microwave discharge on antenna of a rectangular section with a wedge end part is shown in Fig. 6. One can see that the discharge represents uniformly brightly luminous plasma coating the whole surface of a dielectric body. However it is necessary to note also, that in a photo it is visible weakly luminous "halo", existing around antenna. From here by analogy to freely localized microwave discharge it is possible to conclude, that this low-density plasma arises due to photoionization of impurity molecules own ultra-violet radiation of plasma of a surface microwave discharge. It is known, that the surface microwave discharge exists at large values of intensity of an

electric field, at this electric field is located in thin (d < 1 mm) near-surface layer. It results in effective excitation of high-energy levels of molecules and atoms arising in the discharge for the account of dissociation of air molecules, with the subsequent generation of ultra-violet radiation causing photoionization of impurity molecules. This phenomenon can play the important role at use of a surface microwave discharge for assistant combustion of supersonic streams of hydrocarbon fuels.

For studying an opportunity of realization of external ignition of supersonic propane-butane-air stream with flow Mach number $M = 2$ the antenna was located in area of a stream coaxially supersonic nozzle. Thus the direction of surface microwave discharge distribution was opposite to a direction of supersonic stream. The discharge was created both in a stream of pure air, and in a propane-air mixture. Not only a general view of a surface microwave discharge, but also intensity of radiation of excited radical CH^* were registered. Thus with the help of monochromator the area of a spectrum of radiation from plasma of the microwave discharge, corresponding to a band 431.5 nm of radical CH, was chosen. On distinction of values of signals for the discharge in air and in propane-air mixture could judge presence of burning (intensities of bands of CH were compared).

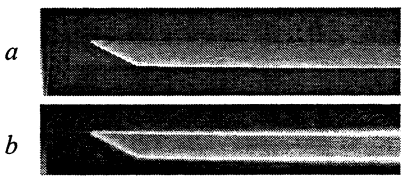

Fig. 6. Side view of flat wedge antenna without (*a*) and with (*b*) microwave discharge on its external surface at $p = 40$ Torr, $W_p = 40$ kW, and $\tau = 100$ μs.

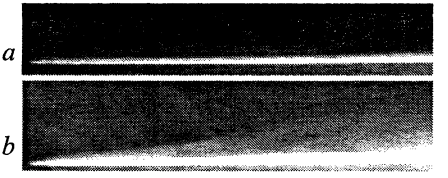

Fig. 7. Side view of a surface microwave discharge on the top part of the flat antenna streamlined by supersonic stream of air (*a*) and propane-butane-air mixtures (*b*) at $M = 2$, $p = 40$ torr, $\tau = 100$ μs and pulsed microwave power $W_p = 40$ kW (mean power $W_m = 40$ W).

The typical integrated photos of the surface microwave discharge in supersonic flow of air (*a*) and propane-air mixture (*b*) are resulted in Fig. 7. It was shown, that at pulsed microwave power $W_p = 40$ kW later of 30–40 μs after the beginning of a pulse the intensity of a luminescence of 431.5 nm CH band starts to grow that testifies about ignition of supersonic stream of propane-air mixtures. Thus in an integrated photo of the surface microwave discharge the characteristic luminescence of a flame in a supersonic stream (look Fig. 7) is ob-

served. In this case the localization place of the greatest burning occurs in a zone of the beginning of the antenna at a supply waveguide where intensity of electric field is maximal. Such spatial distribution of front of burning of a supersonic stream of a propane-butane-air mixture confirms our assumption of the large contribution of own ultra-violet radiation of a surface microwave discharge in kinetics of ignition and burning hydrocarbon fuels. It is necessary to note that process of burning stops with the ending of the microwave pulse duration.

It was received, that in spectrum the intensive bands of the second positive system of nitrogen and bands of sequence $\Delta v = 0$ of CN are observed. In case of supersonic stream of air the gas temperature measured by various molecular bands is equal 800–1000 K. At ignition of supersonic stream of propane-butane-air mixtures the general view of a spectrum in this area of wavelengths essentially varies, namely, intensity of a luminescence of CN bands sharply grows, whereas intensity of a luminescence of bands of the second positive system decreases. The gas temperature measured in this case by CN bands, effectively formed at burning of propane-butane-air mixtures, sharply grows. In this case the gas temperature is equal 2750 K, that also testifies to ignition of supersonic stream of gaseous fuel on an external surface of a plate with the help of a surface microwave discharge.

It was investigated the stabilization of propane-air burning in aerodynamic channel with a cavity. A cavity has allowed us to use a direct current power supply unit with voltage U = 2.5–4.5 kV for creation of the electrode surface discharge. With the help of this power supply unit it is impossible to create the discharge in free stream. However this power supply unit allows supporting the surface electrode discharge in a cavity. The low-current high-voltage pulsed source, generating high-voltage pulses (U = 20 kV) by duration of τ = 10–20 μs and repetition frequency of 50 Hz was used for breakdown of a discharge gap.

The discharge exists only in a cavity and is not flied out downwards on a stream at use of a stagnant zone by depth of $h > 5$ mm. These circumstances are promising from the point of view of a cavity use as a reservoir of the active particles promoting fast ignition and stable combustion of supersonic stream of gas mixture. The typical temporal behavior of CH^* emission (the transition A-X, the band (0,0), the wavelength λ = 431.5 nm), discharge current and voltage on discharge gap is represented in Fig. 8 at use of transversal surface discharge in a stagnant zone in the aerodynamic channel for ignition and combustion of the supersonic propane-air mixture. One can see that after breakdown the voltage on the discharge gap quickly reduces from 4.5 kV till 250 V. At this there is a time delay of stationary combustion of propane-butane-air mixture achievement. Under experimental condition the time delay is about 400 ms

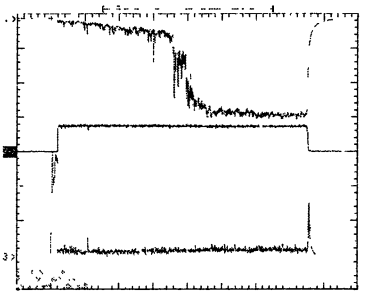

Fig. 8. Combustion of the supersonic propane-butane-air mixture in the aerodynamic channel. Transversal surface discharge in a stagnant zone h = 17 mm, L = 70 mm, p = 150 torr, M = 2, i = 12 A, U_d = 250 V, τ = 750 ms, m_g = 4.4 g/s, m_{air} = 70 g/s; *1* – typical temporal behaviour of CH^* emission, *2* – discharge current, *3* – voltage on discharge gap.

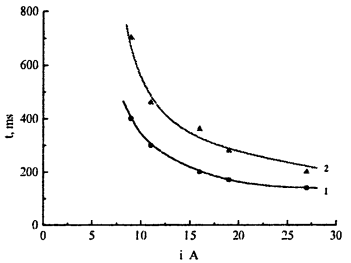

Fig. 9. The beginning ignition time (curve *1*) and time of stationary burning achievement of a propane-butane-air mixture (curve *2*) as a function of discharge current. M = 2, τ = 750 ms, U_d = 250 V, h = 17 mm, L = 70 mm, p = 150 torr, m_g = 5.4 g/s, m_{air} = 70 g/s.

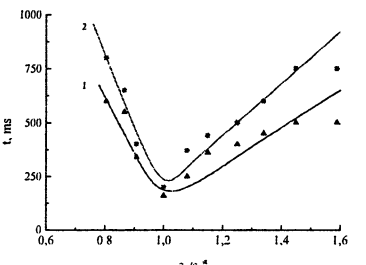

Fig. 10. Time of the beginning of occurrence of burning (a curve *1*) and time of achievement of stationary burning of a propane-butane-air mixture (a curve *2*) as a function of air consumption. M = 2, h = 17 mm, L = 70 mm, τ = 750 ms, p = 150 torr, U_d = 250 V, i = 8 A, m_g = 4.35 g/s, m_{air}^{st} = 70 g/s.

The time t_1 of beginning of process of burning (curve *1*) and time t_2 of an achievement of stationary burning of a propane-butane-air mixture (curve *2*) as a function of discharge current are submitted in Fig. 9. Time of the beginning of process of burning of supersonic propane-air stream was defined as a time interval from gas breakdown and forming of the discharge up to achievement of signal from the photo electronic multiplier, recording intensity of radiation of CH band in the region of spectrum λ = 431.5 nm, of level $I_1 = 0.1 \cdot I_{st}$, and time of achievement of stationary burning was determined on achievement of intensity of a luminescence of level $I_2 = 0.9 \cdot I_{st}$. One can see, that rate of ignition increases with growth of discharge current, thus the stationary mode of burning is established faster.

Process of fuel ignition strongly depends on structure of a combustible mixture. Results of processing of the received data are submitted in Fig. 10. One can see that both in case of a poor mixture, and in case of the enriched mixture, an achievement time of stationary mode of burning increases in comparison with stoichiometry of a mixture.

The general view of the pulse-periodic surface microwave discharge created in a supersonic stream of air in a stagnant zone behind a reverse step of the aerodynamic channel is submitted in Fig. 11. The general view of the combined discharge created in a supersonic stream of air is submitted in Fig. 12. The process of burning the propane-air supersonic stream initiated by the combined microwave and direct current discharge is submitted in Fig. 13. These experiments show, that the combined discharge results in fast ignition and stabilization of propane-air burning. However, efficiency of combustion of a supersonic stream of hydrocarbon fuel not so good, the flame does not pass in the basic flow.

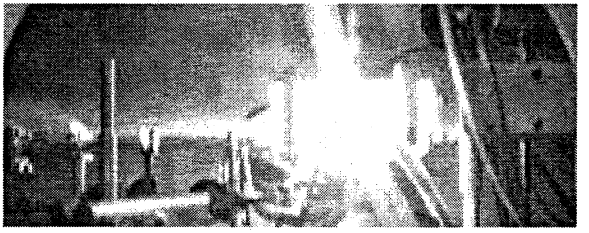

Fig. 11. The general view of the pulse-periodic surface microwave discharge created in a supersonic stream of air (M = 2) in a stagnant zone of the aerodynamic channel at τ = 10 μs, f = 100 Hz, time exposure t_{exp} = 20 ms. The supersonic airflow is directed from right to left.

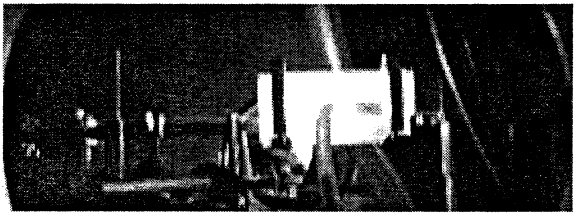

Fig. 12. The general view of the combined discharge created in a supersonic stream of air (M = 2) in a stagnant zone at τ = 10 μs, f = 100 Hz, duration of dc current t_{dc} = 1 s, t_{exp} = 20 ms.

Fig. 13. The general view of the combined discharge created in a supersonic stream of propane-air (M = 2) in a stagnant zone at τ = 10 μs, f = 100 Hz, t_{dc} = 1 s, t_{exp} = 20 ms.

The result of supersonic combustion of the propane-air stream, received at use of a rectangular cavity on wall of the aerodynamic channel as flame stabilizers and flame holders is submitted in Fig. 14. It is visible, that under condition of the combined microwave-dc discharge, created in a rectangular cavity, efficiency of burning increases in comparison with a case of creation of the discharge in a stagnant zone behind a reverse step of the aerodynamic channel. The result of supersonic combustion of the propane-air stream, received at use of a rectangular cavity with angled rear-wall on wall of the aerodynamic channel as flame stabilizers and flame holders is submitted in Fig. 15. Received results testify to efficiency of use of the combined microwave discharge in supersonic aerodynamics.

Fig. 14. The general view of the combined discharge created in a supersonic stream of propane-air (M=2) in a rectangular cavity on wall of the aerodynamic channel at τ = 10 μs, f = 100 Hz, t_{dc} = 1 s, t_{exp} = 20 ms.

Fig. 15. The general view of the combined discharge created in a supersonic stream of propane-air (M = 2) in a rectangular cavity with angled rear-wall on wall of the aerodynamic channel at τ = 10 μs, f = 100 Hz, t_{dc} = 1 s, t_{exp} = 20 ms.

The work was supported by the RFBR (grant 05-02-16532).

References

1. International Space Planes and Hypersonic System and Technologies Conference. Workshop on Weakly Ionized Gases, Proc. AIAA, USA, Colorado,1997; Norfolk,1998, 1999; Anaheim-2001; Reno, 2002, 2003, 2004, 2005.
2. The International Workshops on Magneto- and Plasma Aerodynamics for Aerospace Applications // Proc. Russia, Moscow, IVTAN-1999, 2000, 2001, 2002, 2003, 2005.
3. *Zarin A.S., Kuzovnikov A.A., Shibkov V.M* Freely localized microwave discharge in air, M., Oil and Gas, 1996. 204 p.
4. *Konstantinovskii R.S., Shibkov V.M., Shibkova L.V.* Kinet. Katal., 2005, **46** (6), p. 1-15.
5. *Shibkov V.M., Konstantinovskii R.S.* AIAA Paper No 05–0987, pp. 1–8.
6. *Shibkov V.M. et al.*, AIAA Papers No. 04-0513 and No. 04-0838.
7. *Ershov A.P. et al.*, Appl. Phys., 1999, No. 6, p. 12-19.
8. *Shibkov V.M. et al.*, Vest. Mosk. Univ., Ser. 3: Fiz., Astr., 2000, **41** (6), p. 64–66.
9. *Shibkov V.M. et al.*, Vest. Mosk. Univ., Ser. 3: Fiz., Astr., 2004, **45** (5), p. 67–69.
10. *Dvinin S.A. et al.*, High Temperature, 2004, **42** (2), p.181-191.
11. Ershov A.P. et.al. High Temperature, 2004, **42** (4), p.516–522.
12. *Ershov A.P. et al.*, High Temperature, 2004, **42** (5), p.699–705.
13. *Ershov A.P. et al.*, High Temperature, 2004, **42** (6), p. 856-864.
14. *Shibkov V.M. et al.*, Fizika Plazmy, 2005, **31** (9), p.857-854.
15. *Shibkov V.M. et al.*, Zh. Tekh. Fiz. 2005, **75** (4), p.67-73.
16. *Shibkov V.M. et al.*, Zh. Tekh. Fiz. 2005, **75** (4), p.74-79.

LONG-LIVED PLASMOIDS GENERATED BY MICROWAVE DISCHARGES IN COMBUSTIBLE GASES

N. K. Berezhetskaya, S. I. Gritsinin, V. A. Kop'ev, I. A. Kossyi, David Van Wie[1]

A. M. Prokhorov General Physics Institute, Moscow, Russia
[1]Johns Hopkins University, Laurel, MD, USA

The generation of long-lived microplasmoids is observed after the irradiation of a metal-dielectric surface with a high-power microwave beam in a chemically active gas mixture (H_2+O_2; CH_4+O_2). The lifetime of these plasmoids substantially exceeds the characteristic recombination and cooling times of plasmoids arising at the target surface in a chemically inactive medium.

1. Introduction

In this paper, we study the possibility for the generation of long-lived plasmoids by discharges excited by high-power microwave beams at metal–dielectric surfaces immersed in combustible gas media. This type of discharges was described and studied in a number of works [1, 2]. The experiments [3–5] showed that a dielectric surface with a specially introduced metal grains, when irradiated with a high-power microwave beam, becomes a source of multiple sparks (micron-sized plasma) arising on the metal–dielectric contacts. In the experiments reported on, the key question was as to whether the surface micron-sized plasma produced in a chemically active medium could become a "nucleus" for a long-lived plasmoid like those observed in [6], where experiments were performed with high-current multielectrode gliding discharges.

2. Experimental device

The experimental layout is shown in Fig. 1. The pulsed microwave radiation generated by a magnetron (*1*) is passed through an attenuator (*2*) and a circulator (*3*) to a horn-lens antenna (*4*). The antenna forms a converging microwave beam (*12*), which is launched into a metal chamber (*5*) and then into a reactor chamber (*9*). The reactor chamber is a quartz cell, evacuated and then filled with a working gas or a gas mixture before each particular experiment. The pressure in the cylindrical metal chamber (*5*) is atmospheric.

The microwave beam in the cell (*9*) is focused onto a dielectric target (*10*) whose surface exposed to the microwave beam (*12*) contains metal grains of sizes no more than 1 mm. The surface density of metal grains (their amount per area of 1 cm^2) is chosen such that the target is transparent to low-power microwaves. However, when the microwave intensity is high enough ($I \geq 10$–100 W/cm^2), there arise multiple local sparks on the target surface where the

metal contacts with dielectric. Plasma produced by these sparks absorbs microwaves and substantially affects the transmission coefficient of microwave radiation through the target.

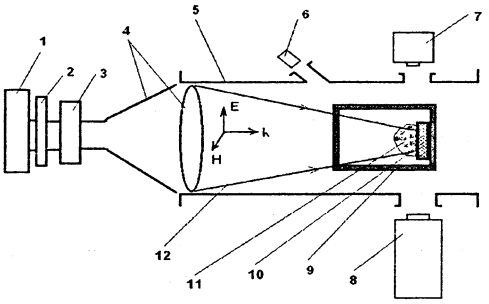

Fig. 1. Scheme of experiment

The microwave radiation parameters are the following: wavelength $\lambda \cong 2.5$ cm, pulse duration $\tau_i \cong 5$–10 μs, peak power $P_i \leq 100$ kW.

The reactor cell (*9*) is filled with argon or a hydrogen–oxygen (H_2:O_2) or a methane–oxygen (CH_4:O_2) gas mixture. The pressure range under study is $10 \leq p \leq 200$ Torr.

The time evolution of glow in the reactor chamber (*9*) is traced with the help of an FER-7 streak camera (*7*) operating in the continuous-sweep mode and a KADR-IOFRAN image intensifier (*8*) operating in the frame-by-frame mode (four frames with a specified exposure time and delays between them) and a collimated photomultiplier (*6*).

3. Experimental results

Typical photographs made with help of KADR-IOFRAN image intensifier are presented in Figs. 2 and 3. Figure 2 shows photographs (negative images) of the target, which were made successively during a microwave pulse. The exposure time of each frame was 30 μs, whereas delay times between frames were equal to 200 μs. The reactor quartz cell was filled with a H_2:O_2 (180:90 Torr) mixture (Fig. 2(*1*)), a CH_4:O_2 (45:90 Torr) mixture (Fig. 2(*2*)), and pure oxygen (135 Torr) (Fig. 2(*3*)).

As may be inferred from Fig. 2(*3a*), the lifetime of surface microwave discharges in the chamber filled with oxygen does not exceed the microwave pulse duration. If the reactor chamber is filled with a chemically active (combustible) medium (Figs. 2(*1*) and 2(*2*)), the duration of the sparking process increases to at least ~200 μs (Figs. 2(*1b*) and 2(*2b*)). Moreover, a few (usually, one or two) sparks appear to be "long-livers", existing for a time longer than 600 μs. This effect is best demonstrated by the example of operation with a methane-oxygen mixture (Figs. 2(*2c*) and 2(*2d*)).

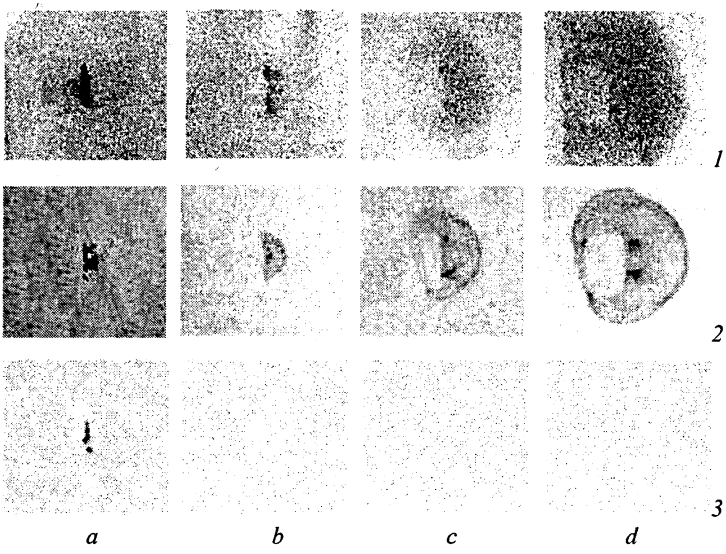

Fig. 2. High speed photographs of microwave discharge

Figure 3 shows the photographs made under conditions identical to those in Fig. 2(*2*), but in the frame-by-frame mode, not in the single-frame mode. The exposure time of each frame was 30 μs as before, and the delay time between the frames was 200 μs. One can see that long-lived plasmoids (in this experiment, a single plasmoid) exist for 1–1.2 ms up to a bright light burst occurring through the chamber and indicating the transition to a fast (based on developed chain reactions) combustion of the gas mixture. In Fig. 2 as well as in Fig. 3, one can notice glow waves initiated by surface discharges and identified as "incomplete-combustion waves" (in terms adopted in [7]).

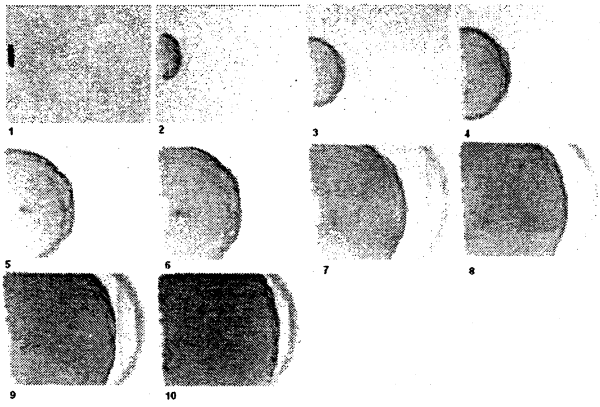

Fig. 3. High speed photographs of microwave discharge

4. Discussion

In [6], mechanisms responsible for maintenance of the long life of plasmoids generated in a chemically active gaseous medium by the high-current multispark surface discharge were discussed and it was hypothesized that any thermal-equilibrium high-temperature plasmoid, irrespective of the method of its production, may be long-lived if its size is less than a certain critical value: $r_p \leq r_{cr}$.

The surface microwave discharge at a metal–dielectric target can also be considered as a candidate for production of plasmoids of this kind. As shown in experiments [1, 2], the irradiation of metal–dielectric targets under conditions such that

$$\Psi \tau_i \geq 0.1 \text{ J/cm}^2$$

(where Ψ is the microwave intensity in (W/cm^2), and τ_i is the microwave pulse duration in [s]) is accompanied by the appearance of multiple plasmoids (sparks) on the contacts of metal grains with dielectric.

Analyzing possible mechanisms of plasma production, the authors of [1, 3] proposed, as the basis for the observed phenomenon, the injection of electrons from the metal to the conduction band of the dielectric where it contacts with the metal. A substantial enhancement of electron emission on the metal–dielectric contact is expected owing to two effects: first, the work function of the metal decreases and, second, the electric field of the electromagnetic wave increases at the metal grains.

The injection of electrons into the dielectric increases its conductivity in a narrow layer adjacent to the metal so that it reaches a level typical of semiconductors (see [8]). Microwave absorption in the dielectric with induced conductivity is accompanied by its heating in the layer adjacent to conducting grains. As the temperature of the metal–dielectric contact grows, the dielectric conductivity increases, and the flow of electrons injected into the dielectric from the metal increases as well. These effects combined lead to thermal instability [8], resulting in explosive energy liberation on the metal–dielectric contacts, which is accompanied by the solid–plasma phase transition.

This process may explain the generation of plasmoids with abnormally long lifetimes observed in our experiment. The life of plasmoids is maintained by inflows of chemically reacting particles from the ambient medium. These plasmoids (like those in [6]), consuming the energy of the ambient medium, in turn can influence the medium and can initiate the volume combustion in the reactor cell.

5. Conclusions

It is shown experimentally that the microdischarge plasma arising under irradiation of metal–dielectric surfaces in hydrogen–oxygen or methane–oxygen

media by high-power microwave beams can evolve into long-lived plasmoids similar to those observed in the experiments with high-current multielectrode gliding discharges.

The experimental results confirm the assumption that the generation of long-lived plasmoids in a chemically active gas mixture can be achieved provided that localized thermal-equilibrium plasmoids with a sufficiently high temperature and sufficiently small sizes are produced, no matter what the method of their production.

In the light of these findings, it is proposed to undertake detailed measurements of the parameters of long-lived plasmoids and a search for new methods of their excitation, including laser sparks.

Of special interest is also the problem of utilizing long-lived plasmoids for initiating the combustion of gas mixtures, particularly, in the version of supersonic flows (see [7, 9]).

This work was supported in part by the Fundamental Researches Program of RAS Presidium 20 and by the ISTC and EOARD (the ISTC project 2681p).

References

1. *Batanov G.M., Bol'shakov E.F., Dorofeyuk A.A., Kossyi I.A., Sapozhnikov A.V., Silin V.A., Brovkin V.G., Kolesnichenko Yu. F., Voronin A.N., Nicholas Koumvakalis, Holly S., Bunn T.L.* // J. Phys. D: Appl. Phys. 1996. V. 29. P. 1641-1648.
2. *Batanov G.M., Gritsinin S.I., Kossyi I.A.* // J. Phys. D: Appl. Phys. 2002. V. 35. P. 2687-2692.
3. *Batanov G.M., Berezhetskaya N.K., Kop'ev V.A., Kossyi I.A., Magunov A.N., Silakov V.P.* // Plasma Phys. Rep. 2002. V. 28. P. 871-876.
4. *Batanov G.M., Berezhetskaya N.K., Kossyi I.A., Magunov A.N., Silakov V.P.* // Strong Microwaves in Plasmas: Proc. Int. Workshop / Ed. by A.G. Litvak. Nizhny Novgorod, 2003. V. 2. P. 631-641.
5. *Batanov G.M., Berezhetskaya N.K., Kossyi I.A., Magunov A.N., Silakov V.P.* // Eur. Phys. J. Appl. Phys. 2004. V. 26. P. 11-17.
6. *Kossyi I.A., Silakov V.P., Tarasova N.M., Taktakishvili M.I., D. van Wie* // Plasma Phys. Rep. 2004. V. 30, № 4. P. 343.
7. *Berezhetskaya N.K., Gritsinin S.I., Kop'ev V.A., Kossyi I A., Popov N.A., Silakov V.P., Van Wie D.* Microwave Discharge as a Method for Igniting Combustion in Gas Mixtures // 43rd AIAA Aerospace Sci. Meeting. Report AIAA-2005-0991. Reno, Nevada, 2005.
8. *Vershinin Yu.N.* Electric Discharge in Solid Dielectrics. Nauka: Novosibirsk, 1968 (in Russian).
9. *Kossyi I.A., Berezhetskaya N.K., Gritsinin S.I., Kop'ev V.A., Silakov V.P., Tarasova N.K., Taktakishvili M.I., Van Wie D.* Long-Lived Plasmoids as Initiators of Combustion in Gas Mixtures // 42nd AIAA Aerospace Sci. Meeting. Report AIAA 2004-836. Reno, Nevada, 2004.

MICROWAVE PLASMA ASSISTED SUPERSONIC HYDROCARBON FUEL COMBUSTION

V. M. Shibkov, A. A. Karachev, R. S. Konstantinovskij, L. V. Shibkova, A. V. Voskanyan, V. V. Zlobin

Physical Department of Moscow State University, Moscow, Russia

A kinetic model is constructed for ignition initiated by non-equilibrium gas-discharge plasma in the hydrogen-oxygen system [1–2]. The model takes into account the effect of the electric field on the dissociation of molecules and on the creation of active radicals, excited species, and charged species (electrons and positively and negatively charged ions). It is demonstrated by mathematical modeling that the induction period depends strongly on the reduced electric field (electron temperature).

One of the problems of modern supersonic aerodynamics is maintenance of steady work of the direct-flow air-breathing engine which main element is the system of ignition of combustible fuel-air mixtures. Control of processes of ignition and burning of fuel in the supersonic jet engine is the major condition for its successful use in a wide range of conditions of flight. For the solution of this problem substantially determining progress in development of hypersonic aircraft, it was offered to use various types of plasma generators [3–11]. The mechanism of the gas-phase oxidation of various combustible gases, including hydrocarbons and hydrogen, has been thoroughly studied, with the emphasis on their ignition mechanism. There are numerous ways of intensifying the chain combustion of hydrocarbons. However, the ignition kinetics is not completely understood even for the rather simple model system hydrogen-oxygen under low-temperature gas-discharge plasma conditions. Here, using the hydrogen-oxygen system as a model, we consider the mechanism of the ignition of a gaseous fuel with nonequilibrium gas-discharge plasma.

A combustible gas mixture can be ignited either by heating it to a high temperature (autoignition) or by the nonthermal creation of free radicals and active species using an external source of energy. The main purpose of this study is to determine the mechanism that is responsible for the ignition of a gas fuel in the presence of nonequilibrium discharge plasma at a high reduced strength of the electric field. Other important tasks of this study are to evaluate the effect of discharge parameters on the ignition kinetics of the gaseous fuel and to simulate the combustion of the fuel under the action of a discharge.

In our laboratory, we initiate ignition with dc discharges (either longitudinal or transverse to the supersonic flow), periodic pulsed discharges, radio-frequency electrode discharges, and freely localized and surface microwave discharges. Initially, the effect of low-temperature plasma on the combustion kinetics of a gaseous fuel was experimentally studied for a supersonic propane-butane-air flow with a Mach number of $M = 2$. Our experimental setup consists

of a cylindrical vacuum chamber with an inner diameter of 1 m and a length of 3 m, a high-pressure air receiver, a high-pressure propane-butane receiver, a system for mixing the propane-butane mixture with air, a system for producing a supersonic propane-butane-air flow, an aerodynamic channel, a discharge section, different types of plasma generators, a pulsed high-voltage power supply, a synchronization system, and a diagnostic system. The air flow rate can be varied between 25 and 100 g/s; the propane-butane flow rate, between 1 and 8 g/s. The basic part of this setup is the vacuum chamber, which serves to produce a supersonic flow and is a reservoir for the exhaust gases and combustion products. The vacuum system allows operation in a wide pressure range of $p = 10^2$–10^5 Pa.

We used three types of gas discharge for ignition: freely localized microwave discharge, surface microwave discharge, and pulsed transverse electrode discharge [1]. The ignition of the supersonic stream was detected as a glow in the aerodynamic channel downstream of the discharge section. No glow was observed when a gas discharge was generated in an air flow, when it was generated in a supersonic propane-butane-air flow but its parameters (pulse duration, discharge current, electric field strength in the plasma, and the electric power deposited in the discharge) were inappropriate for ignition, or when the mixture was far from stoichiometric. Induction time was simultaneously derived from different measurements: (1) the minimum microwave pulse duration resulting in a glowing flame in the aerodynamic channel downstream of the discharge section; (2) the time taken by the intensity of the molecular band of the excited CH^* radical (the (0;0) band due to the $A^2\Delta \rightarrow X^2\pi$ transition), with an edge wavelength of $\lambda = 431.5$ nm, to achieve the maximum growth rate; (3) the time taken by the signal from the double probe to achieve the maximum growth rate; and (4) the time taken by the current through the plane capacitor at the outlet of the aerodynamic channel to achieve the maximum growth rate. The ignition of the supersonic flow was also detected as an increasing output signal from an acoustic noise meter.

Different discharges afford different degrees of gas ionization at the same specific power deposited [12]. The electric energy supplied is nonuniformly distributed among the internal degrees of freedom of the molecular gas. This distribution depends strongly on the reduced strength of the electric field, which, in turn, is determined by the electrodynamics of the discharge. Experiments have demonstrated that a periodic pulsed electrode discharge causes ignition only at a pulse duration of $\tau > 150$ μs. The ignition of a supersonic propane-butane-air flow with a freely localized microwave discharge is possible at $\tau \approx 25$ μs, and the ignition of the same mixture with a surface microwave discharge takes place almost immediately after the microwave generator is turned on. At high reduced field strengths $E/n \geq 10^{15}$ V/cm^2, more than 50% of the power deposited in the discharge is spent for the excitation, dissociation, and electron-impact ionization of molecules followed by the generation of reactive free radicals. Since the self-sustained microwave discharge takes place at high

reduced field strengths, it produces more active species than the electrode discharge. This must exert a strong effect on the kinetics of the processes involving active radicals to shorten the induction period. Therefore, we consider it necessary to thoroughly study the effects of the charged and active species rapidly generated in the discharge on the ignition delay time and hydrocarbon combustion efficiency.

A mathematical model was constructed for a motionless hydrogen-oxygen mixture [1–2]. The model of the ignition of the hydrogen-oxygen mixture is based on a set of equations includes an energy equation, a particle density (concentration) equation, and a state equation. In order to determine the roles of various reaction channels in the ignition of the combustible mixture, we developed a kinetic model including 29 components and 241 forward and back reactions. We took into consideration the neutral unexcited species H_2, O_2, H, O, OH, HO_2, H_2O_2, H_2O, and O_3; the electronically excited oxygen molecules $O_2(a)$ and $O_2(b)$; the positively charged ions O^+, O_2^+, O_4^+, H^+, H_2^+, H_3^+, H_5^+, OH^+, H_2O^+, H_3O^+, $O_3H_2^+$; the negatively charged ions O^-, O_2^-, O_3^-, O_4^-, H^-, OH^- and electrons e. The rate constants included in the model, are taken from works [1–2].

Initially, we simulated the autoignition process. Calculations were carried out on the basis of a kinetic network including 9 components and 60 reactions for various temperatures T_0 and mixture compositions. Under condition of $T_0 = 900$ K, $p_0 = 0.1$ MPa at the early stages of the process (t = 0–1 ms), when the gas temperature is almost constant, reactive atoms and radicals build up, determining the combustion dynamics. Later on, the gas temperature rises sharply and the system passes to a new thermodynamic state. The induction period under these conditions is $\tau_{in} = 1$ ms. The induction period was calculated as a function of the composition of the H_2-O_2 mixture at various temperatures. The ignition delay turned out to depend on both the hydrogen-to-oxygen ratio and gas temperature. As the temperature is raised, the induction period shortens, no matter what the mixture composition. At any temperature, the ignition delay lengthens as the hydrogen-to-oxygen ratio either increases or decreases relative to the stoichiometric composition.

Figure 1 illustrates the effect of a gas discharge on the ignition delay for a stoichiometric (2-1) H_2-O_2 mixture at $p_0 = 0.1$ MPa for instantaneous temperature jumps to various T_0 values. Clearly, the delay time in the ignition induced by nonequilibrium low-temperature plasma decreases by several orders of magnitude as the electron temperature increases. Furthermore, calculations have demonstrated that, as the hydrogen content of the mixture is increased above the stoichiometric value, the gas discharge causes a progressively greater shortening effect on the ignition delay (Fig. 2). At the same time, low-temperature plasma exerts a much weaker effect on lean mixtures. This result is indirect evidence that, at the early stages of the ignition of the H_2-O_2 mixture induced by gas-discharge plasma, electrons form mainly by the ionization of hydrogen mole-

cules. At later stages, the mixture components undergo excitation, dissociation, and ionization by colliding with electrons. Electron attachment and detachment, recharging collisions, and the recombination of charged species take place simultaneously. All these processes lead to the nonequilibrium formation of active species (O and H atoms and OH^* radicals), which participate in branched-chain reactions to intensify the chain combustion of hydrogen.

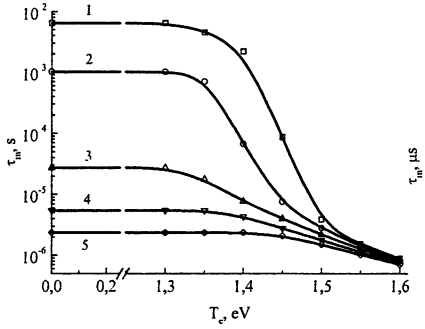

Fig. 1. Effect of the gas discharge on the induction period for the ignition of the stoichiometric (2-1) H_2-O_2 mixture at p_0 = 0.1 MPa with an instantaneous temperature rise to T_0, K: *1* – 800, *2* – 900, *3* – 1000, *4* – 1100, *5* – 1200.

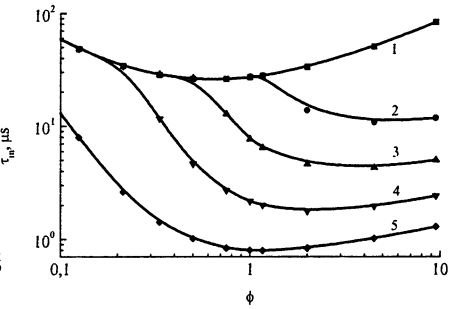

Fig. 2. Induction period as a function of the hydrogen content of the H_2-O_2 mixture at p_0 = 0.1 MPa, T_0 = 1000 K, and T_e, eV: *1* – 0, *2* – 1.3, *3* – 1.4, *4* – 1.5, *5* – 1.6.

Using the basic kinetic network and four reduced networks, we calculated the induction period for gas discharge – induced ignition at various temperatures, pressures, mixture compositions, and electron temperatures [1]. The first reduced kinetic network (RKN1) includes 29 components and 168 reactions, the second (RKN2) includes 23 components and 113 reactions, the third (RKN3) includes 21 components and 89 reactions, and the fourth (RKN4) includes 22 components and 81 reactions. At p_0 = 0.1 MPa, T_0 = 900 K, and various T_e values, RKN1 provides a good description for the ignition of the hydrogen-oxygen mixture. Use of this reaction network instead of the unreduced network generally introduces an error no greater than 10% in the induction period. The largest error is observed for T_e = 1.35 eV. If other conditions, for example, a lower initial temperature is set in the calculations, the error will be greater. For p_0 = 0.1 MPa, T_0 = 800 K, and T_e = 1.4 eV, RKN4 leads to an error greater than 100%. At p_0 = 0.01 MPa, T_0 = 800 K, and T_e = 1.1 eV, even RKN1 leads to an error of 42%. Clearly, the error in τ_{in} depends strongly on process conditions.

These results demonstrate that the basic kinetic network should be reduced in a specific way in each particular case. When reducing the basic kinetic network, it is necessary to perform additional studies to check whether the network chosen is adequate to the given set of conditions.

The work was supported by the RFBR (grant 05-02-16532).

References

1. *Konstantinovskii R S., Shibkov V.M., Shibkova L.V.* Kinet. Katal., 2005, **46** (6), p. 1-15.
2. *Shibkov V.M., Konstantinovskii R.S.* AIAA Paper No. 05–0987, p. 1-8.
3. International Space Planes and Hypersonic System and Technologies Conf., Workshop on Weakly Ionized Gases, Proc. AIAA, USA, Colorado-1997; Norfolk-1998, 1999; Anaheim-2001; Reno-2002, 2003, 2004, 2005.
4. The International Workshops on Magneto- and Plasma Aerodynamics for Aerospace Applications, Proc. Russia, Moscow, IVTAN-1999; 2000, 2001, 2002, 2003, 2005.
5. *Shibkov V.M. et al.*, Vest. Mosk. Univ., Ser. 3. Fiz., Astr. 2000, **41** (6), p. 64-66.
6. *Shibkov V.M. et al.*, AIAA Paper No. 01–3087, p. 1-8.
7. *Shibkov V.M. et al.*, AIAA Paper No. 03–1193, p. 1-7.
8. *Shibkov V.M. et al.*, Vest. Mosk. Univ., Ser. 3: Fiz., Astr. 2004, **45** (5), p. 67-69.
9. *Shibkov V.M. et al.*, Zh. Tekh. Fiz. 2005, **75** (4), p. 67-73.
10. *Shibkov V.M. et al.*, Zh. Tekh. Fiz. 2005, **75** (4), p. 74-79.
11. *Shibkov V.M. et al.*, Fizika Plazmy, 2005, **31** (9), p. 854-857.
12. *Shibkov V.M.,* these proceedings, vol. 2, p. 672-680.

ON THE POSSIBILITY OF TERAHERTZ WAVE GENERATION IN A DENSE GAS OPTICAL DISCHARGE

A. G. Shalashov, E. V. Suvorov, S. V. Golubev

Institute of Applied Physics, RAS, Nizhny Novgorod, Russia

A new method of electromagnetic wave generation in the terahertz range is discussed based on the excitation of Langmuir oscillations by a static electric field in a laser spark produced by an axicon lens in a dense gas, accompanied by the radiation of a coherent broadband electromagnetic pulse through the Cherenkov mechanism.

1. The design of efficient sources of electromagnetic radiation in the terahertz frequency range attracts much attention in the last decade. This relatively new range of electromagnetic radiation opens new perspectives in the analysis of materials, in medicine tomography, in advanced communication systems, etc. In particular, optoelectronic solid-state emitters, detectors, and spectrometers for the analysis of THz signals have now been developed [1]. The development in this direction is mainly associated with the design of the THz oscillators based on the "rectification" of ultrashort optical pulses, in which the shape of radiated signal is close to the envelope (or its derivatives) of a high-frequency optical pulse. Such rectification is accomplished using either crystals with a pronounced nonlinear polarization response or fast photoconductors with a short charge-carrier lifetime. In the latter case, the photocurrent is created by quasi-static fields, either external or internal; illumination of the crystal by a pulsed laser results in the excitation of a surface current, which becomes the source of THz radiation.

In our earlier work [2], we suggested that the aforementioned mechanism operating in the solid-state devices may be realized in a gaseous optical discharge as well. The proposed idea of electromagnetic wave generation in the THz frequency range is based on the excitation of a Langmuir oscillation current in a laser spark plasma using an external quasi-static electric field. The principle of operation of such a source is illustrated in the Fig. 1. An ultrashort laser pulse is focused in a dense gas by an axicon lens into a small dot moving along the focal axis with a velocity larger than the speed of light: $c' = c / \cos\theta_0$ where θ_0 is the lens focusing angle. Accompanied photo-

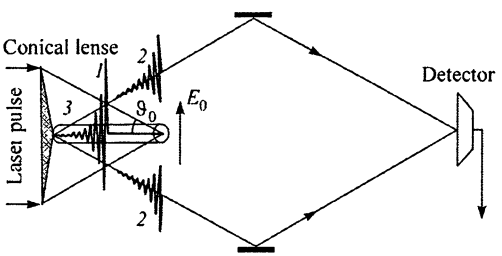

Fig. 1. Scheme of plasma source of THz radiation: *1* – current pulse; 2 – THz pulse; 3 – discharge zone.

ionization wave also propagates along the focusing axis with the super-light velocity. In the presence of an external electric field $\mathbf{E}_0$, a plasma oscillation current wave arises as a result of polarization which radiates a coherent broadband electromagnetic pulse through the Cherenkov mechanism.

Preliminary modeling has demonstrated [2], that such a source can be realized, e. g. at atmospheric pressure breakdown at the subterawatt laser facility operating in the Institute of Applied Physics [3]. In the present communication we amend these results with taking into account dissipation of plasma oscillations due to radiative damping.

2. Let us assume that the laser intensity is so high that the gas tunneling ionization proceeds much faster than all other processes accompanying the terahertz generation. Consider a homogeneous plasma column filling the cylindrical volume around the laser-field focusing axis (Fig. 1). Assume for definiteness that the static electric field $\mathbf{E}_0$ is applied transverse to the cylinder axis resulting in excitation of the transverse plasma oscillations. The main oscillatory mode in this case is related to so-called geometric volume resonance of a cylindrical plasma column (also known as Tonks – Dattner oscillations [4]) with frequency $\omega \approx \omega_p/\sqrt{2}$ where ω_p is the plasma frequency of electrons. Assuming that all electrons exhibit the same displacement $x(t)$ along the electric field relative to the fixed ions, one can obtain the following equation for the electron displacement:

$$x'' + \nu x' + (\omega_p^2/2)x = -eE_0/m\,. \qquad (1)$$

Here ν describes the dissipation of plasma oscillations, which is considered below being of either collisional or radiative nature.

After the instantaneous ionization at $t = t_0$, damped plasma oscillations are excited. They are described by Eq. (1) with zero initial conditions for the displacement and electron velocity: $x(t_0) = x'(t_0) = 0$. In particular, the polarization current density $j = -en_e x'$ caused by the electron motion in the external and charge-separation field can be found:

$$\mathbf{j}(t) = \frac{\mathbf{E}_0\omega_p^2}{4\pi\omega}\begin{cases} e^{-\nu(t-t_0)/2}\sin\omega(t-t_0), & t > t_0 \\ 0, & t \le t_0 \end{cases}, \quad \omega = \sqrt{\omega_p^2/2 - \nu^2/4}\,. \qquad (2)$$

This solution remains valid in the overdamped case, $\nu^2 > 2\omega_p^2$, when ω is purely imaginary (therefore $\sin\omega\tau/\omega$ transforms to $\sinh(\mathrm{Im}\omega\tau)/\mathrm{Im}\omega$). The initial time is defined as $t_0 = z/c'$ corresponding to ionization front movement along the focal axis z with the constant velocity c'. Therefore, the resulting current density is a function of a "retarded" time: $\mathbf{j}(t - z/c')$.

The description of plasma oscillations based on Eq. (1) is valid if (a) oscillations at every space point are mutually independent, i.e. the spatial dispersion is small, (b) the amplitude of these oscillations is small compared to the radius of the oscillating volume, and (c) this radius is small compared to the characteristic radiation wavelength, so the homogeneous electrostatic charge-separation field may be assumed. One can readily verify that, for the atmospheric pressure

discharge, all three conditions may be fulfilled (with a large margin for conditions (a) and (b)).

It should be stressed here, that we omit all effects caused by nonuniformity of the plasma column in a transverse direction as well as a finite time of plasma creation. Recently these effects being inevitable for an optical axicon discharge have been studied within a more detailed model [5]. In particular it is shown that phase mixing of Langmuir oscillations in inhomogeneous plasma may provide additional (very efficient) mechanism of intrinsic plasma losses.

3. The radiation in vacuum from a given current can conveniently be determined through the retarded potentials [6]. In our case, the radiating current wave $\mathbf{j}(t - z/c')$ fills a cylinder volume with radius $a \le 2\pi c/|\omega|$ and length $L >> a$, and propagates along its axis. In the Fraunhofer zone, $r >> L^2 |\omega| \times \times \sin^2\theta /2c$, the vector potential and the electric field may be found in the following form [2]:

$$\mathbf{A}(t) \approx \frac{1}{cr}\int_{-L/2}^{+L/2} \mathbf{j}(t - r/c + z\xi/c)\, \pi a^2 dz\,, \tag{3}$$

$$\mathbf{E}(t) = -\frac{1}{c}\frac{\partial \mathbf{A}(t)}{\partial t} \approx \frac{\pi a^2}{cr\xi}\left\{\mathbf{j}\left(t - r/c + L\xi/2c\right) - \mathbf{j}\left(t - r/c - L\xi/2c\right)\right\}, \tag{4}$$

where $\xi = \cos\theta - c/c'$ is the new angular variable introduced for brevity.

Eqs. (3), (4) describe the Cherenkov emission with a radiation pattern having a maximum at the angle θ_0 to the focusing axis (equal to the focusing angle of laser beam). Width of the radiation pattern may be estimated from the condition $|\xi| < 2c/(L|\omega|)$, where $1/|\omega|$ is the characteristic time of current oscillations. The field amplitude in the vicinity of the radiation pattern maximum can be found by expansion over $\xi << 1$:

$$\mathbf{E}(t) \approx -\frac{V}{c^2 r}\frac{\partial}{\partial t}\mathbf{j}(t') + O\left(\xi^2\right),\ V = \pi a^2 L,\ t' = t - r/c\,, \tag{5}$$

or taking into account plasma-oscillation current (2):

$$\mathbf{E}(t) \approx \mathbf{E}_0 \left(a\omega_p/c\right)^2 \left(L/4r\right)\, e^{-\nu t'/2}\left\{\cos\omega t' - (\nu/2\omega)\sin\omega t'\right\}. \tag{6}$$

In the most interesting and physically relevant cases, the radiation pattern is narrow, $2c/(L|\omega|)<<1$. For this case, the total energy W of the electromagnetic pulse (4) radiated by the plasma current (2) may be defined from the following expression [2]:

$$W \approx V\frac{E_0^2}{4\pi}\left(a\omega_p/c\right)^2\left(\omega_p^2/4\nu\omega\right)\arctan\left(2\omega/\nu\right). \tag{7}$$

Eqs. (6) and (7) are valid both for the oscillatory ($\nu^2 < 2\omega_p^2$, $\mathrm{Im}\omega = 0$) and overdamped ($\nu^2 > 2\omega_p^2$, $\mathrm{Re}\omega = 0$) regimes similar to Eq. (2).

It should be noted that the total radiated energy must not exceed the energy W_0 stored in the plasma oscillations at the initial moment of plasma creation. The latter can be easily estimated as a difference of the energies in final and

initial stages: after all oscillations are damped one obtain a homogeneously polarized plasma cylinder with the energy

$$W_0 = -n_e V\left\{\frac{1}{2}\left(\omega_p^2/2\right)x_0^2 - ex_0E_0\right\} = V\frac{E_0^2}{4\pi}. \qquad (8)$$

Here $x_0 = 2eE_0/m\omega_p^2$ is the stationary displacement of the electrons relative to the fixed ions in the external electric field. The first term in braces describes charge separation energy and the second term describes polarization energy in the external electric field.

4. We now make estimates for a discharge at the atmosphere pressure, so the plasma density corresponded to the initial gas pressure is about $n_e = 3\times10^{19}$ cm^{-3} and the plasma frequency is $\omega_p \approx 3\times10^{14}$ s^{-1}.

The photo-ionization rate by the optical pulse may be estimated e. g. using the average ionization frequency ν_i of a hydrogen atom in a linearly polarized field with amplitude [7]. One then finds that $\nu_i > 2\times10^{14}$ s^{-1} for the laser intensity higher than 2×10^{14} V/cm and the ionization frequency exponentially increases with intensity. At present, such intensities are realized at the Institute of Applied Physics at the subterawatt Ti:Sa laser facility in the experiments with axicon caustic breakdown in dense gases with optical pulse duration about 100 fs [8]. Having in mind possible demonstration experiment with the terahertz generation on this facility, we take the plasma discharge volume to be $L = 1$ cm and $a = 2\times10^{-4}$ cm [8]. Considering that the maximal external electric field strength is limited by the breakdown value, 30 kV/cm at atmosphere pressure, one finds that the energy stored in the plasma oscillations is about $W_0 \approx 10^{-11}$ J. The maximal electric field strength in the pulse at the distance $r = L$ is equal, by the order of magnitude, to the strength of the applied static field (it follows from Eq. (6) with $a\omega_p/c \approx 2$).

In our previous work [2] a purely collisional damping of plasma oscillations was assumed. Then the damping rate may be estimated as defined by electron-ion collisions: $\nu \approx 1.5\times10^{13}$ s^{-1} << ω_p. Therefore, Eq. (2) describes slowly damped current oscillations with the frequency about $\omega_p/\sqrt{2}$ that corresponds to 30 THz, and the decay time about 100 fs. However, the total energy of the electromagnetic pulse radiated by such oscillations is $W \approx 10^{-10}$ J (see Eq. (8)), which is greater than the initially stored energy in the plasma oscillations![1]

Therefore, one should assume that radiation itself provides the dominating mechanism of plasma oscillations damping until all other mechanisms result in condition $W >> W_0$ (so all intrinsic losses are smaller than radiative losses) In this case, the damping rate ν may be introduced basing on the energy balance condition $W = W_0$ (all energy that has been stored is radiated). Using Eqs. (7), (8) this condition may be rewritten as

---

[1] This contradiction has been pointed out in the paper [5], in which radiative losses are taken into account in estimation of the total energy of the electromagnetic pulse (so condition $W \le W_0$ is always fulfilled), but omitted in the modeling of plasma current evolution.

$$\left(a\omega_p/c\right)^2 \frac{\omega_p^2}{2\nu\sqrt{2\omega_p^2-\nu^2}} \arctan\left(\sqrt{\frac{2\omega_p^2}{\nu^2}-1}\right)=1. \qquad (9)$$

Having in mind that our model based on electrostatic plasma oscillations is valid only when radius of the emitting volume is small as compared to a radiation wavelength, the following asymptotic solution[2] to the Eq. (9) may be found in the limiting case of $a\omega_p / c << 2\pi$:

$$\nu \approx \frac{\pi}{2\sqrt{2}}\omega_p\left(\sqrt{\left(a\omega_p/c\right)^2+1}-1\right). \qquad (10)$$

When $\nu < \sqrt{2}\,\omega_p$ the real part of the frequency may be estimated as:

$$\omega \approx \frac{1}{\sqrt{2}}\omega_p\left(1-\frac{\pi^2}{128}\left(a\omega_p/c\right)^4\right). \qquad (11)$$

So, with radiative damping being taken into account plasma oscillations are heavily damped at least at normal pressure, $\nu/\omega \sim (a\omega_p/c)^2 \sim 1$, and all stored energy is emitted within few oscillations. When some intrinsic losses ν_{int} are comparable with the radiative losses, as proposed in [5], the right-hand side in Eq. (9) must be corrected according to reduce in the radiation efficiency: $W = (1-\nu_{int}/\nu)\, W_0$, here ν defines the total (intrinsic plus radiative) losses.

Because of too crude modeling of the radiative losses, details in the shape of the current wave can hardly be described within the approximation based on Eqs. (1) and (9). For more accurate treatment, the Abraham–Lorentz radiation reaction force $f = \tau x'''$ (see, e. g. [6]) with τ defined from the energy conservation may be used in Eq. (1) instead of the friction force $f = \nu x'$. However, this approach is also justified only for the electrostatic plasma oscillations with $a\omega_p / c << 2\pi$. The latter condition may be violated for high pressure discharges (starting from the pressure of several atmospheres). In this case a self-consistent solution to the initial value problem for Maxwell equations is required with taking into account dielectric plasma response in a cylindrical geometry.

The efficiency of the suggested terahertz wave generation technique increases with increasing the ambient gas density. Having in mind that the maximal (breakdown) value of the external static field increases linearly with the gas pressure, one finds that the maximum total energy of the electromagnetic pulse increases as the pressure squared. However, the plasma frequency also increases as a square-root of the pressure (i. e. plasma density); so an increase in the generation efficiency related to the gas pressure is limited by some shift of the frequency range of the electromagnetic pulse to the optical range, which is of little interest. Other possibilities of the efficiency increase are discussed in [5]. In any case, the estimated energy about 10^{-11} J of the terahertz pulse which may be

[2] Deviation of this approximate solution from the exact one is 6% with $a\omega_p/c = \pi$.

generated at the IAP laser stand, is quite measurable with the exiting terahertz radiation detectors.

Authors are grateful to V. B. Gildenburg and N. V. Vvedensky for fruitful discussions and possibility to get acquainted with Ref. [5] before publication. The work is supported by RFBR grant No. 05-02-17517-a.

References

1. *Suvorov E.V., Bratman V.L.,* these proceedings, vol. 1, p. 76-90.
2. *Golubev S.V., Shalashov A.G., Suvorov E.V.*, JETP Lett., 2004, **79** (8), 361.
3. *Babin A.A. et al.*, Usp. Fiz. Nauk, 1999, **169**, 81; Phys. Usp., 1999, **42**, 74.
4. *Tonks L.*, Phys. Rev., 1931, **37**, 1458; *Dattner A.*, Phys. Rev. Lett., 1963, **10**, 205.
5. *Bystrov A.M., Vvedensky N.V., Gildenburg V.B.*, JETP Lett. (submitted 23.09.2005).
6. *Jackson J.D.*, Classical Electodynamics, 3d ed., John Wiley & Sons, Inc., NY, 1999.
7. *Burnett N.H., Corcum P.B.*, J. Opt. Soc. Am. B, 1989, **6**, 1195.
8. *Bodrov S., Kulagin D.*, Technical Digest of IQEC/LAT-YS, Moscow, 2002, 47.

MICROWAVE PROCESSING OF VARIETY OF MATERIALS: DEVELOPMENTS AT PENN STATE MICROWAVE CENTER

Dinesh K. Agrawal

The Pennsylvania State University, University Park, PA 16802 USA

Penn State has been conducting research in microwaves processing of materials for over two decades. In 1980s our activities were mainly confined to oxide ceramics, hydroxyapatites and transparent ceramics. In 1990s we moved on to non-oxide ceramics such as WC/Co based hard composites, synthesis and sintering of important electroceramics, etc. In all these materials we were quite successful in obtaining products with substantial improvements in their properties over conventional product as well as dramatic enhancements in the diffusion and reaction kinetics. Then towards late 1990s, it was found that the metals can also be processed in microwaves very effectively. It is generally known that metals reflect microwaves, however, what was discovered that if the metals are in powder form, they will absorb microwaves and get heated very effectively leading to their sintering and even melting. Almost all metals, including refractory metals (W, Re, Mo, etc.), alloys, steels, and intermetallics were sintered successfully in 5–15 minutes. Then in early 2001, we conducted an extensive investigation of the effect of *E* and *H* fields separation at 2.45 GHz in a single mode cavity on the heating and reactivity of many materials, and found many surprising results, which are not yet fully explained, but they offer important clues to understand the phenomenon of "non-thermal microwave effects".

1. Introduction

The application of microwave energy to process various kinds of materials in an efficient, economic and effective manner is emerging as an innovative technology with great commercial potential and many attractive advantages. In the area of sintering and synthesis using microwave energy, extraordinary enhancements in the materials diffusion and reaction kinetics have been reported. The most recent dramatic results obtained by the use of separation of electric and magnetic fields in a single mode cavity have confounded the scientific community working in this area, and presented new insights to help in understanding the mechanisms of microwave-matter interactions.

At the Microwave Processing and Engineering Center of The Pennsylvania State University, we have been working in the field of microwave materials processing for over two decades. We have conducted research on many materials including oxide ceramics, non-oxides, electroceramics, metallic materials, and *E* & *H* field separation. This paper presents an overview of this research.

2. Microwave sintering of important ceramics

We will confine in this paper only to the high temperature materials processing using microwaves, since this is the area which still needs more

research to be done in order to successful technology transfer to the industry. Only, recently there are reports indicating that some success has been achieved in commercializing the microwave sintering of tungsten carbide based cutting tools [1] and some alumina based products [2]. It is hoped that in near future microwave process will be successfully developed for the commercialization of many other materials where it has shown good promise.

Many traditional and advanced ceramics have been processed in microwave with reported enhancements in reaction and diffusion kinetics and exhibiting better properties than the conventionally processed material. Hereunder only a few selected ceramic materials are reported. All these materials have been processed using 2.45 GHz microwave systems.

Al_2O_3: Alumina is the most common ceramic and has been widely used in microwave sintering research by many scientists working in the field. Because of its highly refractory nature it is difficult to sinter it to full densification unless suitable sintering aids or some special processing techniques are adopted. The full sintering of the alumina using microwave process has been achieved much faster and at lower temperature than the conventional process. Small disc alumina samples microwave sintered at 1400 °C, with no hold time, were 98% dense [3, 4]. In conventional heating it requires at least 1600 °C and 2 hours of soaking time to achieve the same degree of densification but with substantial grain growth. In general, in microwave nearly full density has been achieved at about 200 °C less than the conventional temperature as shown in Fig. 1.

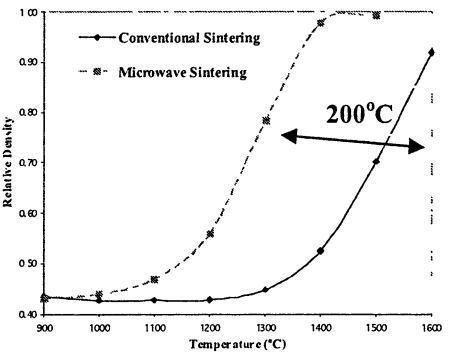

Fig. 1. Sintered density vs. temperature plots for microwave and conventionally sintered alumina.

This work has been extended to fabricate some commercial alumina products with substantial improvement in the quality of the sintered product. For example, sol-gel prepared alumina grit was sintered to full density using a continuous microwave process [5]. The microwave sintering of this material at 1500 °C for 15 minutes provided close to theoretical density. Microwave sintered alumina grit exhibited much higher abrasion index and hardness values

than the standard material. The abrasion index of this grit was 94 and Vicker's hardness 2317 kg/mm^2.

ZrO_2: Zirconia being a refractory oxide ceramic often requires high sintering temperatures and soaking time to obtain high degree of densification. In microwave fine-grained zirconia ceramics were sintered at 1360 °C/2 minutes in a multimode, 2.45 GHz system. The sintered density was about 97.8% and average grain size was 0.25 μm (Fig. 2).

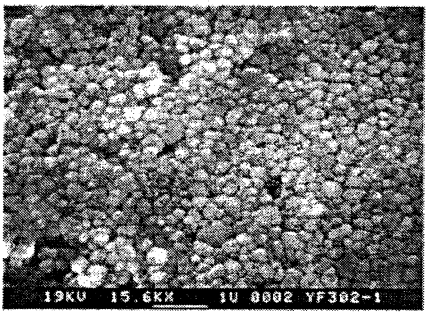

Fig. 2. Microstructure of microwave sintered ZrO_2 (2% Y_2O_3) at 1360 °C for 2 minutes.

$PbZr_{0.52}Ti_{0.48}O_3$ (PZT): PZT is a very common ferroelectric material belonging to perovskite family. It is generally fabricated at temperatures over 1200 °C for several hours of soaking time in a conventional process. One serious problem associated with PZT fabrication is the high loss of PbO due to lengthy sintering soaking time. This is a serious environmental issue. In microwave assisted process single phase PZT was obtained at as low as 600 °C [6] by using TiO_{2-x}. The use of non-stoichiometric TiO_{2-x} enhances the microwave absorption and increases the reaction kinetics many folds. The usage of non-stoichiometric precursors also leads to different reaction pathways for the formation of PZT. In another study PZT samples were microwave sintered at temperatures at 150 °C lower than the conventional process [7] resulting in finer grain size and minimal PbO loss.

$BaTiO_3$ (BT): It is well recognized that virtually all solid state reactions for the synthesis of materials in a conventional process occur under isothermal conditions, i. e. two or more phases involved are at the same temperature. However, the microwave processing for materials synthesis involving two or more phases, may experience a situation known as "anisothermal" state if the reacting phases have different microwave absorption characteristics. Anisothrmal situation is associated with huge temperature differences between the phases at micro-level. This is also one of the key factors to experience dramatic enhancements in reaction and material diffusion rates. In the synthesis of PZT (as shown above) and $BaTiO_3$ the anisothermal approach enhanced reactivity between the starting phases and produced the desired phase in a few minutes. For the synthesis of BT, $BaCO_3$ (a poor microwave absorber) and TiO_{2-x} (an excellent microwave absorber) were used as the precursors. The reaction of the mixture of these two phases in a microwave field occurs radically different from the conventional isothermal heating situation. In the microwave case, at 250 °C, no soak time hexagonal $BaTiO_3$ appears and at 900 °C in 5 minutes nearly phase pure tetragonal $BaTiO_3$ is formed. On the

other hand the conventional process even at 1300 °C for 1 hour soaking time does not produce any XRD detectable $BaTiO_3$ phase [8].

$Ba(Mg_{1/3}Ta_{2/3})O_3$ / $Ba(Zn_{1/3}Ta_{2/3})O_3$: $Ba(Mg_{1/3}Ta_{2/3})O_3$, BMT and $Ba(Zn_{1/3}Ta_{2/3})O_3$, BZT with perovskite crystal structure are good dielectric materials for microwave resonators because of their high quality factors (Q) and moderate dielectric constants. These remarkable materials are, perhaps, the most refractory oxides (melting point > 3000 °C), and therefore very high temperatures (>1600 °C) are required to sinter them in a conventional furnace. However, in the microwave single phase materials using reduced oxide precursors were synthesized and sintered [9, 10]. Use of reduced Ta_2O_{5-x} remarkably enhanced the reaction kinetics and produced single-phase material at 1300 °C/20 min with higher densification than normally obtained by conventional processes. Microwave processed BMT samples exhibited density as high as 97% of theoretical when heated at 1600 °C for 30 minutes. The average grain size in microwave sintered BMT was about 1 μm in contrast to 3 μm in conventional material. BZT samples sintered at 1400 °C for 5 minutes to full density in the microwave had average grain size < 5 μm.

$NaZr_2(PO_4)_3$:[NZP] Compositions: $NaZr_2(PO_4)_3$ is a parent composition of a very large number of family of materials known as [NZP] and characterized by their low thermal expansion behavior [11]. Conventional solid state reaction processes to synthesize and sinter [NZP] compounds require long cycle time and often do not result in to high densification or single phase material. A novel microwave assisted single-step procedure for the synthesis of a number of important members of [NZP] family in less than 20 minutes has been developed [12]. This was made possible by identifying the high microwave absorption of sodium di-dydrogen phosphate monohydrate (NHPM) and using this as one of the reactants. The microwave products exhibited high phase purity and good crystallinity. Specific compounds: $NaZr_2(PO_4)_3$, $NaSn_2(PO_4)_3$, and $NaTi_2(PO_4)_3$ were synthesized at as low as 600 °C in 15 minutes and sintered to more than 97% density.

3. ZnO based ceramic varistors

Zinc oxide varistors are electronic ceramic devices possessing highly non-linear current-voltage characteristics, which enable them to be used as voltage surge suppressors. Various types of zinc oxide varistors under different processing conditions were sintered using microwave heating [13]. Microwave sintering of ZnO varistor samples indicates significant reduction in the cycle time and substantial improvements in the electrical properties. They exhibited better densities, finer grain size, and more uniform microstructure relative to conventional process (Fig. 3). Electrical characterization of the microwave sintered samples showed higher volts and better clamping properties as compared to the conventional sintering. Higher volts/mm response in the

microwaves samples signifies that (i) smaller devices with similar electrical properties can be used, and (ii) it enables to use less material to develop similar devices obtained through conventional process.

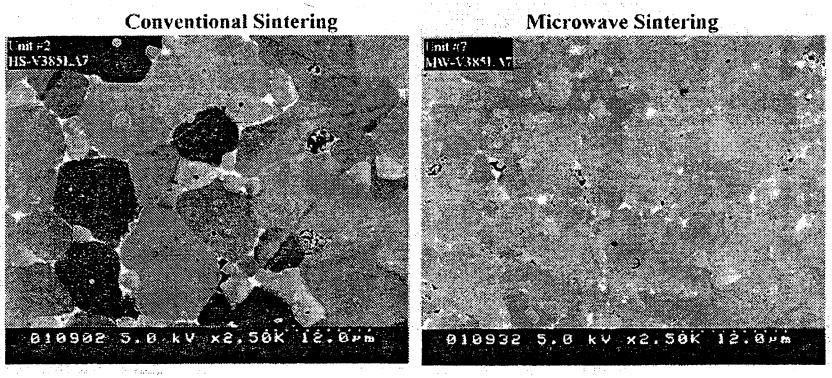

Fig. 3. Typical microstructures of conventional and microwave sintered ZnO based varistor samples.

4. Multi-layer ceramic capacitors (MLCCs)

Microwave sintering of Ni-electrode MLCCs was conducted in an intermediate reducing atmosphere ~ $pO_2 \times 10^{-6}$ atm. It was found that in the temperature range around 1250 °C, the X7R MLCC chips were sintered well, resulting in dense and uniform parts without any delaminations or cracks [14]. Representative SEM micrographs of the fracture surface and free surface of the microwave-sintered Ni-electrode MLCC chips (cross section) are shown in Fig. 4 [15].

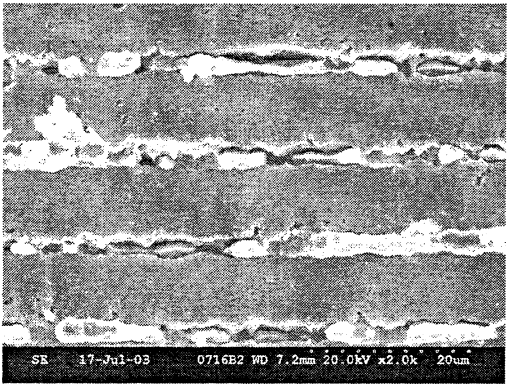

Fig. 4. A typical microstructure of microwave sintered MLCC showing continuity in Ni electrodes and very uniform and homogeneous sintering of $BaTiO_3$ ceramic layers.

5. Transparent ceramics

The conventional methods to fabricate fully dense and reasonably transparent ceramics involve high temperatures, lengthy sintering conditions, and various complex processing steps, which make the processing of transparent ceramics very difficult and uneconomical. However, microwave method has been successfully used to fabricate transparent ceramics due to its ability to minimize the grain growth and produce a fully dense ceramic in a very short period of time without utilizing high-pressure conditions [16]. Hydroxyapatite was fully sintered in to a transparent ceramic at 1100 °C in 10 minutes by microwave processing [17]. The densification was shown to be critically dependent on the starting materials. Transparent ceramics of spinel and alumina were also fabricated [18, 19]. Fully dense alumina [20] and spinel ceramics using high purity and submicron size powders were developed with reasonable degree of transparencies on laboratory size small samples at 1700 °C sintered for 15 minutes in the microwave system. Fully transparent AlON ceramics were also made using multimode microwave system at 1800 °C [21]. Translucent ceramics of AlN, which is a well known high thermal conductivity material, were also developed in microwave at 1900 °C in 60 minutes [22]. Figure 5 shows some of the microwave processed transparent and translucent ceramics of hydroxyapatite, alumina, AlN and ALON.

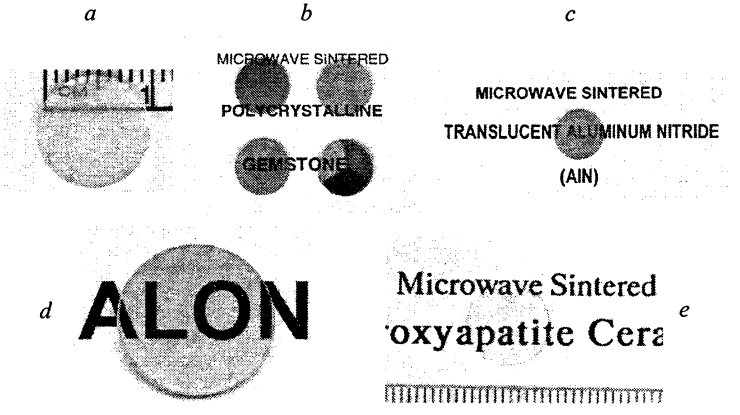

Fig. 5. Various kinds of transparent and translucent ceramics fabricated in microwave: *a* – pure alumina, *b* – doped alumina, *c* – AlN, *d* – ALON, and *e* – hydroxyapatite.

6. WC-Co based ceramic-metal composites

WC-Co based hard metal composites due to their unique combination of hardness, toughness and strength are universally used for cutting tools, machining of wear resistant metals, grinding, mining, and geothermal, oil and

gas drilling operations. Conventional methods for sintering WC with Co as a binder phase involve high temperature (up to 1500 °C) and lengthy sintering cycles (~24 hours) in order to achieve high densification. Such conditions favor undesirable WC grain growth in the presence of Co melts. Consequently, the mechanical strength and hardness of the tools are diminished. In microwave, full sintering of WC commercial green bodies containing 12% and 6% Co was achieved [23], and it was observed that microwave processed WC/Co bodies exhibited better mechanical properties than the conventional parts, fine and uniform microstructure with little grain growth, and nearly full density without adding any grain-growth inhibitors when sintered at 1250–1320 °C for only 10–30 minutes [1, 24, 25]. The microstructural examination of the microwave sintered WC/Co samples, in general, exhibited smaller average grain size than the conventionally sintered sample. Microwave sintered parts also showed significant property improvements without varying the component materials, and without the addition of grain growth inhibitors. The WC/Co part produced by microwave sintering process exhibited an unprecedented improvement in abrasion resistance (15–30% better), erosion resistance (22% better), and corrosion resistance in 15% HNO_3 (20X better) without any noticeable loss in hardness or fracture toughness. These improvements in the properties are believed to be due to the fine microstructure, uniform cobalt phase distribution, and pure Co phase at the grain boundaries in microwave-sintered samples [26]. Figure 6 illustrates some commercial WC/Co parts which have been fabricated very successfully using microwave technology.

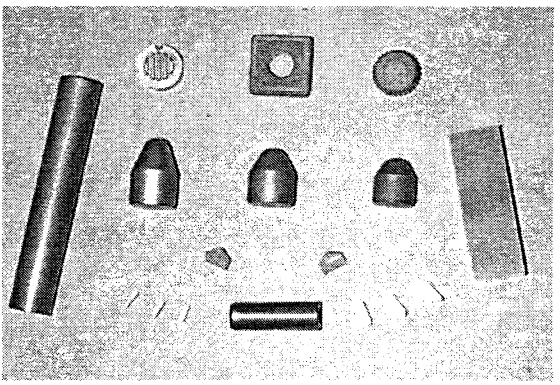

Fig. 6. Microwave sintered cemented carbide based cutting and drilling tools

7. Microwave processing of metallic materials

Until recently, microwave processing of materials mostly was confined to ceramics, semi-metals, inorganic, and polymeric materials. There has been hardly any detailed report on microwave processing of metallic materials. The

main reason for this little work in microwave heating/sintering of metals was due to the misconception that all metals reflect microwave and/or cause plasma formation, and hence cannot be heated in a microwave field. Now, it has been proved that all metallic materials in powder form do absorb microwaves at room temperature, and if even bulk metals are pre-heated to a temperature to at least 400 °C, they also start coupling in microwave field and are heated very rapidly, so much so that they can be melted.

It was only in 1998 that the first attempt of microwave sintering of the powder metals [27] was reported and since then many other researchers have reported successful sintering of many metallic materials [28, 29]. Now it has been shown that the powdered metals are in fact very efficient microwave absorbers and as a result can be very rapidly heated to their sintering temperatures. It has been observed that microwave sintering of metal powders produces a superior product. The steel commercial parts of FC208 and FN208 have been sintered to near net shape. Figure 7 shows some commercial products sintered in microwave. Many commercial powder-metal components of various alloy compositions including iron and steel, Cu, Al, Ni, Mo, Co, Ti, W, WC, Sn, etc. and their alloys have also been sintered in microwaves producing essentially in to nearly fully dense bodies [29–31].

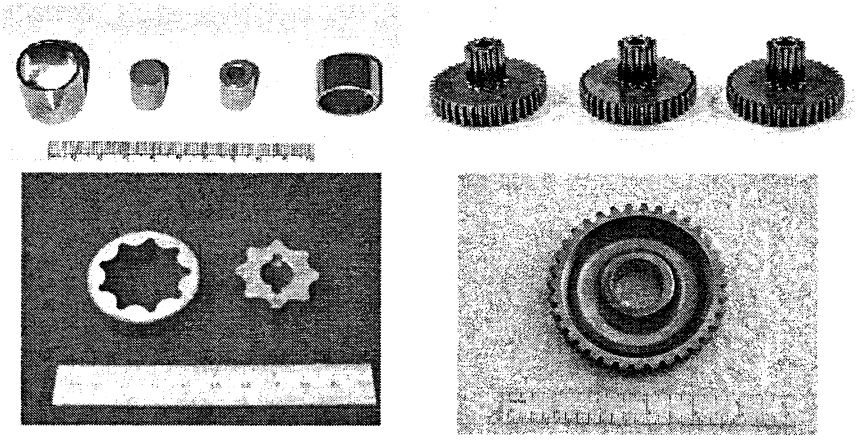

Fig. 7. Various metal/steel parts sintered by microwave process

8. Carbon nanotubes

Carbon nanotubes (CNTs) are hollow cylindrical molecular species that can be conceptually constructed by rolling up a grapheme sheet. Recently, at Penn State using a TE_{103} single mode cavity at 2.45 GHz and *E* and *H* field separation approach, multi-wall carbon nanotubes were synthesized on Fe-coated Si wafers

in the *H* field using acetylene or ethylene as the gaseous carbon source at temperature of 700 °C in 10 minutes (Fig. 8). The diameter of microwave synthesized CNTs could be tailored from 30 nm to 150 nm by adjusting the acetylene/hydrogen ratio. By using thermal oxide on B-doped Si wafer as the substrates, well-aligned CNTs were fabricated with average diameter of ~30 nm and the length of ~10 microns.

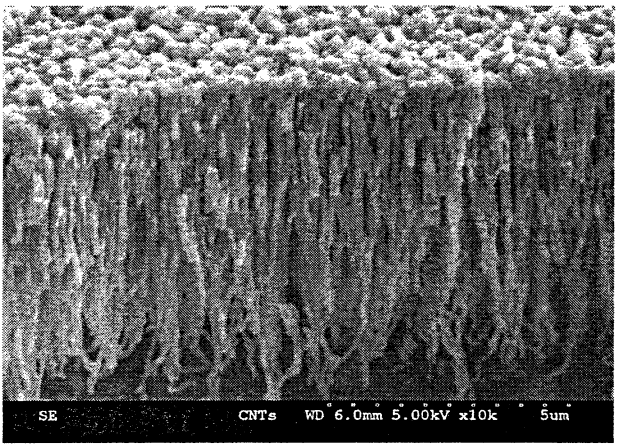

Fig. 8. Multiwalls carbon nanotubes synthesized in a single mode microwave cavity using Si substrate with Fe catalyst in C_2H_2.

9. ZnO single crytal microtubes

ZnO is a promising material for UV and blue light emitting devices because its several advantages over its chief competitor GaN. The single crystal microtube of ZnO has a bandgap of 3.37 eV, with a 60-meV binding energy of the free exciton, and permits excitonic emission at room temperature. To date, most ZnO single crystals have been fabricated in the forms of bulk crystals or thin films or nanowires/nanorods. ZnO single crystal microtubes exhibit strong near band-edge emission, highly selective UV light response, excellent electron field emission, and interesting piezoelectric properties. Recently, ZnO microtubes have been grown by microwave heating and were found to be colorless, fully transparent, contamination-free, and of near-perfect crystallinity [32]. The morphology of the ZnO microtubes observed by optical microscope and SEM is shown in Fig. 9.

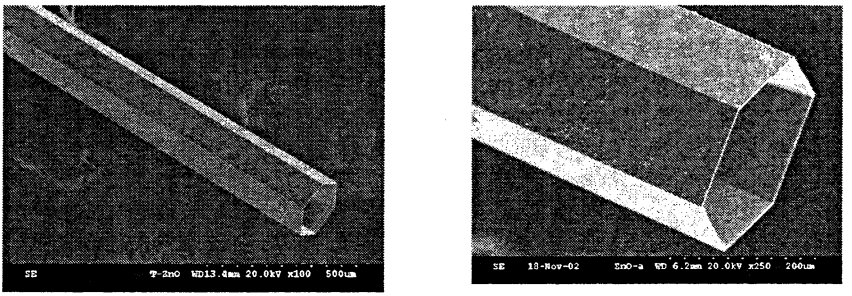

Fig. 9. Single crystal ZnO microtubes synthesized in by microwave process

10. Materials processing in separate *E* and *H* fields at 2.45 GHz

The results of microwave processing of variety of materials presented above (except CNTs) were all produced using multi-mode microwave systems operating at 2.45 GHz frequency, in which various modes of the electric and magnetic components of electromagnetic field are mixed and homogenized. Therefore, in a multi-mode cavity configuration the *E* and *H* fields can not be separated. However, in a single mode cavity the *E* and *H* distributions can be fixed. For example, in a TE_{103} single mode cavity electric and magnetic fields can be separated and materials can be exposed to reasonably pure *E* and *H* fields at 2.45 GHz. In an unloaded cavity where *E* is maximum, *H* is zero and where *H* is maximum, *E* is zero. Therefore small samples placed at *E* or *H* nodes will experience either *E* field or *H* field, respectively.

Cherradi et al. [33] claimed that in most ceramics the dielectric loss mechanism was a minor contribution to the power absorbed compared to the induction losses caused by eddy currents. These researchers also attributed the heating of metals to eddy current losses from the *H* field. Their evidence obtained using different size and shape samples in different orientations, is rather convincing of the role of such eddy current losses as major contributor to the heating of metals. In the Penn State's recent work [34], a survey of a variety of samples of metals, ceramics and composites, showed remarkable differences in their heating behavior depending upon whether they were exposed to *E* field or *H* field at microwave frequency. All metals were very effectively and rapidly heated in the *H* field but not in the *E* field, the reverse was true in case of insulator or ceramics. Further only powder metals could be heated; a solid metallic rod did not get heated at all in either field.

It was also found that many magnetic materials and some special oxides de-crystallize in magnetic field at microwave frequency in 5–90 seconds without going through the actual melting of the material. Such phase transformations are very unusual and the cause of the phenomenon remains to be unexplained [35–37]. Figure 10 gives typical microstructures of barium ferrite ($Ba_4Fe_{12}O_{19}$)

samples processed in E and H field respectively showing that the exposure of 90 seconds in H field made the material totally decrystallized [72]. Similar results were also observed in the case of Fe_3O_4, TiO_{2-x}, CuO, Pr_6O_{11} [73], Si metal [74] and others. Endo et al. [38] explained this observation in magnetic materials in terms of their magnetostriction constant, that higher was the manetostriction constant lower microwave power was required to decrystallize the material. But this can not explain the decrystallization of non-magnetic materials. This work is in its infancy and needs an in-depth investigation of other material systems including metals in order to find the real mechanism to explain this phenomenon.

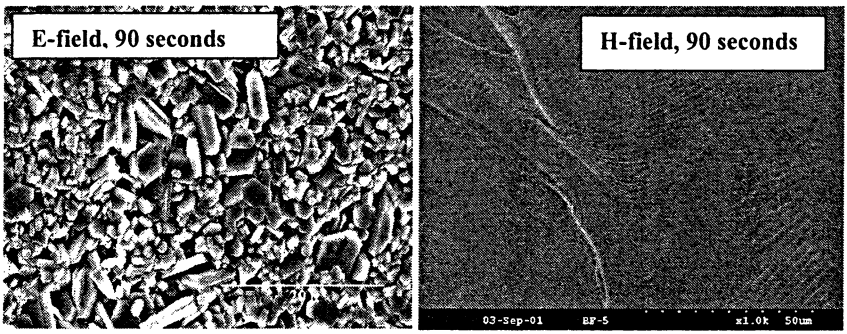

Fig. 10. Typical microstructures of Barium ferrite ($BaFe_{12}O_{19}$) exposed in electric and magnetic fields at 2.45 GHz single mode microwave cavity.

References

1. *Gigl P.D., Breval E., Cheng J., Agrawal D.K., Roy R.*, Structure properties of microwave sintered cemented tungsten carbide materials: Presented at First World Congress on Microwave Processing, Orlando , FL, January 5-9, 1997.
2. *Sato M., Mutoh T., Shimotuma T., Ida K., Motojima O., Fujiwara M., Takayama S., Mizuno M., Obata S., Ito K., Hirai T., Shimada T.*, in Proc. 3rd world congress on Microwave and Radio Frequency Application, Eds., D. Folz, J. Booske, D. Clark, and J. Gerling, ACS Publ., 2003, **281**, p. 189.
3. *Brosnan K.H., Messing G.L., Agrawal D.K.*, J. Am. Ceram. Soc., **86,** 1307 (2003).
4. *Fang Y., Agrawal D., Roy R.*, Mater. Lett., **58**, 498 (2004).
5. *Cheng J., Fang Y., Agrawal D., Roy R., Jayan P.S.*, J. Mat. Process. Tech., **108**, 26 (2000).
6. *Vaidhyanathan B., Singh A.P., Agrawal D.K., Shrout T.R., Roy R.*, J. Am. Ceram. Soc., **84**, 1197 (2001).
7. *Rhee S., Agrawal D., Shrout T., Thumm M.*, Ferroelectrics, **261**, 15 (2001).
8. *Mathis M.D.*, Microwave synthesis using multicomponent and multiphasic systems {Ph.D. Thesis), University Park, The Pennsylvania State University, 1997.
9. *Vaidhyanathan B., Agrawal D.K., Shrout T.R., Fang Y.*, Mater. Lett., **42**, 207 (2000).
10. *Fang Y., Agrawal D., Hackenberher W., Shrout T.R.*, Enhanced Sintering of High-Q $Ba(Zn_{1/3}Ta_{2/3})O_3$ Ceramics, J. Am. Ceram. Soc. (submitted).
11. *Breval E., Agrawal D.K.*, Br. Ceram. Trans., **94**, 27 (1995).
12. *Vaidhyanathan B., Agrawal D.K., Roy R.*, J. Am. Ceram. Soc., **87**, 34 (2004).

13. *Agrawal D., Raghavendra R., Vaidhyanathan B.*, US Patent: 6, 399,012, 4 June 2002.
14. *Fang Y., Agrawal D., Lanagan M., Shrout T., Randall C., Randall M., Henderson A.*, in Ceramic Materials and Multilayer Devices., Cer. Trans., K.M. Nair, Ed., Amer. Cer. Soc., Westerville, OH, 2004, **150**, p. 359.
15. *Fang Y., Lanagan M., Agrawal D., Yang G.Y., Randall C., Shrout T.R., Henderson A., Randall M., Tajuddin A.*, An Investigation Demonstrating the Feasibility of Microwave Sintering of Base-Metal-Electrode Multilayer Capacitors, J. Amer. Ceram. Soc. (In review).
16. *Cheng J., Agrawal D.K., Roy R.*, Am. Ceram. Soc. Bull., **79**, 71 (2000).
17. *Fang Y., Agrawal D.K., Roy D.M., Roy R.*, Mater. Lett., **23**, 147 (1995).
18. *Fang Y., Agrawal D.K., Roy D.M.*, R. Roy, Mater. Lett., **28**, 11 (1996).
19. *Saji T.*, Japn Patent No. 7-187760 (1995).
20. *Cheng J., Agrawal D., Zhang Y., Roy R.*, Mater. Lett., **56**, 587 (2002).
21. *Cheng J., Agrawal D., Zhang Y., Roy R.*, J. Mater. Sci. Lett., **20**, 77 (2001).
22. *Cheng J., Agrawal D., Zhang Y., Roy R.*, J. Electroceram., **9**, 67 (2002).
23. *Cheng J., Agrawal D.K., Komarneni S., Mathis M., Roy R.*, Mat. Res. Innov., **1**, 44 (1997).
24. *Roy R., Agrawal D.K., Cheng J.*, U.S. Patent No. 6,004,505, 21 Dec. 1999.
25. *Agrawal D.K., Cheng J., Roy R., Seegopaul P.*, Microwave sintering of nanocomposite tungsten carbide-cobalt hard materials, Presented at First World Congress on Microwave Processing, January 5-9 1997, Orlando, FL.
26. *Agrawal D., Papworth A.J., Cheng J., Jain H., Williams D.B.*, Proc. 15th Int. Plansee Seminar 2001, G. Kneringer, P. Rodhammer, H. Wildner, Eds., Plansee Holding AG, Reutte, 2001, **2**, p. 677.
27. *Roy R., Agrawal D., Cheng J., Gedevanishvilli S.*, Nature, **399**, 668 (1999).
28. *Takayama S., Saiton Y., Sato M., Nagasaka T., Muroga T., Ninomiya Y.*, Microwave sintering for metal powders in the air by non-thermal effect, 9th Int. Conf. on Microwave and High Freq Heating, Loughborough University, UK, Sep. 2003, 369-372.
29. *Sethi G., Upadhyaya A., Agrawal D.*, Sci of Sintering, **35**, 49 (2003).
30. *Anklekar R.M., Agrawal D.K., Roy R.*, Powder Metall., **44**, 355 (2001).
31. *Anklekar R.M., Bauer K., Agrawal D.K., Roy R.*, Powder Metall., **48**, 39 (2005).
32. *Cheng J., Guo R., Wang Qing-Ming*, Appl. Phys. Lett., **85**, 5140 (2004).
33. *Cherradi A., Desgardin G., Provost J., Raveau B.*, in Electroceramics IV, R. Wasner, S. Hoffmann, D. Bonnenberg, C. Hoffmann, Eds., RWTN, Aachen, 1994, **2**, p. 1219.
34. *Cheng J., Roy R., Agrawal D.*, Mater. Res. Innovations. **5**, 170 (2002).
35. *Roy R., Ramesh P.D., Cheng J.P., Grimes C., Agrawal D.*, J. Mat. Res., **17**, 3008 (2002).
36. *Roy R., Ramesh P.D., Hurtt L., Cheng J., Agrawal D.*, Mat. Res. Innov., **6**, 128 (2002).
37. *Peelamedu R., Roy R., Agrawal D., Drawl W.*, J. Mater. Res. **19**,1599 (2004).
38. *Endo T., Kimura T., Takizawa H., Uheda K.*, Microwave Synthesis of X-ray amorphous ferrites and the magnetic properties, in Proc. Int. Conf. Microwave Chemistry, 2000, p. 335.

STATIONARY THERMAL CONDITIONS THE CERAMIC CYLINDER IN THE FIELD OF MICROWAVE RADIATION

P. V. Kozlov, E. B. Kulumbaev, V. M. Lelevkin

Kyrgyz-Russian Slavic university, Bishkek, Kyrgyz Republic

The numerical analysis of stationary thermal conditions of the ceramic cylinder in the field of electromagnetic radiation of radial type in motionless gas at atmospheric pressure is made.

Introduction

In works [1–3] the model of the SHF-discharge by radial type is developed and the numerical analysis of plasma characteristics in various gases depending on radius of the cylinder, capacity and frequency of a brought electromagnetic field are carried out.

The self-coordinated calculation of microwave heating of ceramic products in real designs on frequencies of an electromagnetic field ~10÷300 GHz is connected to significant difficulties of the numerical decision of an electrodynamic task. It is connected to necessity of the spatial resolution of electromagnetic waves of small length for great volumes of multimodal resonator devices and absence of the data on properties of ceramic materials from temperature, frequency of an electromagnetic field, porosity of products, presence of impurity, etc.

Model

The extended homogeneous ceramic cylinder (Fig. 1) is considered. Stationary of thermal condition of a ceramic product it is provided with power balance between heating due to a dissipation of a brought electromagnetic wave of radial type $\mathrm{E}\left(0;0;E_z=E(r)\right)\exp(i\omega t)$, $\mathrm{B}\left(0;B_\varphi=B(r);0\right)\exp(i\omega t)$ and cooling due to heat removal by heat conductivity in surrounding motionless air.

The equations. Thermal and electromagnetic characteristics of the extended ceramic cylinder in a field of microwave radiation of radial type are defined by the equation of energy balance and the wave equation [1]:

$$\frac{1}{r}\frac{d}{dr}\left(r\lambda\frac{dT}{dr}\right)+\frac{1}{2}\varepsilon_I\omega\varepsilon_0 EE^*=0;\ \frac{1}{r}\frac{d}{dr}\left(r\frac{dE}{dr}\right)+k_0^2\left(\varepsilon_R-i\varepsilon_I\right)E=0;\ B=\frac{1}{i\omega}\frac{dE}{dr}$$

where T – temperature; $\omega=2\pi f$ – frequency; $k_0=\omega/c$ – wave number in vacuum; $\lambda(T)$, $\varepsilon_R(T)$, $\varepsilon_I(T)$ – heat conductivity, the real and imaginary parts of

complex dielectric permeability; c – light speed; ε_0 – an electric constant; i – imaginary unit; the top index * designates in a complex connected size.

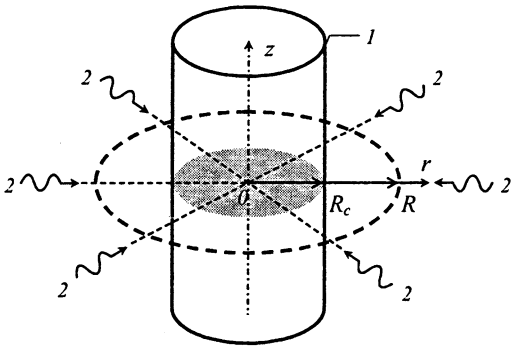

Fig. 1. Scheme of a ceramic cylinder (with radius R_c) (*1*) heating by radial electromagnetic wave (*2*); R – radius of the computational domain.

Boundary conditions surrounding areas $0 \le r \le R$ (Fig. 1) are put for temperature and intensity of an electric field as:

$r = 0$: $dT/dr = 0$; $dE/dr = 0$; $r = R$: $T = T_R$; $E = E_R$;

value E_R is defined from sewing together numerical E and analytical decisions $E_0 = C_1 \mathrm{H}_0^{(1)}(k_0 r) + C_2 \mathrm{H}_0^{(2)}(k_0 r)$ – superposition of the falling and reflected cylindrical waves at $\varepsilon_R = 1$, $\varepsilon_I = 0$ – the wave equation on the preset running power P_I of a brought electromagnetic field [1]:

$r = R$: $E_R = E_0$; $(dE/dr)_R = (dE_0/dr)_R$

under formulas:

$$C_1 = -\frac{i\pi R}{4}\left[k_0 E_R \mathrm{H}_1^{(2)}(k_0 R) + \left(\frac{dE}{dr}\right)_R \mathrm{H}_0^{(2)}(k_0 R)\right];$$

$$C_2 = +\frac{i\pi R}{4}\left[k_0 E_R \mathrm{H}_1^{(1)}(k_0 R) + \left(\frac{dE}{dr}\right)_R \mathrm{H}_0^{(1)}(k_0 R)\right];$$

$$P_I = \frac{\pi R}{2\mu_0}\left(E_R B_R^* + E_R^* B_R\right) = 2|C_1|^2/\omega\mu_0;\ C_{refl} = |C_2/C_1|^2;\ P_R = C_{refl} P_I,$$

here C_{refl} – coefficient of reflection; P_R – running power of the reflected wave; $H_{0,1}^{(1,2)}(k_0 r) = I_{0,1}(k_0 r) \pm i Y_{0,1}(k_0 r)$, $I_{0,1}(k_0 r), Y_{0,1}(k_0 r)$ – Hankel and Bessel 1 and 2 function sorts.

In integrated balance of energy $P_I = P_R + P_d$ dissipated on unit of length of the ceramic cylinder power P_d, finally, is removed by heat conductivity of air through border of considered area (Fig. 1):

$$P_d = \pi \int_0^R \varepsilon_I(T)\omega\varepsilon_0 EE^* r dr = 2\pi\left(-r\lambda\frac{dT}{dr}\right)_R .$$

Method of the solution. The numerical solution of equations system with boundary conditions is made on a non-uniform grid with digitization by a method of control volume [4]. Discrete analogues are solved an iterative method on which each step the method of Gauss exception is applied.

The wave equation defines intensity of an electric field to within any constant multiplier. Therefore, as external parameter of an electrodynamics task brought P_I or dissipated P_d powers it is used.

Results

The numerical analysis of stationary thermal conditions of the ceramic cylinder from sintered aluminum oxide Al_2O_3 (density of 97%) and silicon nitride Si_3N_4 in a field of electromagnetic radiation of radial type in motionless air or nitrogen is carried out at atmospheric pressure (Fig. 1): radius of the cylinder R_c = 15 mm; radius of settlement area R = 50 mm; frequency of an electromagnetic field f = 30 and 130 GHz. Electromagnetic and portable properties Al_2O_3 are taken according to the IAP of the Russian Academy of Science from work [5]; portable properties of air at atmospheric pressure are taken from [6], $\varepsilon_R = 1$, $\varepsilon_I = 0$.

It is visible (Fig. 2) that owing to the "big" heat conductivity in relation to air, temperature drop in a ceramic product is essentially less, than in air, and temperature distribution to interface of two environments ceramics – air tests of characteristic break. Change of temperature on cylinder section is the practically linearly, and small deviations are caused by influence of dependence of heat conductivity factors of aluminum oxide and air from temperature.

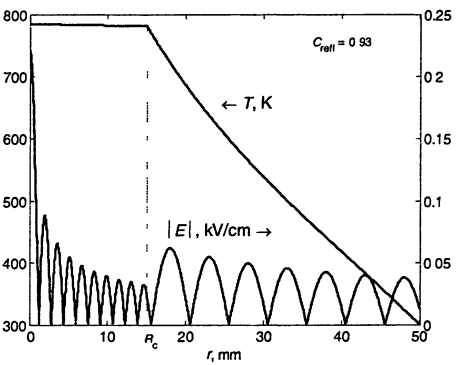

Fig. 2. Radial distributions of temperature and the module of intensity of an electric field: P_I = = 1.5 kW/m; f = 30 GHz; T_{max} = 785 K.

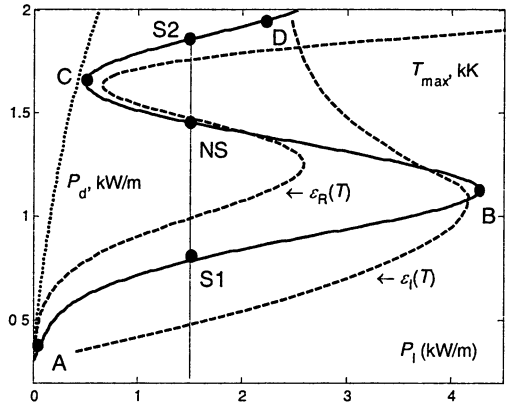

Fig. 3. Dependence of temperature on an axis of cylinder Al_2O_3 from brought power of an electromagnetic wave of radial type $f = 30$ GHz: a continuous line – of temperature dependence of factors of a ceramic material (dot – dissipated power) it is considered; dotted – the constant values of factors from temperature it is preset.

Owing to smallness an imaginary part of complex dielectric permeability of aluminum oxide the weak absorption of microwave radiation in a sample and appreciable heterogeneities of a volumetric source of a thermal emission are realized. Last is shown as system alternating among themselves ring-shaped areas with local maximal and practically zero values of the intensity module of an electric field. Growth of local maximal values $|E|$ from a lateral surface to an axis of the ceramic cylinder is observed (effect of focusing of a field on an axis) (Fig. 2). Such picture of distributions $|E|(r)$ is explained by formation of "quasi-standing" waves as a superposition result of falling and the reflected electromagnetic waves carrying practically identical values of power of microwave radiation (factor of reflection $C_{refl} = 0.93$). Heterogeneities of a volumetric source of a thermal emission do not affect spatial distribution of temperature because of "smoothing" action of heat conductivity.

It is clear (Fig. 3), that stationary thermal conditions of ceramic cylinder Al_2O_3 (R_c = 15 mm, f = 30 GHz) form the S-shaped dependence of the maximal axial temperature on brought power of microwave radiation $T_{max}(P_I)$. At $P_I > P_C$ three stationary thermal conditions of a ceramic product are realized: steady temperatures concerning fluctuations *S1* and *S2* on branches *AB* and *CD*, unstable *NS* on branch *BC*. Connection between T_{max} also P_d is unequivocal. During iterative approach (approximation) the temperature in point *NS* on a unstable branch $T_{max}(P_I)$ is displaced in positions *S2* or *S1* on steady branches of *CD*, *AB* (Fig. 3). Therefore for definition of characteristics of ceramic products on unstable branch BC it is necessary to preset the values of dissipated power of microwave radiation.

The numerical analysis has shown that ambiguity of the attitude $T_{max}(P_I)$ is caused by dependences of the real and imaginary parts of complex dielectric permeability of a ceramic material on temperature (see Fig. 3). At the account

$\varepsilon_I(T)$ and other constant values of factors of a ceramic material from temperature the steady and unstable conditions (a dotted curve $\varepsilon_I(T)$, Fig. 4) are realized. If dependence $\varepsilon_R(T)$ on temperature is taken into account at other constant factors results of calculation qualitatively repeat S-shaped curve $T_{\max}(P_I)$ (a dotted curve $\varepsilon_R(T)$, Fig. 3).

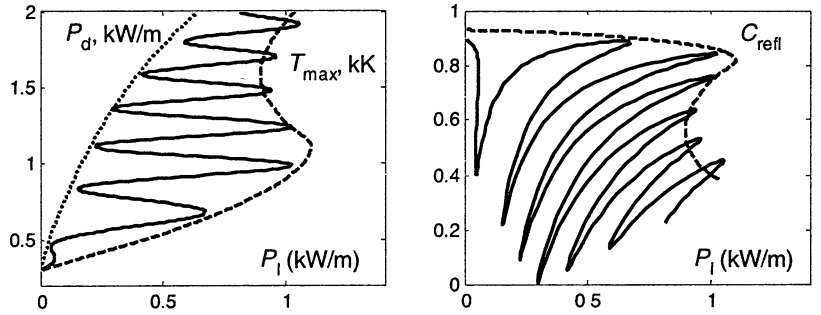

Fig. 4. Dependence of axial temperature and reflection factor of Al_2O_3 from brought power of an electromagnetic wave (f = 130 GHz): a continuous line – temperature dependence of factors of a ceramic material (dot – dissipated power) is considered; dotted – $\varepsilon_I(T)$ and other constant factors are considered.

With increase of an electromagnetic field frequency the nonlinear dependence $T_{\max}(P_I)$ amplifies: the number of the maximal and minimal values T_0 (steady and unstable modes of heating of a ceramic material) has increased in 6 times (Fig. 4). The factor of reflection C_{refl} of microwave radiation depending on brought power of electromagnetic fields changes by complex way. It is typical, that a curve which is taking into account $\varepsilon_I(T)$ at constant factors $\lambda(T)$, $\varepsilon_R(T)$, is bending around the maximal values of reflection factor and axial temperature of the ceramic cylinder (see Fig. 3).

Conclusions

The numerical analysis of stationary thermal conditions of ceramic materials in a field of electromagnetic radiation has shown nonlinear dependence of temperature of a ceramic material on brought power and frequency of the microwave radiation, caused by change of complex dielectric permeability from temperature, presence of unstable conditions, increase (focusing) of an electric field in a direction to an axis of symmetry and, as consequence, strengthening of a dissipation of electromagnetic power.

Despite of a strict correctness of a thermal and electrodynamics problem the given calculations have preliminary and estimated character since there is the big uncertainty connected to the task of ceramic materials properties from temperature, by frequency of an electromagnetic field, porosity, presence of impurity and phase transformation.

References

1. *Dresvin S.V., Bobrov A.A., Lelevkin V.M. et al*, *RF* and Microwave Plasmotrons., Nauka, Novosibirsk, 1992, Vol. 6.
2. *Lelevkin V.M., Otorbaev D.K., Schram D.C.*, Physics of non-equilibrium plasmas, North-Holland, Amsterdam, 1992.
3. *Lelevkin V.M., Otorbaev D.K.*, Experimental methods and theoretical models in physics of nonequilibrium plasma, Ilim, Frunze, 1988.
4. *Patankar S.*, Numeral Heat Transfer and Fluid Flow., McGraw-Hill, New York, 1980; Énergoatomizdat, Moscow, 1984.
5. *Bulls Yu.V., Egorov S.V., Fishermen K.I et al.*, Gas-dynamic calculation of a mode of microwave heating of ceramic materials: Materials of the international seminar Problems of modeling and development of technology of reception of ceramics, ISTC, KRSU, Bishkek, 2005.
6. *Éngel'sht V.S., Gurovich V.Ts., Desyatkov G.A. et al.*, The Theory of Electric Arc Column, Nauka, Novosibirsk, 1990, Vol. 1.

GAS-DYNAMIC MODELING OF THE MICROWAVE HEATING OF CERAMIC MATERIALS

Yu. V. Bykov, S. V. Egorov, K. I. Rybakov, V. E. Semenov, O. N. Kanygina[1], E. B. Kulumbaev[1], V. M. Lelevkin[1]

Institute of Applied Physics, Russian Academy of Sciences, Nizhny Novgorod, Russia
[1]Kyrgyz-Russian Slavic University, Bishkek, Kyrgyz Republic

The temperature distributions arising in a low-loss dielectric sample in the process of microwave heating in air have been studied using a numerical gas-dynamic model. The convective heat removal has been demonstrated to play the determining role in the energy balance of the sample. The obtained temperature distributions have been compared with the results of a microwave heating experiment with multi-channel temperature measurement. The results suggest that the temperature distribution is strongly influenced by air convection and the electromagnetic field structure in the microwave-heated sample.

Introduction

High-temperature microwave processing of materials is an emerging field of science and technology that attracts a growing interest of researchers worldwide [1, 2]. In developing microwave processing applications, an important role is played by numerical simulation that can be an efficient tool to cut down the costs of application development. However, to be usable for this purpose, a simulation method must possess sufficient accuracy. In particular, solid-state diffusion and other thermally activated processes are highly sensitive to temperature, and it is important to be able to control and simulate the temperature of the material undergoing microwave processing to an accuracy better than 1%.

An important factor that affects the temperature distribution under microwave heating is heat removal from the sample. In contrast to conventional furnaces where the heat is delivered to the sample from the outside, in a microwave heating system the heat is generated inside the sample due to dissipation of the microwave energy. The temperature distribution establishes as a result of concurrent heat generation in the volume of the sample and heat removal through the sample surface. The objective of this paper is to determine the role played by convection in a microwave heating process by comparing calculated and measured temperature distributions.

Experiment

The experiments on multichannel temperature measurement were performed on a 30 GHz/10 kW gyrotron system for microwave processing of materials [3]. The microwave radiation from the gyrotron is fed into the applicator,

which comprises a cylindrical supermultimode cavity. Hundreds of modes excited simultaneously in the cavity are additionally stirred by a rotating mode stirrer, in order to obtain a more uniform distribution of the electromagnetic field.

A cylindrical alumina ceramic sample was positioned in the cavity on a support made of porous quartz. The dimensions of the cavity, sample and support are shown in Fig. 1, *a*. Although in the majority of experiments the sample undergoing the processing is surrounded by thermal insulation, in this particular experiment no thermal insulation was used, to facilitate the comparison with simulation described below. The temperature was measured at eight points of the sample by type K thermocouples, positioned as shown in Fig. 1, *b*.

The gyrotron system is equipped with a feedback-loop power control circuit for automatic control over the gyrotron output power in accordance with a preset temperature-time schedule. The reading from one of the temperature sensors is compared with the scheduled temperature, and the power is increased or decreased depending on the difference. The accuracy of sustaining the preset temperature-time schedule in the system is about 1%. In the described experiments, a constant heating rate, 20 K/min, was preset, and the reading from the thermocouple № 38 was used in the feedback loop of the power control circuit.

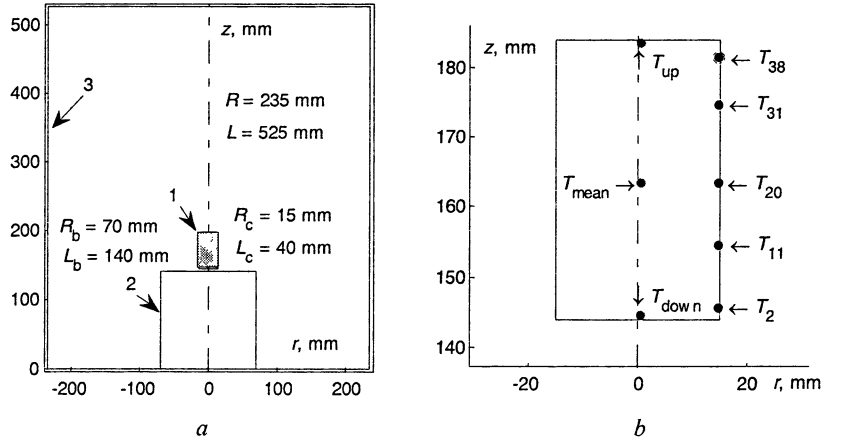

Fig. 1. Dimensions of the ceramic sample *1* on the support *2* in the supermultimode cavity applicator *3* of the gyrotron system (*a*). Positions of the thermocouple sensors of the multichannel system for temperature measurements (*b*).

Model

The evolution of the temperature distribution is described by a model that accounts for volumetric microwave heating of the sample and its cooling by

conductive and convective heat transfer into the surrounding air (the radiation heat losses are negligibly small since the temperatures do not exceed 400 °C). As a rough approximation, the power deposition due to microwave heating is assumed to be uniform within the volume of the sample. The limitations of this approximation are discussed below in the Discussion section.

The heating process is described by the equations of continuity, Navier–Stokes, and energy balance. In cylindrical coordinates (see Fig. 1) for the axially symmetric case the equations take the following form:

$$\frac{\partial \rho}{\partial t}+\frac{1}{r}\frac{\partial}{\partial r}(r\rho v)+\frac{\partial}{\partial z}(\rho u)=0,$$

$$\rho\left(\frac{\partial v}{\partial t}+v\frac{\partial v}{\partial r}+u\frac{\partial v}{\partial r}\right)=-\frac{\partial p}{\partial r}+\frac{2}{r}\frac{\partial}{\partial r}\left(r\eta\frac{\partial v}{\partial r}\right)-\frac{2\eta v}{r^2}+$$

$$+\frac{\partial}{\partial z}\left[\eta\left(\frac{\partial u}{\partial r}+\frac{\partial v}{\partial z}\right)\right]-\frac{\partial}{\partial r}\left[\frac{2}{3}\eta\left(\frac{1}{r}\frac{\partial rv}{\partial r}+\frac{\partial u}{\partial z}\right)\right],$$

$$\rho\left(\frac{\partial u}{\partial t}+v\frac{\partial u}{\partial r}+u\frac{\partial u}{\partial z}\right)=-\frac{\partial p}{\partial z}+2\frac{\partial}{\partial z}\left(\eta\frac{\partial u}{\partial z}\right)+$$

$$+\frac{1}{r}\frac{\partial}{\partial r}\left[r\eta\left(\frac{\partial u}{\partial r}+\frac{\partial v}{\partial z}\right)\right]-\frac{\partial}{\partial z}\left[\frac{2}{3}\eta\left(\frac{1}{r}\frac{\partial rv}{\partial r}+\frac{\partial u}{\partial z}\right)\right]+(\rho_\infty-\rho)g,$$

$$\rho C\left(\frac{\partial T}{\partial t}+u\frac{\partial T}{\partial z}+v\frac{\partial T}{\partial r}\right)=\frac{1}{r}\frac{\partial}{\partial r}\left(r\lambda\frac{\partial T}{\partial r}\right)+\frac{\partial}{\partial z}\left(\lambda\frac{\partial T}{\partial z}\right)+P(t).$$

Here $\vec{V}=\left(V_r=v,\ V_\varphi=0,\ V_z=u\right)$ is velocity of air, T is temperature, p is pressure, g is free fall acceleration, ρ, λ, C, η are density, thermal conductivity, heat capacity and viscosity, respectively, ρ_∞ is density of "cold" air. $P(t)$ is the heat source term that expresses microwave power deposition.

The boundary conditions are defined on the rectangular contour of the simulation area, $0\le r\le R$, $0\le z\le L$ (Fig. 1). They include axial symmetry, fixed temperature and zero velocity of air at the cavity walls:

$$0\le z\le L;\ r=0:\quad \frac{\partial T}{\partial r}=0;\quad \frac{\partial u}{\partial r}=0;\ v=0;\ r=R:\quad T=T_R;\ u=v=0,$$

$$0\le r\le R;\quad z=0;L:\quad T=T_R;\quad u=v=0.$$

The microwave-induced heat source is the primary cause of temperature evolution in the system. However, in order to accomplish proper comparison with experiment, where the microwave power is controlled to implement a preset temperature-time schedule, an inverse problem is solved in this simulation. A certain temperature-time schedule is given for one point of the sample, and the temperature evolution in all other points of the simulation volume, as well as the time dependence of the microwave power, $P(t)$, are obtained.

The computation method is based on a through calculation, in which conjugation of problems in the solid bodies and in the air is achieved by introducing harmonic-average transport coefficients on the boundaries between them [4]; inside the solid bodies the viscosity values are taken high enough to ensure zero velocities. The equations are digitized using the control volume method. The pressure field is computed by the SIMPLER procedure [4]. The microwave power, $P(t)$, at any given moment of time is obtained from the energy balance equation at the point of the sample for which the temperature-time schedule is prescribed.

Results and discussion

An example of the simulation results is shown in Fig. 2. The temperature-time schedule of the upper point of the side surface of the sample, $T_{38}(t)$, was chosen as $T_{38} = T_R + \alpha t$, where the heating rate, α, was chosen equal to 20 K/min in accordance with experiment.

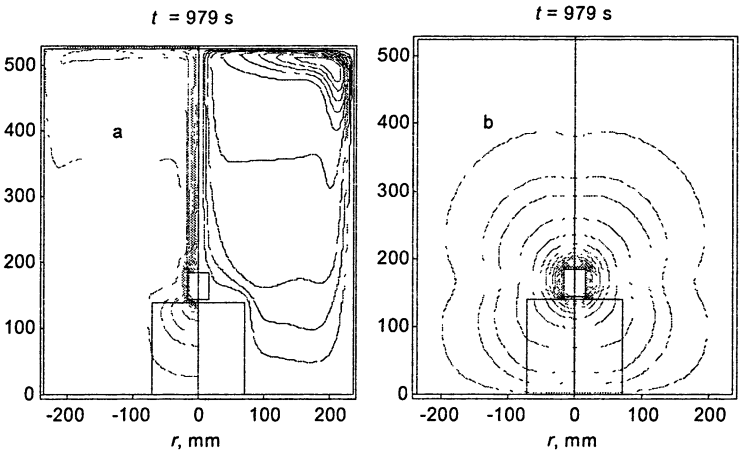

Fig. 2. Calculated dynamics of microwave heating with an account for convective and conductive heat transport (*a*): left – the temperature field (isotherms 301 K, 305 K, 310 K, 325 K and so on with a step of 25 K), right – gas flow lines (from 0.1 with a step of 0.1). The case of conductive heat transport only (no convection, isotherms only) (*b*).

As the sample is heated due to dissipation of the energy of the microwave electromagnetic field, the air surrounding the sample also heats up and its density decreases. Gradients of air density form within the applicator and they cause convective air flows. Hot air goes up, transports heat to the applicator walls, cools down and descends along the walls. As a result, a gas flow with a non-uniform temperature distribution is established in the applicator (Fig. 2, *a*).

For comparison, the case of conductive heat transport only (no convection) is illustrated by Fig. 2, *b*.

Figure 3 shows the time dependencies of the microwave power, $P(t)$, normalized by its maximum value. For comparison, the microwave power recorded in a microwave heating experiment with constant heating rate is shown (curve *1*). The microwave power has been computed for three cases: with an account for both convective and conductive heat removal from the sample (curve *2*), conductive heat removal only, no convection (curve *3*), and no heat removal from the sample (curve *4*). In the latter case the power factor is determined analytically,

$$P(t) = \rho C(T)\frac{\partial T}{\partial t} = \rho C(T)\frac{(T_* - T_R)}{t_*}.$$

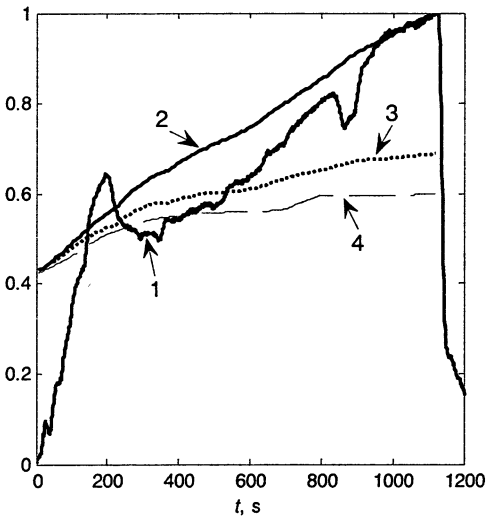

Fig. 3. Time dependencies of the microwave power, $P(t)$, normalized by its maximum value: *1* – experimental curve from a microwave heating experiment with the same heating rate (20 K/min), *2* – calculated with an account for both convective and conductive heat removal from the sample, *3* – calculated with conductive heat removal only (no convection), *4* – calculated with no heat removal from the sample.

It can be seen that the simulation result that accounts for convective and conductive heat removal is, on the average, the closest to the experimental curve. By comparing curves *2*, *3* and *4* it can be seen that convective heat removal is prevailing over conductive during the entire process, except its initial stage, when the temperature difference between the sample and the applicator walls is insignificant. At higher temperatures the convective heat removal is about 4 times stronger than conductive.

Figure 4 shows comparison of the calculated and measured temperatures at eight points of the sample. It can be seen that while the measured temperatures on the side surface of the sample agree well with the simulation (taking both convective and conductive heat removal into account), the measured temperatures on the axis of the sample (T_{down}) and especially in its core (T_{mean}) are noticeably higher than those predicted by simulation. This suggests that the heat source inside the sample is essentially non-uniform, which is apparently associated with the inhomogeneity of electric field distribution [5].

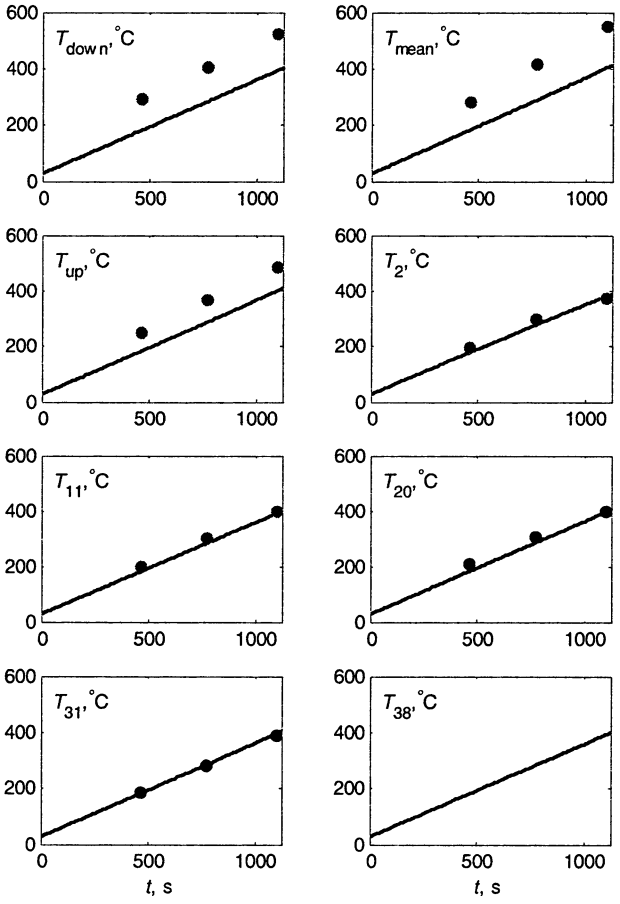

Fig. 4. Temperature evolution at different points of the sample (solid lines – simulated, dots – measured). The temperature-time schedule $T_{38}(t)$ was preset as a constant heating rate, 20 K/min. See Fig. 1, *b* for positions of the points.

Conclusion

A comparative experimental and numerical study of the process of microwave heating of a dielectric sample in air in a multimode cavity applicator has been accomplished. It has been shown that convective heat removal prevails over thermal conduction of air, starting from early stages of the process. The simulation taking convection into account results in a good agreement of the measured and calculated values of temperature on the surface of the sample. However, the measured temperature in the bulk of the sample is higher than predicted by simulation. This is associated with the non-uniformity of electromagnetic field inside the sample, which was not accounted for in the simulation.

The results of this research demonstrate that commonly used simple models are inadequate for correct simulation of microwave heating processes. Accurate simulation should account for heat removal by convective air flows and the distribution of electromagnetic field in the sample.

Acknowledgement

Partial support of this research by the International Science and Technology Center (project KR-727), INTAS (project 03-51-5345), and the U.S. Civilian Research and Development foundation (BRHE fellowship Y1-PE-01-03) is acknowledged.

References

1. *Clark D.E., Sutton W.H., Lewis D.A.*, Annu. Rev. Mater. Sci., **26**, 299-331 (1996).
2. *Bykov Yu.V., Rybakov K.I., Semenov V.E.*, J. Physics D: Appl. Phys., **34**, R55-R75 (2001).
3. *Bykov Yu. et al.*, Ceramic Transcations, **59**, 133-140 (1995).
4. *Patankar S.*, Numeral Heat Transfer and Fluid Flow, McGraw-Hill, New York, 1980.
5. *Rybakov K.I. et al.*, J. Appl. Phys., **99**, 023506-023514 (2006).

EVIDENCE FOR NON-THERMAL EFFECTS DURING MICROWAVE SINTERING OF ZIRCONIA CERAMICS

G. Link[1], *M. Wolff*[2], *S. Takayama*[1], *G. Falk*[2], *R. Clasen*[2], *M. Thumm*[1,3]

[1]Forschungszentrum Karlsruhe, IHM, Germany
[2]Saarland University, Dep. of Powder Technology, Saarbrücken, Germany
[3]University of Karlsruhe, IHE, Germany

The potential of microwave sintering has been investigated in field of sintering Y_2O_3 stabilized, tetragonal and cubic ZrO_2 in comparison to conventional sintering techniques. Ceramic green bodies with high green densities and homogeneous pore size distribution were produced by electrophoretic deposition technique. So produced samples were microwave sintered in a multimode applicator of a compact 30 GHz gyrotron system and in a 2,45 GHz single mode cavity. The subsequent microstructure analysis in comparison to equivalent results from conventional sintering gave evidence for microwave specific non-thermal effects.

Introduction

The material properties of ceramic materials are significantly determine by the microstructure and the residual porosity. The sintering process as well as powder conditioning and powder compaction technology are important processing steps to control the microstructure. In this work, the potential of microwave sintering (MWS) for the production of dense and fine grained zirconia ceramics was investigated in combination with advanced green body shaping techniques.

Microwave technology gathered growing industrial interest for thermal processing of various kinds of materials. The benefits of volumetric heating by microwaves can be exploited to significantly shorten processing times, especially if large volumes of materials with low thermal conductivity have to be processed. Furthermore, enhanced sintering as a result of microwave heating has been reported in literature used to explain phenomenological observations such a significant reduction in processing temperature and time [1]. Recently theoretical models have been developed, which try to explain such non-thermal effects revealed by microwave sintering of ceramics [2].

One of the major focuses of this work were to examine the effects of microwave heating onto the microstructure evolution in ceramics. Therefore nanocrystalline powder compacts of zirconia ceramics were produced by the advanced eletrophoretic deposition technique [3]. Then these compacts were microwave sintered in a multimode cavity as well as in a linear polarized electric field of a single mode waveguide applicator. The microstructures of the sintered samples were compared to results obtained in a conventional, resistive heated furnace with respect to grain size and pore geometry.

Experimental

The green bodies used for the following investigations were manufactured from nanosized powders of 3 mol-% Y_2O_3, tetragonal stabilized ZrO_2 (TZ3YS) and of 10 mol-% Y_2O_3, cubic stabilized ZrO_2 (TZ10YS) from Tosoh Corp., Japan. The TZ3YS powder had a mean grain size of 27 nm. TZ10YS had a mean grain size of 62 nm determined by XRD and an aggregate size of 0.5 μm.

For optimal shaping with electrophoretic deposition (EPD) a deaggregation and dispersion of the powders into an agglomerate-free suspension with a high solids loading was realized. The so produced green bodies were dried for 24 h at room temperature and then in a drying chamber at 120 °C for 24 h. The samples made of TZ3YS had a green density of approximately 53% of the theoretical density (TD) and those of TZ10YS, 54%TD. Hg-porosimetry revealed a homogenous and monomodal pore size distribution. The mean pore size was 45 nm and 60 nm for TZ3YS and TZ10YS, respectively. The conventional sintering (CS) experiments were carried out in a resistive heated lab-scaled furnace. The MWS experiments were performed in a highly overmoded, untuned cavity of a compact 30 GHz gyrotron system [4] with an installed maximum power of 15 kW. In parallel similar experiments were performed in a TE_{103} waveguide applicator, at 2.45 GHz with a maximum power of 1.2 kW, where the samples were placed in the maximum of the linear polarized electric field.

To avoid the evolution of an inverse temperature profile, which is a specific feature of microwave volumetric heating, in both microwave-systems the samples were sintered within a ZrO_2 crucible, placed in a box of mullite ceramic fiber boards, for thermal insulation. Density of the sintered samples was measured using the Archimedes principle, assuming a theoretical density of 6.07 g/cm^3 for the tetragonal and 5.95 g/cm^3 for the cubic ZrO_2. To determine the grain sizes, the cut and polished samples were thermally etched at 1240 °C for 30 min and at 1200 °C for 1 hour in case of sintering at 30 GHz and 2.45 GHz, respectively. Characterization of grain structure was performed by high resolution scanning electron microscopy (HRSEM).

Results and discussion

Sintering experiments were performed at a heating rate of 10 K/min in case of CS, while MWS in the 30 GHz multimode applicator was conducted at 50 K/min. The thermal insulation and thus cooling behavior of the conventional furnace was different from the cooling behavior in the gyrotron system. Beside higher heating rates, the gyrotron system allowed higher cooling rates than did the conventional furnace, since the mass of the thermal insulation was much smaller. In the left graph of Fig. 1, the densification behavior of TZ10YS as a function of temperature is shown. The samples were cooled down directly after reaching the desired temperatures. It demonstrates a difference in densification behavior as a function of temperature if CS is compared with MWS. But before

drawing the conclusion that so called non-thermal microwave effects are responsible for this behavior, one should be aware of the fact that systematic errors in temperature measurement can feign the same behavior. For a reliable comparison of process temperatures from different sintering techniques as presented in this work, the different heating mechanisms between CS and MWS and the resulting differences in temperature distribution within the ceramic body must be considered [5].

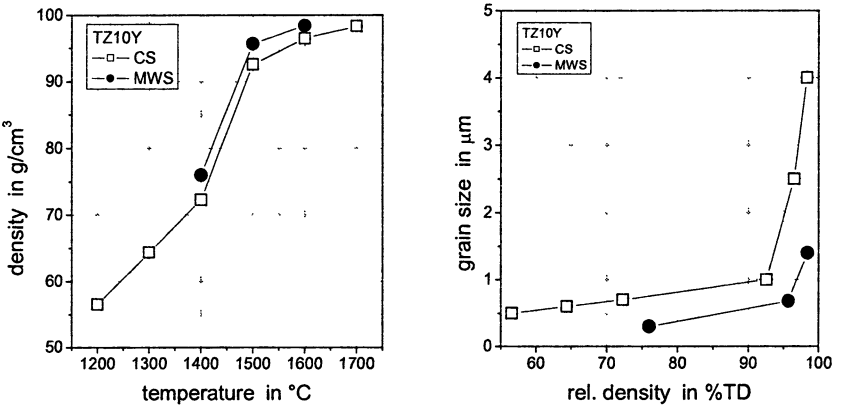

Fig. 1. Density as a function of sintering temperature (left) and grain size as a function of density (right) for CS and MWS of TZ10YS.

As exact comparison of temperature is difficult for the different sintering methods, a reliable comparison of densification behavior can be done, showing the relationship between density and grain size. Here the temperature parameter is not necessary to discuss microwave specific effects on sintering. In the right graph of Fig. 1, where grain size is shown as function of density, it can clearly be seen that the different sintering methods resulted in different microstructures evolution. Using MWS in TZ10YS the grains were significantly smaller than after CS.

The results obtained for tetragonal stabilized zirconia TZ3YS are shown in Fig. 2. The left graph gives the grains size evolution during densifications where millimeter-wave power was switched of as soon as the preset sintering temperatures were achieved. Although the effect is not as pronounced as found with TZ10YS, the grain size with millimeter-wave sintering is still smaller compared to CS. But when a soaking time of 1 hour is applied the picture changes as can be seen in the right graph of Fig. 2. Annealing in the millimeter-wave field led to stronger grain growth as compared to annealing in a conventional furnace.

The motivation for doing sintering experiments in a single mode cavity was to investigate the influence of the linear polarized electric field onto the evolution of the microstructure. Theoretical reflections of the materials diffusion within a pore structure under the influence of a linear polarized field [6], led to predictions that pores could develop an elliptical shape. In order to promote potential non-thermal microwave effects versus thermal effects, sintering ex-

periment in the single mode applicator were performed at temperatures as low as possible so that reasonable densities with closed porosity could be achieved in still acceptable processing time. So samples from TZ3YS were sintered at 1250 °C and 1260 °C for 7 days and 4 days, respectively. Thus sintered densities of 98.8%TD and 99.1%TD could be achieved. A number of SEM pictures have been produced. There from the ratio of pore diameters perpendicular and parallel to the direction of the applied electric field were estimated for a larger number of pores. The average values obtain from three independent persons are shown in Fig. 3, together with the average value and standard deviation thereof. From these preliminary results it can be seen that after microwave sintering pores show an aspect ration significantly grater than one.

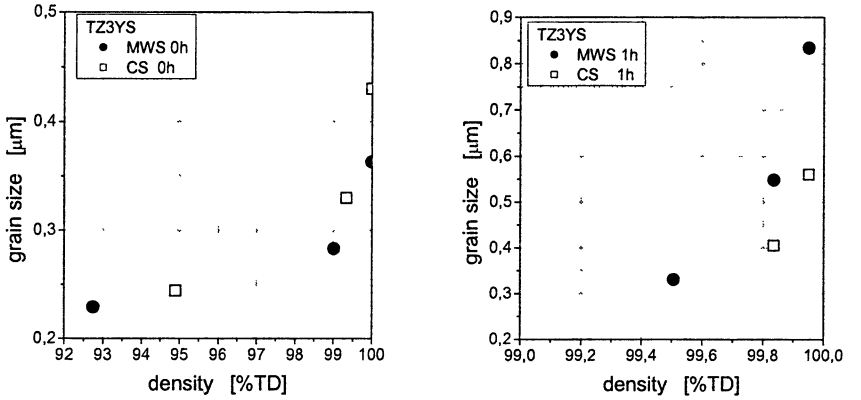

Fig. 2. Grain sizes as a function of density for TZ3YS without soaking time (left) and with 1 h soaking (right) at sintering temperature.

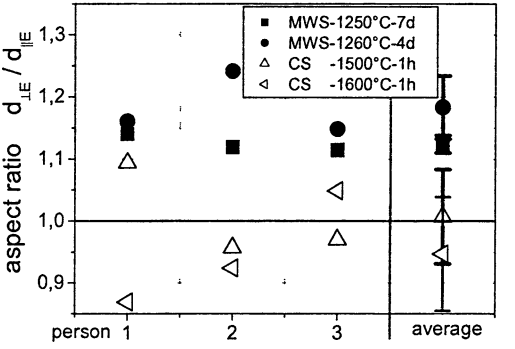

Fig. 3. Average ratio of measured pore diameter perpendicular and parallel to the applied electric microwave field for MWS samples of TZ3YS and CS samples of TZ10YS.

In parallel cubic stabilized TZ10YS samples were sintered in a conventional furnace. The geometry of the residual pores were analyzed the same way. The mean values of the pore diameter aspect ratios are shown in Fig. 3. As can be seen CS samples in average the pores show no significant deviation from a circular shape.

Although this results are still preliminary and the comparison of CS and MWS was done with different zirconia materials, these so far shown results give some evidence for non-thermal effects as indicated by Booske et al. [6]. To get more confidence in the discovered effect further experiments will have to be done.

Conclusions

The application of high frequency (30 GHz) MWS techniques in comparison with CS on tetragonal and cubic zirconia was investigated. Homogeneous green bodies with reasonable densities were formed by means of electrophoretic deposition. For high frequency microwave and conventional sintering, different densification behavior was found. Distinct differences in grain growth in relation to the densification state of the zirconia ceramics were observed. With MWS smaller grain sizes could be achieved for tetragonal as well as for cubic zirconia in case of fast sintering. With elongated processing time larger grain growth was found for MWS. All these results demonstrate that the ratio between the different diffusion mechanisms responsible for densification and grain growth, respectively can be influence by the application of MWS. At the intermediate and final stage of sintering, the influence of microwave heating shifts the balance of densification and grain growth towards densification. Whereas when densification is finished increased grain growth can be achieved by microwave heating.

Preliminary investigations of sintering in a linear polarized electric field gave some evidence, that grain boundary and surface diffusion in the near vicinity of pores is influence by the field direction. Thus the resulting pores in average developed an elliptic geometry with an aspect ratio of the order of about 1.15.

Acknowledgements

The financial support from the Deutsche Forschungsgemeinschaft (DFG, Graduiertenkolleg 232) and the Helmholtz-Gemeinschaft (VH-FZ-024) is gratefully acknowledged.

References

1. *Nightingale S.A., Dunne D.P., Worner H.K.*, J. Mater. Sci., **31**, 5039-5043 (1996).
2. *Rybakov K.I., Semenov V.E.*, Phys. Rev. B, **49** (1), 64-68 (1994).
3. *Tabellion J., Clasen R.*, J. Mater. Sci., **39**, 803-811 (2004).
4. *Bykov Yu. et al.*, ITG-Fachberichte **132**, VDE-Verlag, ISBN 3-8007-2086-8, 103-108 (1995).
5. *Link G., Takayama S, Thumm M.*, Proc. 9th. Int. Conf. Microwave and High Frequency Heating, ed. J. Binner, Loughborough University, 473-476 (2003).
6. *Booske J.H. et al.*, **5** (5), 1664-1670 (1988).

MILLIMETER WAVE IRRADIATION AND INVASION INTO LIVING BODIES USING A GYROTRON AS A RADIATION SOURCE

T. Tatsukawa, A. Doi, M. Teranaka, H. Takashima, F. Goda, S. Watanabe, T. Idehara[1], S. Mitsudo[1], T. Kanemaki[1], T. Namba[2]

School of Medicine, Kagawa University, Kagawa 761-0793, Japan
[1]Research Center for Development of Far Infrared Region, University of Fukui, Fukui 910-8507, Japan
[2]Kagawa prefectural College of Health Science, Kagawa 761-0123, Japan

Microwave invasion into living bodies through a millimeter wave catheter irradiation is described. As radiation sources for millimeter wave irradiation tests both a gyrotron and an impatt oscillator were used. Irradiated samples are cow livers and living rats. A newly designed wave-guide vent antenna with an anti-reflecting layer is used as a launcher for the irradiation and the reflectance measurements. The correlation between the denaturation of the tissue and the reflectance from the antenna is studied in detail.

1. Introduction

In the field of medical radiology, there is a growing interest in the possibility to treat various diseases (such as cancer) by catheter irradiation with millimeter and submillimeter wave radiation because of the following advantages: 1) Millimeter- and submillimeter-wave radiology allows irradiation of a localized spot size on a living body tissue by use of a waveguide vent antenna (WVA) and a Teflon rod antenna [1–3]. 2) The power absorption of a living body surface is large in these wavelength regions, because the reflection of the wave are well hold down (impedance-matching) by the anti-reflecting layers (ARL) of dielectrics. 3) Millimeter- and submillimeter-waves can be transmitted by a slim catheter into the living body. 4) The irradiation power can be controlled well in real time measuring waves reflected from the samples.

A novel system for applied medical studies, using one of the gyrotrons developed at the University of Fukui (Gyrotron FU-IV) [1, 2], has been designed in collaboration with Kagawa University. As the irradiated region of the living body is characterized by irradiation antennas used, many antennas with various shapes have been designed and tested as reported previously elsewhere [3, 4]. We also present and discuss data resulting from investigation of a WVA with an ARL for millimeter wave received using two kinds of solid state radiation sources (Impatt oscillator and Gunn oscillator). The use of the WVA with the anti-reflecting layer is suitable for the millimeter wave irradiation system. In our experiments, we tested the apparatus developed for irradiating a living animal tissue in vivo and in vitro specimens.

2. Experimental setup

The experimental setup used is shown in Fig. 1. The left-hand side of the figure shows the gyrotron oscillator and the right-hand side, the catheter radiation system. The gyrotron FU-IV is one of the gyrotrons in the FU series which can operate in both CW and pulse modes [6, 7]. The maximum beam energy and current applied to gyrotron are 18 keV and 200 mA, respectively. The superconducting magnet produces a magnetic field with a maximum intensity of 12 T. The gyrotron covers a broad frequency range from 199 GHz to 305 GHz, and delivers a CW output power of up to 20 W at fundamental cyclotron operations. The output power is transmitted by a circular waveguide whose length and inner diameter are 6 m and 28 mm, respectively and with two corner bends. Then, the diameter is changed by a taper waveguide which is inserted between the 28 mm waveguide and a catheter waveguide. The catheter waveguides are a straight or bend copper waveguides with inner diameters of 3.5 to 5 mm.

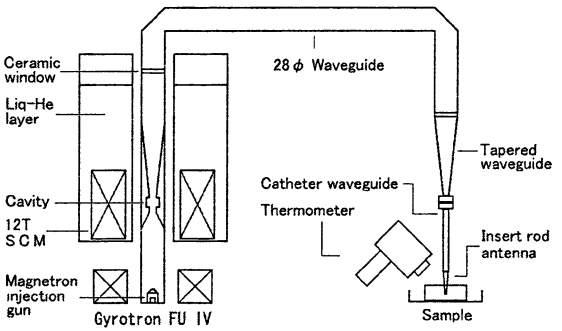

Fig. 1. Schematic of millimeter- and submillimeter-wave catheter irradiation apparatus for a living body using a rod antenna as a radiation antenna.

Irradiation antennas used are a circular WVA, a Teflon rod dielectric antenna and a conical horn antenna. The irradiated samples are beef, livers of living rats and malignant tumors implanted in living mice. The samples are located several tens of mm away from the antennas. In the case of the Teflon rod dielectric antenna, the tip of the rod is inserted into the samples. The maximum insertion depth is 20 mm. The living animals were irradiated under an anesthetic state.

During the irradiation, the surface temperature of irradiated parts was measured using an infrared radiation thermometer in order to estimate the absorbed energy as in a previous report [1]. For measurement of the irradiated area, the images recorded by a camera and subsequently converted into computer graphics were observed.

The another millimeter wave irradiation apparatus is shown in Fig. 2. It includes an oscillator, a rectangular to circular waveguide transition section, a taper waveguide, a circular feeding waveguide and a transmitting antenna. It includes also an attenuator, a phase shifter, a circulator and a detector. The upper side of the figure shows the Impatt oscillator (IO) while the bottom side presents the catheter radiation system. The IO is able to operate at the frequency

of 94.26 GHz and the power of 0.3 W in CW modes. In this system, we can measure characteristics of a WVA with an ARL located between the waveguide vent and a living body for direct coupling of the millimeter wave radiation.

Figure 2 shows also another similar apparatus which was used for studying the characteristics of the antennas and for measurement of reflections from the biological samples. In this case, a Gunn oscillator was used as a radiation power source. Its operating frequency and output power are 90.05 GHz and 13 mW, respectively. Both apparatuses are equipped with a hot plate holder for the specimens in order to keep the temperature of the irradiated tissue close to the normal physiological temperature (around 36 degree Celsius) of a living body.

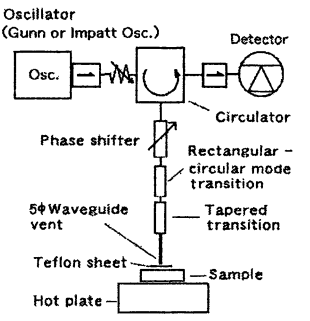

Fig. 2. Block diagram of millimeter wave irradiation apparatus for a living body.

3. Results and discussion

3.1. Thermal denaturation by the irradiation

During the irradiation, the gyrotron FU-IV is operated in the CW mode at a frequency of 302 GHz (TE_{03} cavity mode) [1]. The irradiation antennas used are conical horn and a Teflon rod antennas. The typical output powers were 5 W at the output vent of the 28 mm waveguide and 2 W at the Teflon rod antenna. Figure 3 shows the denaturation of cow livers after 3 min irradiation, at 30 mm distance below the 28 mm waveguide vent antenna (*a*), conical horn antenna (*b*) and at a 20 mm insertion depth using the rod antenna (*c*). On the samples, a black carbonized region and a gray thermal denaturation region surrounding it are observed. Both area and depth of denaturation region increase with irradiation time. However, in the case of using a 5 mm waveguide vent antenna, no denaturation region is observed. The power density in that case is approximately 3 W/cm^2 in the cases of 28 mm waveguide vent antenna and 0.5 W/cm^2 in the cases of conical horn antenna as reported previously [1].

Figure 4 shows the photographs of typical irradiation of the living rat liver. Figure 5 shows the typical irradiation time dependence of the surface temperature which was measured by a spot thermometer. As shown in the figure, the surface temperature rapidly increased on the initial stage (up to ~10 s) and after then, the temperatures reach to the range of 90 ~100 ℃ with the increase of irradiation time. These results are similar to the experimental results of irradiation of beef. In results, the cellular tissue in the denaturation region is dead because of surface temperature and the size of the denaturation in these living bodies.

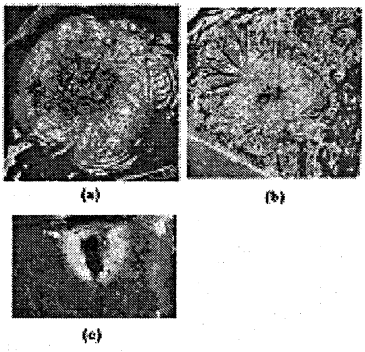

Fig. 3. Thermal denaturation by various irradiation antennas.

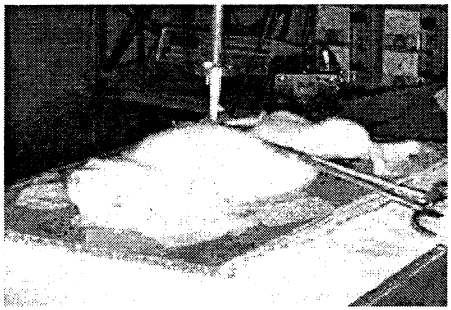

Fig. 4. Photograph of an irradiation of the living rat liver.

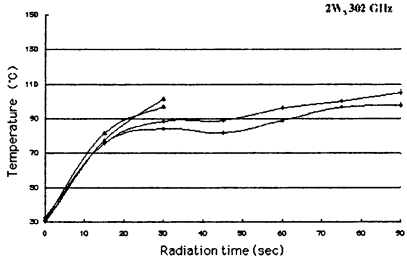

Fig. 5. Typical temperature change on the surface of living rat livers after irradiation through horn antenna by submillimeter wave (TE_{03} mode, 302 GHz).

3.2. Reflection characteristics

In order to evaluate the intensity of the reflected and transmitted (irradiated) waves, we measured detail reflection voltage from water, cow liver, cow heart, lard, vegetable oil, glycerol and silicone rubber using the apparatus as shown in Fig. 2. Figure 6 shows the reflection voltage from various samples using WVA with Teflon sheet. As can be seen, the reflection from WVA for all samples has the same period of the thickness of the layer as suggested by normal ARL theory. In the case of biological samples and water, the reflection decreases with the thickness of Teflon, but is practically independent from the changes of the thickness of the silicone rubber. According to the well-known theory, the reflection from an absorbing medium such as water, changes the polarization of the incident wave. Thus the reflected wave is an elliptically polarized [5]. Therefore, we think that the decrease of the reflection in Fig. 6 could be attributed to the interference between incident and the reflected waves.

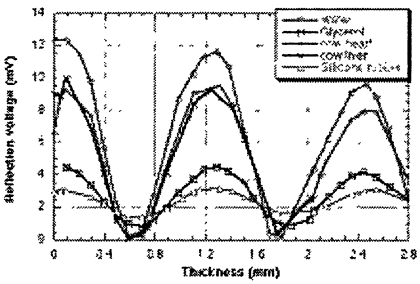

Fig. 6. Reflection voltage from various samples versus thickness of Teflon sheets.

Figure 7 shows the changes of the denaturation areas in cow livers with time during the irradiation. These data are obtained through computer graphics registered in successive moments of time during the experiment and simultaneously measuring the reflection voltage from the WVA with a Teflon sheet. The denaturation region increases rapidly with the irradiation time up to 3 minute, and after then, increases moderately with irradiation time. Generally, the reflection power decreases with the irradiation time, except at the initial period with duration about one minute. We are considering that the rapid increase at the initial stage arises from the variation of the surface temperature and denaturation of cow liver.

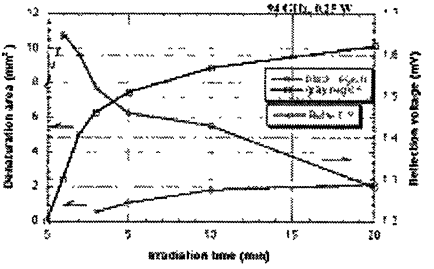

Fig. 7. Irradiation time dependenc of the denaturation area and the refection power from the waveguide vent antenna with a Teflon sheet.

4. Summary

In summary, we have developed a catheter apparatus suitable for irradiation of a living body. Tests of time and insertion depth dependent irradiation of a cow liver confirm the normal operation of the irradiation apparatus for living bodies because only the irradiated local part is damaged. Measurement results of the denaturation region and the surface temperature of irradiated samples in a previous report [1] suggest that the apparatus using a gyrotron is appropriate for use as a common catheter irradiation apparatus for living bodies such as liver cancer and brain cancer tissues.

While, we have also studied a WVA with ARL for the irradiation on the living body at millimeter wavelength region. Obtained experimental data and studied relations give deeper insight in the processes involved during microwave invasion in biological samples and living body, and are important for the further optimization of the submillimeter slim catheter and used set of specialized antennas with ARL.

Further developments are underway to improve the slim catheter waveguide and to develop an effective antenna to enable localized irradiation.

References

1. *Tatsukawa T. et al.*, Int. J. Infrared Millim. Waves, **21,** 1155 (2000).
2. *Idehara T. et al.*, Proc. 3rd Conf. Strong Microwave Plasmas, **2,** 634 (1997).
3. Tatsukawa T. et al., Jpn. J. Appl. Phys., **41,** 5486 (2002).
4. *Tatsukawa T. et al.*, Jpn. J. Appl. Phys., **42,** 7147 (2003).
5. *Tatsukawa T. et al.*, Int. J. Infrared Millim. Waves, **26**(4), 591 (2005).

INPUT IMPEDANCE AND PLASMA PARAMETERS OF A FERROINDUCTOR-BASED PLASMA SOURCE

Ya. Z. Slutsker, Yu. P. Bliokh, J. Felsteiner, P. M. Vaisberg

Physics Department, Technion–Israel Institute of Technology, Haifa, Israel

Characteristics of a low-frequency inductively coupled discharge where instead of an inductor-like rf antenna was used a ferromagnetic core with a primary winding ("ferroinductor") have been investigated A dense, highly ionized homogeneous plasma was obtained in this ferroinductor at low gas pressures Almost purely active input impedance in combination with high efficiency and low driving frequency makes this kind of discharge attractive for many applications.

We have obtained highly ionized dense plasma in a low-pressure gas discharge using a novel version of the well-known inductively coupled plasma (ICP) source. In an ordinary ICP source the plasma exists due to the induced electric field near the inductor-like antenna when rf voltage is applied to its input. The electric field is maximal in the inductor neighborhood and falls down to zero in the center even without plasma screening. It should be noted that the rf magnetic field of the inductor penetrates into the plasma and it may restrict the energy of the plasma electrons in the rf electric field. Instead of this rf antenna we suggest to use a ferroinductor, namely, a magnetic core with a few turns of winding (see Fig. 1). In this case the electric field fills the whole device and does not vanish in the core axis. Also most of the magnetic field of the winding is inside the magnetic core and does not penetrate into the plasma. Due to the magnetic core the inductance of the ferroinductor is high. Therefore it becomes possible to drive this ferroinductor coupled plasma (FCP) discharge with a much lower rf-frequency and even to work with comparatively long single pulses which simplifies the power supply. Also this FCP device may achieve a considerably denser plasma due to the greatly increased coupling brought in with the closed core. To be complete we should also mention the transformer-like version of the ICP source where a toroidal vacuum vessel surrounds a magnetic core and serves as a secondary winding. The disadvantage of such a device is the small plasma volume and its complicated shape, which result in big surface losses.

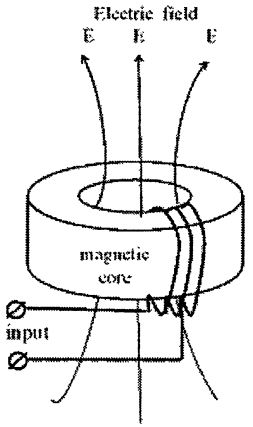

Fig. 1. Sketch of the ferroinductor coupled plasma source.

In this paper we present experimental results showing that the ferroinductor setup caused gas discharge at very low pressures with highly ionized plasma. Also it was found that almost all of the energy delivered from the power supply

to the magnetic core could be transmitted to the plasma. These results were obtained for FCP driven by single current pulses and by AC current as well. For AC driven FCP the input impedance was found to be almost purely active and determined by the number of turns N. It could be easily fitted with an RF oscillator. In our expements we used the setup shown in Fig. 1 which was placed in a vacuum chamber. We used two vacuum chambers: a small glass one with inner diameter of 30 cm and length 50 cm and a big one with inner diameter of 66 cm and length of 89 cm made of stainless steel. These chambers could be pumped to a pressure $p \leq 5 \cdot 10^{-6}$ Torr and then filled with gas (usually Xe or Ar) to the working pressure $p = 10^{-4}$–10^{-2} Torr. We used different ferromagnetic cores with inner diameters 10, 20 and 30 cm and height of 2.5 or 10 cm. These cores were composed from different materials: supermendure with $\mu \sim 300$–1000 and high saturation level ~3 T, ferrite with $\mu \sim 1000$ and low losses and Co-based amorphous ribbon with high $\mu \sim 5 \cdot 10^4$.

The number of turns N were varied in the range 3–20. This FCP device could be driven by a simple one stage Pulse Forming Network (PFN) with output resistance 50–70 Ω, pulse duration T with 70–170 μs and output voltage $U \leq 6$ kV. This PFN driver could be used just with supermendure core because of its high saturation level. Another option was to drive this FCP device with a powerful RF oscillator which could deliver up to 2 kW of RF power at 30–70 Ω loading in the frequency range 40–2000 kHz. For plasma diagnostics we used movable single and double probes, the microwave cut-off method, movable Rogovsky coils, current view resistors and compensated voltage dividers.

Typical waveforms for FCP driven by single current pulses from PFN are shown in Fig. 2. These experiments were performed at $p = (1$–$10) \cdot 10^{-4}$ Torr of Xe, with driving current $I_d = 20$–80 A and 6 turns of winding. The plasma density n and current density j_p via the plasma were measured in the core center. As it is seen there the discharge was formed not later than 15–30 μs after the beginning of the current pulse. The voltage per turn V_1 before the breakdown was found to be about U/N but abruptly fell down to $V_1 = 10$–20 V after the

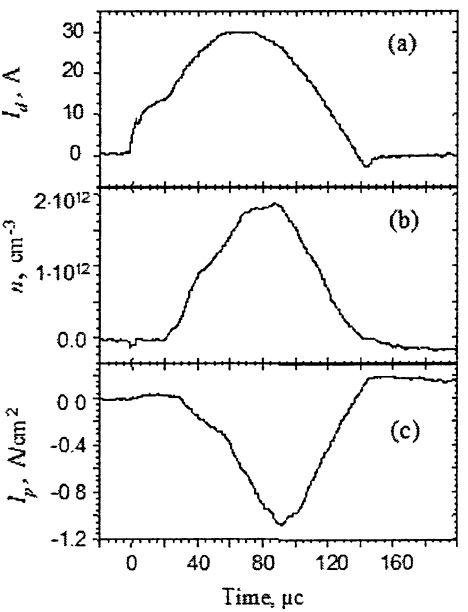

Fig. 2. Driving current I_d (*a*); plasma density n (*b*); current via plasma j_p (*c*).

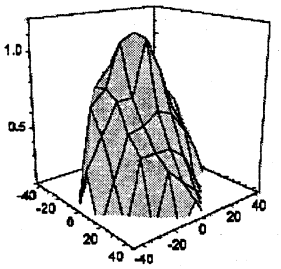

Fig. 3. Normalized distribution of the plasma density n in the FCP core cross section. Core inner diameter 10 cm.

plasma formation. The spatial distribution of n in the core cross-section is shown in Fig. 3. The spatial distribution of j_p looks similarly. We found that $\int_s J_p\, ds \approx I_d N$ which is evidence for low core losses. The plasma density spatial distribution along the core axis also fell down far away from the core. The level of ionization, as it is seen in Fig. 4, *a*, could achieve 90% at low pressure (~10^{-4} Torr) while the plasma density could reach 10^{13} cm^{-3} at pressure ~$3\cdot10^{-4}$ Torr. The efficiency of this FCP source also could be about 90% (see Fig. 4, *b*) but just for comparatively long pulses and high pressures. This is understood because at short pulses the core losses become significant and at low pressures more energy is wasted for electron acceleration with no ionization. The main disadvantage of the FCP source driven by single pulses is that the maximal energy stored in the magnetic core is limited by its volume (and weight correspondingly) even for the best materials we used. As a consequence the product nT is also limited. Thus $T \sim 140$ μs and $n \sim 10^{13}$ cm^{-3} appear to be the limit.

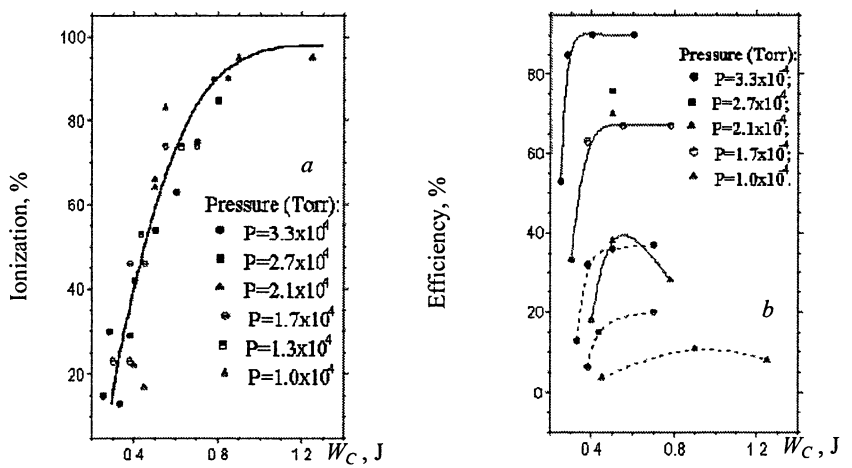

Fig. 4. Ionization level in the middle of the FCP core (*a*); Efficiency for 140 μc pulse (solid line) and for 70 μc pulse (dashed line) (*b*).

The obvious way to overcome these disadvantages is to drive the FCP by a series of periodical comparatively short pulses instead of a long single one. On the one hand for short pulses it is easy to achieve high values of V_l with no core saturation, but on the other hand when the period of these pulses is shorter than the plasma decay time τ it will not affect the plasma density too much. In our case τ ~ 15–50 μs, so the pulse repetition rate should be tens to hundreds kHz. Obviously in such a case the pulse shape does not matter and a simple sinusoidal driving current may be used.

In our experiments we used the above-mentioned powerful RF oscillator in the frequency range 40–300 kHz. It was found that the plasma density does not depend on the number of turns but directly depends just on the RF power W delivered to the core: $n \sim W$. On the other hand it was found that the input impedance was always almost purely active ($\cos\varphi \geq 0.9$) and this impedance R did depend on the number of turns similarly to an ordinary transformer: $R \sim N^2$.

For the whole investigated frequency range 40–300 kHz, pressure range $p = 3 \cdot 10^{-4}$–10^{-2} Torr of Xe gas and $W \leq 2$ kW the value of V_1 could always be found in the range 5.5–11 V. For Ar gas $V_1 \sim$ 8–16 V. This value weakly depended on the core sizes and gas pressure but mainly did depend on the driving power W with a shallow minimum at $W \sim 0.3$–1 kW. When W was kept *constant* and the pressure p grew up, the plasma density n also increased monotonically but slowly, namely $n \sim p^{\alpha}$, $\alpha \sim 0.25$–0.5. The input resistance R of the FCP source also weakly depended on the gas pressure and the driving frequency as well, while it was mainly determined by the driving power $W \sim n$. On the other hand the behavior of R *vs* W definitely depended on the core sizes. Thus for the core with a diameter of 10 cm the input resistance might be well approximated by the dependence $R \sim W^{-1}$ (see Fig. 5, *a*) while for FCP with a diameter of 30 cm the input resistance also went down but more slowly (see Fig. 5, *b*). It may be qualitively understood by the fact that for our pressure range and plasma density ($\sim 10^{12}$ cm^{-3}) for the small chamber and small core the main role is played by electron collisions in the inner parts of the device while for the big core and big chamber the main role is played by electron-neutral and electron-ion collisions.

Note that for all the FCP versions we tested, the electron temperature T_e was always found to be in the range 3.5–5.5 eV. Taking into account values of our working frequencies $f \leq 300$ kHz, the working pressures and the inner distances in our devices, one can easily derive that the total electron collision frequency $\nu >> 2\pi f$. This, in turn, explains why the input impedance of the FCP source appeared almost purely active.

Note that the above-mentioned dependencies led us to estimate the number of turns required to achieve a convenient value of the input resistance, say $R = 50\ \Omega$, which, in turn, led us to eliminate any fitting box and connect the FCP directly to a standard RF oscillator. Indeed, one can easily obtain that $N = \sqrt{WR/V_1}$, where W is the power required to achieve a given plasma density n at a given working pressure p (e. g. for 10 cm core at $n \sim 10^{12}$ cm^{-3} and $p = 3 \cdot 10^{-4}$ Torr of Xe gas, $W \approx 200$ W).

Another interesting fact is that in the RF driven FCP source the plasma density spatial distribution appears to be very homogeneous in both the axial and radial directions (see Fig. 6). This is contrary to the results obtained with the single pulse driven FCP. The reason may be that during a comparatively short, not rectangular, single pulse the plasma did not reach its steady state. On the other hand during a 1 ms RF pulse, a steady state was always achieved.

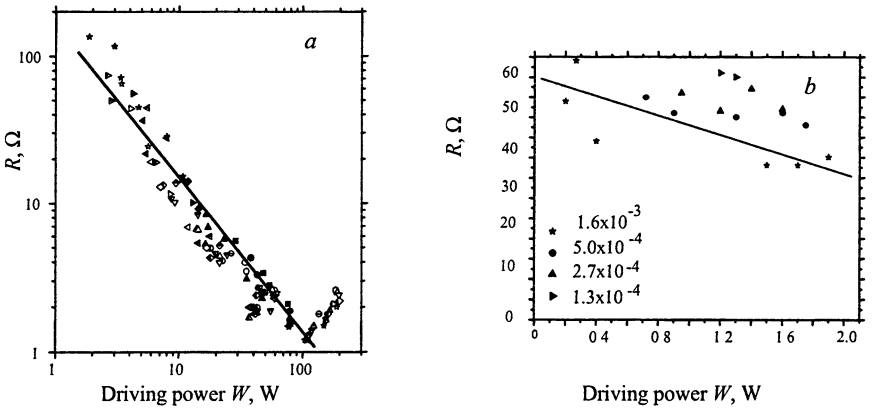

Fig. 5. FCP core with diameter of 10 cm (*a*). The different symbols correspond to different combinations of pressures in the range $1.7 \cdot 10^{-4}$–$1 \cdot 10^{-2}$ Torr and driving frequencies in the range 40–300 kHz. FCP core with diameter of 30 cm (*b*). Pressures are in Torr. Both of these graphs correspond to $N = 17$ turns.

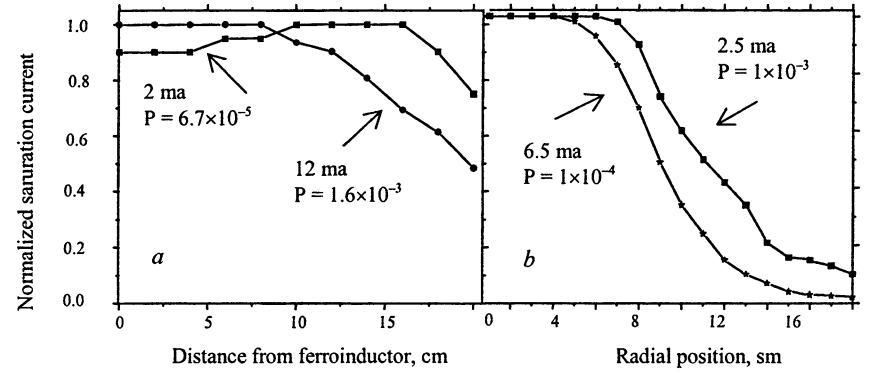

Fig. 6. Axial (*a*) and radial (*b*) plasma inhomogeneities for FCP with inner diameter of 20 cm. Xe gas, pressures are in Torr.

To conclude the following points should be mentioned:

1). The FCP source may achieve ionization level up to 90%. 2). The efficiency of the FCP source can achieve 90%. 3). The FCP source may be driven by either single current pulses or low RF frequency (about 10^2 times less than for typical ICP). 4). Due to the absence of input reactance, the FCP source may be easily fitted to any standard RF oscillator by varying the number of turns, and no fitting box is needed. 5). Very homogeneous plasma is obtained.

References

1. *Hopwood J.*, Plasma Sources Sci. Technol., 1992, **1**, 109, and references therein.
2. *Bliokh Yu.P., Felsteiner J., Slutsker Ya.Z., Vaisberg P.M.*, Appl. Phys. Lett., 2004, **85**, 1484.

ELECTRODE MICROWAVE DISCHARGES. RECENT RESULTS OF MODELLING AND EXPERIMENTS

Yu. A. Lebedev, I. L. Epstein, A. V. Tatarinov, V. A. Shakhatov

Topchiev Institute of Petrochemical Synthesis RAS, Moscow, Russia

Brief report of general properties of electrode microwave (2.45 GHz) discharge (EMD) is presented. EMD was generated at gas pressures ranged between 0.5 and 400 Torr in Ne, Ar, H_2, N_2, O_2, air and mixtures containing CH_4 и C_2H_2. Electrodes/antennas of different shapes were used to ignite the discharge: solid and tube cylindrical antennas with diameter of 1–6 mm, needle, spiral and trident antennas etc. The concept of "self-sustained-non-self-sustained" mechanism of EMD was concluded from analysis of publications on microwave discharges and results of study of EMD. Recent results of emission spectroscopy study and EMD modelling are described.

Introduction

A lot of publications are now devoted to the processes of plasma self-organization and to formation of plasma structures at reduced pressures. These phenomena are clear appeared in the electrode microwave discharge (EMD) [1]. Here we call as EMD the discharge when plasma is ignited near the tip of powered electrode/antenna and luminous plasma region is less than dimensions of discharge chamber. Discharge turns into the ordinary discharge mode at smaller distance between the electrodes.

Interest to the electrode microwave discharge is caused by its distinctive features:

- Extremely low maintaining discharge power (1–2 W).
- Wide range of operation pressures.
- Generation of compact plasma structures.
- Generation of plasma active particles in large vessels.
- Generation of plasma in the chosen point of space (localization of plasma region).
- Generation of plasma active particles near the treated surface.
- Absence of pollution of plasma treated surfaces by the products of electrode erosion.
- The area of plasma region is controlled by the electrode shape.

Electrode microwave discharge gives the possibility: to study and realize the plasma chemical processes, to intensify physical-chemical processes in gas phase, including the process of burning, to study of interaction of plasma with solids, to study the behavior of solids surrounded by plasma with gas flows, to study of interaction of plasma clots with gas flows.

Intensive study of EMD was started in 1997 and now we have fund of knowledge on discharge physics and on application of the discharge.

Experimental set-up

Detailed description of experimental set-up was presented in [1–4]. Stainless steel cylindrical discharge chambers with diameters of discharge vessel of R_1 = 7 cm and R_2 = 4.2 cm were used for experiments. Plasmas in both arrangements revealed similar features, thus the properties of the described plasmas seem to be typical for the electrode microwave discharge systems. Plasma gases were Ar, Ne, H_2, N_2, O_2, CH_4, C_2H_2, air, and their mixtures at pressures 0.5–400 Torr. Gas flow systems were used providing the total gas flow rate less than 1000 sccm. System "gas feeding-pumping" provides possibility to operate with mixtures of 3 gases. The latest modification of setup (stand EMD-3) is shown in Fig. 1.

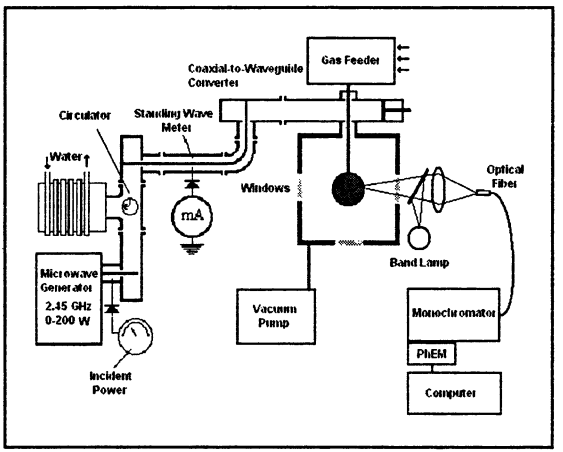

Fig. 1. Schema of experimental setup EMD-3

A tubular and solid stainless steel and copper electrodes of different shapes (direct cylinder and bent electrodes, trident electrode, spiral electrode, etc.) with diameters of 0.5–6 mm have been used as the antennas.

Most of results have been obtained when the discharge was ignited at the end of cylindrical electrode (antenna). Microwave power (2.45 GHz) was transmitted from the magnetron generators with output powers of 2.5 kW or 150 W. The power absorbed in the system was measured by the directional coupler. The power absorbed in the discharge was obtained by subtracting of power losses in chamber without plasma from the power losses with plasma at the same incident power.

The set-up was equipped with the system of optical measurements (monochromators MDR-4 and MDR-23 with photo registration, spectrograph Ava

Spec-2048). Discharge visualization was made with video camera (exposition times were ranged between 1/20 and 1/8000 s) or with digital photo camera.

Methods used for experimental study:

- Photometry of the discharge (study of EMD structure).
- Double probe method (determination of local values of electron temperature and density) [3–8].
- Emission spectroscopy in visible range of spectrum with spatial resolution (determination of plasma particles concentrations, gas temperature and electric fields, etc) [10–12, 14, 15].
- Electrodynamic measurements (determination of plasma absorbed power).

Methods of EMD simulation:

- Self-consistent one dimension modelling in quasi-static approximation [9].
- Self-consistent 2D modelling on the base of Maxwell equation [13, 14, 16].

General features of EMD and results

I. Discharge properties are independent of diameter of the chamber

II. Discharge consists of:

- bright thin (1–3mm) near electrode plasma region which covers the tip of the electrode (overcritical plasma density);
- ball-like plasma region (undercritical plasma density);
- dark external (non zero plasma density) space, separated from the luminous part by the double layer).

III. Ball dimension increases with microwave power and decreases with pressure.

IV. Upper limit of microwave power exists. It is impossible to keep the plasma region at the tip of electrode at higher power (discharge runs away along the antenna towards the microwave generator).

V. At high microwave power and pressure, when only thin near electrode plasma exists, the electrode can be destroyed because of melting and even explosion.

Analysis of results for hydrogen EMD together with known literature data on microwave plasmas gives possibility to formulate the concept of "self-sustained-non-self-sustained" mechanism of EMD: near electrode overcritical self-sustained plasma is surrounded by undercritical non-self-sustained plasma ball-region [11, 14].

Spectroscopic study of nitrogen EMD [15]

The method of determination of electric field strength and electron concentration in nonequilibrium plasma of electrical discharges is based on the modeling of measured vibration distribution function (VDF) of nitrogen molecules in

electronic state $C^3\Pi_u$. The measured VDF, specific absorbed power and gas pressure were the data for calculations. The model of plasma processes in nitrogen was developed on the base of balance equations for plasma components and homogeneous Boltzmann equation for plasma electron. The gas temperature was estimated from the thermal conductivity equation. The following plasma particles were taken into account in the model: nitrogen molecules in the ground state $X^1\Sigma_g^+$ (47 vibrational levels), molecules in the electronic excited states $A^3\Sigma_u^+$, $B^3\Pi_g$, $W^3\Delta_u$, $B'^3\Sigma_u^-$, $C^3\Pi_u$ (5 vibrational levels), $E^3\Sigma_g^+$, $D^3\Sigma_u^+$, $a'^1\Sigma_u^-$, $a^1\Pi_g$, $w^1\Delta_u$, $a''^1\Sigma_g^+$; nitrogen atoms in the ground ^4S and excited states ^2P and ^2D, electrons. Reliability of the model was verified by the modeling of the plasma condition of LTE, by the modeling of the literature data on excitation constants of electronic states of nitrogen, electron energy distribution function, drift velocity of electrons, first ionization coefficient, characteristic electron energy, and by the modeling if glow DC plasma with known values both the VDF and electric field strength and electron density. Qualitative agreement of measured and calculated values was achieved. For example good agreement was obtained for measured and calculated VDF in electronic state $C^3\Pi_u$ in the glow DC discharge. The method is non-intrusive and has obvious advantages for diagnostics of plasma generated by RF and microwave fields.

First measurements of electric field strengths and electron densities were fulfilled in plasma of EMD at pressure of 1 Torr. It was shown that situation is the same as it was in hydrogen discharge: near electrode plasma region is overcritical one and ball region is undercritical plasma.

Recent results of modeling [16]

Problems of matching of discharge chamber with microwave generator, dependence of plasma structure on dimensions of discharge chamber, pressure, and incident power were studied on the base of numerical 2D self-consistent modeling of hydrogen discharge in diffusion controlled regime [13, 14].

It is known that considered discharge is not the only form of the discharge in such a system. It is possible generate several discharge zones along the antenna or the discharge is located near the window at the entrance of antenna into the chamber. Here we consider the discharge at the tip of the electrode only and the problem of matching is analyzed regarding this type of discharge.

Calculations showed that at pressures below 2 Torr close to full matching was achieved at the length of antenna $L_{el} \approx n\lambda$, where λ is the wave length in free space, n is the integer. At higher pressures the best matching was observed at $L_{el} \approx \lambda(n + 1/4)$. The problem of matching is related with problem of determination of maximum absorbed power at which the discharge exists at the tip of

the electrode. This problem can be solved only on the base of solution of Maxwell equations.

It was shown that electrodynamics of discharge chamber defines the maximal power consumption. At small incident powers the discharge is initiated at the tip of antenna where electric field strength is several times increased. The size of plasma region increases with increasing incident power and discharge begins to spread towards the generator along the antenna, but its center is still fixed at the tip of antenna. The increased size of plasma shields the field penetration to the tip. The role of this point in the discharge position stabilization is decreased. At definite conditions the discharge is detached from the tip of antenna and moves towards the generator. At the same time the electric field strength at the entrance in the chamber also increases with increased incident power (the diameter of outer electrode in this zone is much less than in the chamber and the electric field strength is higher). The probability to ignite discharge in this region increases and it absorbs the main part of power.

Thus the upper level of power exists which can be absorbed in the discharge at the tip of the electrode. This power corresponds to the largest size of plasma region which is defined by the value of the order of the quarter of the wave length.

Acknowledgements. This study was supported by RFBR Grant 02-02-16021, Project 20 of the Program of fundamental researches of the Presidium of the Russian Academy of Sciences and NWO-RFBR grant 047.016.019.

References

1. *Bardos L , Barankova H., Lebedev Yu.A., Nyberg T., Berg S.*, Diamond and Related Materials, 1997, 6, 224.
2. *Bardos L., Lebedev Yu.A.*, Technical Phys., 1998, 43, 1428.
3. *Bardos L., Lebedev Yu.A.*, Plasma Phys. Rep., 1998, 24, 956.
4. *Lebedev Yu.A., Mokeev M.V., Tatarinov A.V.*, Plasma Phys. Reports, 2000, 26, 272.
5. *Lebedev Yu.A., Mokeev M V.*, High Temp., 2000, 38, 338.
6. *Bardos L., Lebedev Yu.A.*, High Temp., 2000, 38, 528.
7. *Bardos L , Lebedev Yu.A.*, Plasma Phys. Rep., 2001, 27, 418.
8. *Lebedev Yu.A., Mokeev M.V.*, Technical Phys., 2002, 47, 135.
9. *Lebedev Yu.A., Tatarinov A.V., Epstein I.L.*, Plasma Sources: Sci. & Technol., 2002, 11, 146.
10. *Lebedev Yu.A., Mokeev M.V.*, Plasma Phys. Rep., 2003, 29, 251.
11. *Lebedev Yu.A., Mokeev M.*, Plasma Phys. Rep., 2003, 29, 983.
12. *Lebedev Yu.A., Mokeev M.*, High Temp., 2003, 41, 725.
13. *Lebedev Yu.A., Tatarinov A.*, Plasma Sources: Sci. & Technol., 2004, 13, 1.
14. *Lebedev Yu.A., Mokeev M.V., Tatarinov A.V., Epstein I.L.*, Plasma Phys. Rep., 2004, 30, 91.
15. *Lebedev Yu A., Shakhatov V.A.*, Plasma Phys. Rep., 2005 (in press).
16. *Lebedev Yu.A., Tatarinov A.V., Epstein I.L.*, High Temp., 2006 (in press).

MICROWAVE DISCHARGE ON EXTERNAL SURFACE OF DIELECTRIC ANTENNA

V. M. Shibkov, A. D. Abramova, V. A. Chernikov, A. S. Dvinin, A. P. Ershov, R. S. Konstantinovskij, L. V. Shibkova, O. S. Surkont, A. V. Voskanyan

Physical Department of Moscow State University, Moscow, Russia

The basic properties of the surface microwave discharge created on an external surface of the dielectric antenna at low pressure $p = 10^{-3}$–20 Torr of air under conditions when frequency of collisions of electrons with molecules less than circular frequency of an electromagnetic field are investigated. Dependences of the longitudinal and transversal sizes and also longitudinal and transversal speeds of propagation of the surface microwave discharge on pressure, microwave power and time are measured. Spatiotemporal distributions of electron density and gas temperature, and also intensity of a luminescence of the discharge are obtained.

For successful application of low-temperature gas discharge plasma it is necessary to study the physical processes proceeding in various types of gas discharges. Because of the unique properties the microwave discharges are excellent means for numbers of practical tasks, such as nano- and microelectronics, plasma chemistry, and also, in particular, supersonic plasma aerodynamics. Earlier it has been shown by us [1] that the self-sustained freely localized and surface microwave discharges exist at high values of the reduced electric field. It conducts to the effective contribution of energy to plasma, to a high gas heating rate, to a high degree of ionization of gas and dissociation of molecules, to creation of a plenty of active radicals and the excited atoms and molecules. The listed above properties should render huge influence, for example, on ignition of supersonic streams of hydrocarbon fuel.

In the report essentially new type of a plasma source on a surface wave was investigated. It is known that at creation of the microwave discharges inside dielectric tube, filled by gas at low pressure, the electromagnetic energy delivered to system is transformed to a surface wave. Thus, there is a self-sustaining system when a plasma medium created by the surface wave is necessary for a surface wave existence, i.e. the presence of plasma is a necessary condition for propagation of a surface wave. The surface wave is travelled in space so long as its energy is sufficient for creation of plasma with electron density no less then a critical value. This report deals with a surface microwave discharge outside a dielectric body in a low-pressure chamber. In this case plasma supported by a surface microwave is formed on an external surface of a dielectric antenna. Due to high speed of a wave distribution it is possible to create a plasma source of extremely big diameter ~1 m. As the microwave discharge on a surface wave exists only at electron concentration exceeding the critical value, the offered type of the discharge is extremely perspective as a source of dense plasma with

electron concentration ~10^{13} cm^{-3}. The main properties of surface microwave discharge were obtained.

In previous our works [2–10] new type of the microwave discharge on a surface wave has been offered for creation of plasma in a supersonic stream of air at pressure about 100 Torr. Thus the discharge was created on an external surface of the dielectric antenna. It represents a plasma wave guide on which the surface wave supporting ionization of gas is distributed. Thus in a wide range of frequencies it is possible to receive plasma area of significant extent and form. Feature of such discharge is a basic opportunity of creation of plasma with ultrahigh concentration of the charged particles as a surface microwave discharge can exist only at electron density n_e the greater, than critical n_{cr} concentration of electrons. Under experimental conditions, when frequency of an electromagnetic field f ~ 12.4 GHz, the critical concentration of electrons $n_{cr} \sim 2 \cdot 10^{12}$ cm^{-3}.

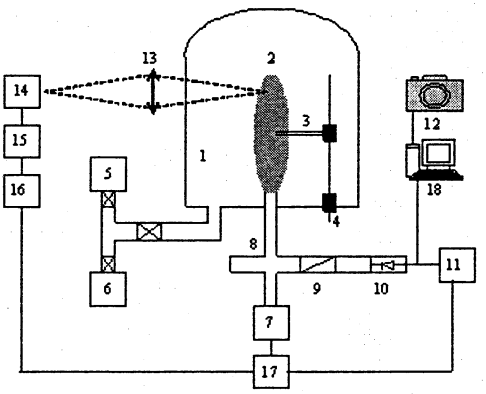

Fig. 1. The block-scheme of experimental installation: *1* – the discharge chamber; *2* – a surface microwave discharge on the dielectric antenna; *3* – a double probe; *4* – system of fastening and moving of a double probe; *5* – a pumping system; *6* – a cylinder; *7* – the magnetron generator; *8* – a directional coupler; *9* – attenuator; *10* – a crystal detector; *11*, *16* – digital oscilloscopes; *12* – a digital photo camera; *13* – system of lenses; *14* – spectrograph; *15* – the photo electronic multiplier; *17* – the block of synchronization; *18* – a personal computer.

The block-scheme of experimental installation is resulted in Fig. 1. The microwave source is a pulsed magnetron generator operating in the centimeter wavelength range. The parameters of the magnetron generator are as follows: the wavelength is λ = 2.4 cm, the pulsed microwave power is W_p < 100 kW, the pulse duration is τ = 1–200 μs, and the period-to-pulse duration ratio is Q = 1000, thus mean power did not exceed 100 W. The magnetron is powered from a pulsed modulator with a partial discharge of the capacitive storage. Microwave power was delivered to the discharge chamber through a 9.5×19 mm

rectangular waveguide. The input microwave power was measured with the help of a directional coupler installed in the waveguide so that a fraction of microwave power was directed to the measuring arm containing an attenuator and a section with a crystal detector. The microwave pulse envelop at the detector output was recorded using a digital oscilloscope. The pulse envelop was nearly flat-top. The same signal was fed to a pulsed digital voltmeter measuring the pulse amplitude. The voltmeter was preliminarily calibrated with the help of a calorimetric power meter connected to the output of the main arm of the directional coupler. All the components of the microwave transmission line were sealed. To avoid electric breakdowns inside the waveguide, it was filled with an insulating gas (SF_6) at a pressure of 4 atm. The vacuum system allowed us to carry out experiments at air pressures of $p = 10^{-3}$–10^3 Torr.

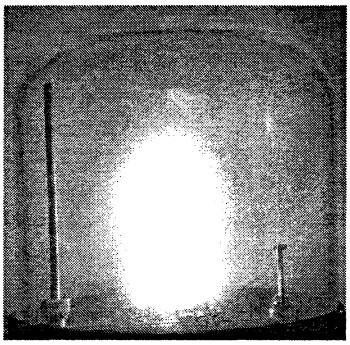

Fig. 2. Common side view of surface microwave discharge in air at $p = 0.5$ Torr, $\tau = 200$ μs, and $W_p = 35$ kW.

The general view of a surface microwave discharge on the quartz antenna at air pressure of $p = 0.5$ Torr, microwave pulse duration $\tau = 200$ μs, and microwave pulsed power $W_p = 35$ kW is submitted in Fig. 2.

The time dependence of the discharge transversal size was studied for air pressure in the chamber $p = 0.1$–20 Torr and microwave pulse powers $W_p = 15$–55 kW. Fig. 3 shows the semilog plots of the discharge transversal size versus the microwave pulse duration at different values of air pressure. With the pulse duration fixed, the transversal size of the surface microwave discharge decreases at increase in the air pressure.

Under experimental conditions longitudinal velocity of surface microwave discharge spreading at an initial stage of the discharge more than on the order of value exceeds transversal velocity of the discharge whereas on late times of the discharge existence longitudinal and transversal velocities of discharge are equal each other (Fig. 4). The breakdown wave defines the longitudinal velocity of the discharge at its early stages. Ambipolar diffusion governs the longitudinal and transversal propagation of the surface microwave discharge at the stage of its evolution.

Spatial distribution of electron density is submitted in Fig. 5. It can be seen that concentration of electrons in a narrow boundary layer where the electric field of a surface wave is located, reaches value of 10^{14} cm^{-3}. The transversal sizes of plasma areola increase when air pressure decreases. As tentative estimations show that the processes of photoexcitation, photodissociation and photoionization of air bring the certain contribution to formation of the measured distribution of electron density.

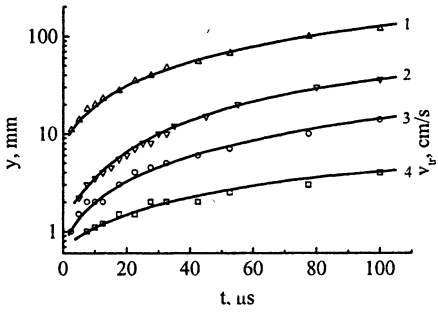

Fig. 3. Time dependencies of transversal size of the surface microwave discharge at W_p = = 55 kW, and different values of air pressure p, Torr: *1* – 0.1; *2* – 0.5; *3* – 5; *4* – 20.

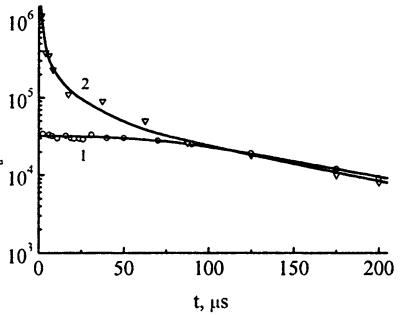

Fig. 4. Time dependencies of longitudinal (*1*) and transversal (*2*) velocity of the surface microwave discharge spreading at p = 0.5 Torr, and W_p = 35 kW.

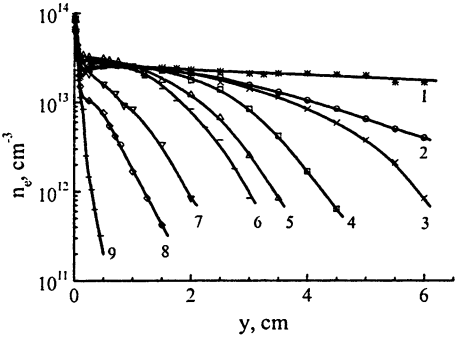

Fig. 5. Transversal distribution of electron density in plasma of a surface microwave discharge at a pulse duration τ = 100 μs, input pulse power W_p = 55 kW and various air pressure p, Torr: *1* – 0.1; *2* – 0.2; *3* – 0.3; *4* – 0.5; *5* – 1; *6* – 2; *7* – 5; *8* – 10; *9* – 20.

Longitudinal distributions of gas temperature at low air pressure and threshold values of an input microwave power are submitted in Fig. 6. It is visible, that with increase of air pressure the gas temperature increases, and in a direction of the discharge propagation the gas temperature insignificantly decreases. When microwave power increases the longitudinal distribution of gas temperature smoothes out. It is defined by that with increase in power longitudinal speed of the surface microwave discharge propagation grows, the discharge occupies whole antenna length, thus there is an effective reflection ($R \sim 85\%$) surface wave from the forward end of the antenna. Under these conditions the energy input to gas in discharge on unit of length of plasma is constant on the discharge length.

Under conditions of a surface microwave discharge effective dissociation molecules of oxygen and nitrogen takes place. Time dependence of the transver-

sal sizes of area of localization of atomic oxygen in plasma of the surface microwave discharge, measured on a luminescence of a triplet line of atomic oxygen (λ = 777.1 nm, 777.4 nm and 777.5 nm), is submitted in Fig. 7 at air pressure p = 0.5 Torr. It is possible seen the distribution of the discharge in time and space. The transversal sizes of localization of atomic particles practically coincide with the sizes of plasma measured by a probe method (see Fig. 5). Now researches of the surface microwave discharge in our laboratory proceed. The received results allow drawing the basic conclusion that the surface microwave discharge because of its unique properties is excellent means for its application in various applied problems.

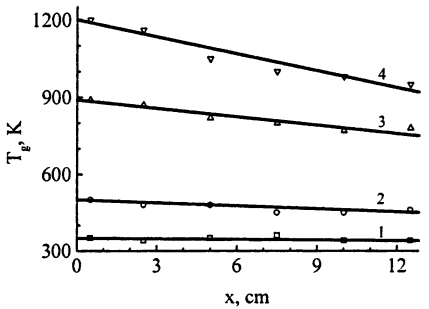

Fig. 6. Longitudinal distributions of gas temperature at threshold values of an input microwave power and air pressure p, Torr: *1* – 0.01; *2* – 0.1; *3* – 1; *4* – 10.

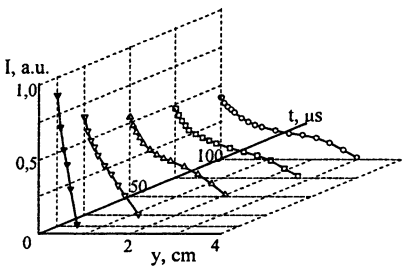

Fig. 7. Transversal sizes of area of localization of atomic oxygen in plasma of the surface microwave discharge at input microwave power W_p = 55 kW and air pressure p = 0.5 Torr.

The work was supported by the NWO (grant 047-016.019) and the RFBR (grant 05-02-16532).

References

1. *Zarin A.S., Kuzovnikov A.A., Shibkov V.M.*, Freely localized microwave discharge in air, M.: Oil & Gas, 1996, 204 p.
2. *Shibkov V.M. et al.*, Vest. Mosk. Univ., Ser. 3: Fiz., Astr., 2000, **41** (6), p. 64-66.
3. *Shibkov V.M. et al.*, Microwave Discharges: Fundamentals and Applications, M.: Yanus-K, 2001, p. 145-153.
4. *Shibkov V.M. et al.*, 15th Int. Symposium on Plasma Chemistry. Orleans, France, 2001, v. 1, p. 179-184.
5. *Shibkov V.M. et al.*, AIAA Paper No. 01–3087, p. 1-8.
6. *Shibkov V.M. et al.*, AIAA Paper No. 03–1193, p. 1-7.
7. *Shibkov V.M. et al.*, Vest. Mosk. Univ., Ser. 3: Fiz., Astr., 2004, **45** (5), p. 67-69.
8. *Shibkov V.M. et al.*, Zh. Tekh. Fiz., 2005, **75** (4), p. 67-73.
9. *Shibkov V.M. et al.*, Zh. Tekh.Fiz., 2005, **75** (4), p. 74-79.
10. *Shibkov V.M. et al.*, Fizika Plazmy, 2005, **31** (9), p. 857-854.

WAITING TIME PHENOMENON OF MICROWAVE BREAKDOWN

D. Anderson, D. Dorozhkina[1], U. Jordan, L. Lapierre[2], M. Lisak, T. Olsson[3], J. Puech[2], V. Semenov[1]

Chalmers University of Technology, Göteborg, Sweden
[1]Institute of Applied Physics RAS, Nizhny Novgorod, Russia
[2]Centre National d'Etudes Spatiales, Toulouse, France
[3]Powerwave Technologies Sweden AB, Täby, Sweden

Theoretical and experimental investigations have been made of the statistical properties of rf corona breakdown thresholds for the case where no artificial electron seeding is used. Comparisons between theoretical predictions and experimental results show good agreement.

Further development of compact microwave communication systems requires particular consideration of the problem of microwave breakdown. The phenomenon of microwave breakdown is manifested as an avalanche-like increase of the electron density, driven by electron impact ionization of neutral gas molecules. The growth rate of the electron avalanche, γ, is determined by the difference between the impact ionization frequency, ν_i, and the effective frequency of electron losses, ν_l. The latter includes both attachment of electrons on neutral molecules and electron diffusion out from the breakdown region. Therefore, for CW operation, the breakdown criterion is usually formulated as the inequality:

$$\gamma = \nu_i - \nu_l > 0 . \qquad (1)$$

Typically $\nu_i - \nu_l$ increases with increasing microwave power and Eq. (1) determines the power threshold, I_{th}, at which breakdown occurs.

The conservative way to avoid breakdown is to keep the microwave power, I, always below I_{th}. However this requirement is very difficult to combine with current progress in rf communication. A less conservative approach could be based on the breakdown criterion for the pulsed operation regime which allows short pulses with $I > I_{th}$. Actually, breakdown is dangerous only when the electron number, N, exceeds some high critical value N_c. On the other hand, the initial number, N_0, of electrons is often relatively small inside the breakdown-prone volume. Therefore even an exponential increase of the electron number during a microwave pulse with high power, but of short duration, is not dangerous if $\gamma\tau_p < \ln(N_c/N_0)$, where τ_p is pulse duration. Usually it is considered that about 20 exponentiations are enough to reach a dangerous level and the pulse breakdown threshold is taken as $\gamma\tau_p \approx 20$. The time

$t_b = \gamma^{-1} \ln(N_c/N_0)$ can be considered as a temporal delay of the microwave breakdown process. It implies that a first part of a powerful microwave signal, used e. g. to measure the pulse breakdown threshold for a certain device, is transmitted through the system without perturbation. In addition, if some particular sources are not used to produce sufficiently high number of initial electrons, it may happen that no free electrons are available in the breakdown volume at the beginning of the microwave signal. Therefore in the case, when this waiting time for the appearance of a first electron is comparable with the pulse duration, τ_p, breakdown will be stochastically observed with different degrees of probability, depending on the pulse power.

The electron creation inside the breakdown volume can be described as a stochastic process in terms of the probability, S, per unit time. Assuming that one electron is enough to start the breakdown avalanche, the breakdown time delay, t_b, is typically presented as the sum:

$$t_b = \gamma^{-1} \ln N_c + 1/S, \tag{2}$$

where the first term gives the systematic delay and the second one denotes the stochastically varying waiting time for the first electron to appear. According to Eq. (2) only the systematic delay depends on the value of the microwave power over the breakdown threshold $I - I_{th}$. However this feature is not confirmed by experiments where also the spread of the breakdown delay time is found to depend on the difference $I - I_{th}$. One reason for this discrepancy is that the processes of impact ionization and electron losses are also stochastic by nature. Therefore a consistent theory should not treat the breakdown avalanche as a deterministic process, but instead consider the temporal evolution of the probability distribution over the electron number, N, inside the breakdown volume.

A general way to study the stochastic breakdown process is to treat the number of electrons N in the breakdown volume as a stochastic process with a probability function, $f(N,t)$, which varies in time due to ionization, electron losses, and seeding:

$$\begin{aligned} &\textstyle\sum_{N=0}^{\infty} f(N,t) = 1, \ \frac{d}{dt} f(0,t) = -S f(0,t) + \nu_l f(1,t), \\ &\frac{d}{dt} f(N,t) = S f(N-1,t) - S f(N,t) + \nu_l (N+1) f(N+1,t) - \\ &\quad - \nu_l N f(N,t) - \nu_i N f(N,t) + \nu_i (N-1) f(N-1,t), \quad N \geq 1. \end{aligned} \tag{3}$$

Here the parameter S denotes the probability per unit time for creation of one electron in the breakdown volume by the seeding source and ν_i and ν_l denote the ionization frequency and the effective frequency of electron losses respectively. Note, that ν_i and ν_l are related to the probability per unit time for one electron to produce a new electron or to disappear respectively.

The kinetic equations (3) can be solved exactly by means of the generating function, $F(z,t)$:

$$F(z,t)=\sum_{N=0}^{\infty} z^N f(N,t), \quad f(N,t)=\frac{1}{N!}\left(\partial^N F(z,t)/\partial z^N\right)_{z=0}, \tag{4}$$

$$\partial F/\partial z=(z-1)\left[SF+(z\nu_i-\nu_l)\partial F/\partial z\right]. \tag{5}$$

When the initial value of the average electron number is zero, i. e. $\langle N_0\rangle=0$, this implies, $F(z,0)=1$ and the solution of Eq. (5) is

$$F(z,t)=\left[\frac{1-\nu_l/\nu_i}{z-\nu_l/\nu_i+(1-z)\exp(\gamma t)}\right]^{S/\nu_i}. \tag{6}$$

In the case of particular interest ($\alpha\equiv S/\nu_i<<1$, $\exp(\gamma t)>>1$), Eq. (6) reduces to the following solution for $f(N,t)$:

$$f(N,t)\approx\alpha N^{\alpha-1}\exp\left(-\alpha N/\langle N\rangle\right)f(0,t),\ f(0,t)\approx(\gamma/\nu_i)^{\alpha}\exp(-\alpha\gamma t), \tag{7}$$

where $\langle N\rangle$ is the average electron number. It can be shown that the evolution $\langle N\rangle$ coincides with that obtained from the deterministic breakdown theory, viz $\langle N(t)\rangle=(S/\gamma)\left[\exp(\gamma t)-1\right]$.

The integral probability of breakdown, P_b, can be defined as:

$$P_b(t)=\sum_{N=N_c+1}^{\infty} f(N,t)=1-\sum_{N=0}^{N_c} f(N,t), \tag{8}$$

where the function $P_b(t)$ gives the probability of the event that breakdown has happened before time t. Based on Eq. (7) it can be shown that P_b is negligibly small, if $\langle N\rangle<<\alpha N_c$, whereas in the opposite limiting case, $\langle N\rangle>>\alpha N_c$, the breakdown probability can be expressed as follows: $P_b(t)\approx 1-\left(\alpha N_c/\langle N\rangle\right)^{\alpha}=1-\left(\gamma N_c/\nu_i\right)^{\alpha}\exp(-\alpha\gamma t)$. The dependence of the integral breakdown probability, P_b, on $\langle N\rangle$ is illustrated in Fig. 1 for different values of the parameter $\alpha\equiv S/\nu_i$. As can be seen from Fig. 1, breakdown becomes probable, when $\langle N\rangle$ reaches extremely high values, which means very long delay of the breakdown event as compared to predictions of the deterministic model.

The average waiting time for breakdown and its characteristic spread are estimated to be

$$\langle t_b\rangle=(\gamma\alpha)^{-1}+\gamma^{-1}\left[\ln(N_c)+\ln(\gamma/\nu_i)\right],\ \sqrt{\langle t_b^2\rangle-\langle t_b\rangle^2}=1/\gamma\alpha. \tag{9}$$

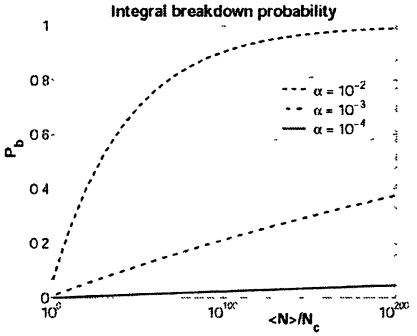

Fig. 1. The integral breakdown probability, P_b, as a function of average electron number $\langle N \rangle$.

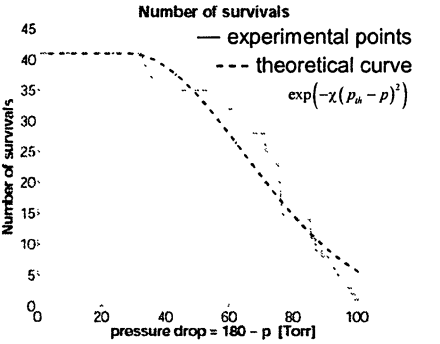

Fig. 2. Distribution over pressure of 41 breakdown events in experiments with the rf power fixed at 300 W and pressure ramp-down speed 1.5 ± 1 Torr/s.

When the microwave field is so strong that $\nu_i >> \nu_l$, $\gamma \approx \nu_i$, the waiting time (9) is close to its traditional estimate (2) and the characteristic spread of the waiting time is of the order of $1/S$ in complete agreement with commonly accepted notions. However when one is close to the breakdown threshold ($\nu_i \approx \nu_l$, $\gamma << \nu_i$), the spread of the waiting time increases in inverse proportion to γ and $\langle t_b \rangle$ exceeds the estimate (2). For very weak seeding source, i. e. $\alpha << \ln(\gamma N_c/\nu_i)$, the average waiting time is close to its spread ($\langle t_b \rangle \approx 1/\gamma\alpha$) and is determined mainly by the delay for the "reliable" appearance of a first electron.

The statistical properties of breakdown phenomena were studied in experiments with several different filters, which are prototypes for commercial use. The system was designed to keep a fixed level of pressure or to scan pressure down with any desirable rate. In experiments both regimes were used while keeping the parameters of the rf signal fixed. A breakdown event was detected by measuring a sufficient increase in the level of reflected rf power. The control system measured the waiting time for breakdown to occur after the turn-on the rf signal. When breakdown occurred, the rf power was switched off, the test tank was re-pressurized, and the next experimental cycle began. The typical total time for one experimental cycle was about half an hour during which the plasma products were vented.

A detailed experimental study of the breakdown statistics was carried out, first in the case when the pressure was ramped down and the rf power was fixed to 300 W, which corresponded to an empirical breakdown threshold of $p_{th} = 153$ Torr. The experimental series included 41 identical cycles. Each cycle started with the pressure 180 Torr and after the rf power had been turned on,

the pressure was reduced with a fixed rate of 1.5±1 Torr/s until breakdown occurred. The results are presented in Fig. 2 (solid line) in terms of the number of survivals (number of experimental runs without breakdown) vs. pressure.

In the next experimental series, the spread of the observed breakdown waiting time was studied under conditions of constant rf power (300 W) and air pressures, which were fixed at different levels below the threshold pressure. In this case each experimental series included as much as 80 runs. The experiments demonstrated that the number of tests without breakdown decreases approximately exponentially with increasing testing time (Fig. 3). The rate of this decrease was found to depend almost linearly on the pressure (Fig. 4). The closer the pressure to the threshold value, the smaller the decay rate, which means an increasing spread of breakdown waiting times when approaching the breakdown threshold.

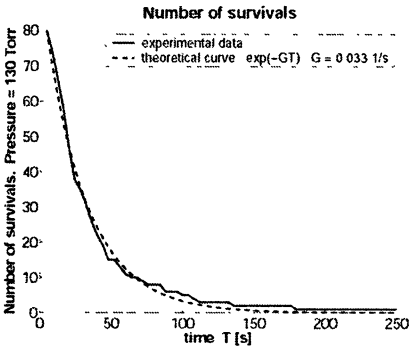

Fig. 3. Number of surviving tests samples as function of time, T, for fixed microwave power 300 W and pressure 130 Torr.

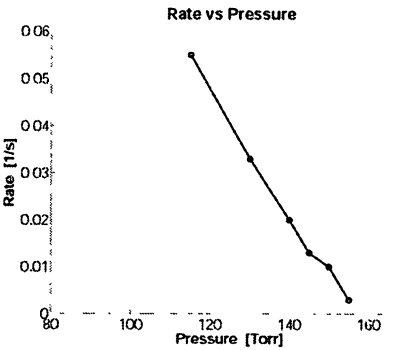

Fig. 4. Rate of decay of survivals as function of pressure around the breakdown pressure. The experimental error in the estimated rates is ±20%.

In order to discuss the statistics of the experimental results, we draw some further conclusions from the statistical theory presented above. In a series of sufficiently great number of identical experimental tests, the number of survivals, K_s, is associated with the probability, W_0, to have no breakdown in a single test, which is $W_0(T) = K_s(T)/K_t = 1 - W_b(T)$, where $W_b(T)$ stands for the breakdown probability in an experimental run of duration T and K_t is the total number of experimental runs in the series. Assuming independence of breakdown events between separate pulses, the probability $W_0(T)$ can be calculated as the product of the probabilities to have no breakdown in separate pulses:

$$W_0(T) = \prod_{k=1}^{M(T)} \left[1 - P_{bk}(\tau_p)\right], \; M(T) = f \times T, \tag{10}$$

where $M(T)$ is the number of rf pulses in the experimental run, f denotes the pulse repetition frequency, and $P_{bk}(\tau_p)$ is the breakdown probability in the *k*-th separate rf pulse of duration τ_p. In the experiments with fixed pressure, the breakdown probability is the same for all pulses ($P_{bk} = P_b$). Therefore Eq. (10) implies:

$$W_0(T) = \exp(-GT),\ G = -f \ln[1 - P_b].$$

The parameter *G*, which depends also on the source rate *S*, is not known in the experiment. However the theoretically predicted exponential decay with time *T* is in quantitative agreement with the experimental results (Fig. 3) where the value $G = 0.033$ has been used in the comparison.

Theory explains also the linear dependence of the decay rate, G, on pressure (Fig. 4). Since in the second set of experiments, the pressure was only slightly below the breakdown level, p_{th}, G can be estimated as $G \propto (p_{th} - p)$ in good agreement with the observed pressure scaling. Furthermore, in this limit it is possible to calculate the probability $W_0(T)$ in the first experimental series with permanent pressure drop. Actually, $W_0(T)$ can be represented as a Gaussian distribution (the dotted line in Fig. 2): $W_0(T) = \exp\left(-\chi(p_{th} - p)^2\right)$, where χ is determined by known parameters (f, pressure sweeping rate etc) and the unknown parameter *S*. Based on the decay rates with time and pressure observed in Figs. 2, 3, and 4, it is possible to estimate the source rate *S*, which is found to be of the order of 0.4–0.6 s^{-1} in good agreement with the source rates to be expected from cosmic radiation in a breakdown prone volume on the order of 0.1 cm^3 which, is relevant for the limiting resonator in the tested filter.

PLASMA SOURCES AND PLASMA CHEMISTRY

D. C. Schram, J. H. van Helden, R. A. B. Zijlmans, R. Engeln

Eindhoven University of Technology, Eindhoven, The Netherlands

In this presentation the mechanisms in fast plasma deposition, surface modification and molecule synthesis will be discussed. The various processes in the plasma and at the surface will be summarized at the hand of a particular plasma source in a remote plasma process. In view of the need of high rate processing new aspects of plasma-surface interaction with large flows of radicals will appear. From radicals adsorbed at the surface new molecules are generated, which at high re-cycling conditions can replace injected monomers. Detection of new molecules forms thus a diagnostic for the surface processes at hand and thus for the mechanisms for the formation of new molecules, modified surfaces, or thin layers amorphous or structured material.

1. Introduction

Plasma deposition, surface modification, etching, oxidation have become increasingly important for various applications. Also synthesis of molecules gains significance, as selective generation is possible at low ambient pressure and temperature [1]. At present most applications are of a high added value character and allow low to moderate process rates. If the rate of the process could be enlarged to 10–100 nm/s over large areas with unaltered or even improved properties, various large-scale applications would become within reach as thin layer solar cell fabrication [2]. One can discern in the process a dissociating phase in which the injected molecules are dissociated to fragments and an associating phase, in which molecules are formed and atoms are deposited. It appears that very roughly speaking the plasma dissociates and the surface associates: plasma chemistry can be seen as plasma physics and surface chemistry.

At the surface radicals formed in the plasma are adsorbed and interact with each other and form a molecule, which desorbs. Also radicals can lead to deposition and be built in the growing layer. The quality of the deposited layer depends on the various sub-processes. Thus the generated molecules form an indication of the deposition mechanism.

It is likewise interesting to study molecule generation [3] in non-depositing cases. In short the question is: is the (deposition) process physical, with the right radical at the right place. Or is a more chemical picture relevant, in which all radicals contribute to the adsorbed layer and in which the result depends more on effective temperature and atomic composition than on the right type of radicals arriving at the surface. In the latter case more strategic freedom exists: one could probably separate in time the flows of depositing radicals and of energy: deposition and annealing and still obtain a high quality layer.

2. Plasma methodology

To reach higher rates one has to turn to remote plasma processing [4], i. e. the plasma production is separated from the plasma process, cf. Fig. 1. The reason

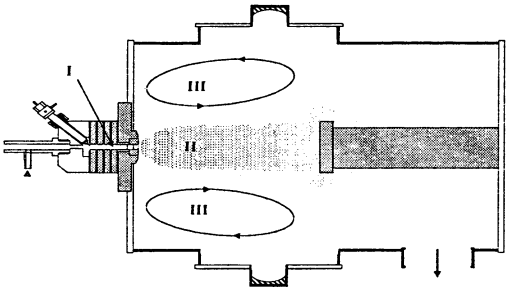

Fig. 1. Sketch of remote plasma processing; the expanding thermal plasma approach; *I* – cascade arc source, *II* – expansion, *III* – re-circulation.

is simple: only then the required fluxes are reached with acceptable energy flux to the surface. If the source is remote then the energy flow associated with the production of plasma will not reach the substrate and the ratio between growth flux and energy flux is more favorable. The flux of radicals depends on the efficiency of the source; the higher the efficiency, the more radicals are produced at a specific power. The cascade arc (expanding thermal plasma, ETP) methodology forms a pertinent example of the remote source approach [4]. A primary plasma is created in the sub atmospheric cascade arc, with a DC current of 30–100 A and gas flows of 30–100 scc/s (1 scc/s ~ $2.5 \cdot 10^{19}$ atoms/s). With large pumps the downstream vessel can be pumped to a working pressure down to 10 Pa. The plasma is ionizing in the source, whereas it becomes recombining when it enters the vessel. The expansion is at first supersonic: the density decreases with $1/z^2$ because of expansion, the temperature decreases and the velocity increases [5]. After a stationary shock front a subsonic plasma beam results, in which radicals are formed from injected and generated molecules by charge transfer and dissociative recombination with the primary e. g. Ar^+ ions, or by abstraction reactions with e. g. H atoms from the source [6]. The formed radicals (the type depends on the application, etching, deposition) may grow by polymerization reactions in the flight to the substrate. There they may lead to deposition, or they may be adsorbed, interact and form a new molecule. Also they may reflect and enter the recirculation vortices in the periphery of the plasma chamber. There they have the residence time to react in the plasma or at the chamber walls; at pressures below 10 mbar surface production is more im-

portant than volume reactions. As new molecules are generated the gas composition will be altered. This new admixture is admixed in the primary plasma beam from the source and new radicals are produced until a stationary mixture is reached. Therefore the measurement of the depletion of injected molecules and the generation of new molecules are an important help to uncover the mechanisms in the surface process [4].

In the remote plasma approach the ionizing part of the plasma is restricted to the source; here the plasma is created. The downstream plasma in the chamber is recombining or passive: no plasma is created; only chemical transfer and (dissociative) recombination takes place. In this passive plasma the electron temperature is low and direct excitation, dissociation and ionization are absent. In pure atomic plasma, as in argon, recombination is weak and the flow of ions is constant. If hydrogen is admixed charge transfer leads to ArH^+ ions, which dissociatively recombines to Ar and H atoms, observed in H_α emission [6]. In that case ions are lost effectively and H atoms form the primary agents. Hence the source can be used either as a plasma ion source or as an atomic radical source. With other molecules as N_2 and O_2 the chemistry is again governed by charge transfer between ions and molecules and dissociative recombination of molecular ions and by abstraction reactions with H, N or O atoms.

Also in more classical in situ treatment plasmas, as the planar microwave discharge of the INP in Greifswald [7], a similar sequence of processes exists. Also here in the bright ionizing region the plasma is created, whereas in the recombining region radicals are formed from interactions between ions and electrons and injected and produced monomers.

To compare different plasmas we need to estimate the dissociation power and the produced radical densities and fluxes. We will do so by relating the radical production to the ion-electron production in the source (region). This follows from the consumed power P and the energy cost per electron-ion pair: $\xi_P E_{ion}$, in which E_{ion} is the ionization energy. The correction factor ξ_P, which describes additional energy losses, as radiation and heat conductivity can be as high as 100 for low pressure plasmas and as low as 3 for high pressure equilibrium plasmas. This gives one major advantage of a high-pressure source in the remote source approach. Other advantages are independent operation of the source with no spurious deposition and the possibility of operation at higher pressure, which is important for diamond deposition.

For the remote ETP method we can as a first estimate use for ξ_P a vale of 3, which gives an ion production of $1 \cdot 10^{17}$ ions/Ws, in rough agreement with a measured ion flow of $3 \cdot 10^{20}$ ions/s at a few kW. For the planar microwave reactor at 1 mbar a value of $\xi_P = 30$ can be used, which for 1 kW gives an ion production of $1 \cdot 10^{19}$ ions/s. The radical production can then be estimated as $5 \cdot 10^{20}$ s^{-1} for the ETP method and $3 \cdot 10^{19}$ s^{-1} for the planar microwave discharge.

3. Radical production and types in deposition

We will describe the dissociation pathways for two important examples: the dissociation of hydrocarbons and of silane for respectively carbon and silicon deposition. There are two main strategies: the first one is by charge transfer between ions from the source and molecules and subsequent dissociative recombination of the resulting molecular ion by low energy electrons [8]:

$$C_2H_2 + Ar^+ \rightarrow C_2H_2^+ + Ar, \quad (1)$$

$$C_2H_2^+ + e \rightarrow C_2H + H. \quad (2)$$

Other dissociative recombination pathways lead to CH + CH, or to C_2 + H + H. In all cases the radical products can be electronically and ro-vibrationally excited as typically 10 eV or more is available. Hence in recombining plasmas the emission of a characteristic molecular band or atomic line is not so much a sign of the presence of these radicals but indicates the recombination of ions and the birth of these radicals.

The C_2H radical can be a deposition precursor, as [9] are C_3H, C_4H formed by reactions with the main hydrocarbon C_2H_2. It is generally assumed that these C_2H based radicals lead to the formation of a dense layer, whereas CH and C_2 are assumed to stick readily and promote a more open polymer like layer with more hydrogen. Note that the densities of CH and C_2 are low, as they are easily lost at the wall. The time constants of these radicals are short, but the ratio of density and time constant can still have a large value, indicating an appreciable production and use.

If CH_4 is injected the following reaction pathway is dominant:

$$CH_4 + Ar^+ \rightarrow CH_3^+ + H + Ar, \quad (3)$$

$$CH_3^+ + e \rightarrow CH_2 + H. \quad (4)$$

The CH_2 radicals have a low sticking coefficient and reflect from the surface rather than contribute to layer deposition. They will build up density in the recirculation until the effective sticking gives sufficient loss to the surface and compensate production. New molecules, like C_2H_2, are produced. The CH_2 density may be high and the time constant long, but with a ratio of n/τ similar to the one for hard radicals, indicating similar use.

If SiH_4 is injected for silicon deposition a similar reaction chain occurs. Charge transfer with Ar^+ ions and dissociative recombination leads to SiH_2 and SiH, both hard radicals with high sticking coefficient. These are readily built in the growing layer and therefore a highly structured layer is produced. If a denser amorphous layer is desired the softer SiH_3 radical is desired. These radicals can be obtained by an abstraction reaction [10]:

$$H + SiH_4 \rightarrow SiH_3 + H_2. \quad (5)$$

This SiH_3 radical has a high mobility at the surface and can readily react at a defect site. But also it can reflect from the surface or can form SiH_4 by a pick up reaction of a hydrogen atom. It has been shown that for high quality a-Si:H deposition a dominance of SiH_3 is needed.

Another example is crystalline diamond deposition. At substrate temperatures of 1000K and a high admixture of H_2 and a small CH_4 flow diamond is deposited. It proves that the best quality diamond is obtained at the highest pressure, which gives also the highest growth rate of 50 μm/h [11]. It is the first example that quality improves with growth rate. One explanation could be the improved re-cycling at the higher pressure and thus a better deposition/etching cycle, which removes improperly bound atoms. Another more general reason might be the increased importance of weakly adsorbed, mobile radicals at the surface in high flux conditions.

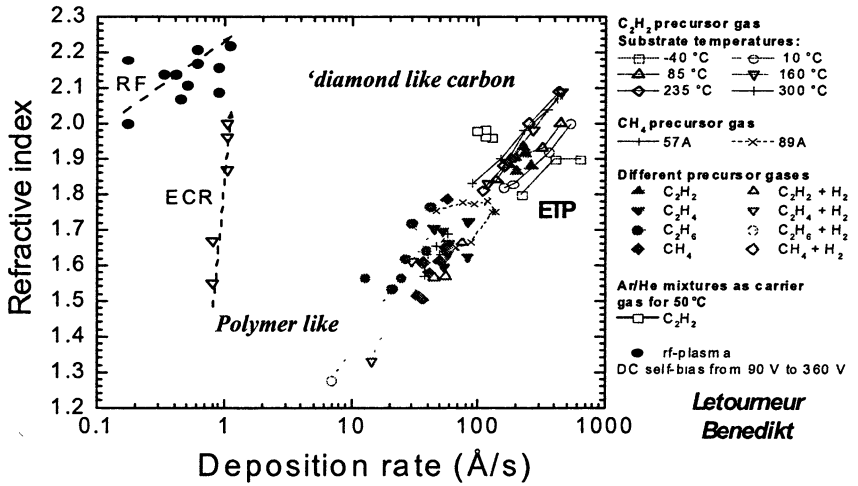

Fig. 2. Refractive index as function of deposition rate

At lower substrate temperatures and smaller or no admixture with hydrogen, amorphous hydrogenated carbon is deposited. In Figure 2 the density of the layer, expressed as index of refraction is given as function of deposition rate [12]. Again the density of the deposited layer, a direct measure for the quality, improves with rate. Also points are given (von Keudell [12]) of an ECR plasma and of a RF plasma, for which cases the ion energy is important and the quality improvement is ascribed to ion pinning. However for ETP this cannot be the mechanism as the ion fraction is small and the ion energy 1 eV. Note that the deposition result does not depend on the injected monomer; only the surface

temperature has an influence. The highest growth rates are reached with C_2H_2, which can be ascribed to the lowest H/C ratio with less H_2 generated. The behavior can be explained at least partly by the contribution of specific radicals in the growth process. At low rates the monomer flow is smaller than the Ar^+ ion flow and thus two cycles of fragmentation by charge transfer and dissociative recombination become possible. This gives a large fraction of hard radicals and thus an open polymer like layer. At the higher growth rates the C_2H radical becomes dominant, and at even higher densities C_3H_n and larger molecules [9]. These are intermediate type radicals and have a high mobility at the surface. Why the quality keeps increasing with rate is still not fully clear. It may be connected with the existence of additionally adsorbed radicals as C_2H, which reside long enough at the passivated surface to react with each other or with a radical arriving from the plasma. This mechanism would only work at high rates with large fluxes; it would indicate a new domain of surface chemistry.

4. Processes at the surface and molecule generation

In the preceding discussion it appears that deposition of a-C:H is quite independent of which hydrocarbon is used. This may in first instance be seen as an indication of the chemical nature of the deposition process. But it can also be connected with the fact that if the injected hydrocarbons are all dissociated that then full conversion of molecules is possible, besides deposition. This is what happens if e. g. methane is injected: it is largely converted to acetylene as has been measured with infrared absorption [13]. Thus actually in both cases the deposition precursor comes from C_2H_2 and is CH and C_2 for low flows and C_2H for higher CH_4 flows. It explains also the emission of C_2 and CH light, which is observed in these types of plasmas. Apparently for C-H systems the tendency is to generate C_2H_2 and to a lesser extent with H_2, C_2H_6 and CH_4.

In order to obtain information on the mechanisms and to which extent freedom exists in deposition strategies also molecule formation has been investigated for non-depositing systems. In particular the generation of NH_3 and of NO_x in nitrogen and hydrogen, respectively oxygen, containing mixtures has been investigated [14].

An ammonia production of up to 12% has been reached in nitrogen hydrogen mixtures [15]. At small hydrogen flows it is even so that the fraction of the admitted H_2, which is used for NH_3 formation increases to 50 %. One way to explain this production is that on passivated (stainless steel) surface only H atoms, N atoms and NH_2 radicals are adsorbed. At small hydrogen fractions only N and NH_2 radicals remain. The few H atoms impinging at the surface will form NH_3 or be used to form new NH_2 radicals at the surface. N atoms will form N_2 with N atom precursors. It is then temperature and stochiometry which determine the formation of precursors at the surface. Then in a direct pick up

reaction or in reactions between two adsorbed radicals new molecules are formed, with a preference of molecules with a higher binding energy.

In nitrogen and oxygen containing mixtures the molecule NO is observed for a typical fraction of a few percent. In this case the sum of the bond energies for N_2 and O_2, (9.8 + 5.1) eV = 14.85 eV, is larger than that of two NO molecules: 13.0 eV. Hence the dominance of formation of O_2 and N_2 can be understood, but the significant appearance of NO is somewhat unexpected. From time dependent studies it can be concluded that in N-O mixtures primarily N atoms and NO molecules are adsorbed at the passivated surface. One explanation could thus be that in fact N_2O (N rich) or NO_2 (O rich) are formed at the surface with excess energy in the form of electronic and/or ro-vibrational energy. These molecules are in the gas phase effectively reduced by N or O atoms and form NO and N_2 from N_2O for O poor mixtures and NO, O_2 and N_2 from NO_2 in N poor mixtures. In this respect it is important to note that bond energies of N_2O and NO_2 are closer to those of the appropriate $N_2 + O_2$ mixtures.

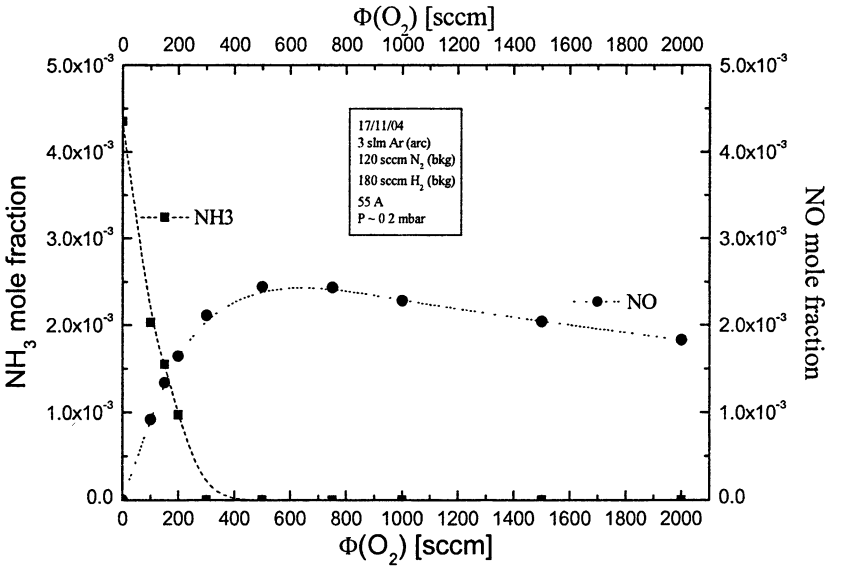

Fig. 3. NH_3 and NO mole fractions in N_2, H_2 and varying O_2 seeded argon plasma

In a third experiment the influence of H_2 addition to NO forming plasmas and of oxygen to NH_3 formation has been studied. It appears [16] that with admixture of oxygen to hydrogen/ nitrogen mixture the formation of NH_3 decreases drastically, and H_2O is formed instead. Contrarily the presence of hydrogen in NO forming plasma does not influence the formation of NO appreciably, cf. Fig. 3. This behavior can certainly not be expected from bond ener-

gies alone. One must conclude that the occurrence of specific saturated radicals at the surface determines the fate of molecule formation. If oxygen is added, OH radicals will replace NH_2 radicals at the surface, with as a consequence that H_2O is formed rather than NH_3. Apparently, the NO radical is less affected, or forms a HNO molecule, with which on impact NO can be formed. One must conclude that formation at the surface is chemical of nature but that the presence of specific adsorbed precursor radicals plays an important physical role in the production of specific molecules. This could explain the fact that very similar mixtures are observed in totally different experiments as has been shown from results in a planar microwave reactor in INP in Greifswald [17]. Similar studies in C/N/H/O mixtures give the same conclusion.

A final remark can be given with regard to the production of excited molecules at the surface. At large flows of atomic nitrogen radicals the appearance of $B \rightarrow A$ (first positive system) is observed as well as the first negative system of N_2^+ ($B \rightarrow X$) [14]. At that location the electron temperature is 1000 K and electron excitation can be excluded. The only way to explain this observation is that excited N_2 molecules desorb from the surface. Also in N/O mixtures excited molecular radiation has been observed as an orange glow close to the substrate [14]. This glow is known as the shuttle glow. Also here the reaction of two radicals at the substrate can explain the observation if they are weakly bound on top of a passivated surface.

5. Implications and conclusions

For molecule generation the presence of specific precursors at the surface is important for the type of molecules. We have seen that NH_2, NO, OH are examples of such radicals besides the atomic radicals N and H; these can explain the appearance of specific molecules as H_2O, NO, NH_3 and in the presence of C atoms HCN and CO. In deposition circumstances it is important which type of radicals are present. Soft radicals lead in general to more dense layers as then the radicals can migrate over the surface. A dominance of hard radicals will give rise to more structured layers. For the generation of molecules in deposition circumstances similar mechanism as described above applies. If the surface is sufficiently passivated it is expected that the result is not too dependent on the composition. Actually the difference in surface structure with differences in effective surface may have an equal influence on the resulting composition of generated molecules. At any rate it is more informative to measure also new molecules than to focus on radicals only. A low density of radicals does not mean that it is unimportant; a high density likewise does not exclude that it is unimportant. The ratio of density and time constant is the determining quantity.

We have also shown that the dissociation power of the plasma, remote or not remote, is the first item to consider. In this respect a remote ETP source performs better than a microwave source. However in the lower pressure sec-

tion also the recombination effect is crucial and in this respect the low electron temperature in ETP plasma expansion is a disadvantage. Therefore a combination of an effective plasma source of the cascade arc type and microwave/ millimeter wave heating of the lower pressure in the expansion would be ideal. If then e.g. diamond would be deposited a large deposition rate could be achieved over a large area.

Acknowledgement. The support of Netherlands Organization for Scientific Research (NWO) in the framework of scientific cooperation between The Netherlands and the Russian Federation is gratefully acknowledged.

References

1. *Liebermann M.A., Lichtenberg A.J.*, Principles of plasma discharges and material processing, John Wiley, New York, 1994.
2. *Martinu L., Poitras D.*, J. Vac. Sci. Techn., **A18** (2000), 2619.
3. *Capitelli M., Ferreira C.M., Gordiets B.F., Osipov A.I.*, Plasma Kinetics in Atmospheric gases, Springer, 2000.
4. *Schram D.C.*, Pure Appl. Chem., **74** (2002), 369.
5. *Schram D.C., Mazouffre S., Engeln R., van de Sanden M.C.M.*, The physics of plasma expansion, in Atomic and Molecular Beams, Ed. R. Camparque, Springer, Berlin, 2001.
6. *Mazouffre S., Vankan P., Engeln R., Schram D.C.*, Phys. Plass. **8** (2001), 3834.
7. *Hempel F., Davies P.B., Loffhagen D., Mechold L., Röpcke J.*, Plasma Sources Sci. Technol., **12** (2003), S98.
8. *Benedikt J., Letourneur K.G.Y., Wisse M., Schram D.C., van de Sanden M.C.M.*, Diamond and Related Materials, **11** (2002), 989.
9. *Benedikt J., Eykman D.J., Vandamme W., Agarwal S., van de Sanden M.C.M.*, Chem. Phys. Lett., **402** (2005), 37.
10. *Smit C., van Swaaij R.A., Hamers E.A.G., van de Sanden M.C.M.*, J. Appl. Phys., **96** (2004), 4076.
11. *Beulens J.J.*, Surface modification using a cascade arc source, Thesis Eindhoven university of Technology, 1992; *Buuron A.J.M.*, Plasma deposition of carbon materials, Thesis Eindhoven university of Technology, 1993.
12. *Letourneur K., von Keudell A.*, personal communication.
13. *van Hest M.F., de Graaf A., van de Sanden M.C.M., Schram D.C.*, Plasma Sources Sci. Technol., **9** (2000), 615.
14. *van Helden J.H., Zijlmans R.A.B., Engeln R.A.H., Schram D.C.*, IEEE Trans. Plasma Sci., **33** (2005), 390.
15. *Vankan P.J.W., Rutten T., Mazouffre S., Schram D.C., Engeln R.*, Appl. Phys. Lett., **81** (2002), 418.
16. *Zijlmans R.A.B., Gabriel O., Welzel S., Ropcke J., Engeln R., Schram D.C.*, to be published.

HYDROCARBON PLASMA CHEMISTRY IN CW MICROWAVE DISCHARGE

A. M. Gorbachev, A. B. Muchnikov, A. L. Vikharev, D. B. Radishev, V. A. Koldanov

Institute of Applied Physics, Nizhny Novgorod, Russia

Hydrocarbon plasma chemistry in microwave discharge (frequency 2.45 GHz) during diamond deposition in H_2-CH_4 gas mixture was studied. Experimental investigation of growth rate of diamond film at different synthesis conditions was carried out. Optical emission spectroscopy (OES), used to examine CH, C_2 radicals and atomic hydrogen (H), shown a certain correlation between diamond film growth rate and relative intensities of CH (4310 Å) and H_γ (4340 Å) lines. Also, the changing of gas phase chemistry with variation of discharge parameters was observed by OES. Zero-dimensional numerical modeling of hydrocarbon chemistry is presented. Qualitative agreement between experimental results and theoretical approach is reported.

The problems of hydrocarbon plasma chemistry are associated with one of the applications of the microwave discharge: CVD diamond synthesis. The works in the field of CVD technologies have been performed for quite a long time already. But still now the interrelations between the external parameters of CVD reactor, the plasma parameters, the diamond film growth rate and diamond film properties have not been sufficiently studied yet. This work describes the study of the influence of external parameters (percentage of methane in the mixture, pressure, gas flows) on the concentrations of carbon-containing species and the diamond film (DF) growth rate.

The experiments were performed using 2.45 GHz microwave plasma CVD reactor described in detail in [1]. The microwave discharge (shaped as a hemisphere) was ignited in the quartz dome, located in a cylindrical resonator excited at the TM_{013} mode by a magnetron. The discharge touched substrate surface, where DF was deposited. The DF synthesis was carried out in a hydrogen-methane mixture, which was fed into the quartz dome. Figure 1 shows the experimental dependence of the DF growth rate on the percentage of the methane content in the gas mixture.

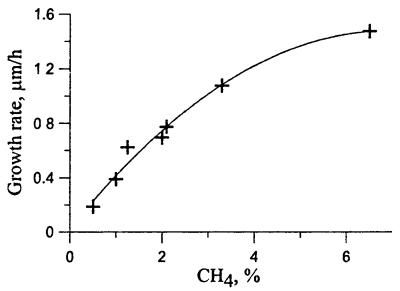

Fig. 1. DF growth rate as a function of the percentage of methane content in the gas mixture. Microwave power 3 kW, pressure p = 90 Torr, hydrogen flow 200 sccm.

Optical emission spectroscopy was used for diagnostics of gaseous species in the CVD reactor. The radiation of the discharge was focused by a lens to

an optical fiber, connected to the input slit of the SOLAR TII monochromator. The signal from the Hamamatsu R928 photomultiplier (connected to the output slit of the monochromator) was registered with a digital oscilloscope and sent to a computer.

The main attention was given to the study of the following species: C_2 radical ($d^3\Pi_g \rightarrow a^3\Pi_u$ transition of the Swan band, 5166 Å), CH radical (4310 Å), atomic hydrogen H (H_α, H_β, and H_γ lines: 6563 Å, 4861 Å, and 4340 Å, respectively). Small amount of argon was added to the process gas mixture for the actinometric measurements [2]. The H_2 dissociation degree was assumed to be proportional to the ratio of the intensities of the H_γ and Ar (8115 Å) lines [1].

Figure 2 shows experimentally determined intensities ratios of emission lines – $I_{CH}/I_{H\gamma}$, $I_{C_2}/I_{H\gamma}$, and $I_{H\gamma}/I_{Ar}$. Note that the intensity ratios of H_α, H_β, and H_γ lines remained equal in all cases; it indicates that the electron temperature did not vary either. It was assumed that in our conditions the radiating levels were excited from the main state by electron impact, and quenched by collisions with molecules. In this case the ratios of line intensities are proportional to the ratios of concentrations of the corresponding species.

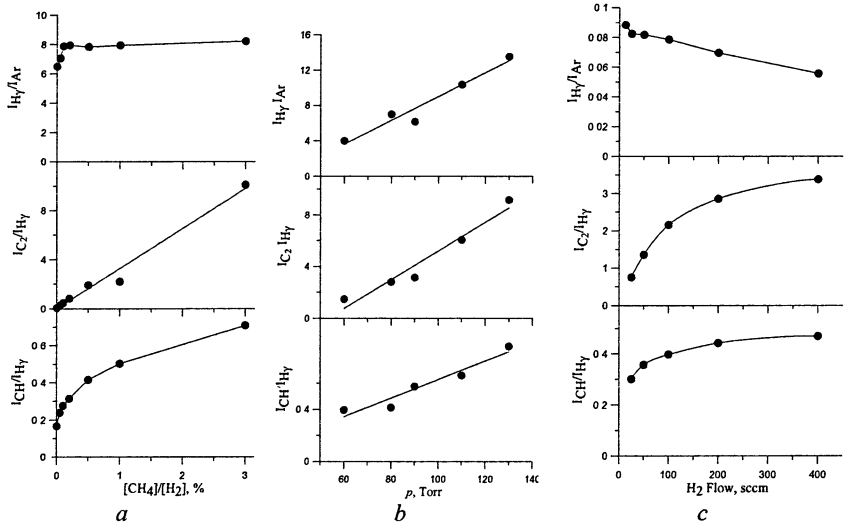

Fig. 2. Ratios of lines intensities: $I_{CH}/I_{H\gamma}$, $I_{C_2}/I_{H\gamma}$, and $I_{H\gamma}/I_{Ar}$ for the microwave power of 3 kW: *a* – as a function of the methane content in the mixture at $p = 90$ Torr and hydrogen flow 200 sccm; *b* – as a function of the pressure in mixture of 1% CH_4 in H_2, hydrogen flow 200 sccm; *c* – as a function of the H_2 flow in mixture of 1% CH_4 in H_2, $p = 90$ Torr.

It is seen from Fig. 2, *a* the $I_{H\gamma}/I_{Ar}$ ratio becomes somewhat higher when the methane content is raised to 0.5%, and then stays the same. It shows that the H_2

dissociation degree is weakly dependant on the methane content in the mixture. Note that the value of the I_{C_2}/I_{H_γ} ratio is proportional to the methane content, and the I_{CH}/I_{H_γ} ratio grows much slower, as the percentage of the methane content rises. Figure 2, *b* shows the dependencies on the gas pressure: the ratio I_{H_γ}/I_{Ar} grows in parallel with the pressure, and, hence, the molecular hydrogen dissociation degree also increases. This is explained by the increase of the specific microwave power absorbed in the plasma, since the volume of the plasma contracts as the pressure grows (at a constant level of the incident microwave power) [1, 3]. Due to the fact that the ratios of line intensities depend on the gas flow (Fig. 2, *c*), one can conclude that surface reactions influence the concentrations of carbon-containing species, thus causing these concentrations to decrease at low values of gas flow.

Comparing Fig. 1 and Fig. 2, *a* one can see the similar character of dependencies of the DF growth rate and the I_{CH}/I_{H_γ} ratio on the methane content in the mixture. The authors of [4] obtained the following formula for the DF growth rate G and relative density of diamond defects, X_{def}:

$$G \propto \frac{[CH_3]_{sur}[H]_{sur}}{3\cdot 10^{15}\,\mathrm{cm}^{-3} + [H]_{sur}} \propto [CH_3]_{sur}[H]_{sur}, \quad X_{def} \propto \frac{G}{[H]^2_{sur}} \propto \frac{[CH_3]_{sur}}{[H]_{sur}}, \qquad (1)$$

where $[H]_{sur}$ is atomic hydrogen concentration, and $[CH_3]_{sur}$ is concentration of the CH_3 radical near the substrate surface. The distribution of C_1 species can be explained by partial equilibria of hydrogen shift reactions [5], thus, there is an algebraic connection between concentrations of the C_1 hydrocarbons and the $[H]/[H_2]$ ratio, from which it follows that $[CH_3][H] \propto \frac{[CH][H_2]^2}{[H]}$. In this case, according to Eq. (1), the DF growth rate will be proportional to the $[CH]/[H]$ ratio.

In order to analyze the hydrocarbon plasma chemistry we used the zero-dimensional model of chemical kinetics, that took into account the reactions between the following gas-phase species: H_2, H, CH_4, CH_3, CH_2, CH, C, C_2H_6, C_2H_5, C_2H_4, C_2H_3, C_2H_2, C_2H, and C_2. The rates of forward reactions were taken from [6], and the rates of reverse reactions were calculated using the principle of detailed balancing. The concentration of atomic hydrogen was found from the following equation:

$$\frac{\partial[H]}{\partial t} = k_d^*[H_2]\cdot N_e - 2k_R[H]^2 N - \nu_d[H] + k_T[H_2]N, \qquad (2)$$

where k_d^* is the electron impact dissociation rate (which takes into account the dissociation both from the ground-state and vibrationally excited levels), k_R is three-body recombination rate, k_T is thermal dissociation rate, N is density of gas molecules, N_e is electron density, $\nu_d = \frac{D_H}{\Lambda^2}$ is efficient frequency of diffu-

sion losses, determined by the diffusion coefficient, D_H, and diffusion length Λ. The values of the reaction rates in (2) were chosen basing on the results of the self-consistent modeling of the discharge in hydrogen [3].

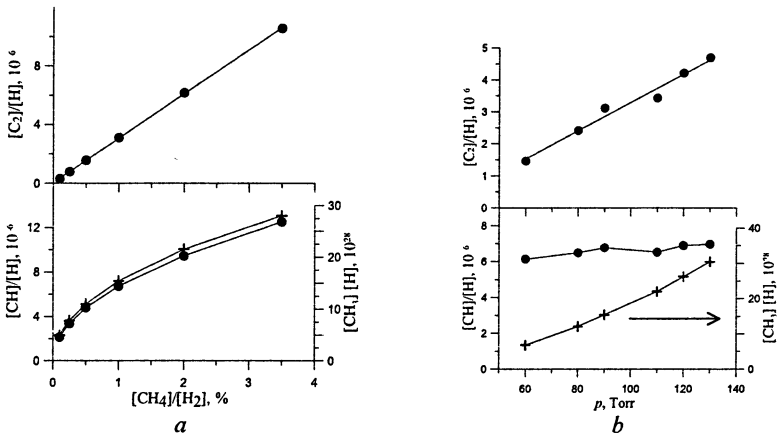

Fig. 3. Calculated concentrations ratios of [CH]/[H] and $[C_2]/[H]$ (circles) and $[CH_3][H]$ concentrations product (crosses) depending on methane percentage in the gas mixture (*a*); gas pressure (*b*).

Figure 3 shows the results of numeric modeling. By comparing Fig. 2 and Fig. 3 one can see that the observed dependencies on the methane content and gas pressure are quite well described by the model. The dependence on gas flow cannot be described within this model, due to the interaction with the surface that has not been taken into account.

The authors of [7, 8] proposed to use the ratios of intensity of different lines to control the process of CVD diamond synthesis. Let us check the methods proposed using the obtained experimental dependencies and the results of numerical modeling.

The said results showed that the species concentrations are linked by the formula $[CH_3][H] \propto \frac{[CH]}{[H]}$, Fig. 3, *a*. Assuming that the DF growth rate is determined by Eq. (1) and is proportional to $[CH_3]\cdot[H]$ we can treat the I_{CH}/I_{H_γ} ratio as a parameter to control the DF growth rate.

As the methane content in the mixture grows, the ratio of concentrations $[C_2]/[H]$ increases linearly. The methane that enters the reactor is converted into acetylene, which is the main carbon-containing species in the reactor, since its concentration exceeds the concentration of other carbon-containing species by several times. C_2 is formed from acetylene in the following chain of reactions: $C_2H_2 \leftrightarrow C_2H \leftrightarrow C_2$. Calculations show that the concentration ratio $[C_2]/[H]$ is proportional to the molecular hydrogen dissociation degree and the percentage

of carbon in the mixture: $\frac{[C_2]}{[H]} = \frac{[H]}{[H_2]}\frac{[C_2H_2]}{[H_2]}$. Therefore, ratio I_{C_2}/I_{H_α} used in [7] to control the DF growth rate, correlates with the DF growth rate taking into account the combined effect of two factors: the H_2 dissociation degree and the stabilized percentage of carbon in the mixture.

The authors of [8] used the I_{C_2}/I_{CH} ratio to control the composition of the plasma. The performed calculations show that the corresponding concentration ratio characterizes the share of CH_3 among the carbon-containing species: $\frac{[C_2]}{[CH]} \propto \frac{[C_2H_2]}{[CH_3]}$. Accounting for this, the parameter that determines the DF quality is expressed as follows: $K = \frac{1}{X_{def}} \propto \frac{[H]}{[CH_3]} \propto \frac{[H][C_2]}{[CH][C_2H_2]} =$

$= \frac{[C_2]}{[CH]}\frac{[H]}{[H_2]}\frac{[H_2]}{[C_2H_2]}$. Therefore, for the dissociation degree and methane percentage of being constant we obtain $K \propto [C_2]/[CH]$. It should be noted that comparison of the results of [8] and this paper may be not completely accurate, since the authors of [8] made their experiments in the mixture of H_2 and C_2H_5OH, and, hence, the composition of the plasma in the compared experiments was different.

Thus, among the lines of atomic hydrogen and carbon-containing species observed in the discharge radiation, the following ratios may be used: I_{C_2}/I_{H_γ} depends on the H_2 dissociation degree and the stabilized carbon percentage in the mixture. The I_{C_2}/I_{CH} ratio tracks the DF quality at constant H_2 dissociation degree and constant established percent of carbon content in the mixture. The I_{CH}/I_{H_γ} ratio is proportional to the DF growth rate.

This work has been supported by the Netherlands Scientific Society (NWO Project 047.16.019), and the CRDF, under the Basic Research and Higher Education (BRHE) program, grant Y1-P-01-04.

References

1. *Vikharev A.L., Gorbachev A.M., Koldanov V.A., Radishchev D.B.*, Plasma Phys. Rep., 2005, **31** (4), 1.
2. *Coburn J.W., Chen M.*, J. Appl. Phys. 1980, **51**, 3134.
3. *Koldanov V.A., Gorbachev A.M., Vikharev A.L., Radishchev D.B.*, Plasma Phys. Rep., 2005, **31** (11), 965.
4. *Goodwin D.G.*, J. Appl. Phys., 1993, **74** (11), 6888 and 6895.
5. *Goodwin D.G., Butler J.E.*, Theory of Diamond Chemical Vapor Deposition, ed. Prelas, Popovici, Bigelow, Marcel Dekker Inc., 1998, 527-583.
6. *Baulch D.L., Cobos C.J., Cox R.A. et al.*, Combustion and Flame, 1994, **98**, 59.
7. *Sevillano et al.*, US Patent N 5,405,645.
8. *Dvorkin V.V.*, Fizika Plazmy, 2003, **29** (9), 851.

POSSIBILITIES OF THE PULSED-PERIODICAL REGIME OF DIAMOND FILMS DEPOSITION IN MPACVD REACTOR

V. A. Koldanov, A. L. Vikharev, A. M. Gorbachev, A. B. Muchnikov, D. B. Radishev

Institute of Applied Physics, Nizhny Novgorod, Russia

This paper demonstrates that the usage of a pulsed-periodical regime of discharge maintenance makes it possible to sufficiently (in 2–3 times) increase the growth rate of the diamond films in comparison with CW regime.

Introduction

The influence of the pulsed-periodical regime of a CVD reactor operation on growth rate and quality of diamond films (DF) is being investigated in this work. In comparison with the previous works [1, 2] the present investigation has been made at a higher level of microwave power and at different pulse repetition frequencies. Due to the high level of microwave power growth of DF on a bigger diameter substrates at pressures of 20–200 Torr is possible.

The dynamics of chemically active particles during a microwave pulse was investigated with optical emission spectroscope method (OES). The short diagnostic pulse was used to investigate the processes between the pulses.

The influence of pulse repetition frequencies on growth rate and morphology of DF was studied. The comparison of growth rate and quality of DF in CW and pulsed regimes was made.

Experimental setup

In this work we used the CVD reactor (Fig. 1) similar to one developed in Michigan State University [3]. This setup allows us to investigate the DF depositions in CW and pulsed-periodical regimes at average microwave power up to 5 kW; pulse repetition rate up to 1000 Hz; hydrogen flow rate up to 400 sccm (standard cubic centimeters per minute); methane percentage in hydrogen-methane mixture up to 10%. The silicone substrate with diameter up to 75 mm was used for DF deposition.

Investigations of the discharge characteristics

It was discovered with OES method that small methane addition in hydrogen discharge leads to substantial increase of atomic hydrogen lines intensities (Fig. 2). At the same time the ratio of different atomic hydrogen lines inten-

sities doesn't change. Evidently, it shows that electron temperature in the discharge changes only slightly.

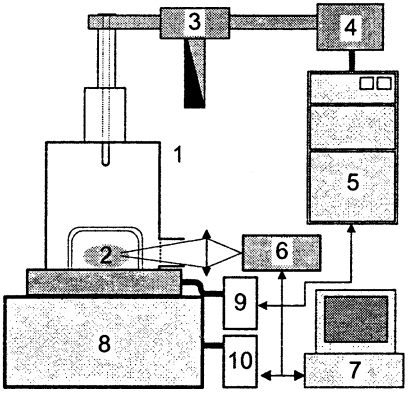

Fig. 1. Scheme of the experimental setup: *1* – resonator, *2* – microwave discharge, *3* – waveguide with circulator, *4* – magnetron, *5* – power supply, *6* – monochromator, *7* – computer, *8* – vacuum chamber, *9* and *10* – gas-feed and pump-out systems.

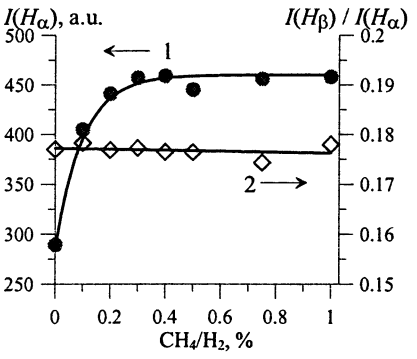

Fig. 2. The dependence of H_α line intensity (*1*) and ratio of intensities of H_β and H_α (*2*) as a function of methane mole fraction in the mixture at pressure 90 Torr and microwave power 3 kW (CW regime).

The effect of the discharge plasma emission intensity increase can be explained by a slight growth of the electrons temperature in the discharge. A small methane addition leads to the change of the main ion from H_3^+ to CH_5^+, which has a larger recombination constant. Simulations made on our model [5], show that a small increase of electric field in the discharge (<5%) followed by a significant change of excitation rate of particle electron levels occurs.

For investigation of processes between microwave pulses with OES method we used a short diagnostic pulse (duration 50–200 μs, power 5 kW) sent with a delay after the main pulse. This short diagnostic pulse due to a small pulse energy, according to our estimations, doesn't significantly influence the parameters of the gas mixture. The time-dependence of a relative atomic hydrogen concentration is presented in Fig. 3 (obtained with actinometrical method).

Unfortunately, the tracking of the concentration of such radicals as CH and C_2 between the pulses was impossible with this method. The intensity of their luminescence in a diagnostic pulse appeared to decrease quickly (< 0.5 ms) with the increase of the diagnostic pulse delay. Furthermore, the afterglow of these radicals continues for a long time after the end of the microwave pulse and the disappearance of atomic hydrogen lines emission (Fig. 4). Perhaps, the after-

glow of carbonic radicals is due to a low excitation threshold (CH – 2.9 eV, C_2 – 2.6 eV) and the collisions with gas particles may be the main mechanism of emission levels excitation of these radicals.

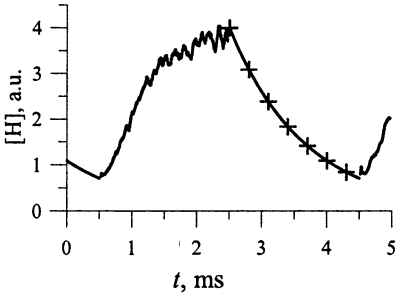

Fig. 3. Modulation of atomic hydrogen concentration in the discharge (average microwave power 3 kW, pulse repetition frequency 250 Hz, gas pressure 100 Torr).

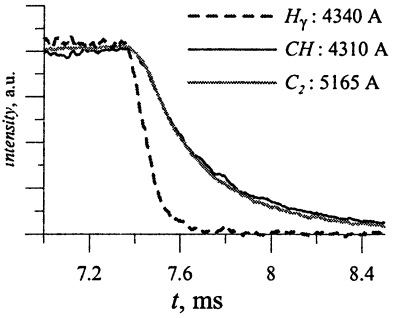

Fig. 4. The dynamics of luminescence of different radicals after the end of the microwave pulse.

The influence of the pulse repetition rate on DF growth

In this series of experiments the diamond films growth was performed on substrate of 40 mm in diameter in the following regime: growth temperature 730–820 C, average microwave power 3 kW, methane mole fraction 1%, hydrogen flow rate 200 sccm, deposition time 7 h. The gas mixture pressure was 90 Torr in CW regime and 130 Torr in pulsed regime. Here the visible plasma volume, deposition area and substrate temperature were approximately equal in both regimes. The conditions for comparison of CW and pulsed regimes of CVD reactor operation were discussed earlier in the article [1]. The results of these experiments with DF deposition in CW and pulsed regimes are presented in Fig. 5. Despite large dispersion of experimental results it's seen that the growth rate in pulsed regime is 2–3 times higher than in CW one.

The points *A* and *B* marked in Fig. 5, correspond to DF growth in long (100 h) deposition processes. The growth rate in these processes was 1.2 μm/h in CW regime and 5.5 μm/h in the pulsed one. At the same time, the Raman scattering plots (Fig. 6) show that the quality of DF grown in pulsed regime is higher than that of DF grown in CW regime. So, pulsed regime does not only increase the growth rate of DF but can also improve the DF quality in comparison with CW regime.

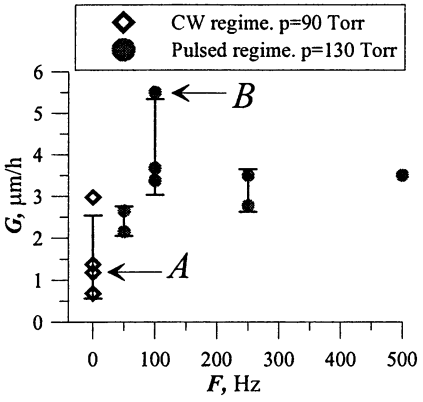

Fig. 5. Dependence of DF growth rate on pulse repetition frequency. Average microwave power 3 kW, methane mole fraction 1%.

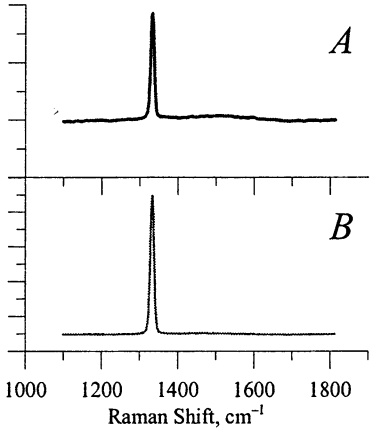

Fig. 6. Raman scattering plots of DF grown in CW (*A*) and pulsed (*B*) regimes in long (at 100 h) deposition processes.

The microphotographs of DF grown in pulsed regime at different pulse repetition rate are presented in Fig. 7. As it's seen on photos, the morphology of DF depends strongly on the pulse repetition rate. At a low pulse repetition rate (50 Hz) there is a spot of 4–6 mm diameter in the center of the substrate. The average crystal size in the spot is 1–2 μm. The main part of the DF consists of crystals of about 10–20 μm with dominating <110> orientation.

The DF grown at pulse repetition rate of 100 Hz has a completely different morphology. The central part of this film is made of big crystals (30–50 μm) with dominating <100> orientation. When moving away from the center the average crystal size decreases and crystal orientation gradually changes. At the edge of the film there are mostly crystals with <111> orientation and 10–20 μm size.

At a high pulse repetition rate (500 Hz) DF has a high degree of homogeneity. All surface consists of crystals with <111> orientation and average size of 10–20 μm.

So, investigations show that the size and orientation of DF crystals depend on the pulse repetition rate. The DF growth rate depends on the pulse repetition rate slightly. Therefore the pulsed regime can be used for DF deposition with the given surface morphology.

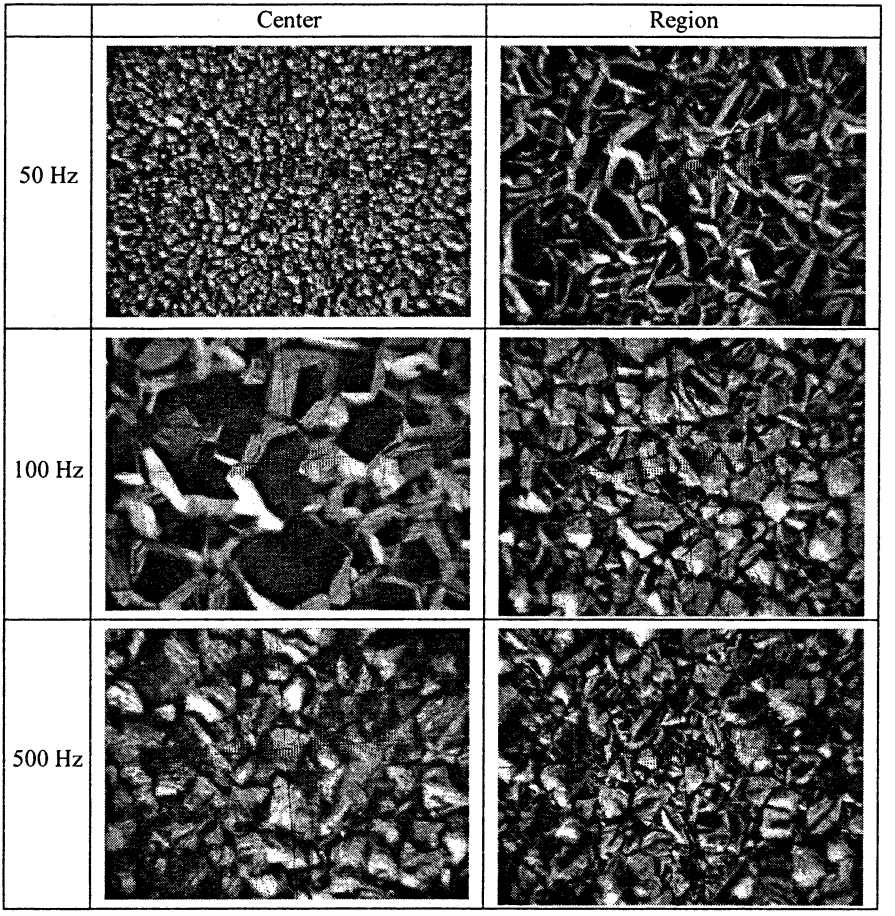

Fig. 7. The microphotographs of DF grown in pulsed regime at different pulse repetition rate.

Conclusion

As the result of DF deposition investigations it has been demonstrated that pulsed periodical regime makes it possible to increase the growth rate of DF substantially (2–3 times). The morphology of the DF depends on the pulse repetition rate.

With the use of a short diagnostic pulse the dynamics of atomic hydrogen concentration during the whole pulse period has been investigated.

The afterglow of carbonic radicals CH and C_2 has been observed. This effect may be connected with these radicals excitation due to their collisions with gas molecules.

It has been demonstrated that addition of 0.2–0.3% CH_4 to pure hydrogen leads to the increase of atomic hydrogen lines intensity by 1.5–2 times. We explain this effect by a slight (less than 5%) increase of the discharge maintenance field, which is due to the change of plasma ionic composition.

References

1. *Vikharev A.L., Gorbachev A.M, Koldanov V.A., Radishev D.B.* // Strong microwaves in plasmas: Proc. Int. Workshop. Nizhny Novgorod, 2003. V. 2. P. 693-699.
2. *Vikharev A.L., Gorbachev A M., Koldanov V.A., Radishchev D.B.* // Plasma Phys. Rep. 2005. V. 31, № 4. P. 338-346.
3. *Grotjohn T.A., Asmussen J.* Microwave plasma-assisted diamond film deposition // Diamond Films Handbook / Ed. by J. Asmussen and D.K. Reinhard. New York: Marcel Dekker, 2001.
4. *Lebedev Yu.A., Épshteoen I.L.* // Teplofiz. Vys. Temp. 1998. V. 36. P. 534.
5. *Koldanov V.A., Gorbachev A.M., Vikharev A.L., Radishev D.B.* // Plasma Phys. Rep. 2005. V. 31, № 11. P. 965-977.

MICROWAVE COAXIAL TORCH AS PLASMACHEMICAL REACTOR

I. A. Kossyi, S. I. Gritsinin, V. Yu. Knyazev, N. A. Popov[1]

General Physics Institute, Moscow, Russia
[1]Moscow State University, Moscow, Russia

A microwave coaxial plasma torch is described. The efficiency of production of nitrogen oxides (NO and NO_2) was determined for different operating conditions of the torch. It is shown that the nitrogen oxides production is followed intensive gas heating and subsequent fast gas cooling i.e. quenching of reaction products.

1. Introduction

Microwave coaxial plasma sources find wide application in production with the use of various plasma technologies, as well as useful tools in various scientific applications (see, e. g., [1, 2]).

A coaxial microwave plasma torch (CMPT) considered in this paper is different from conventional plasma sources in that it produces a large volume of nonequilibrium plasma with a high density. From this point of view, it is interesting to consider the possibility to use the proposed CMPT as a plasma chemical reactor. In particular, in the present paper it is proposed that the CMPT be used to produce nitrogen oxides from air. It is well known that this reaction proceeds successfully at equilibrium heating of a gas to 3000–4000 K with the subsequent fast quenching of the reaction products or at nonequilibrium excitation of vibrational and electronic energy levels of molecules. The aim of our experiments was to determine the density of nitrogen oxides (NO and NO_2) under different operating conditions of the torch and to clarify the mechanism of oxidation of nitrogen in air at operation of this device.

2. Experimental device

The design of the proposed CMPT has some important characteristic features and advantages over other known discharge systems (see, e. g., [1]). The construction is described in details in [3, 4]; here, we only outline its characteristic features.

A basic component of the CMPT is a coaxial waveguide. The inner electrode of the coaxial waveguide is shorter than the outer electrode. Therefore, in the absence of a flame, the coaxial waveguide is ended in a circular beyond-cutoff waveguide reflecting the incident electromagnetic wave. A maximum electric field of the wave takes place near the nozzle edge, where the reflection occurs. As the energy is accumulated in the coaxial waveguide, the field increases up to the breakdown of a gas, resulting in the formation of a plasma jet

in the gas stream flowing through the hollow central electrode of the coaxial waveguide (cavity).

The construction allows us to achieve a stable generation of the plasma jet near the nozzle by using a production magnetron with a power of $W < 1$ kW and a radiation frequency of 2.45 GHz. The increase of the electric field up to the threshold intensity make possible operating with almost all gases and gas mixtures (air, argon, nitrogen, methane, etc.).

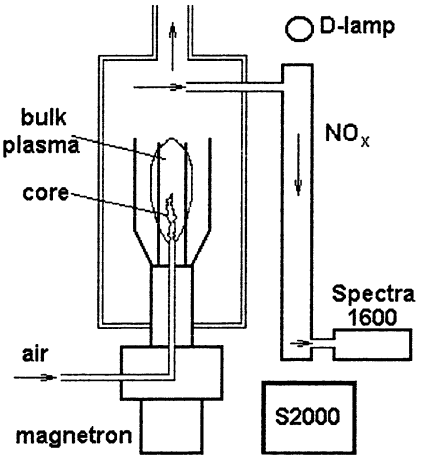

Fig. 1. Experimental setup

The CMPT of this type was studied as a plasmachemical reactor for production of NO_x ($x = 1, 2$). The experimental setup is shown in Fig. 1. Air at atmospheric pressure passes through the central hollow electrode, which is an inner electrode of the coaxial waveguide. We used a nozzle with a channel diameter of nearly 1.5 mm (the length was 10 mm).

Treated by discharge, the gas flowed into the chamber open at its end. After short-time operation of the torch, the concentration of produced oxides in the chamber came to a steady-state level, and their percentage was exactly defined by their production in the jet. Downstream from the end of the torch, we introduced a ceramic pipe to take gas samples. The gas-analyzing system consisted of a spectrometer unit for measuring the NO_2 concentration and a Spectra-1600 GL gas analyzer measuring the NO concentration to within 10% of a measured value. The gas analyzer, using the electrochemical effect for its operation, has a built-up pump drawing the sampled gas through the entire diagnostic system. The spectrometer unit for NO_2 concentration measuring consists of a deuterium lamp, a tube with transparent ends for transportation of the sampled gas, and an S2000 (200–800 nm) spectrometers measuring the spectrum of the lamp radiation passed through the tube.

3. Experimental results

In the experiments we varied the gas flow rate determining the released energy density in the gas.

The results of these experiments are presented in Fig. 2. It is seen that the concentrations of produced NO and NO_2 are comparable and amounts to several tenth percent. As the gas flow rate was increased to a maximum attainable

value, the oxide production decreased. At the same time, the energy efficiency of the process changed insignificantly.

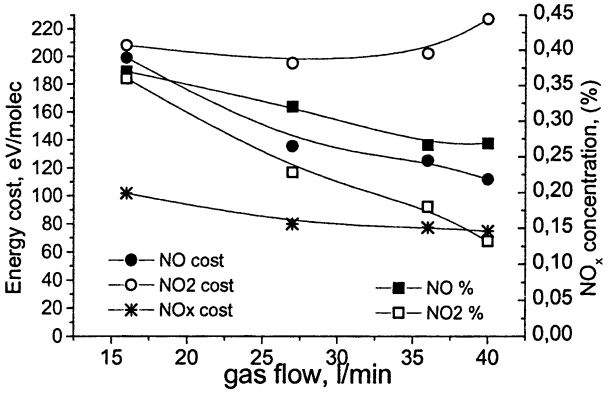

Fig. 2. NO_x concentration and energy cost vs. gas flow

4. Description of a model

We consider the NO_x production in the CMPT discharge in air at atmospheric pressure. The discharge channel is a axisymmetric plasma of radius $R \sim 1$ mm [3, 4]. At a distance of $L_d \leq 1.5$–2 cm from the electrode, the gas in the channel is heated to temperatures exceeding 4000–4500 K [4]. Under these conditions, most of the discharge energy is expended for exciting vibrational degrees of freedom of nitrogen molecules. At a gas temperature $T \geq 4000$ K, the rate constant for VT relaxation of N_2 ($v = 1$) by oxygen atoms exceeds $k_{VT} \geq \geq 10^{-12}$ cm^3/s [5], whereas the equilibrium density of O(^{3}P) atoms in air amounts to $\sim 5 \cdot 10^{17}$ cm^{-3} [6]. Hence, this discharge may be considered as a heat source.

The air is admitted into the discharge plasma through the central electrode. Intense ionization and heating of the gas occur in the region of strong field near the electrode. The formed hot plasma is then entrained by the gas flow; hence, the electromagnetic field energy is expended only for maintaining the conductivity and for an additional heating of the created channel region. The discharge action on every elementary volume of the gas occurs while this volume of the gas is driven through the region of microwave action. In calculations we used a one-dimensional axisymmetric model. The radial profile of the specific power of a heat source was assumed to be Gaussian with characteristic radius R_0.

The kinetic block of the model included a system of processes describing the evolution of concentrations of dominant neutral components: N(^{4}S), O(^{3}P), O_3, NO, NO_2, O_2, N_2. The main reactions and dependences of the rate constants on T were taken from [7, 8].

For every component, we solved the equation

$$\frac{\partial N_k}{\partial t}+\frac{1}{r}\frac{\partial(uN_k)}{\partial r}=\frac{1}{r}\frac{\partial}{\partial r}(rD_k\frac{\partial N_k}{\partial r})+F_k^+-F_k^-, \quad (1)$$

where N_k is the concentration of the k-th species, D_k is the diffusion coefficient, F_k^+ and F_k^- account for the production and loss of these particles, respectively.

In modeling the radial expansion of the hot gas channel, we used the set of one-dimensional (axisymmetric) time-dependent equations

$$\frac{\partial \rho}{\partial t}+\frac{1}{r}\frac{\partial \rho ur}{\partial r}=0, \quad \frac{\partial \rho u}{\partial t}+\frac{1}{r}\frac{\partial \rho u^2 r}{\partial r}+\frac{\partial P}{\partial r}=0,$$

$$\frac{\partial \rho E}{\partial t}+\frac{1}{r}\frac{\partial \rho ur(E+P)}{\partial r}=\frac{1}{r}\frac{\partial}{\partial r}(r\lambda\frac{\partial T}{\partial r})+W_T, \quad (2)$$

where ρ, u, P are the mass density, velocity, and pressure of the gas; $E = \varepsilon + u^2/2$, and ε is the internal energy in unit volume of the gas. The heat conductivity coefficient for air λ was taken from [9]. The set of Eqs. (2) was solved numerically on a mesh uniform on r (by using a modified McCormack method of second order of accuracy), simultaneously with equations of chemical kinetics (1).

5. Discussion

To verify the kinetic block of the model, we performed calculations of the temperature T dependence of the equilibrium concentration of nitrogen oxides in air at atmospheric pressure (Fig. 3). The results of comparison with data [6] show that the elaborated kinetic model adequately describes the equilibrium concentrations in hot air [6] in the temperature range $T = 2500$–7000 K.

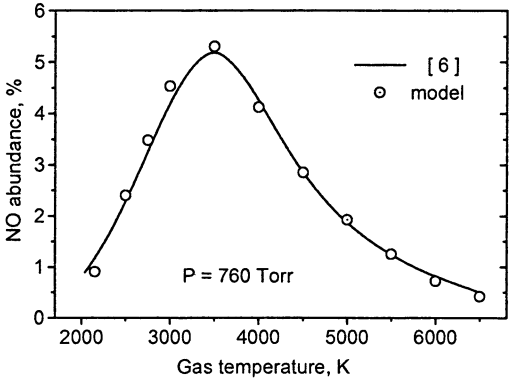

Fig. 3. NO thermoequilibrium content in air at 1 atm vs. gas temperature. Curve – [6], points – our computation.

Simulation of the NO_x production in the microwave torch discharge was performed at a given discharge power per unit length (400 W/cm), known from the experiment. In calculations, the microwave absorption in the plasma was varied from 70 to 100%. It was assumed that all absorbed power is converted into the gas heat.

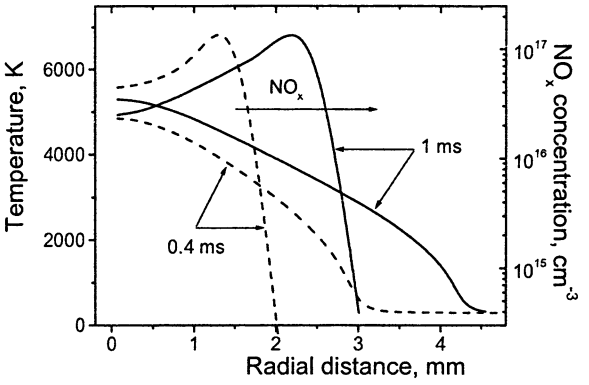

Fig. 4. Radial profiles of gas temperature and NO_x concentration in air at $P = 1$ atm in different time moments: $t = 0.4$ ms (dotted), $t = 1$ ms (solid), $R_0 = 1$ mm.

Figure 4 shows the calculated radial profiles of T and of NO_x in air at atmospheric pressure at times $\tau = 0.4$ and 1 ms, assuming $R_0 = 1$ mm. An interesting result is a nonmonotonic radial profile of NO_x with a maximum at the periphery, that is a consequence of the nonmonotonic dependence of the equilibrium NO_x concentration on T (Fig. 3). The lower the temperature, the longer the time it takes for NO_x to attain equilibrium values. For this reason, the radial profile in this region is steep, and NO_x concentrations are lower than their equilibrium values.

The calculated value of the energy cost of the nitrogen oxide production is estimated as $\varepsilon = 75 \pm 5$ eV/molec(NO_x) agree with the experimental data on ε and its dependence on the discharge action time.

6. Conclusions

The analysis of experimental and theoretical results leads us to the following conclusion. The decisive factor in the process of NO_x production is air heating to temperatures 3500–4000 K with the subsequent quenching of reaction products. The energy cost of the NO_x production achieved in this system is much lower than its values obtained experimentally for nonequilibrium-plasma of microwave discharges operating with relatively cold ($T \leq 800$ K) air (see [10]).

According to [11], high energy efficiency of the nitrogen oxide production (ε = 3–10 eV/molec(NO_x)) is best achieved by employing microwave discharges. However, such record levels may only be achieved when discharge parameters are varied within a relatively narrow range, at pressures of several ten Torr. Our reactor developed on the basis of a microwave torch discharge, even though it ranks below these systems in efficiency, is superior to them in performance because operates at atmospheric pressure.

This work was supported in part by the Netherlands Organization for Scientific Research, project NOW 047.016.019.

References

1. *Moisan M., Sauve G. et al.*, Plasma Sources Sci. Technol., 1994, **3**, 584.
2. *Jonkers J., Hartgers A. et al.*, Plasma Sources Sci. Technol., 1999, **8**, 49.
3. *Gritsinin S.I., Knyazev V.Yu. et al.*, Plasma Phys. Rep., 2004, **30,** 255.
4. *Barkhudarov E.M., Gritsinin S.I. et al* , Plasma Phys. Rep., 2004, **30,** 531.
5. *Breshears W.D., Bird P.F.*, J. Chem. Phys., 1968, **48**, 4768.
6. *Predvoditelev A.S., Stupochenko E.V. et al.*, Air thermodynamic functions tables, Moscow, Comp. Center AS USSR, 1962.
7. *Krivonosova O.E., Losev S.A. et al.*, Reviews of Plasma Chemistry, **1**, ed. B.M. Smirnov. New York· Consultants Bureau, 1991. P. 1.
8. *Baulch D.L., Cobos C.J., Cox R.A. et al.*, J. Phys. Chem. Ref. Data, 1994, **23**, 847.
9. Physics and Engineering of low temperature plasmas. Ed. S.V. Dresvin. Moscow, Atomizdat, 1972 (in Russian).
10. *Askaryan G.A., Batanov G.M. et al.*, Trudy IOFAN, Physics and Chemistry of Gas Discharge, Excited by Microwave Beam, Moscow, Nauka, 1994, **47**, p. 9 (in Russian).
11. *Rusanov V.D., Fridman A.A.*, Physics of Chemical Active Plasmas, Moscow: Nauka, 1984 (in Russian).

MICROWAVE DISCHARGE IN THE PRESENCE OF PLASMA RESONANCES AND STOCHASTIC HEATING

N. A. Azarenkov, Vi. V. Gushchin, V. V. Gushchin

V.N. Karazin Kharkov national university, Ukraine, Kharkov

In present report the nonlocal approach for discharges sustained by surface wave (SWDs) at the low pressures is generalized. The self-consistent set of equations for the kinetic description of nonlocal inhomogeneous plasma is received. It consist from the averaging kinetic equation (KE) for electron energy distribution function (EEDF), nonlocal Maxwell equations for the high frequency (HF) field of the surface wave (SW) and hydrodynamic ion equations. The possibility of meaningful increase of the collisionless SW energy absorption is showed.

The gas discharges sustained by surface waves, are investigated intensively in relation to an opportunity of the appendix in various technological and plasmochemical problems [1]. The basic problem of the theory of plasma sources is based on a finding of coupling between external and internal discharge parameters. The discharge geometry, gas pressure and a kind, frequency of the external HF fields, its intensity and current (etc) can be related to external (set) parameters. The internal discharge parameters are the electron energy distribution function (EEDF), distributions of plasma density, distributions of the quasystationary and HF fields, distributions of frequencies of excitation, ionization and others. Knowledge of the electron energy distribution function (EEDF) is a basic requirement for the modeling of low temperature plasmas. The modeling has been based on local and nonlocal approaches [2], i. e. without and with according for radial plasma nonuniformity and for the stationary field of spatial charge. In this situation, is, the so-called nonlocal approach [2, 3] the most perspective. The essence of this method is based on that the kinetic equation is averaged on the cross-section which is available for particles with energy ε. As a result of such procedure the differential equation in partial derivatives passes in the ordinary differential equation.

The nonlocal approach was successfully used to describe the capacitive (the electric field is directed normally to border) [4] and inductive discharges (the electric field, lays in a plane of border) [5]. The nonlocal approaches have been generalized on region of low pressure in the work [6] where the effects of collisionless heating such as anomalous skin-effect [7] become essential. The kinetic description of electron components in the discharges on surface waves taking into account of nonlocal and nonequilibrium effects was offered in work [8]. It has been made for enough big pressure when the basic mechanism of heating was Ohmic heating. These approaches have generalized in the work [9] by the account of collisionless damping in a vicinity of a plasma resonance point that has led to appearance additional, quasylinear diffusions. It is necessary to note, that these approaches were not completely self-consistent since they assumed to use the dielectric permittivity of cold plasma with preset values of frequencies

of collisions and ionization. A modern trend in plasma technology aims at decreasing the gas pressures down to millitorr range. For these low pressures it is easier to maintain uniform plasmas with well controlled parameters. Due to the large value of the mean free path the main mechanism of electron heating turns out to be collisionless one rather than conventional Joule heating dominant for higher pressures. Collisionless electron heating is the dominant heating mechanism in low pressure plasma [6, 7, 10]. It can be describe quantitavely in terms of the surface impedance for uniform plasma [11, 12] and the energy diffusion coefficient for nonuniform case [6].

For accurate calculation of the discharge characteristics at the low pressures the EEDF needs to be computed self-consistently. Self-consistency is an important and difficult issue for the kinetic simulation of plasma. The EEDF, nonlocal conductivity and plasma density profile are all nonlinear and nonlocally coupled. The basic purpose of the present work is obtaining of completely self-consistent set of the equations describing the discharge, sustained by surface wave (SW). Let's consider the plasma sustained by HF field of a surface E-wave with components E_x, H_y, E_z, in a planar dielectric waveguide thickness d (the wave with components E_r, H_φ, E_z in cylinder is analogous to E-wave). It propagates in a z direction, along borders $x = 0; d$. We assume that for the description of electrons it is necessary kinetic description, and ions can be described with the help of the hydrodynamical equations. The set of the discharge equations is self-consistent and will consist of kinetic equation (KE) to define the electron energy distribution function (EEDF), set of Maxwell equations for HF fields of the SW and LF equations for a stationary field of a spatial charge, ion density and speeds. Two-partial decomposition applied to Boltzmann equation [2, 3] is used for simplification of the KE the method. Taking into account of anomalous skin-effect the KE becomes simpler a method of integration on trajectories [6]. Further, similarly to [6, 7, 8], it is possible to obtain the electron KE in the discharge sustained by a surface E-wave:

$$\frac{d}{d\varepsilon}(\bar{D}_\varepsilon \frac{df_0^0}{d\varepsilon} + \bar{V}_\varepsilon f_0^0) = \bar{S}_0; \qquad D_\varepsilon = D_z + D_x + D_{ql},$$

where such designations are entered: $\varepsilon = w + e\phi_s$ is full electron energy; w is the electron kinetic energy; u is the speed; ϕ_s is the potential of a spatial charge field; $f_0^0(\varepsilon)$ – isotropic part of EEDF dependent only from full energy. The expression for the quasylinear diffusion coefficient for plasma sustained by SW was received in [13]:

$$D_{ql} = \frac{\pi e}{2m_e}\frac{w^{3/2}}{\omega}\left|E_x(x)\right|^2 d(\xi), \quad d(\xi) \approx \frac{\xi}{2}\exp(-\xi), \quad \xi = \frac{2\nu_{eff}L}{u}$$

where $\nu_{eff} = \max\{\nu_{en}; \omega(\frac{u_T}{\omega L})^{2/3}\}$; $L = \left|\frac{\partial \ln n}{\partial x}\right|^{-1}_{x=x^*}$ is the density length at the

resonant point. Using of this coefficient is unique nonself-consistent place in our equations.

$\bar{D}_\varepsilon$ and $\bar{V}_\varepsilon$ – diffusion coefficient and drift speed in power space respectively; they are defined as follows:

$$D_z = -\frac{em_e^{3/2}}{\sqrt{2}}\{\int_0^\varepsilon (\varepsilon-\varepsilon_x)d\varepsilon_x \int_0^{2\pi} d\varphi\cos^2\varphi \int_{x_-}^{x_+} dxE_z^*(x)V_z^{HF}\},$$

$$D_x = -\frac{em_e^{3/2}}{\sqrt{2}}\{\int_0^\varepsilon \varepsilon\varepsilon_x d\varepsilon_x \int_0^{2\pi} d\varphi\cos^2\varphi \int_{x_-}^{x_+} dxE_x^*(x)V_x^{HF}\}$$

(for convenience we went in spherical system of coordinates in space of speeds), φ is azimuthal angle in space of speeds; speed of electron oscillations along a trajectory with energy ε_x. Because of bulkiness their obvious kind here is not resulted. For the surface wave sustaining plasma at the low pressure, set of Maxwell equations, is reduced to the standard equations [9]. The current j_z is defined from the nonlocal Ohm law. Because of bulkiness it obvious kind here is not resulted. The third block of the discharge equations – low frequency (LF) – are the standard hydrodynamic equations for ions with next inelastic terms [15]:

$$R_{ion}^\alpha = n^\alpha \nu_{inel}^\alpha = N_a\sqrt{\frac{2e}{m_e}}\int_{-e\phi_s}^{\infty} \sigma_{ion}^\alpha(u)f_0(u)\{\varepsilon-e\phi_s\}d\varepsilon,$$

where α can mean the most probable inelastic processes (i – direct ionization, sw – step-wise ionization, etc.) in discharge plasma at low pressure.

If the quasyneutrality condition ($n_i = n_e$) occur then the equation for ϕ_s is next:

$$\frac{\partial\phi_s}{\partial x} = T_{scr}^e \frac{\partial \ln n_i}{\partial x},$$

where the "screening" temperature looks like:

$$T_{scr}^e = \{\frac{e}{2n_e}\int_{-e\phi_s}^{\infty} \frac{f_0(\varepsilon)d\varepsilon}{\sqrt{\varepsilon-e\phi_s}}\}^{-1}.$$

If the quasyneutrality condition isn't always executed we can use condition

$$n_e(x) = n_i(x)\{1-\frac{\zeta(x)}{\pi}\},$$

which was suggested in [14] for CCP discharge. Here ζ is the phase where electron interacts with a transitive layer. According to our assumption that SWD there is "superposition" of ICP and CCP, the transitive area at border of plasma can be considered as "superposition" of a skin-layer and sheath. The resonant electrons of plasmas effectively interact with a HF field in this region. But by virtue of that the field in this region varies in time and in space, the phase ζ has random character, as provides stochastic character of heating. If $\zeta \to 0$, plasma

can be counted quasyneutral, and if $\zeta \to 2\pi$ quasyneutrality the condition of is broken. It is possible to define a phase from the equation of electron movement in transitive range $l(t)$, by analogy with [14]:

$$-en_e(l)\frac{\partial l}{\partial t} = -j_1(t,\zeta),$$

where j_1 – the HF current on border of the transitive range, caused by presence of a HF field. Thus, the full set of the equations of the LF block for the discharge sustained by field of SW is reduced to following:

$$\frac{\partial \phi_s}{\partial x} = T_{scr}^e \{\frac{\partial \ln n_i}{\partial x} - \frac{1}{\pi - \zeta}\frac{\partial \zeta}{\partial x}\}.$$

The set of the obtained discharge equations is the most general self-consistent set of the equations for the discharges sustained by SW. Let's show it. In the beginning we shall consider block KE. First, if the condition $\nu_{en} > \Omega_b$ is valid (where Ω_b – is the frequency of bounce-oscillations) the relation of the electron oscillation speeds V_x^{HF} and V_z^{HF} with fields E_x and E_z respectively, becomes local. Expressions for the power diffusion coefficients derive in formulas (26)–(27) work [9] for Ohmic plasma heating (collision diffusion). Second, if $k_z \to 0$ and $E_x \to 0$, that $V_x^{HF} = 0$, and V_z^{HF} passes in the formula (6) of the work [6], and the diffusion coefficient behaves similarly to the formula (52) of the same work. Thirdly, if $k_z \to 0$ and $E_z \to 0$ then V_z^{HF} addresses in zero. Thus it is obtained from expressions for the diffusion coefficient in CCP.

Now we look at the HF block. At first, under conditions of $k_z \to 0$ and $E_x \to 0$ in expression for a current j_z address in zero V_x^{HF}. Then the HF equations for ICP [6] are obtained. Transition to results CCP ($E_x = \text{const}$) [16] takes place under conditions $k_z \to 0$ and $E_z \to 0$. And under condition of $\nu_{en} > \Omega_b$ the relation between a current j_z and E_x also E_z becomes local. And the HF field equations pass in the results SWD [9].

It is obviously, that the set obtained equation can be solved generally only numerically. But it is beyond the submitted report. However, at all not solving system of the equations it is possible to approve, that all discharge parameters and their distributions will change.

In the nonuniform plasma at first compare the diffusion coefficients with results [9] for energy diffusion coefficient [9]. Introduce next function:

$$\Theta_1 = \frac{D_x^{stoc}}{D_x^{Ohm}} \sim (\frac{\omega}{\nu_{en}})^2 (\frac{\omega - \Omega_b}{\nu_{en}})^{-2} > 1,$$

where $\Omega_b(\varepsilon_x) = \pi\{\int_{x_-}^{x_+} \frac{dx}{|u_x(\varepsilon_x)|}\}^{-1}$ is the bounce frequency.

Secondly we compare values of diffusion coefficients with quasylinear diffusion coefficient which arising in the vicinity of plasma resonant point. Investigate the next function:

$$\Theta_2 = \frac{D_x^{stoc}}{D_x^{ql}} \sim \frac{1}{d(\xi)} \frac{\omega}{\nu_{en}} [1 + \frac{(\omega - \Omega_b)^2}{\nu_{en}^2}]^{-1} > 1.$$

We determine role of spatial inhomogeneity at the wave dissipation – for this case we compare absorbed power in uniform and nonuniform plasmas. This relation is determined by next function:

$$\Theta_3 = \frac{P_{abs}^{un}}{P_{abs}^{nonun}} = \frac{\beta \mathrm{Re} Z_{pl}}{4\pi \int_0^\infty d\varepsilon \sqrt{\varepsilon} D_\varepsilon^{stoc} \frac{\partial f_o}{\partial \varepsilon}} \sim \frac{\delta_n}{d} (\frac{\omega}{\omega_{pl}})^2 (\frac{e|E|}{m\omega u_T})^2 >> 1.$$

References

1. *Moisan M., Hubert J.*, Advanced Technologies Based on Wave and Beam, NATO ASI, Series B: Physics, Sozopol, 1998.
2. *Kortshagen U., Bush C., Tsendin L.D.*, Plasma Sources Sci. Technol., 1996, 5, 126.
3. *Kolobov V.I., Godyak V.A.*, IEEE Tram. Plasma Sci., 1995, 23, 503.
4. *Berezhnoi S.V., Kaganovich I.D., Tsendin L.D.*, Plasma Phys. Rep., 1998, 24, 556.
5. *Kolobov V.I., Hitchon W.N.G.*, Phys. Rev. E, 1995, 52, 972.
6. *Kaganovich I.D., Polomarov O.V.*, Phys. Rev. E, 2003, 68, 026411.
7. *Kolobov V.I., Economou D.J.*, Plasma Sources Sci. Technol., 1997, 6, Rl.
8. *Kortshagen U., Schluter H., Shivarova A.P.*, J. Phys. D.: Appl. Phys., 1991, 24, 1571.
9. *Aliev Y.M., Maximov A.V., Kortshagen U., Schluter H., Shivarova A.*, Phys. Rev. E, 1995, 51, 6091.
10. *Lieberman M.A., Godyak V.A.*, IEEE Tram. Plasma Sci., 1998, 26, 955.
11. *Kondratenko A.N.*, RF Field Penetration into plasma, Moscow: Atomizdat, 1979 (in Russian).
12. *Shaing K.C., Aydemir A.Y.*, Phys. Plasmas, 1997, 4 (3), 163.
13. *Aliev Y.M., Bychenkov V.Y., Maximov A.V., Schluter H.*, Plasma Sources Sci. Technol., 1992, 1, 126.
14. *Lieberman M.A.*, IEEE Trans Plasma Sci., 1988, 16, 638.
15. *Kaganovich I.D., Ramamutri B., Economou D.J.*, Plasma Sources Sci. Technol., 2003, 12, 170..
16. *Aliev Y.M., Kaganovich I.D., Schluter H.*, Phys. Plasmas, 1997, 4, 2413.

CREATION OF SUPER DENSE PLASMA DUE TO CONTRACTING OF MICROWAVE DISCHARGE ON SURFACE OF DIELECTRIC

V. A. Ivanov, M. E. Konyzhev, V. P. Gavrilenko, E. Oks[1], *A. A. Letunov*

A. M. Prokhorov General Physics Institute of Russian Academy of Sciences, Moscow, Russia
[1]Auburn University, Auburn, Alabama, USA

The emission spectra from a contracted microwave discharge on the surface of dielectrics exited by microwave radiation (2 MW power, 3μs pulse duration) have been investigated. It has been found experimentally that the FWHM of H_α spectral line (originally centered at wavelength 656.3 nm) of atomic hydrogen can be as large as 7 nm. The main line broadening mechanism is the Stark effect in electric microfields produced by ions and electrons in dense plasma of a contracted microwave discharge. Based on the experimental data of the H_α line profiles and on the results of corresponding theoretical calculations, the maximum electron plasma density in a contracted microwave discharge was determined to be about 2×10^{18} cm^{-3}.

Introduction

The interaction of microwave radiation with dielectrics is accompanied by the following phenomena: 1) generation of plasma on the surface of dielectrics, 2) significant microwave energy absorption in the plasma, 3) rapid release of plasma energy in dielectrics, 4) onset of strong local destructions in dielectrics [1, 2]. The aim of the present study is to measure an electron density and to estimate an electron temperature in dense plasma of a contracted microwave discharge on dielectrics.

Experimental conditions and diagnostic equipment

All experiments were carried out in the BRUS device (Fig. 1) operating under high vacuum (pressure 0.1 mPa). Pulsed microwave radiation produced by a magnetron (2 GHz, H_{10} mode, power $\leq$ 2 MW, pulse duration of 3 μs) was transmitted through a waveguide system and was injected into an evacuated waveguide through a window transparent to microwaves. The evacuated waveguide of rectangular section 12×5.8 cm was short-circuited at its end by a flat metal flange. The incident microwave and the microwave reflected from the flange formed a standing wave. A dielectric sample was placed at the antinode, where the microwave electric field was maximum, at a distance of $0.75\lambda = 15$ cm ($\lambda = 20$ cm is the wavelength in the waveguide) from the end metal flange.

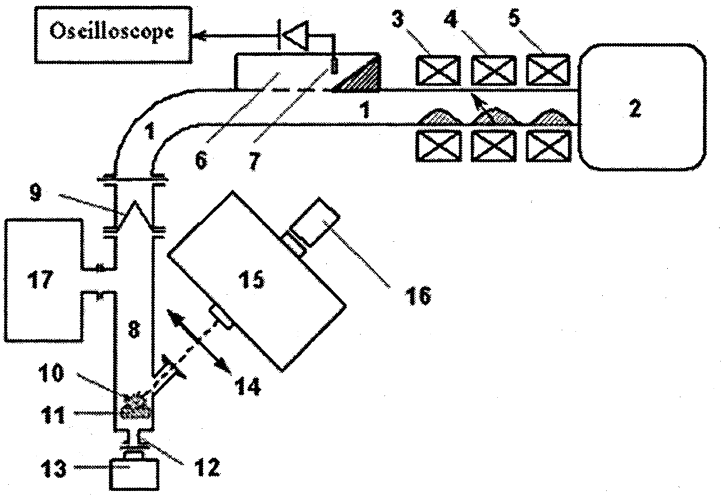

Fig. 1. Schematic of the BRUS experimental device: *1* – waveguide, *2* – magnetron, *3*, *5* – magnetoferrite decoupling valves, *4* – magnetoferrite absorbing attenuator, *6* – directional coupler, *7* – microwave antenna, *8* – evacuated waveguide, *9* – microwave-transparent vacuum window, *10* – plasma, *11* – dielectric sample, *12* – cylindrical beyond-cutoff waveguide, *13* – photographic camera, *14* – focusing optical lens, *15* – MDR-2 monochromator, *16* – FEU-79 photomultiplier, and *17* – high-vacuum pump.

The envelope of the reflected microwave pulse was monitored with a help of a semiconductor diode detector and a microwave antenna which was installed in a directional coupler. The plasma floating potential near the dielectric surface was measured by a Langmuir probe made of a thin graphite rod. In our experiments, attention was focused on spectral measurements of the emission from the plasma in different stages of a microwave discharge. In order to achieve high spectral resolution, the radiation emitted from a contracted microwave discharge excited at the surface of dielectric samples was collected by a 12-cm-diameter lens and was focused onto the 0.1-mm-wide entrance slit of an MDR-2 monochromator. The width of the instrumental function of the monochromator was about 0.4 nm. In the experiments it was possible to achieve a spatial resolution of about 0.1 mm and a spectral resolution of 0.4 nm. The spectrum was measured by a FEU-79 photomultiplier. All signals (incident and reflected microwave power, plasma potential and plasma radiation) were recorded by a Tektronix TDS-3014 four-channel digital oscilloscope with a time resolution of 10 ns.

The method based on Stark broadening of the atomic hydrogen lines was used to measure the electron density in microwave discharge plasma. In particular, the broadening of H_α 656.3-nm line in the plasma emission spectrum is due

to the interaction of hydrogen atoms with microfields produced by electrons and ions in plasma. Under optimal conditions, the spectral measurement of the Stark broadening of the H_α line is a reliable tool for determining the plasma density [3]. To realize such conditions, it was necessary to solve the following two problems: 1) to ensure the spatial stability of the contracted microwave discharges and 2) to provide a sufficient amount of hydrogen atoms in the microwave discharge plasma in order to ensure stable detection of the broadened H_α spectral line. These two problems were resolved by using specially prepared dielectric samples. At the surface of such sample made of quartz glass 100×10×1 mm in size, we made a narrow strip of organic glass dissolved in acetone. When acetone evaporated, a narrow (1 mm wide and 30 mm long) strip of organic glass was produced on the sample surface. Organic glass (polymethylmethacrylate) is applied because it contains a large quantity of atomic hydrogen: chemically, it is composed of 54% atomic hydrogen, 33% atomic carbon, and 13% atomic oxygen. In this way both problems were successfully resolved: contracted microwave discharges were located at such a strip which, in turn, ejected a sufficient amount of atomic hydrogen into the microwave discharge plasma.

Types of microwave discharges excited at dielectric surfaces

There are three types of electrodeless discharges that can be excited by a high-power pulsed microwaves at the surfaces of dielectrics in vacuum [1, 2]: nonresonant secondary-electron-emission microwave discharge (SEEMD), surface microwave breakdown (SMB) of dielectrics, and plasma-flare microwave discharge (PFMD) at dielectric surfaces. Photographs of these types of microwave discharges are shown Figs. 2*a*, 2*b*, 2*c*.

SEEMD is excited at a dielectric surface in vacuum (Fig. 2*a*) when the electron oscillatory energy ε in the electric field E_0 of a standing microwave is higher than the characteristic energy of the dielectric W_1 – first cross over point of the secondary emission curve at which the secondary electron emission coefficient is equal to unity: $\varepsilon = e^2E_0^2/2m\omega^2 > W_1$ [2, 4], where e and m are the charge and mass of an electron and ω is the angular frequency of the microwave field. For most dielectrics, the energy W_1 is in the range 10–100 eV. When an incident pulsed microwave radiation with a power of P = 0.6–2 MW excites a standing H_{10} wave in the rectangular waveguide, the mean electron energy in an SEEMD varies within a range of 200–600 eV. The electron density n_e in such discharge is much lower then the cutoff (critical) density $n_c = m\omega^2/4\pi e^2 = 4\times10^{10}$ cm^{-3} for the incident microwaves, $n_e < 0.25n_c$, the microwave absorption coefficient being ~0.01.

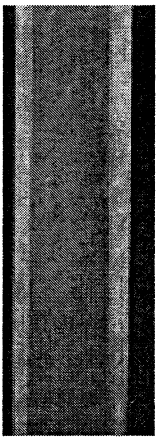

Fig. 2*a*. Photograph of light emission of potassium bromide (KBr) single crystal excited by the electrons of SEEMD (1000-fold amplification of light).

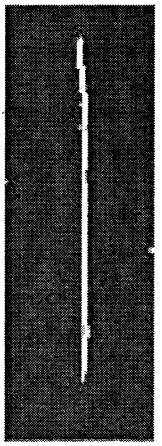

Fig. 2*b*. Photograph of light emission of contracted microwave discharge on the surface of organic glass (without amplification).

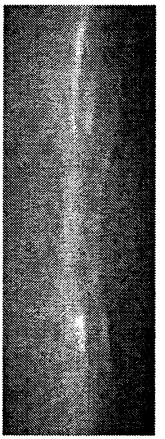

Fig. 2*c*. Photograph of light emission of plasma-flare microwave discharge at the surface of Teflon sample (5-fold amplification of light).

SMB [1, 2, 5] occurs due to a strong excitation of the dielectric surface layer by the electrons of SEEMD stage of a microwave discharge, the fraction of the incident microwave power that is absorbed by the discharge plasma increases very rapidly on time scale of ~50 ns: from 1% of absorbed microwave power (in the SEEMD stage) to 50–100% of absorbed microwave power (in the stage of microwave breakdown). In the stage of microwave breakdown the incident microwave power is absorbed by dense plasma of contracted discharge (Fig. 2*b*). The microwave breakdown stage lasts 0.2–0.05 μs. The higher the incident power the shorter the breakdown stage.

PFMD [1, 2] develops after the microwave breakdown of a dielectric as a result of the expansion of dense plasma of a contracted microwave discharge at the dielectric surface (Fig. 2*c*). During 1 μs after the microwave breakdown, the maximum expansion velocity of the plasma with a critical density is ~10^6 cm/s. During the next 2–3 μs the expansion velocity decreases to about 10^6–10^5 cm/s. The expanding plasma evolves into a large dense cloud. The size of the plasma cloud at the level of cutoff density is about 3–5 cm. Measurements with a 8-mm interferometer show that the electron plasma density in the PFMD stage increases inward from the periphery of the plasma cloud. The electron plasma density near the dielectric surface exceeds the value 2×10^{13} cm^{-3}, which is three orders of magnitude higher than the cutoff density $n_c \approx 4\times10^{10}$ cm^{-3}. In the

PFMD stage, the incident microwave power is fairly strongly absorbed in the plasma resonance region: the fraction of the absorbed power amounts to about 20–50%.

Study of temporal evolution of microwave discharges

We studied such issues as the dynamics of the microwave absorption by the plasma in different stages of a microwave discharge (Fig. 3*a*), the time evolution of the plasma potential (Fig. 3*b*), and the time evolution of H_α emission from microwave discharge plasma (Fig. 3*c*, 3*d*). In the SEEMD stage (during 1 μs before the breakdown) only about 1% of incident microwave power is absorbed by electrons of SEEMD. The largest portion of the incident microwave power (about 60%) is absorbed during a time interval of 1–1.2 μs in the microwave breakdown stage in a form of contracted microwave discharge. During a time interval of 1.2–3 μs in the PFMD stage, the plasma absorbs about 30% of the incident power. The incident microwave power in these particular experiments was 620 kW.

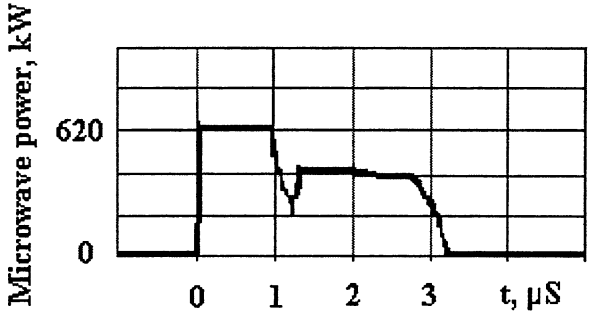

Fig. 3*a*. Oscillogram of the envelope of pulsed microwave power reflected from the discharge plasma.

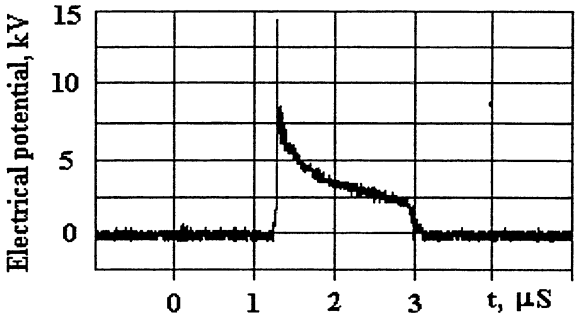

Fig. 3*b*. Oscillogram of plasma potential near the surface of a dielectric sample. The parameters of microwaves are the same as in Fig. 3*a*.

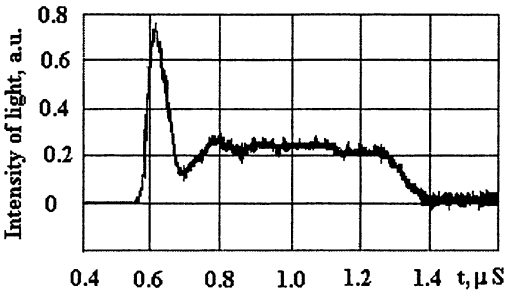

Fig. 3*c*. Oscillogram of light emission of microwave discharge plasma at the wavelength of 656.3 nm (i. e. originally wavelength of the H_α spectral line of atomic hydrogen). Microwave power is 2 MW, pulse duration is 1.3 μs.

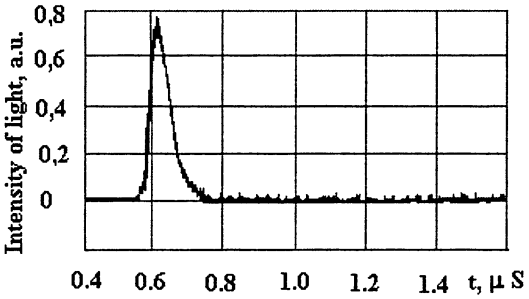

Fig. 3*d*. Oscillogram of light emission of microwave discharge plasma at the wavelength of 656.8 nm (the shift from the central H_α line is 0.5 nm). The parameters of the microwaves are the same as in Fig. 3*c*.

In the contracted discharge stage, the plasma potential is low and amounts to only several tens of volts. During the evolution from the contracted discharge stage to the plasma flare stage the plasma acquires a high positive potential of about 15 kV (Fig. 3*b*). The high plasma potential is the consequence of the acceleration of electrons in the strong electric field in the plasma resonance region and their escape from the plasma [6]. Such behavior of the plasma floating potential shows that the electric field in the plasma resonance region becomes amplified in the PFMD stage rather than in the breakdown stage. This result can be explained as follows: in the contracted microwave discharge stage, the transverse plasma dimensions are so small and the gradients of the electron density in the resonance region are so steep that intense Langmuir waves cannot be excited there [6]. In contrast, in the plasma flare stage, the gradients of the electron plasma density become gentler because of the plasma expansion, with the result that the resonance conditions can be satisfied for Langmuir waves excitation in the plasma resonance region. Nonlinear processes that come to play are responsible for the self-breaking of Langmuir waves and for the electron acceleration to a maximum energy of about 15 kV [7, 8]. The maximum energy of the fast electrons, which corresponds to the positive plasma potential of +15 kV, is observed during the transition from the contracted discharge stage to the plasma-flare stage. In SEEMD stage, the light emission from dielectrics is the lumines-

cence of short-lived color centers induced in dielectrics due to bombardment by electrons of SEEMD [9]. During the production of dense plasma in contracted discharge bright emission from hydrogen atoms was observed at the central wavelength of the H_α line and also over a broad wavelength range around the central wavelength. From the oscillograms presented in Fig. 3*c*, 3*d* it is seen that the H_α line is wide enough in the contracted microwave discharge stage and is narrow in the PFMD stage. The profile of the H_α spectral line measured during the contracted microwave discharge is displayed in Fig. 4. In this stage, the FWHM of the H_α line profile is about 7 nm for an incident microwave power of 2 MW and decreases with decreasing incident power (2.5 nm for 620 kW). As for the PFMD stage, the FWHM of H_α profile is less than 1 nm.

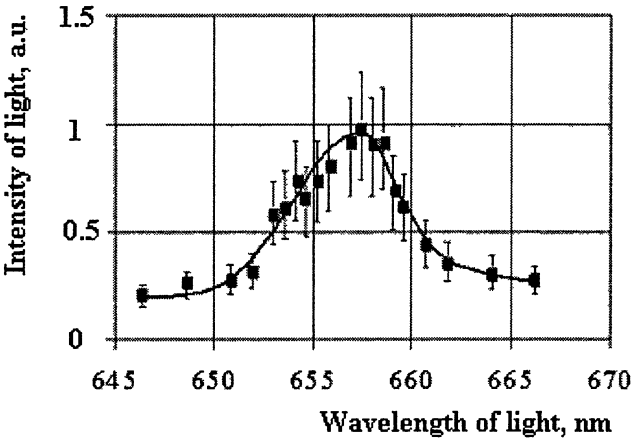

Fig. 4. Profile of the H_α spectral line of atomic hydrogen in the stage of contracted microwave discharge. Microwave power is 2 MW.

Discussion of the experimental results

The main mechanism responsible for the broadening of the H_α line in the discharge is related to collisions of hydrogen atoms with the electrons and ions of the discharge plasma. This mechanism is the Stark effect in the electric fields that are produced by the plasma ions and electrons and act upon hydrogen atoms in their collisions with the charged plasma particles [3]. Based on the experimental data, we calculated the electron density in the contracted microwave discharge. It was found that in contracted microwave discharge the electron density can reach the value $2\times10^{18}cm^{-3}$ at an incident power of 2 MW, and the electron density can reach the value $6\times10^{17}cm^{-3}$ at an incident power of 620 kW [3]. This leads to the following conclusion: the electron plasma density in the contracted microwave discharge stage is approximately proportional to the incident

microwave power. At the same time, the fraction of the incident power that is absorbed by the plasma is approximately the same (~60%) for incident powers 620 kW and 2 MW. This fact implies that the microwave absorption by the discharge plasma depends weakly on the level of incident power. Therefore we can conclude that the plasma electric conduction in a contracted microwave discharge is independent of the electron plasma density. Consequently, the plasma electric conduction in the contracted microwave discharge stage is governed by Coulomb collisions between the plasma electrons and ions and depends only on the electron temperature. On this basis, the electron plasma temperature can be estimated to be about $T_e = 4–10$ eV. The estimates for the electron temperature were obtained by calculating the diameter of the dense plasma (10–20 μm) during microwave breakdown.

On the basis of Stark measurements for the PFMD stage and corresponding theoretical calculations the electron density in plasma may be estimated as not more than 5×10^{16} cm^{-3}. On the other hand, the measurements carried out with a microwave interferometer at the wavelength of 8 mm showed that the electron density in the discharge plasma in the PFMD stage is higher than 2×10^{13} cm^{-3}.

Conclusion

We have experimentally determined the electron plasma density in the stages of contracted microwave discharge and in the plasma-flare discharge. In the plasma of contracted microwave discharge the electron density was varied from 6×10^{17} to 2×10^{18} cm^{-3} when the power of the incident microwave radiation was varied from 0.6 to 2 MW. Under the same irradiation conditions, the electron plasma density in the stage of a plasma-flare microwave discharge lies in the range 2×10^{13}–5×10^{16} cm^{-3}. Therefore, in the stage of surface microwave breakdown of dielectrics in the form of contracted discharge, and in the stage of plasma-flare microwave discharge the electron density of plasma is much higher than the critical plasma density 4×10^{10} cm^{-3}.

Acknowledgments. We are grateful to A.S. Gerasimov, A.A. Dorofeyuk (Mrs.), E.F. Bol'shakov, T.I. Kamolova (Mrs.), S.N. Satunin, and A.M. Spirin – the scientists of the A.M. Prokhorov Institute of General Physics of the Russian Academy of Sciences – for their help in preparing the diagnostic equipment and for technical assistance in experiments.

This work was supported in part by the Russian Foundation for Basic Research (project No. 06-02-17471-a) and the U.S. Civilian Research and Development Foundation (grant No. RU-P1-2594-MO-04).

References

1. *Ivanov V.A., Konyzhev M.E.* Breakdowns and destructions of dielectrics in strong microwave fields // Strong Microwaves in plasmas / Ed. A. Litvak. Nizhny Novgorod, 2003. V. 2. P. 684-692.
2. *Ivanov V.A., Konyzhev M.E.* Destructions produced in dielectrics by pulsed microwave discharges // Microwave Discharges: Fundamentals and Applications: Proc. 5th Int. Workshop / Ed. A. Ohl. INP, Keibu-Druck GmbH. Greisfwald, 2003. P. 247-254.
3. *Flih S.A., Oks E., Vitel Y.* Comparison of the Stark width and shifts of the H-alpha line measured in a flash tube plasma with theoretical results // J. Phys. B: At. Mol. Opt. Phys. 2003. V. 36. P. 1-14.
4. *Grishin L.V., Dorofeyuk A.A., Kossyi I.A.* Investigation of secondary-electron-emission discharge at large transit angles of the electrons // Dissipation of electromagnetic waves in plasma. Moscow: Nauka, 1977. P. 82–131.
5. *Batanov G.M., Ivanov V.A., Konyzhev M.E.* Microwave breakdown of ionic crystals initiated by a secondary-electron-emission discharge // JETP Lett. 1994. V. 59, No. 10. P. 690-694.
6. *Batanov G.M., Ivanov V.A., Kossyi I.A.* Strong Langmuir Turbulence and Particle Acceleration in the Plasma Corona // Nonlinear and Turbulent Processes in Physics. Gordon and Britch Harw. Acad. Publ, 1984. V. 1. P. 45-55.
7. *Ivanov V.A., Konyzhev M.E., Losa M.I., Ravaev A.A.* Generation of High Potentials and Fast Electron Diagnostic in Microwave Produced Plasma Flare // XX Int. Conf. Phenomena in Ionised Gases. V. 5. Pisa, Italy, 1991. P. 1091-1992.
8. *Batanov G.M., Ivanov V.A., Khomenko A.I., Konyzhev M.E., Ravaev A.A., Seleznev V.D.* Generation of High Potentials in the Plasma by the Interaction with Intense Microwave Radiation // Strong Microwave in Plasma / Ed. A. Litvak. Nizhny Novgorod: Inst. Appl. Phys., 1991. V. 2. P. 553-558.
9. *Batanov G.M., Ivanov V.A., Konyzhev M.E., Konyushkin V.A., Mirov S.B.* Microwave Discharge Method for Formation of Optically-Dense Submicron-Thickness Layers with High Concentrations of Color Centers on the Surfaces of Alkali-Halide Crystals // Proc. I. XXI Int. Conf. Phenomena in Ionised Gases. Rurh-University, Bochum, Germany, 1993. P. 37-38.

MULTIPACTOR DISCHARGE ON A DIELECTRIC IN THE X-BAND TE_{01} MODE CAVITY

O. A. Ivanov, M. A. Lobaev, A. L. Vikharev, V. A. Isaev, D. B. Radishev

Institute of Applied Physics, Nizhny Novgorod, Russia

This work presents the results of studying the multipactor discharge that occurs on a dielectric surface in an X-band TE_{01}-mode cavity. These experiments determined the threshold of the multipactor and the density of electrons in the discharge plasma. A numerical discharge model has been constructed based on solving the set of equations that describe electron motion in a high-frequency electromagnetic field.

Introduction

It is known that in the microwave fields in vacuum are a specific form of a discharge, the multipactor (secondary-emission) discharge, which develops on the surface of a dielectric. The mechanism of discharge development is associated with multiplication of electrons as they bombard a dielectric surface. Usually, two phases of discharge evolution on the dielectric surface are discerned. At the first stage the multipactor discharge proper occurs; at the second, gas is desorbed from the surface, and, consequently, the formed gas cloud is broken down by microwaves. The plasma that is formed near the surface changes the electrodynamic characteristics of microwave devices and may cause destruction of the dielectric surface. Studying the conditions for appearance of multipactor discharges and the methods of quenching them is especially important for development of vacuum windows used in high-power microwave generators, accelerating structures with dielectrics, and plasma switches of high-power microwave pulse compressors [1–3]. This work presents the results of studying the microwave discharge, which occurs on the quartz surface, experimentally under the conditions close to those in plasma switches [3].

Experimental setup and results of the experiment

Interaction of high-power electromagnetic radiation with a dielectric surface was studied in a specially designed setup. The scheme of the setup is shown in Fig. 1.

The setup is based on a resonator excited at the TE_{012} mode formed by a cylindrical waveguide 45 mm in diameter that is constrained by two diaphragms. The diameter of the input diaphragm is D_1 = 29 mm, and of the output one, D_2 = 27 mm. A quartz plate was filled at one of the electric field loops formed in the resonator by a standing wave. The measured Q-factor of the resonator was Q_0 = 960. This Q-factor provided high intensity of the electric field on the dielectric surface even when the level of the microwave generator power was low. The resonator was placed in the vacuum chamber evacuated down to the

pressure of $p = 5 \cdot 10^{-5}$ Torr. The distance between the diaphragms (length of the resonator) and the position of the dielectric plate in the resonator could be changed from the outside by means of special devices. The discharge was observed and measured optically through the window on the end of the vacuum chamber. The resonator was excited at the frequency of $f_0 = 9.4$ GHz. Microwave pulses with their power $P \leq 150$ kW and duration $\tau = 2$–6 μs were fed to the input of the resonator through the Mariet converter that formed the TE_{01} mode of a circular waveguide and a non-reflective vacuum window. In the course of the experiment we registered the incident power reflected from the microwave resonator, and the power that has passed through it. Tuning of the resonator to resonance made the signal reflected from the resonator weaker, and the transmitted signal, stronger. The value of the electric field on the surface of the dielectric was determined from the measured microwave power with the field structure in the resonator, Fig. 2, taken into account. The structure of the electric field in the resonator was calculated using the FDTD method [4].

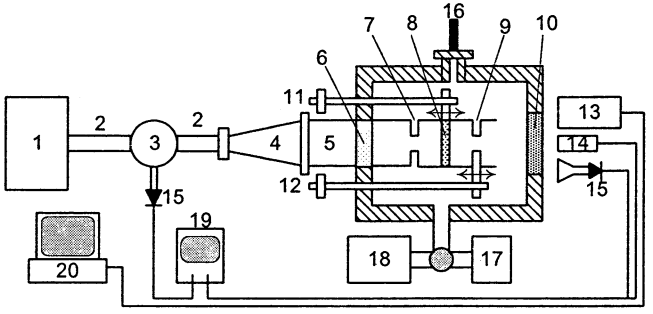

Fig. 1. Scheme of the experimental setup: *1* – magnetron, *2* – rectangular waveguide, *3* – circulator, *4* – mode converter, *5* – circular waveguide, *6* – microwave-transparent window, *7* – diaphragm, *8* – dielectric plate, *9* – movable diaphragm, *10* – dialectric window, *11* – window drive, *12* – diaphragm drive, *13* – spectrograph, *14* – photo multiplier, *15* – microwave detector, *16* – pressure controller, *17* – forevacuum pump, *18* – ion pump, *19* – oscilloscope, *20* – PC.

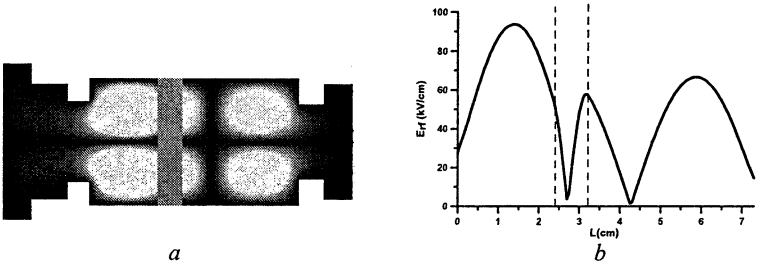

a *b*

Fig. 2. Distribution of the field in the resonator (*a*) and the dependence of the amplitude of the mean-square field on the longitudinal coordinate (*b*). Incident power $P_i = 100$ kW.

A multipactor discharge occurred when the threshold power was exceeded and was registered by observing variations in the shapes of the transmitted and reflected microwave signals. The threshold field was 21 kV/cm for a rough surface, and 27 kV/cm for a smooth one. The characteristic breakdown time of discharge was determined from the durations of the edges of the reflected and transmitted signals and was 40–80 ns. When the duration of the microwave pulse was short (≤ 1 μs) the glow of the discharge was shaped as a homogenous ring localized near the surface of the quartz plate. When the duration or power of the pulse increased against the background of homogenous glow, bright plasma formations appeared (usually, from one to three). The dimensions of those formations were 5–10 mm, and they were torn away from the dielectric surface. This associates with the fact that secondary electrons, when bombarding the surface, cause desorbtion of the surface and a breakdown of the gas cloud spreading from the surface into vacuum.

Appearance of the discharge detuned the resonator and caused a rise of a reflected signal. Typical oscillograms of the signals in the absence of the discharge and during the breakdown of the dielectric are shown in Fig. 3.

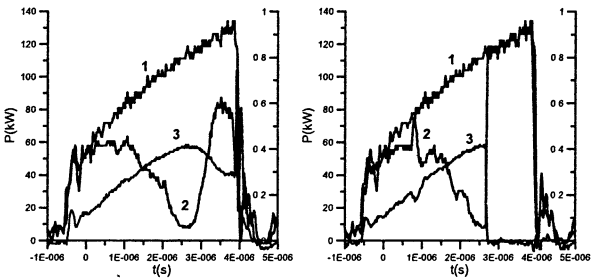

a) without discharge *b*) with discharge

Fig. 3. Oscillogramms of the incident (*1*) reflected (*2*) and transmitted (*3*) microwave pulses.

By observing the variations of the eigenfrequency of the resonator one can determine electron density in the discharge basing on the perturbation theory. The electron density measured in this way was $n_e = 10^{11}$–10^{12} см$^{-3}$.

The influence of microwave field inhomogeneity near the surface on the breakdown threshold has been studied. It is known that an electron in an inhomogeneity field is affected by the averaged ponderomotice force (Miller force) [5]. In the experiment, the dielectric plate was positioned in such a way as to make the ejected electron affected by the force attracting it to the surface, on the one of the plates sides, and by the repelling force, on the other. In this case the thickness of the plate was chosen to match the amplitudes on the both sides. According to the existing ideas, the discharge on the surface with the repelling force should not develop; however, in the experiment the discharge occurred on

that surface. We can suppose that the repellent gradient force causes rapid quartz electrostatic charging and thus returning electrostatic force. Note, that a similar experimental investigation of the single surface multipactor discharge in the field of the standing wave did not display any influence of the Miller force on the multipactor breakdown condition [6].

The well-known effect of dielectric surface conditioning by microwave breakdowns was observed in the experiment [7]. The threshold of discharge occurrence rose with time and achieved the values of 45–55 kV/cm. This is associated with the fact that initially the dielectric surface is covered with a film of adsorbed gases. Imposing the surface to electron impacts, one can remove the film from the surface and raise the discharge occurrence threshold. This can be demonstrated by analyzing the optical spectra of the discharge, which are shown in Fig. 4.

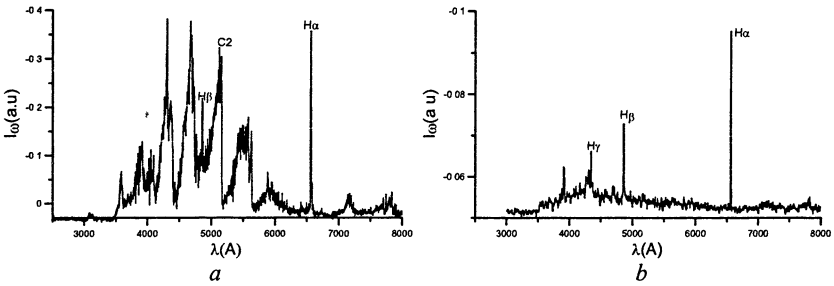

Fig. 4. Optical spectra of the discharge for different incident powers: P_i= 70 kW (*a*), P_i= 160 kW (*b*).

It is seen from the figure that the main contribution into the radiation is made by the lines of hydrogen and carbon. This is associated with the fact that the main contaminations of the quartz surface are vapour of water and CO_2. At a low level of microwave power, the water vapours contained in the surface film are desorbed under the effect of the discharge. Therefore, the spectrum contains only hydrogen lines. As the power grows (the threshold becomes higher) the energy of electrons in the discharge increases. This yields higher intensity of the radiating lines. Besides, the gases dissolved in the quartz start to be desorbed from deeper layers. As the result, the lines of CO_2 molecules appear in the spectrum.

Numerical model of the multipactor discharge

In order to calculate the thresholds of multipactor discharge occurrence, we used the model from [8]. Within that model, an electron ejected from the sur-

face with arbitrary velocity V_0 at arbitrary angle φ moves in a variable, E_{rf}, and constant, E_{dc}, field, Fig. 5.

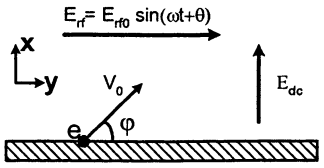

Fig. 5. Model of a single-surface multipactor in a parallel rf and normal dc electric fields.

It is supposed that initial energy $E_0 = mV_0^2/2$ and angle φ are described with the following distribution functions:

$$f(E_0) = \frac{E_0}{E_{0m}^2}\exp\left(-\frac{E_0}{E_{0m}}\right), \quad g(\varphi) = \frac{1}{2}\sin(\varphi), \tag{1}$$

where E_{0m} is the energy, at which secondary emission coefficient has a maximum value, $0 \le \varphi \le \pi$. The force that returns the electrons to the surface may be associated with an external constant electric field, E_{dc}, the discharge of the surface, inhomogeneity of the microwave field near the surface, or the influence of the magnetic field of the microwave. In this case the set of equations for electron motions in fields E_{rf} and E_{dc} have the following form:

$$\ddot{x} = -\frac{e}{m}E_{dc}, \qquad \ddot{y} = -\frac{e}{m}E_{rf0}\sin(\omega t + \theta). \tag{2}$$

In the E_{rf} field the electron oscillates along the surface and acquires energy. E_{dc} field does not change the electron energy, but only distorts its trajectory and returns it to the surface. The discharge will be evolving if the energy of electrons lies in the range of energies $E_1 < E < E_2$, when the coefficient of secondary emission of the dielectric is more than unity. The set of equations (1) and (2) was solved numerically using the Monte-Carlo method to model random values. Based on the calculations, the boundaries for the region of existence of the multipactor discharge at the plane of parameters E_{rf} and E_{dc}, Fig. 6, were determined. In this case the lower boundary of the region corresponds to energy E_1, and the upper one, to E_2. Comparison of the results of this calculation with the analytical method [9] demonstrated their qualitative agreement, see Fig. 6.

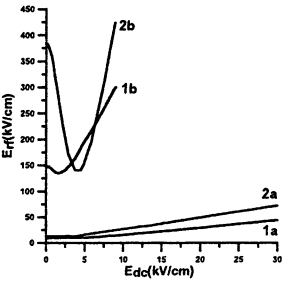

Fig. 6. Upper and lower boundaries of the multipactor discharge existence: *1a* and *1b* – Monte-Carlo simulation, *2a* and *2b* – analytical method [6].

Conclusion

The thresholds of the multipactor discharge on a quartz surface have been measured in TE_{01} mode cavity. The density of electrons in the discharge and the characteristic breakdown time of multipactor have been found. Based on the analysis of the optical radiation spectra, it has been shown that the gases adsorbed in the dielectric influence significantly on the thresholds of the breakdown and discharge evolution dynamics. The calculations of the multipactor threshold using the Monte-Carlo and analytical methods have been compared.

References

1. *Preist D.H., Talcott R.C.*, IRE Trans. Electron Devices, 1961, 8, 243.
2. *Wang C., Yakovlev V.*, J. Hirshfield, PAC 2005.
3. *Vikharev A.L., Gorbachev A.M., Ivanov O.A. et al.*, Proc. of the Intern. Workshop: Strong Microwave in plasmas; Ed. by A.G. Litvak, IAP, Nizhny Novgorod, 2003, 1, 90.
4. *Yee K.S.*, IEEE Trans. Antennas Propagat, 1966, AP-14, 302.
5. *Gaponov A V., Miller M.A.*, Sov. Phys. JETP, 1958, 7, 168.
6. *Grishin L.B., Dorofeyuk A.A., Kossyi I.S. et al.*, Trudi FIAN. M.: Nauka, 1977, 92, 82 (in Russian).
7. *Neuber A., Dickens J., Hemmert D. et al.*, IEEE Trans. on Plasma Scince, 1998, 26, 296.
8. *Kishek R.A., Lau Y.Y.*, Phys. Rev. Let., 1998, 80, 193.
9. *Sazontov A., Semenov V., Buynova M. et al.*, Phys. Plasma (to be published).

STATISTICAL THEORY OF SINGLE-SURFACE MULTIPACTOR DISCHARGE ON A DIELECTRIC

A. G. Sazontov, V. A. Sazontov, V. E. Semenov, N. K. Vdovicheva[1]

Institute of Applied Physics RAS, Nizhny Novgorod, Russia
[1]Institute for Physics of Microstructures RAS, Nizhny Novgorod, Russia

The present paper proposes a novel theory of initial stage of single-surface multipactor discharge on a dielectric. The calculation employs the statistical method based on an exact analytical solution for the arrival time probability density of secondary electrons. The general integral equation allowing prediction the steady-state emission phase distribution and the threshold of multipactor growth is formulated. We obtain the susceptibility diagram, applicable to a wide range of materials, in terms of the rf electric field, the dc electric field, and the magnetic field. It has been found that the shape of susceptibility curves predicted from the statistical model is in a good qualitative agreement with the ones obtained through Monte Carlo simulations.

During the recent decade, extensive theoretical attention has been focused on the problem of multipactor discharge on a dielectric. Most of the recent studies of such type of discharge are based on Monte Carlo simulations [1–3]. Such consideration led to construction of generalized susceptibility diagrams bounding the regions of external parameter space in which multipactor is possible. However, the use of Monte Carlo simulations requires tremendous computation time when it is necessary to carry out calculations within a wide range of parameters.

In this paper we present a novel theory of initial stage of single-surface multipactor discharge on a dielectric extending the existing statistical theory proposed in Ref. [4] to the subject of interest. The general integral equation allowing prediction the steady-state emission phase distribution and the threshold of multipactor growth is formulated.

Problem formulation

We consider a single-surface multipactor discharge on a dielectric surface exposed to spatially uniform rf electric field $\mathbf{E}_{rf}\sin(\omega t+\varphi_s)$, (with amplitude $\mathbf{E}_{rf}$, frequency ω, initial phase φ_s) which is *parallel* to that surface. The plate is assumed to have a net positive charge, which creates uniform dc electric field $\mathbf{E}_{\rm dc}$, restoring emitted electrons back to a dielectric.

The geometry of the problem for the case of an external magnetic field $\mathbf{H}$ is shown in Fig. 1. A secondary electron emitted with a random velocity v_0 and a random angle ϕ with respect to the positive x-axis is subjected to the forces imposed by $\mathbf{E}_{\rm rf}$, $\mathbf{E}_{dc}$, and $\mathbf{H}$.

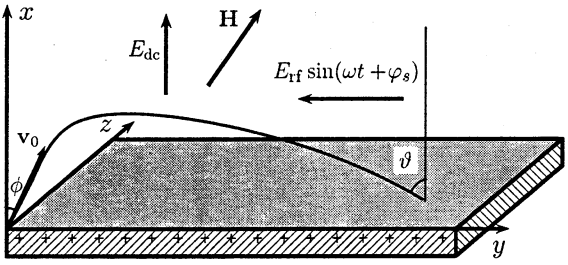

Fig. 1. Schematic of a single-surface multipactor in a parallel rf, normal dc electric fields, and external magnetic field lying in the $x-y$ plane.

The 3-D distribution function $f(\mathbf{v}_0)$ for the emission velocities is assumed in a separable form: $f(\mathbf{v}_0)=f_v(v_0)f_\phi(\phi)$, where

$$f_\phi(\phi)=2\cos\phi,\ f_v(v_0)=\frac{2}{(2\pi v_T^2)^{3/2}}\exp\left(-\frac{v_0^2}{2v_T^2}\right), \tag{1}$$

and v_T is the thermal velocity.

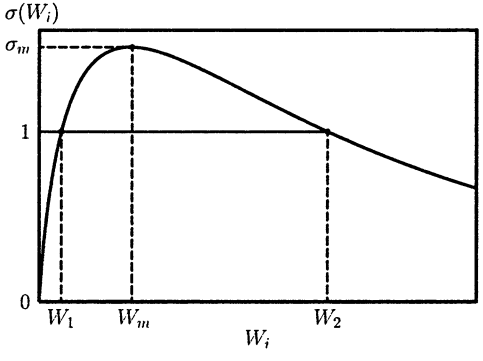

Fig. 2. Secondary electron yield vs. impact energy

Having gained energy from $\mathbf{E}_{rf}$, the electrons strike the surface with impact energy W_i and impact angle ϑ. Multipactor is possible, when the impact energy lies between W_1 and W_2, the first and second crossover energy points, respectively, of the secondary yield curve (see, Fig. 2).

The dependence of the secondary electron yield on the impact energy and the impact angle is adopted from Vaughan's empirical formula [5]

$$\sigma(w)=\sigma_m\left[w\exp(1-w)\right]^{k(w)},\ k(w)=\begin{cases}0.62 & \text{if } w<1;\\ 0.25 & \text{if } w>1,\end{cases}$$

where $w=W_i/W_m$, σ_m is the maximum value of the secondary emission yield, and W_m is the impact energy which corresponds to σ_m. For impact at an angle ϑ, the parameters W_m and σ_m are adjusted in calculating the yield, according to the following equations:

$$W_m = W_{\max}\left(1+\frac{k_s\vartheta^2}{\pi}\right), \quad \sigma_m = \sigma_{\max}\left(1+\frac{k_s\vartheta^2}{2\pi}\right),$$

where $W_{\max}$ and $\sigma_{\max}$ are the parameters for an impact angle normal to the surface, and k_s is a surface smoothness factor ranging from 0 for a rough surface to 2 for a polished surface. Since the electron gain their energy from the parallel rf, most impacts will be at almost grazing incidence ($\vartheta \approx \pi/2$) .

In this paper, we set $k_s = 1$, representing a typical dull surface, pick $\sigma_{\max} = 2$, and $W_{\max} = 400$ eV. Then, systematically vary both $E_{\rm dc}$ and $E_{\rm rf}$ we determine the boundaries of the multipactor region for different values of $\mathbf{H}$.

Theoretical development

The resulting electron equations of motion are

$$\ddot{\mathbf{r}} = -\frac{e}{m}\left(\mathbf{E}+\frac{1}{c}[\mathbf{v}\times\mathbf{H}]\right), \quad \mathbf{r}\big|_{t=0} = 0, \quad \dot{\mathbf{r}}\big|_{t=0} = \mathbf{v}_0, \tag{2}$$

where c is the speed of light, m and e stand for electron mass and charge respectively.

For the further analysis it is convenient to introduce the following dimensionless variables

$$\varphi = \omega t,\ \Omega = \omega_H/\omega,\ \mathbf{u} = \mathbf{v}_0/v_{\rm rf},\ e_{\rm rf} = E_{\rm rf}/E_{\max},\ e_{\rm dc} = E_{\rm dc}/E_{\max},$$

where $v_{\rm rf} = eE_{\rm rf}/m\omega$ is the oscillatory velocity, $\omega_H = e\mathbf{H}/mc$ is the cyclotron frequency, and $E_{\max} = (m/e)\omega\sqrt{2W_{\max}/m}$.

The force equation (2) can be solved exactly to find the trajectories $\mathbf{r}(\tau|\varphi_s,\mathbf{u},\mathbf{e},\Omega)$, velocities $\mathbf{v}(\tau|\varphi_s,\mathbf{e},\Omega)$, and time of flight $\varphi = \tau$ defined as a smallest positive root of the transcendental equation $x(\tau|\varphi_s,\mathbf{e},\Omega) = 0$, or $\tau = \tau(\mathbf{u};\varphi_s,\Omega,\mathbf{e})$, where $\mathbf{e} = (e_{\rm dc}, e_{\rm rf})$. Since the emitted electrons have velocity distribution, they will hit the dielectric surface at different instants. The corresponding probability density of the time of flight, $G(\tau|\varphi_s,\Omega,\mathbf{e})$, can be evaluated by using the well known formula from the statistical theory

$$G(\tau|\varphi_s,\Omega,\mathbf{e}) = \int_0^\infty du_x \int_{-\infty}^{\infty} du_y \int_{-\infty}^{\infty} du_z\, \delta\left(\tau-\tau(\mathbf{u};\varphi_s,\Omega,\mathbf{e})\right) F(\mathbf{u}), \tag{3}$$

where $F(\mathbf{u}) = v_{\rm rf}^3 f(v_{\rm rf}\mathbf{v}_0)$.

Knowledge of the arrival time distribution makes it possible to construct the general integral equation allowing for prediction the steady-state emission phase distribution $f_{\rm st}(\varphi_s)$ and the threshold of multipactor growth [5]:

$$f_{st}(\varphi_s) = \mu \int_0^{2\pi} K_1\left(\varphi_s|\varphi_s';\mathbf{e},\Omega\right) f_{st}(\varphi_s')\, d\varphi_s', \quad \mu = \sigma_{max}, \tag{4}$$

$$K_1\left(\varphi_s \,|\, \varphi_s';\mathbf{e},\Omega\right) = G\left(\varphi_s - \varphi_s' \,|\, \varphi_s';\mathbf{e},\Omega\right) \varsigma\left(\varphi_s|\varphi_s';\mathbf{e},\Omega\right)\Theta(\varphi_s,\varphi_s')$$

$$+\sum_{n=1}^{\infty} G\left(\varphi_s - \varphi_s' + 2\pi n|\varphi_s';\mathbf{e},\Omega\right) \varsigma\left(\varphi_s + 2\pi n \,|\, \varphi_s';\mathbf{e},\Omega\right),$$

where $\varsigma(\varphi_s|\varphi_s';\mathbf{e},\Omega) = \left(1+\frac{\vartheta^2}{2\pi}\right)\left[w\exp(1-w)\right]^{k(w)}$, $w = w(\varphi_s - \varphi_s' \,|\varphi_s';\mathbf{e},\Omega)$

and $\Theta(\varphi_s,\varphi_s')$ is the step function.

For given parameters $\mathbf{e}$ and Ω, electron multipaction occurs when the maximum yield σ_{max} exceeds some threshold value (above which there is multipactor growth). From the mathematical point of view, the corresponding value coincides with the smallest characteristic value μ of the integral equation (4) (which depends on Ω and $\mathbf{e}$, i.e. $\min\mu = \min\mu(\mathbf{e},\Omega)$). Hence, in order to calculate the multipactor region boundaries, it is necessary to find $\min\mu(\mathbf{e},\Omega)$ from Eq. (4) and compare it with σ_{max}: $\min\mu(\mathbf{e},\Omega) = \sigma_{max}$. The latter condition defines the regions of parameter space in which multipactor is possible.

Susceptibility diagram. Effect of magnetic field

We begin with the case, when the magnetic field is parallel to dc electric field. Such configuration of magnetic field does not affect the electron motion in the x-direction. As a consequence, the time of flight is exactly the same as in the case of zero magnetic field, i.e. $\tau = 2e_{rf}u_x/e_{dc}$. For the given velocity probability density (1), the time of flight distribution can be found exactly from Eq. (3). The result is

$$G(\tau, e_{dc}) = \frac{e_{dc}^2}{2w_T}\,\mathrm{erfc}\left(\frac{e_{dc}\tau}{2\sqrt{2w_T}}\right), \quad w_T = W_T/W_{max}$$

where $W_T = \frac{1}{2}mv_T^2$ and $\mathrm{erfc}(z) = \frac{2}{\pi}\int_z^{\infty} e^{-x^2}\,dx$ is the complementary error function.

Figure 3 shows the susceptibility diagram for various values of Ω_x, assuming $w_T = 2/400$. The dotted line corresponds to the case of zero magnetic field. As can be seen from this figure that the effect of magnetic field is realized first for the upper boundary. By increasing the cyclotron frequency from zero to one, the upper boundary is lowered. The upper boundary may be raised if Ω_x greater than unity.

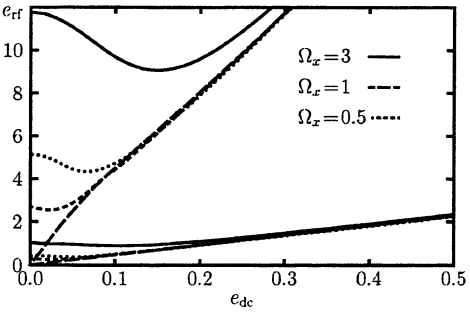

Fig. 3. Multipactor region boundaries in the plane of (e_{dc}, e_{rf}) for various values of Ω_x.

Consider now the case when magnetic field is parallel to rf field. In this case the flight time can be expressed as

$$\tau = \frac{2}{\Omega_y}\arctan\left(\frac{u_x}{e_{dc}/(e_{rf}\Omega_y) - u_z}\right), \quad \tau \in [0, \pi/\Omega_y]. \tag{5}$$

$$G(\tau, e_{dc}, \Omega_y) = \frac{\sin(\Omega_y\tau/2)}{2}\left\{\left[\Omega_y + \frac{e_{dc}^2}{w_T\Omega_y}\left(2\cos^2(\Omega_y\tau/2) - \sin^2(\Omega_y\tau/2)\right)\right]\right.$$

$$\left.\times \operatorname{erfc}\left(\frac{e_{dc}\sin(\Omega_y\tau/2)}{\sqrt{2w_T}\Omega_y}\right) + \frac{2e_{dc}\sin(\Omega_y\tau/2)}{\sqrt{2\pi w_T\Omega_y^2}}\exp\left(-\frac{e_{dc}^2\sin^2(\Omega_y\tau/2)}{2w_T\Omega_y^2}\right)\right\}.$$

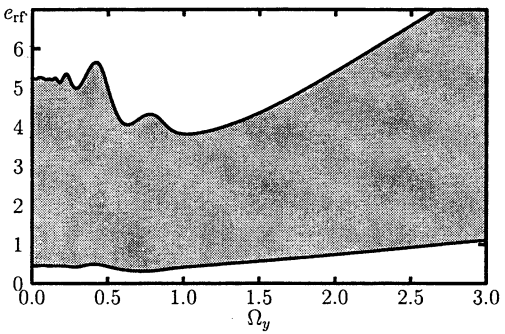

Fig. 4. Multipactor regions for $e_{dc} = 0$

Substituting Eq. (5) into Eq. (3) and performing the necessary calculations, for the time of flight distribution we obtain

For the scenario considered the multipactor is possible even in the limit of zero dc field. Thus, at $e_{dc} = 0$ the multipactor region boundaries are depicted in Fig. 4. They do not depend on the velocity spread. At large values of Ω_y they are linear asymptotically. When the dc field differs from zero, the multipactor region boundaries behave as depicted in Fig. 5.

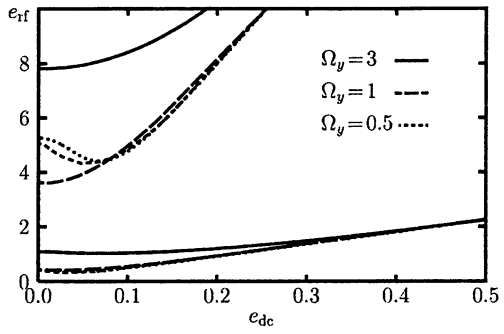

Fig. 5. Multipactor region boundaries in the plane of (e_{dc}, e_{rf}) for various values of Ω_y.

The corresponding curves qualitatively similar to the previous case: the effect of magnetic field is more pronounce for the upper boundary. However, the effect of Ω_y is negligible if $0<\Omega_y<1$.

Note also that the shape of susceptibility curves predicted from statistical model is in a good qualitatively agre-ement with the ones obtained through Monte Carlo simulations [1–3].

Conclusions

A single-surface multipacor discharge on a dielectric has been studied in detail using a statistical approach. We obtain the susceptibility diagram, applicable to a wide range of materials, in terms of the rf electric field, the dc electric field, and the magnetic field. It has been found that the shape of susceptibility curves predicted from the statistical model is in a good qualitative agreement with the ones obtained through Monte Carlo simulations. Magnetic field qualitatively changes the upper boundary. However, it has only minimal effects on the saturation mechanism (since saturation occurs on the lower boundary).

This work was partially supported by INTAS under Grant No 03–53–4213 and by Russian Foundation for Basic Research under Grant No 03–02–16357a.

References

1. *Kishek R.A., Lau Y.Y., Ang L.K., Valfells A., Gilgenbach R. M.*, Phys. Plasmas, 1998. **5**. 2120.
2. *Kishek R.A., Lau Y.Y.*, Phys. Rev. Lett., 1998. **80**, 193.
3. *Valfells A., Ang L.K., Lau Y.Y., Gilgenbach R.M.*, Phys. Plasmas, 2000. **7**. 750.
4. *Vdovicheva N.K., Sazontov A.G., Semenov V.E.*, Radiophysics and Quantum Electronics, 2004. **47**, 580.
5. *Vaughan J.R.M.*, IEEE Trans. Electron Devices, 1989. **36**. 1963.

TWO APPROACHES TO THE PROBLEM OF MULTIPACTOR DISCHARGE ON A DIELECTRIC RF-WINDOW

M. N. Buyanova, V. E. Semenov

Institute of Applied Physics, Russian Academy of Sciences,
Nizhny Novgorod, Russia

The special statistical theory for multipactor research [3] was modified in order to implement new time-dynamical approach that concludes in describing the multipactor on a dielectric window in real time. The special software for numerical simulations either for frequently used trajectory analysis and novel time-dynamical method was developed. Both multipactor threshold and the process of growing avalanche were studied. Some simple analytical estimates of multipactor threshold were analyzed also. A comparative analysis of two approaches was carried out.

At present the accurate theoretical predictions of multipactor development are a necessary stage in design of microwave components. Such predictions could hardly be accomplished using analytical calculations when the particular system geometry is of interest. Therefore numerical simulations become inevitable. Currently two qualitatively different approaches are used in simulations of the multipactor process. The particle-in-cell (PIC) codes [1] simulate a process of multipactor development in real time taking into account space charge effects. Therefore these codes are considered as the most appropriate numerical tool to simulate the multipactor. Unfortunately they require tremendous computer resources in case of realistic system geometry. As a result the Monte Carlo simulations are very popular in practical applications because they are considerably faster. Typically the Monte Carlo approach is based on independent computing of successive series of electron trajectories and an analysis of average electron number after given number of electron impacts with the device walls [2]. Such an approach does not allow getting information on the multipactor avalanche rate in real time which makes the simulation results uncertain in case of short microwave pulse.

Recently the statistical theory [3] was applied to study the multipactor. An implementation of this theory allows developing codes which are even faster than the Monte Carlo ones. Originally this theory was also based on the multipactor analysis following a number of electron impacts. It was shown that such statistical calculations are identical to the Monte Carlo ones. Therefore an applicability of the original statistical codes to simulate the multipactor avalanche rate in real time is also under a question. However the statistical theory can be modified and applied to consider the multipactor development in real time [4]. This gives an opportunity to examine an accuracy of the standard Monte Carlo approach as well as the original statistical theory in case when the multipactor avalanche rate and its threshold are of interest. To realize such a purpose in this paper the problem was studied using a particular example of single-surface mul-

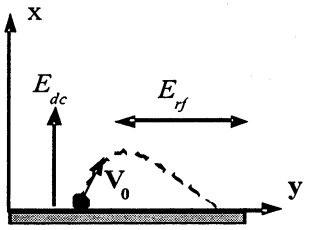

Fig. 1. The model geometry

tipactor on dielectric plate irradiated by plane electromagnetic wave with electric field parallel to the plane surface.

A conventional approximation [2] was used to consider electron motion in this case. Specifically it was assumed that a dielectric plate is exposed to spatially uniform rf electric field and spatially uniform dc electric field. The rf field E_{rf} with frequency ω is parallel to the plate and the dc field E_{dc} is normal to the surface and restores emitted electrons back to the plate (Fig. 1).

The dc field may result from dielectric charging; however, in this study the space charge effects are ignored. Electrons are emitted with a random velocity $\mathbf{V}_0$ and angle, but it is sufficient for the current research to analyze only normal component of emission velocity and omit the take-off angle. A motion of electron is governed by simple equations (1), which give the expressions for flight time and tangentional component of impact velocity (2), (3) that determines the impact energy and the effective coefficient of secondary emission.

$$m\ddot{x} = -eE_{dc}, \quad m\ddot{y} = eE_{rf}\sin\omega t, \tag{1}$$

$$\Delta t = \frac{2mV_x^{emission}}{eE_{dc}}, \quad t^{impact} = t^{emission} + \Delta t, \tag{2}$$

$$V^{impact} \approx V_y^{impact} = \frac{eE_{rf}}{m\omega}\left\{ \cos[\omega(t^{impact} - \Delta t)] - \cos[\omega t^{impact}] \right\}. \tag{3}$$

Unlike two-sided multipactor, for example, single surface multipactor in these conditions does not depend on any resonance condition and all electrons return to the surface of emission. The only condition for multipactor growth is that the sufficient part of electrons impacts with appropriate energy. Due to this it is necessary to consider the spread over electrons motion parameters, and use numerical simulations.

The process can be described with a help of several distribution functions. Since the transit time τ is uniquely concerned with the normal component of electron emission velocity V_{x0}, the distribution over that component of emission velocity $\tilde{G}(V_{x0})$ can be easily expressed through the distribution over transit time $G(\tau)$. Also, secondary emission yield σ is function of impact velocity V_y, which is determined by the emission moment $t^{emission}$ and the transit time Δt, therefore the secondary emission coefficient can be considered as function of emission phase and dimensionless transit time (4):

$$\sigma = \sigma(\varphi, \tau), \quad \tau = \omega\Delta t, \quad \varphi = \omega t^{emission}. \tag{4}$$

Then the multipactor process can be described by the distribution function of secondary electrons over emission phases $F^{dyn}(\varphi)$. The following integral equation (5) can be obtained [4]:

$$F^{dyn}(\varphi) = \int_0^{\infty} F^{dyn}(\varphi - \tau) K(\varphi, \tau) d\tau, \quad K(\varphi, \tau) = G(\tau)\sigma(\varphi, \tau). \tag{5}$$

The kernel $K(\varphi,\tau)$ is periodical, so the particular solution can be represented by a periodical distribution on a base of average growth, that describes the avalanche development process (6). The multipactor threshold corresponds to a case when the growth increment γ is zero.

$$F^{dyn}(\varphi) = \exp(\gamma\varphi)\Psi(\varphi). \tag{6}$$

The new time-dynamical approach can be compared to the statistical trajectory analysis [3]. For trajectory analysis the electron distribution function over emission phases for any separate electron transit $F_{k+1}^{iter}(\varphi)$ can be introduced in similar way. The main equation turns into a recurrent relationship for a successive series of distribution function (7). In this case the particular solution and the growth of electron number is described with the geometric-progression low:

$$F_{k+1}^{iter}(\varphi) = \int_0^{\infty} F_k^{iter}(\varphi - \tau) K(\varphi, \tau) d\tau, \; F_k^{iter}(\varphi) = \lambda^k \tilde{\Psi}(\varphi). \tag{7}$$

Generally the integral equation for periodical part of distribution function over emission phase for the time-dynamical method does not coincide with the one for trajectory method ((8a), (8b) respectively) and this fact leads to unavoidable discrepancies between the results of these two approaches. The comparison between numerical results of these methods is the way to examine the accuracy of trajectory analysis.

$$\Psi(\varphi) = \int_0^{\infty} \Psi(\varphi - \tau) K(\varphi, \tau) \exp(-\gamma\tau) d\tau, \tag{8a}$$

$$\lambda\tilde{\Psi}(\varphi) = \int_0^{\infty} \tilde{\Psi}(\varphi - \tau) K(\varphi, \tau) d\tau. \tag{8b}$$

It should be mentioned that the difference between two methods could disappear in some particular cases; the most clear is the threshold case ($\lambda = 1$ or $\gamma = 0$), which results in complete equivalence between equations. In the threshold case operating speed of two methods can be measured. Also analytical estimates of the threshold should be compared to the results of numerical simulations.The following model distribution over transit time is used (9):

$$G(\tau) = \alpha \exp(-\alpha\tau), \quad \langle\tau\rangle = \frac{1}{\alpha}. \tag{9}$$

The average transit time is a parameter concerned either with the emission velocity distribution and dc field: low values of $<\tau>$ correspond to strong dc electric field and high $<\tau>$ values correspond to weak dc electric field.

Near the multipactor threshold the most of electrons have impact energy close to the first crossover point, where the effective secondary emission coefficient can be approximated as linear function of impact energy (10):

$$\sigma(\varphi,\tau)=\frac{W_{impact}(\varphi,\tau)}{W_1}=\mu(1-\cos\tau)(1-\cos(2\varphi-\tau)). \tag{10}$$

Evaluating the threshold, the coefficient $\mu=\frac{1}{2}\frac{mV_\omega^2}{W_1}$ can be considered as a control parameter: $\mu\geq\mu_{threshold}\Leftrightarrow\lambda\geq 1$ (trajectory analysis), $\gamma\geq 0$ (time-dynamical method).

The general analytical estimate says that at the threshold the average secondary emission yield over both emission phase and transit time is unity [2]. The distribution over emission phases is approximated by uniform distribution. It gives an estimate of the threshold value of μ (11):

$$\left\langle\left\langle\sigma\right\rangle\right\rangle_{\tau,\varphi}=1,\quad \Psi(\varphi)=const\quad\Rightarrow\quad \mu=1+\left(\frac{1}{\langle\tau\rangle}\right)^2. \tag{11}$$

Another two estimates for limit cases of low and high values of average transit time are more precise. In the case of weak restoring dc electric field (high $<\tau>$ values) the distribution function at the threshold is not uniform but smooth enough (12):

$$\Psi(\varphi)\propto 1+2(\sqrt{3/2}-1)\cos(2\varphi),\quad \mu=4\left(\sqrt{3/2}-1\right). \tag{12}$$

In the case of strong restoring dc field the distribution over emission phases $\Psi(\varphi)\propto e^{S(\varphi)}$ becomes rather sharp (13):

$$S'(\varphi)=\sqrt[3]{\frac{2\mu\sin^2\varphi}{<\tau>}}-\frac{1}{<\tau>},\quad \mu=\frac{1}{2<\tau>^2\left\langle(\sin\varphi)^{2/3}\right\rangle^3}. \tag{13}$$

The threshold value of secondary emission was studied in dependence on an average transit time. It was verified that the time-dynamical method and the method of iterations show the same results although the time-dynamical method proved to be much faster. The most interesting result was obtained from comparison between numerical simulations and analytical estimates. Even the estimate made on a base of assumption of uniform distribution over emission phases can give relatively good results (Fig. 2). It indicates that during the multipacting process the periodical part of electron emission distribution is formed so to generate almost the same number of secondaries, which is generated in case of the uniform distribution.

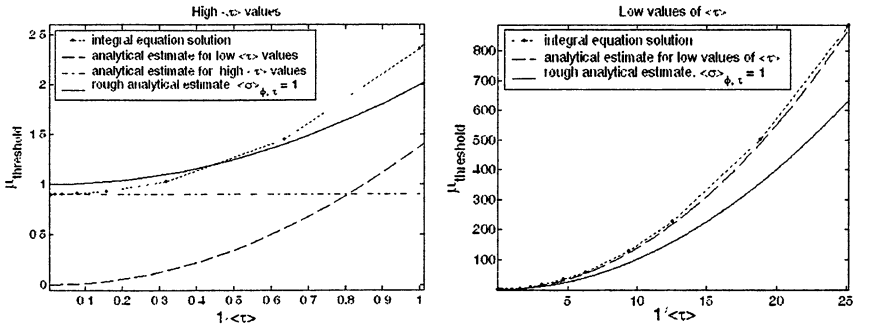

a *b*

Fig. 2. The threshold value of secondary emission as a function of average transit time

But the detailed analysis shows that even in the case of weak dc field (high <τ> values) the distribution over emission phases is far from uniform (Fig. 3). The results of numerical calculations and precise analytical estimates are in good agreement for both limit cases of weak and strong dc field.

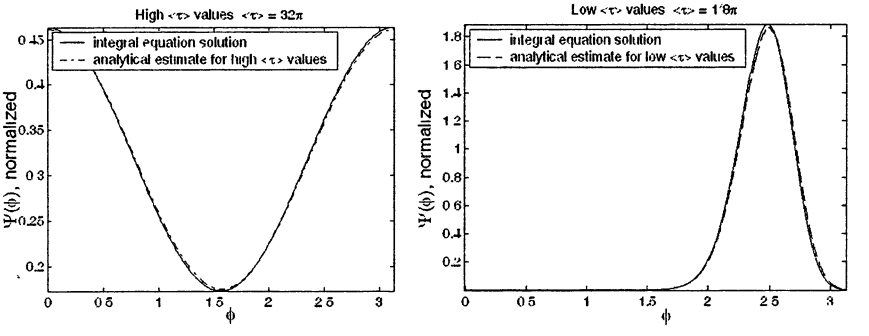

a *b*

Fig. 3. The distribution over emission phases at the threshold, with the period equal to a half of rf cycle, obtained from numerical simulations and calculated from analytical estimates.

Nevertheless, the application of the trajectory analysis to the over-threshold research is more doubtful. It was shown that the periodical parts of the distributions over emission phases do not coincide in principle (Fig. 4). Therefore the trajectory method is not quite correct for description of the multipactor avalanche, and the time-dynamical method represents a considerably good alternative approach.

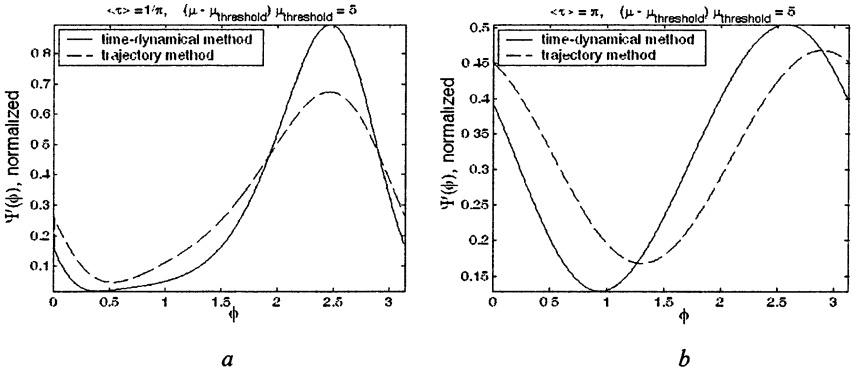

Fig. 4. The distribution over emission phases above the threshold obtained from numerical simulations based on the trajectory analysis and the time-dynamical method.

The statistical theory was modified to describe the multipactor on a dielectric rf window in real time and the special software was developed to solve it numerically. The new time-dynamical method of calculations is shown to be relatively fast as compared to the method of trajectory analysis. Detailed comparison of these approaches showed that the multipactor threshold could be accurately determined by the simulations of successive electron trajectories. However this method is not quite correct for the description of the multipactor avalanche. It was also shown that both cases of weak and strong dc field could be estimated analytically with good accuracy. Even the estimate based on the assumption of uniform distribution over emission phases describes the threshold value of secondary emission well.

This work was partially supported by INTAS under Grant No. 03-53-4213 and by the Russian Basic Research Foundation through grant No. 03-02-16357a.

References

1. *Verboncoeur J.P., Alves M.V., Vahedi V., Birdsall C.K.*, J. Comput. Phys., 1993, **104**, 321.
2. *Kishek R.A., Lau Y.Y.*, Phys. Rev. Lett., 1998, **80**, 193.
3. *Vdovicheva N.K., Sazontov A.G., Semenov V.E.*, Radiophys. Quantum Electron., 2004, **47**, 580.
4. *Sazontov A., Semenov V., Buyanova M., Vdovicheva N., Anderson D., Lisak M., Puech J., Lapierre L.*, Multipactor Discharge on a Dielectric: Statistical Theory and Simulation Results, Physics of Plasmas (accepted for publication).

CONTENTS OF VOLUME 2

CURRENT DRIVE AND PLASMA HEATING BY MICROWAVES IN NUCLEAR FUSION DEVICES

MICROWAVE DISCHARGES IN GASES AND OTHER APPLICATIONS OF HIGH-POWER MICROWAVES

STRONG MICROWAVES IN PLASMAS

PROCEEDINGS
OF THE INTERNATIONAL WORKSHOP

In two volumes

Volume 2

Institute of Applied Physics,
Russian Academy of Sciences

46 Ul'yanov Street, 603950 Nizhny Novgorod, Russia

Printed by Printing House №2, "Nauka" Publishers,
6 Shubinsky Pereulok, 121099 Moscow